Testing Technology of METAL MATRIX COMPOSITES

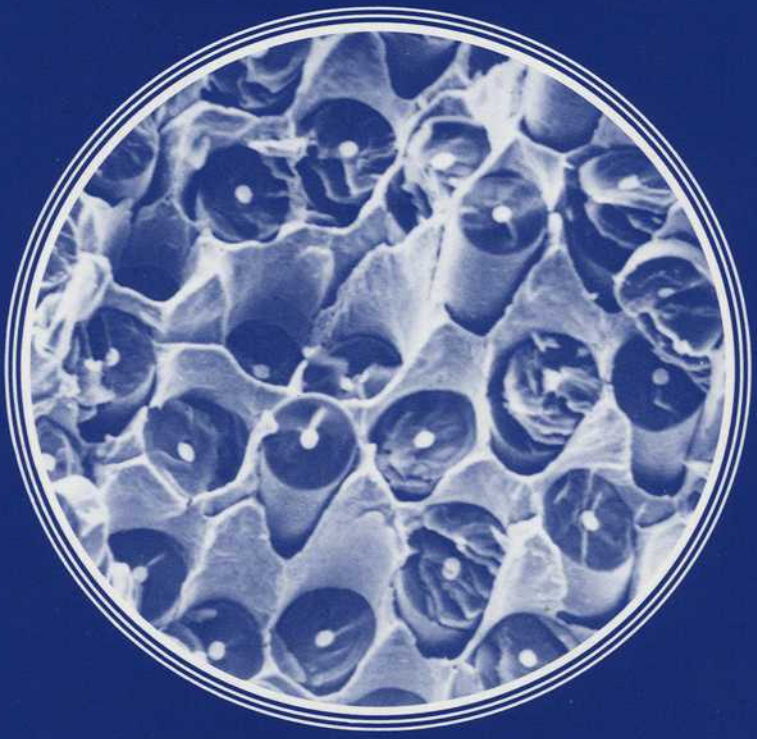

DiGiovanni/Adsit
EDITORS

ASTM STP 964

STP 964

Testing Technology of Metal Matrix Composites

Peter R. DiGiovanni and Norman Ray Adsit, editors

ASTM
1916 Race Street
Philadelphia, PA 19103

Library of Congress Cataloging-in-Publication Data

Testing technology of metal matrix composites / Peter R. DiGiovanni and Norman Ray Adsit, editors.
(STP ; 964)
"The symposium on Testing Technology of Metal Matrix Composites was held 18–20 November 1985 in Nashville, Tennessee. ASTM Committee
D-30 on High Modulus Fibers and Their Composites sponsored the symposium"—Foreword.
"ASTM publication code number (PCN) 04-964000-33."
Includes bibliographies and index.
ISBN 0-8031-0967-9
1. Metallic composites—Testing—Congresses. I. DiGiovanni, Peter R. II. Adsit, N. R. III. ASTM Committee D-30 on High Modulus Fibers and Their Composites. IV. Series: ASTM special technical publication; 964.
TA481.T48 1988
620.1'18'0287—dc19 88-15451
CIP

NOTE

The Society is not responsible, as a body,
for the statements and opinions
advanced in this publication.

Peer Review Policy

Each paper published in this volume was evaluated by three peer reviewers. The authors addressed all of the reviewers' comments to the satisfaction of both the technical editor(s) and the ASTM Committee on Publications.

The quality of the papers in this publication reflects not only the obvious efforts of the authors and the technical editor(s), but also the work of these peer reviewers. The ASTM Committee on Publications acknowledges with appreciation their dedication and contribution of time and effort on behalf of ASTM.

Printed in West Hanover, MA
September 1988

Foreword

The symposium on Testing Technology of Metal Matrix Composites was held 18–20 November 1985 in Nashville, Tennessee. ASTM Committee D-30 on High Modulus Fibers and Their Composites sponsored the symposium. Peter R. DiGiovanni, Raytheon Company, and Norman Ray Adsit, Rohr Industries, served as symposium cochairmen and coeditors of this publication.

Contents

NONDESTRUCTIVE EVALUATION AND PHYSICAL TESTS

FRACTURE BEHAVIOR AND NONDESTRUCTIVE EVALUATION

MECHANICAL TEST METHODS AND MATERIAL CHARACTERIZATION

Overview

While the use of Metal Matrix Composites (MMCs) has increased significantly in recent years and there are many future applications, standard test procedures and an understanding of the failure mechanisms have not kept pace. This symposium and the resulting book is a first attempt to address this specific issue.

The keynote address given at the symposium by Jerome Persh, of the Office of the Undersecretary of Defense for Research and Engineering, gave a clear prospective of the need and the importance of MMCs. Mr. Persh dealt with the need to have standard methods of evaluating competing systems so that one can arrive at the system with the most appropriate material.

A total of forty-one papers were initially scheduled for presentation. Eleven had to be cancelled and two more were not included in this book. The resulting twenty-eight papers are divided topically into:

1. Special Topics (Including High Temperature)
2. Theoretical Considerations
3. Nondestructive Evaluation and Physical Tests
4. Fracture Behavior and Nondestructive Evaluation
5. Mechanical Test Methods and Material Characterization

Work included in this volume covers material systems from the continuous silicon carbon/titanium system to the particulate reinforced aluminum system. The form of the material varied from precast block to braided pieces. While the end applications of these systems vary, the need to obtain accurate and reliable test data does not vary. Tests and test methods are given for elevated temperature tests, dynamic modulus tests, coefficient of expansion tests, compression and buckling tests, among others. In all cases there is a need for an evaluation of the material before the destructive tests are conducted, that is, a need for nondestructive evaluation.

N. R. Adsit
Rohr Industries, Chula Vista, Ca 92012; symposium co-chairman and co-editor.

Special Topics

Leonard J. Westfall[1] *and Donald W. Petrasek*[1]

Thermal-Mechanical Fatigue Test Apparatus for Metal Matrix Composites and Joint Attachments

REFERENCE: Westfall, L. J. and Petrasek, D. W., **"Thermal-Mechanical Fatigue Test Apparatus for Metal Matrix Composites and Joint Attachments,"** *Testing Technology of Metal Matrix Composites, ASTM STP 964,* P. R. DiGiovanni and N. R. Adsit, Eds., American Society for Testing and Materials, Philadelphia, 1988, pp. 1–17.

ABSTRACT: Two thermal-mechanical fatigue (TMF) test facilities were designed and developed, one to test tungsten fiber reinforced metal matrix composite specimens at temperatures up to 1700 K (2600°F) and another to test composite/metal attachment bond joints at temperatures up to 1030 K (1400°F). The TMF facility designed for testing tungsten fiber reinforced metal matrix composites permits test specimen temperature excursions from room temperature to 1700 K (2600°F) with controlled heating and loading rates. A strain-measuring device measures the strain in the test section of the specimen during each heating and cooling cycle with superimposed loads. Data are collected and recorded by a computer. The second facility was designed to test composite/metal attachment bond joints and to permit heating to a maximum temperature of 1030 K (1400°F) within 600 s and cooling to 420 K (300°F) within 180 s. A computer controls specimen temperature and load cycling.

KEY WORDS: metal matrix composites, composite tubes, root attachments, thermal fatigue, thermal-mechanical fatigue

Tungsten fiber reinforced-superalloy matrix composites have demonstrated a potential for use as high-temperature structural materials [*1*]. The use of these materials for turbine applications often depends on their ability to withstand cyclic loading. Studies have been performed on the mechanical and thermal fatigue of fiber reinforced metal matrix composites [*1–9*]. However, combined effects of thermal and mechanical fatigue have not been fully investigated. Thermal-mechanical fatigue, however, is one of the primary failure modes considered in the design analysis of high-temperature components, and thermal-mechanical failure data for these materials have not been obtained. In the testing of these materials it is desirable to simulate, as closely as possible, the pertinent environmental conditions the structure will experience in service.

The efficient joining of metal matrix composite components to supporting structures is of major concern facing users of these materials. It is essential that the fatigue behavior of bonded joints between composite material components be understood in order to have available design principles and rationale to take advantage of the desirable characteristics of composite materials. It is necessary to develop high efficiency joints so that load will be transferred efficiently from the composite to the supporting structure. To date few experi-

[1] Materials engineers, National Aeronautics and Space Administration, Lewis Research Center, Cleveland, OH 44135.

mental studies of composite/metal attachment bond joints have been conducted under cyclic loading, and no cumulative damage theories have evolved. Data must be generated that will permit designers to develop allowables for joints between advanced composites and metals. The need to evaluate the thermal-mechanical fatigue behavior of fiber reinforced metal matrix composites and composite/metal joint attachments and to simulate as closely as possible the pertinent conditions the material will experience in service, stimulated the design and development of fatigue test apparatus for this purpose.

The purpose of this paper is to describe two thermal-mechanical fatigue (TMF) test facilities which were designed and developed at the National Aeronautics and Space Administration, Lewis Research Center. One TMF apparatus was designed to test fiber reinforced metal matrix composite specimens and another was designed to test composite/metal attachment bond joints. Test procedures and typical results obtained on tungsten fiber reinforced superalloys and composite attachment bond joints are also described in this paper.

Apparatus for Thermal-Mechanical Fatigue Testing of Composite Specimens

Design Considerations

A thermal-mechanical fatigue test facility was required in which tests could be conducted that would simulate the pertinent loading and environmental conditions that a metal matrix composite component might be exposed to during service. Consideration was given to the following factors in the design capability of the test facility:

1. Testing in either an air or inert atmosphere.
2. Specimen test temperature excursions from room temperature to 1700 K (2600°F).
3. Heating rates on the order of 22 K (40°F)/s.
4. Varying the load on the test specimens during each heating and cooling cycle from a zero load condition to a maximum load of 2270 kg (5000 lb).
5. Varying the loading rates on the specimen from 1 kg (2 lb)/s to 18 kg (40 lb)/s.
6. Measuring strain occurring in the specimen test section during loading and each heating and cooling cycle.

Component Layout

A photograph of the test apparatus is shown in Fig. 1. The apparatus consists of a commercially available high load capacity (9100 kg (20 000 lb)) frame with a 20 to 1 lever arm system to impose loads onto test specimens. Loads are applied to the lever arm through a chain connected to a variable speed motor. The load applied by the motor is measured by use of a strain gage attached to a metal bar in line with the test specimen as shown in Fig. 1. An electrical signal is sent from the load strain gage to a control device having upper and lower adjustable limits to control the minimum and maximum loads applied to the test specimen. The load on the test specimen can be varied from 0 to 2270 kg (5000 lb), and loading rates can be also varied from 1 kg (2 lb)/s to 18 kg (40 lb)/s. Specimens can be tested either in air or in an inert atmosphere.

The specimens which were tested consisted of hollow tubes with threaded ends that were screwed into grip fixtures. The diameter of the tubes was approximately 0.017 m (0.67 in.) with a wall thickness of 0.0014 m (0.55 in.). Specimens are heated to the desired temperature by direct resistance heating using a current transformer which is capable of generating approximately 1000 A at 5 V. Large copper cables are connected to both ends of the test specimen using water cooled copper connectors to carry the high currents required to heat the specimen. The water cooled copper connectors served the dual purpose of maintaining

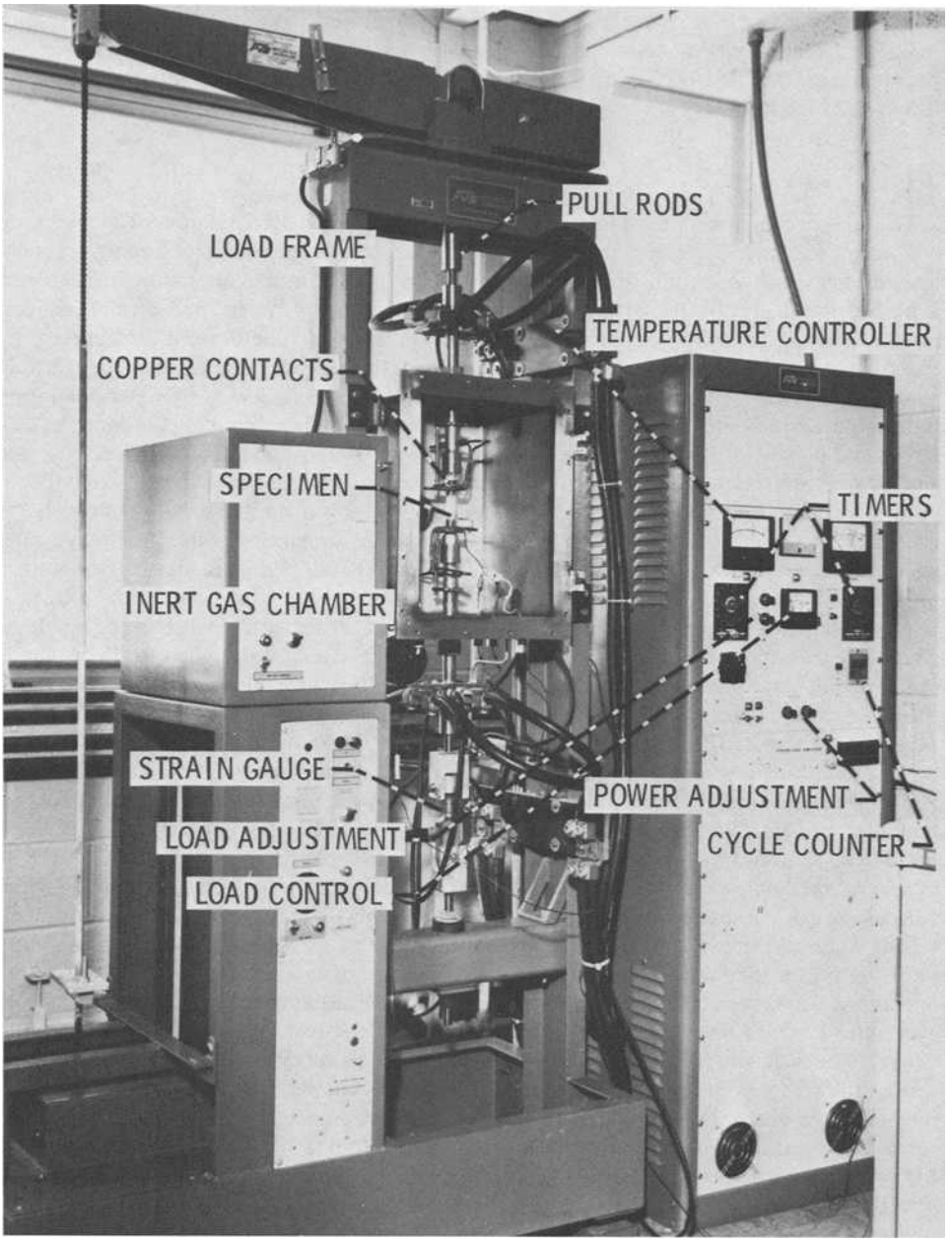

FIG. 1—*Photograph of thermal mechanical fatigue apparatus.*

a good electrical contact and cooling the ends of the specimen. The bottom grip fixture pull rod connected to the lower portion of the load frame is insulated to ensure that all the current passes through the specimen. The total power used to heat the specimen is controlled by adjusting a variable resistor. An adjustable temperature controller enables the upper temperature to be maintained for up to 3600 s. Specimen test temperature excursions from room temperature to 1700 K (2600°F) can be obtained as well as rapid heating rates, on the order of 22 K (40°F)/s.

Test Procedure

The test specimen is installed in grip fixtures which are attached to pull rods. The minimum and maximum loads applied to the specimen are selected and set on the load control device. The rates at which the motor will apply the load is also set. In normal operation the specimen is loaded and heated at the same time with the specimen being cycled from zero to full load in 30 s. During the load operation the specimen is heated to the desired temperature by direct resistance heating. The total power used to heat the specimen is controlled by adjusting a variable resistor. The proper variable resistor adjustment is selected by determining the time required to heat the specimen to the desired temperature. Normal procedure was to adjust the power settings to produce a 30-s specimen heating time. The specimen cooling rate is not controlled. The power is shut off, and the specimen is allowed to cool. An adjustable temperature controller having an upper and lower limit is used to establish the specimen temperature limits for the heating excursion. Normal procedure was to cycle the specimen temperature between 700 K (800°F) and 1360 K (2000°F). The upper temperature limit was maintained, if desired, by using the upper limit switch to transfer the electrical power signal to another circuit having a lower power setting. The switch in power level causes the specimen to slowly cool. The second electrical circuit is designed to allow a small specimen temperature drop of approximately 10 K (20°F) before the main power is returned to the specimen. This procedure allows a fast heating rate without an accompanying temperature overshoot. The temperature of the specimen is maintained at the upper temperature limit setting by allowing the power to fluctuate and the temperature to vary within the 10 K (20°F) range. A timing device is connected to the upper temperature limit switch of the temperature controller which enables the upper temperature to be maintained for intervals up to 3600 s. In normal operation the high-temperature hold times were 120 to 300 s.

Several methods were evaluated to measure the temperature. Attempts to measure the temperature of the specimen with a thermocouple attached to the hot section of the specimen failed. Thermocouples spot welded to the hot section of the specimen were damaged by diffusion of the thermocouple material into the surface of the test specimen. Oxidation at the spot weld was another problem encountered during testing. After a number of thermal cycles the oxidized thermocouple spot weld would fatigue, resulting in an insufficient bond between the weld and the specimen to produce accurate temperature readings. This situation caused the temperature to overshoot. Tying the thermocouple onto the specimen also was not successful since the thermocouple junction could not be kept securely fastened to the surface of the specimen. This resulted in a large error of up to 100 K. An attempt was made to correct this error by insulating the area around the thermocouple with alumina wool. The insulation caused the surface of the specimen to oxidize under the insulation which resulted in premature specimen failure.

A procedure was developed to accurately measure specimen temperature which involved the use of an optical pyrometer in conjunction with a control thermocouple spot welded to the specimen. The optical pyrometer was calibrated using a dummy specimen that had two thermocouples spot welded onto it, one spot welded to the hot section of the specimen and

the other to the cooler region. The optical pyrometer reading was determined when the hot section thermocouple was reading 1360 K (2000°F). The thermocouple reading in the cool region was also determined at this time. The dummy specimen was cooled down to 700 K (800°F) as indicated by the thermocouple situated in the hot test section. The temperature of the cooler thermocouple was also recorded at this time. The actual test specimens only had one thermocouple which was spot welded to the cool section and placed as accurately as possible in the exact location that was used for the dummy specimen run. This thermocouple was connected to and operated the power controller which had an upper and lower limit setting.

The test specimen was heated up to 1360 K (2000°F) by adjusting the upper limit on the control thermocouple setting and reading the hot section temperature of the specimen with the optical pyrometer until the desired temperature of the hot section was reached. The thermocouple was used to control the power to the specimen on each cycle which produced the desired maximum temperature on the specimen. The lower limit setting of the control thermocouple for the cool-down of the specimen was determined previously from the trial run on the dummy specimen. Cool-down to 700 K (800°F) was achieved by duplicating this lower limit control setting on each specimen. This technique allowed the control thermocouples to be spot welded to a cool section of the specimen which resulted in long thermocouple junction lives.

The optical pyrometer was used to establish the relationship between the test section temperature and the cooler control thermocouple temperature. The control thermocouple limits were set to the proper values to produce the desired temperature limits on the specimen test section. The optical pyrometer was used to measure the temperature of the specimen test section during the hold time. Small adjustments were made to the control thermocouple setting to maintain the proper test section temperature.

The axial strain in the specimen was measured during the complete thermal cycle using the strain measuring device shown in Fig. 2. The strain measuring device consists of a scissor mechanisms with the pivot point located in the center of the scissor arms. The tips of the device consist of ceramic points which contact the specimen surface. The ceramic tips prevent the conduction of electricity and heat to the metal arms of the device. A linear variable displacement transducer (LVDT) capable of producing an electrical signal that has a known relationship with distance is located on the opposite end of the metal arms. A signal is sent from the displacement device to a computer and a digital display. A simple system was developed to calibrate the strain measuring device. A displacement standard was produced by drilling several sets of small holes into a flat metal plate. The distance between holes was within the range of the desired specimen gage length. The distance between the holes was accurately measured and recorded. The tapered ceramic tips of the measuring device were inserted into the holes, and the corresponding voltages produced by the displacement device was recorded. This information was used to produce a plot of distance versus voltage, and the equation of the displacement curve was determined by the computer. Subsequent displacement voltages were converted to axial strain.

The strain measuring device was used in the following manner. The ceramic tips were positioned on the specimen test section at a distance apart from one another of approximately 0.0175 m (0.7 in.) prior to starting the test. The voltage output was recorded which accurately determined the exact distance between the tips. The test cycle was started and the voltage variations produced by the straining of the test specimen could be recorded manually at the high- and low-temperature limits of the cycle and later converted to distances. A computer was installed in the test facility to be used as a high-speed recorder. The computer was programmed to record the variation in load, temperature, and displacement in real time. The software for the computer was developed to allow the data to be printed in a graphical

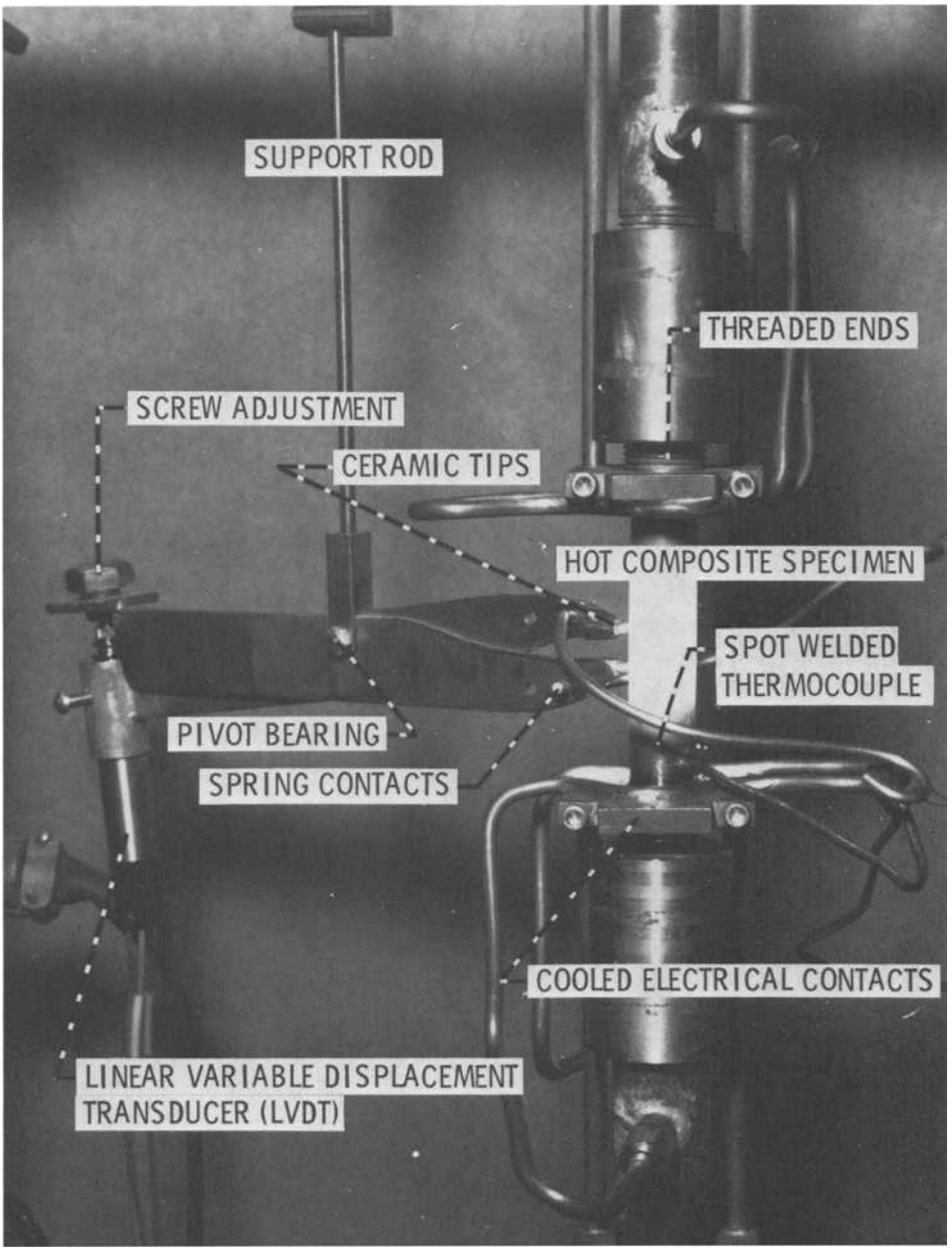

FIG. 2—*Photograph of strain gage attached to specimen.*

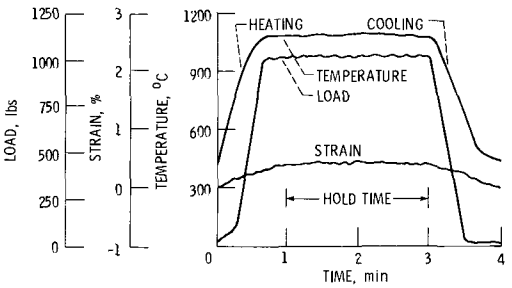

FIG. 3—*Typical load and heat cycle plot for thermal-mechanical fatigue test.*

form if a significant change in displacement had occurred. This system produced a periodic recording of data plus a recording of all of the data for cycles that produced a significant change in displacement.

Test Results

A typical plot of temperature, load, and displacement for a tungsten fiber reinforced superalloy matrix composite cycled between 700 K (800°F) and 1360 K (2000°F) under a load of 70 MPa (10 000 psi) is shown in Fig. 3. The plot displays the load, temperature, and strain that occurred in the specimen test section as a result of one loading and heating cycle.

At the end of a specified number of cycles the data were graphically displayed. These types of data representation displays the maximum temperature and load along with the change in specimen strain as a function of the number of heating and cooling cycles. A typical plot of a complete test is shown in Fig. 4.

Apparatus For Thermal-Mechanical Fatigue Testing Of Composite/Attachment Bond Joints

Design Considerations

A thermal-mechanical fatigue test facility was required in which tests could be conducted that would simulate the pertinent loading and environmental conditions that a metal matrix

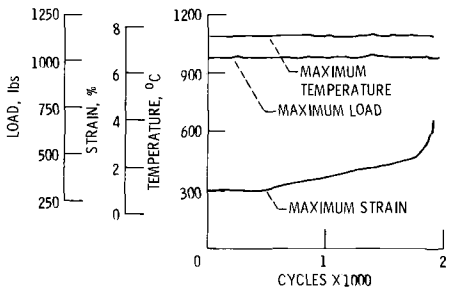

FIG. 4—*Typical plot for completed thermal-mechanical fatigue test.*

composite/attachment bond joint might be exposed to during service. Consideration was given to several factors in the design of the test facility. The test facility was designed to be capable of the following:

1. Testing in either an air or inert atmosphere.
2. Specimen test temperature excursions from room temperature to 1030 K (1400°F).
3. Heating composite/metal attachment bond joint specimens from room temperature to 1030 K (1400°F) in 10 min and cooling to 420 K (300°F) in 3 min.
4. Varying the load on the test specimens during each heating and cooling cycle from a zero load condition to a maximum load of 2270 kg (5000 lb).

Component Layout

The essential features of the test apparatus are shown in Fig. 5. The apparatus consists of a commercially available high load capacity (9100 kg (20 000 lb)) frame with a 10 to 1 lever arm system to impose loads onto test specimens. Loads are applied to specimens by a series of large metal plates that are connected to the lever arm which is connected to a specimen load chain. A mechanically driven load elevator is positioned below the weights and is used to apply and remove the load. The elastic deformation of the mechanical linkage allows the load to be applied in a gradual manner. A computer installed in the test facility was programmed to control the mechanically driven load elevator so that the maximum load is applied at the start of the heating cycle and removed at the start of the cooling cycle. Test specimens can either be tested in air or in an inert atmosphere.

A platinum wound resistance furnace is used to heat specimens to 1030 K (1400°F) within 600 s. The heating rate and temperature limits the specimen is exposed to is controlled by a computer programmed to control the power input to the furnace. Nitrogen gas is blown onto the surface of the specimen to rapidly cool the specimen to the minimum temperature selected. The computer is programmed to activate a solinoid switch which allows the nitrogen gas to be released onto the specimen. Specimens can be cooled from 1030 K (1400°F) to 420 K (300°F) within 180 s.

Conventional resistance furnaces were not available in which test specimens mounted in grip fixtures could be heated and cooled at the required rate, or that could withstand the heating and cooling cycle without the furnace components fatiguing after a very few cycles. A furnace was designed that in some respects resembled a toaster as shown in Figs. 6 *a* and *b*. A furnace shell was made that consisted of thin ceramic plates that surrounded the specimen. Small ceramic pins were located in the top and bottom of the plates. A small diameter coil of platinum was fabricated and wound vertically between the ceramic pins to create a series of closely spaced heating coils. The furnace was constructed so that the heating coils were positioned close to the grip fixture surface to allow maximum heat flux to the grip and test specimen. This type of furnace design allowed specimens to be heated at the required heating rate and cooling rate since there was less furnace mass to heat and cool.

Test Procedure

Test specimen configurations were designed to simulate a potential component application for metal matrix composites, namely, that of a turbine blade. Figure 7 illustrates a probable construction for a metal matrix composite blade. The composite airfoil would be bonded to a root block which in turn would be installed in an engine disk. The airfoil must be securely bonded to the root block such that centrifugally induced loads and thermal loads

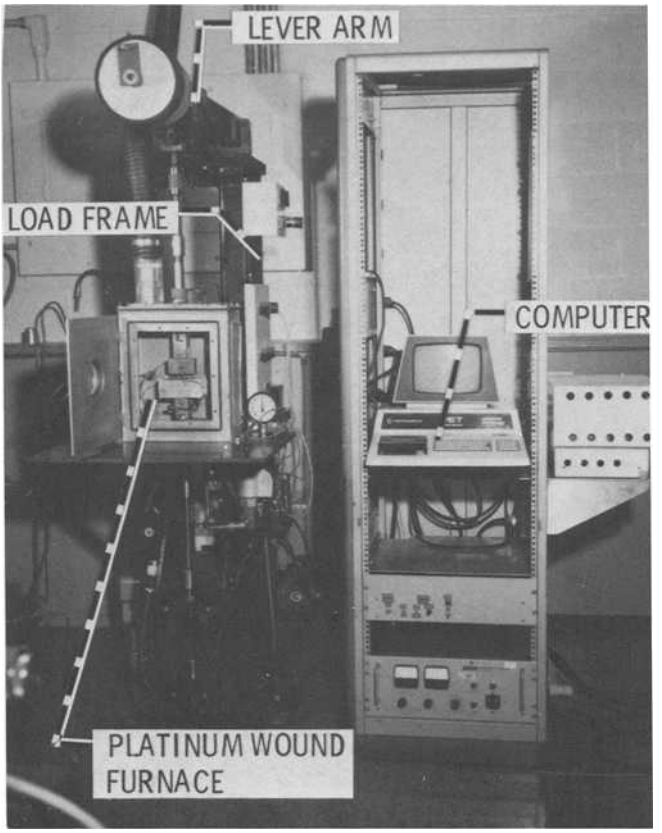

FIG. 5—*Photograph of root block test apparatus.*

do not cause failure at the composite/metal attachment bond joint interface. One design consisted of a composite panel containing fibers oriented parallel to the load axis of the specimen and bonded onto a metal root block attachment also parallel to the load axis as shown in Fig. 8. Another design consisted of a composite panel in which the fibers were flared out at an angle to the load axis of the specimen and bonded to a metal attachment at an angle to the load axis as shown in Fig. 9. Specimen grip fixtures were designed to match the contour of the two specimen designs. The grip fixtures were fabricated from a strong nickel base alloy, Udimet 700, and had internal passages machined in them to allow an inert cooling gas to be passed through the mass of the grip to permit high specimen cooling rates. The specimens were installed in the grip fixtures as shown in Fig. 10.

Specimen test temperature were determined using chromel-alumel thermocouples which were inserted into two holes machined in the grip fixtures. This test temperature measuring procedure was used to eliminate the need to machine holes in test specimens to measure internal temperatures. A dummy test specimen was machined to allow thermocouples to be inserted into holes extending into the midsection of the test specimen so that the internal temperature could be measured. The relationship between the grip thermocouple readings and the dummy test specimen reading was determined when the specimen was at the selected

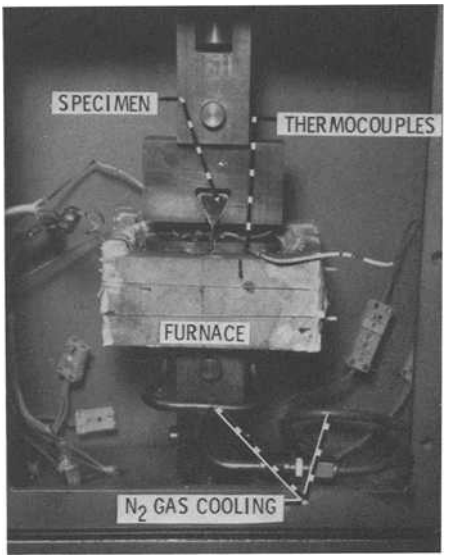

(a) Photograph of furnace and test specimen.

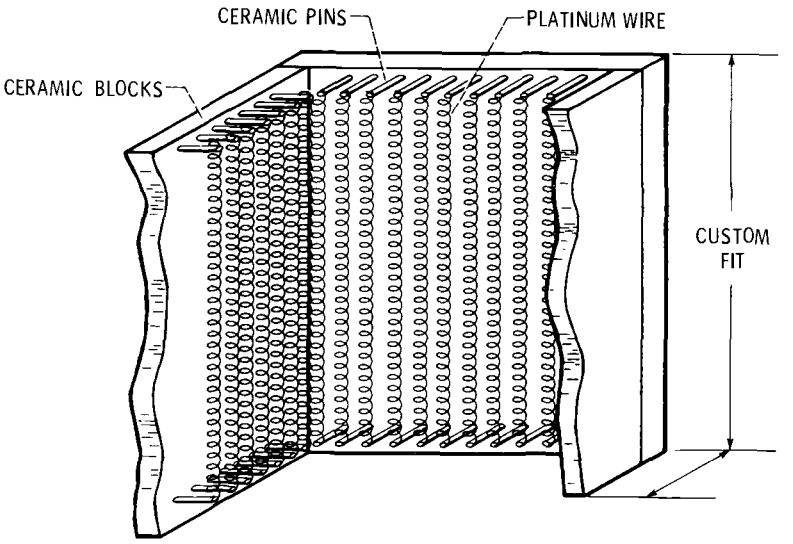

(b) Schematic of furnace design.

Figure 6.

FIG. 6—*Furnace apparatus.*

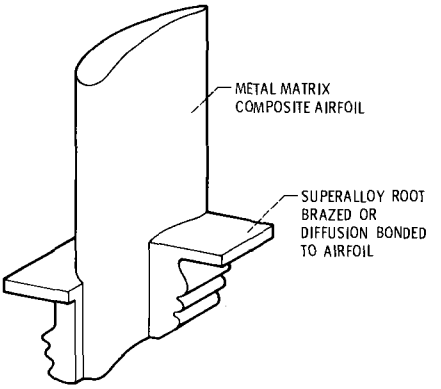

FIG. 7—*Metal matrix composite turbine blade.*

test temperature. The grip thermocouples were subsequently used as the controlling thermocouples for the temperature excursions used in these tests.

A predetermined load was then placed on the load elevator and the chamber closed and double purged with an inert gas and then evacuated with a large mechanical vacuum pump. Test conditions parameters were then inputted into a computer program to control the test facility. Desired load, power to the furnace, and duration or number of cycles required for the test were inputted into the computer. The computer then turned on the power supply to the furnace. The power supply was previously set at an amperage selected to allow the fastest specimen heating rate without overheating and failing the furnace coil. Load was then gradually applied to the specimen during the heating cycle through a computer command to the elevator motor which lowered the elevator stand. The test specimen temperature reached 1030 K (1400°F) within 600 s after the start of heating. At this time the computer sent a command to a power shut-off switch and load elevator which turned off the furnace, removed the load from the specimen, and also activated a solinoid switch. The solinoid switch allowed cool nitrogen gas to be forced through cooling passages machined in the grip fixtures and also to be exhausted onto the composite specimen just above the point where the composite panel was bounded to the root attachment. The grip fixture and test specimen was cooled to 420 K (300°F) within 180 s. After the test specimen temperature reached 420

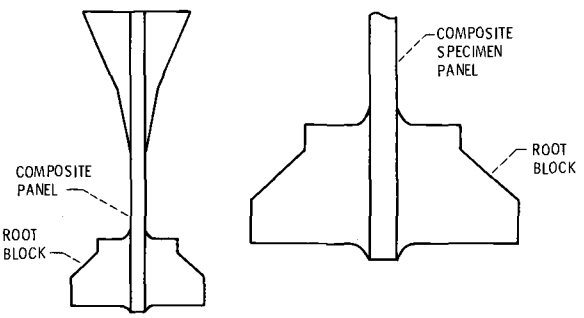

FIG. 8—*Root block attachment specimen.*

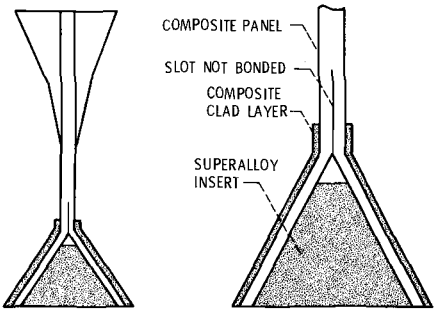

FIG. 9—*Dovetail root attachment specimen.*

K (300°F) the computer gave the necessary command to repeat the cycle until the number of cycles initially inputted was attained. The test specimen was then removed from the grip fixtures and examined for debonding or shearing at the joint interface.

Test Results

Typical types of test specimen failures for tungsten fiber reinforced Incoloy 903 composite panels bonded to Udimet 700 attachments using the specimen designs described previously and the thermal mechanical test facility are shown in Figs. 11 to 14. The test specimen shown in Fig. 11 failed at the bond between the composite panel and root block attachment. The disbond originated at the section of the test specimen exposed to an exhaust of cool nitrogen gas. The test was stopped before complete disbonding occurred at the bond joint interface.

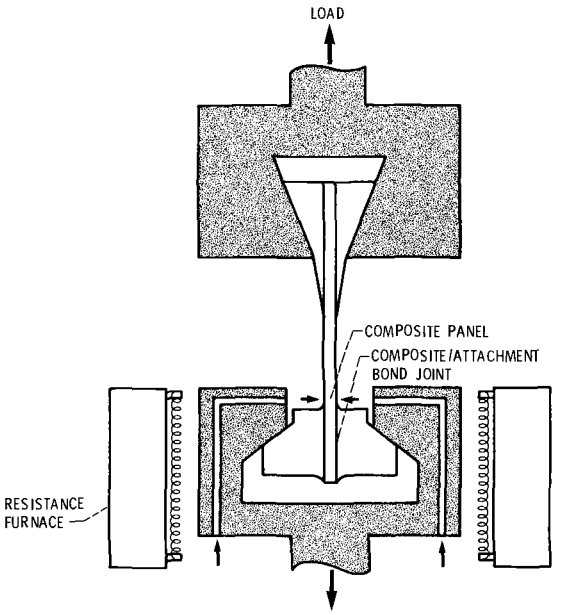

FIG. 10—*Root block thermal cycle test.*

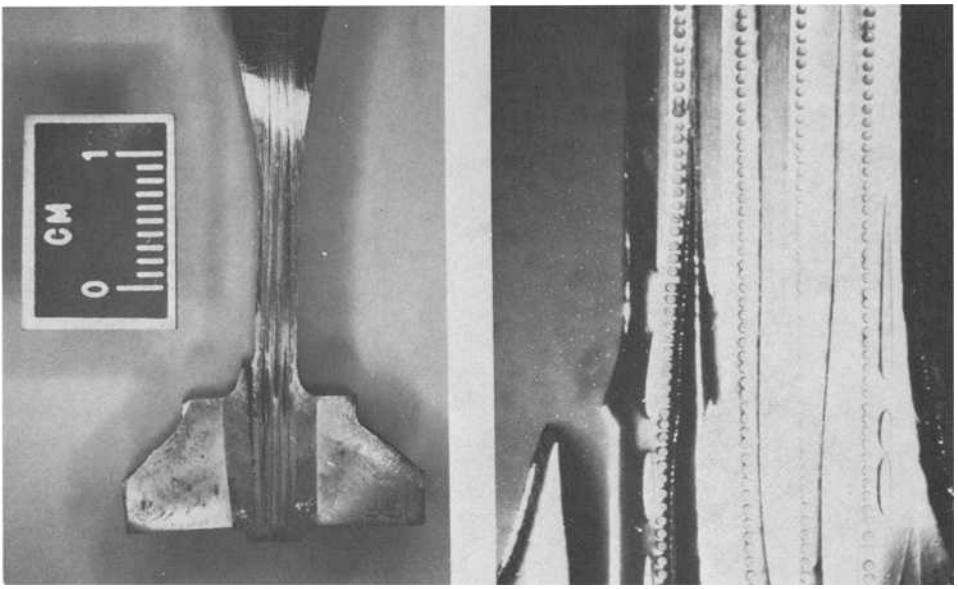

FIG. 11—*Typical composite-attached bond joint thermal-mechanical fatigue failure.*

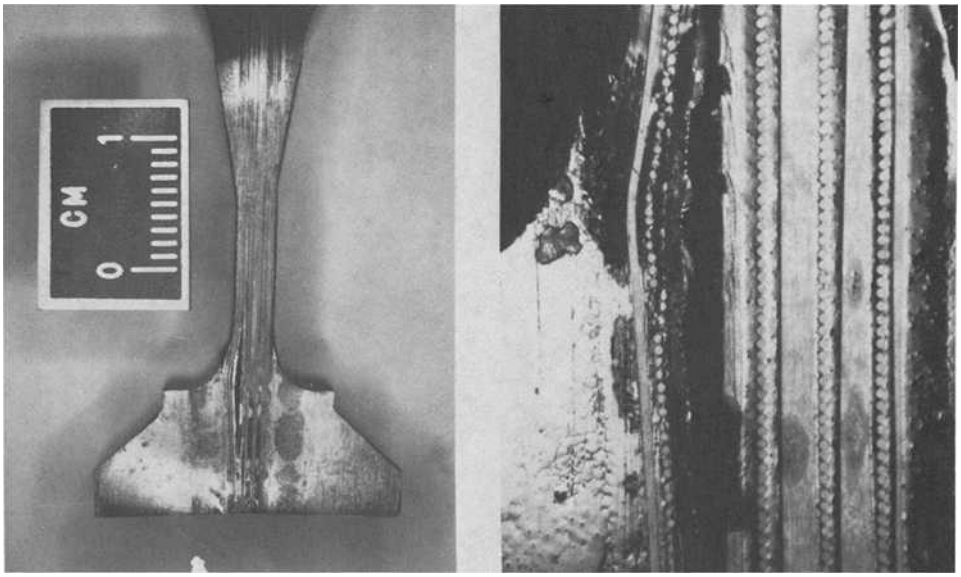

FIG. 12—*Typical composite panel delamination due to thermal-mechanical fatigue.*

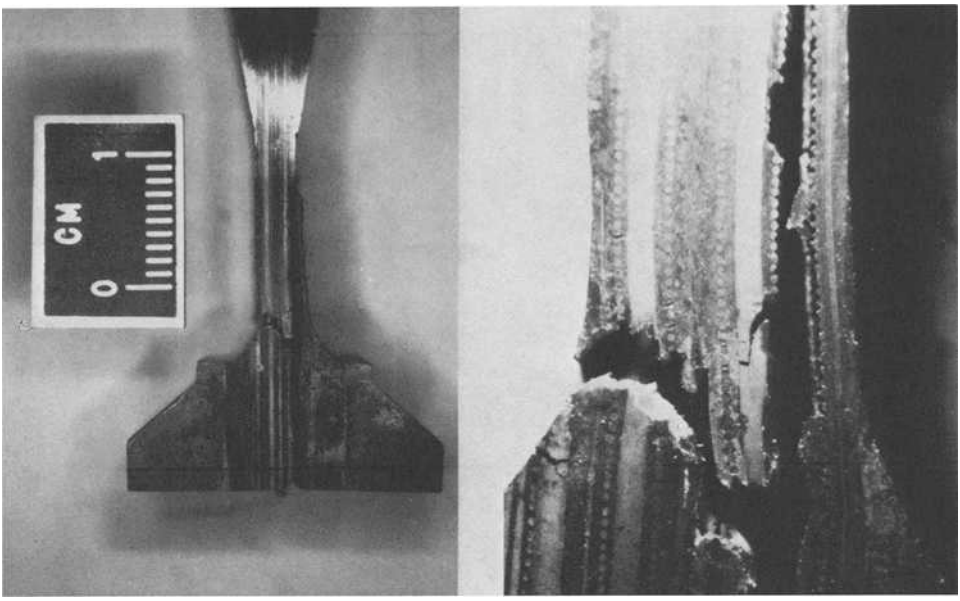

FIG. 13—*Typical combination panel and delamination failure due to thermal-mechanical fatigue.*

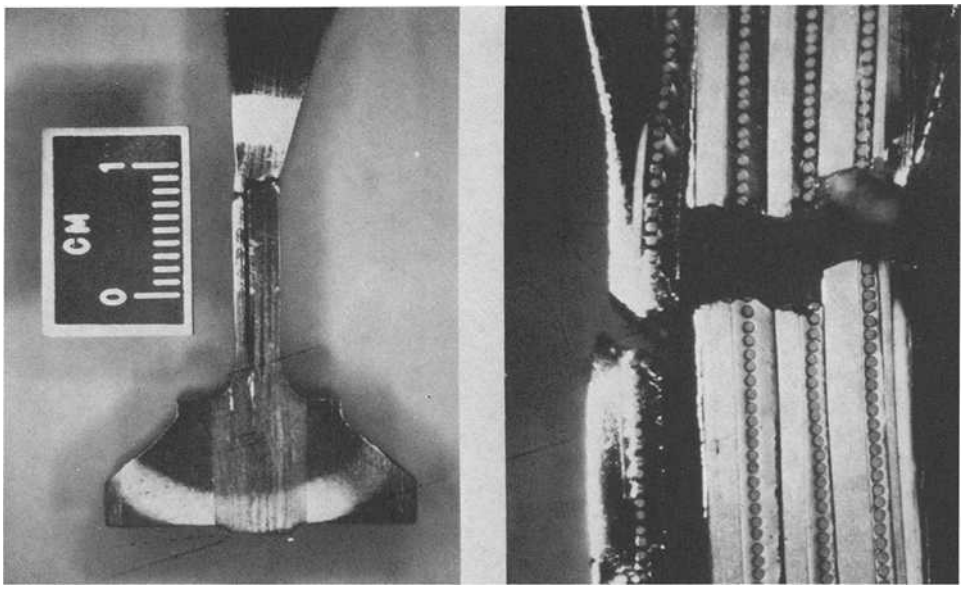

FIG. 14—*Typical failure due to thermal-mechanical fatigue.*

Figure 12 shows another type failure which can occur during thermal mechanical fatigue, namely, delamination of the composite panel. The method of loading the test specimen introduces a separation force perpendicular to the longitudinal axis of the composite panel caused by a bending movement. The separation force was sufficient to cause delamination of the panel. The bond joint between the panel and the root block remained intact. Figures 13 and 14 show a third type of failure observed due to thermal mechanical fatigue. In both cases the composite panel completely fractured while the bond joint between the panel and the root block attachment remained intact. Figure 13 shows a composite panel failure at the highly stressed root fillet. Figure 14 demonstrates a composite tensile failure away from the root attachment.

Concluding Remarks

The need to evaluate the thermal-mechanical fatigue behavior of fiber reinforced metal matrix composites and joint attachments and to simulate as closely as possible the pertinent conditions the material will experience in service stimulated the design and development of fatigue test apparatus for this purpose.

Two thermal-mechanical fatigue (TMF) test facilities were designed and developed. One TMF apparatus was used to test tungsten fiber reinforced super-alloy matrix composite specimens and another was used to test composite/metal attachment bond joints.

Both test apparatus are designed to produce a thermal cycle that coincides with an increasing load. Where possible, the strain of the specimen was measured. All data were collected by a computer and represented graphically if possible. In both apparatus maximum flexibility was maintained to allow a wide variety of test conditions. Reproducible test conditions were also maintained.

References

[1] Morris, A. W. H. and Burwood-Smith, A., "Fiber Strengthened Nickel-Base Alloy. High Temperature Turbines," AGARD-CP-73-71, Advisory group for Aeronautical Research and Development, 1971, pp. 19-1 to 19-3.

[2] Dean, A. V., "The Reinforcement of Nickel-Base Alloys with High-Strength Tungsten Wires," *Journal of Institution Metallurgy*, Vol. 95, 1967, pp. 79–86.

[3] Baskey, R. H., "Fiber-Reinforced Metallic Composite Materials," AFML-TR-67-196, Air Force Materials Laboratory, Wright-Patterson Air Force Base, OH, 1967.

[4] Fleck, J. N., "Fabrication of Tungsten-Wire/FeCrAlY-Matrix Composites Specimens," TRW Report ER-8076, TRW, Inc., Cleveland, OH, 1979.

[5] Dudnik, G. I., Banas, F. P., and Aleksandrov, B. V., "Nature of Failure of Reinforced Sheets Subjected to Thermal Cycling," *Strength Materials*, Vol. 5, No. 1, Oct. 1973, pp. 106–107.

[6] Nilsen, N. and Sovik, J. H., "Fatigue of Tungsten Fiber Reinforced Nickel," *Practical Metallic Composites*, Institution of Metallurgists, London, 1974, pp. B51–B54.

[7] Banas, F. P., Baranov, A. A., and Yakoveleva, E. V., "Deformation of Composite Materials During Alternate Heating and Cooling," *Strength Materials*, Vol. 7, No. 6, March 1976, pp. 744–748.

[8] Brentnall, W. D. and Moracz, D. J., "Tungsten Wire-Nickel Base Alloy Composite Development," ER-7849, TRW; NASA Contract NAS3-17816, NASA CR-135021, 1976.

[9] Friedman, G. I. and Fleck, J. N., "Tungsten Wire-Reinforced Superalloys for 1093°C (2000°F) Turbine Blade Applications," ER-8135, TRW; NASA Contract NAS3-20084, NASA CR-159720, 1979.

Dick J. Chang,[1] *Gary L. Steckel,*[1] *William D. Hanna,*[1] *and Francisco Izaguirre*[1]

Compressive Properties and Laser Absorptivity of Unidirectional Metal Matrix Composites

REFERENCE: Chang, D. J., Steckel, G. L., Hanna, W. D., and Izaguirre, F., **"Compressive Properties and Laser Absorptivity of Unidirectional Metal Matrix Composites,"** *Testing Technology of Metal Matrix Composities, ASTM STP 964,* P. R. DiGiovanni and N. R. Adsit, Eds., American Society for Testing and Materials, Philadelphia, 1988, pp. 18–30.

ABSTRACT: Metal matrix composite (MMC) use has been impeded because there is no well qualified property data base. Elevated temperature compressive properties and laser absorptivity data are in great demand in the design, modelling, and analysis of MMC structures in elevated temperature applications and survivability assessment. Testing methods were developed for room-temperature and elevated-temperature compressive modulus and strength measurements of single-ply unidirectional graphite-aluminum (Gr/Al) and graphite-magnesium (Gr/Mg), and to generate laser absorptivity data for these two types of materials.

An effective gage length was established for valid compression tests to eliminate buckling failure. The measured failure strength values for Gr/Al and Gr/Mg are approximately 50 to 60% lower than the material tensile strength. Small gage strain gages are being used to measure the compressive modulus as a function of temperature.

The laser absorptivities of Gr/Al and Gr/Mg were measured by the use of an in-house developed differential calorimeter. The calorimeter has been used to measure total hemispherical emittance and normal laser absorptance of specimens as a function of temperature from 200 to 700°C.

Test results indicated that the laser absorptances of Gr/Al and Gr/Mg at 10.6 μm wavelength remain more or less constant over most of the temperature range tested.

KEY WORDS: metal matrix composites, graphite-aluminum, graphite-magnesium, compressive properties, laser absorptivity

The development of metal matrix composite (MMC) materials was initiated in the early 1950s. The goal of the development work was to fabricate composite materials that offer characteristics such as high strength and modulus, light weight, and high temperature load carrying capability. Early work included the investigation of boron aluminum, boron titanium, silicon carbide aluminum, silicon carbide titanium, and alumina (Du Pont FP) reinforced composites [*1–2*]. Significant data have been presented over the past decades, especially for boron aluminum composites [*3–13*] because of the high modulus and strength and low density of boron fibers.

Graphite fiber reinforced composites have been shown to have lower density, which is a very important selection parameter for space applications. Furthermore, graphite fibers

[1] Research scientist, section manager, member of the technical staff, and member of the technical staff, respectively, Materials Sciences Laboratory, The Aerospace Corporation, El Segundo, CA 90245.

generally have a negative coefficient of thermal expansion (CTE) over the temperature range of specific interest. Much work has been done to demonstrate that graphite fiber reinforced composite materials can be fabricated with nearly zero thermal dimensional growth [*14,15*]. Thus, it provides great dimensional stability to fulfill stringent distortional requirements. The dimensional stability provided by graphite fiber reinforced composite is unique and cannot be achieved by other known MMC materials.

Recent development of graphite fibers has resulted in higher stiffness fibers (P100, P120, and P140) with 6.89 to 9.65 $\times$ 10^5 MN/m^2 (100 to 140 Msi) moduli. Unidirectionally reinforced MMC fabricated from these types of fibers offers greater axial stiffness for structure components such as struts, booms, and tower structures. Thin-ply fabricability and the feasibility of producing complex shapes have been demonstrated for graphite-aluminum (Gr/Al) and graphite-magnesium (Gr/Mg). Mechanical properties, such as tensile moduli and strengths, and thermal physical properties have been measured for these materials by various investigators [*15–17*].

However, other basic properties such as compressive moduli and strengths, shear moduli and strengths, fracture behavior, and optical absorptance and emittance for these materials are at best very limited in the literature. Data to evaluate these properties for the design, analysis, and modelling of MMC are useful to permit development of structural components for room and high-temperature applications. The utilization of the potential of MMC will be severely hindered unless these properties become available. Work has been performed at The Aerospace Corporation to develop the testing methodology and to generate data for some of the basic properties. These investigations have included the compressive properties and laser absorptance for Gr/Al and Gr/Mg materials as a function of temperature. The results of the work will assist the establishment of standard testing techniques, and the broadening of the data base for design, modelling and analysis, and failure criteria.

Procedure

Two types of MMC were utilized in the project: 6061 graphite aluminum and AZ91C graphite magnesium with AZ61A surface foils. The graphite fibers were P100 (VS-0054) mesophase pitch fibers with an average axial modulus of elasticity of 7.24 $\times$ 10^5 MN/m^2 (105 $\times$ 10^6 psi) and average density and ultimate strength of 2.15 g/cm^3 (0.078 lb/in.^{3}) and 2.24 $\times$ 10^3 MN/m^2 (325 $\times$ 10^3 psi), respectively. The fibers were manufactured by Union Carbide Corp. and the 6061 Gr/Al and AZ91C Gr/Mg wires were made by Materials Concepts, Inc. (MCI), Columbus, Ohio. Two types of specimens were fabricated. Unidirectional single layer Gr/Al and Gr/Mg plates were fabricated by DWA Composite Specialties, Inc., Chatsworth, California, with 0.089-mm (3.5-mil)-thick 6061 aluminum and 0.061-mm (2.4-mil)-thick AZ61A magnesium surface foils, respectively. The compressive specimens were machined from these plates. Their nominal dimensions are 11.43 cm long by 0.64 cm wide (4.5 in. long by 0.25 in. wide). The use of single-ply specimen was dictated by the lightweight requirement in actual applications. For the laser absorptance tests, thicker specimens were fabricated because of the design requirements of the apparatus employed. The panels were diffusion bonded by DWA by stacking up ten single-layer unidirectional layups. The fabrication parameters include: 588°C (1090°F) at 24 MN/m^2 (3.5 $\times$ 10^3 psi) for 20 min for Gr/Al; 477°C (890°F) at 24 MN/m^2 (3.5 $\times$ 10^3 psi) for 40 min for Gr/Mg. Table 1 shows the fiber, matrix, and fiber volume of the fabricated panels. Since the thick panels had the same diffusion bonding parameters, it is expected that they had surface conditions similar to those of the single layer panels.

Thermooptical properties of engineering materials are generally not available. This is particularly true for properties at elevated temperatures. Furthermore, such properties are

TABLE 1—*Panel Composition and Configuration of Unidirectional Gr/Al and Gr/Mg Materials.*

Materials	Matrix	Surface Foil	Fiber Volume Fraction, %	Specimen Thickness, mm (in.)	Remarks
Gr/Al	6061	0.089 mm (3.5 mil) 6061 Al	33.0	0.686 (0.027)	for unidirectional compression tests
Gr/Mg	AZ91C	0.061 mm (2.4 mil) AZ61A	37.0	0.655 (0.026)	for unidirectional compression tests
Gr/Al	6061	0.089 mm (3.5 mil) 6061 Al	32.6	6.50 (0.256)	for emittance and laser absorptance tests
Gr/Mg	AZ91C	0.076 mm (3.0 mil) AZ61A	32.8	5.75 (0.226)	for emittance and laser absorptance tests

affected by handling and other environmental or processing conditions to such an extent that direct measurements taken on specific materials of interest are often the only means of obtaining data with which one can confidently model material response to thermal radiation inputs. Total hemispherical emittance and directional laser absorptance of MMC materials can vary considerably depending, among other things, on surface deformations due to the underlying matrix, thermal diffusivity through the normal axis of the matrix, and surface alloy composition.

Experimental Work

Compression Tests

All compression tests were performed with the use of a modified ASTM D3410 Celanese fixture. The fixture had a smaller overall diameter so that it could be fit in a quad-elliptical, high-intensity, infrared, radiant heating chamber for high-temperature testing. The fixture

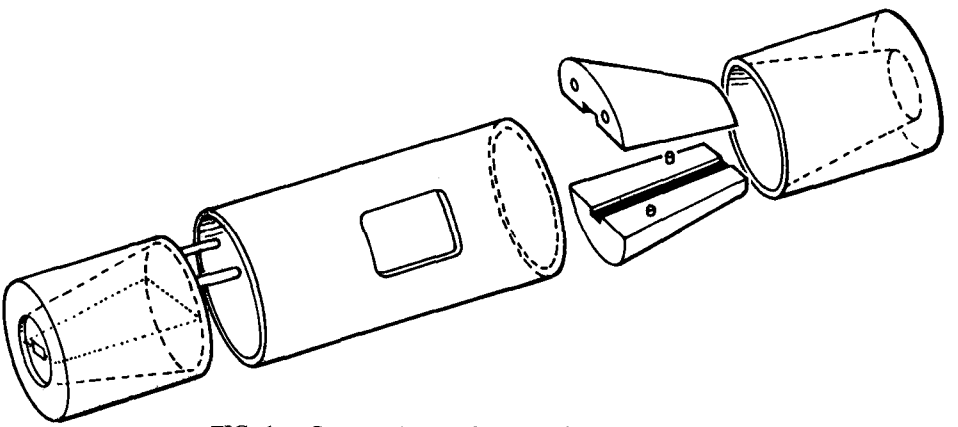

FIG. 1.—*Compressive test fixture with conical wedges.*

was fabricated from Inconel 625 alloy so that testing at temperatures over 500°C (~930°F) could be performed. Figure 1 is a sketch of the compressive test fixture, and Fig. 2 is a photograph of the fabricated fixture.

The modified D3410 fixture was selected for the testing because it was found by Adsit [*18*] to give valid compression results. Although the pyramidal wedges [Illinois Institute of Technology Research Institute (IITRI) method] appear to give equivalent modulus and strength values for thin composite materials, such as graphite-epoxy, it may not have a symmetric temperature gradient when heated in an annular clamshell-type heater.

Tabs made from hard file material were used to transfer the shear load from the shell frustra to the specimens. Each of the four tabs was tapered at one end to produce uniform

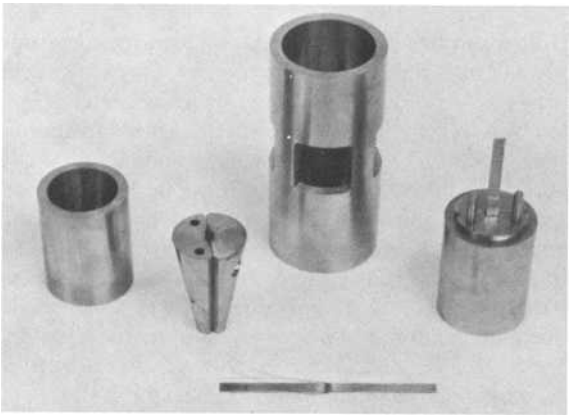

(a)

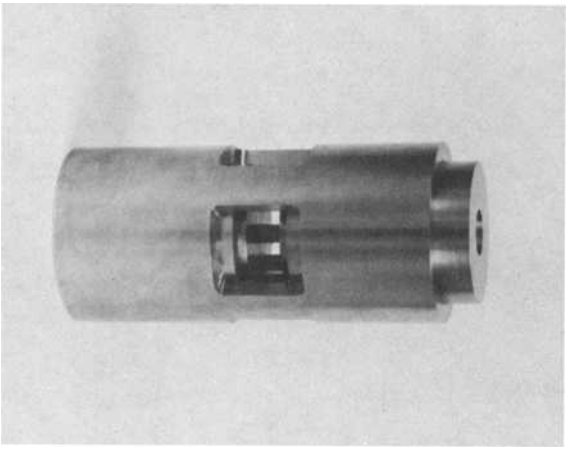

(b)

FIG. 2.—*Photograph of compressive test fixture* (a) *disassembled parts,* (b) *assembled fixture.*

load transfer between the tabs and specimens. Moreover, the tabs acted as lateral supports to reduce possible transverse deflections which can cause the specimens to fail in a buckling rather than a compressive mode.

The compressive loads were applied using an Instron universal loading fixture, model 1135. Two Micro-Measurement Unidirectional EA-06-015-EH-120 strain gages were mounted at the center of the two surfaces of each specimen. The small strain gages, which have 0.38 mm (0.015 in.) gage length and 0.64 mm (0.025 in.) overall length, were chosen because a short unsupported specimen length was required to give valid compressive strengths, as discussed in the results section.

Absorptance and Emittance Tests

The normal spectral absorptance $\alpha_N(\lambda,T)$ and total hemispherical emittance $\epsilon(2\pi,T)$ testing of Gr/Al and Gr/Mg materials was performed as a function of temperature. The tests were carried out using an Aerospace-developed dual calorimeter [*19*]. The Gr/Al and Gr/Mg specimens tested were disks 5.08 cm (2 in.) in diameter and approximately 0.64 cm (1/4 in.) (ten-plies) thick. A control specimen of 6061-T6 aluminum was also tested.

A schematic diagram of the calorimeter is shown in Fig. 3. The central part of the calorimeter is an oxygen-free, high-conductivity (OFHC) copper housing that provides a high-temperature environment for two specimen assemblies. The housing consists of a main body and two end pieces. Each specimen to be tested is mounted against an OFHC copper block in which two cartridge heaters are imbedded. The two specimen assemblies are then positioned in the openings in both end pieces and are held in place by point contact with threaded stainless steel rods. The specimen is mounted flush to the front surface of the end piece. An annular gap of about 0.64 mm (0.025 in.) separates the specimen assembly from the end piece. The housing is heated separately from the dual specimen assemblies by a clamshell-type heater. The assembled calorimeter is encased in a gold-coated stainless steel jacket. The temperatures of each specimen and of the housing of the calorimeter are controlled independently. To allow the recording equipment to constantly monitor the power output, the temperature and power controllers are current proportional rather than time

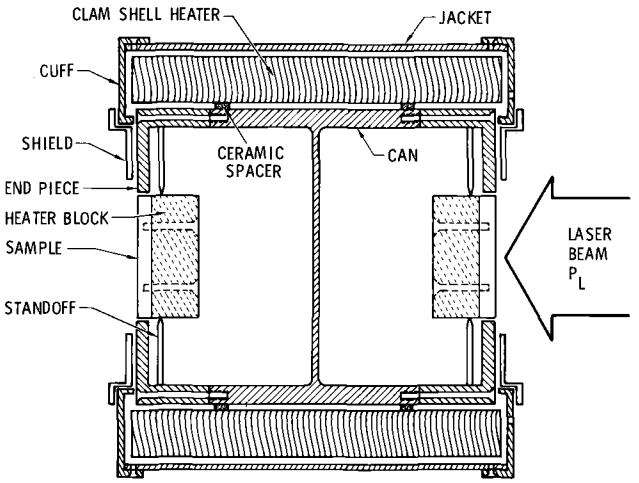

FIG. 3.—*Schematic diagram of calorimeter.*

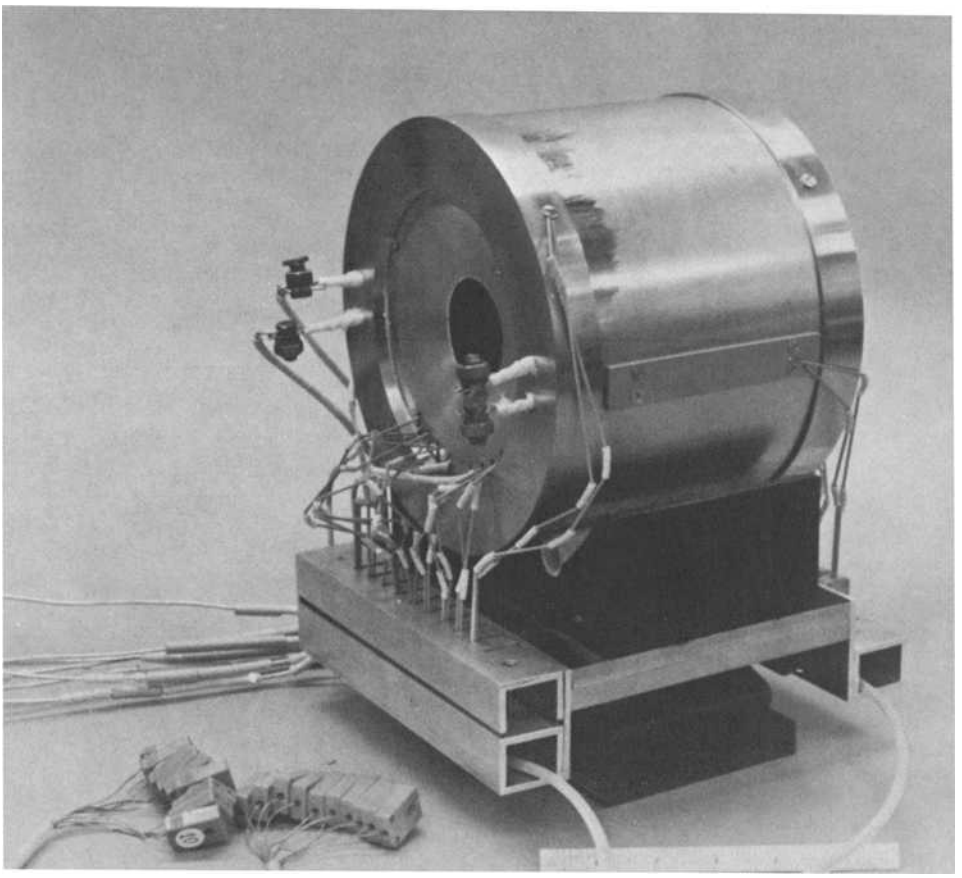

FIG. 4.—*Photograph of calorimeter.*

proportional. Power transducers continuously monitor the output of the power controllers and provide proportional voltage signals that are recorded. All electronic devices are hard-wired into a single console. To track the temperature of critical areas the assembly is instrumented with 20 thermocouples (Fig. 4).

During the experiment, the assembled calorimeter is placed in a vacuum chamber. The interior of the chamber is surrounded with a cooling shroud. Calculations of the view factors [*19*] show that of all the surfaces seen by the specimen, the largest view factor corresponds to the one between the specimen and the shroud. To minimize the errors introduced by the uncertainty in the emmittance of the shroud surface, the cooling passages in the shroud are filled with liquid nitrogen, and its temperature is measured with thermocouples.

Figure 5 shows the CO_2 laser beam path. A sodium chloride wedge splits the beam. One reflection from the wedge is directed to a focusing mirror and into a power meter. The other reflection is steered toward the test chamber. The last mirror in this optical path focuses the beam onto the specimen. The calorimeter is positioned and aligned in the vacuum chamber so that the beam is about the same size as the test specimen and incident on the entire specimen. The advantage of a dual calorimeter design is that it provides a convenient way of differentiating thermal damage from purely laser damage. If, when the absorptance

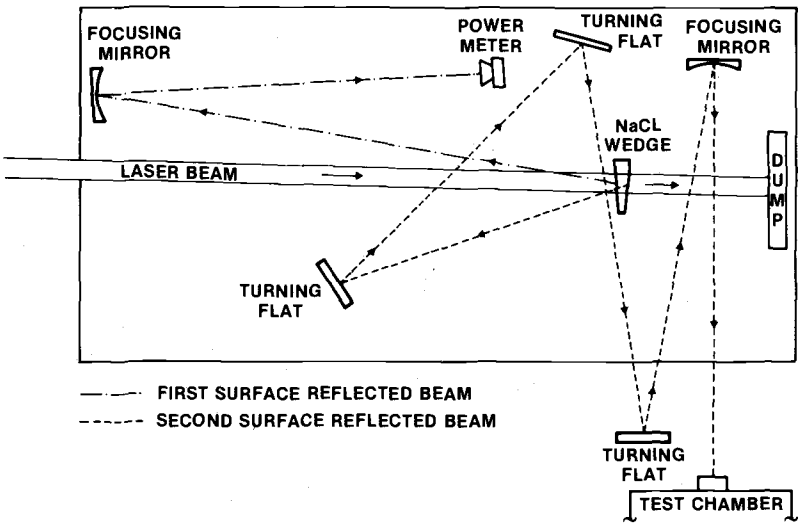

FIG. 5.—*Laser beam path.*

is measured, the illuminated specimen degrades while the other specimen does not, then degradation is due to the absorptance of the specimen at the particular wavelength of the laser being used.

The equation used to determine the normal spectral absorptance at a particular laser wavelength and a pre-determined temperature is

$$\alpha_N(\lambda,T) = \frac{P_2 - P_1}{P_L} \tag{1}$$

where

$\alpha_N(\lambda,T)$ = normal absorptance as a function of wavelength and temperature,
P_2 = net electrical power delivered to the specimen heating block before illumination of the specimen with the laser,
P_1 = net electrical power delivered to the specimen while the specimen is being illuminated by the laser, and
P_L = power delivered to the specimen by the laser.

Equation 1 assumes that all three powers, P_2, P_1, and P_L are measured at an equilibrium temperature and the temperature is the same before and after illumination of the specimen by the laser. A graphic derivation of this equation can be deduced from Fig. 6.

The equation used to determine the total hemispherical emittance is

$$\epsilon(2\pi,T) = \frac{P_2}{A\sigma \sum_{i=2}^{n} F_{1,i}(T_1^4 - \epsilon_i T_i^4)} \tag{2}$$

where

$\epsilon(2\pi,T)$ = total hemispherical emittance as a function of temperature,
P_2 = net electrical power delivered to the specimen heating block,
A = area of emitting surface,
σ = Stefan-Boltzmann constant,
$F_{1,i}$ = view factors between specimen and surfaces seen by the specimen,
T_1 = temperature of specimen,
T_i = temperature of the surfaces seen by the specimen, and
ϵ_i = emittance of the surfaces seen by the specimen

The major uncertainty in this equation is in ϵ_i. The uncertainty is negligible when $T_1 >> T_i$. This condition can be attained by chilling the walls of the shroud as described previously. For other surfaces, where it is not possible to lower the temperature, the view factors are small, and the error remains negligible.

The preparation of the test specimens included several steps. Blind mounting holes were drilled and tapped into the back of each specimen, and this surface was polished to ensure good thermal contact with the heating block. The surface to be tested for emittance and absorptance was cleaned with fine and very fine 3M Scotch Brite. Particular care was taken to avoid altering the surface roughness. Acetone was used to remove any residue from the cleaning process.

In addition to the two MMCs, a solid block of 6061-T6 aluminum was machined and used as a baseline specimen. Its surface was cleaned in the same manner as the metal matrix specimens. However, to eliminate machine oil, this specimen was degreased in a hot bath of trichloroethane.

At the center of the back (nonexposed) surface of each specimen, a small blind hole was drilled and a thermocouple inserted as near as possible to the front (exposed) surface. An additional thermocouple was sandwiched between the specimen and the heating block. By means of these thermocouples the temperature gradient between the front and back surface

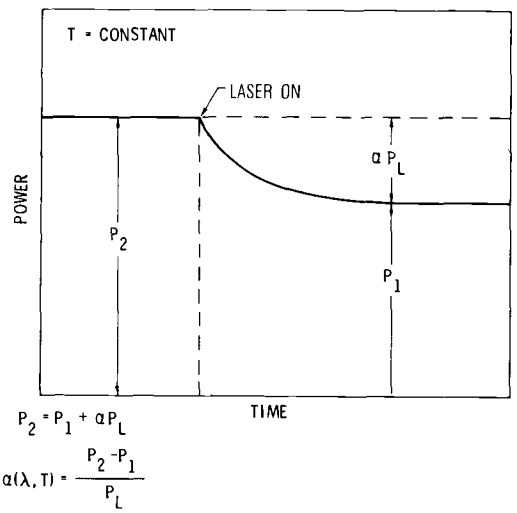

FIG. 6.—*Expected behavior of power controllers' output.*

of each specimen during testing was observed to be no larger than 1°C. The test specimen disks were anchored with screws to the heating blocks and then assembled in the calorimeter. The calorimeter was then placed in a vacuum chamber and the shroud of the chamber cooled with liquid nitrogen. The operational pressure was about 200 mT at the low end of the temperature scale, increasing to about 300 mT at the high end.

Results

Compressive Tests

Compressive tests were performed at 24, 149, and 260°C (75, 300, and 500°F) for compressive modulus and strength measurements. A 2.5 mm (0.1 in.) unsupported gage length between the tips of two tabs was used. This dimension was established after compression testing at several different gage lengths. It was found that failure occurred prematurely in buckling modes when the unsupported gage length was greater than 2.5 mm (0.1 in.) for single layer unidirectional Gr/Al and Gr/Mg composites. Table 2 summarizes the compressive modulus results, and Table 3 lists the results of the compressive strength. The room-temperature tensile modulus and strength for specimens from the same panels as the compressive specimens were also tested and are shown in the two tables for comparison purposes. It can be seen from these two tables that the average room-temperature compressive modulus for Gr/Al material is 2.12×10^5 MN/m^2 (30.7 Msi) which is about 78% of the room-temperature tensile modulus, and the room-temperature compressive strength is 272 MN/m^2 (39.4 ksi) which is about 36% of the room-temperature tensile strength. The corresponding ratios for Gr/Mg material are 89% for room-temperature modulus and 58.1% for the room-temperature strength.

The compressive modulus of a single graphite fiber is almost impossible to measure since it is only $7 \sim 10$ μm ($2.76 \approx 3.94 \times 10^{-4}$ in.) in diameter. It is believed to be similar to the tensile modulus. In general, the compressive modulus of a unidirectional graphite fiber reinforced composite is lower than the tensile modulus. The primary reason is that the graphite fibers can never be straight. There are kinks, bends, or even off-angle layups which would make the compressive modulus lower even if the fiber tensile and compressive moduli were the same. In addition, the high-processing temperature of Gr/Al and Gr/Mg puts the graphite fibers in compression as a result of cooling. This would either make the kinks and bends more pronounced or create new kinks and bends due to weak lateral support which would further lower the compressive modulus. Therefore, a compressive modulus of Gr/Al and Gr/Mg composites lower than the tensile modulus is expected.

No elevated temperature tensile modulus and strength measurements were made on the

TABLE 2—*Compressive moduli of unidirectional Gr/Al and Gr/Mg.*

Material	Room Temperature Tensile Modulus, 10^5 MN/m^2 (Msi)	Temperature °C	Temperature (°F)	Compressive Modulus, 10^5 MN/m^2 (Msi)
Gr/Al	2.71 (39.4)	24	(75)	2.12 (30.7)
		149	(300)	2.51 (36.4)
		260	(500)	2.71 (36.8)
Gr/Mg	2.90 (42.1)	24	(75)	2.58 (37.4)
		149	(300)	2.47 (35.9)
		260	(500)	2.63 (38.1)

TABLE 3—*Compressive Strength of Unidirectional Gr/Al and Gr/Mg.*

Material	Room Temperature Tensile Strength, MN/m^2 (ksi)	Temperature °C	Temperature (°F)	Compressive Strength, MN/m^2 (ksi)
Gr/Al	751.4 (109)	24	(75)	271.6 (39.4)
		149	(300)	283.3 (41.1)
		260	(500)	228.9 (33.2)
Gr/Mg	488.8 (70.9)	24	(75)	284.0 (41.2)
		149	(300)	294.0 (42.2)
		260	(500)	213.7 (31.0)

same lots of materials that were used for compression tests. However, tension tests were performed for 30% fiber volume fraction of Gr/Al and 45% fiber volume fraction of Gr/Mg fabricated by DWA using the same techniques. The data show a 9% tensile modulus decrease from room temperature (RT) to 260°C (500°F) and an 18% tensile strength variation. The corresponding values for Gr/Mg are 3% tensile modulus decrease for RT to 300°C (572°F) and 2% tensile strength variation for RT to 313°C (595°F). The large variation of tensile strength for Gr/Al was due to some failures in the grip areas which do not reflect the tensile strength of the material. It is believed that both the tensile and compressive modulus variations of Gr/Al and Gr/Mg material are small in the RT to 260°C (RT to 500°F) range. Thus, the 20% increase in the compressive modulus of Gr/Al from RT to 260°C (500°F) was surprising. More data are required to substantiate this observation.

During the test series, it was found that both the tensile and compressive moduli depend upon the thermal and loading history. Two Gr/Al specimens were heat treated to T6 condition for the aluminum matrix material and then were compressively tested at room temperature. A 33% compressive strength increase was observed for the heat-treated specimens over the average compressive strength for the as-received condition. The higher strength was apparently due to a higher matrix contribution to the composite strength resulting from the heat treatment. This may be the result of stronger lateral support for the graphite fibers. The matrix heat treatment does not affect the tensile strength of Gr/Al to such an extent. Thus, it is postulated that the matrix strength properties have much more influence on the composite strength in compression than in tension. Two additional Gr/Al specimens, which were cooled to RT from a 260°C (500°F) preheating operation, had a measured tensile modulus of 2.32 and 2.42 $\times$ 10^2 MN/m^2 (33.6 and 35.1 Msi) at RT, a 15 and 9% reduction, respectively, from the average RT tensile modulus without any preheating operation. The Gr/Al compressive specimen, which had similar cooldown to RT from 260°C (500°F) preheating, had a compressive modulus of 2.65 $\times$ 10^5 MN/m^2 (38.5 Msi) following an RT tension retest. This value is much higher than the average compressive modulus of nonpreheated specimens and is closer to the tensile modulus. It is postulated that the residual stresses in the filament and the aluminum matrix as a result of cooldown changes the mechanical characteristics of the composites. Further investigation is needed in this area.

Absorptance and Emittance Tests

The results of the absorptance measurements as a function of temperature under CO_2 laser illumination (10.6 μm) for all three specimens are shown in Fig. 7. The absorptance for Gr/Al, Gr/Mg, and 6061 -T6 aluminum between 200 and 500°C (392 and 932°F) remains constant at 0.06 to 0.08 with the exception that there is a dramatic increase in the absorptance

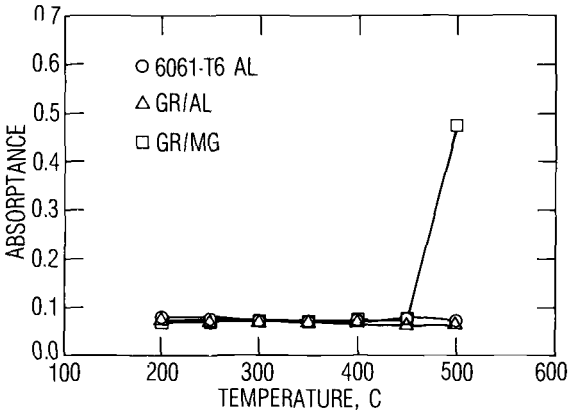

FIG. 7.—*Absorptance of 6061-T6 aluminum, graphite-aluminum, and graphite-magnesium as a function of temperature.*

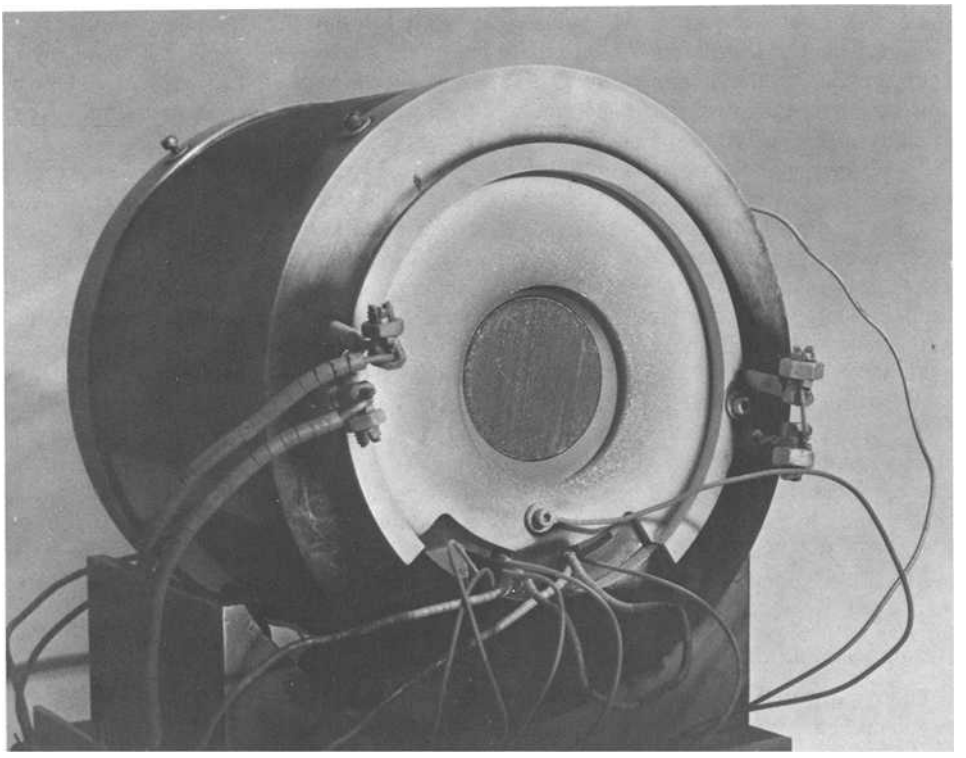

FIG. 8.—*Calorimeter partially disassembled after absorptance tests.*

of Gr/Mg (0.47) at 500°C (932°F). [When the calorimeter was disassembled, it was found that the carbon fibers were no longer embedded in magnesium, and the calorimeter surfaces closest to the specimen were coated with a coarse silvery substance (Fig. 8). This would explain the anomalous last point].

The total hemispherical emittance measurements are shown in Fig. 9. The emittance for Gr/Mg is 0.2 at 200°C (392°F) and gradually decreases to about 0.17 at 400°C (752°F). As with the absorptance, there is a drastic change in the emittance (0.63) at 500°C (932°F). The emittance of 6061-T6 aluminum remains approximately constant between 200 and 300°C (392 and 662°F) at about 0.2. Between 300 and 500°C (572 and 932°F) there is a slight increase to about 0.22. The emittance for the Gr/Al agrees with that of the 6061 aluminum values at low temperature. At temperatures higher than 400°C (752°F), the emittance decreases. At 500°C (932°F) the emittance is 0.18.

Conclusions and Recommendations

It can be seen from Tables 2 and 3 that the compressive modulus and strength values for Gr/Al and Gr/Mg differ from the tensile values. Room temperature compressive moduli for as-received Gr/Al and Gr/Mg materials are approximately 78 and 89%, respectively, of the tensile values. The corresponding room temperature compressive strength values are approximately 36% for Gr/Al and 58% for Gr/Mg of the tensile strength. There seems to have been a modulus increase at both 149 and 260°C (300 and 500°F) relative to room temperature for Gr/Al, whereas the modulus differences between 149 and 260°C (300 and 500°F) are negligible. For Gr/Mg material, the modulus difference for all temperatures up to 260°C (500°F) seems to be within the scatter band of the measurements.

The compressive strength values at 149°C (300°F) for Gr/Al and Gr/Mg are very close to the room temperature values. At 260°C (500°F), however, there is a significant drop in the compressive strength. The aluminum or magnesium matrices in either composite are much softer at 260°C (500°F). It is postulated that the softening of the matrix reduces the lateral support to the graphite fibers. Therefore, the fibers failed prematurely in buckling.

The values for the emittance and absorptance of Gr/Al, Gr/Mg, and 6061-T6 aluminum are very similar and appear reasonable. Even though small blisters were noticed when the

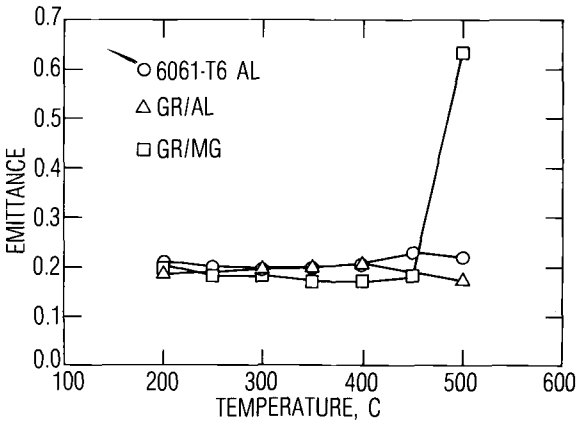

FIG. 9.—*Total hemispherical emittance of 6061 aluminum, graphite-aluminum, and graphite-magnesium as a function of temperature.*

Gr/Mg specimens reached 300°C (572°F), they appeared on both specimens, the one illuminated by the laser and the control specimen. The small blisters cannot be attributed to laser damage, nor do they seem to have affected the overall experiment in any other way. Because of the low eutectic temperature of the constituents in AZ91C and AZ61A (such as zinc), the application of Gr/Mg at temperatures higher than 450°C is not recommended.

Acknowledgment

This work was sponsored by the U. S. Naval Sea Systems Command under Air Force Space Division Contract No. F04701-83-C-0084.

References

[1] Stuhrke, W. R., "The Mechanical Behavior of Aluminum-Boron Composite Material," *Metal Matrix Composites, ASTM STP 438,* American Society of Testing and Materials, Philadelphia, 1958, pp. 108–133.

[2] Metcalfe, A. G., "Fiber Reinforced Titanium Alloys," *Composite Materials, Vol. 4,* Chapter 6, K. G. Kreider, Ed., Academic Press, New York, 1974.

[3] "Structural Analysis Methods for Advanced Composites: 4. Structures and Materials," Report CASD-ERR-73-029, General Dynamics/Convair Aerospace Division, Dec. 1973.

[4] "Design, Manufacture, Development, Test and Evaluation of Boron/Aluminum Structural Components for Space Shuttle, Vol. II—Materials and Processing," Report GDCA-DBG73-006, General Dynamics/Convair Aerospace Division, Aug. 1973.

[5] "Development of Engineering Data on the Mechanical and Physical Properties of Advanced Composite Materials," AFML-TR-72-205, Part II, Contract No. F33615-71-C-1713, IIT Research Institute, Chicago, IL, Feb. 1974.

[6] "Composite Box Beam Optimization: Experimental Data Supporting Technology Development and Preliminary Design," AFML-TR-73-13, Grumman Aerospace Corp., June 1973.

[7] "Advanced Development of Conceptual Hardware—Fuselage," Report NA-73-662-8, Rockwell International/Los Angeles Aircraft Division, March 1974.

[8] "Composite Box Beam Optimization, Vol II, Increased Structural Efficiency of Boron/Aluminum," AFML-TR-74-105, Grumman Aerospace Corp., May 1974.

[9] "Boron/Aluminum Skins for the DC-10 Aft Pylon," NASA CR-132645, McDonnell Douglas Corp/Douglas Aircraft Co., May 1975.

[10] "Manufacturing Methods for Metal Matrix Structural Components," Interim Report IR-304-4(W) for Contract F33615-74-C-5151, General Dynamics/Convair Division, 15 July 1975.

[11] "Optimum Boron/Aluminum Design for a B-1 Wing Rib," NA-74-584-15, Contract 70-00626 (General Dynamics/Convair Division) Rockwell International/Los Angeles Aircraft Division, 1975.

[12] "Boron/Aluminum Landing Gear for Navy Aircraft," Report CASD-NADC-76-003, General Dynamics, Convair Division, Sept. 1978.

[13] Schromm, R. E., "Cryogenic Mechanical Properties of Boron, Graphite, and Glass Reinforced Composites," *Materials Sciences and Engineering,* Vol. 30, 1977, pp. 197–204.

[14] Wolff, E. G., Kendall, E. G., and Riley, W. C., "Thermal Expansion Measurements of Metal Matrix Composites," *Advances in Composite Materials,* A. R. Bunsell, Ed., ICCM III, Pavis, Pergamon Press, New York, 1980.

[15] Armstrong, H. H., Ellison, A. M., Kintis, D. H., Sullivan, P. G., "Development of Graphite/Metal Advanced Composites for Spacecraft Applications," LMSC-D758140, 15 April 1980.

[16] Taylor, R. E. and Groot, H., "Thermophysical Properties of Fiber-Reinforced 6061," PRL524, Properties Research Laboratory, West Lafayette, IN, May 1980.

[17] Taylor, R. E. and Groot, H., "Thermophysical Properties of Graphite Aluminum and Graphite Magnesium," PRL 330, Properties Research Laboratory, West Lafayette, IN, June 1984.

[18] Adsit, N. R., "Compression Testing of Graphite/Epoxy," *Compression Testing of Homogeneous Materials and Composites, ASTM STP 808,* Richard Chait and Ralph Papirno, Eds., American Society for Testing and Materials, Philadelphia, 1983, pp. 175–186.

[19] Izaguirre, F. and Fishman, L., "A Calorimetric Approach for Measuring Emittance and Normal Spectral Absorptance at Elevated Temperatures," in *AIAA 19th Thermophysics Conference,* American Institute of Astronautics and Aeronautics, Snowmass, CO, 25–28 June 1984.

Azar P. Majidi,[1] *Jenn-Ming Yang,*[1] *and Tsu-Wei Chou*[1]

Mechanical Behavior of Three-Dimensional Braided Metal Matrix Composites

REFERENCE: Majidi, A. P., Yang, J-M, and Chou, T-W, **"Mechanical Behavior of Three-Dimensional Braided Metal Matrix Composites,"** *Testing Technology of Metal Matrix Composites, ASTM STP 864.* P. R. DiGiovanni and N. R. Adsit, Eds., American Society for Testing and Materials, Philadelphia, 1988, pp. 31–47.

ABSTRACT: The results of an on-going experimental study to characterize the mechanical properties and failure mechanisms of a novel 3-D braided composite of α-alumina fiber (fiber FP) in a matrix of aluminum +2.5% lithium have been presented. Quasi-static tension, compression, and shear tests have been conducted. Acoustic emission data have been collected during tension tests to provide additional information about failure. Fracture toughness and drop-weight impact characteristics have been also evaluated and compared with those of unidirectional FP/aluminum-lithium composites.

The 3-D braiding of fibers not only provides reinforcement in the thickness direction and reduces or eliminates potential for interlaminar failure, but also appears to be an effective approach to increasing the resistance of the composite to crack propagation under both static and impact conditions of loading.

KEY WORDS: 3-D braided composites, α-alumina fiber, aluminum-lithium matrix, metal matrix composites, mechanical properties

Metal matrix composites incorporating the new potentially low cost/high performance ceramic reinforcements such as alumina (Al_2O_3) or silicon carbide (SiC) whiskers, particles, or filaments have recently received much attention on account of their outstanding corrosion resistance, wear resistance, and high temperature capabilities. The state-of-the-art fabrication and characterization of metal matrix composites has been recently published in a general review of Chou, Kelly, and Okura [*1*].

In this paper the mechanical characteristics and capabilities of an innovative 3-D braided composite of fiber FP,[2] a polycrystalline α-alumina fiber, in an aluminum +2.5% lithium matrix have been explored. This composite has been manufactured by a novel braiding process which allows fabrication of a nonorthogonal, fully integrated, 3-D fiber reinforced structure directly to the shape of the component by multidimensional manipulation of fibers in the loom. Technologically, the main advantages of 3-D integrated composites are their superior damage tolerance and higher interlaminar strength and stiffness as compared with conventional 2-D laminates.

The experimental and theoretical characterization of multidimensional fabric composites is still in an infantile stage. The thermoelastic properties of these materials were recently treated by Yang, Ma, and Chou using two different approaches and geometric models [*6*–

[1] Assistant professor, graduate student, and professor, respectively, Department of Mechanical Engineering and Center for Composite Materials, University of Delaware, Newark, DE 19716.

[2] FP is a tradename of Du Pont Company, Wilmington, DE.

10]. Their "fiber interlock model" [*7*] contains seven reinforcement axes within the unit block of composite and takes into account interactions between the interlacing fiber bundles. The "fiber inclination model" [*8*] assumes only four fiber orientations and does not consider fiber interactions at the "interlocks."

The focus of this paper is experimental characterization of the mechanical properties of 3-D braided FP/aluminum-lithium (Al-Li) composites. This work is part of an on-going research to establish the basic thermo-mechanical properties and failure mechanisms of this composite in tension, compression, and shear and to characterize its fracture toughness and impact behavior. The results of logitudinal tension, compression, and in-plane and interlaminar shear tests have been already presented in a previous publication [*11*]. In this paper, detailed description of results are given for those properties not previously reported.

Experimental Procedures

Materials

The 3-D braided fiber FP preforms were prepared by Dr. Frank Ko at Drexel University, Philadelphia, Pennsylvania. The preforms had a 1 by 1 braid structure with an average braid angle of about 20° (the angle between the fiber bundle and the axis of braiding) and were each fabricated to the final specimen dimensions along the width and thickness directions. Each fiber bundle in the preform contained twelve yarns. The preforms were then infiltrated with the aluminum matrix containing 2 to 3% lithium by means of the liquid metal vacuum infiltration technique. The infiltration process was carried out at E. I. Du Pont Company in Wilmington, Delaware. All specimens were tested in the as-cast condition and cutting or machining was avoided as much as possible in order to maintain the integrated fiber structure.

The composites reported in this paper were the first batch of 3-D braided FP/Al-Li specimens made; thus, due to the experimental nature of the fabrication process, they had a low fiber volume percent, V_f, of about 17%.

All specimens were examined prior to testing by ultrasonic C-scan technique and were found to contain occasional flaws due to an insufficient infiltration of fibers.

Tensile, Compressive, and Shear Tests

The experimental procedures for tension, compression, and shear tests have been previously described [*11*]. Tension tests were conducted on parallel sided composite specimens parallel and perpendicular to the braiding axis and on specimens of unreinforced matrix material. Acoustic emission (AE) data were collected during tension tests with a Physical Acoustics Corporation (PAC) Model 3000/3004 AE System to gain information about the onset and perhaps the mechanism of failure.

Compressive tests were performed parallel to the braiding axis on specimens with reduced width in the gage length. These were done in an Illinois Institute of Technology Research Institute (IITRI) fixture.

Shear testing of the braided composite proved difficult as discussed previously [*11*]. In-plane shear tests were conducted both parallel and perpendicular to the braiding axis utilizing the Iosipescu shear test method [*14*]. While the strength measurements obtained from the Iosipescu test were quite reproducible, the strain readings were highly inconsistent, giving questionable data for the shear modulus. The interlaminar shear strength was measured by the double-slotted shear test described in ASTM Test method for In-Plane Shear Strength of Reinforced Plastics (D 3846).

Fracture Toughness Tests

Fracture toughness was measured in both longitudinal (crack running perpendicular to the braiding axis) and transverse (crack running parallel to the braiding axis) directions. For these, 6.3 mm thick compact tension (CT) specimens were used. The geometry and dimensions of the compact tension specimens, shown in Fig. 1*a*, were in accordance with those specified in the ASTM Test Method for Plain-Strain Fracture Toughness of Metallic Materials (E 399) standard practice except that the machined crack was not sharpened by fatigue loading. A standard clip gage was used to monitor the crack opening displacement (COD) during the test. Tests were conducted on an Instron testing machine at a crosshead speed of 0.008 mm/s.

Each specimen was loaded until a load drop was observed in the load-COD curve upon which the material was unloaded, and the crack extension was measured under a rolling microscope. This loading-unloading process was repeated several times for each specimen until the crack length to specimen width ratio, a/w, became larger than 0.6. Some specimens were broken in halves for microscopy.

In addition to the compact tension specimens, a few tests were also conducted on the work of fracture (WOF) type of specimens [*15*] shown in Fig. 1*b*. The specimen was broken in halves in three-point bending and the total energy absorbed during the complete fracture was measured by a weighing method.

Drop-Weight Impact Tests

Instrumented drop-weight impact tests were carried out on square plates of composites with 76 by 76 by 6.3 mm dimensions. The impactor was a steel hemisphere of 12.7 mm diameter, and the specimen was clamped to a circular support of 50 mm diameter. In addition to the 3-D braided material, specimens of unidirectional FP/Al-Li with a fiber volume loading of 34% and the unreinforced Al-Li matrix material were also tested for comparison. These specimens had the same dimensions as the braided composites.

Impact tests for the braided composite and the unreinforced matrix material were conducted on a "Dynatup" impact instrument at dart energies of 292 and 614 J, respectively. The unidirectional composite was tested with an impact equipment designed and built by the Imperial Chemical Industries Company in Wilmington, Delaware at a dart energy of 135 J.

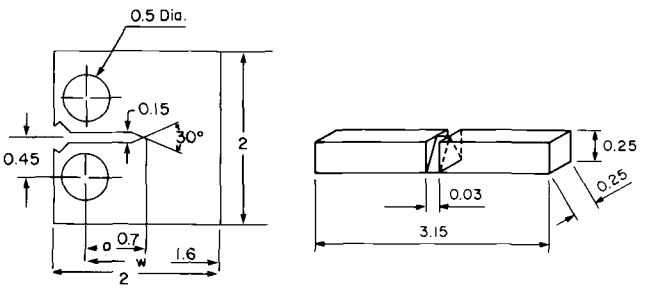

FIG. 1—*Schematic of* (a) *compact tension and* (b) *work of fracture specimens.*

Microscopy

Some of the specimens were sectioned after failure and prepared for examinations by scanning electron (SEM) and optical microscopes. Specimens for optical microscopy were mounted in a cold setting resin and were ground and polished down to a 1 μm finish with diamond paste and minimum applied pressure to avoid further damage. Those for SEM were given a thin coat of gold to enhance electrical conductivity.

Results

Tensile, Compressive, and Shear Properties

The mechanical properties are summarized in Table 1. Details of most of the results shown in Table 1 can be found in Ref *11*. Figure 2 shows the stress-strain curves and acoustic emission data for the axial and transverse specimens in tension. For comparison, data for the unreinforced Al-Li matrix are also shown in Fig. 3. In axial tension, the stress-strain curve demonstrated a "knee" at about 0.03% strain. In spite of the considerable fiber misalignment, the ultimate failure strain was only 0.3%, that is, almost identical to that obtained for unidirectional FP/Al-Li composites [*16,17*]. Specimens were believed to fail

TABLE 1—*Mechanical properties of FP/Al-Li Composites* (V_f = *17%*).

Property	3-D Braided[a]		±20° Angle Ply[b] theoretical	0° Unidirectional[c] theoretical
	Experiment	Theoretical		
		TENSION		
Ultimate strength (MPa)				
axial[d]	189	...	281.3	307.7
transverse	105	...	114.6	94.7
Young's modulus (GPa)				
axial[d]	97	113.4	114.3	135.0
transverse	87	97.6	97.7	87.1
Poisson's ratio				
axial[d]	0.33	0.33	0.36	0.31
transverse	0.31	0.29	...	0.20
		AXIAL COMPRESSION		
Ultimate strength (MPa)[d]	837.6	...	...	1482
Young's modulus (GPa)[d]	106.0	115.6	114.3	153
Poisson's ratio	0.30	0.33	0.36	0.31
		SHEAR		
Interlaminar strength (MPa)[d]	144.5	...	...	100.8
In-plane strength (MPa)				
parallel to fibers	126.5	...	151.2	100.8
perpendicular to fibers	142.3	...	...	...
In-plane modulus (GPa)	...	37.4	42.3	32.5

[a] Based on the "fiber inclination model" [*8*].

[b] Calculated from the classical lamination theory.

[c] The axial tensile strength and elastic moduli are predicted from the rule of mixtures; transverse tensile and shear strengths are based on equations given by Chamis [*19*]; and compressive strength is calculated from equation suggested by Rosen et al. [*23*].

[d] Data from Ref *11*.

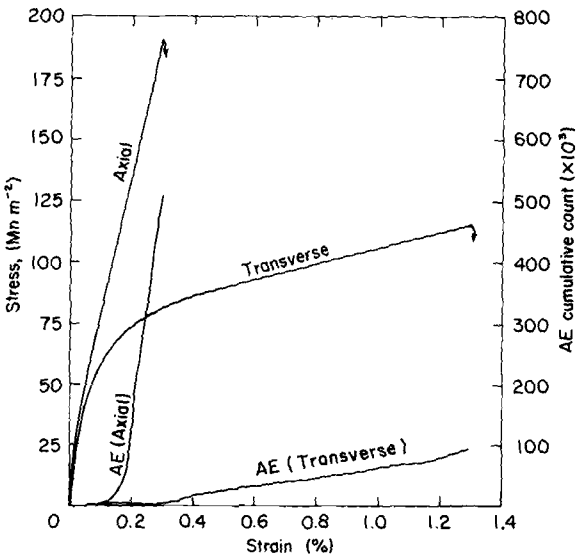

FIG. 2—*Stress-strain behavior and acoustic emission output for braided FP/Al-Li composite (V_f = 0.17) in the axial and transverse directions.*

by a cumulative fiber fracture mechanism in which as soon as enough fibers in one fiber bundle broke, catastrophic failure of the whole composite would occur. The fracture surface did not show any fiber pullout indicating the presence of a strong fiber-matrix interface.

In transverse tension, the stress-strain curve was highly nonlinear. The onset of nonlinearity was at a strain of approximately 0.05%. While the Young's modulus was only slightly lower, the ultimate strength in the transverse direction was considerably lower than that for

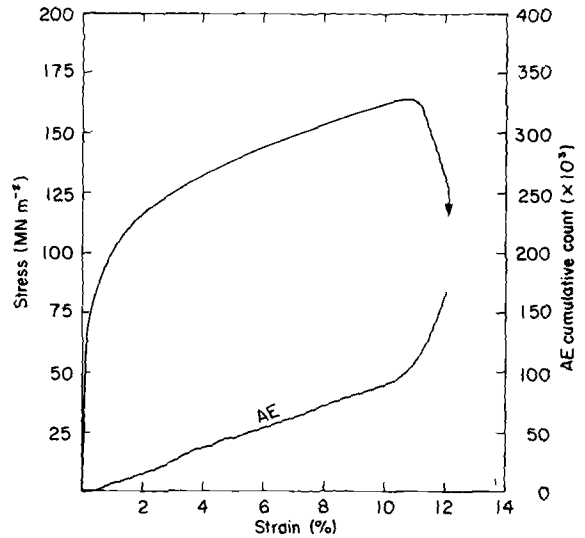

FIG. 3—*Stress-strain behavior and acoustic emission response for the neat Al-Li matrix material.*

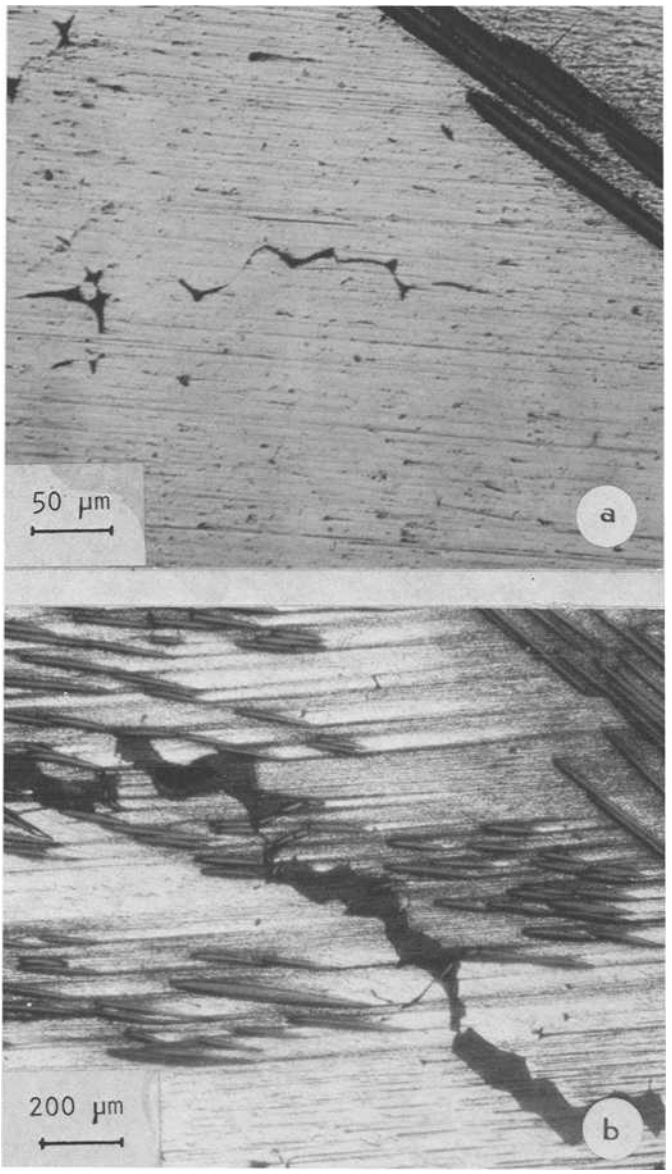

FIG. 4—*Crack morphology in transverse tension depicting* (a) *crack initiation in the matrix and* (b) *crack running through the fiber bundle in the braided FP/Al-Li composite.*

the axial specimen and for that matter considerably smaller than that of the unreinforced matrix material shown in Fig. 3. From the microscopic examinations after failure, it appeared that transverse cracks had started within the matrix-rich areas between fiber bundles from what seemed to be microscopic voids in the matrix, Fig. 4. Some of these cracks had extended along the interface of the fiber bundles with the matrix. In contrast to the strength, the

failure strain in the transverse direction (~1.3%) was much larger, by a factor of four, than that in the axial direction.

The amplitude distribution of AE signatures, shown in Fig. 5, revealed some distinct differences in the AE response of the three types of tension specimens tested. For the unreinforced Al-Li material, the amplitude of events was in the range of 20 to 60 db with maximum events occurring at around 20 db. The amplitude distribution for the transverse tension specimen was very similar to that of the matrix material indicating that transverse tensile failure was predominated by a matrix failure mode. It must be pointed up that the threshold amplitude used for the matrix specimens was somewhat lower than that for the composite materials. For the longitudinal tension specimen, however, the AE events had significantly larger amplitudes between 50 to 90 db. It was noted that in all three specimens events generated during initial stages of loading generally had lower amplitudes and that the higher amplitude events began only after the initial rapid rise in the AE counts shown in Figs. 2 and 3. For the axial tension specimen, the high amplitude events (>70 db) mostly occurred just prior to the final failure.

Detailed descriptions of the compressive and shear properties have been previously reported [*11*]. Briefly, the axial compressive stress-strain curve was considerably nonlinear, and specimens broke at a strain of about 1.7%. Kinking was the prevailing mode of compressive failure as also found for unidirectional FP/Al-Li composites [*16,18*].

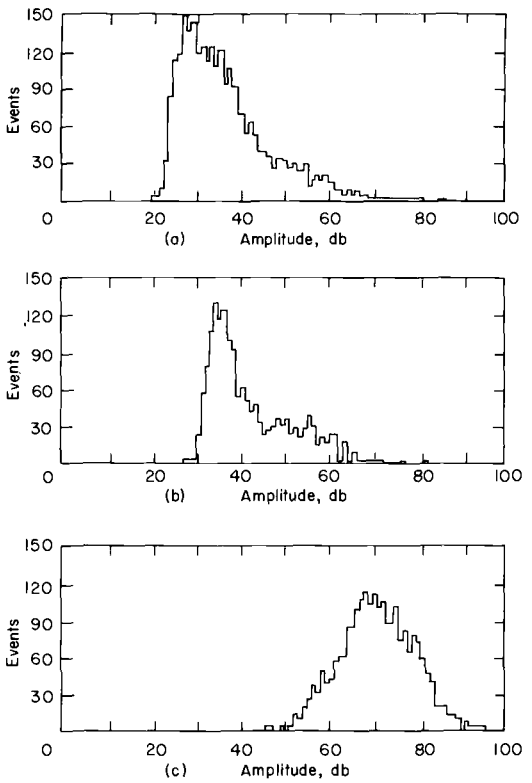

FIG. 5—*Amplitude distribution of acoustic emission events obtained during tension testing of* (a) *neat matrix material,* (b) *braided composite in transverse direction and* (c) *braided composite in axial direction.*

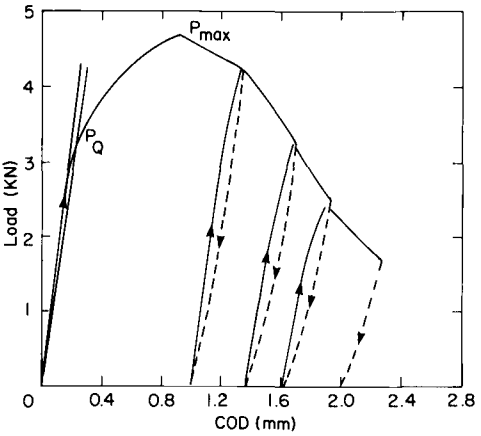

FIG. 6—*Typical load-COD curve obtained during repeated loading of compact tension specimen of braided FP/Al-Li composite in the axial direction.*

Fracture Toughness Results

The load-COD curves for repeated loading-unloading of axial and transverse compact tension specimens demonstrated a significant amount of hysteresis. An example of this is given in Fig. 6 for the longitudinal specimen. For the first loading cycle, the specimen had a machined crack. The load-COD curve for the machined crack was highly nonlinear, and COD increased rapidly as load approached its failure value. For the subsequent loading cycles, the crack was naturally sharpened and the load-COD curve was much less nonlinear. This decreased nonlinearity could be due to a number of factors including a higher stress concentration at the tip of the sharp crack, crack tip work hardening of the matrix, and the presence of damage from the previous loading event. Also, note that for subsequent loadings, failure occurred at a load somewhat smaller than the original load from which the specimen had been unloaded. Recent experiments employing AE measurements indicated that on reloading, the onset of AE signals occurred at a load appreciably below the level from which the specimen had been unloaded.

The stress-intensity factors for axial and transverse specimens are shown in Table 2. K_Q-values are calculated from the load P_Q which is determined by drawing a secant line with a slope 5% less than the initial slope of the load-COD curve as specified in the ASTM E 399 standard procedure. The K_{max}-values are based on the maximum load, P_{max}, achieved during each loading increment. Note that for the initial machined crack, K_Q-values are significantly smaller than K_{max}-values due to the highly nonlinear load-COD curves.

Figure 7 depicts the variation of K_{max} with a/w ratios, showing a reasonable amount of scatter.

Crack propagation characteristics for both axial and transverse compact tension specimens are shown in Fig. 8. In the axial case, there was a great deal of fiber fracture ahead of the crack tip and crack propagated by tensile fracture of fiber bundles and shearing of the matrix. These specimens showed some pullout of the whole fiber bundle to a length of 1 to 2 mm. In the transverse specimen, crack propagation was mostly along the interface of fiber bundles with the matrix.

Table 2 also reports the fracture surface energies obtained from CT and WOF specimens.

TABLE 2—*Fracture toughness data for 3-D braided FP/Al-Li composite* (V_f = 17%).

	CT Specimen				WOF Specimen
Test Direction	$\overline{K}_Q$,MPa · $m^{1/2}$ Machined Crack	$\overline{K}_Q$,MPa · $m^{1/2}$ Natural Crack	$\overline{K}_{max}$,MPa · $m^{1/2}$	$\overline{\gamma}_i$,KJ m^{-2}	$\overline{\gamma}_f$,KJ m^{-2}
Longitudinal	16.48 ± 2.14	22.80 ± 3.10	24.85 ± 3.04	3.4	7.9
Transverse	10.64 ± 1.34	16.58 ± 2.13	17.37 ± 2.26	2.4	...

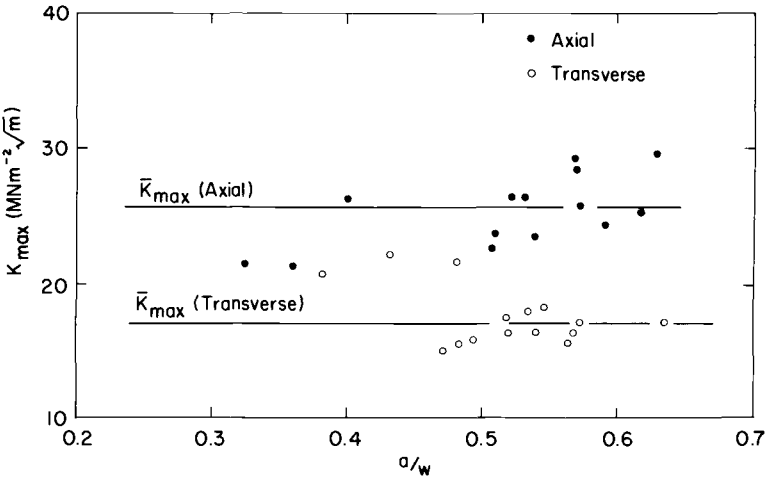

FIG. 7—*Variation of the stress intensity factor,* K_{max}, *with crack length to width ratio,* a/w, *for compact tension specimens of braided FP/Al-Li composite.*

γ_i is the fracture surface energy for crack initiation calculated from the maximum load on CT specimens, and γ_f is the effective fracture surface energy obtained by dividing the total energy absorbed during the complete separation of the two halves of the WOF specimen by the surface area of the unnotched portion of the cross section.

Drop-Weight Impact Behavior

A typical load-deflection and absorbed energy curve obtained during the instrumented impact testing of 3-D braided composite is shown in Fig. 9. The impact data are also given in Table 3 for the case of through-the-thickness penetration of the impactor for the three materials tested. In Table 3, the crack initiation energy is the amount of energy absorbed by the specimen from the start of the impact up to the maximum load, and propagation energy is that from the maximum load to the end of the impact event.

From the energies given in Table 3 and damage characteristics shown in Figs. 10 and 11, it is clear that the 3-D braided composite has a greater damage tolerance than the unidirectional laminate. The unidirectional composite fractured like a brittle material with cracks propagating through the entire length of specimen; while, in the braided composite, damage was restricted to a small region, and the material showed a ductile type of behavior. The inferior impact properties of the unidirectional composite could be partly due to its higher, by a factor of two, fiber volume fraction. Both composites showed considerably smaller crack initiation energies than the unreinforced metal matrix; however, the energy for the unidirectional composite was almost five times smaller than that for the braided material. During the crack propagation stage, the braided composite absorbed more energy than the unreinforced matrix, thus bringing its total impact energy close to that of the monolithic material. The crack propagation and total energies reported for the unidirectional composite could be somewhat overestimated because of the occurrence of circumferential cracks in this material, Fig. 11. Circumferential cracks which develop in later stages of the impact event lead to increases in the propagation and total impact energies. This secondary damage mode, which often occurs during testing of brittle materials, was not observed for the 3-D braided composite.

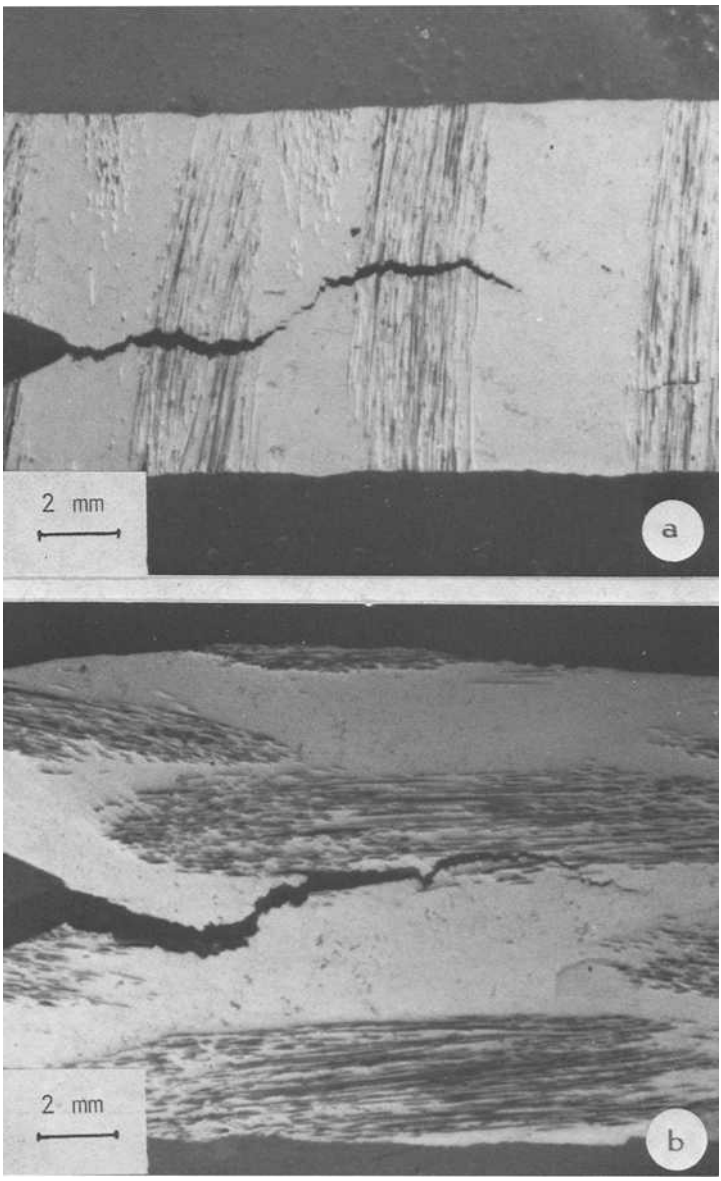

FIG. 8—*Crack morphology in compact tension specimens of the braided FP/Al-Li composite in the* (a) *axial and* (b) *transverse directions. Note the broken fiber bundle ahead of the crack tip in* (a).

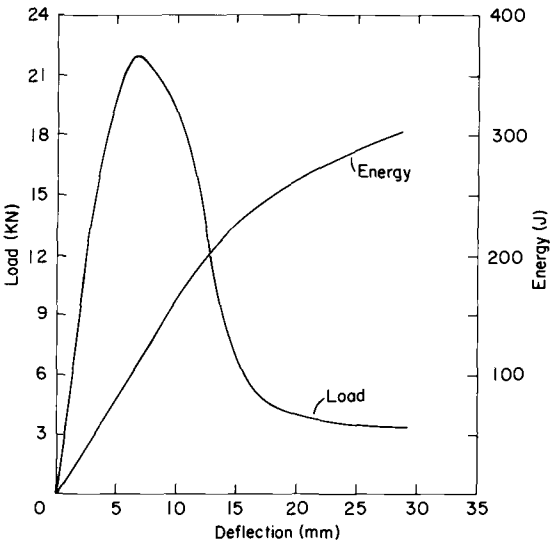

FIG. 9—*Typical load-energy-deflection curve obtained during instrumented drop-weight impact testing of the braided FP/Al-Li composite for a through-the-thickness penetration.*

Discussion and Conclusions

In both areas of damage tolerance and interlaminar shear strength where 3-D braided composites are believed to out-perform the conventional 2-D laminates, the braided FP/Al-Li composite displayed a strong performance. The interlaminar and in-plane shear strengths of the composite with a fiber volume fraction of 17% tested in this work were only slightly smaller than its axial tensile strength (Table 1). The instrumented drop-weight impact tests also showed that the impact resistance of the braided composite is superior to that of the unidirectional laminate in terms of both the amount of energy absorbed and the size of damage zone. These data are presented in Table 3 and Figs. 10 and 11. While the lower fiber volume fraction of the braided composite may have an important part in its higher impact energy, there are clear indications from comparisons with monolithic Al-Li material and damage characteristics of the two composites that the 3-D integrated structure also has an effective role in providing crack arresting mechanisms that control the fracture and increase the impact energy. The braided composite absorbed almost as much energy

TABLE 3—*Drop-weight impact properties.*

Material	Impact Energy Absorbed, J			Maximum Load, KN
	Initiation	Propagation	Total	
3-D braided FP/Al-Li (V_f = 0.17)	68	196	264	25.6
Unidirectional FP/Al-Li (V_f = 0.34)	14	112	126	11.7
Al-Li alloy	173	145	318	28.9

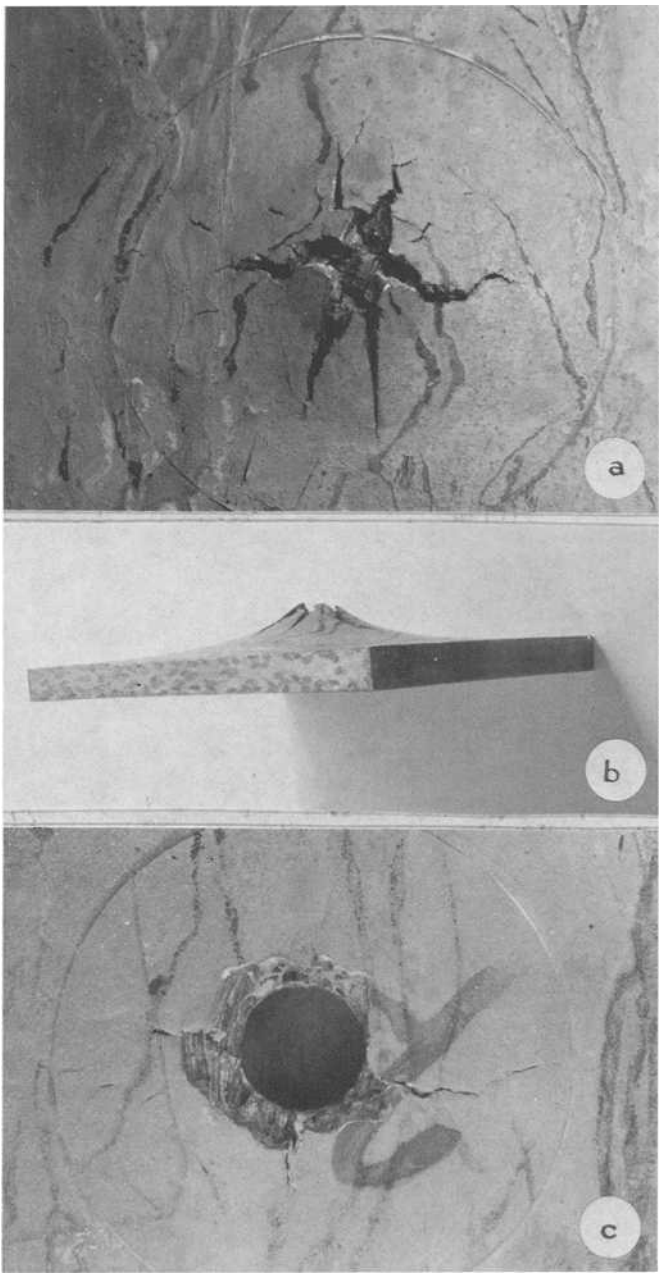

FIG. 10—*Failure characteristics of braided FP/Al-Li composite* (V_f = *0.17*) *subjected to drop-weight impact loading at* (a) *and* (b) *126J and* (c) *264J absorbed energy levels.*

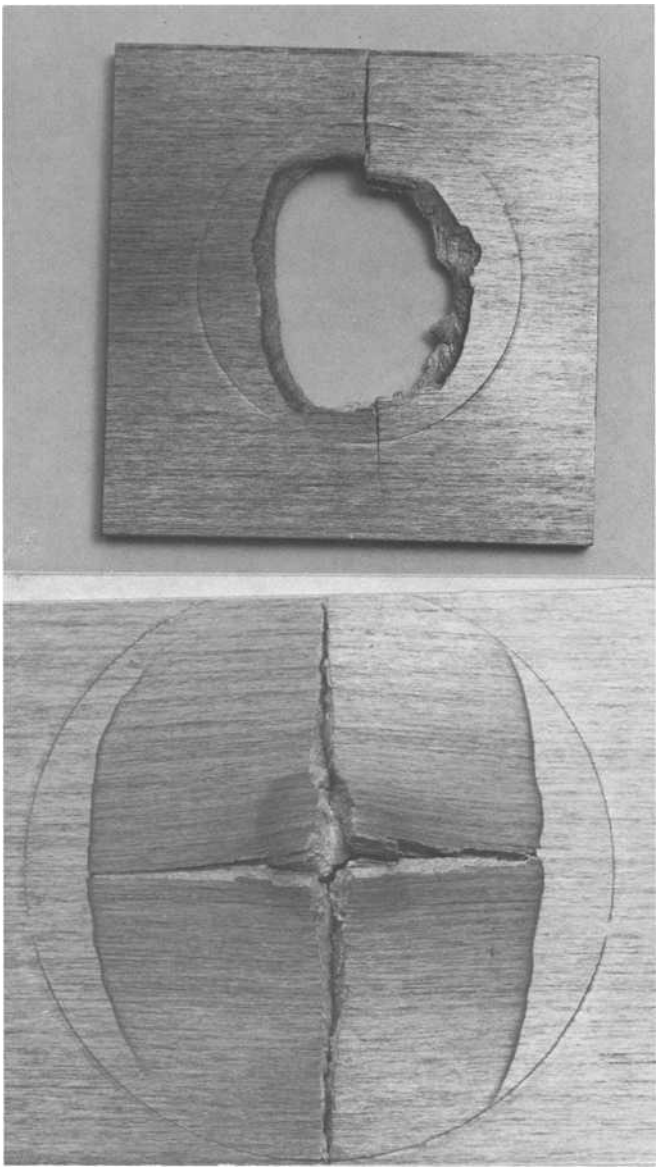

FIG. 11—*Failure due to drop-weight impact testing of unidirectional FP/Al-Li composite* (V_f = *0.34*). *Note circumferential cracking of the specimen.*

as the unreinforced matrix material. This was resulted from the larger crack propagation energy of the material even though it showed a considerably smaller crack initiation energy than the unreinforced Al-Li matrix. The difference in impact energies of the braided and unidirectional composites is expected to be even larger than that shown in Table 3 because of the occurrence of secondary, circumferential cracks in the unidirectional composite.

Circumferential cracks usually occur after the formation of main, radial cracks in a brittle material and result in false increases in the crack propagation and, therefore, total energies.

The in-plane properties of the braided FP/Al-Li composite having an average braid angle of 20° were very similar to those predicted for a ±20° angle-ply laminate (Table 1) except for the axial tensile strength and failure strain that were appreciably lower. The axial failure strain (~0.3%) was almost identical to that for 0° unidirectional laminates [*16,17*]. In contrast, unidirectional FP/Al-Li composites tested at 22.5° with respect to the fiber axis have shown a failure strain of 1.14% [*17*]. One reason for the low failure strain of the braided composite could be that fiber bundles go through 0° orientation as they change angle within the braided structure. These 0° segments of fibers, therefore, fail first at a composite strain equal to the failure strain of the 0° unidirectional laminate, and they thus trigger failure of the whole composite. Another possibility for the poor axial strength is fiber damage and bending induced by the braiding process. Fiber FP is very brittle and can be easily damaged during handling. In addition to fiber damage, there were other process-related defects such as flaws due to an inadequate infiltration and microscopic matrix voids that could further reduce the strength of the composite. These material defects could also account for the consistently lower experimental elastic moduli than those predicted by the "fiber inclination model" [*8*] as shown in Table 1.

In transverse tension, the braided composite broke at a stress of 105 MN m^{-2} which is considerably lower than the bulk matrix strength of 156 MN m^{-2}. Transverse failure was found to initiate in the matrix-rich regions from what appeared to be microscopic voids (Fig. 4). For unidirectional FP/Al-Li composites with a V_f of 55%, a transverse tensile strength of 213 MN m^{-2} has been reported [*16*]. It is possible that, in composites with high V_f where fibers are closely spaced, there is increased work hardening of the matrix leading to a higher *in situ* matrix strength and, therefore, higher composite transverse strength. Calculating the *in situ* strength of the matrix from the composite transverse strength of 213 MN m^{-2} using the equation given by Chamis [*19*] yields a value of 252 MN m^{-2}; an increase of almost 40% over the bulk matrix strength.

In addition to the matrix plastic deformation, fiber straightening in tension (or, deflection in compression) due to initially curved fibers [*20*] and off-axis shear caused by fiber misalignment may also contribute to the nonlinear behavior of braided composite. In axial tension, however, these effects are not expected to be significant because of the low failure strain of the material. The compressive strength is particularly sensitive to fiber curvature. Failure may be expected to occur by local microbuckling of fibers once the matrix yields under lateral stresses and fibers are more free to deflect. A simple model based on this mechanism has been developed by Piggot [*21*] for the compressive strength of composites with fibers having a sinusoidal shape. In the braided composite under investigation, fiber bundles assume an almost helical configuration within the structure, and the situation is therefore more complex particularly when fiber interactions are also taken into account.

The fracture toughness results shown in Table 2 indicate that the effective fracture surface energy, γ_f, obtained from WOF specimens is considerably larger than crack initiation energy, γ_i, calculated from K_{max}-values of CT specimens. The higher γ_f shows that crack propagation requires more energy than its initiation, thus meaning a slow crack growth. For CT specimens in both axial and transverse directions, the load-COD curve (Fig. 6) was highly nonlinear for the initial machined crack. K_{max} was therefore considerably larger than K_Q for the first load-COD curve. For subsequent loading cycles, the nonlinearity largely disappeared and K_Q approached K_{max}. The rapid increase in COD as specimen approached failure denotes extensive damage ahead of the crack tip such as fiber fracture, matrix plastic deformation, and void extension. Fracture surface of the axial specimen showed frequent pull out of the whole fiber bundle to a length of 1 to 2 mm.

The braided composite had a lower fracture toughness (K_{max}) in the axial direction than the unidirectional FP/Al-Li composite with 34% V_f [22], that is, 24.85 MPa $\sqrt{m}$ versus 31.7 MPa $\sqrt{m}$, respectively. In transverse direction, however, both materials showed virtually similar values of K_{max}.

Finally, because of the low V_f of FP/Al-Li composite tested, it is difficult to demonstrate the full capabilities of braided metal matrix composites or to provide a meaningful comparison of the properties with those of the unidirectional composites. It is hoped that a better understanding of the intricate nature of these composites and the advantages they offer over the conventional laminates can be achieved by investigating braided composites with a high fiber volume fraction.

Acknowledgments

This work is supported by the Office of Naval Research. Dr. L. H. Peebles, Jr., is the technical monitor.

References

[1] Chou, T. W., Kelly, A., and Okura, A., *Composites,* Vol. 16, 1985, p. 187.
[2] Shu, L. S., "Omniweave Composites," General Electric Company, Report No. GE-OMSD, PIR 2990-69, July 1969.
[3] Florentine, R. F., "Low-Cost High Performance Composites-Magnaweave Reinforcements for Pultrusion," Papers 10A and 10B, *Proceedings,* 37th Annual Conference, Reinforced Plastics/Composites Institute, The Society of Plastics Industry, Jan. 1982.
[4] Ko, F. K., "Three-Dimensional Fabrics for Composites-an Introduction to the Magnaweave Structure," in *Progress in Science and Engineering of Composites,* T. Hayashi and K. Tokyo, Eds., Japan, 1982; Proceedings of the ICCM-IV, Tokyo, Japan, 1982.
[5] Ko, F. K., "Developments of High Damage Tolerant, Net Shape Composites through Textile Structural Design," *Proceedings,* Fifth International Conference on Composite Materials, ICCM-V, W. C. Harrigan, J. Strife, and A. K. Dhingra, Eds., San Diego, CA, 29 July-1 Aug., 1985.
[6] Yang, J. M., Ma, C. L., and Chou, T. W., "Elastic Stiffness of Biaxial and Triaxial Woven Fabric Composites," in *Proceedings*, 29th National SAMPE Symposium, Society of Aerospace Materials and Process Engineers, April, 1984 pp. 292-303.
[7] Ma, C. L., Yang, J. M., Chou, T. W., "Elastic Stiffness of Three-Dimensional Braided Textile Structural Composites," in *Composite Materials: Testing and Design* (Seventh Conference, *ASTM STP 893,* American Society for Testing and Materials, Philadelphia, PA, 1986, pp. 404-421.
[8] Yang, J. M., Ma, C. L., and Chou, T. W. "Fiber Inclination Model of Three-Dimensional Textile Structural Composites," *Journal of Composite Materials,* in press.
[9] Yang, J. M. and Chou, T. W., "Thermo-Elastic Analysis of Three-Dimensional Fabric Composites," in *Advances in Aerospace Science and Engineering,* U. Yuceoglu and R. Hesser, Eds., American Society of Mechanical Engineers, New York, 1984.
[10] Chou, T. W., Shehata, B. I., and Yang, J. M., "Analytical and Experimental Studies of Textile Structural Composites," *Proceedings,* International Conference on Rotorcraft Basic Research, American Helicopter Society and Army Research Office, 1985.
[11] Majidi, A. P., Yang, J. M., Pipes, R. B., and Chou, T. W., "Mechanical Behavior of Three-Dimensional Woven Fiber Composites," *Proceedings,* Fifth International Conference on Composite Materials, ICCM-V, W. C. Harrigan, J. Strife, and A. K. Dhingra, Eds., San Diego, CA, 29 July-1 Aug., 1985.
[12] Dhingra, A. K., Champion, A. R., and Krueger, W. H., "Fiber FP Reinforced Aluminum and Magnesium Composites," in *Proceedings,* First Metal Matrix Composite Workshop, Paper Number C-501, Institute for Defense Analyses, Washington DC, Sept. 1975.
[13] Dhingra, A. K., Philosophical Transactions of the Royal Society, London, A294, 1980, p. 559.
[14] Walrath, D. E. and Adams, D. F., "The Iosipescu Shear Test as Applied to Composite Materials," *Experimental Mechanics,* Vol. 23, 1983, p. 105.
[15] Tattersall, H. G. and Tappin, G. J., Journal of Materials Science, 1966, p. 296.
[16] Shetty, H. R. and Chou, T. W., *Metallurgical Transactions,* Vol. 16A, 1985, p. 853.

[17] Page, R. A. and Leverant, G. R., "Relationship of Fatigue and Fracture to Microstructure and Processing in Al_2O_3 Fiber Reinforced Metal Matrix Composites," *Proceedings,* Fifth International Conference on Composite Materials, ICCM-V, W. C. Harrigan, J. Strife, and A. K. Dhingra, Eds., San Diego, CA, 29 July-1 Aug., 1985.
[18] Pattnaik, A., Koczak, M. J., and Rogers, H. C., "Compressive Failure Behavior of FP Alumina/Aluminum Composites," *Proceedings,* AIME Conference, American Institute of Mining, Metallurgical, and Petroleum Engineers, St. Louis, MO, 1978.
[19] Chamis, C. C., SAMPE Quarterly, Society for the Advancement of Material and Process Engineering, 15, 1984, p. 41.
[20] Chou, T. W. and Takahashi, K., submitted to *Metallurgical Transactions.*
[21] Piggott, M. R., *Journal of Materials Science,* Vol. 16, 1981, p. 2837.
[22] Richter, M. A., "Mechanical Characterization and Fracture Investigation of FP/Aluminum Unidirectional Composite Materials," M.A.S. thesis, Center for Composite Materials, University of Delaware, Newark, DE, Dec. 1984.
[23] Dow, N., Rosen, B. W., and Hashin, Z., NASA-CR-492, National Aeronautics and Space Administration, Washington, DC, June 1966.

Frank Ko,[1] *Ali Razavi,*[1] *and H. C. Rogers*[1]

An Evaluation of the Failure Behavior of 3-D Braided FP/Aluminum-Lithium Composites Under Static and Dynamic Blanking

REFERENCE: Ko, F., Razavi, A., and Rogers, H. C., **"An Evaluation of the Failure Behavior of 3-D Braided FP/Aluminum-Lithium Composites Under Static and Dynamic Blanking,"** *Testing Technology of Metal Matrix Composites, ASTM STP 964,* P. R. DiGiovanni and N. R. Adsit, Eds., American Society for Testing and Materials, Philadelphia, 1988, pp. 48–64.

ABSTRACT: The adiabatic shear stability of unreinforced, unidirectionally reinforced and 3-D braid reinforced aluminum-lithium were studied by static and dynamic blanking at various deformation levels. Comparing to Hadfield steel, no apparent adiabatic shear was detected in any of these materials. The failure mechanism of these structures were identified by microstructural analysis.

KEY WORDS: adiabatic shear, aluminum-lithium, unidirectional fiber reinforcement, metal matrix composite, 3-D braid, static blanking, dynamic blanking, microstructural analysis

As part of a study on the failure behavior of braided 3-D composites, static and dynamic blanking were used to characterize the penetration resistance of FP[2] Al_2O_3/Al-2.5Li composites. The blanking process, used extensively to evaluate the shear behavior of metallic materials, was also found to provide useful information on the through-thickness shear resistance of 3-D braided metal matrix composites. Braided composites were tested under an impact velocity of 44 m/s. The shear behavior of the composites is characterized and compared to that of the unreinforced aluminum-lithium (Al-Li) matrix material and of FP uniaxial tape reinforced Al-Li composites.

One important aspect of the response of these materials to dynamic shear loading examined in this study is their respective susceptibilities to adiabatic shear localization.

Adiabatic shear bands are the most extreme manifestation of localized flow produced by high strain rate deformation. In monolithic metals these bands tend to form during ballistic penetration as well as high rate machining and forming processes. The two principal factors contributing to dynamic flow localization are: (1) 95% of the work of plastic deformation is converted to heat and (2) the flow stress of materials decreases with increasing temperature. Thus, during high strain rates, the heat generated by localized plastic deformation cannot be dissipated by thermal conductivity; the resultant adiabatic temperature rise weakens the material locally stimulating further deformation localization [*1–4*]. Thus with many speci-

[1] Associate professor, research associate, and professor, respectively, Fibrous Materials Research Center, Drexel University, Philadelphia, PA 19104. Dr. Razavi is currently with Materials Engineering Department, Wilkes College, Wilkesbarre, PA 18766.

[2] FP is a registered trademark of Du Pont's α-alumina fiber.

men/indenter geometries, a shear band in which the deformation is much greater than in the surrounding microstructure is generated. Furthermore, the highly localized strain associated with an adiabatic shear band often leads directly to fracture of the impacted target. At normal deformation rates, however, thermal conductivity permits only a modest increase in temperature, thus reducing substantially the degree of strain localization in the specimen. Accordingly, the objective of this study was to examine the usefulness of the blanking process for the evaluation of the failure behavior of metal matrix composites. Specifically, the static and dynamic response of Al-Li reinforced by unidirectional fiber and by 3-D braided fiber were compared to that of pure Al-Li alloy. The microstructure of these composites were examined to detect the occurrence of adiabatic deformation.

Experimental Procedure

Target Material and the Blanking Process

The target materials used for this study are the Al-Li alloy in the as-cast condition, unidirectional FP fiber reinforced Al-Li and 3-D braided FP fiber reinforced Al-Li. These target materials were selected so that the merit of various fiber reinforcements could be assessed. Specifically, the effect of fiber architecture was examined. The reinforcing FP fiber is a continuous polycrystalline α-alumina yarn produced by the Du Pont Co. Table I provides a summary of its properties. The 3-D braided preforms were fabricated in our laboratory with a 1 by 1 braid construction. The formation of this fabric preform has been detailed in Refs *5* and *6*. The composites were prepared at Du Pont by the vacuum infiltration process. The Al-Li specimens and the unidirectionally reinforced FP/Al-Li composites were obtained from Du Pont. The fiber volume fraction for the 3-D braid composites ranged from 17 to 40%, while it was approximately 34% for the unidirectionally reinforced Al-Li composite. Square target specimens 25.4 by 25.4 by 6.25 mm, (1 by 1 by 0.25 in.) were cut from the FP composites and homogeneous Al-Li alloy. For both unidirectional and 3-D fiber targets, the edges of the specimens were cut perpendicular to the fiber orientation.

Blanking and similar industrial processes such as punching are by no means new. Chang and Swift [*7*] carried out a comprehensive study of shearing. Later, Johnson and Slater [*8*] carried out an extensive study of slow and fast blanking of homogeneous materials. This work in particular provides a background for the current interest in the effects of the rate of deformation, temperature, and stress wave propagation. Since blanking can be studied using simple geometrical configurations, it is relatively easy to examine a number of im-

TABLE 1—Fiber FP filament properties.

Tensile strength	1380 MPa (200 ksi)
Tensile modulus	345 to 380 GPa (50 to 55 Msi)
Compressive strength	6900 MPa (1000 ksi)
Compressive modulus	345 to 380 GPa (50 to 55 Msi)
Tensile elongation	0.4%
Density	3.90 g/cm^3 (0.141 lb/in.^{2})
Specific strength	3.56 $\times$ 10^6 cm (1.4 $\times$ 10^6 in.)
Specific modulus	8.89 $\times$ 10^8 cm (3.5 $\times$ 10^8 in.)
Melting point	2045°C (3713°F)
Filament diameter	20 to 5 μm
Cross section	round
Filaments/yarn	210

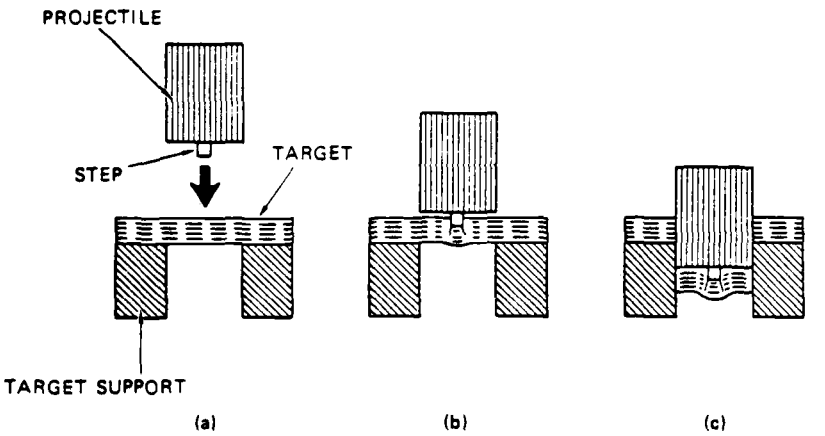

FIG. 1—*Schematic presentation of* (a) *the blanking process and* (b, c) *penetration steps.*

portant fundamental aspects of fracture behavior during blanking. These include shear instability, the initiation and propagation of cracks, and damage to the structure both at low and high velocities.

The blanking test configuration used for both static and dynamic impact in the present investigation is shown schematically in Fig. 1. The target materials were inserted into a blanking die with a hole in the back support plate having a 12.5 mm (0.5 in.) diameter. The projectiles used for static blanking had a step 4.0 mm in height and 6.25 mm in diameter. Low velocity (static) blanking was carried out on an Instron testing machine at a crosshead velocity of 0.5 mm/min. The depth of penetration as revealed in the sectioned specimens provides a measure of the punch and projectile displacements. Close agreements were noted between the measurements of the deformation shown in the sectioned specimen and the autographic record.

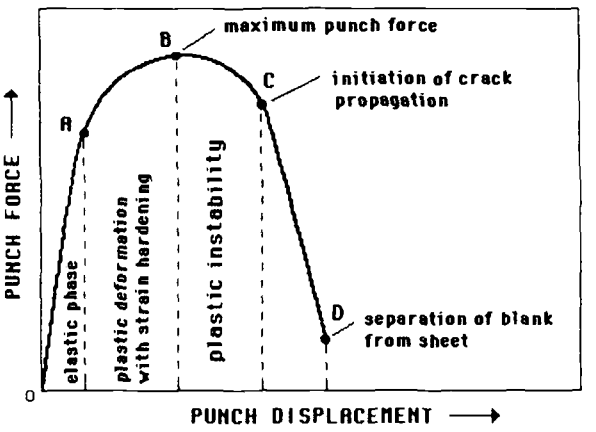

FIG. 2—*Schematic presentation of the force-displacement diagram for the static and dynamic blanking process.*

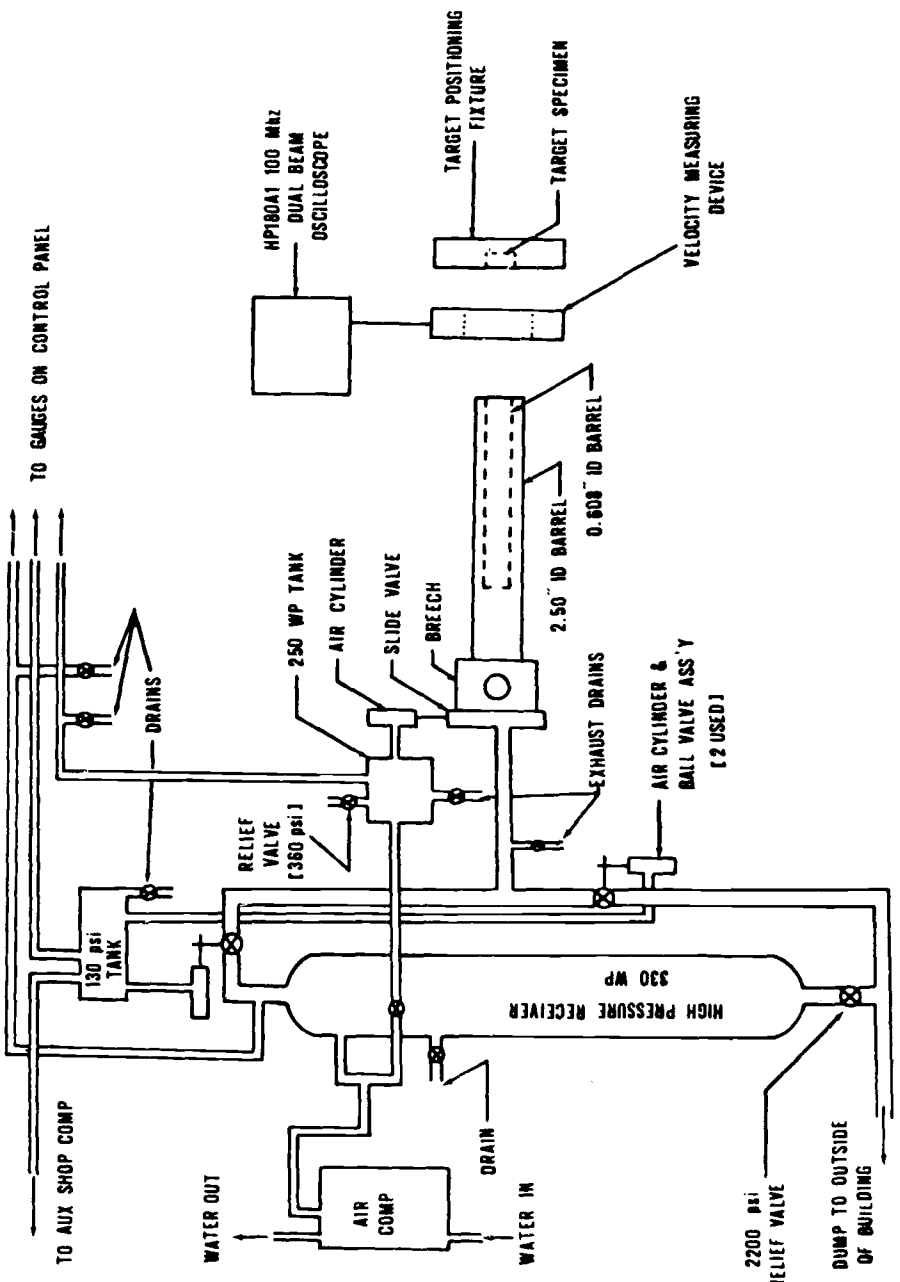

FIG. 3—*A schematic diagram of the air gun and the velocity measurement device.*

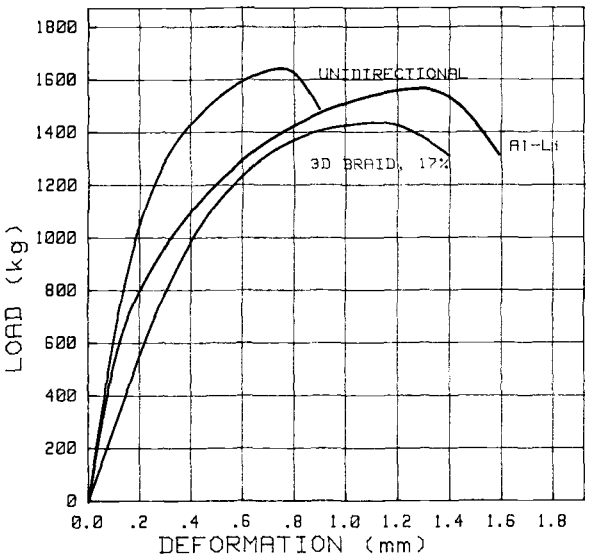

FIG. 4—*Load-deformation relationships of various target materials under static blanking.*

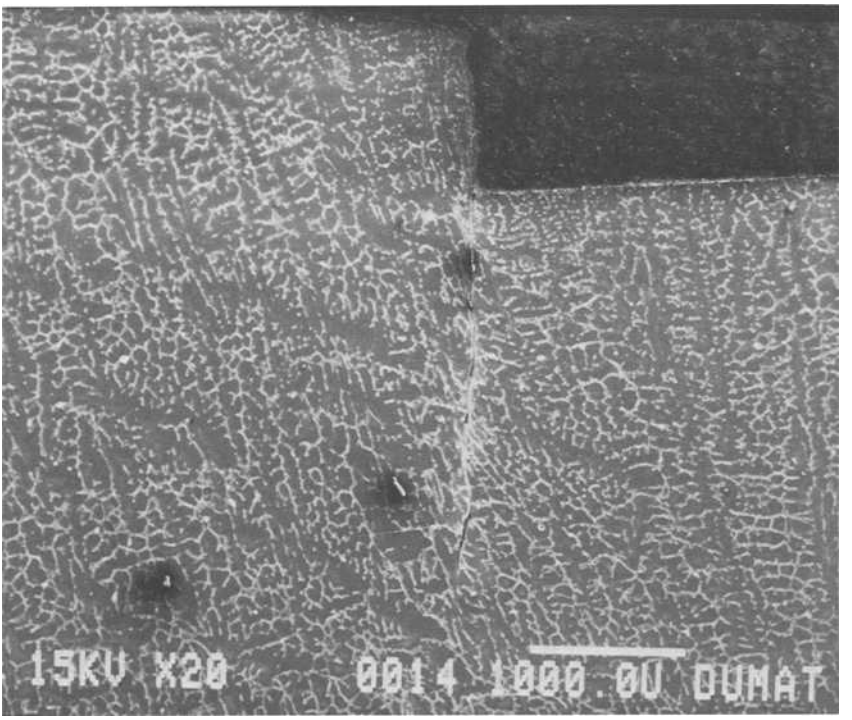

FIG. 5—*SEM picture of the penetration side of the homogeneous Al-Li target after static blanking.*

In addition, a schematic force-displacement diagram for both low and high velocity blanking processes at ambient temperature is shown in Fig. 2 with the individual stages of the process labeled. Although plastic deformation increases between A and C in Fig. 2, the punch force attains its maximum at some intermediate displacement, B. This implies some form of plastic instability phenomenon or cracking or both. During the post-instability phase between B and C, plastic flow localizes, and microcracks may be initiated somewhere within the initially crack-free body. Beyond C, the punch force drops dramatically as a result of the coalescence of small cracks and subsequent propagation of the resulting macrocrack. This terminates in the separation of the blank (plug) from the sheet.

Compressed Air Gun and Velocity Measurement

Stepped projectiles of hardened steel were fired at different velocities into composite targets using a compressed air gun, shown schematically in Fig. 3. The velocity of a projectile prior to target impact was measured by an opto-electronic system with the detectors positioned between the shotgun barrel and the target fixture (Fig. 3). The velocity was measured by allowing the projectile to interrupt two light beams having a known separation. The output from each of the two photodiodes illuminated by the beams was fed into a storage oscilloscope, enabling the average time for the projectile to travel between light beams to be calculated and hence the average projectile velocity.

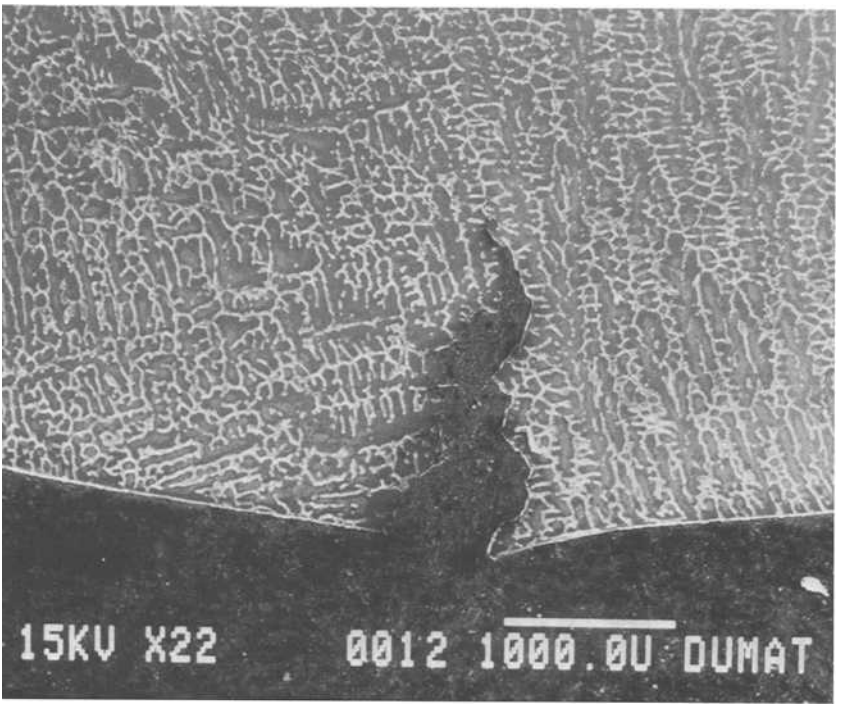

FIG. 6—*SEM picture of the back side of the homogeneous Al-Li target after static blanking.*

Results and Analysis

Static Blanking

The autographic load versus deformation test results are shown in Fig. 4. To study instability and fracture under static blanking conditions, each target material was sectioned after they were loaded beyond the maximum loading at 0.9 and 1.4 and 1.6% deformation for unidirectional, 3-D braiding, and pure Al-Li, respectively. The Al-Li alloy, seen in Fig. 5, shows fracture propagation well inside the unsheared section of the target, parallel to the penetration. Figure 6 shows the intergranular fracture on the back side of the target caused by the bending strain imposed by the punch. An intergranular fracture mode was also observed on the back side of the FP composite. The large grain size of the cast material is the reason for this behavior. Figure 7 shows a severe double shear strain localization for a unidirectional composite. Fiber failure within the shear zone is also evident. The 3-D FP

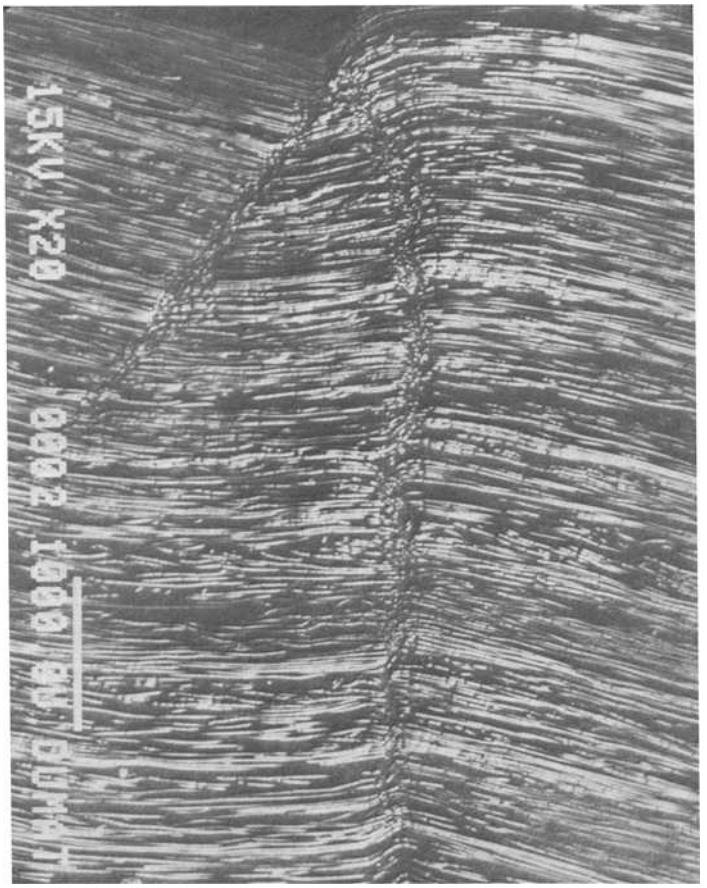

FIG. 7—*SEM picture of the penetration side of the unidirectionally reinforced FP/Al-Li composite.*

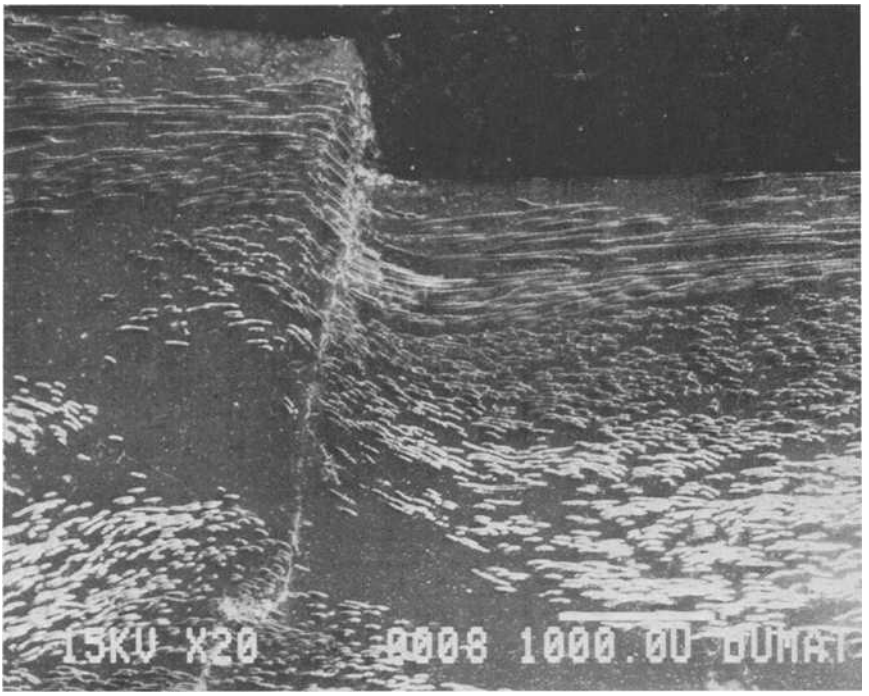

FIG. 8—*SEM picture of the penetration side of the 3-D braid reinforced Al-Li composite.*

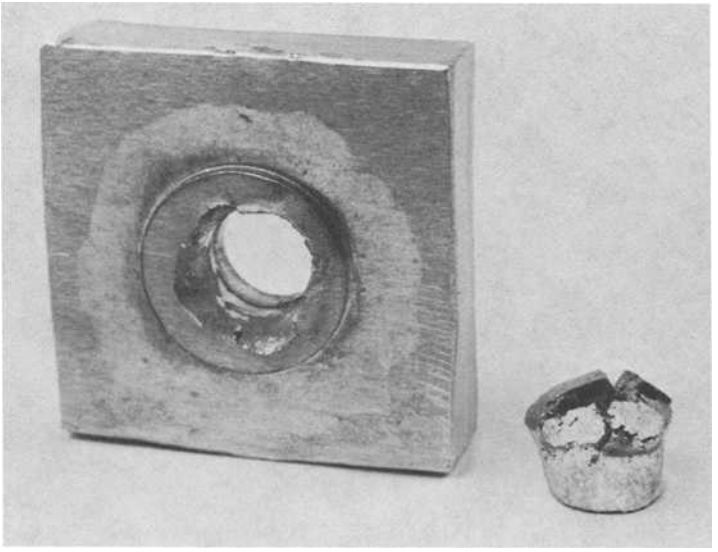

FIG. 9—*Light microscope picture of the homogeneous Al-Li target and the plug formed by dynamic blanking.*

composite behavior, shown in Fig. 8, demonstrates a more diffuse type of shear strain localization. The statically blanked Al-Li alloy and FP composites were susceptable to shear strain localization leading to instability and fracture. The severe shear strain localization observed in the unidirectional composite could be the cause of its limited ductility under static blanking and lack of intra- and inter-laminar reinforcement.

Dynamic Blanking

Under high velocity blanking conditions all three target materials showed little resistance to plug formation. When impacted by a projectile having a 4.0 mm step height at 44.0 m/s velocity, the step on the front of the projectile penetrated the impacted face of the target completely, shearing out a plug from the back side of the target. As shown in Fig. 9, plug formation was observed for all the target material. To further investigate the nature of fracture initiation in the zone of adiabatic shear, these targets were impacted by projectiles having step heights of only 0.7 mm but with the same impact velocity (44.0 m/s).

The deformed structures resulting from these small step projectiles are shown in Figs. 10 to 12 for the three types of target. Two indentation steps are observed for targets impacted by projectiles having small step heights. The deeper indentation on the left side of each picture is caused by impact of the shoulder of the projectile, whereas the shallower indentation on the right side is produced by the full penetration of the shallow step. The defor-

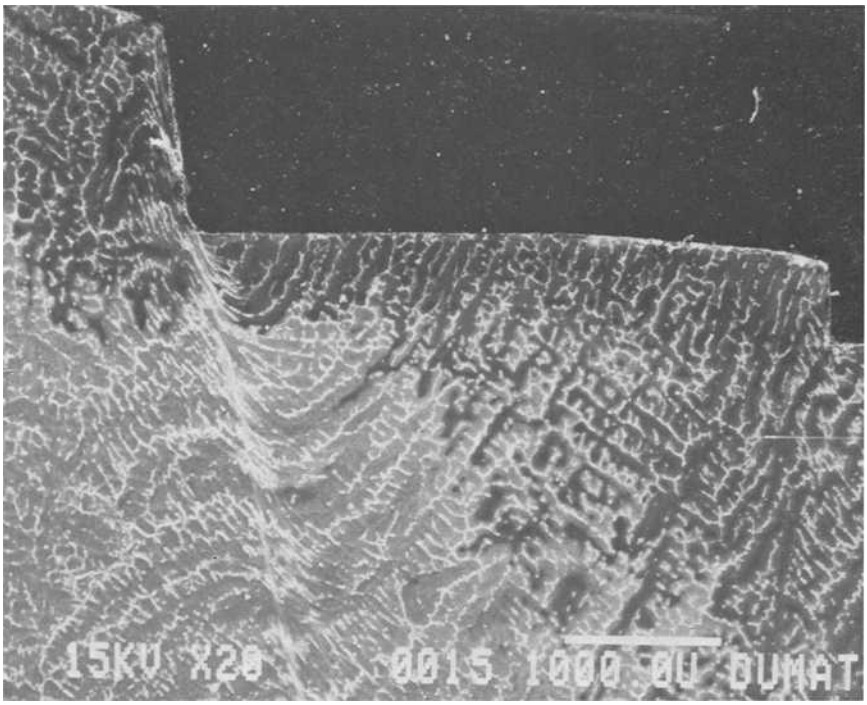

FIG. 10—*SEM picture of the deformation pattern of the homogeneous Al-Li target produced by a small step projectile under dynamic blanking* (note: step penetration is on the right hand side).

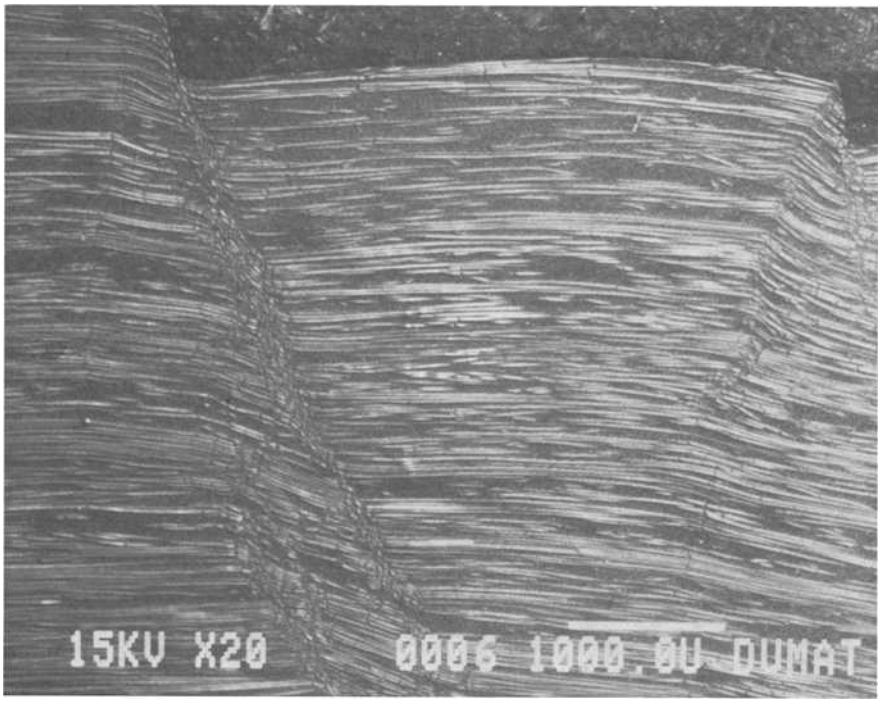

FIG. 11—*SEM picture of the deformation pattern of the unidirectionally reinforced Al-Li target produced by a small step projectile under dynamic blanking* (note: step penetration is on the right hand side).

mation pattern on the right side is the one that should be compared and analyzed with respect to possible adiabatic shear localization. For comparison the microstructure of Hadfield steel, which had been studied previously [*9*] using the same projectile velocity and a similar blanking die and which showed failure initiation by adiabatic shear localization, is included here (Fig. 13) for identification of this mode of failure. The contrast between the heavily deformed grains and the so-called "white band" which crosses many grains at the corner of the indentation is obvious. The band has a much higher hardness and finer grain size compared with the surrounding material.

This earlier study also showed that this localized shear zone was the locus of fracture initiation and propagation. Figure 12 shows the general diffuse strain localization that occurs in the Al-Li target under this impact mode. The unidirectional FP composite behavior, shown in Fig. 13, exhibits double shear band localization and propagation parallel to the penetration direction of the projectile. Conversely, the 3-D composite exhibits a diffuse type of shear band behavior (Fig. 14). Thus none of the Al-Li FP composite targets, at least under these impact conditions, exhibited the type of adiabatic shear localization reported earlier for Hadfield steel.

Scanning electron micrographs of the fracture surface of plugs formed during impact by 4.0 mm step height projectiles are shown in Figs. 14–18. Figure 14 shows that the entire surface of the Al-Li plug was created by ductile shear failure. This is similar to the failure mode of homogeneous materials during dynamic blanking, reported previously [*9*]. Figures

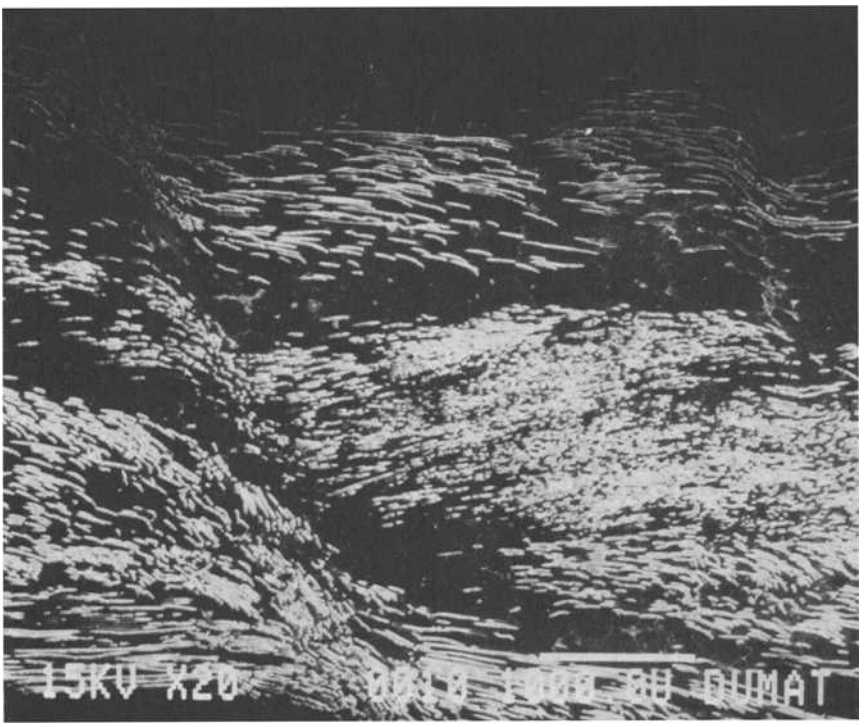

FIG. 12—*SEM picture of the deformation pattern of the 3-D braid Al-Li target produced by a small step projectile under dynamic blanking* (note: step penetration is on the right hand side).

15 to 18 show the fracture surface of unidirectionally reinforced composites. Careful examination of the failure surface shows that this composite fractured with two different failure modes. Figure 15 shows the portion of the plug that failed by shear which may have occurred during the early stages of penetration. The observed pattern of grooves is produced by the rubbing of the plug against the matrix during plug ejection. Figure 16 presents that portion of the fracture surface of the plug closer to the back side of the target. The difference in fracture appearance may be related to bending during the failure process. The same area shown in Fig. 16 is shown in Fig. 17 at much higher magnification, illustrating the ductile failure of the Al-Li matrix and the brittle fracture pattern of FP alumina fibers. The fracture surface of a 3-D FP/Al-Li composite, shown in Fig. 18, reveals a similar groove pattern plus the shear fracture surface of Al-Li matrix.

Conclusions

The blanking process is a valuable test method for evaluating the through-thickness properties of composite materials. It can be adapted for the study of shear fracture resistance and fracture propagation under both low and high velocity modes. Static testing plus structural analysis for the three targets material tested (Al-Li, unidirectional and 3-D FP/Al-Li composites) identified the main mechanism for instability and fracture as shear localization following by shear failure. Unidirectionally reinforced FP alumina fiber composites showed

severe shear localization and, hence, limited deformation before fracture. 3-D reinforcement with similar fibers, however, postponed this shear localization to larger displacements by spreading and diffusing the deformation. The specific displacement required for localization is undoubtedly dependent on the specific fiber architecture employed in a particular composite.

The fracture study of the plugs from the three different target materials showed clear evidence that unidirectional composite is very sensitive to the bending strain produced by the blanking process employed. The 3-D FP/Al-Li composite showed no sign of this bending fracture mode on the surface of plugs from this target material. Structural analysis of the indentation deformation caused by small step projectiles indicates that adiabatic strain localization is not a major factor in the initiation of fracture in any of the target materials studied as was the case in Hadfield steel.

Finally, it should be cautioned that this study is preliminary in nature. A more conclusive depiction of the shear failure behavior of the various composite systems will require more extensive experimental work with several step heights and a recording of the stress-strain response under dynamic blanking.

FIG. 13—*Light microscope picture of a typical adiabatic band formation in a Hadfield steel under dynamic blanking.*

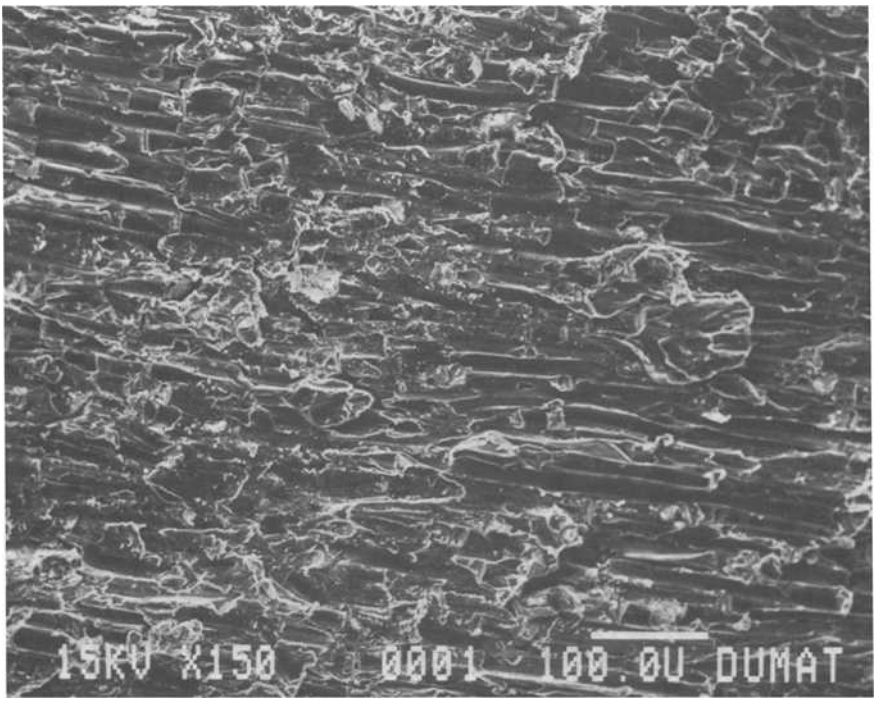

FIG. 14—*SEM picture of the fracture surface on the penetration side of the plug from the homogeneous Al-Li target produced by a large step height projectile under dynamic blanking.*

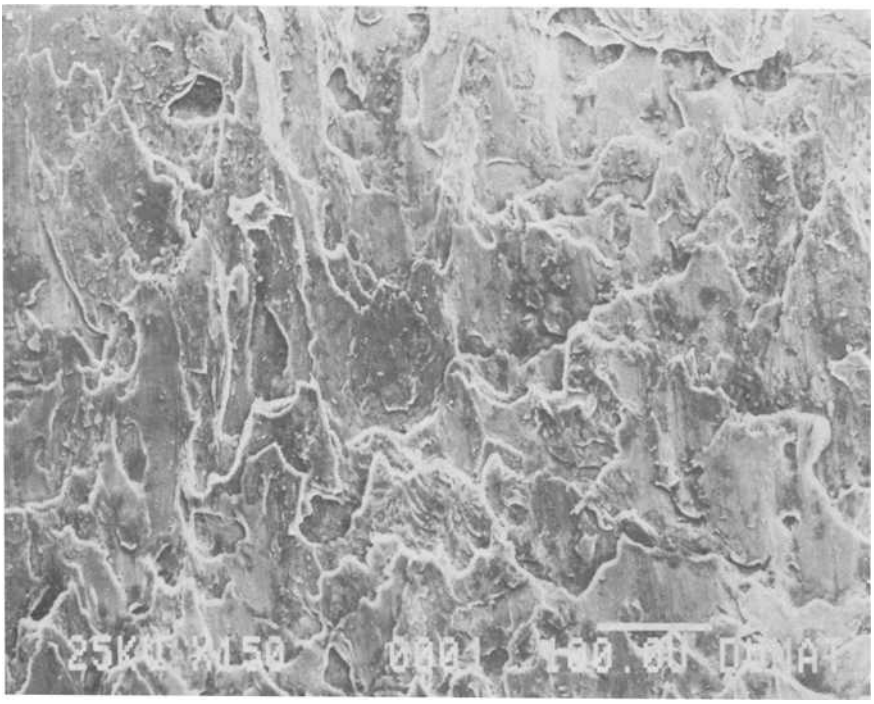

FIG. 15—*SEM picture of the fracture surface on the penetration side of the plug from the unidirectionally reinforced Al-Li target produced by a large step height projectile under dynamic blanking.*

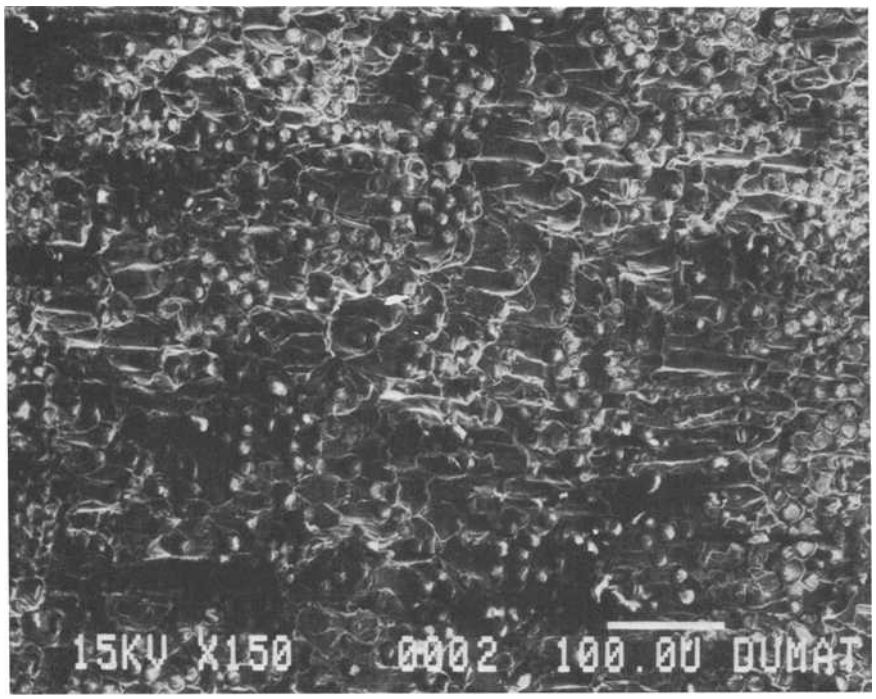

FIG. 16—*SEM picture of the fracture surface on the bending side of the plug from the unidirectionally reinforced Al-Li target produced by a large step height projectile under dynamic blanking.*

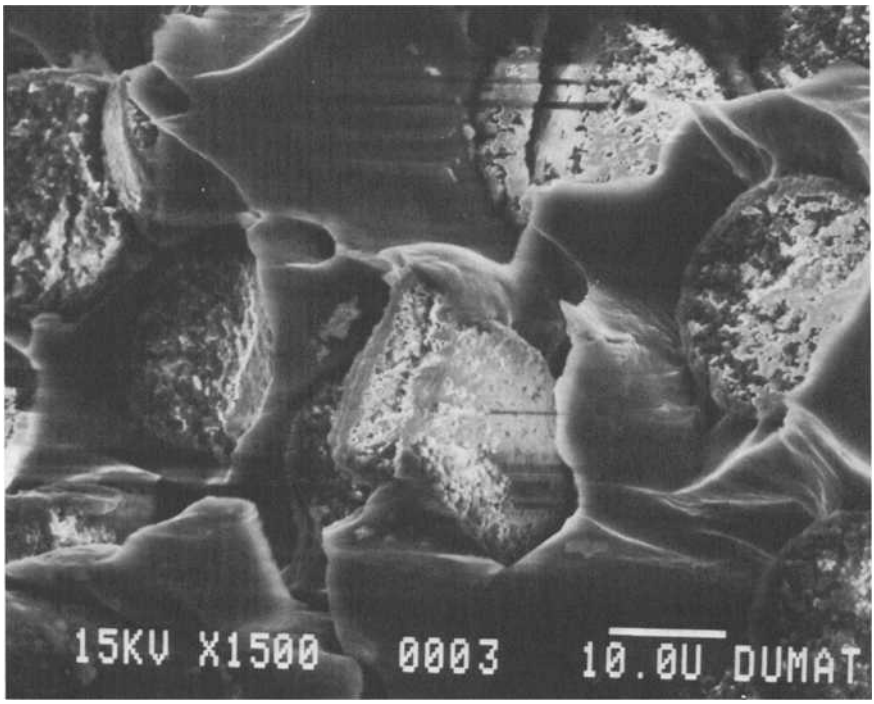

FIG. 17—*A higher magnification of the same SEM picture shown in Fig. 15.*

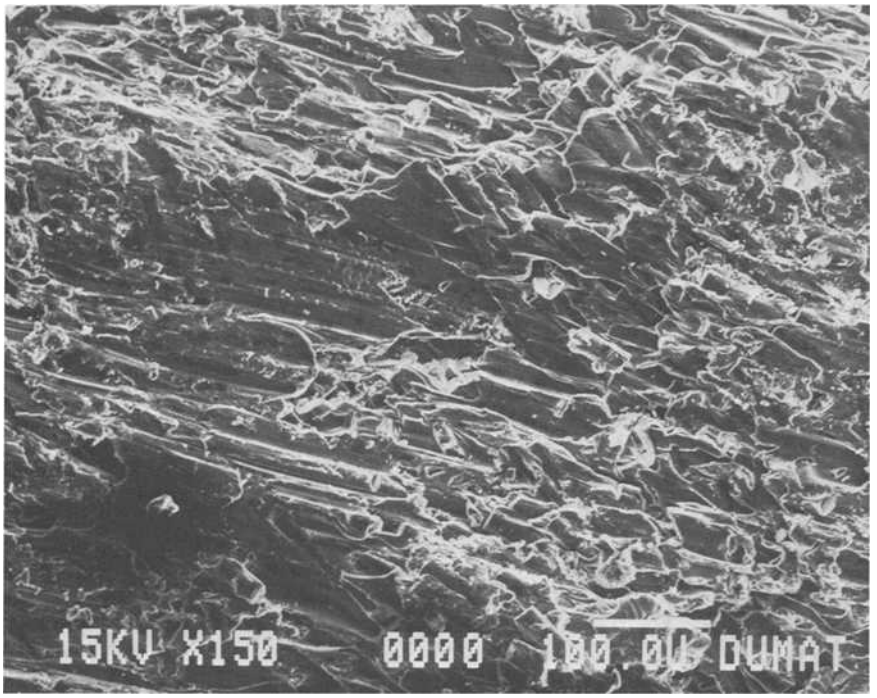

FIG. 18—*SEM picture of the fracture surface on the penetration side of the plug from the 3-D braid reinforced Al-Li target produced by a large step height projectile under dynamic blanking.*

Acknowledgment

Partially supported by the Office of Naval Research under grant No. N00014-83-K-0415.

References

[1] Bedford, A. J., *Journal of the Australian Institute of Metals,* 1974, Vol. 19, pp. 61–73.
[2] Backman, M. E. and Finnegan, S. A. *Metallurgical Effects at High Strait. Rates,* R. W. Rohde, B. M. Butcher, J. R. Holland, and C. H. Karnes, Eds., *Plenum,* New York, 1973, pp. 531–43.
[3] Rogers, H. C., *Annual Review Materials Science,* 1979, Vol. 9, pp. 283–311.
[4] Olson, G. B., Mescall, J. F., and Azrin, M., *Proceedings, International Conference on Metallurgica, Effects of High Strain Rate Deformation and Fabrication,* Plenum, New York, 1980, pp. 221–47.
[5] Ko, F., "Three Dimensional Fabrics for Composites—An Introduction to the Maganweave Structure," *Progress in Science and Engineering of Composites,* Hayashi et al., Eds., ICCM IV, Tokyo, 1982, pp. 1609–1616.
[6] Ko, F. and Pastore, C., "Structure and Properties of an Integrated 3-D Fabric for Structural Composites," *Recent Advances in Composites in the United States and Japan, ASTM STP 864,* J. Vinson and M. Taya, Eds., American Society for Testing and Materials, Philadelphia, pp. 428–439.
[7] Chang, T. M. and Swift, H. W., *Journal of the Institute of Metal,* 1950–1951, Vol. 19, pp. 119–146.
[8] Johnson, W. and Slater, R. A. C., *Proceedings, International Conference on Manufacturing Technology,* 1967, CIRP-ASTME 825.
[9] Razavi, A. and Rogers, H. C., presented in AIME meeting Sept. 13, Detroit MI, 1984.

Ronald P. Tye[1] *and Stephen E. Smith*[1]

Factors Affecting the Determination of Thermophysical Properties of Metal Matrix Composites

REFERENCE: Tye, R. P. and Smith, S. E., **"Factors Affecting the Determination of Thermophysical Properties of Metal Matrix Composites,"** *Testing Technology of Metal Matrix Composites, ASTM STP 964,* P. R. DiGiovanni and N. R. Adsit, Eds., American Society for Testing and Materials, Philadelphia, 1988, pp. 65–78.

ABSTRACT: Methods, techniques, and models available for the measurement or estimation of thermal conductivity, electrical conductivity, thermal diffusivity, thermal expansion, and heat capacity, are reviewed with respect to their applicability to metal matrix composite materials and systems.

Various factors influencing the choice of method used to obtain reliable properties information are discussed. These include: (*a*) application and use of the material or system; (*b*) continuous and discontinuous reinforcement of the matrix; (*c*) layered and other combination of materials; (*d*) size and form; (*e*) anisotropy; and (*f*) temperature and accuracy requirements.

Considering the unique problems represented by these materials and systems, recommendations are made regarding the most appropriate means currently available to obtain reliable thermal properties information. Areas are identified where further information and work are required in order to improve existing models and measurement techniques.

KEY WORDS: anisotropy, continuous reinforcement, discontinuous reinforcement, electrical resistivity, heat capacity, honeycombs, layered materials, models, rule of mixtures, structural performance, thermal conductivity, thermal expansion, thermal resistance, thermal stresses

Reinforced metal composites offer a number of potential advantages over their polymer counterparts, including:

(*a*) higher temperatures of operation;
(*b*) higher modulus of the matrix leading to higher moduli of the composite for stresses below the maximum yield point;
(*c*) higher ductility and strength of the matrix providing improved off-axis properties and interlaminar shear strength;
(*d*) stronger joints due to more control of matrix;
(*e*) improved chemical, environmental, and erosion resistance; and
(*f*) higher thermal conductivity and electrical conductivity.

There are still a number of problems associated with the development of light weight, strong, stiff metal matrix composites for temperatures in excess of 1000°C, especially high

[1] Manager, Market Development and manager, Thermophysics Laboratory, respectively, Dynatech Scientific Inc, Cambridge, MA 02139.

cost and degradation due to thermal cycling. However, a wide variety of such materials, based on lower melting point metals such as aluminum, magnesium, and copper or their alloys, are now becoming available in a variety of forms.

During the past decade, significant advances have been made in developing better, continuous, and more economic processes for the fabrication of metal matrix composites [*1,2*] having improved and more reproducible properties. Weight critical applications, where the high strength to weight ratio and other desirable property characteristics are utilized, have continued to increase. This is particularly true for the areas of space structures, missile components, and engines. Such factors now enable these types of materials to be considered for other applications where the original high costs were considered to be prohibitive. As a result, the use of both current and new metal matrix composites of various types is forseen to increase during the next decade.

In the development of composite materials, most attention, quite justifiably, has been directed towards the evaluation and understanding of their structural performance and their integrity under the conditions of use. However, because of the anisotropic nature of many of these materials, combined with their limited availability in forms suitable for evaluation of properties along appropriate axes, the determination of various mechanical properties in a reproducible manner in accordance with "standard" test criteria has proved to be a difficult exercise. This has been compounded by the fact that even though "standard" tests were used, specimen size and form, testing criteria, and experimental techniques have not been consistent. In consequence, it has been very difficult to develop a totally reliable data base [*3*] for these materials such that properties can be used for design purposes, and much work is still on-going to assess the situation for structural properties.

For the case of thermal properties, there is little or no information available for any current production material. Information is scattered and in most cases related to uncharacterized developmental materials and specimens, with little information provided on the method of measurement. Alternatively, the data have been derived utilizing questionable analytical approaches combined with uncertain values for the constituent materials, particularly the reinforcing medium. The concept of a data base for thermal properties is some years away. In order to avoid similar problems and issues which developed during measurements of the structural properties, consideration of factors which influence the determination of reliable thermal property data should be also given when undertaking programs of work to characterize current materials.

Several promising candidate materials, including both continuous graphite and alumina reinforced metals and alloys and discontinuous silicon carbide reinforced metals, are now being produced in substantial quantities in different shapes and forms for use in various applications where high-thermal conductivity is necessary. In addition, a variety of layered metal composites, especially in the form of a honeycomb with metallic or reinforced plastic facers, are being considered or used in a variety of applications where lower thermal conductivity or conductance is more advantageous. The design and reliable operation of systems utilizing such materials now becomes more dependent upon a knowledge of their thermal properties, particularly thermal expansion, thermal conductivity, and thermal conductance. These properties, while providing the required data base, may also provide a means of determining and understanding behavior of reinforced materials and particularly how service life of higher temperature components is affected by interactions between the metal and the reinforcement [*1,4*].

The present discussion attempts to outline the various issues which have to be addressed when considering how to obtain reliable properties information on the different types and forms of metal matrix composites. The major properties emphasis will be placed on thermal conductivity and thermal conductance, but thermal expansion and heat capacity will be also

addressed where these properties are relevant to the issue. The major materials emphasis will be placed on the fibrous reinforced systems.

Problem Definition

As indicated earlier, there are two major types of metal matrix composites. These are the continuous fiber and the discontinuous fiber, whisker or other solid particle reinforced matrix. These are supplemented with one other type, namely, the layered systems. These consist of a metal matrix in forms varying from cellular, honeycomb, fiber, and solid sandwiched between other materials. These can include metals, ceramics, and plastics, any of which may be reinforced composites.

The major thermal properties of current interest are:

(*a*) thermal conductivity (including electrical conductivity) and thermal conductance;
(*b*) thermal diffusivity;
(*c*) thermal expansion; and
(*d*) heat capacity.

In addition, total hemispherical emittance and spectral emittance are other properties which become necessary for future higher temperature applications. These properties are not addressed in this paper.

Unlike heat capacity (C_p), thermal conductivity (λ) and thermal expansion (α) are properties which are influenced considerably by form, while thermal conductance is a unique property for a particular component. Materials which can exist in forms ranging from highly porous powders, particulates, and fibrous masses to high-density solids can have property values, particularly of λ, which differ by at least four orders of magnitude.

When two or more materials are combined, the ensuing composite may have properties which cannot be modelled simply and which can be much different to those of the constituents especially if the resultant composite has preferred orientation which induces anisotropy of the property. Finally, current composite materials can in some instances be fabricated only in limited forms and sizes such as thin-walled tubes or flat plates which are not suitable for providing the best type of specimen configuration. These factors present challenges to those trying to measure or model the properties of any or all of these materials.

In trying to derive or measure the thermal properties of metal matrix composites, there are a number of factors which are found to influence the choice of model or measurement technique which can be used [*5*]. These are:

(*a*) type and form of the material;
(*b*) property required:
(*c*) measurement; and
(*d*) temperature and other external variables.

Those factors, which are often interrelated, are now discussed in relation to the desired thermal property.

Thermal Conductivity

In general, λ of fiber and whisker reinforced metal matrix composites will reflect the high conductivity of the metal and, therefore, will be likely to be in excess of 10 W/m · K. The absolute value will depend upon the matrix, the type and form of the reinforcement fiber

or particle, the volume loading, and the orientation of the continuous fiber. The latter is particularly true if it is not unidirectional but laid up in two or more directions in order to try to obtain optimum strength and matched or low α characteristics.

A number of models [*6–9*] have been postulated to derive λ for a composite utilizing values of the individual constituents. Essentially, these are modified forms of the simple rule of mixtures

$$\lambda = \lambda_f V_f + \lambda_m V_m$$

where V_f and V_m are the volume fractions of the reinforcement and metal of appropriate λ_f and λ_m. This λ is derived for the composite either if it is isotropic or for the direction of the longitudinal reinforcement. Additional, more complex analyses are required to derive λ for the transverse and other directions [*10,11*].

These models need reliable information for the properties of the constituents. In most cases, such results for λ_m are available from a prime source in the literature [*12*]. However, little reliable information is available for many of the reinforcing fibers or materials. In most cases, the assumption is made that λ_f is that for the monolithic bulk form. However, this is not necessarily true since, for example, some reinforcing fibers and particles are amorphous or partially crystalline, and λ will be different than the assumed for the solid crystalline form. In addition, some fibers such as carbon and graphite will have values of λ which not only are anisotropic but also depend on the type of fiber, its surface condition and the degree of graphitization. Similar models [*13–16*] have been proposed for α and the same reasons can be postulated to question their efficacy.

A major problem with these models for λ is the basic assumption that the thermal resistances at the contacting surfaces between the matrix and reinforcement are zero or are constant. This assumption may not be valid for a majority of cases since there may be often good mechanical contact existing but relatively poor thermal contact. In addition, these contact resistances may not be uniform throughout the system and will probably change with temperature. This is due to the mismatch between the thermal expansion coefficients of the constituents. This is a factor which also affects the models used to derive α. Finally, a further complicating issue concerns the fact that different fiber types of one material, such as carbon, have different surface morphologies which again lead to differing contact resistances which can affect both λ and α. Thus, while modelling can provide guidelines on average or upper and lower limit values of λ and α, in many cases it will be necessary for measurements to be made.

Measurements on materials having λ in excess of 10 W/m · K are normally made by a guarded longitudinal heat-flow method such as the axial rod [*17,18*] or comparative cut-bar technique [*19,20*]. The axial rod method, shown schematically in Fig. 1, is the technique which is the most suitable for materials having high λ-values and an accuracy of $\pm 2\%$ is obtainable. The major consideration is that the specimen should have a length to diameter ratio which exceeds eight wherever possible. This can be normally attained with discontinuous reinforced matrices and where λ is desired for the direction of heat flow along the length of a continous reinforced fiber material in the form of a flat sheet or a tube. However, it is less easy to attain for the heat flow normal to axial direction of the latter anisotropic configurations or for heat flow in the circumferential direction for the case of the tubular form.

The comparative method shown schematically in Fig. 2 is utilized in many cases due to its ready adaptability to λ-values in the range 1 to 200 W/m · K and to specimen configuration. Its operation is absolutely dependent upon the availability of stable reference materials of similar values of λ to those expected for the materials. A limited number of

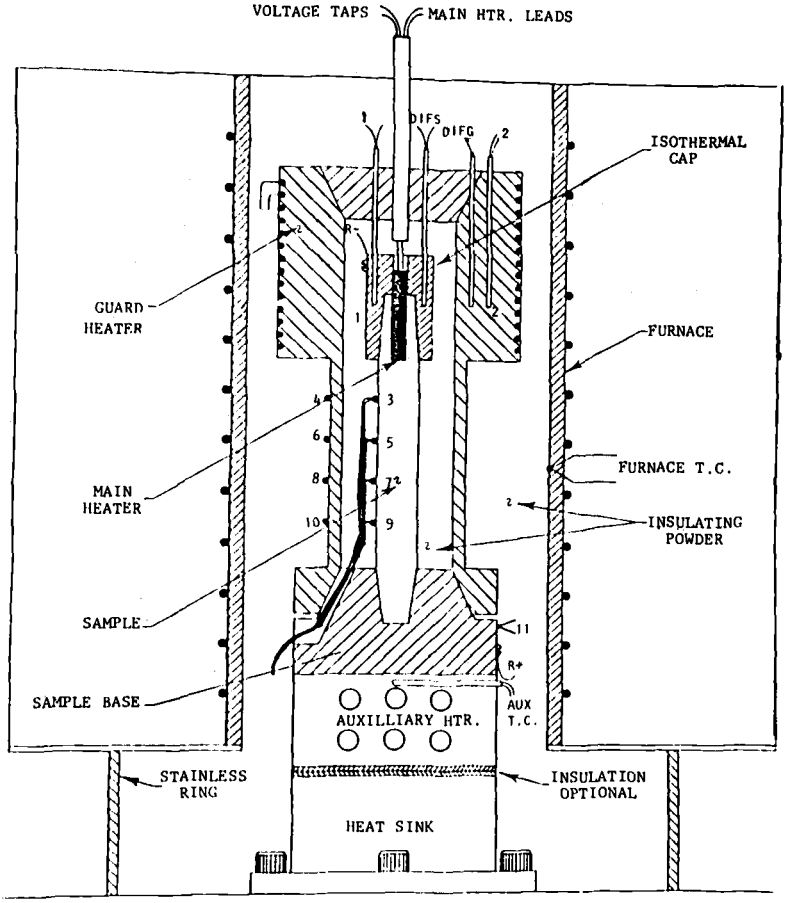

FIG. 1—*Longitudinal guarded axial rod method: schematic arrangement.*

ceramics, alloys, and pure metals are available [*21*] for the expected λ range of the metal matrix materials. The accuracy of the method is highly dependent on the material and the specimen. Providing a specimen of the correct dimensions with flat parallel faces is available, accuracies of ±5% can be attained [*22*].

The basic criteria for measurements by this method is that a representative specimen of suitable geometry having a length to diameter ratio which is large or at least 1 be available. This is necessary in order to establish and measure a reasonable temperature gradient in or across the specimen such that the inherent accuracy of the method is attained. The same limitations regarding material form and availability for the axial rod method apply to a somewhat lesser extent to this technique.

For materials in the form of thin sheets, or thin walled tubes, suitable specimens for the axial direction can be fabricated in the form of a number of strips of the same width and length clamped together tightly at each end to form a rod or bar specimen of appropriate dimensions. For the axial rod, this can be up to 10 to 12 mm square and 100 mm long and for the comparative 25 to 50 mm square and from 10 to 25 mm in thickness, as shown in Fig. 3. If measurements are made on a tube form it is essential that the central hole be filled

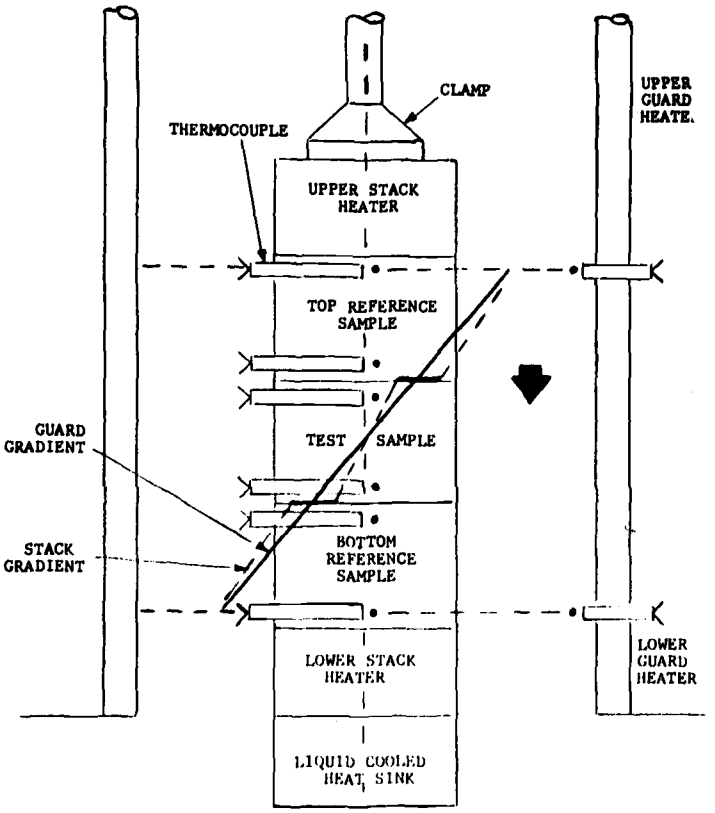

FIG. 2—*Longitudinal guarded comparative method: schematic arrangement.*

with a powder or other insulation in order both to eliminate convection and to minimize cross radiation in the central hole within the specimen.

Since a major source of error can be incorrect measurement of temperature or temperature difference, significant attention must be paid to this parameter [*23*]. In the axial rod method, temperature sensors can be attached directly into or onto the exterior surfaces at suitable positions along the length of a solid specimen or thick-walled tube. Alternatively, for the strip form, the sensors can be clamped between the central two strips. For the comparative method, sensors can be placed in small holes drilled into the specimen if the length is sufficient or in fine grooves cut into the surfaces for thinner specimens.

If the thickness of the specimen is such that these grooves or holes are a significant percentage of the total thickness, temperature measurements have to be obtained from sensors in the reference materials alone. In this case, every effort has to be taken to ensure that the contact resistances at the surfaces are eliminated or are minimized and remain constant. This can be accomplished by using liquid indium, or other nonreacting metal film, at the interfaces in conjunction with an applied load.

For the heat flow normal to reinforcement direction, there is a major problem because λ is high and the length of specimen, that is, thickness, is very limited. In such cases, one can consider bonding a number of strips together to form a layered composite and use the axial rod or comparative techniques. However, in this case, considerable uncertainties exist

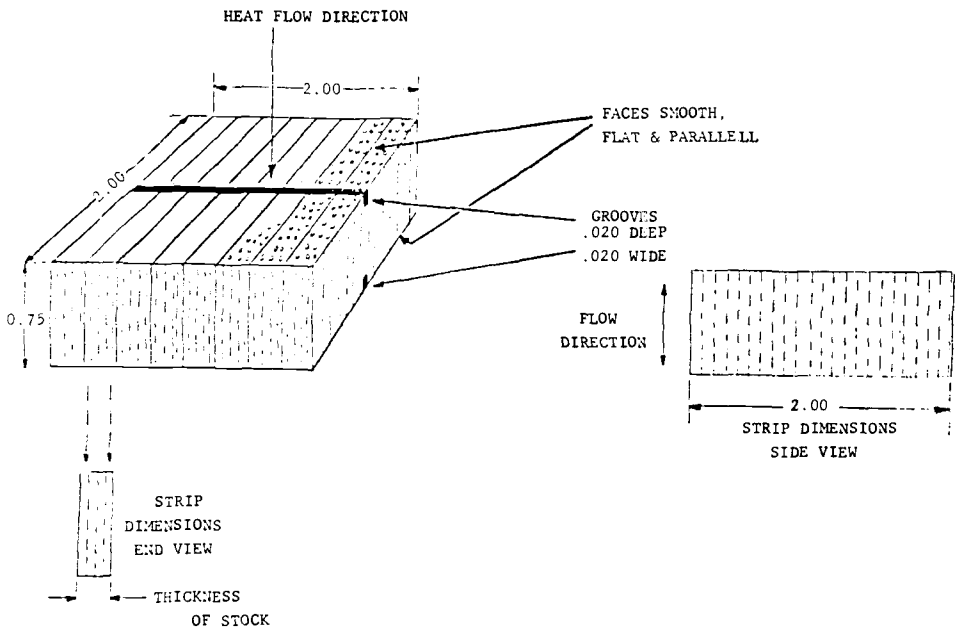

FIG. 3—*Suitable test specimens from thin sheets of composite materials.*

concerning the matter of such a specimen being representative of the bulk material. The bonding medium may also affect the results unless the amount used is minimized. It must be accepted that reliable measurements for this direction are difficult and alternative means must be sought.

If accurate measurements can be made for one direction of reinforcement, it is possible to consider measuring the anisotropy ratio and deriving λ for the other direction. Providing suitable flat plate type of specimens can be made available or fabricated, the old method of Ingen-Hauz [*24*] and de Senarmont [*25*] modifications can be utilized.

The specimen can be cooled at its center by means of small pieces of solid carbon dioxide, and once the specimen cools below the dew point, frost will appear in the form of a well-defined ellipse. The major axes of the ellipse are proportional to square root of the thermal conductivities for the two principal axes of the plate. This is a somewhat simple technique and is suitable only for a limited temperature range, but it can be quite accurate [*26*].

Since metal matrix composites, in general, will be electrical conductors, it is recommended that electrical conductivity or resistivity be measured. The measurement is more direct and simple than that for λ and requires a more simple specimen configuration. Measurements in the axial and in various reinforcement directions can be also made more easily.

The four-point probe method is the most widely used [*26*] especially where relatively large length-to-diameter ratios specimens are available. However, it is quite possible to undertake measurements on a comparative basis on thin specimens using the same technique. For this, reference specimens of the same order of dimensions cut from materials to provide specimens of known electrical resistance are used to calibrate a four-point probe and to eliminate contact resistance effects. If it is possible to cut cubical or rectangular specimens having suitable cross sections, anisotropy in the properties can be measured directly on one specimen.

For metals and alloys, there is a direct relationship between the thermal and electrical

conductivities. This is usually in the form of the Lorenz Number, L, for electronic conduction only [27], modified by Wiedemann-Franz to include a contribution due to lattice conduction [28].

While it is not probable that a direct Wiedemann-Franz or Lorenz relationship will exist for such materials, some empirical modifications of the relationship may be found to exist. Under these circumstances, the easier measured electrical property can be used on a larger number of specimens of each direction in order to help determine a more reliable value of λ, especially for the through thickness direction.

Thermal Conductance

In a number of applications, metal matrix composites may have configurations with non-uniform sections. Under such circumstances, the properties will be dependent, for example, on the number, thickness, and type of layers or on the pore or honeycomb size. In addition, they may be used for applications where specific conditions of temperature, gaseous environment, and applied load are governing criteria.

In such cases, the measured property will be a thermal conductance (λ/thickness) for the specific conditions, and the value will apply only to the particular configuration and conditions. In general, values for other configurations and conditions cannot be derived from the results unless reliable information, and its parametric variation, is available for the individual constituents.

Measurements of this type can be made by the comparative method or the guarded hot-plate method [29]. The major criteria concerning the choice of method have been covered previously [5] and are summarized as follows:

(*a*) ensuring that the test specimen is representative of that of the application;
(*b*) ensuring that the condition of test are those that apply for the application; and
(*c*) ensuring that the size of the test specimen is appropriate for the type of apparatus.

The guarded hot-plate method and its utilization for composites has been well documented [30–31]. It is normally used where the higher accuracy is required and where the specimen has a relatively low-thermal conductance value. In some cases, this can only be attained with large specimen thicknesses which may necessitate the use of large apparatus. Such hot plates especially for use at elevated temperatures are difficult to design and operate such that one is assured that the basic design criteria needed to establish uniform heat flow and zero or minimal lateral heat loss, etc. are attained. For metal matrix composite systems, because of the relative high value of λ of some components, it is essential that the central metering section of the specimen is separate from the surrounding guard section and the gap filled with a fibrous or particulate thermal insulation to minimize lateral conductive heat flow as well as eliminating or minimizing convective and radiative heat transfer between the two sections.

With materials having hard surfaces, large areas, and somewhat higher thermal conductance values than typical thermal insulations, there is always a tendency for thermal resistances caused by air gaps to exist at contacting surfaces [32]. In addition, due to differential expansion on heating, the test specimen may tend to warp, thereby increasing the effects of such air gaps. An important experimental technique for such types of specimens is to ensure that temperature sensors are attached to the surfaces of the specimen, preferably in fine grooves, with no reliance placed on those in the surface plates of the apparatus for calculation of the experimentally determined value.

Thermal Diffusivity

For some applications, thermal diffusivity (D), defined as the ratio of thermal conductivity to specific heat per unit volume ($D = \lambda/\rho C_p$) is the parameter governing heat transfer. If the three individual properties are known then D can be calculated. These are often not known for metal matrix materials and direct measurement of the property is more desirable. The property is potentially easier and quicker to measure and utilizes, in general, a smaller and more simple specimen configuration than for determination of λ alone.

However, another attraction to the measurement of D is the fact that λ can be calculated from the results finding providing values of C_p and ρ are available. If experimental results for C_p are unavailable, values are more readily calculated by method of mixtures, whole ρ can be measured very simply and small temperature adjustments can be made if thermal expansion, α, values are also available.

It must be pointed up that in the calculation of λ from D, the basic analysis assumes that:

(*a*) the temperature distribution at any plane within the specimen is isothermal at any time; and
(*b*) λ is due only to solid conduction within a homogeneous specimen.

Most metal matrix composites are highly anisotropic while others, particularly the layered and honeycomb types, are inhomogeneous, and for these the first assumption particularly may not apply. Thus, some care has to be taken in deciding when the calculation of λ is appropriate. In addition, when a method which utilizes quite small specimens is used, such specimens may not necessarily be representative of the bulk material especially for the layered composites or for the application where a thermal conductance is required.

The attractive features of transient methods are based on the fact that they involve the complete differential equation for heat flow with the time and space variables being of equal importance. Thus, for any set of boundary conditions, there is a unique solution on which to develop a method. Furthermore, heat losses can be handled easier by the inclusion of an additional term either in the equation or in the choice of boundary conditions. This will appear as a constant in the solution of the equation and can be eliminated by suitable choice of measurement parameters.

Thus, the measurement of D has stimulated that ingenuity of many experimentalists such that a profusion of methods and techniques have been developed. This is particularly true during the past two decades where significant advances in instrumentation especially for accurate measurement, recording, and analysis of the temperature with time relationship has allowed measurement times to be reduced often to the subsecond level.

The basic details of the many and varied methods available and analyses on which they are based have been well documented and assessed [*33*]. The major consideration becomes one of choosing or adapting a technique which is the most suitable for the type or form of the material for which D or λ or both is desired at an appropriate accuracy. Alternatively, a combination of both techniques can be used to determine D for continuous reinforced materials in the form of sheets or thin plates.

Transient techniques fall into two categories, periodic temperature and transitory temperature methods, respectively. Most of the current information on metals and metal matrix composites have used one basic method from each category.

The most widely used method currently is a transitory temperature one generally described as the "flash method." In this, one face of a specimen usually a small flat disk of the order of 6 to 12 mm in diameter and a thickness of 1 to 6 mm, depending on the thermal properties, is subjected to a flash of thermal energy in a time interval which is very short compared to the time during which the resultant thermal transient propagates through the specimen.

The method is illustrated schematically in Fig. 4. During the past decade, the source most widely used is a laser having an appropriate power density to provide sufficient response in the material. The temperature response at the rear surface measured originally with a thermocouple is now usually measured with a sensitive indium antimonide radiation detector.

The value of D is then calculated from a characteristic time obtained from the temperature time response curve together with the specimen thickness: various characteristic time analyses, based upon a function of the maximum temperature attained, have been developed depending upon the technique and boundary conditions used or assumed.

The major advantages of the basic techniques are the utilization of thin specimens and consequent short measurement times. The latter overcomes possible contamination problems at high temperatures which can restrict the use of the more time consuming steady-state methods. Accuracies of $\pm 5\%$ or better for values of D can be obtained by this technique. However, if λ is derived from such values its uncertainty will depend also upon those for the values of C_p and ρ used in the calculation.

This method obviously lends itself well to measurements on discontinuous reinforced metal matrix composites and to continuous fiber reinforced materials where the anisotropy may not be significant. However, it is less readily suited for more highly oriented fiber reinforced materials unless suitable disk specimens can be fabricated from the materials with their axes normal to the respective major fiber orientations. In addition, this specific method requires significant modifications of technique for measurements to be carried out on highly curved or very thin specimens such as those from metal matrix materials fabricated as thin-walled tubes.

The periodic temperature method which has been used to a limited extent for metal matrix materials [*34*] is based upon that developed originally by Angstrom [*35*] for long thin semi-infinite rods. This involves essentially a long thin radiating specimen heated at one end with a source having a sinusoidal variation of temperature and time.

The method is shown schematically in Fig. 5. The period of the heat source can be adjusted to suit the capabilities of the temperature recording facilities and the dimensions of metallic specimens should be of the order of 2 to 10 mm diameter and lengths of 50 to 300 mm. Shorter specimens with thermocouple spacings 2 to 3 mm have been used for metals having $\lambda < 10$ to 15 W/m · K.

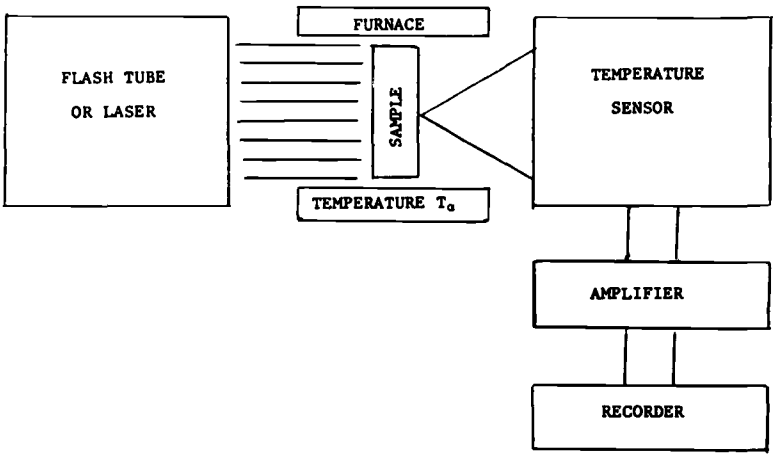

FIG. 4—*Transitory "flash" method for thermal diffusivity: schematic arrangement.*

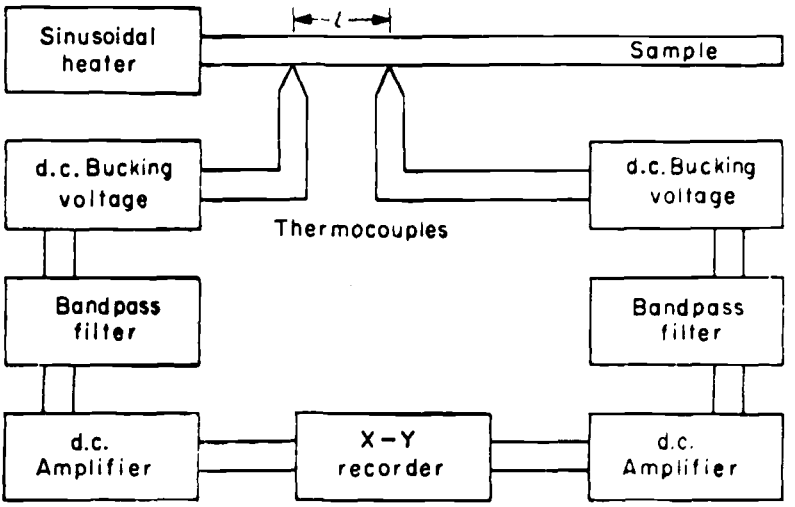

FIG. 5—*Periodic "Angstrom" method for thermal diffusivity: schematic arrangement.*

The temperatures are sensed at the two positions along the length and the electromotive forces (emfs) are opposed by d-c bucking potential such that the output corresponding to the "ambient" temperature is eliminated. The residual small sinusoidal component is amplified and recorded on an X-Y system. The resulting ellipse produced by the X- and Y-deflections due to the respective thermocouple is analyzed to yield D from a knowledge of the phase angle between the X- and Y-displacements, the distance between the temperature sensors and the absolute temperature.

This method is more suited for measurements on discontinuous reinforced materials and on thin-walled tubes and other materials where D is required for the reinforcement parallel to axial direction. It is less suited for the other directions unless suitable specimens can be made available.

In deriving λ from measurements of D, accurate values of C_p and density are necessary. As mentioned earlier, values of the former not available in the reliable literature [*12*] may be calculated by the method of mixtures knowing the specific heat and volume fractions of the components. However, in many cases, small specimens may not necessarily contain the design volume fractions, and thus C_p may be in error and measurements are required.

Specific Heat

In general, this property can be determined accurately by either drop or adiabatic calorimetry. Both methods are well researched and documented [*36,37*] and need not be discussed here. Accuracies of ±2% and better are attainable for large or high mass (>100 g) specimens. More recently, differential scanning calorimetry [*38*] utilizing very small (milligram) specimens has become more widely used. However, the accuracy of this technique, while often quoted to be better than ±5%, is affected by a number of variables including form of specimen, heating rate, and similarity of both D and emittance values of the test specimen with those of the calibration material. In addition, since the specimens are very small there is the possibility that they will be even less representative of the bulk material than the relatively small specimen used to measure D.

Thermal Expansion

Thermal expansion is the one thermal related property which has been studied on composites including metal matrix systems and for which some information is available. It is one of the necessary properties required in order for thermal stresses to be analyzed for particular applications of a material.

One of the major advantages of fiber reinforced composites is the ability to tailor the reinforcement of a matrix such that desired strength and expansion properties can be obtained in components. Thus, metal matrix systems like their organic and carbon matrix counterparts can have a wide range of α from small negative coefficients to those of the basic metal. This range is of the order of -5×10^{-7} to $+15 \times 10^{-6}\,K^{-1}$.

In general, expansion coefficients in the range above $1 \times 10^{-6}\,K^{-1}$ can be measured to required accuracies utilizing conventional single calibrated or double comparative push rod techniques [*39*]. These are based on a carefully designed system of fused silica and utilizing reference materials such as platinum, Invar, and a low expansion glass for calibration.

Typical specimen configurations are small rods or bars or tubes, of appropriate cross section to remain rigid, with lengths of 25 to 75 mm and the ends machined flat or to a desired radius. Such specimens are readily available for discontinuous reinforced materials and for the continuous reinforced material for the reinforcement parallel to axis direction of the sheet plate or tube. For other directions, specimens particularly of sheet or plate are often fabricated in the form of a number of pieces stacked together. Accuracies for such specimens are less easy to determine due to the fact that it is highly unlikely that the individual pieces will be perfectly flat. Thus, the initial length of the stacked specimen will be uncertain, and the individual pieces may behave differently during the subsequent heating or cooling.

For measurements on very low expansion materials or on specimens of limited thickness interferometric techniques as discussed by Wolff et al. [*40*] are necessary. These methods, which are contactless, are attractive since they are not restricted by specimen size or shape. Using a two channel Michelson interferometer, changes in dimension as low as 10^{-12}m can be detected, and the overall accuracy is stated to be of the order of $\pm 10^{-8}$m.

In measurements of α, there is another important experimental parameter which is often neglected. This is the issue of maintaining and measuring the temperature uniformity of the complete specimen at each of the temperatures of the interval over which the change in length is determined. If there is any significant temperature gradient within the specimen this will be reflected as an uncertainty in the temperature at which the length is measured. Since α depends on measurements at two distinct temperatures such affects could be additive. These uncertainties can contribute to significant errors particularly for low expansion materials.

In this context, it is recommended that the designed constant temperature zone of the furnace or environmental chamber in which a specimen is placed be at least 1.5 times the length of the test specimen. Furthermore, for most accurate determinations, it is recommended that measurements be made at successive equilibrium temperatures rather than utilizing a continuous slow heating or cooling rate.

Summary

Various factors which influence methods and techniques available to determine reliable thermophysical properties of metal matrix composites are discussed for the different types and forms of materials currently used. Recommendations on the choice of technique and improvements which can be made in order to improve accuracy are suggested.

References

[1] Piggott, M. A., *Load-Bearing Fibre Composites,* Pergamon Press, New York, 1980.
[2] *Progress in Science and Engineering of Composites,* T. Hayashi, K. Kawata, and S. Umekawa, Eds., Pergamon Press, New York, 1982.
[3] Metal Matrix Composites Information and Analysis Center, Operated by Kaman Tempo, Santa Barbara, CA.
[4] Loomis, K. E. and Ahmad, I., *Proceedings,* Thirteenth Thermal Conductivity Conference, University of Missouri-Rolla Extension Division, Nov. 1973, pp. 207–210.
[5] Tye, R. P., *High Temperature–High Pressures*, Vol. 17, 1985, p. 311.
[6] Springer, G. S. and Tsai, S. W., *Journal of Composite Materials,* Vol. 1, 1967, p. 166.
[7] Hashin, Z., *Mechanics of Composite Materials,* Pergamon Press, New York, 1983.
[8] Chen, F. C., Choy, C. L., and Young, K., *Journal of Physics D.*, Vol. 10, 1976, p. 517.
[9] Bergman, D. J., *Physics Reports*, Vol. 43, 1978, p. 377.
[10] Behrens, E., *Journal of Composite Materials,* Vol. 2, 1968, p. 2.
[11] Schulgasser, K., *Journal of Mathematical Physics,* Vol. 17, 1976, p. 382.
[12] *Thermophysical Properties of Matter,* Y. S. Touloukian, C. Y. Ho, R. W. Powell, and P. G. Klemens, Eds., Plenum Press, New York, 1969.
[13] Halpin, J. C., *Journal of Composite Materials,* Vol. 3, 1969, p. 732.
[14] Levin, V. M., *Mekhanika Tverdogo Tela.*, Vol. 2, 1967, p. 88.
[15] Wolff, E. G. and Eselun, S. A., *Journal of Composite Materials,* Vol. 11, 1977, p. 30.
[16] Hale, D. K., *Journal of Materials Sciences,* Vol. 11, 1976, p. 105.
[17] Laubitz, M. J. *Thermal Conductivity,* Vol. I. R. P. Tye, Ed., Academic Press, New York, 1969.
[18] Tye, R. P. and Brazel, J. P., *Revue Internationale des Hautes Temperatures et Refractaires,* Vol. 7, 1970, p. 326.
[19] Mirkovich, V. V., *Journal of the American Ceramics Society*, Vol. 48, 1965, p. 387.
[20] Tye, R. P. and Clougherty, E. V., *Proceedings* Fifth Symposium on Thermophysical Properties, American Society of Mechanical Engineers, New York, 1970, pp. 396–401.
[21] Powell, R. W., Ho, C. Y., and Liley, P. E., "Thermal Conductivity of Selected Materials," NSRDS-NBS8, National Bureau of Standards, Washington, DC, 1966.
[22] Tye, R. P., "The Thermal and Electrical Conductivities of Porous Copper and Stainless Steel to Elevated Temperatures," Paper 73-HT-46, ASME-AIChE Heat Transfer Conference, Atlanta, GA, 1973.
[23] Tye, R. P. and Hurley, J. R., "The Measurement of Thermal Conductivity with Particular Reference to Temperature Measurement" Proceedings, Fifth Temperature Measurement Society Conference, II C-1, March 1967.
[24] Ingen-Hausz, J., *Journal of Physical Radium,* Vol. 34, 1789, pp. 68 and 380.
[25] Senarmont, H., de, *Comptes Rendus,* Vol. 29, 1849, p. 279, see also *Annales de Chimie,* Vol. 28, 1850, pp. 257 and 259.
[26] Powell R. W., *Proceedings, Royal Society A,* Vol. 209, 1951, p. 525.
[27] Lorenz, L., *Annales de Physik,* Vol. 3, No. 13, 1881, p. 422.
[28] Wiedemann, G. and Franz, R. *Annales de Physik,* Vol. 89, 1853, p. 497.
[29] ASTM C 177-1976 "Test for Steady-State Thermal Transmission Properties by Means of the Guarded Hot Plate," American Society for Testing and Materials, Philadelphia.
[30] Glaser, P. E., Black, I. A., Lindstrom, R. S., Ruccia, F. E., and Wechsler, A. E., *Thermal Insulation Systems,* NASA SP5027, National Aeronautics and Space Administration, Washington, DC, 1967.
[31] Bourne, J. G. and Tye, R. P., *Heat Transmission Measurements in Thermal Insulations,* ASTM STP 544, American Society for Testing and Materials, Philadelphia, 1974, pp. 297–305.
[32] Tye, R. P. and Spinney, S. C., Annex 1976-2 Bulletin, Institute International du Froid, 119–127, 1976.
[33] Danielson, G. C. and Sidles, P. H., *Thermal Conductivity,* Vol. II, R. P. Tye, Ed., Academic Press, New York, 1969.
[34] Ostenson, J. E., Finnemore, J. D., Verhoeven, E., and Shanks, H. R., *Journal of Applied Physics,* Vol. 55, No. 1, 1984, p. 1.
[35] Ångström, A. J., *Annales de Physik,* Vol. 64, 1861, p. 513.
[36] Ginnings, D. C. and Corruccini, R. J., *Journal of Research,* National Bureau of Standards, Vol. 38, 1947, p. 592.

[37] Hoagland, L. C., DeWinter, F., and Reti, A. R., *Transactions of Instrument Society of America,* Vol. 6, 1967, p. 111.
[38] Watson, E. S., O'Neill, M. H., Justin, J., and Brenner, N., *Analytical Chemistry,* Vol. 36, 1964, p. 1233.
[39] ASTM E 228-1979, Test for Linear Thermal Expansion of Rigid Solids With a Vitreous Silica Dilatometer, American Society for Testing and Materials, Philadelphia.
[40] Wolff, E. G., Kendall, E. G., and Riley, W. C., *Advances in Composite Materials,* A. R. Bunsell et al, Eds., Pergamon Press, New York, pp. 1140–1176, 1980.

Dattatraya P. Dandekar,[1] *J. Frankel,*[2] *and William J. Korman*[2]

Pressure Dependence of the Elastic Constants of Silicon Carbide/2014 Aluminum Composite

REFERENCE: Dandekar, D. P., Frankel, J., and Korman, W. J., **"Pressure Dependence of the Elastic Constants of Silicon Carbide/2014 Aluminum Composite,"** *Testing Technology of Metal Matrix Composites, ASTM STP 964,* P. R. DiGiovanni and N. R. Adsit, Eds., American Society for Testing and Materials, Philadelphia, 1988, pp. 79–89.

ABSTRACT: Adiabatic elastic constants of a composite composed of 25 volume percent of silicon carbide (SiC) whiskers in 2014 aluminum matrix are measured to 1.5 GN/m^2. Whereas the pressure derivative of bulk modulus of the composite exceeds those of its two constituents, the pressure derivative of the shear modulus of the composite lie between those of its constituents. Calculated values of the upper and lower bounds of these moduli of the composite appear to be insensitive to the pressure derivative of the shear modulus of SiC. A new modified and simple model of such a composite predicts the values of the elastic constants of this composite fairly well at both the ambient pressure and 1.5 GN/m^2.

KEY WORDS: composite material, whiskers, metal-matrix composite, elastic constants, anisotropy, pressure derivative of elastic constants, equation of state

The present work represents one part of a comprehensive research effort to determine physical and mechanical properties of a composite fabricated from silicon carbide (SiC) whiskers and 2014 aluminum alloy. This work deals with the variation in the elastic constants of this composite at elevated pressures to 1.5 GN/m^2 (GPa). Obtaining the values of the elastic constants of this composite at elevated pressure allows reseachers (1) to determine the equation of state, and (2) to verify theoretical models which estimate the elastic constants of this composite not only at ambient pressure but also at elevated pressures, from knowledge of the pressure dependence of the elastic constants of its constituents SiC whiskers and 2014 aluminum alloy. As high-pressure elastic constants data are not available for SiC, use of shock wave data for SiC was made to estimate the values of its elastic constants at high pressures. These estimates of the elastic constants of SiC in conjunction with the high-pressure elastic constants data of 2014-T6 aluminum were used to compute elastic constants of the composite at elevated pressure.

To the best knowledge of the authors, this is the first time such calculations have been done for any composite. Comparisons are made between a model due to Hashin and Shtrikman [*1*] and a model recently developed by Maewal and Dandekar [*2*] which is based on a generalization of the method developed by Mori and Tanaka [*3*], Taya and Chou [*4*], Weng [*5*], and Tandon and Weng [*6*] for composites in which inclusions are either spherical or

[1] Research physicist, Army Materials Technology Laboratory, Watertown MA 02172.
[2] Physicist and electronic technician, respectively, U.S. Army Armament Research and Development Command, Benet Weapons Laboratory, Watervliet, NY 12183.

oriented along some direction. Further we present in sequence (1) a description of the composite, (2) the ultrasonic technique used to determine the elastic constants of the composite, (3) results of the ultrasonic experiments, (4) a brief outline of technique to estimate pressure derivatives of the elastic constants of SiC from the shock wave data, (5) calculations of the elastic constants of the composite on the basis of the elastic constants of its two constituents SiC and 2014-T4 aluminum, and (6) conclusions based on this research.

Material

The metal matrix composite used in the present investigation consisted of randomly dispersed 25 volume percent SiC whiskers in a 2014 aluminum alloy matrix. The whiskers were 0.2 to 0.5 μm in diameter and have a length-to-diameter ratio between 50 and 80. These whiskers were obtained from ARCO. Materials with the previously mentioned starting composition was fabricated by hot isostatic pressure (HIP) technique in the form of thick-walled cyclinders. The HIP material was subsequently given the conventional heat treatment which brings 2014 aluminum to the standard T4 condition. Fabrication of the SiC/2014-T4 aluminum composite hereafter also referred to as SiC/Al, when no confusion is likely to arise, was done at Fiber Materials, Inc., Biddeford, Maine.

Right circular solid cylindrical specimens of SiC/Al composite used for the measurements of the elastic wave velocities had their faces either normal to the axis of the thick-walled cyclinder (z-axis) or normal to the radial direction (r) of the thick-walled cylinders (Fig. 1). The specimens of SiC/Al with face normal in z- and r-directions are, respectively, identified as SiC/Al(z) and SiC/Al(r) in this paper.

Elastic wave velocities in SiC/Al(z) and SiC/Al(r) were determined at room temperature, that is, 295 ± 2 K to detect presence of elastic anisotropicity in the material. Elastic wave velocities at elevated pressures and at room temperature were measured only in SiC/Al(z) because the room temperature measurements of the elastic wave velocities in SiC/Al(z) and SiC/Al(r) failed to indicate elastic anisotropy in SiC/Al (see the section on Experimental Results). The specimens of SiC/Al used for the elastic wave velocity measurements at the ambient condition were right circular cylinders with a diameter of 25.5 ± 0.5 mm and a thickness of 38.06 ± 0.01 mm. The specimen of SiC/Al(z) used for the measurements of elastic wave velocities at elevated pressures was a right circular cylinder with a diameter of

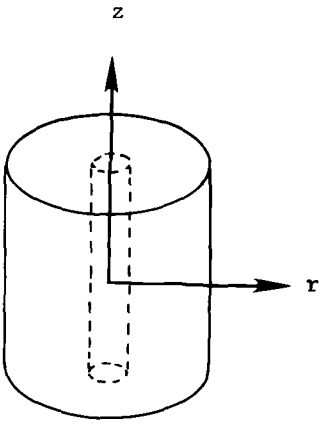

FIG. 1—*A schematic of the orientations of the thick-wall cyclinders of SiC/Al.*

TABLE 1—*Physical properties of SiC/2014-T4 aluminum as a function of orientation of specimens.*

Physical Properties	Orientation[a]		
	Z	*R*	Small Specimen
Density, Mg/m^3	2.908 ± 0.028	2.904 ± 0.006	2.906
Density range, Mg/m^3	2.890 – 2.915	2.900 – 2.907	
Elastic velocity, km/s			
Longitudinal	7.284 ± 0.050	7.329 ± 0.02	7.381 ± 0.015
Shear (1)	3.870 ± 0.02	3.866 ± 0.010	3.902 ± 0.008
Shear (2)	3.885 ± 0.02	3.918 ± 0.014	

[a] These values represent an average of measurements performed on 9 diffferent specimens of each orientation.

12.5 ± 0.1 mm and a thickness of 11.821 ± 0.002 mm. It is identified as the small specimen when necessary as in Table 1.

Experimental Technique

Elastic wave velocities in SiC/Al were measured by the pulse-echo overlap technique developed by Papadakis [7]. In the Papadakis method the echoes are overlapped on the cathode tube screen by triggering the oscilloscope at a frequency which corresponds to the inverse of transit time between echoes. The correct cycle and hence the correct time for the echo in the pulse echo overlap technique is difficult to discern, and the following method was suggested based on the properties of a composite resonating system. The resonant frequency of the transducer is found, and then a cycle overlap is chosen for the two echoes, and the transit time is found. The frequency exiting the transducer is then reduced to nine-tenths of the resonant frequency, and the transit time thus obtained for the same cycle overlap is subtracted from the transit time obtained when the resonant frequency was used. This procedure is followed when the cycle for cycle overlap between the two echoes is switched by one cycle at a time. The differences in times thus obtained should change by a constant amount as one progresses from cycle to successive cycle comparisons. The correct cycle overlap can then be found by noting the spacing of the difference in transit times obtained, as the cycles of overlap are changed by one at a time. The method of choosing the correct cycle for overlap is further discussed in Ref 7.

We found, however, that some uncertainty is removed from the selection by repeating the above procedure with a transducer of a different frequency. In that case, all the previously mentioned intervals should change, but the correct cycle overlap retains the same value. The velocities at the resonant frequency of each transducer should equal each other at the correct overlap. This method assumes that there is no dispersion of sound waves in the material. This technique was used only on the small specimen subiected to high pressure.

The longitudinal and shear wave velocity data on large specimens were obtained at 10 and 5 MHz, respectively. The longitudinal and shear wave velocity measurements in the small specimen were made at two different frequencies, that is, 10 and 15, and 5 and 10 MHz, respectively. During the measurements of transit times between echoes at elevated pressures, only changes in times were measured. Nine sets of measurements were performed as a function of pressure; three of these were for longitudinal velocity mode, and the remaining six with random polarization were for shear velocity mode. The absolute velocity values are estimated to have an accuracy of 2×10^{-3}.

Pressure was generated in a Birch-Bridgman high-pressure cell manufactured by Harwood Engineering Co., Inc., Walpole, Massachusetts. The pressure medium was a 50-50 mixture of Pentane-Isopentane. The pressure was determined by a Manganin Coil calibrated via a dead weight tester.

Results

Table 1 summarizes the results of measurements performed on the specimens of SiC/Al at the ambient condition.

Density

The densities of SiC/Al were measured by the immersion technique. Measured densities of nine specimens of each of the two orientation, that is, SiC/Al(z) and SiC/Al(r) were determined to be 2.908 ± 0.028 and 2.904 ± 0.006 Mg/m^3, respectively. The expected density of the present composite composed of 25 volume percent of SiC with a density of 3.21 Mg/m^3 and 75 volume percent of 2014-T4 aluminum with a density of 2.81 Mg/m^3 was calculated to be 2.910 Mg/m^3. Thus the measured densities of SiC/Al used in the present investigation are not significantly different from the theoretical density of the composite and hence can be considered to be pore free. The average density of the previously mentioned 18 density measurements is 2.906 ± 0.02 Mg/m^3 for SiC/Al. This value of density is used in all the subsequent calculations.

Elastic Constants at the Ambient Condition

Velocities of three elastic waves were determined in each of the nine large specimens of SiC/Al(z) and SiC/Al(r). The two shear wave velocity modes were measured to yield a maximum difference in their measured values. These shear wave velocities are identified as Shear (1) and Shear (2) in Table 1. The values of elastic wave velocities given in Table 1 do not appear to be significantly different in SiC/Al(z) and SiC/Al(r) directions. Hence, it is concluded that the composite SiC/Al used in the present work is elastically isotropic. The representative values of longitudinal and shear wave velocities for this composite calculated as the arithmetic average of the respective velocity measurements are 7.307 ± 0.05 and 3.884 ± 0.027 km/s, respectively. It should be noted that even though the precisions of the density and elastic wave velocity measurements are no worse than 0.2%, the actual errors associated with these parameters are larger and around 0.7% possibly due to materials variability of the 19 specimens of SiC/Al used in these measurements. Thus one may regard the variability in the values of the previously mentioned three parameters of SiC/Al as inherent in the method of fabrication of this composite.

Table 2 gives the values of densities and elastic properties of SiC/2014-T4 aluminum and 2014-T4 aluminum measured in the present work. The values of these parameters for SiC and 2014-T6 aluminum are from Refs *8* and *9*, respectively. The values of density and elastic constants of the last three materials are subsequently also used to calculate the elastic constants of SiC/2014-T4 aluminum based on theoretical models for composites due to Hashin and Shtrikman [*1*] and Maewal and Dandekar [*2*].

TABLE 2—*Density and adiabatic elastic properties of SiC/2014-T4 Aluminum, SiC, 2014-T4 Aluminum, and 2014-T6 Aluminum.*

Properties	Units	SiC/2014-T4 Aluminum[a]	SiC[b]	2014-T4 Aluminum[a]	2014-T6 Aluminum[c]
Density	Mg/m^3	2.906	3.21	2.81	2.81
Elastic wave velocity	km/s				
Longitudinal, v(l)		7.307	12.37	6.378	6.353
Shear, v(s)		3.884	7.81	3.145	3.199
Bulk, v(b)		5.769	8.47	5.243	5.169
Elastic Modulus	GPa				
Youngs, E		114 ± 2	458.0	74.5	76.4
Shear, μ		43.8 ± 0.7	196.0	27.8	28.7
Bulk, K		96.7 ± 1.3	230.2	77.2	75.1
Poisson's ratio (ν)		0.303 ± 0.006	0.168	0.341	0.330
Pressure derivative					
Bulk modulus		5.42	2.8[d]		4.23
Shear modulus		2.48	2.9[d]		2.25

[a] Present work.
[b] Reference *8*.
[c] Reference *9*.
[d] Estimated from shock data, see text for details.

Elastic Constants at Elevated Pressures

The changes in the elastic wave velocities in SiC/Al were obtained from the measured changes in frequencies of longitudinal and shear wave modes as a result of changing the pressure. The results of three sets of frequency measurements for longitudinal wave velocities and six sets of similar measurements for shear wave velocity in SiC/Al are shown in Figs. 2 and 3, respectively. These figures show that the measured frequencies for both longitudinal and shear wave velocities in SiC/Al vary almost linearly with pressure. The least squares fit to these data yield

$$F(1,P)/F(1,0) = 1.00010 + (2.61363 \times 10^{-2})P \tag{1}$$

and

$$F(s,P)/F(s,0) = 0.998949 + (2.70908 \times 10^{-2})P \tag{2}$$

for longitudinal and shear wave velocities, respectively, to 1.5 GPa.

In Eqs 1 and 2 P is pressure in GPa. In Eq 1, $F(1,P)$ and $F(1,0)$ are the frequencies (reciprocal of transit time for elastic wave) for longitudinal elastic wave at pressure P and one atmospheric pressure, respectively. Similarly, $F(s,P)$ and $F(s,0)$ are the frequencies for shear eleastic wave at pressure P and one atmospheric pressure, respectively. The correlation coefficient for these respective least squares fits are 0.998 and 0.995.

It should be noted that under ideal circumstances, the first coefficients in Eqs 1 and 2 would be identical and equal unity. However, in the subsequent calculations, we have used the Eqs 1 and 2 so as not to artificially remove the inherent error incurred in representing the frequency variations with pressure by a straight line. The changes in the elastic wave velocities and elastic constants with pressure were calculated by applying the self-consistent iterative method to obtain the numerical values of these constants without a prior knowledge of the compressibility of the material developed by Dandekar, the details of which will be found in Ref *10*. These computations require values of volume thermal expansion coefficient (β) and specific heat at constant pressure (Cp). Since the value of β is not yet measured for SiC/2014-T4 aluminum, the measured value of the volume thermal expansion coefficient for a composite consisting of 25 volume percent of SiC whiskers in 2024-T6 aluminum matrix is used instead. The value of β is $5.076 \times 10^{-5}\ K^{-1}$ [*11*]. Similarly, the value of the specific heat is computed by using the thermal model given in Ref *12* and the measured values of specific heat, thermal expansions, and bulk moduli of SiC and 2014-T6 aluminum. The calculated value of Cp for SiC/2014-T4 aluminum is 919.6 J kg^{-1} K^{-1}. These values of β and Cp were used because their values for SiC/2014-T4 aluminum remains to be determined. However, it can be shown that even an error of 10% in the values of either of these two parameters will change the calculated values of elastic constants by only 0.4%. Isothermal pressure derivatives of adiabatic bulk and shear moduli of SiC/2014-T4 determined from the sound wave velocity measurements are displayed in Table 2.

These pressure derivatives can be used with confidence to 1.5 GPa and probably may be used above this pressure to obtain pressure-volume curve to a much higher pressure.

The adiabatic compression curve of SiC/2014-T4 aluminum when expressed in the form of Bridgman's equation, that is

$$-\Delta V/V_o = aP + bP^2 \tag{3}$$

where a is adiabatic compressibility, that is, K^{-1}

and

$$b = -0.5\{1 + (\partial K/\partial P)_T\}/K^2(P) \text{ as } P \longrightarrow 0 \tag{4}$$

and $\Delta V/V_o$ is the change in volume with respect to the volume V_o of the material at the ambient pressure, is given by

$$-\Delta V/V_o = (1.0341 \times 10^{-2})P - (3.4323 \times 10^{-4})P^2 \tag{5}$$

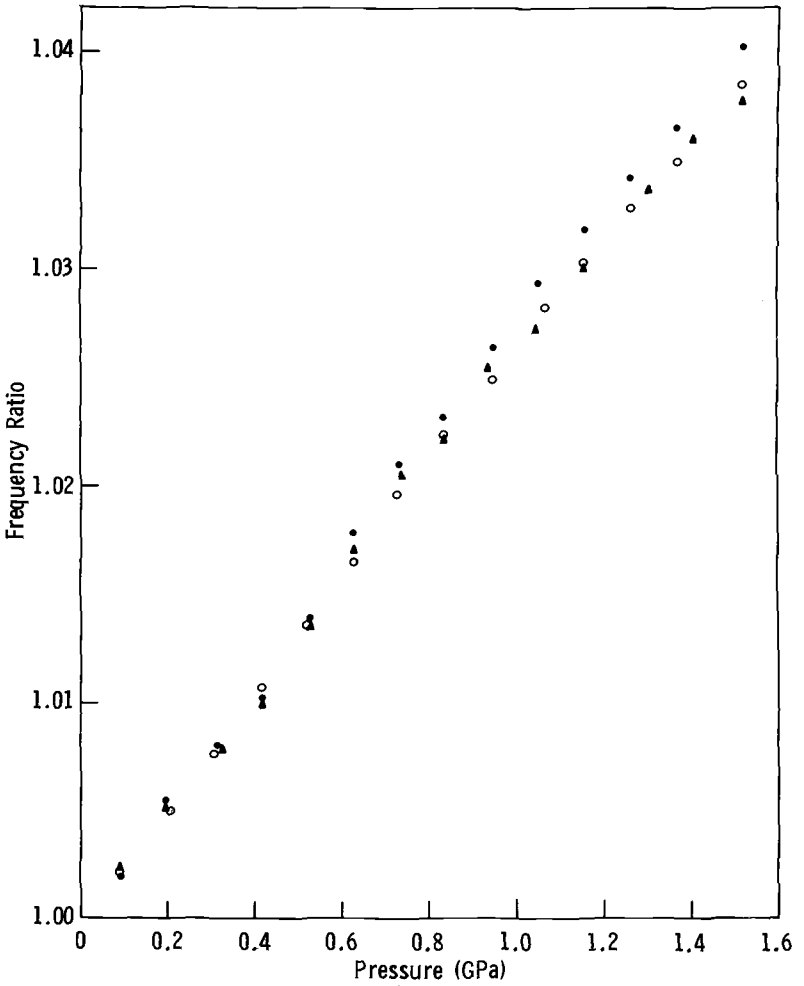

FIG. 2—*Frequency ratio for longitudinal elastic wave velocity versus pressure in SiC/Al in three different experiments.*

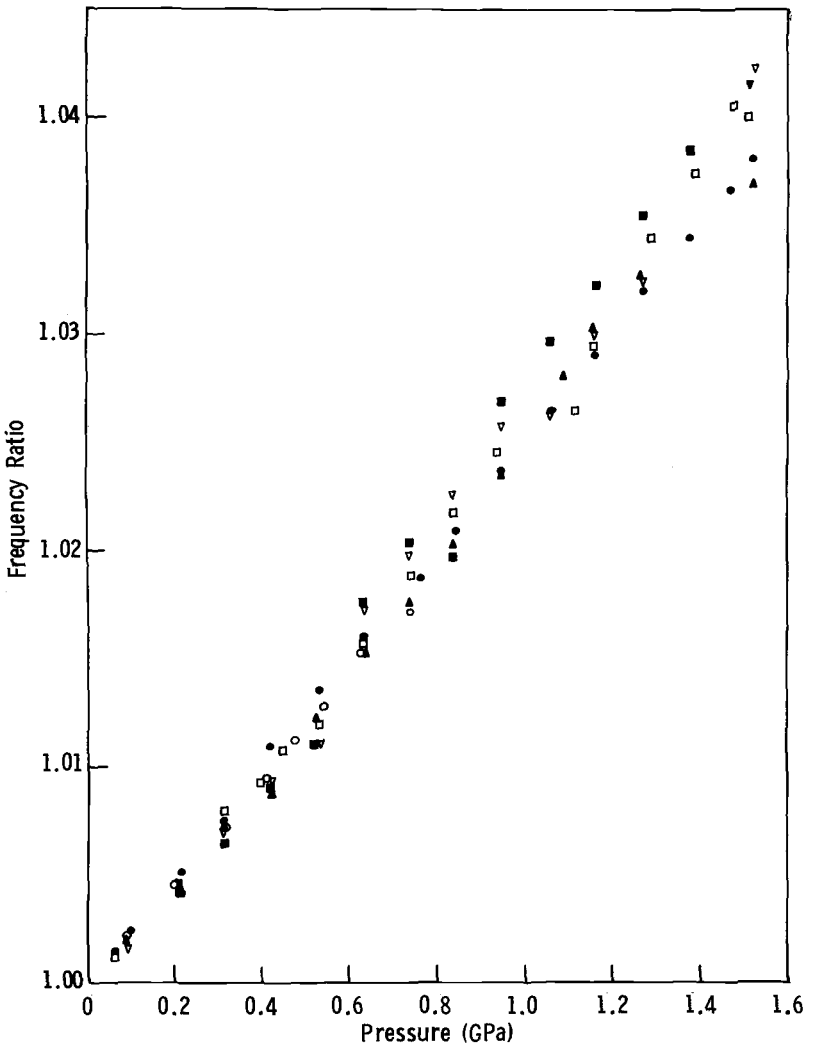

FIG. 3—*Frequency ratio of shear elastic wave velocity versus pressure in SiC/Al in six different experiments.*

Discussion

It is of interest to note that the pressure derivatives of the elastic moduli obtained for SiC/2014-T4 aluminum exceed the respective pressure derivatives for 2014-T6 aluminum. Since tempering of 2014 aluminum to T4 and T6 conditions do not change their elastic constants significantly, it is reasonable to assume that the pressure derivatives of the bulk and shear moduli of 2014-T4 aluminum could not be significantly different from those experimentally determined for 2014-T6 aluminum in Ref *9*. Unfortunately, no high-pressure elastic constant measurements of SiC is yet available for such a direct comparison. However, one can estimate the pressure derivatives of the bulk and shear moduli of SiC by using the existing shock wave data given in Refs *13* and *14*. McQueen et al. [*13*] showed that the

shock wave velocity, U_s, in SiC was linearly dependent on the particle velocity, U_p, and this dependency can be written as

$$U_s = 8.00 + 0.95\ U_p \tag{6}$$

where U_s and U_p are in km/s. This relationship was determined by conducting shock wave experiments where the maximum pressure reached in SiC was 110 GPa. Whenever such a linear relationship is found to exist for a material, it implies that the pressure derivative of the bulk modulus (K') for the material as the presssure goes to zero is given by

$$K' = 4s - 1 \tag{7}$$

where s is the rate of change of U_s with respect to U_p, that is, for SiC, the value of s is 0.95 as in Eq 6. Therefore, the value of the pressure derivative of the bulk modulus is 2.8. It is this value which is listed in Table 2 for SiC.

The shear modulus of SiC at high pressure is calculated from the relation between the modulus μ, and the Hugoniot elastic limit (HEL) σ_H, relative volume change at HEL η_H, and Hugoniot pressure P_H, at η_H [*15*]. Hugoniot pressure P_H, at low pressures, say below 10 GPa, is very close to hydrostatic pressure. Therefore, the shear modulus μ, at pressure P_H is given by

$$\mu = 0.75\ (\sigma_H - P_H)/\eta_H \tag{8}$$

where $\eta_H = 1 - V_H/V_o$.

The average value of η_H for SiC on the basis of eight shock wave experiments where HEL was observed in Ref *14* is found to be 1.92×10^{-2}. The average initial density of SiC used by Gust et al. [*14*] was 3.08 Mg/m^3. The observed HEL for this low density SiC was 8.0 GPa. The value of σ_H for fully dense SiC, assuming that η_H do not depend on porosity, can be estimated from the equation

$$\sigma_H = \rho_o v^2(1,o) \cdot \eta_H \tag{9}$$

where ρ_o is the initial density and $v(1,o)$ is the longitudinal velocity at one atmospheric pressure [*16*]. Substituting the values of ρ_o and $v(1,o)$ for SiC listed in Table 2, we get a value of 9.44 GPa for σ_H of fully dense SiC.

When a similar correction is done for the determination of P_H for fully dense SiC from the data of McQueen et al. [*13*], we obtain a value of 4.115 for P_H at $\eta_H = 1.92 \times 10^{-2}$. Substituting the values of σ_H, P_H, and η_H in Eq 8 gives a value of shear modulus (μ) equal to 207.9 GPa. This can be treated as the value of μ of SiC at pressure P_H, that is, 4.115 GPa. The value of shear modulus of fully dense SiC at one atmospheric pressure is 196 GPa (Table 2). Hence, the calculated pressure derivative of the shear modulus is 2.9, as listed in Table 2.

Table 2 shows that the pressure derivative of bulk modulus of SiC/Al is larger than the presssure derivatives of this modulus for each of the two constituents. However, the pressure derivative of the shear modulus of SiC/Al is comparable to those of its two constituents. The physical reason for this is not clear at present.

Following the works of Hashin and Shtrikman [*1*] and estimates of the elastic constants using the procedure of Maewal and Dandekar [*2*], we obtain the numbers given in Table 3. Both models predict elastic constants values for SiC/Al composite by using the elastic

TABLE 3—*Elastic constants (in units of GPa) of SiC/Al as a function of pressure.*

	Pressure, GPa			
	0.0001		1.5	
	Bulk Modulus	Shear Modulus	Bulk Modulus	Shear Modulus
Measured	96.7	43.8	104.8	47.5
Hashin and Shtrikman				
Lower Bound	96.3	41.3	103.3	45.8 (45.6)
Upper Bound	105.7	54.5	112.1 (112.0)	58.3 (57.7)
Maewal and Dandekar	100.0	45.3	106.7 (106.7)	49.5 (49.2)

constants of its constituents SiC and 2014-T4 aluminum. Comparison shows that the measured values of the elastic constants of SiC/Al do lie within the Hashin and Shtrikman [*1*] bounds both at the ambient and elevated pressures. The estimates of bulk and shear moduli following Maewal's [*2*] procedure are within 4% of the preceding results. Since the errors involved in the estimation of shear modulus of SiC at high pressure from shock wave data of Refs *13* and *14* could be large, we include in Table 3 the computed values of bulk and shear moduli of SiC/Al at 1.5 GPa with a drastic assumption that shear modulus of SiC does not change with presssure. These calculations are shown within parentheses in Table 3 and reveal that the calculated values of the constants are only negligibly changed due to this drastic assumption.

Conclusions

1. The equation of state of SiC/Al, when expressed in the form of Bridgman's equation, is given by

$$-\Delta V/V_o = (1.0341 \times 10^{-2})P - (3.4323 \times 10^{-4})P^2$$

where P is in GPa.

2. The model developed by Maewal seem to provide reasonable estimates of the elastic constants of SiC/Al as a function of pressure and is consistent with the Hashin and Shtrikman bounds.

3. The calculated values of the elastic constants of SiC/Al at high pressure are relatively insensitive to the pressure derivative of the shear modulus of SiC.

References

[*1*] Hashin, Z. and Shtrikman, S., *Journal of the Mechanics and Physics of Solids,* Vol. 11, 1963, pp. 127–140.
[*2*] Maewal, A. and Dandekar, D. P., *Acta Mechanica,* Vol. 66, 1987, pp. 191–204.
[*3*] Mori, T. and Tanaka, K., *Acta Metallurgica,* Vol. 21, 1973, pp. 571–574.
[*4*] Taya, M. and Chou, T. W., *International Journal of Solids and Structures,* Vol. 17, 1981, pp. 553–564.
[*5*] Weng, G. J., *International Journal of Engineering Science,* Vol. 22, 1984, pp. 845–856.
[*6*] Tandon, G. P. and Weng, G. J., *Polymer Composites,* Vol. 5, 1984, pp. 327–333.
[*7*] Papadakis, E. P., *Journal of Acoustical Society of America,* Vol. 42, 1967, pp. 1045–1051.
[*8*] Schreiber, E. and Soga, N., *Journal of American Ceramic Society,* Vol. 49, 1966, p. 342.

[9] Babcock, S. G., Langan, J. J., Norvey, D. B., Michaels, T. E., Schierloh, F. L., and Green, S. G., "Characterization of Three Aluminum Alloys," AMMRC CR 71-3, Army Materials and Mechanics Research Center, Watertown, MA, January 1971.
[10] Dandekar, D. P., *Journal of Applied Physics*, Vol. 41, 1970, pp. 667–672.
[11] Gubbay, J. D., "Micromechanical Properties of Al/SiC Metal Matrix Composite," The Charles Stark Draper Laboratory Final Report CSDL-R-1578, The Charles Stark Draper Laboratory, Inc., Cambridge, MA, June 1982.
[12] Christensen, R. M., *Mechanics of Composite Materials*, John Wiley and Sons, New York, 1979, pp. 311–339.
[13] McQueen, R. J., Marsh, S. P., Taylor, J. W., Fritz, J. N., and Carter, W. J. in *High Velocity Impact Phenomena*, Ray Kinslow, Ed., Academic Press, New York, 1970, Chapter VII, and Appendix E, pp. 293–417 and p. 549.
[14] Gust, W. H., Holt, A. C., and Royce, E. B., *Journal of Applied Physics,* Vol. 44, 1973, pp. 550–560.
[15] Fowles, G. R., *Journal of Applied Physics*, Vol. 32, 1961, pp. 1475–1487.
[16] Steinberg, D. J., "Equations of State for the Ceramics BeO and B_4C," UCID-16946, Lawrence Livermore National Laboratory, Livermore, CA, Nov. 1975.

Theoretical Considerations

Donald F. Adams[1]

Micromechanical Modeling of Yielding and Crack Propagation in Unidirectional Metal Matrix Composites

REFERENCE: Adams, D. F., "**Micromechanical Modeling of Yielding and Crack Propagation in Unidirectional Metal Matrix Composites**," *Testing Technology of Metal Matrix Composites, ASTM STP 964,* P. R. DiGiovanni and N. R. Adsit, Eds., American Society for Testing and Materials, Philadelphia, 1988, pp. 93–103.

ABSTRACT: A two-dimensional finite element micromechanics analysis was used to predict the response of a unidirectional graphite/aluminum composite subjected to transverse tensile, longitudinal shear, or axial-transverse tensile biaxial loadings. Processing-induced thermal residual stresses and the temperature dependence of the highly nonlinear aluminum matrix properties were included, along with the anisotropy of the graphite fibers. A parametric study was made of the influence of matrix heat treatment condition and fiber-matrix interface bond strength on composite response to the various loadings. The correlations with available experimental data suggested that the actual composite material may have been in an intermediate heat treat condition, and a moderate interface strength degradation state.

KEY WORDS: metal matrix composites, graphite/aluminum composites, unidirectional composites, micromechanics analysis, crack propagation

The high degree of matrix material nonlinearity and the possibility of a weak interface in many metal-matrix composites requires the use of special analysis capabilities. Most existing analytical tools are based on elastic response of a continuum, that is, no plastic flow and no local microcracking. The author and his colleagues have, over a period of years, developed a much more general two-dimensional, generalized plane-strain finite-element micromechanics analysis of unidirectional composite response. Early work [*1,2*] did include material properties temperature-dependence and crack propagation, but only normal stress loadings. Also, computers available during that time period were limited in storage capacity and computational speed, thus severely limiting the size of the finite element grids which could be used. Thus, while very informative in a qualitative sense, these analyses did not permit detailed interpretations.

During the past decade, improvements in both computers and computational techniques have been rapid. Correspondingly, the micromechanics analysis capabilities have steadily improved, to permit combined shear and normal loadings [*3,4*], time-dependent viscoplastic effects [*5*], and much more computationally efficient solution routines [*6*]. The particular computer program used in the present study, WYO2D, includes all of these two-dimensional micromechanics features except time-dependent material effects, which were not considered here, only static properties experimental data being available.

The unidirectional graphite fiber-reinforced, aluminum matrix composite experimental

[1] Professor of Mechanical Engineering, director Composite Materials Research Group, University of Wyoming, Laramie, WY 82071.

data were generated as a part of a study in conjunction with Vought Corporation for the Naval Surface Weapons Center [7], as also reported separately in unrestricted distribution form in Ref *8*. The brief analysis performed at that time utilized an earlier version of the micromechanics analysis [9], which did not include crack propagation. The present program WYO2D was later used to model cracking, as briefly reported in Ref *10*. For the present publication, all of this prior analysis has been repeated, using matrix material properties that more closely describe the actual 201 aluminum alloy matrix of the composites being modeled.

Capabilities of the WYO2D analysis and related computer program are presented and discussed in Ref *10* and thus need not be repeated here.

Constituent Material Properties

The material tested as part of the NSWC program [7] was a unidirectional graphite/epoxy composite fabricated by DWA Composite Specialties, Inc. in December 1981, and sent directly to the University of Wyoming. One plate measuring 430 mm (17 in.) by 430 mm (17 in.) by 1.0 mm (0.04 in.) was received, additional material being sent directly to Vought Corporation. This plate was ultrasonically C-scanned and determined to be of acceptable quality [8]. Axial and transverse tension and compression, Iosipescu shear, axial, and transverse thermal expansion, and cruciform-shaped biaxial loading specimens were then cut from this plate for testing. Complete details of specimen preparation and testing procedures, and all test results, are included in Ref *8*.

The fiber was Union Carbide VSB-32 (P-55), a pitch-precursor graphite fiber. The assumed properties for this fiber are listed in Table 1. This fiber was assumed to be transversely isotropic, to remain linearly elastic to fracture, and to have properties independent of temperature in the range of interest here.

The matrix material of the graphite/aluminum wire preform used was 201.0 aluminum alloy, the plate being fabricated with thin face sheets of 2024 aluminum alloy. The compositions of these two alloys are very similar, as discussed in Ref *8*. These composites are typically processed at 566°C (1050°F) [13]. However, the actual alloy heat treat condition as fabricated was not known. The assumed mechanical and physical properties of the 201 aluminum alloy matrix were established based on data available in Refs *14* and *15*. Plots of the uniaxial tensile, room temperature stress-strain curves for three different assumed heat treat conditions, namely, 0, T2, and T6, are presented in Fig. 1. As will be discussed, the T2 condition provided the best agreement with the available experimental data. Plots of the variation of modulus and coefficient of thermal expansion of the 201 aluminum alloy as a function of temperature are presented in Fig. 2.

TABLE 1—*Material properties for Union Carbide VSB-32 pitch-based graphite fiber.*

Longitudinal modulus	E_l = 379 GPa (55 Msi) [11]
Transverse modulus	E_t = 10.3 GPa[a] (1.5 Msi[a])
Major Poisson's ratio	ν_{lt} = 0.20[a]
In-plane Poisson's ratio	ν_{tt} = 0.25[a]
Longitudinal shear modulus	G_{lt} = 28 GPa[a] (4 Msi[a])
Longitudinal thermal expansion	α_l = -0.54×10^{-6}/°C[b] (-0.30×10^{-6}/°F[b])
Transverse thermal expansion	α_t = 18×10^{-6}/°C[b] (10×10^{-6}/°F[b])

[a] Estimated.
[b] Based on data for Hercules HMS fiber (E = 345 GPa) [12].

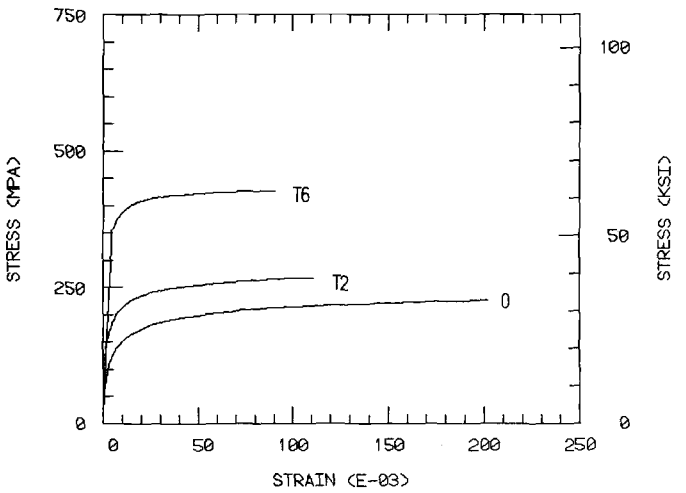

FIG. 1—*Room temperature tensile stress-strain curves for the 201.0 aluminum alloy matrix material in various heat treat conditions.*

As can be seen in Figs. 1 and 2, the matrix stress-strain response is strongly influenced by heat treat condition, and for a given condition, by the test temperature. The latter is significant in that the composite is processed at elevated temperature, even if only tested at room temperature. Cooldown from the processing temperature induces thermal residual stresses, which must be modeled by the analysis. Thus, properties as a function of temperature are needed.

Micromechanical Modeling

The VSB-32 graphite fibers were modeled as being circular in cross section, and arrayed in a square packing in the 201 aluminum alloy matrix. The experimentally determined fiber volume of 45% was modeled. Because of the periodic array assumed, it was necessary to model only one quadrant of a fiber and the surrounding matrix. The finite element grid used for this purpose is shown in Fig. 3. This is the same grid as used in the work of Ref *10*; it contains 704 constant strain elements and 384 node points. Using reduced integration and a frontal solution technique, an average of 17 CPU seconds per solution increment was required on a Control Data Corporation CDC CYBER 760 mainframe computer. The grid model includes layers of small elements at the fiber-matrix interface, as can be seen in Fig. 3. Any of the material properties of a layer of these elements can be selectively reduced as desired, typically to a fraction of the corresponding matrix values, to model a degraded interface. In the present study, interfacial degradation was analytically characterized by the simultaneous percentage reduction of one-dimensional tensile and compressive yield and ultimate matrix strengths. All other material properties, such as extensional and compressive moduli, shear modulus, Poisson's ratios, maximum shear stress, etc., were not degraded. Also, the degraded region was limited to the narrow annulus of matrix material surrounding the fiber, as shown in Fig. 3.

Although yielding is dictated by an octahedral shear stress criterion in the present version of WYO2D, the failure criterion can be selected as desired. For the present study, octahedral shear stress (distortional energy) and maximum principal stress failure criteria were both evaluated.

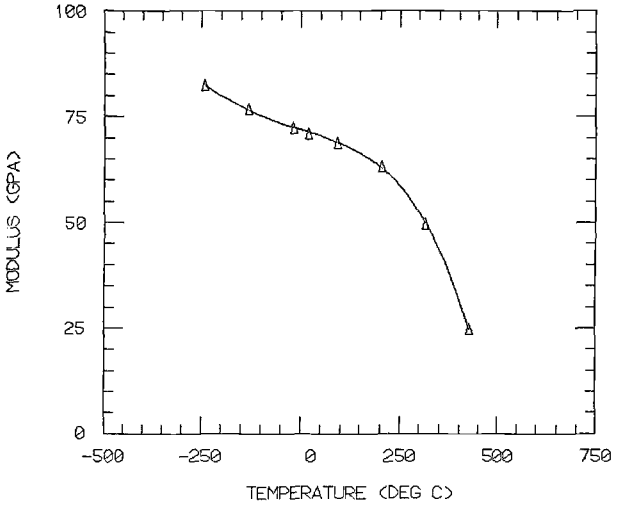

a) Tensile Modulus

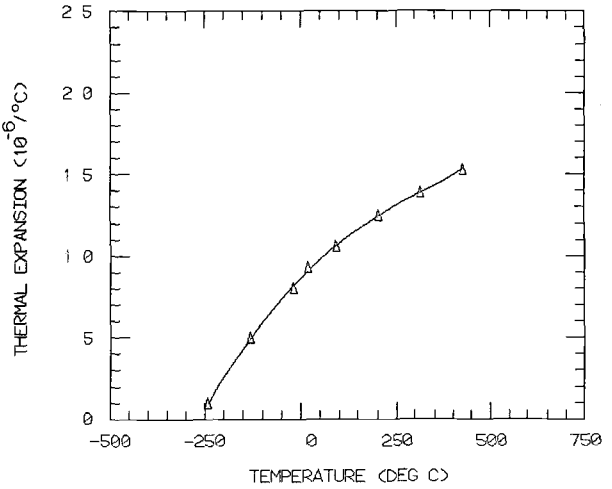

b) Coefficient of Thermal Expansion

FIG. 2—*Temperature dependence of the tensile modulus and coefficient of thermal expansion of the 201.0 aluminum alloy matrix material.*

Analytical/Experimental Results

The experimental data available for correlation purposes were previously published in Refs *7* and *8*, and included axial and transverse tension, axial and transverse compression, Iosipescu shear, and biaxial loading tests. The axial tensile response is fiber dominated, and hence of limited interest for a micromechanics analysis, as demonstrated in Refs *8* and *10*. Axial compression was dominated by fiber microbuckling, which is not modeled in the present analysis. Thus, attention was focused here on the transverse tensile, Iosipescu shear, and biaxial tensile loading data. These will be discussed in order.

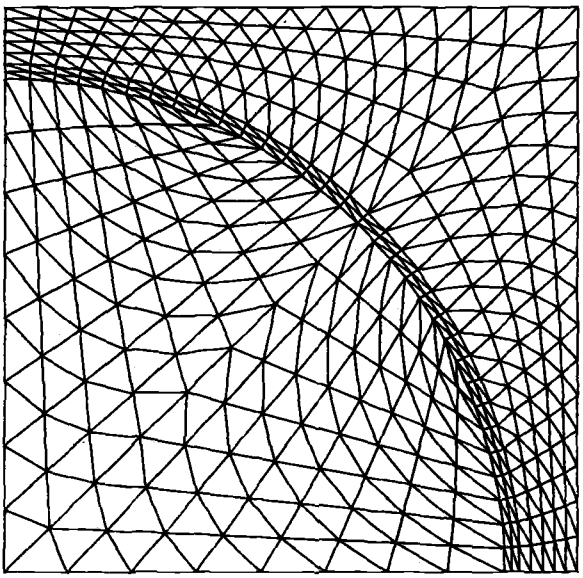

FIG. 3—*Finite element grid model of one quadrant of a repeating unit cell representing a square array of circular fibers in a matrix.*

Of the many parametric variations considered relating to matrix heat treat condition, fiber-matrix interface degradation, and failure criterion, nine will be discussed here. These are listed and described in Table 2. The goal was to analytically define a matrix heat treat condition, failure criterion, and interface bond condition that would predict with reasonable accuracy the actual experimental response for all three types of loadings considered.

TABLE 2—*Parametric Variations Considered.*

Variation No.	Matrix Condition	Interface Condition (percent degraded[a])	Failure Criterion
1	0	0	octahedral shear for shear loading, maximum principal stress for others
2	T2	25	octahedral shear for shear loading, maximum principal stress for others
3	T2	35	octahedral shear for shear loading, maximum principal stress for others
4	T2	50	octahedral shear for shear loading, maximum principal stress for others
5	T6	0	maximum principal stress
6	T6	0	octahedral shear stress
7	T6	10	octahedral shear stress
8	T6	25	octahedral shear stress
9	T6	35	octahedral shear for shear loading, maximum principal stress for others

[a] Interface yield and alternate strengths were reduced by the indicated fractions of the corresponding matrix properties.

Transverse Tension

The available experimental data [*7,8*] for five individual transverse tensile test specimens are shown plotted in Fig. 4. The typical scatter for this type of experimental data will be noted. Also plotted in Fig. 4 are the results of the nine parametric variations defined in Table 2, although not all are significant. For example, Variation 4, that is, a 201-T2 aluminum matrix with 50% degradation of the fiber-matrix interface, proved to be too severe, leading to predicted total failure prior to mechanical loading. That is, the thermal residual stresses induced during cooldown from the 566°C processing temperature were in themselves sufficient to fail the material.

For Variation 1, the only variation to include the 201-0 (fully annealed) matrix condition, the interface failed completely during cooldown, but not the matrix between fibers. These thin webs of matrix material then failed relatively soon in the transverse tensile loading process. The low composite stiffness due to the fiber-matrix interface bond failure, that is, the lack of load carrying ability of the isolated fibers, is evident in Fig. 4.

Variations 5 and 6, for a T6 matrix condition and no interface degradation, resulted in little nonlinear response of the composite, as shown in Fig. 4, even though the matrix itself was quite nonlinear (see Fig. 1). This was associated with the highly triaxial stresses that developed in the matrix under loading, thus inhibiting plastic deformation. Neither Variation 5, using a maximum principal stress failure criterion, nor Variation 6, using an octahedral shear stress failure criterion, produced any matrix yielding up to the loadings indicated in Fig. 4, much less microcracking, and thus the computer runs were terminated.

Similar results were obtained for Variations 7 and 8, for an octahedral shear failure criterion, and for Variation 9, for a maximum principal stress failure criterion, for 10, 25, and 35% interface degradations, respectively. These computer runs were terminated at 79 MPa (11.5 ksi).

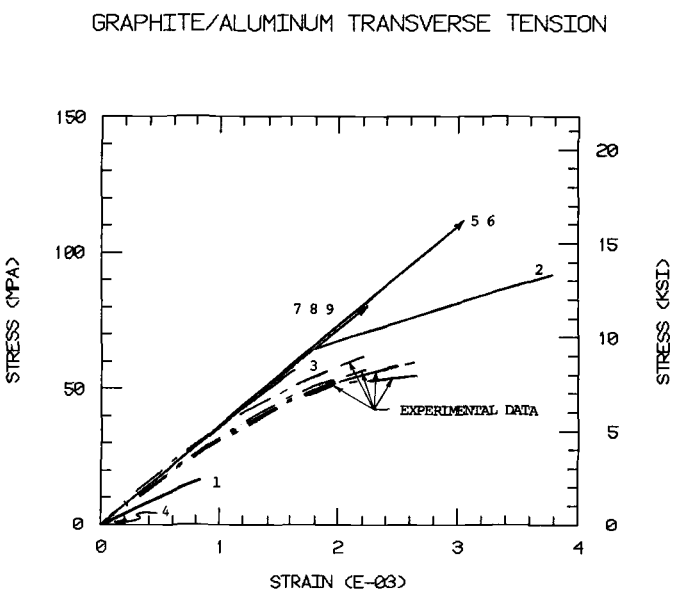

FIG. 4—*Correlations of the various analytically predicted transverse tensile stress-strain responses with available experimental data for a unidirectional graphite/aluminum composite.*

Variation 3 was similar to Variation 4, which resulted in total failure during cooldown, but for a 35% interface degradation rather than 50%. First failure, at the interface, was predicted at approximately 21 MPa (3 ksi), with total failure of the composite at 56 MPa (8.1 ksi). A relatively high yield stress was assumed for this 201-T2 matrix, and thus the composite stress-strain response was relatively linear to failure.

Variation 2 was similar to Variation 3, but for only a 25% interface ultimate strength degradation rather than 35%. First failure occurred at the interface, at 50 MPa (7.3 ksi), but then spread transversely in the matrix between fibers before proceeding further around the interface. Total failure occurred at approximately 90 MPa (13 ksi), but with a relatively high degree of nonlinearity and strain to failure, as can be seen in Fig. 4.

In summary, a maximum normal stress failure criterion, a moderate degradation of the fiber-matrix interface (on the order of 25%) and a mild matrix hardening, somewhere near a T2 condition, appears to best model the present graphite/aluminum transverse tensile data.

Longitudinal Shear

Available experimental data [*7,8*] for three individual Iosipescu shear tests of the unidirectional graphite/aluminum composite are plotted in Fig. 5. Predicted responses for the parametric variations listed in Table 2 are also shown.

Variations 6, 7, and 8, for the 201-T6 aluminum at increasing levels of interface degradation, resulted in no failures up to 160 MPa (23 ksi), where the computer simulations were terminated as already being above the measured shear strength of approximately 145 MPa (21 ksi). As can be seen in Fig. 5, essentially no composite nonlinearity was predicted. The 25% interface degradation case (Variation 8) did indicate interface yield initiation at about 138 MPa (20 ksi), but no microcracking.

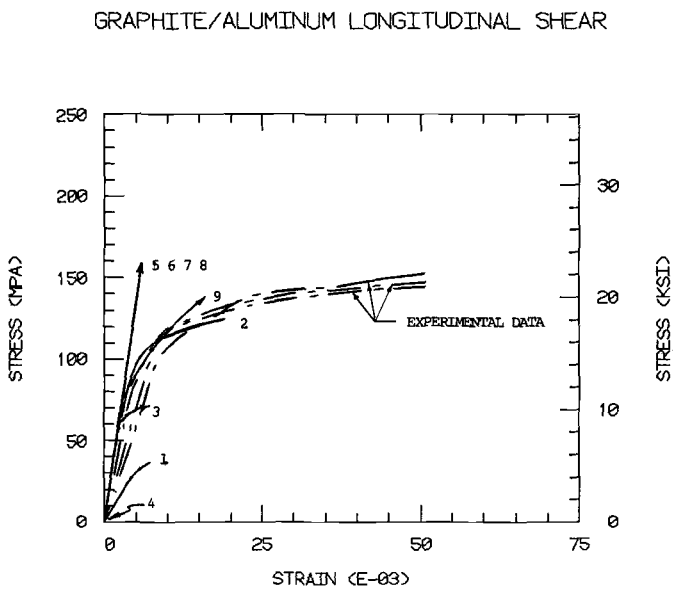

FIG. 5—*Correlations of the various analytically predicted longitudinal shear stress-strain responses with available experimental data for a unidirectional graphite/aluminum composite.*

The 35% interface degradation case (Variation 9) resulted in somewhat more severe response. The interface began to fail at a low stress level, being completely failed at 83 MPa (12 ksi). However, the matrix then continued to yield with no further crack propagation, the run being terminated at 152 MPa (22 ksi).

Similar response was predicted for Variation 1. That is, the interface failed and the low strength (annealed) matrix yielded readily, resulting in low stiffness and strength, and high strain to failure.

Variations 2, 3, and 4 represent the T2 condition matrix. The 50% interface degradation was too severe, causing failure during cooldown, as previously discussed. The 35% degradation (Variation 3) was more reasonable, the entire matrix yielding at a low stress level, followed by complete interface failure at about 6 MPa (9 ksi). No further matrix cracking occurred, however, and the predicted composite yield point was too low, as shown in Fig. 5. For Variation 2 (25% degradation) the matrix yielded extensively also, being fully yielded at about 48 MPa (7 ksi). The interface did not begin to fail until a shear stress of 97 MPa (14 ksi) had been applied, however, at which point it rapidly failed completely. This accounts for the relatively abrupt yield shown in Fig. 5, which correlates well with the available experimental data. The large strains to failure indicated for the experimental data may be exaggerated by the test method used, which did not result in abrupt failures for this material.

An octahedral shear stress failure criterion was assumed for the longitudinal shear loading in all cases except Variation 5. A maximum principal stress criterion did not predict the measured response well. Variation 5 was one such attempt, the response being similar to that for Variation 6.

In summary, a shear stress-based failure criterion, a moderate interface degradation (about 25%), and a mild matrix hardening (T2) resulted in the best correlation with the available shear data. This is the same interface and matrix condition that was found to be most suitable for the transverse tensile data.

Biaxial Loadings

For the present study, the three biaxial tests in the first quadrant of the loading space, that is, the tensile-tensile loadings, were selected from Ref *8*. These represented axial-to-transverse load ratios of 2:1, 5:1, and 10:1.

Both axial and transverse stress-strain response were monitored experimentally; the transverse stress-transverse strain plots are shown in Fig. 6 through 8, for the 2:1, 5:1, and 10:1 ratios, respectively. These transverse loading curves would be expected to exhibit the composite material nonlinearity if it occurred. The actual experimental curves are shown in Figs. 6 and 7. For the 10:1 loading ratio of Fig. 8, the measured strains were very small and scattered. Thus, the experimental curve is not shown. The measured transverse tensile stresses at failure, as tabulated in Ref *8*, were 73 MPa (10.6 ksi), 57 MPa (8.3 ksi), and 37 MPa (5.4 ksi) for the three load ratios, respectively. The 2:1 and 5:1 load ratio specimen failures were identified to be transverse tensile failures, while the 10:1 load ratio specimen failed in a combined axial tension (fiber failure) and transverse tension mode.

The predicted transverse strains were consistently greater than measured, but not excessively so considering the small values involved.

The T6 matrix condition (Variations 6 through 9) again proved to be too strong. No yielding or interface failure occurred for Variations 6 through 8 before the analysis was terminated at applied stress levels well above the experimental values. Interface failures did occur for Variation 9 (35% degradation), being minimal for the 2:1 ratio case, and extensive for the 10:0 ratio case. This explains the considerable nonlinearity at the high stress level for Variation 9 in Fig. 8. An octahedral shear stress failure criterion was used in Variations 6 through 8.

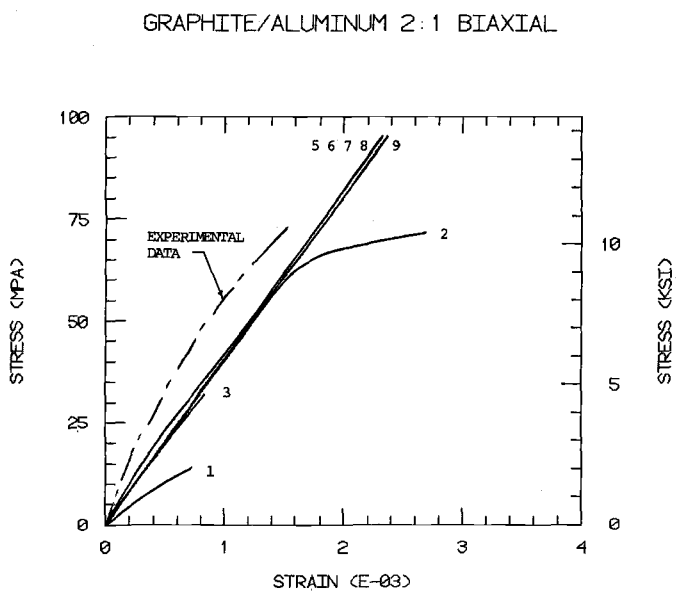

FIG. 6—*Correlations of the various analytically predicted 2:1 ratio biaxial loading transverse tensile stress-strain responses with available experimental data for a unidirectional graphite/aluminum composite.*

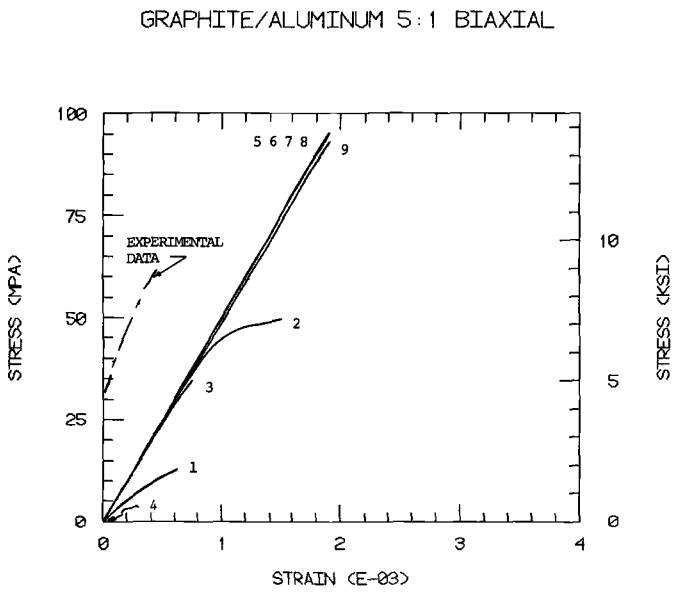

FIG. 7—*Correlations of the various analytically predicted 5:1 ratio biaxial loading transverse tensile stress-strain responses with available experimental data for a unidirectional graphite/aluminum composite.*

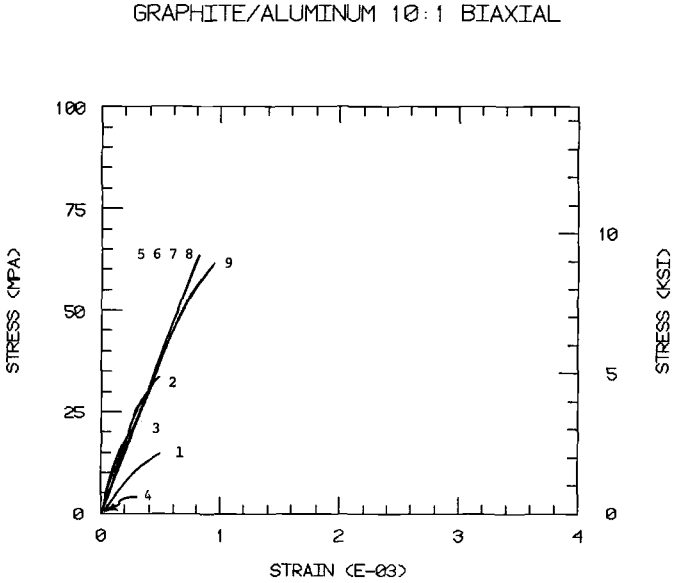

FIG. 8—*Correlations of the various analytically predicted 10:1 ratio biaxial loading transverse tensile stress-strain responses for a unidirectional graphite/aluminum composite.*

The 201 (annealed) matrix condition (Variation 1) again proved to be too weak, for all three loading ratios, resulting in low composite stiffnesses and strengths.

As noted for the uniaxial loadings, that is, transverse tension and longitudinal shear, the severely degraded (50%) interface, 201-T2 matrix simulation was too drastic, resulting in failures during cooldown. At 35% degradation (Variation 3), the interface failures initiated at low levels, spreading around the interface progressively with increasing loading, resulting in predicted composite strengths lower than measured.

At 25% degradation (Variation 2), the failures also occurred at the fiber-matrix interface, but did not propagate as rapidly. In fact, for the 2:1 and 5:1 loading ratios, that is, those cases where the transverse tensile loading was a higher percentage of the axial loading, the crack was predicted to move into the matrix before it completely isolated the fiber. The stress levels at which failures were predicted were relatively close to those measured, for all three biaxial loading conditions. Transverse failures were predicted, as experimentally observed. A maximum principal stress failure criterion was used.

In summary, a maximum principal stress failure criterion, a moderate interface degradation (25%), and a mild matrix hardening (T2) resulted in the best correlation with the experimental data.

Conclusion

The present study suggests that the various parameters which influence metal matrix composite stress-strain response and strength, for example, matrix heat treatment condition and interface bond strength, can be modeled by a micromechanics analysis. Predicted response is strongly influenced by the failure criterion assumed, with a normal stress-based criterion being appropriate for cleavage failures, and a shear stress-based criterion being most suitable for shear failures, as might be expected.

The most significant conclusion was that one combination of matrix hardening and level

of interface strength degradation was found to best fit all of the data for the loading conditions considered. This is as it must be, of course, if the analysis is to be significant, since the test material was the same for all loading conditions. Likewise, the values of the parameters used, that is, matrix material properties representative of a T2 heat treatment condition, and a 25% interface strength reduction, were well representative of the probable properties of the particular graphite/aluminum composite material tested, these properties not having been measured.

The present results also indicate the potential benefit of improving the fiber-matrix interface bond strength, and of achieving a higher matrix heat treatment condition.

Acknowledgments

The author wishes to acknowledge the assistance of Dennis K. McCarthy, Mechanical Engineering graduate student, in performing the many computer runs. The support of the Vought Corporation and the Naval Surface Weapons Center in generating the experimental data is also gratefully acknowledged.

References

[1] Adams, D. F., "Elastoplastic Crack Propagation in a Transversely Loaded Unidirectional Composite," *Journal of Composite Materials,* Vol. 8, Jan. 1974, pp. 38–54.

[2] Adams, D. F., "A Micromechanical Analysis of Crack Propagation in an Elastoplastic Composite Material," *Fibre Science and Technology,* Vol. 7, No. 4, Oct. 1974, pp. 237–256.

[3] Adams, D. F. and Crane, D. A., "Combined Loading Micromechanical Analysis of a Unidirectional Composite," *Composites,* Vol. 15, No. 3, July 1984, pp. 181–192.

[4] Adams, D. F. and Crane, D. A., "Finite Element Micromechanical Analysis of a Unidirectional Composite Including Longitudinal Shear Loading," *Computers and Structures,* Vol. 18, No. 6, 1984, pp. 1153–1165.

[5] Schaffer, B. G. and Adams, D. F., "Nonlinear Viscoelastic Analysis of a Unidirectional Composite Material," *Journal of Applied Mechanics,* Vol. 48, No. 4, Dec. 1981, pp. 859–865.

[6] Cilensek, R. F., "WYO2D Finite Element Analysis Computer Program User Instructions and Documentation," Composite Materials Research Group, University of Wyoming, Laramie, WY, June 1984.

[7] Standard, C. M. and Ho, T., "Metal Matrix Materials for Navy Systems Program," Final Report on Naval Surface Weapons Center Contract N60921-81-C-0114, LTV Aerospace, Dallas, TX, Jan. 1984.

[8] Zimmerman, R. S., Walrath, D. E., and Adams, D. F., "Biaxial Loading Characterization, Failure Mode Study, and Micromechanical Predictions and Correlations for Graphite/Aluminum Composites," Report UWME-DR-504-104-1, Department of Mechanical Engineering, University of Wyoming, Laramie, WY, July 1985.

[9] Crane, D. A. and Adams, D. F., "Finite Element Micromechanical Analysis of a Unidirectional Composite Including Longitudinal Shear Loading," Report UWME-DR-101-101-1, Department of Mechanical Engineering, University of Wyoming, Laramie, WY, February 1981.

[10] Adams, D. F., "Analytical/Experimental Correlations of Failure Modes in Composites," Proceedings of the SESA Symposium on Fracture Mechanics of Composites, 1985 Spring Conference on Experimental Mechanics, Las Vegas, NV, June 1985.

[11] Technical Information Bulletin No. 465-252, Union Carbide Corporation, May 1982.

[12] "Hercules Magnamite Graphite Fibers," Hercules Incorporated, Wilmington, DE, 1978.

[13] Gaebler, G., DWA Composite Specialties, Inc., Telecon Communication, Feb. 1982.

[14] Military Handbook 5D, "Metallic Materials and Elements for Aerospace Vehicle Structures," Department of Defense, Washington, DC, June 1983.

[15] *Metals Handbook,* Ninth Edition, American Society for Metals, Volume 2, 1979.

Edward M. Wu[1] *and S. C. Chou*[2]

Statistical Strength Comparison of Metal-Matrix and Polymeric-Matrix Composites

REFERENCE: Wu, E. M. and Chou, S. C., **"Statistical Strength Comparison of Metal-Matrix and Polymeric-Matrix Composites,"** *Testing Technology of Metal Matrix Composites, ASTM STP 964,* P. R. DiGiovanni and N. R. Adsit, Eds., American Society for Testing and Materials, Philadelphia, 1988, pp. 104–120.

ABSTRACT: The reliability of a composite structure depends on the materials strength variability. Unidirectional composites fail sequentially initiating from the very weakest fiber sites with matrix binder providing local redundancy by transferring load to neighboring fibers until cumulation and clustering of these sites lead to sever stress concentration and ultimate structure failure. As a consequence, the variability of the metal matrix structure is traceable to the strength variability of the constituent fiber, the metal matrix coating process, and the composite wire consolidation process. This report focuses on the partitioning of the first two sources of variability, identification and modeling of the dominant parameters, together with experimental measurment on a current graphite-aluminum composite. The statistical strength of several graphite spools are measured by testing single filament specimens at the beginning and at the end of the spools, thereby characterizing the statistical parameters associated with the strength variability among the spools and within each spool. The graphite-aluminum wire, produced from continuous liquid infiltration process are tested in tension. The metal matrix composite statistical strengths from differ spools are compared with the respective statistical strength of the parent fiber. The results suggest that, given proper interpretation, single filament fiber strength is a sensitive parameter for quality assurance of metal matrix composites.

KEY WORDS: statistical strength, dimensional scaling, size effect, testing methods, filament testing, metal matrix composites, Weibull distribution

Objective

The objective of this investigation is to perform experimental and analytical studies to:

1. Understand the failure process of metal matrix composites.
2. Identify the parametric roles of the fiber and the matrix which contribute to the *statistical* composite strength.

The results of this investigation will identify and quantify the attributes of metal matrix composites especially in comparison to polymeric composites. This understanding and characterization methodology discussed herein are relevant to:

(*a*) materials development and fabrication technology for metal matrix composites, and
(*b*) reliability design and quality assurance methodology for critical applications.

[1] Professor of Aeronautics, Department of Aeronautics, Naval Postgraduate School, Monterey, CA 93943.
[2] Army Materials Technology Laboratory, Watertown, MA 02172.

Background

Current PAN-based and pitch-based graphite fibers are achieving substantial improvement in strength largely through reduction of the fiber diameters. On the one hand, the smaller fiber diameter limits the maximum flaw size, thereby contributing to the strength increase. On the other hand, the smaller fiber approaches a geometrically true weakest-link-of-chain configuration, therefore causing a concurrent increase in variability. A strength scatter of 20 to 25% is not uncommon for current graphite fibers. Ordinarily, such high variability would render them unsuitable as an engineering structural material. However, the addition of a matrix binder causes a dramatic reduction in scatter to around 4% (for polymeric matrix composites).

The mechanism for the scatter reduction lies in the local structural redundancy provided by the matrix binder resulting in a sequential failure process rather than a catastrophic failure process. The sequential failure process is initiated by failure of weak fibers at very low load (as low as 15% of the ultimate load).

Through the adhesion of the matrix binder, the loads carried by these weak sites are transferred to neighboring fibers, thereby forestalling catastrophic failure of the entire composite. In fact these earlier fiber failures are not detectable except by acoustic emission detection instruments. Upon further load increase, more and more of the weak lower tail fibers fail leading to an increase in the spatial density of the failure sites and the companion increase in the probability of occurrence of *contiguous* failure sites. The contiguous fiber failure sites give rise to stress concentrations; the most severe of which causes ultimate catastrophic failure.

This sequential failure process caused by the micro-redundancy due to the presence of the matrix was qualitatively noted by Rosen [*1*], Zweben [*2*], and quantitatively modeled by Harlow and Phoenix [*3,4*], Phoenix and Smith [*5*]. The Harlow-Phoenix-Smith model predicts a reduction of strength scatter when fibers are bonded by a matrix binder in addition to the scatter reduction predicted by the Coleman's bundle theory. This is experimentally substantiated in Figs. 1*a* and 1*b* for graphite-epoxy composites. In Fig. 1*a*, the strength variability of the parent gaphite fibers were obtained by tension test of single filaments and presented in a linearized Weibull cumulative distribution function: $F^* = \ln(-\ln(1 - F))$ versus measured specimen strengths. The linear appearance of the data in this representation suggests a two parameter Weibull distribution model where the probability of failure is given by

$$F(\sigma) = 1 - \exp\{-(\sigma/\beta)^{\alpha}\} \tag{1}$$

where

σ = strength,
β = scale parameter (relatable to the mean strength), and
α = shape parameter (relatable to the variability) which is the slope in Fig. 1.

The good fit of the data to the Weibull model substantiates that the single filament fiber strength is well approximated by a weakest-link-of-chain process. From these data representations, we can observe (by noting the left-hand intercept of the curve with the ordinate) that at a stress level approximately 25% of mean strength (fiber stress 5 g), the probability of fiber failure is 10^{-3}. This is equivalent to a failure density of one fiber per cm^2 of a single layer of lamina [typically 0.0127 cm (.005 in.) thick]; a rather startling numbers of failures at such low stress level.

The scatter reducing effect of the matrix is demonstrated (in Fig. 1*b*) by the strength of graphite/epoxy composite strands, that is, epoxy impregnated tows of the same graphite

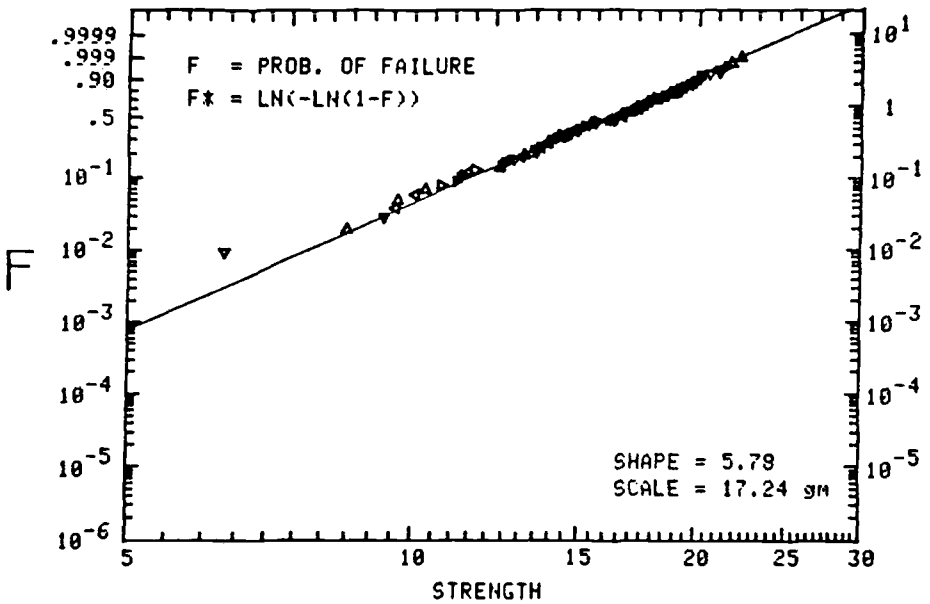

FIG. 1*a*—*Graphite fiber strength (force per fiber) with high variability, single filament without matrix binder.*

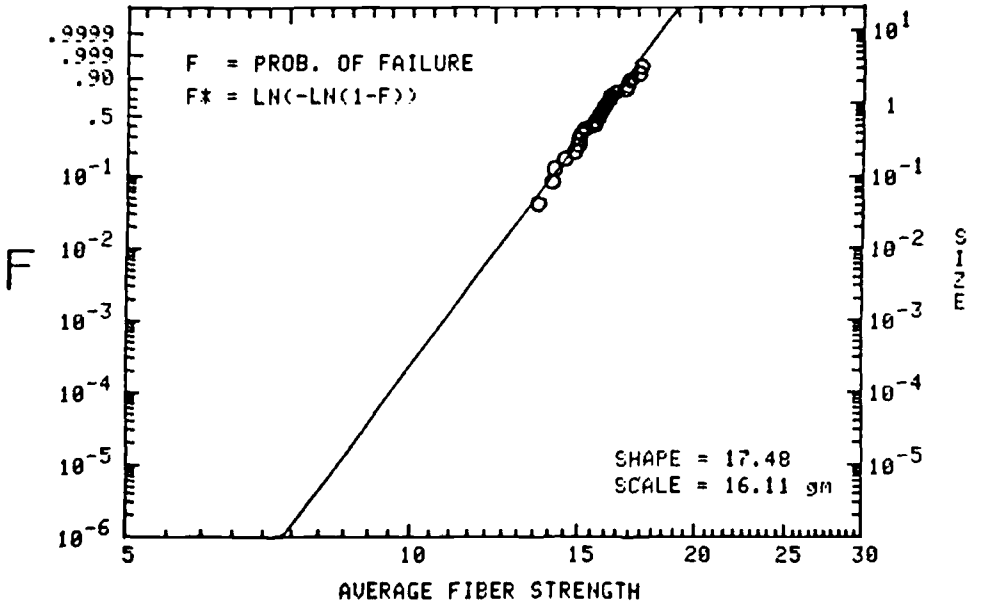

FIG. 1*b*—*Graphite fiber strength (force per fiber) with lower variability, composite with polymeric matrix binder.*

fiber. A dramatic reduction of variability can be observed through the slope increase (or rotation to vertical) of the strength distribution curve. As a result of this rotation, the probability of failure (at 25% mean stress) is reduced from 10^{-3} to 10^{-8}; a five orders of magnitude improvement as a result of the microredundancy provided by the matrix.

An important practical consequence of the strength variability is the strength dependency on the physical volume of a structure. The larger the volume, the higher the probability of encountering a fatal flaw, therefore the lower the mean strength. It follows that the larger the materials strength variability, the more severe the size effect. For the materials database presented in Figs. 1; given the fiber without matrix, an increase of physical size by 10^6 (that is, from a single layer 1 cm^2 lamina to 10 layer 3 m^2 laminate) would result in an expected decrease of mean strength by 90%! However, with this polymeric matrix, because of the reduction of scatter (the shape parameter α increases from 5.8 to 17.5), the expected decrease in mean strength (for the same size increase) is 45%. Table 1 summarizes the materials performance in the fiber form and that in the composite form with a polymeric matrix.

TABLE 1—*Materials performance in the fiber form and in the composite form with a polymeric matrix.*

Material	Scale, g	Shape	Mean, g	Coefficient of Variation, %
Fiber filament AS4	17.2	5.78	16	21
Fiber + polymer AS4 + DER332/T403	16.1	17.5	15.6	7

From this comparison, it is evident that high performance fibers can be a viable structure material only when used in conjunction with an effective matrix binder. The variability of composite and structure reliability in strength and life has been investigated by Phoenix and Wu [6]. The parametric roles of the statistical properties of the fiber and matrix and their interacted contribution to the composite properties must be *qualitatively* assessed. We can assess the dominating parameters through our understanding of the sequential failure process.

1. The demand on the matrix performance is inversely proportional to fiber variability. In the ideal limiting case where fiber strength has no variability, all fiber fail simultaneously, and no matrix load sharing will be needed.
2. The matrix effectiveness is proportional to the ratio of matrix-strength to fiber-strength (τ_m/σ_f) so that the load sharing can be maximized.
3. Matrix effectiveness is proportional to the ratio of matrix-shear modulus to fiber modulus (G_m/E_f) so that the ineffective length around the failure site can be minimized.
4. Matrix effectiveness is proportional to the ratio of matrix-ultimate strain to fiber-ultimate strain (ϵ_m/ϵ_f) so that stress singularity around the broken fiber will not be a catastrophic crack initiation site.

TABLE 2—*Typical values of dominating parameters for typical polymeric and aluminum matrices.*

Matrix Material	Matrix Strength τ_m / Fiber Strength σ_f	Matrix Shear Modulus G_m / Fiber Exterior Modulus E_f	Matrix Strain ϵ_m / Fiber Strain ϵ_f
Polymer	1/100	1/1000	2
Aluminum	1/50	1/5	4

We compare the typical values of these dominating parameters for typical polymeric matrix and aluminum matrix in Table 2.

From this comparison, we observed that aluminum matrix excels in all of the preceding strength governing parameters. We expect that, given the same fiber, aluminum should be more effective than polymer as a matrix binder material for high performance composites. We report on an experimental program to investigate the attributes of graphite-aluminum composites.

Experimental Program

The experimental program consists of selecting one spool of VSB64 pitch-base graphite fiber. Materials properties are listed in Appendix II and fabrication details are in accordance with standard ASTM practices. Specimens are sequentially made from the spool according to the following sequence starting from the beginning of the spool to the end of the spool:

1. Single filament fiber specimens.
2. Composite strand specimens with epoxy impregnation.
3. Composite wire specimens with aluminum impregnation.
4. Composite strand specimens with epoxy impregnation.
5. Single filament fiber specimens.

The statistical strength properties of the respective specimens were thoroughly charac-

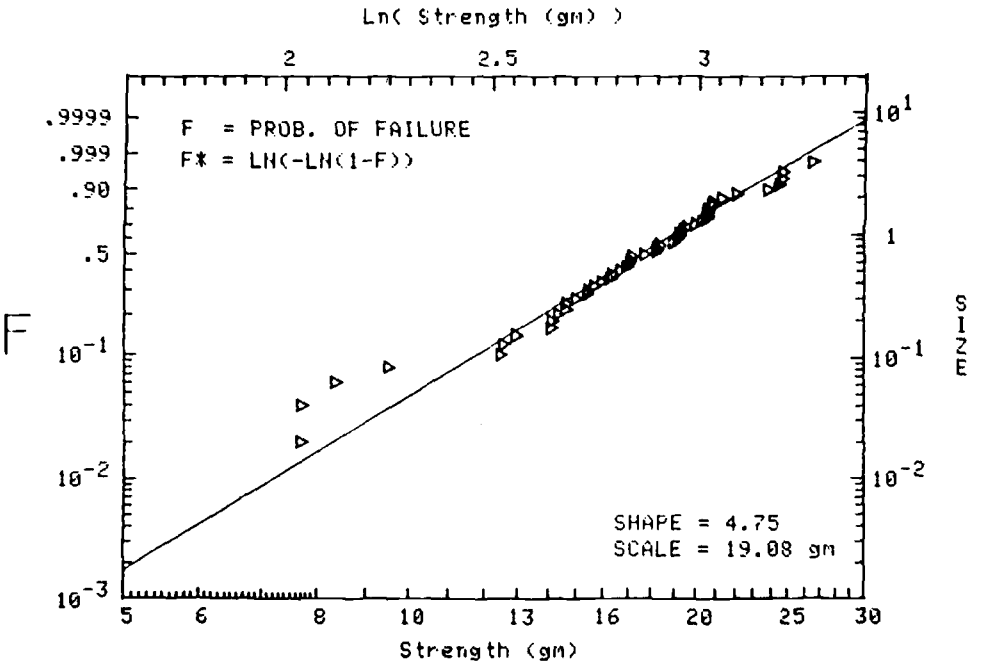

FIG. 2a—*Graphite fiber strength (force per fiber) single filament strength, specimen 1 from beginning of spool.*

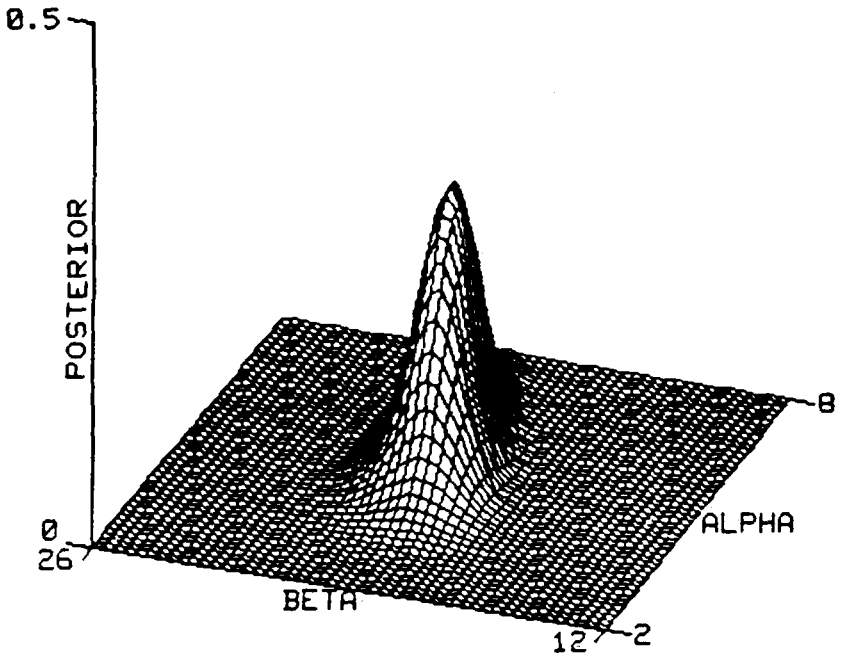

FIG. 2b—*Posterior density of the Weibull parameters* α, β *given data in Fig.* 2a.

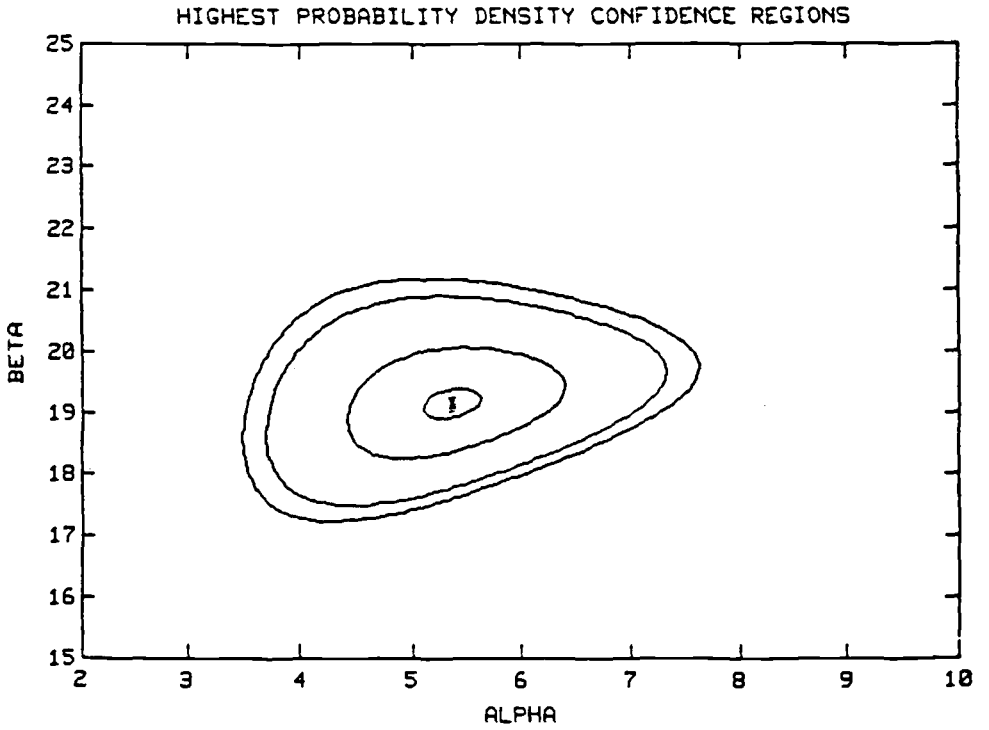

FIG. 2c—*Confidence contours of the Weibull parameters* α, β *given data in Fig.* 2a.

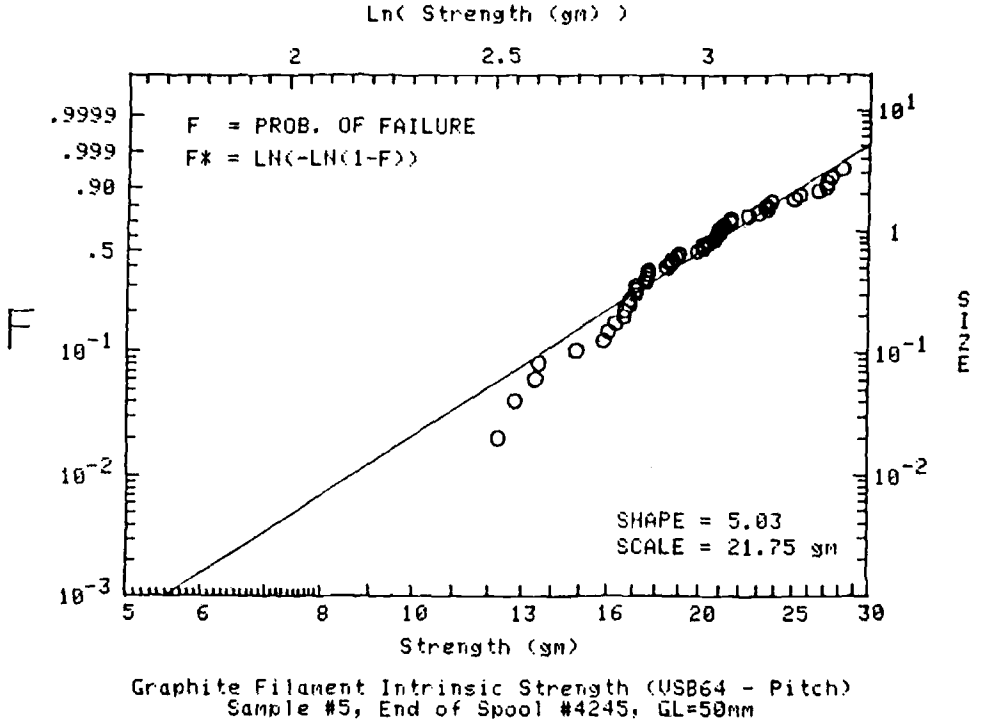

FIG. 3*a*—*Graphite fiber strength (force per fiber) single filament strength, specimen 5 from end of spool bracketing graphite/epoxy and graphite/aluminum composites for comparison.*

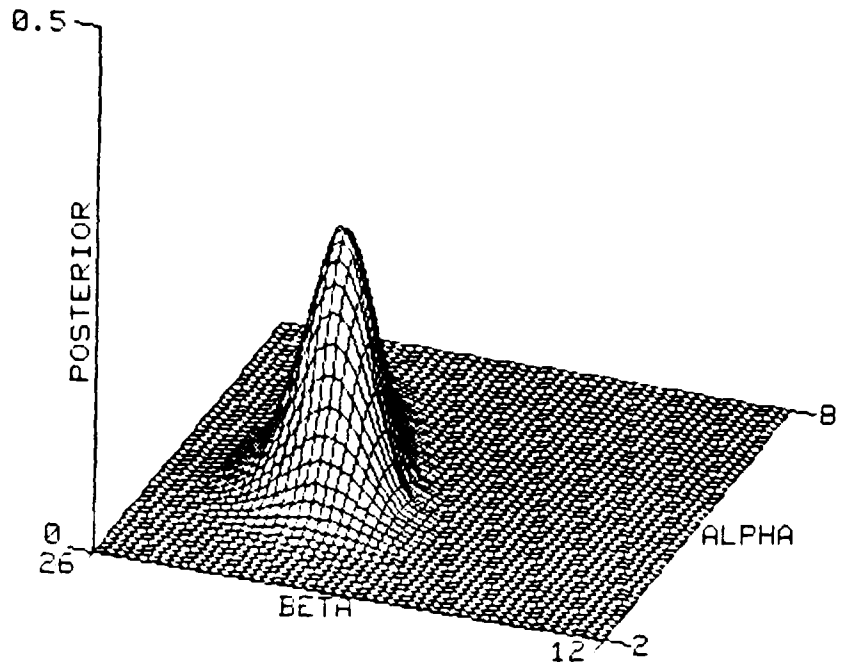

FIG. 3*b*—*Posterior density of the Weibull parameters* α,β *given data in Fig. 3a.*

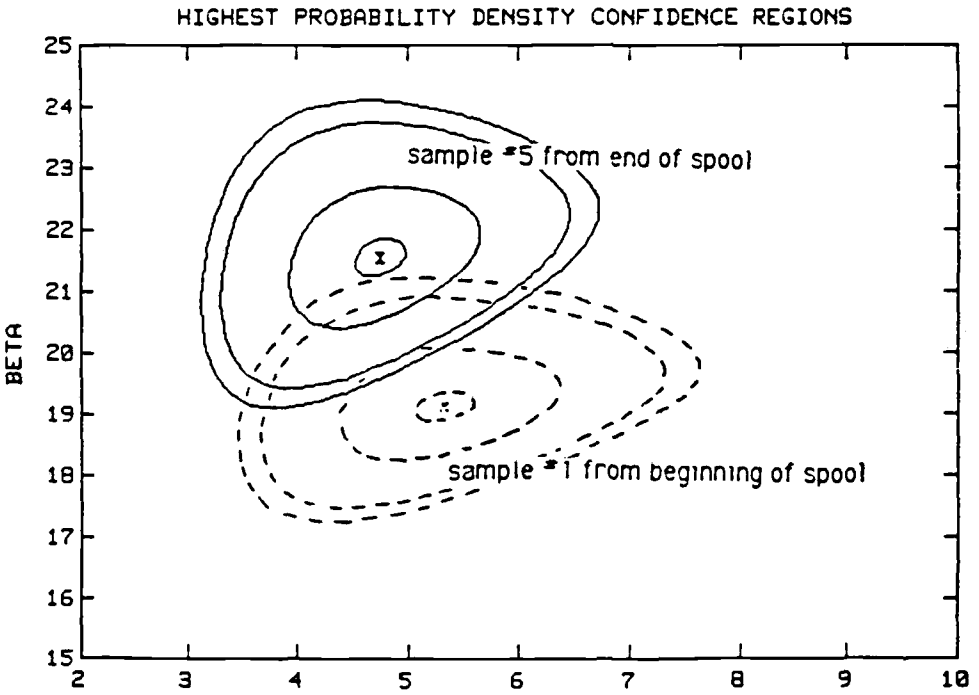

FIG. 3c—*Confidence contours of the Weibull parameters* α,β *given data in Fig.* 3a.

terized by tension test of an adequate number of specimens with respect to the observed scatter. That is, the number of test specimens are proportional to the variability observed. The testing methodology for each type of specimens are described in the Appendix I. This specimen allocation allows us to bracket the fiber strength variations within the spools so that an unambiguous relation between the graphite fibers and their composites can be established.

Results and Discussion

The results of the tension strength tests of each of the five specimen groups (as described in the "Experimental Program" section) are tabulated in Appendix III. From these data sets, we desired to examine the strength variability within the spool by comparing the strength at the beginning of the spool (data from Specimen 1) to the strength at the end of the spool (data from Specimen 5). If the strength variations are within the range of experimental resolution, we may infer that the constituent fibers in the composites Specimens 2, 3, and 4 are uniform and that they are from the same population. This would provide justification for merging data from Specimens 2 and 4 to form an unbiased representation of the graphite/epoxy composite strength.

This merged graphite/epoxy strength can be then compared to the graphite/aluminum strength from Specimen 3. Because of the statistical nature of the strength data such careful bracketing is necessitated in order to provide meaningful confidence level of the inferred conclusions.

In order to interpret the tabulated strength results we will select an appropriate statistical model, estimate the parameters of the model given the data from the respective specimens,

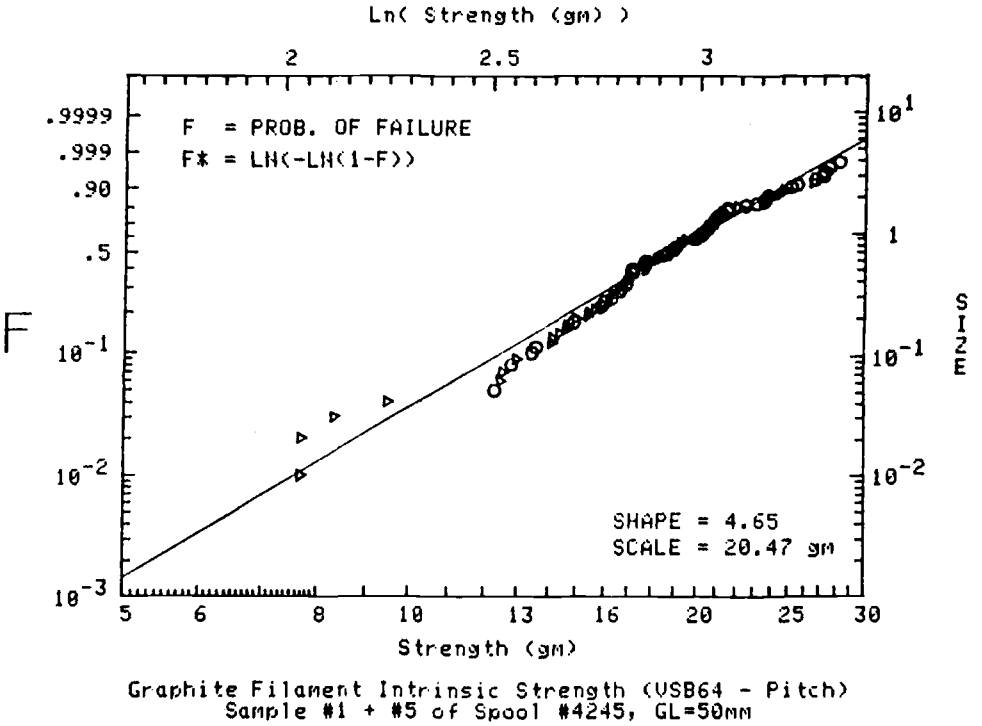

FIG. 4—*Graphite fiber strength (force per fiber) single filament strength, merged specimen 1 (beginning) and specimen 5 (end) of spool, bracketing benchmark for comparing the role of polymeric and metal matrix.*

then finally compare the parameters in accordance with the strategy outline previously. The two parameter Weibull model Eq 1 is selected to analyze the strength data. The selection is based on the physical failure process and substantiation by former experimental experiences (as described in the "Background" section). The shape α and scale β parameters for a given data specimen are obtained using the maximum likelihood estimator (MLE) numerically implemented based on the variable metric algorithm (BFGS) or the conjugated gradient algorithm (Beale). The confidence interval of the estimated parameter given a specimen data is calculated from Baye's formula

$$f(\alpha, \beta|D) = \frac{f(D|\alpha, \beta)f(\alpha, \beta)}{\int_{\alpha,\beta} f(D|\alpha, \beta)f(\alpha, \beta)\, d\alpha\, d\beta} \tag{2}$$

where

$f(\alpha, \beta|D)$ = posterior density given the data D,
$f(D|\alpha, \beta)$ = density of the data, and
$f(\alpha, \beta)$ is the prior density.

A flat prior $f(\alpha, \beta)$ = constant is used in all of the calculations herein.

Following the preceding procedure, the strengths of the fiber filament at the beginning of the spool (Specimen 1) are represented under linearized Weibull cumulative distribution

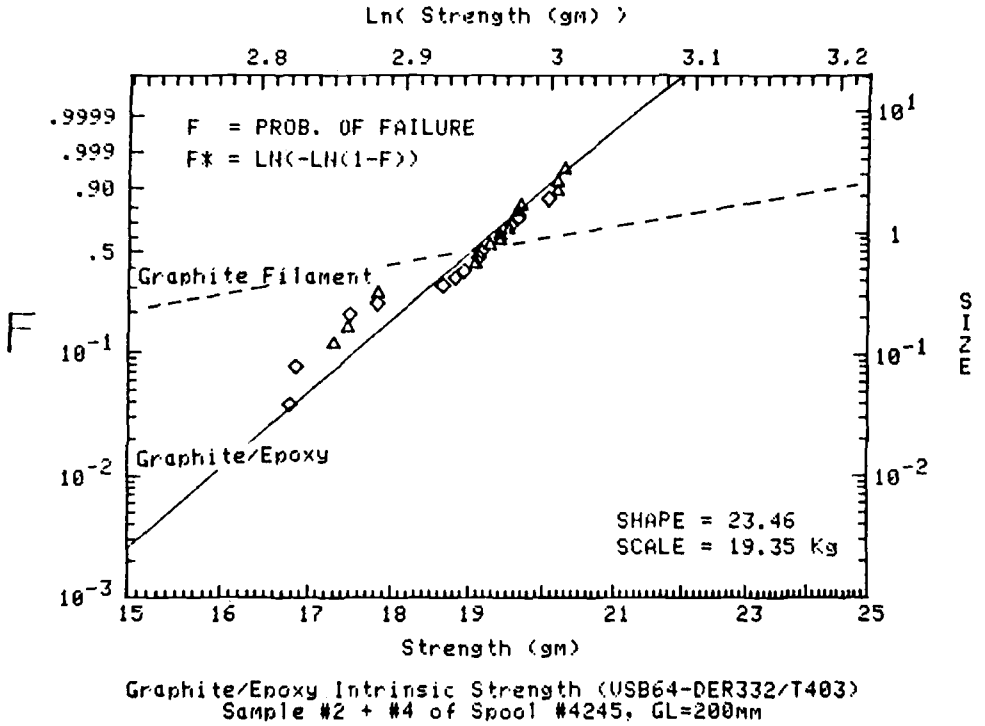

FIG. 5—*Graphite fiber strength (force per fiber) in graphite/epoxy composite, merged specimen 2 and specimen 4 bracketing graphite/aluminum composite. Scatter reduction is reflected by the vertical rotation.*

function and presented in Fig. 2*a*. We note, consistent with previous discussion, the large variation of the filament strength (indicated by $\alpha = 4.8$ or approximately a coefficient of variation of 25%). Figure 2*b* presents the posterior density of the parameters α, β. This density is a measure of the confidence of the parameter estimation given the current data set; the more peaky the density, the more confident the estimation. The equi-confidence contours of 5, 50, 90, and 95% of the posterior density function are presented in Fig. 2*c*. The interpretation of the 5% innermost contour is that the parameters measured by another specimen of equal size will have a 5% probability of lying within this contour.

The corresponding representation of the fiber filament data at the end of the spool (Specimen 5) are presented in Figs. 3*a*, 3*b*, and 3*c*. The dashed curves in these figures are transferred from (Specimen 1). Comparison of the numerical values of the shape α and scale β parameters (and also from cursory comparison between Fig. 2 and Fig. 3) suggests that the statistical strength of the fiber filament at the beginning and from the end of the spool are similar. This is confirmed by the Chi-square tests which indicated that there is over 50% probability that the two specimens are the same. It is therefore justified to merge Specimens 1 and 5 together to represent the statistical strength of the fiber filaments as presented in Fig. 4.

The graphite/epoxy data from Specimen 2 and Specimen 4 are interpreted in similar manner. They are inferred to be similar, and the two data sets are merged to form one combined data set which is presented in Fig. 5. Physically, it means that the two graphite/epoxy specimens which bracket the graphite/aluminum specimens belong strength-wise to

the same population. The dashed curve is transferred from the filament strength distribution (Fig. 4).

The graphite/aluminum data (Specimen 3) is in the center of the bracket and can be interpreted directly. The statistical strength of this graphite/aluminum composite is presented in Fig. 6. The dashed curves are transferred from Figs. 4 and 5 for comparison.

Interpretation

We collected a carefully planned and implemented data base of the parent fiber (Fig. 4), their graphite/epoxy composites (Fig. 5), and their aluminum composites (Fig. 6). For quantitative comparison, the respective value of the parameters are tabulated in Table 3.

We noted that current high performance graphite fibers have a natural high scatter and will have unavoidable early failures. This is observed and presented in Fig. 4. According to the physical failure process of composites, the role of the matrix binder is understood to provide local microredundancy around the early weak fiber failure sites. From Fig. 5, we note, consistent with the failure process, the epoxy matrix leads to a dramatic reduction of the scatter (α = 23.5 or a coefficient of variation of 5%).

From consideration of the parametric roles of stiffness, strength, and ultimate strain capacity, we surmise that aluminum could be a superior matrix material in comparison to polymeric matrix. The higher stiffness of aluminum minimizes the zone of load sharing (the

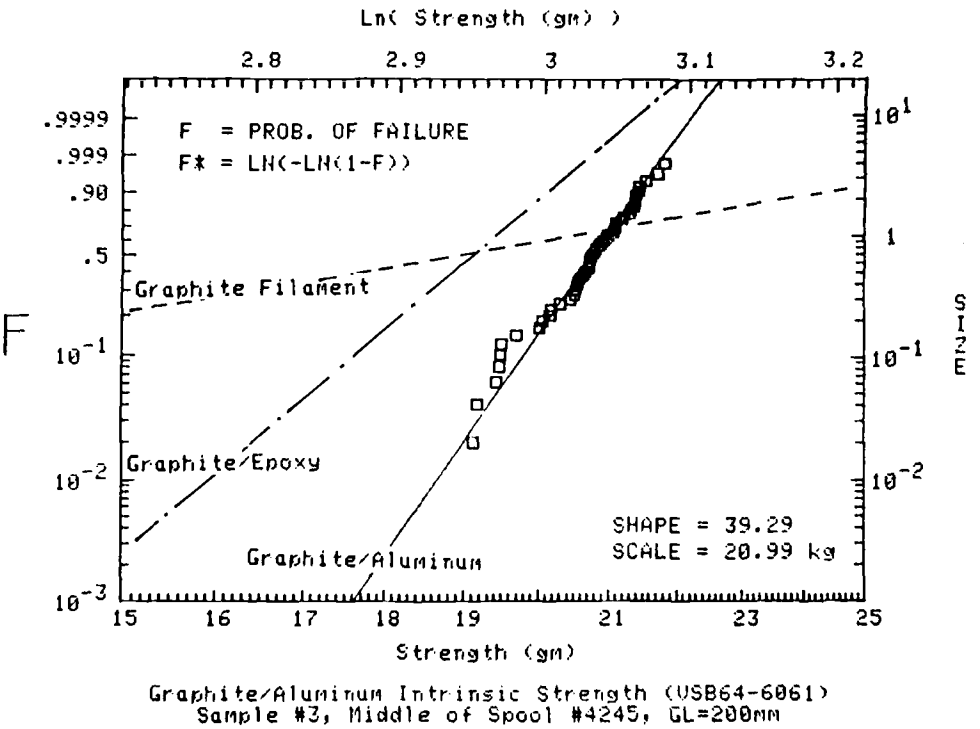

FIG. 6—*Graphite fiber strength (force per fiber) in graphite/aluminum composite specimen 3, bracketed by graphite/epoxy composite specimens (2 and 4) and single filament specimens (1 and 5). Scatter reduction is reflected by the vertical rotation; strength increase is reflected by the right shift.*

TABLE 3—*Respective values of the polymers.*

Materials	Scale, β (g)	Shape, α	Mean, μ (g)	Coefficent of Variation, cv
Fiber filament	20.4	4.6	19	26
Graphite/epoxy	19.4	23.5	18	5
Graphite/aluminum	21.0	39.3	21	3

ineffective length). The higher strength maximizes the magnitude of load sharing. The higher ultimate strain capacity increases the fracture toughness around the stress singularity of broken fiber end. Figure 6 confirms that aluminum leads to an even greater reduction of scatter (α = 39.3 or coefficient of variation of 3%).

Conclusions and Recommendations

This investigation identified and quantified the role of aluminum matrix in reducing strength scatter. This attribute of metal matrix is not generally recognized. It is of great practical importance in reducing strength dependence on the size (or volume) of a structure. A shape parameter change from 20 to 40 will result in a minimization of strength reduction by 250%. In other words, it is feasible to build large graphite aluminum structures with high structural efficiency (higher stress) *and* high reliability.

The results of this investigation suggest additional explorations in the following areas:

1. Strength size effect.
2. Stress singularity around broken fiber tip in the presence of matrix with plasticity.

Acknowledgment

This work was performed under the auspices of the U.S. Army, Materials Technology Laboratory, under BMD Materials, program manager, John Dignam.

References

[*1*] Rosen, B. W., "Tensile Failure of Fiberous Composites," *AIAA Journal,* American Institute of Aeronautics and Space Administration, Vol. 2, 1964, pp. 1985–1991.

[*2*] Zweben, C. and Rosen, B. W., "A Statistical Theory of Material Strength with Application to Composite Materials," *Journal of the Mechanics and Physics of Solids,* Vol. 18, 1970, pp. 189–206.

[*3*] Harlow, D. G. and Phoenix, S. L., "The Chain-of-Bundles Probability Model for Strength of Fibrous Materials I: Analysis and Conjectures," *Journal of Composite Materials,* Vol. 12, 1978, pp. 195–214.

[*4*] Harlow, D. G. and Phoenix, S. L., "The Chain-of-Bundles Probability Model for Strength of Fibrous Materials II: A Numerical Study of Convergence," *Journal of Composite Materials,* Vol. 12, 1978, pp. 314–334.

[*5*] Phoenix, S. L. and Smith, R. L., "A Comparison of Probabilistic Techniques for the Strength of Fiberous Materials Under Local Load-Sharing Among Fibers," *International Journal of Solids Structures,* Vol. 19, No. 6, 1983, pp. 479–496.

[*6*] Phoenix, S. L. and Wu, E. M., "Statistics for the Time Dependent Failure of Kevlar-49/Epoxy Composites: Micromechanical Modeling and Data Interpretation," *Mechanics of Composite Materials-Recent Advances,* Hashin and Herakovich, Eds. Pergamon Press, Elmsford, N.Y., 1982, pp. 135–162.

APPENDIX I

Experimental Method of Graphite-aluminum Tension Test

This appendix describes the experimental methods for measuring the tensile strength of graphite-aluminum composites. The specimen configuration considered herein is that of a strand (wire) which is a matrix impregnated tow of graphite fibers. Specifically in this investigation, the matrix is 6061 aluminum and the tow consists of 1000 fiber ends. The constituent properties of the fiber and the matrix are listed in Appendix II. The composite wire is nominally straight as fabricated, and multiple wires can be consolidated into tapes which can in turn be consolidated into laminae, then laminates, finally, the end structure. Hence, the composite wire may be considered as the primary building block for graphite aluminum structures. A proper characterization of the strength properties of the wire is the basis for quantitatively assessing material process development and ultimately for predicting the strength and reliability of the end composite structure. For such purposes, the pertinent strength properties include: the mean, the variability, and the strength dependency on the size (volume) of the specimen.

Tensile Strength Properties Are Measured in This Investigation

Tension testing of composites is simple in concept but difficult in experimental implementation. In tension testing of homogeneous material, a specimen configuration of reduced cross section within the gage length (the "dog-bone" configuration) can be used to reduce the stress in the gripping region and to assure a uniform tension state of stress within the gage section. As a result, evaluation of each individual test datum is straightforward. Those with failure sites within the gage length are valid tests, and any strength variation within the valid test can be accepted as the characteristic of the material. Those with failure sites outside the gage length can be discarded with assurance that the underlying materials characteristic will not be biased.

However, for heterogeneous composites, the reduced cross-section solution is not always applicable. In fiber reinforced composites, the stiff fibers carry the primary portion of the load, and the transfer of the gripping force (which is in shear) to the interior fibers depends on the shear transfer ability of the matrix. The complex state of stress in the grip area increases the likelihood of failure in the grip vicinity therefore does not provide the representative strength value. On the other hand, identification and censoring of these specimens are not straightforward. For a specimen of slender configuration under tension, propagation of stress wave initiated from the failure site causes multiple secondary failures sites breaking the specimen into many segments rendering the identification of the original failure site exceeding difficult and uncertain. In this investigation, we developed experimental methods to:

1. Increase the shear transfer capacity of the adhesive between the grip and the specimen.
2. Increase the shear transfer capacity of the matrix in the neighborhood of the grip.
3. Protect the specimen from fragmentation by the failure initiated stress wave, thereby allowing positive identification whether failure initiated around the grip vicinity and unambiguously accept or censor a specific test datum.

Gripping Method of Composite Wire Specimen

Conventional method of load introduction by adhesive bonding of the specimen to a tab has two limitations. The first limitation is that there exist a high shear stress concentration where the tab terminates toward the gage section, this lead to adhesive failure and loss of

definition of the gage dimension. The second limitation is that the applied tension from the testing machine is transferred through shear of the adhesive into the specimen which in turn transfers via shear of the matrix into tensile load of the fiber. The shear stress is maximum at the bonding adhesive and decreases to zero at the interior center of the specimen. This nonuniform stress distribution gives rise to a tension peeling stress at the edge of the tab and specimen interface. Such peeling tension stress is known to severely reduce the adhesive strength.

To overcome these limitations, we developed a tubular tab to fully enclose the wire. The tubular tab is made of thin-walled copper tubing with an internal diameter to give nominal 0.01 mm (.004 in.) diametrical clearance with the wire. Prior to bonding to the specimen the copper tube is annealed and de-scaled in an acid bath. Graphite/aluminum wire specimens are cut to length with diameters and the weight measured and recorded. Appropriate fixtures are designed to assure the concentric alignment of the tubular tab and the wire specimen at the proper gage location. An anaerobic adhesive is injected into the space between the tubular tab and specimen and allowed to set. Specimens are now ready for tension testing.

For measuring the intrinsic strength (that is, the short time static strength) of the composite wire, chucks (commercially available for jeweler's lathe) are mounted to a universal tension testing machine with precision alignment to minimize any bending. Special jaws are sized for tubular tab such that when the jaws are fully tightened in the chuck, the tubular tabs are subjected to a 1.5% diametrical strain. Since the jaw reduces tab diameter uniformly, a state of hydrostatic compression strain is applied to the specimen and adhesive in the bonding region. This state of hydrostatic strain is retained by the strain hardening action of the copper tubing. This hydrostatic strain provides two important functions:

1. The hydrostatic stress simultaneously cancels the tension peel stress and increases the strength of the adhesive.
2. The hydrostatic stress is uniformly transferred to the composite and increases the shear strength of the matrix.

The combination of these two functions leads to minimization of failure in the grip vicinity to less than 5% of the specimens tested.

APPENDIX II

Constituent Properties of Fiber and Matrix

Fiber Properties	
Manufacturer	Union Carbide Corporation
Type	Pitch Based Graphite (VSB-64)
Modulus E_f	55 Msi
Diameter	10 μm
Density	0.072 lb/in.^{3}
Bundle (tow)	1000
Matrix Properties	
Aluminum	
Type	6061-F condition, T-4 estimated
Modulus E_m	10 Msi (69 GPa)
Shear Modulus G_m	3.8 Msi (26 GPa)
Yield τ_{yield}	27 ksi (0.19 GPa) estimated
Fiber volume V_f	46% (nominal)

Appendix II—*Continued.*

Epoxy	
Type	DER-332/T403[a]
Modulus E_m	0.48 Msi (3.3 GPa)
Shear Modulus G_m	0.16 Msi (1.1 GPa)
Yield τ_{yield}	11.5 ksi (0.079 GPa) estimated
Fiber volume V_f	55% (nominal)

[a] A bisphenol-A-based epoxy resin (Dow Chemical: DER-332) cured with an aliphatic polyether triamine (Jefferson Chemical: Jeffamine T403). The stoichiometric ratio of resin to curing agent is 55/45 by weight, cured at 60°C for 16 h.

APPENDIX III

Tabulation of Ordered Tensile Strength of Specimens 1, 2, 3, 4, and 5

Graphite filament intrinsic strength (VSB64-pitch) Specimen 1, beginning of Spool 4245, GL = 50 mm.

No.	Strength, g	Code	No.	Strength, g	Code
1	7.680	1.	26	18.170	1.
2	7.700	1.	27	18.230	1.
3	8.340	1.	28	18.360	1.
4	9.490	1.	29	18.940	1.
5	12.440	1.	30	19.120	1.
6	12.540	1.	31	19.200	1.
7	12.950	1.	32	19.200	1.
8	14.080	1.	33	19.370	1.
9	14.110	1.	34	19.500	1.
10	14.330	1.	35	19.960	1.
11	14.590	1.	36	20.220	1.
12	14.630	1.	37	20.450	1.
13	14.950	1.	38	20.480	1.
14	15.360	1.	39	20.480	1.
15	15.400	1.	40	20.540	1.
16	15.650	1.	41	20.730	1.
17	15.910	1.	42	20.790	1.
18	16.290	1.	43	21.250	1.
19	16.350	1.	44	22.000	1.
20	16.680	1.	45	23.740	1.
21	16.930	1.	46	24.380	1.
22	17.020	1.	47	24.580	1.
23	17.060	1.	48	24.640	1.
24	17.150	1.	49	26.490	1.
25	17.660	1.			

NOTE—
Two-parameter Weibull distribution maximum likelihood estimates.
Shape parameter = 4.7458.
Scale parameter = 19.0846 g.
49th root of maximum likelihood function = 0.0577.
0-points progressively censored.

Graphite/epoxy intrinsic strength (VSB64-DER332/T403) Specimen 2, beginning of Spool 4245, GL = 200 mm.

No.	Strength, kg	Code	No.	Strength, kg	Code
1	17.300	4.	8	19.530	4.
2	17.470	4.	9	19.650	4.
3	17.840	4.	10	19.690	4.
4	19.080	4.	11	20.190	4.
5	19.260	4.	12	20.190	4.
6	19.390	4.	13	20.290	4.
7	19.400	4.			

NOTE—
Two-parameter Weibull distribution maximum likelihood estimates.
Shape parameter = 27.3933.
Scale parameter = 19.5971 kg.
13th root of maximum likelihood function = 0.2797.
0-points progressively censored.

Graphite/aluminum intrinsic strength (VSB64-6061) Specimen 3, middle of Spool 4245, GL = 200 mm.

No.	Strength, kg	Code	No.	Strength, kg	Code
1	19.120	8.	26	20.800	8.
2	19.180	8.	27	20.810	8.
3	19.430	8.	28	20.860	8.
4	19.460	8.	29	20.890	8.
5	19.480	8.	30	20.930	8.
6	19.500	8.	31	20.970	8.
7	19.700	8.	32	20.990	8.
8	20.020	8.	33	21.070	8.
9	20.060	8.	34	21.080	8.
10	20.160	8.	35	21.100	8.
11	20.180	8.	36	21.100	8.
12	20.310	8.	37	21.180	8.
13	20.460	8.	38	21.210	8.
14	20.520	8.	39	21.300	8.
15	20.530	8.	40	21.320	8.
16	20.550	8.	41	21.360	8.
17	20.570	8.	42	21.370	8.
18	20.600	8.	43	21.390	8.
19	20.640	8.	44	21.390	8.
20	20.670	8.	45	21.430	8.
21	20.710	8.	46	21.440	8.
22	20.720	8.	47	21.530	8.
23	20.730	8.	48	21.710	8.
24	20.740	8.	49	21.810	8.
25	20.770	8.			

NOTE—
Two-parameter Weibull distribution maximum likelihood estimates.
Shape parameter = 39.2892.
Scale parameter = 20.9907 kg.
49th root of maximum likelihood function = 0.3890.
0-points progressively censored.

Graphite/epoxy intrinsic strength (VSB64-DER332/T403) Specimen 4, end of Spool 4245, GL = 200 mm.

No.	Strength, kg	Code	No.	Strength, kg	Code
1	16.780	5.	7	18.930	5.
2	16.850	5.	8	19.120	5.
3	17.490	5.	9	19.150	5.
4	17.830	5.	10	19.560	5.
5	18.660	5.	11	19.640	5.
6	18.820	5.	12	20.060	5.

NOTE—
Two-parameter Weibull distribution maximum likelihood estimates.
Shape parameter = 22.3987.
Scale parameter = 19.0453 kg.
12th root of maximum likelihood function = 0.2445.
0-points progressively censored.

Graphite filament intrinsic strength (VSB64-pitch) Specimen 5, end of Spool 4245, GL = 50 mm.

No.	Strength, g	Code	No.	Strength, g	Code
1	12.280	9.	26	20.180	9.
2	12.800	9.	27	20.220	9.
3	13.440	9.	28	20.480	9.
4	13.570	9.	29	20.730	9.
5	14.870	9.	30	20.860	9.
6	15.870	9.	31	21.000	9.
7	16.040	9.	32	21.000	9.
8	16.290	9.	33	21.050	9.
9	16.640	9.	34	21.180	9.
10	16.680	9.	35	21.500	9.
11	16.890	9.	36	21.500	9.
12	16.930	9.	37	22.460	9.
13	17.150	9.	38	23.040	9.
14	17.150	9.	39	23.480	9.
15	17.150	9.	40	23.480	9.
16	17.570	9.	41	23.740	9.
17	17.610	9.	42	25.080	9.
18	17.650	9.	43	25.400	9.
19	17.700	9.	44	26.620	9.
20	18.480	9.	45	27.130	9.
21	18.610	9.	46	27.210	9.
22	18.680	9.	47	27.460	9.
23	18.860	9.	48	28.160	9.
24	18.990	9.	49	30.540	9.
25	19.890	9.			

NOTE—
Two-parameter Weibull distribution maximum likelihood estimates.
Shape parameter = 5.0262.
Scale parameter = 21.7505 g.
49th root of maximum likelihood function = 0.0558.
0-points progressively censored.

Jonathan Awerbuch,[1] *Jonathan Goering,*[2] *and Kent Buesking*[2]

Minimechanics Analysis and Testing of Short Fiber Composites: Experimental Methods and Results

REFERENCE: Awerbuch, J., Goering, J., and Buesking, K., **"Minimechanics Analysis and Testing of Short Fiber Composites: Experimental Methods and Results,"** *Testing Technology of Metal Matrix Composites, ASTM STP 964,* P. R. DiGiovanni and N. R. Adsit, Eds., American Society for Testing and Materials, Philadelphia, 1988, pp. 121–142.

ABSTRACT: This paper describes a study performed to experimentally investigate the constitutive behavior of silicon carbide whisker reinforced aluminum and to provide data for a companion material modelling study. The experimental program included measurement of material stress-strain curves, assessment of the acoustic emission response of the material, and examination of the material failure surfaces.

The results of the mechanical tests showed that as the whisker content increases, stiffness, strength, and rate of strain hardening increases, whereas the strain to failure decreases. Changes in the extrusion ratio have little effect upon the composite properties although the extruded bulk aluminum was significantly different from commercial aluminum alloy 6061-T6. The acoustic emission results showed that the failure modes of the composites and unreinforced materials were similar. The scanning electron microscopy results showed that failure of the materials was due to microyielding within the aluminum. Therefore, the composite failure is believed to be caused by matrix plasticity and whisker pullout.

KEY WORDS: metal matrix composites, silicon carbide whiskers, aluminum matrix, mechanical properties, acoustic emissions, failure modes, stiffness, strength, strain to failure, strain hardening

Recent advances in the field of metal matrix composites have made short fiber reinforced materials, such as silicon carbide/aluminum (SiC/Al), structurally very attractive. The addition of the SiC whiskers to the aluminum matrix results in a material that is significantly stiffer and stronger than homogeneous aluminum. Furthermore, the fact that the reinforcement is in the form of whiskers allows the composite to be formed, machined, and handled very much like a conventional metal. Because of these characteristics, whisker reinforced metals are being investigated for applications which range from deep submergence structures to satellite components.

The structural properties of a whisker reinforced composite depend most strongly upon factors such as the matrix material properties, whisker volume fraction, aspect ratio and orientation, and whisker material properties. In order to better understand the effects of these parameters upon the composite behavior, a combined experimental and theoretical study was undertaken. This paper describes an experimental study in which the mechanical

[1] Associate professor, Department of Mechanical Engineering and Mechanics, Drexel University, Philadelphia, PA 19104.

[2] Research engineer and director of Advanced Materials, respectively, Materials Sciences Corporation, Spring House, PA 19477.

behavior, acoustic emissions, and fracture surfaces of SiC/Al composites with different reinforcement volume fractions and extrusion ratios were investigated. A companion paper describes a theoretical study in which the stress-strain behavior of the composites was computed based upon the material properties of the constituents and correlated with the experimental results [*1*].

Experimental Procedure

Material and Specimen Preparation

The material tested in this program was 6061 aluminum reinforced with SiC whiskers. The composite materials were fabricated as described in Ref *2* by first blending the proper volume fraction of SiC whiskers with a powdered aluminum matrix. The blends are vacuum hot-pressured into cylindrical billets which are assumed to contain a random and homogeneous dispersion of whiskers. The billets are then extruded at ratios of 5:1 and 10:1 into long cylindrical rods which are subsequently machined into test specimens.

Specimens of three different volume fractions were tested: 0, 15, and 25%, randomly oriented and having an extrusion ratio of 10:1. Specimens with 25% by volume (V/O) were also manufactured with an extrusion ratio of 5:1. Two types of specimens were manufactured and machined: cylindrical tension specimens with a gage length of 44 mm (1.75 in.) and a diameter of 4.05 mm (0.16 in.); and compression specimens 38 mm (1.50 in.) long and 7.87 mm (0.31 in.) in diameter. In order to determine the effect of fabrication on the mechanical properties of the aluminum matrix, commercial aluminum 6061-T6 was also tested. The data obtained with the commercial aluminum alloy were compared with those obtained with extruded aluminum, V/O = 0%. The specimen designation in the figures of this paper consists of five digits. The first three digits indicate the supplier's code number, the fourth identifies the specimen number within each lot and the fifth identifies the type of test, that is, T for tension, C for compression. The letters XCT identify the commercial aluminum alloy.

Mechanical Test Program

Quasi-static uniaxial tension test and compressive tests were performed on a closed loop servohydraulic Instron testing machine (Model 1331). Specimens were loaded under stroke control mode at a rate of 0.07 mm/min (0.003 in./min). Each tension specimen was instrumented with an extensometer (1.0 in. gage length, 25.4 mm) to obtain the global stress-strain curves. A selected number of tension specimens were strain-gaged to obtain the local stress-strain curves and to ensure that the extensometer data were reliable. Two gages (Micro-Measurements EA06-031DE-120) were applied along opposite sides of the specimens to minimize the effect of bending and to ensure axiality of loading. The compression specimens with the original length-to-diameter ratio ($L/D = 4.8$) experienced significant buckling, and, although buckling occurred much beyond the elastic region, no reliable ultimate strength data could be obtained. Therefore, most of the specimens were first machined into two L/D ratios. The group of specimens with the higher ratio ($L/D = 2.0$) was tested for stiffness, while the group of the lower ratio ($L/D = 1.0$) were not instrumented and were only tested for ultimate strength. All specimens of $L/D = 2.0$ were instrumented with two strain gages (Micro-Measurements EA06-031DE-120) to ensure loading axiality and to compensate for bending during initial loading. Selected specimens of $L/D = 4.8$ were instrumented with an extensometer for comparison with the results obtained using strain gages on the short L/D ratio specimens. A total of 48 mechanical tests were performed, 21 tension and 28 compression tests. For all specimens tested, initial stiffness, stress-strain curves, and strength data were recorded.

Test results were recorded on *X-Y-Y* recorders to monitor the test progression in real time. The testing system was also interfaced with a data acquisition system (PDP 1103 Model MINC-11 of Digital Equipment Corporation). Post-test analyses provided complete load-displacement curves, stress-strain curves, and mechanical properties such as strength and stiffness. Printouts of stress-strain data in tabular form were also obtained.

Failure Modes and Damage Progression

For a selected number of specimens subjected to tensile loading, fracture surfaces were examined through the scanning electron microscope (SEM). The purpose of these examinations was to evaluate the fabrication quality of the specimen material and to examine the dominant microfailure mechanisms.

For a few specimens photomicrographs were prepared to evaluate the void content. Energy dispersion analysis of X-ray, using Phillips SEM 500 Model with ECON (energy dispersion analysis of carbon, oxygen, and nitrogen), and element analysis of the fracture surfaces were performed in order to determine whisker/matrix bonding quality and for qualitative evaluation of the whisker volume fraction, respectively.

Damage initiation and progression under tensile loading was monitored via acoustic emission (AE) as well. Due to the limitation in specimen length, a single transducer was utilized. This is not considered to be the optimum instrumentation for monitoring AE since the use of two transducers enables more accurate detection of damage initiation, location of existing damage, tracking damage progression, and identification of potential fracture sites, and also allows for spatial filtering to eliminate unwanted emission generated from the grips. Therefore, the AE results obtained in this study are to be considered as preliminary.

It should be noted, however, that preliminary tests conducted using two transducers with sufficiently long specimens indicated that relatively little emission has been generated from the grips. Therefore, the test results are considered to be quite reliable for the purpose of assessing the applicability of AE as a nondestructive testing technique for monitoring damage initiation and progression in the subject material.

For all specimens tested in this program, acoustic emission was monitored using Dunegan/Endevco 3000 series AE instrumentation. The most pertinent operating parameters are: Transducer Type S9204, system threshold level of 1V, fixed gain of 40 dB preamplifier, post-amplifier gain control of 40 dB, dead time = 3 ms and envelope = 10 ms. To ensure a good contact area between the specimen's round surface and the flat surface of the transducer, a waveguide has been used, in which a groove has been machined to match the surface of the specimen. Acoustic emission results include events, counts and count rate as a function of load, and amplitude distribution histograms of events.

Experimental Results

Stiffness and Strength

The experimental results on initial stiffness and strength for all specimens are summarized in Table 1. Clearly, increasing whisker volume fraction strongly affects both initial stiffness and strength. However, very little, if any effect of extrusion ratio has been noticed on either mechanical property.

The significant effect of reinforcement on both stiffness and strength can be best seen by comparing the results for the 25% reinforced aluminum and commercially available aluminum alloy, for example, 6061-T6. Such a comparison indicates that the combination of fabrication procedure and whisker reinforcement significantly increases both stiffness and strength over that of commercial aluminum alloy, Table 2.

TABLE 1—*Summary of average experimental measurements on whisker reinforced SiC/AL composites.*

	No. of Specimens	Volume Fraction, %	Extrusion Ratio	Average[b] Stiffness		S.D.[c] Stiffness		Average[b] Strength		S.D.[c] Strength	
				10^6 psi	GPa	10^6 psi	GPa	ksi	MPa	ksi	MPa
				TENSION							
Commercial 6061-T6	4	0	N/A	10.03	69.11	0.21	1.47	47.16	325.1	0.66	4.6
0 V/0, ER = 10:1[a]	5	0	10:1	10.44	71.97	0.21	1.46	58.97	406.5	4.72	32.5
15 V/0, ER = 10:1	3	15	10:1	14.75	101.70	0.69	4.77	71.33	491.8	3.63	25.0
25 V/0, ER = 10:1	5	25	10:1	18.30	126.20	0.50	3.47	84.68	583.8	5.16	35.6
25 V/0, ER = 5:1	4	25	5:1	17.97	123.87	0.58	4.02	83.91	578.5	1.21	8.3
				COMPRESSION							
Commercial 6061-T6	4	0	N/A	10.23	70.51	0.21	1.42	...	...	...	...
	2	0	N/A	...	...	...	...	>135	>932	...	...
0 V/0, ER = 10:1[a]	3	0	10:1	10.95	75.49	0.77	5.34	...	...	...	...
	2	0	10:1	...	...	...	...	>135	>932	...	...
15 V/0, ER = 10:1	3	15	10:1	14.04	96.77	1.00	6.87	...	...	...	...
	2	15	10:1	...	...	...	...	97.57	672.70	7.55	52.1
25 V/0, ER = 10:1	4	25	10:1	17.87	123.23	0.53	3.71	...	...	...	...
	3	25	10:1	...	...	...	...	109.59	755.60	5.91	40.8
25 V/0, ER = 5:1	3	25	5:1	17.46	120.39	0.93	6.40	...	...	...	...
	1	25	5:1	...	...	...	...	118.75	818.73	...	...

[a] Aluminum fabricated according to same procedure as SiC/Al composites.
[b] Average of all strain gages and extersometer results.
[c] Standard deviation.

TABLE 2—*Effect of SiC whisker reinforcement on stiffness and strength.*

Volume Fraction	Aluminum 6061-T6	0%[a]	15%	25%
	TENSION			
Percent increase in stiffness	···	4	47	83
Percent increase in strength	···	25	51	80
	COMPRESSION			
Percent increase in stiffness	···	7	37	75

[a] Aluminum fabricated according to the same procedure as the SiC/Al composites.

The effect of fabrication procedure alone on the matrix properties is seen in the comparison between data obtained from specimens of 0% V/O (extruded specimens) and those obtained for commercial aluminum alloy 6061-T6. The extruded specimens have approximately the same stiffness as the commercial alloy under both tension and compression, as expected. However, the extruded specimen has a much higher tensile strength, by about 25%, than the commercial aluminum alloy. The data for the extruded specimens are most comparable to those listed in Alcoa handbooks for solution heat treated, artificially aged, and then cold worked, that is, T9 condition, and are significantly higher than those obtained for the T6 conditions. It should be noted that no compressive strength data could be obtained for the commercial or extruded specimens since neither failure nor drop in the stress-strain curve was obtained up to a strain level beyond 50%, at which stage the test was terminated.

Stress-Strain Curves

Stress-strain curves for all five material systems tested having different whisker volume fractions (V/O) and extrusion ratios (ER) were measured and examined. The stress-strain curves for different material systems were compared to investigate the effects of whisker volume fraction, extrusion ratio, fabrication procedure, and tensile versus compressive loading upon the mechanical behavior of the composites. Representative stress-strain curves are shown in Figs. 1–7 obtained under tension and compression. The results shown in these figures were selected to reflect average rather than extreme values. The applied stress was determined based on the original cross section of the specimens. Generally, there was very little scatter in the results for a given material system.

In order to compare the effect of whisker volume fraction on the overall stress-strain curves, representative results are plotted in Fig. 1. Results indicate that whisker volume fraction significantly affects initial stiffness and strength of the subject material, both of which increase with higher whisker volume fraction. Increasing the whisker volume fraction also increases the strain hardening rate. The percent of elongation to failure, however, decreases with increasing whisker volume fraction, as expected. Actual elongation to failure could not be accurately determined since several specimens failed outside the extensometer gage length. However, the presence of the SiC whiskers does significantly limit the global deformation of the composite to failure.

The effect of extrusion ratio on the mechanical properties of the composite were studied as well, Fig. 2. Stiffness, strength, rate of strain hardening, and deformation to failure are practically not affected by the extrusion ratio.

The effect of fabrication procedure on the mechanical properties of the aluminum matrix is shown in Fig. 3. A specimen of commercially available aluminum alloy 6061-T6 and a specimen fabricated according to the same procedure as the composite but without the SiC whiskers were both tested. The comparison between the stress-strain curves of the two

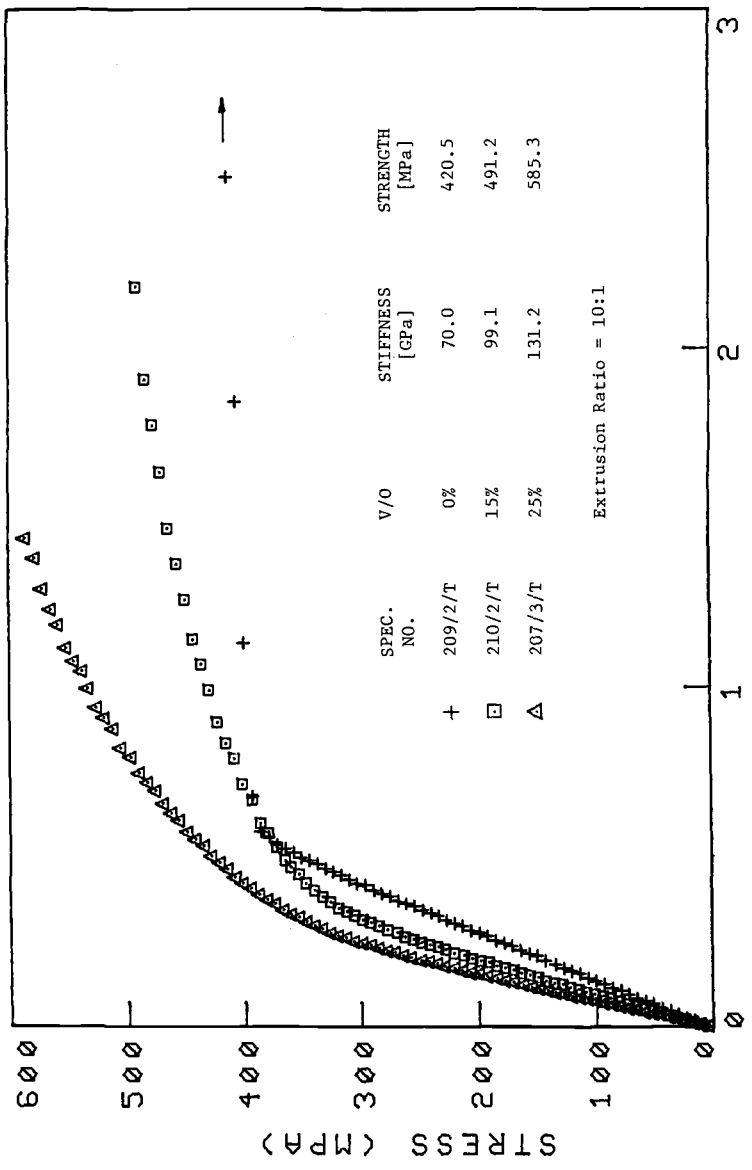

FIG. 1—*Stress-strain curves in tension of various SiC/Al composites showing effect of whisker volume fraction.*

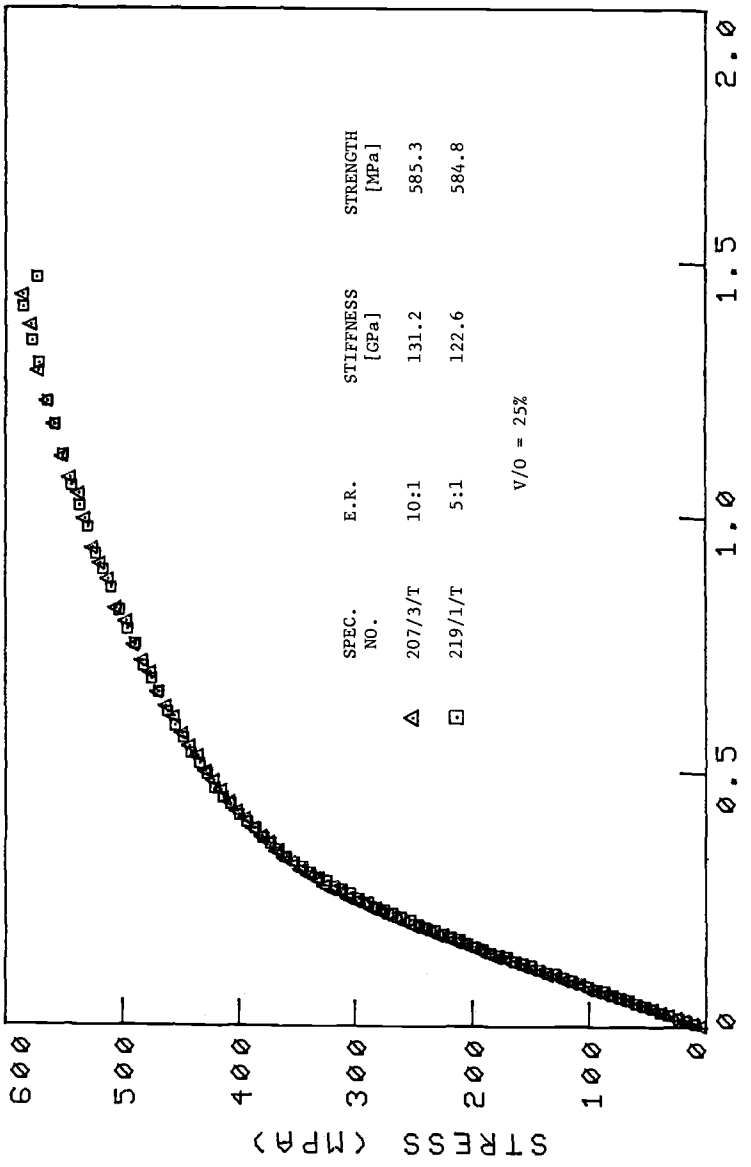

FIG. 2—*Stress-strain curves in tension of various SiC/Al composites showing effect of extrusion ratio.*

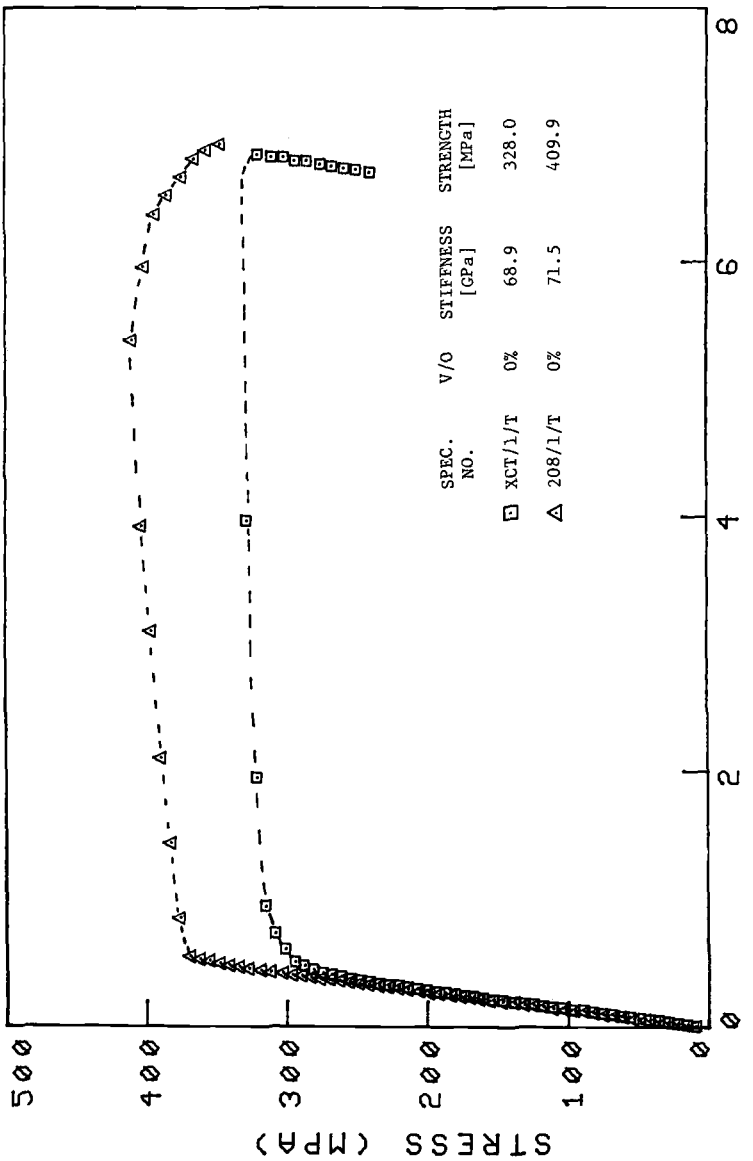

FIG. 3—*Stress-strain curves in tension of aluminum showing effect of composite fabrication procedure on aluminum behavior.*

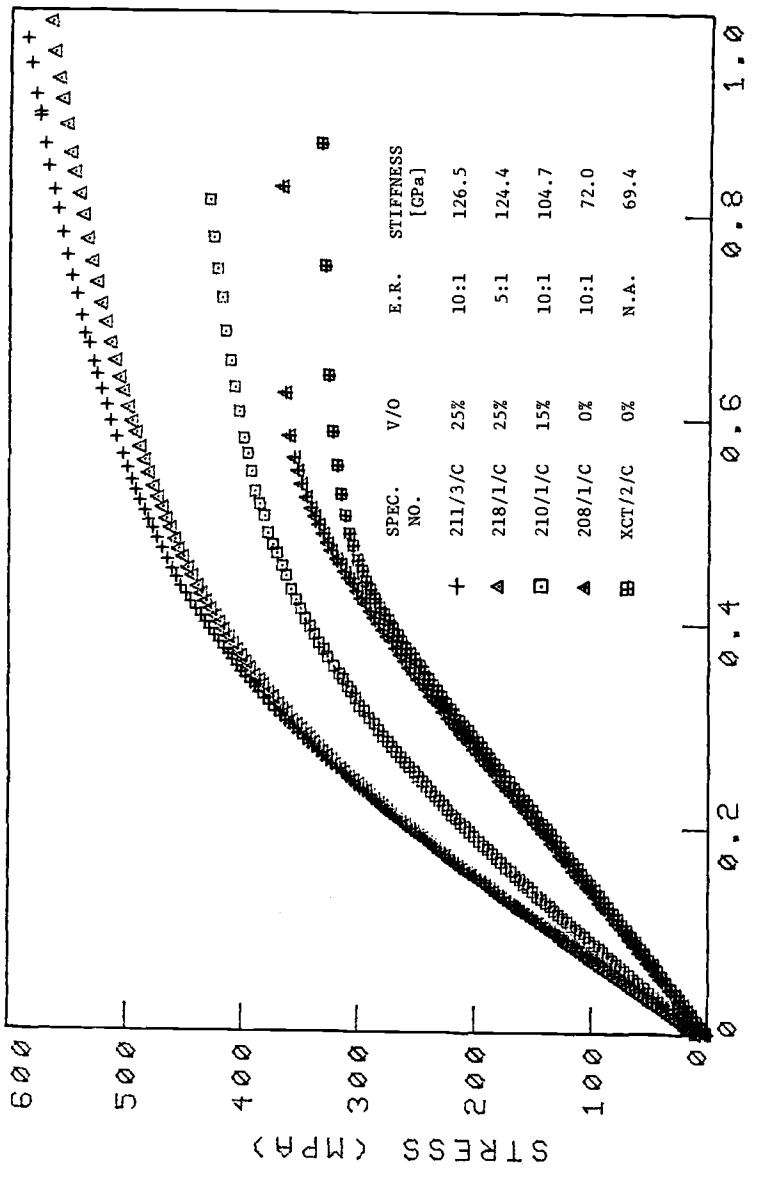

FIG. 4—*Stress-strain curves in compression of various SiC/Al composites showing effect of whisker volume fraction.*

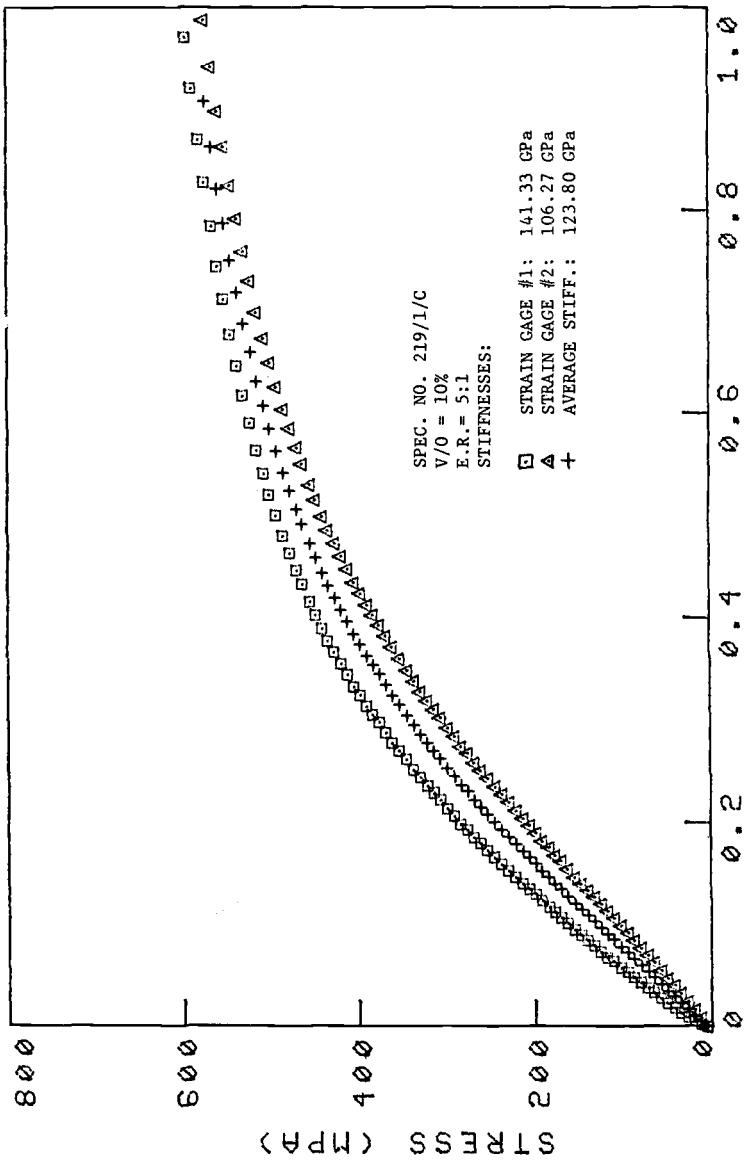

FIG. 5—*Stress-strain curves in compression obtained with two single strain gages bonded on opposite sides of the specimen.*

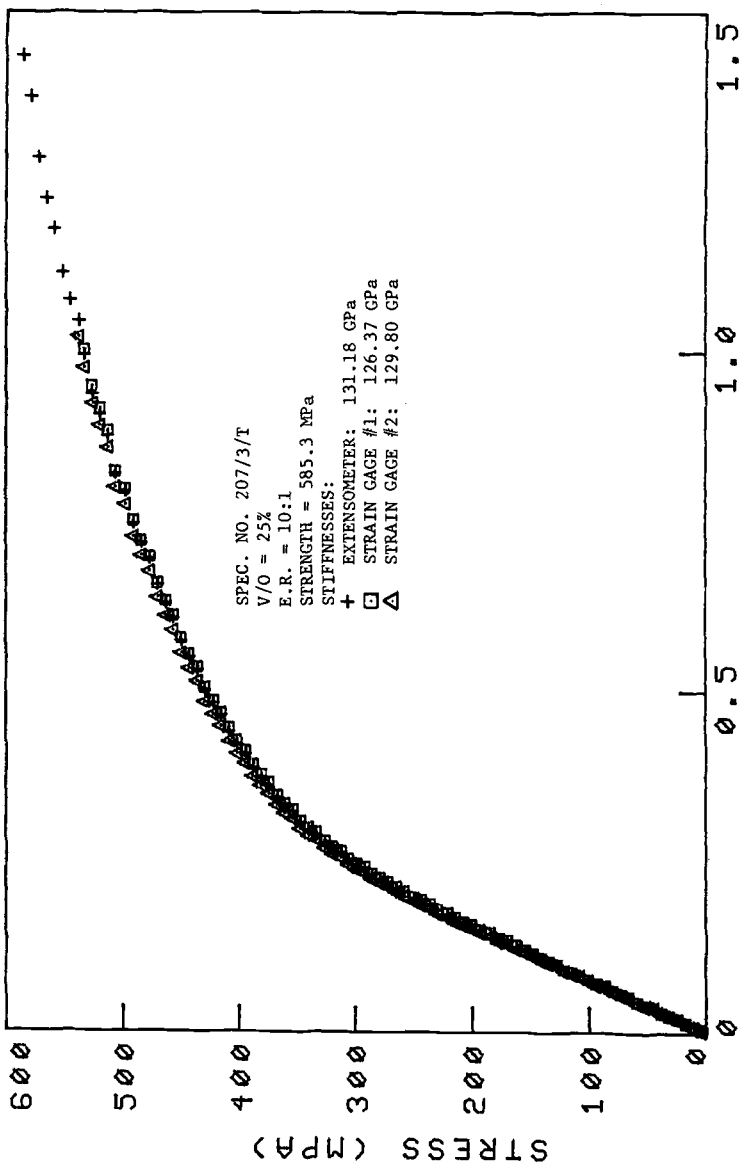

FIG. 6—*Stress-strain curves in tension obtained with an extensometer and with two single strain gages bonded on opposite sides of the specimen.*

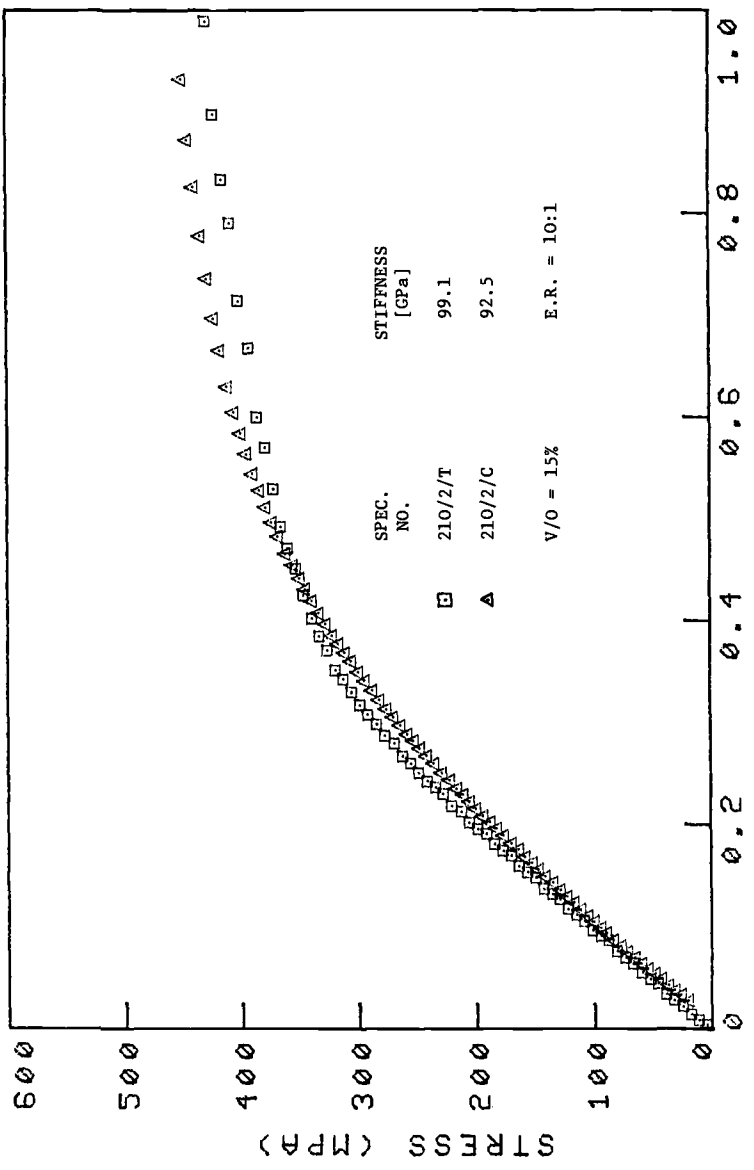

FIG. 7—*Comparison of stress-strain curves under tensile and compressive loading.*

specimens, Fig. 3, indicates that while the stiffness is similar, the strength of the extruded aluminum is higher by about 25%. Consequently, the effect of the fabrication of the composite on the mechanical properties of the aluminum should be taken into account in analyzing the performance of the composite.

Representative stress-strain curves obtained for all five material systems tested under compression are shown in Fig. 4, indicating the effects of whisker volume fraction, fabrication procedure, and extrusion ratio. From the results it could be concluded that whisker volume fraction significantly affects initial stiffness as well as strain-hardening rate. The comparison between the stress-strain curves of the commercially available aluminum alloy 6061-T6 and the extruded aluminum (V/O = 0%) indicates a relatively small effect on ultimate strength, and very little, if any effect on initial stiffness. The effect of extrusion ratio on the mechanical properties, namely, stiffness, strength, rate of strain-hardening, and the overall stress-strain curve is marginal.

Each curve shown in Fig. 4 is the average of the two curves obtained from the two strain gages which were mounted on opposite sides of the specimen. Typical stress-strain curves obtained from both strain gages are shown in Fig. 5 indicating some degree of bending. However, the average curve, used for comparison among the different material systems, was identical to that obtained with the extensometer. In the case of the tension tests a perfectly uniaxial loading was achieved, Fig. 6.

A comparison between the stress-strain curves obtained under tensile and compressive loading for one of the five material systems is shown in Fig. 7. These depict a representative result for the 15 V/O, 10:1 ER material system. It should be recalled here that the tensile stress-strain curves were obtained with an extensometer, while the specimens loaded under compression were instrumented with strain gages. Although a comparison of tension versus compression is shown for only one composite, the same comparison for the other four material systems resulted in very similar trends. For each material system, the stress-strain curves under both loading conditions are similar in stiffness and rate of strain-hardening, although the compressive yield strength is slightly higher than that recorded under tension, Figs. 1 and 4. The increased compressive yield strength may be due to a higher matrix compressive yield strength, residual thermal stresses caused by the differential thermal expansion of the whiskers and matrix, or a combination of both effects.

Acoustic Emission

Damage initiation and progression during tensile loading has been monitored through acoustic emission (AE) for a selected number of specimens. The correlation between the deformation characteristics and the AE results can be best seen in Fig. 8, indicating that emission initiates approximately when yielding occurs. Thus, for the extruded aluminum (V/O = 0%), emission initiation load is approximately 90% of ultimate load, while for all three other reinforced systems, emission initiates at load levels which are approximately 65% of ultimate load. Some random emission occurred at much lower load levels; however, it seems that this can be attributed primarily to grip noise during the initial loading, which cannot be filtered when a single transducer is used.

Events as a function of load accumulated during the entire loading to failure for all four material systems are shown in Figs. 9 and 10, which depict representative results from each of the material systems studied. The results, which were highly reproducible, show that the larger the volume fraction, the lower the slope of the events-versus-load curves. This is in agreement with the characteristic stress-strain curves recorded for the four material systems, Figs. 1 and 2, that is, the higher the rate of strain hardening, the lower the slope of the event versus load. Thus, the effect of fiber volume fraction on the acoustic emission results in quite noticeable. The extrusion ratio has little if any effect on the AE results, Figs. 8 and

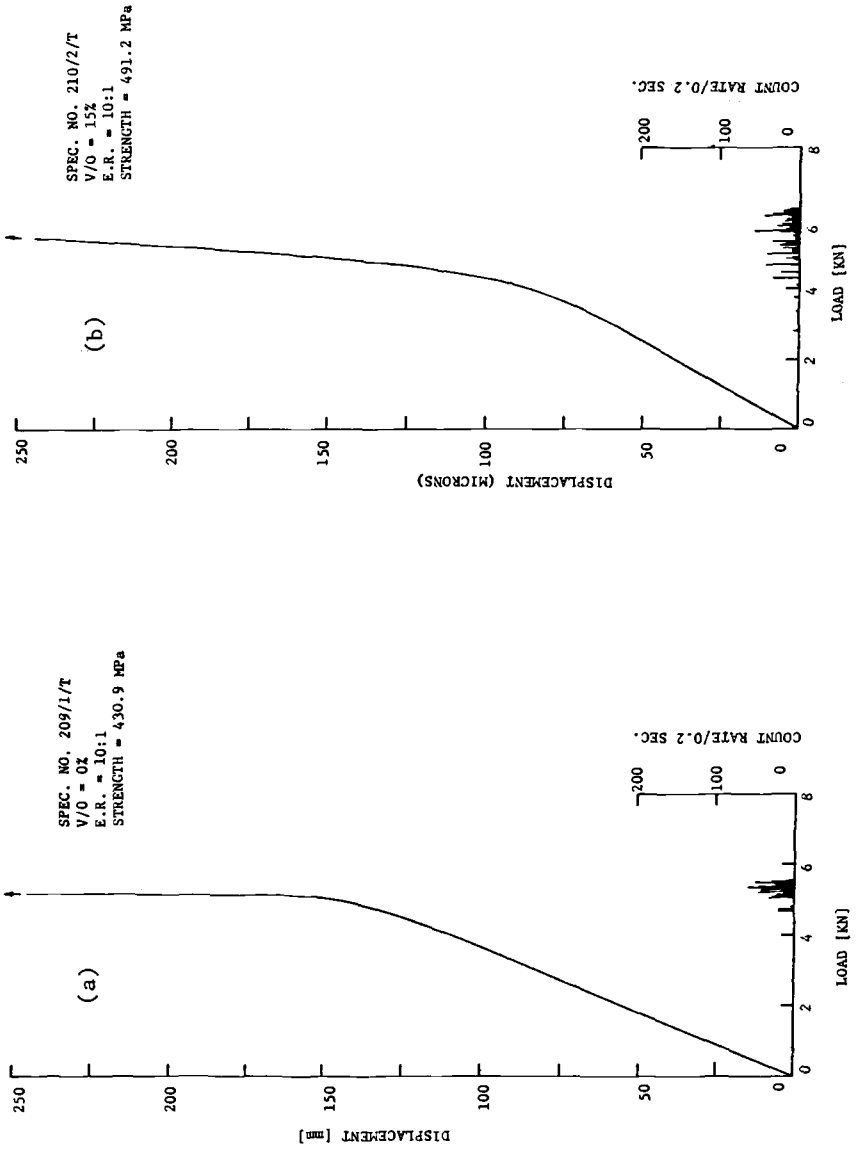
SPEC. NO. 209/1/T
V/O = 0%
E.R. = 10:1
STRENGTH = 430.9 MPa
(a)
DISPLACEMENT [mm]
LOAD [KN]
COUNT RATE/0.2 SEC.
SPEC. NO. 210/2/T
V/O = 15%
E.R. = 10:1
STRENGTH = 491.2 MPa
(b)
DISPLACEMENT (MICRONS)
LOAD [KN]
COUNT RATE/0.2 SEC.

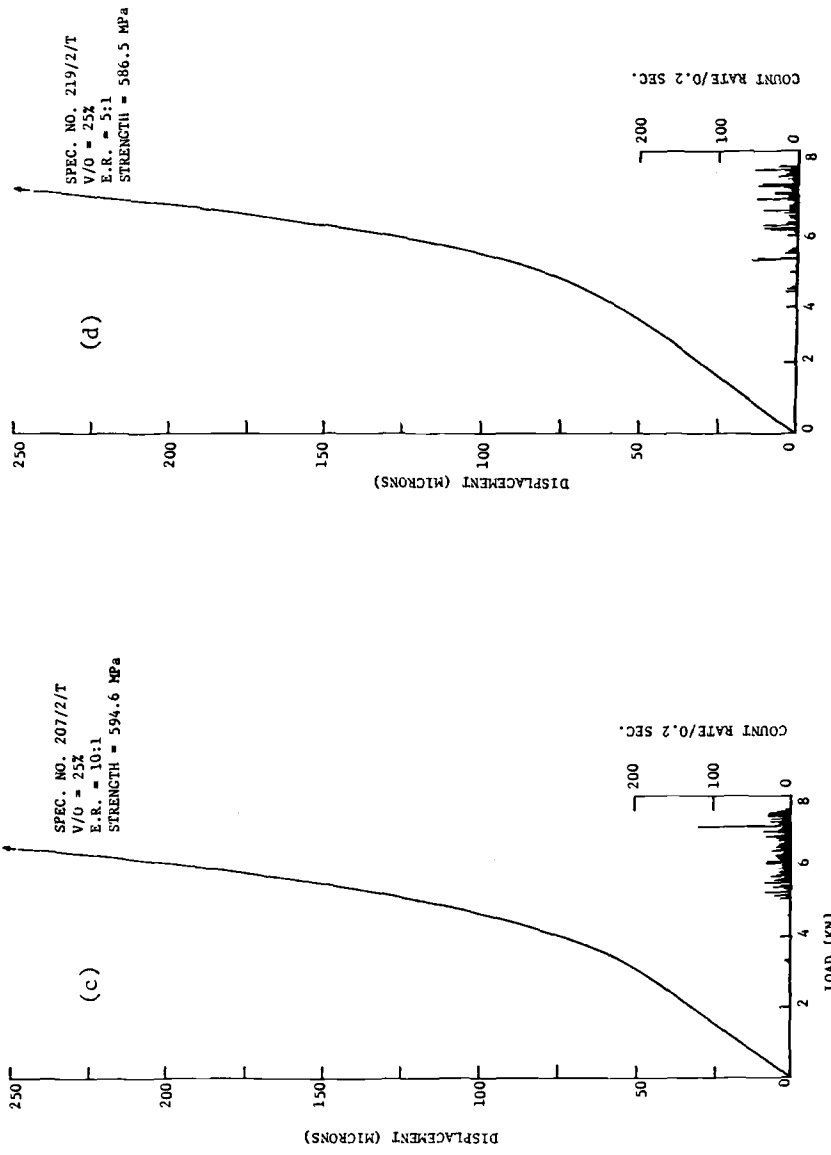

FIG. 8—*Far-field displacement and count rate as a function of load for:* (a) *V/O = 0%, ER = 10:1;* (b) *V/O = 15%, ER = 10:1;* (c) *V/O = 25%, ER = 10:1; and* (d) *V/O = 25%, ER = 5:1.*

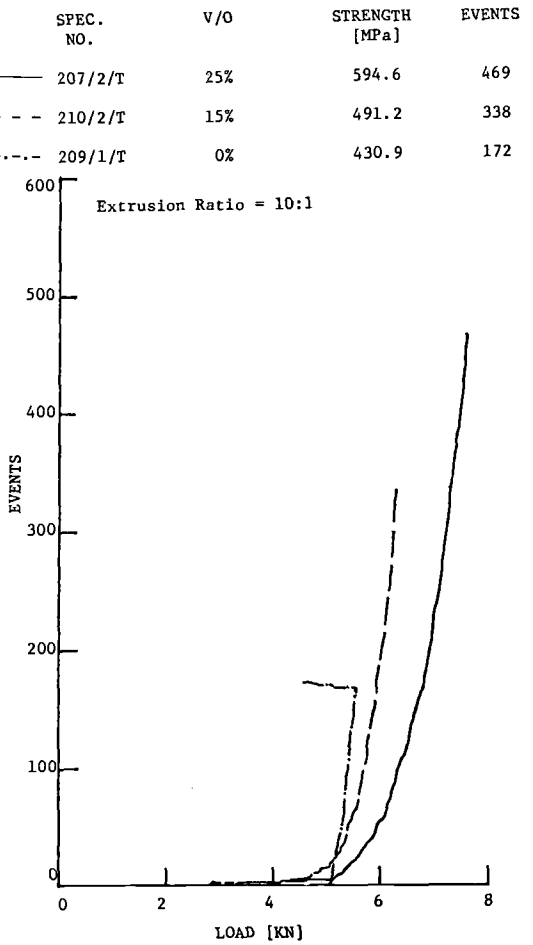

FIG. 9—*Accumulative events as a function of load for SiC/Al with different fiber volume fraction, subjected to tensile loading.*

10, and this is expected recalling that both extrusion ratios resulted in similar rates of strain hardening, Fig. 2.

From the results shown in Figs. 9 and 10 it could be concluded that the total number of events is higher for the stronger specimens, as expected. In particular, the total number of events accumulated through the loading to failure is much higher for the reinforced specimens than it is for the unreinforced extruded specimens. Within each material system, however, due to the small scatter in strength, such a correlation could not be found.

Determination of the major failure mechanisms using acoustic emission can be based upon a variety of AE source intensity signatures, such as events amplitude, duration, energy, counts per events, frequency spectrum, etc. In this study, emphasis has been placed on analyzing the amplitude distribution histogram of events, which is the most commonly used, to determine the potential of the AE technique in determining the dominant failure mechanisms. It is assumed that high amplitude events correspond to whisker fracture, while lower amplitude events correspond to matrix inelastic deformation and whisker-matrix interfacial failure. Although there is some evidence for this distinction, relatively little work on metal matrix composites is available in the literature.

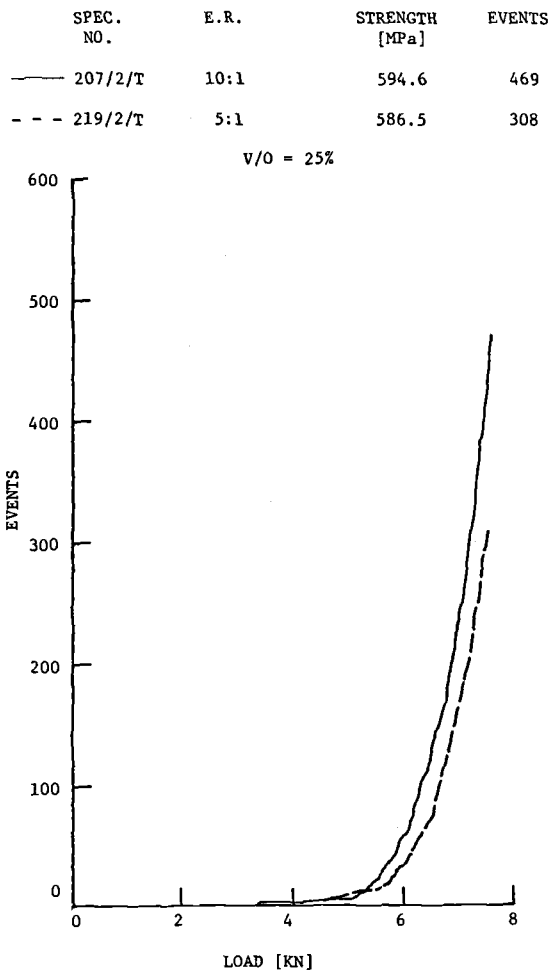

FIG. 10—*Accumulative events as a function of load for SiC/Al with different extrusion ratios (V/O = 25%), subjected to tensile loading.*

Amplitude distribution histograms of events for all four material systems (excluding the commercial aluminum) accumulated during the entire load to failure are shown in Fig. 11. Most of the histograms have a peak amplitude in the range of 40 to 60 dB. Very few events have higher amplitude, and these occurred as the load approached its ultimate value. It is assumed, therefore, that most of the emission is generated either by plastic deformation or whisker-matrix interfacial failure, or a combination of these, since only limited fiber breakage is expected to occur. Since all four material systems yielded similar amplitude distributions (including the 0% V/O specimens) it can be concluded from the AE results that neither whisker breakage nor significant whisker-matrix interfacial failure occurred. This observation has been confirmed by examination of the fracture surface morphologies, which will be discussed in the next section.

The results obtained from monitoring acoustic emission are obviously not conclusive, primarily due to limitations imposed by specimen length. However, they do offer a general indication of the potential of acoustic emission as a nondestructive test technique to monitor damage initiation and progression, and determine major failure mechanisms, all in real time

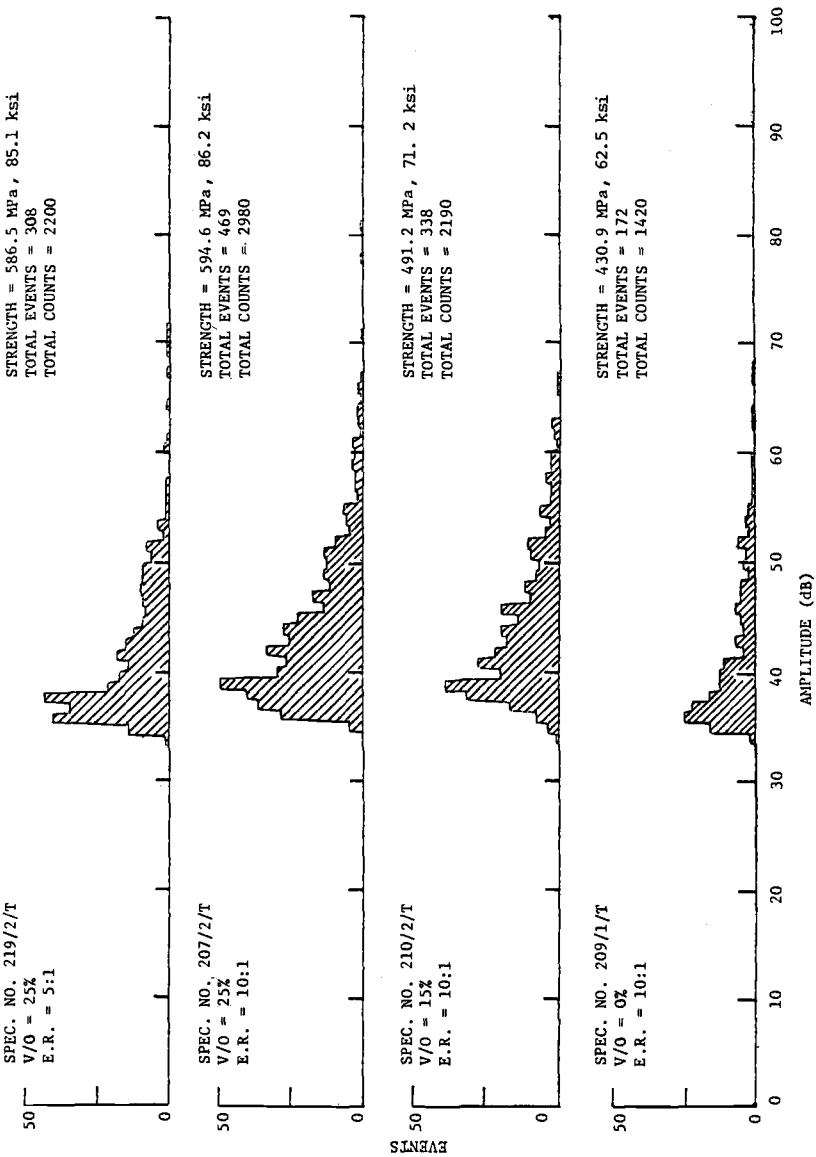

FIG. 11—*Amplitude distribution histograms of events accumulated during the entire loading to failure in tension for four material systems.*

The results obtained in this study are promising since they do correlate with the deformation characteristics of the subject material.

Failure Modes

A selected number of specimens subjected to tensile loading have been examined under the scanning electron microscope (SEM). An overall view of the fracture surfaces of five specimens representing the five materials systems is shown in Fig. 12. The commercial aluminum alloy 6061-T6 exhibits the typical cup-and-cone ductile failure which is associated with significant yielding and necking at the fracture site, Fig. 12*a*. On the other hand, the extruded aluminum (V/O = 0%) specimen has an inclined fracture surface, typical to shear failure observed in high strength aluminum alloys, Fig. 12*b*. The amount of yielding and necking in this specimen is much more limited. All three reinforced composite specimens also exhibit some amount of ductility; however, it is significantly more limited, which confirms the stress-strain diagrams, that is, the higher the volume fraction, the more limited is the amount of ductility. For example, the fracture surface of the 15% V/O specimen, Fig. 12*c*, exhibits higher ductility than the 25% V/O specimen, Fig. 12*d*, while the effect of the extrusion ratio is not noticeable, Fig. 12*e*.

Details of the fracture surfaces of the commercial aluminum and the three reinforced systems are shown in Fig. 13. The fracture surface of the commercial aluminum alloy 6061-T6, Fig. 13*a*, indicates a very large amount of microvoid coalescence with relatively large dimples, all typical to the microyielding associated with failure of the aluminum 6061 system. Fracture surface morphologies of the three composite systems tested are shown in Figs. 13*b* through 13*d* all of which exhibit largely intergranular failure, as was expected considering the manufacturing procedure of the composite. All three specimens also exhibit local yielding and microvoid coalescence; however, the main feature consists of fine equiaxial dimples. The whiskers shown in these figures generally seem to be randomly oriented; however, no precise evaluation of preferred directionality is possible and additional examinations are warranted. Very little fiber pullout is observed, for example, Fig. 13*d*, and it seems that very little interfacial failure occurred.

In order to obtain a better view of the fracture surfaces and better characterize the different modes of failure, stereo (three dimensional) views of the fracture surfaces were prepared. The pairs of photographs were obtained by rotating the specimens by three degrees. Viewing the two resulting photographs through the stereo viewer clearly revealed the details of these dimples, that is, shape, depth, and orientation, as well as the amount and length of fiber pullout, quality of whisker/matrix bonding, etc. Careful examination of the fracture surfaces indicates little effect of fiber volume fraction and extrusion ratio on the fracture surface morphologies of the reinforced systems. These examinations also indicate good bonding between the aluminum matrix and whiskers. In order to more accurately determine the quality of bonding between the whiskers and the aluminum matrix, an element mapping of the whisker surface has been performed using energy dispersion analysis of X-ray. Traces of both aluminum and silicon were detected throughout the entire area under examination. Consequently, the results were not considered sufficiently conclusive. However, the results of the SEM suggest the presence of aluminum on the whisker surfaces. A general element analysis of specimen cross sections has been performed as well, resulting in a relative average of the percentages by weight of the elements detected on the fracture surface. The comparison among the different specimens indicated that the whisker volume fraction was very close to that reported by the supplier.

In order to qualitatively determine the whisker uniformity and the void content, photomicrographs were prepared for cross sections of all five material systems, both perpendicular and parallel to the axis of symmetry of the specimens (that is, the extrusion direction).

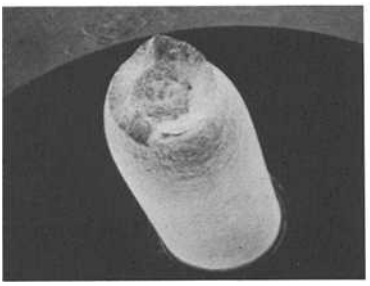

(a) Com'l 6061-T6 Alum.

(b) V/O=0%, E.R.=10:1

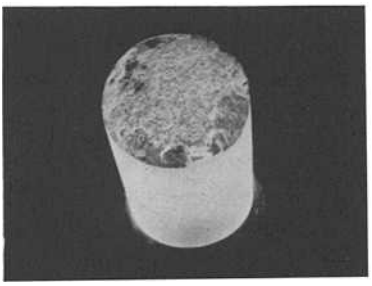

(c) V/O=15%, E.R.=10:1

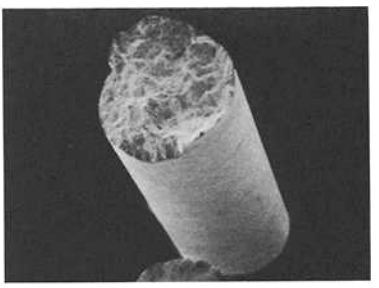

(d) V/O=25%, E.R.=10:1

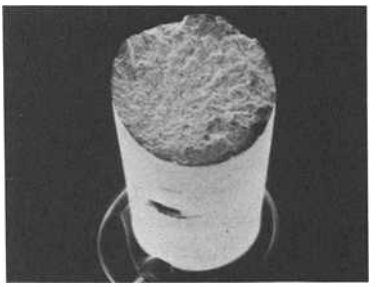

(e) V/O=25%, E.R.=5:1

FIG. 12—*Scanning electron micrographs of aluminum and SiC/Al composites subjected to tensile loading, showing general views of the fracture surfaces.*

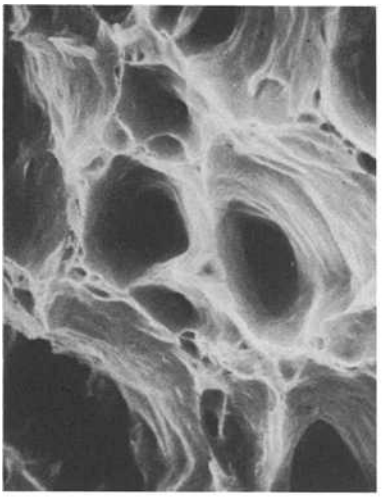

(a) Com'l 6061-T6 Alum.
~ x=5000

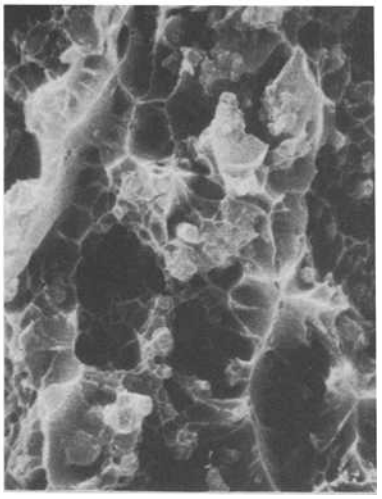

(b) V/O 15%, E.R.=10:1
~ x=5000

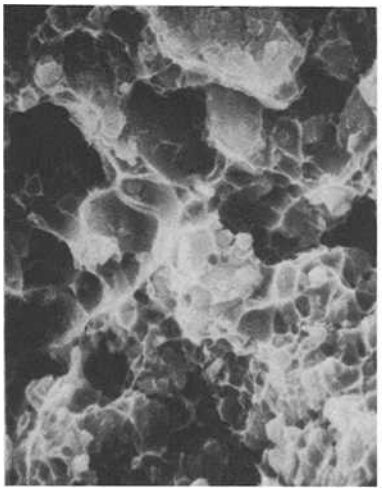

(c) V/O 25%, E.R.=10:1
~ x=5000

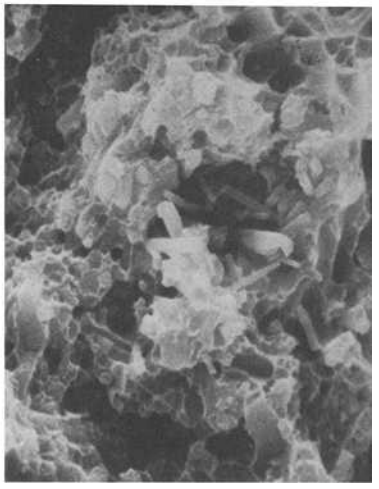

(d) V/O 25%, E.R.=5:1
~ x=5000

FIG. 13—*Scanning electron micrographs of aluminum and SiC/Al composites subjected to tensile loading, showing details of fracture surfaces.*

These photomicrographs indicated that the SiC whiskers are bundled together. In other words, a clear distinction between whisker-rich and whisker-poor areas can be made.

Very few voids were observed throughout the cross sections and the features of the microstructure were very similar within each cross section. Most of the larger voids were located in the whisker-rich areas. The voids were quite equiaxial; however, they were significantly distended along the extrusion direction, as expected. Generally, very few voids could be found in the reinforced materials.

Conclusions

The mechanical properties of whisker reinforced SiC/Al subjected to uniaxial tensile and compressive loading can be summarized as follows:

1. Fiber volume fraction strongly affects stiffness, strength, rate of strain hardening, and ultimate strain, as expected. This effect is more pronounced in the case of tensile loading.
2. The extrusion ratios studied (5:1 versus 10:1) have little if any effect on the stress-strain behavior.
3. However, the 10:1 extruded aluminum, designated 6061-T6, is stronger than the commercial aluminum 6061-T6. Therefore, the fabrication process alters the *in situ* aluminum matrix properties.
4. The subject material appears to have equal stiffness in tension and compression. The recorded compressive strengths are, however, somewhat higher than the tensile strengths, which is probably related to the higher matrix compressive strength or to residual stresses in the matrix.
5. A qualitative correlation between the acoustic emission results and the deformation characteristics could be established.
6. The amplitude distribution histograms of events, recorded for the reinforced and unreinforced materials, are similar. It could be concluded therefore, that the dominant mode of failure is matrix plasticity and whisker pullout. There is no evidence that whisker failure governs failure of the composite, although additional studies on this issue are warranted.
7. Examinations of the fracture surface morphologies of all material systems reveal a significant amount of microyielding, manifested by the microvoid coalescence. Good whisker-matrix bonding has been observed in all fracture surfaces examined. The degree to which the composite fracture surface appears brittle, on the macroscale, could be qualitatively correlated with the recorded stress-strain behavior.

Acknowledgment

The authors wish to thank Drs. S. Fishman, C. Crowe, and J. Tydings of the Naval Surface Weapons Center (NSWC) for serving as technical monitors on this program. This work was supported by NSWC under contract number N60921-82-C-0133 during the period July 1982 to March 1983. The assistance of Dr. M. S. Madhukar and Mr. S. Ghaffari in performing the experimental work is acknowledged with great appreciation.

References

[*1*] Goering, J., Buesking, K., and Awerbuch, J., "Minimechanics Analysis and Testing of Short Fiber Composites: Analytical Model and Data Correlation," this publication, pp. 143–158.

[*2*] Hood, P., "Base-Line Property and Fabrication Data for SiC Whisker Reinforced Aluminum Alloy," Arco Technical Final Report, NSWC Contract Number N60921-81-C-A328, Dec. 1982.

Jonathan Goering,[1] *Kent Buesking,*[1] *and Jonathan Awerbuch*[2]

Minimechanics Analysis and Testing of Short Fiber Composites: Analytical Model and Data Correlation

REFERENCE: Goering, J., Buesking, K., and Awerbuch, J., **"Minimechanics Analysis and Testing of Short Fiber Composites: Analytical Model and Data Correlation,"** *Testing Technology of Metal Matrix Composites, ASTM STP 964,* P. R. DiGiovanni and N. R. Adsit, Eds., American Society for Testing and Materials, Philadelphia, 1988, pp. 143–158.

ABSTRACT: This paper describes an analytical modeling effort designed to study the stress-strain behavior of silicon carbide whisker reinforced aluminum. The objective of the study was to develop an approximate method for predicting the stress-strain response of whisker reinforced metals as a function of constituent properties, whisker geometry, volume fraction, and extrusion ratio. The study utilized experimental results (described in a companion paper) for qualitative understanding of the material behavior and quantitative data correlations with the model.

KEY WORDS: metal matrix, silicon carbide, analytical model, extrusion, stress-strain behavior, plasticity

Recent advances in the field of metal matrix composites have made short-fiber reinforced materials, such as silicon carbide/aluminum (SiC/Al), very attractive as structural materials. Most of the previous research and development work with these composites has concentrated upon fabrication and testing of specific materials. Although this approach has been successful, it becomes very inefficient due to the large number of variables associated with these materials.

The mechanical properties of a whisker reinforced composite depend most strongly upon factors such as: matrix material properties; whisker volume fraction, aspect ratio and orientation; and whisker material properties. A theoretical model of the material can be postulated, allowing the material behavior to be quantified analytically. This analytical model can then be exercised to gain an understanding of the effects of the various material parameters upon the mechanical behavior of the composite.

This paper describes the development of such an analytical material model for short-fiber reinforced composites. The model is complex enough to account for the effects of the major material parameters, yet simple enough to serve as a useful tool. This analysis focuses upon the behavior of silicon carbide (SiC) whisker reinforced aluminum, but is applicable to the analysis of other short-fiber reinforced composites. The analytical model is used to estimate the nonlinear stress-strain response of a SiC/Al composite as a function of whisker volume fraction, aspect ratio, and preferred orientation, and is verified by comparison with experimental results.

[1] Research engineer and director of Advanced Materials, respectively, Materials Sciences Corporation, Gwynedd Plaza II, Spring House, PA 19477.

[2] Associate professor, Department of Mechanical Engineering and Mechanics, Drexel University, Philadelphia, PA 19104.

Material Model

To understand the assumptions utilized in the material model, it may prove helpful to examine the physical characteristics of SiC/Al. The composite is fabricated by mixing silicon carbide whiskers with aluminum at high temperatures. The composite, which is somewhat like cast aluminum, can be then formed by typical metal working procedures such as extrusion. The aluminum is generally a typical aluminum alloy such as 6061. The SiC whiskers can be envisioned as small ellipsoids. They have diameters ranging from 5 to 10 μm and an average aspect ratio on the order of 5. Thus, the whiskers are very small in comparison to typical structural dimensions. This implies that in the as-cast form they can be assumed to have a homogeneous, random distribution in space. It is assumed that a material model of a small representative volume element is sufficient to predict the bulk properties of the composite material.

The silicon carbide whiskers themselves are treated as isotropic, brittle materials, and the aluminum matrix is assumed to be isotropic and ductile. Thus, the model must account for potential plasticity within the matrix.

Another characteristic of the material results from the extrusion process. As the bulk, random composite is extruded, the silicon carbide whiskers tend to develop a preferred orientation along the extrusion direction. Therefore, the initial material, which was globally isotropic because of the random whisker orientations, can become transversely isotropic after extrusion. This implies that the model will need to predict properties that vary with local whisker orientation.

In summary, the material model considers a composite consisting of a ductile, isotropic matrix reinforced with brittle, isotropic whiskers. The whiskers may have either random or preferred orientations, and are assumed very small in diameter with aspect ratios that are constant in an average sense.

The analytical development utilizes two fundamental assumptions in creating the material model. First, it is assumed that a representative volume element of the composite can be treated as an infinite number of randomly oriented unidirectional whisker bundles. Secondly, it is assumed that a random distribution of bundles can be adequately represented by a finite number of specially oriented bundles. These assumptions are shown schematically in Fig. 1.

These two concepts form the basis of the material model. That is, it is postulated that the bulk properties of a whisker reinforced composite will be similar to those of a representative volume element (RVE) consisting of a finite number of specially oriented unidirectional whisker bundles. Further, it is assumed that by incrementally loading this RVE and accounting for any matrix yielding that might occur, the nonlinear stress-strain relationship of the whisker reinforced composite will be estimated.

The actual model utilizes the self consistent scheme for an ellipsoidal inclusion in an infinite matrix to determine the effective properties of the unidirectional whisker bundles [*1*]. Stiffness matrices of the effective bundles are then transformed into a global coordinate system and volume averaged to yield the effective stiffness matrix of the composite. Details of this procedure are included in the appendix.

Loads are applied to the composite incrementally, while stresses or strains are monitored at the bundle level. After each load increment, Hill's yield criterion [*2*] is used to predict matrix yielding within a given bundle. When matrix yielding is predicted, the effective properties for the yielding bundle are calculated using the tangent modulus of the matrix. The reduced effective bundle properties are then used to calculate effective composite properties for subsequent load steps. This incremental procedure results in a piecewise linear stress-strain response for the effective composite. The flow chart for the analysis is shown in Fig. 2.

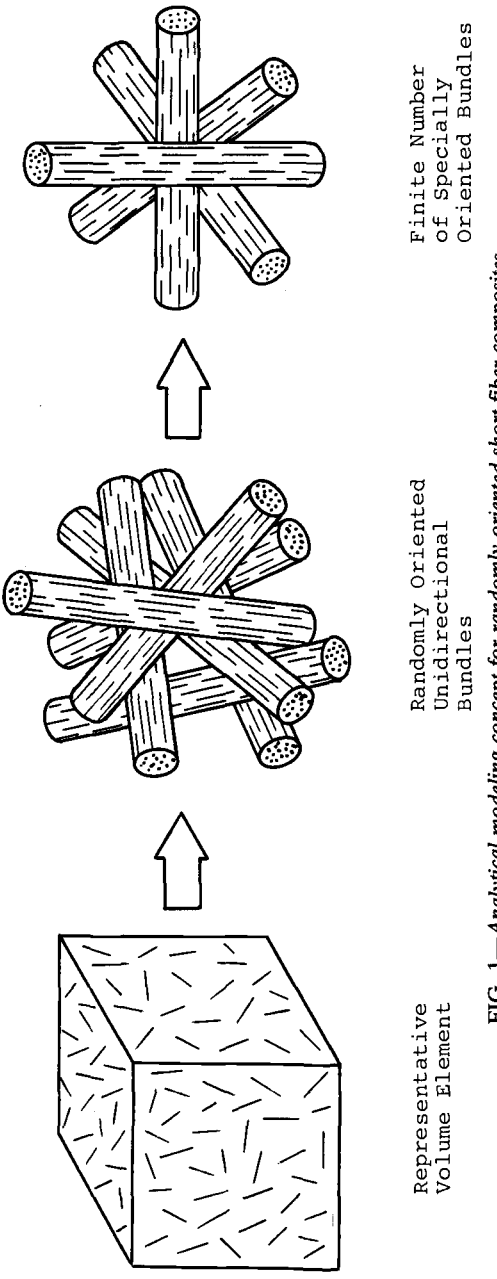

FIG. 1—*Analytical modeling concept for randomly oriented short-fiber composites.*

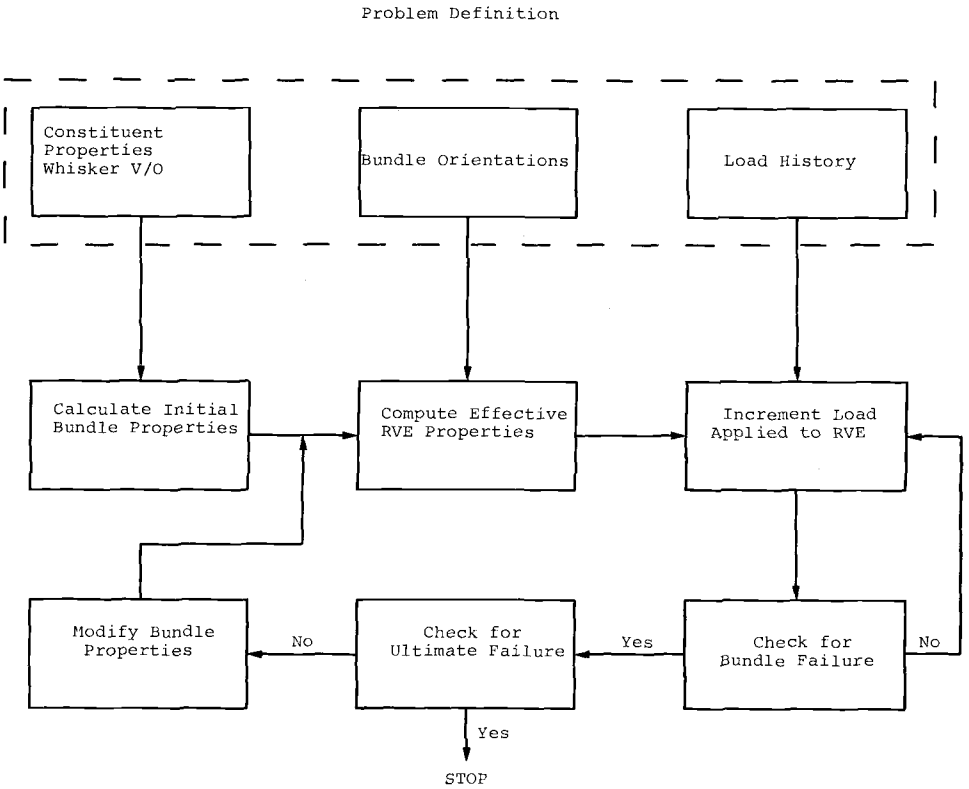

FIG. 2—*Flow chart of the analytical procedure.*

It was found that 16 unidirectional bundles could be used to approximate the random whisker reinforced composite. These bundles were oriented such that they passed through the vertices and face centers of a dodecahedron, as shown in Fig. 3. It is known that isotropic elastic properties for randomly reinforced composites can be predicted by properly orienting a finite number of reinforcing bundles [*3,4*]. An analogy for isotropic strength is not obvious and can be only demonstrated, in an approximate sense, numerically. Three predicted stress-strain curves for the 16 bundle composite are shown in Fig. 4. Each of these curves represents a uniaxial load in one of the global coordinate directions, only one of which is parallel to a bundle direction. As demonstrated by this figure, the material model provides a sufficient approximation to isotropic strength to warrant its use as an engineering tool.

Experimental Study

An experimental study was undertaken in conjunction with the model development efforts. The experimental program utilized material supplied by the Naval Surface Weapons Center and was performed at Drexel University under the direction of Dr. Jonathan Awerbuch. The goal of the experimental studies was to produce typical stress-strain curves of the material which could be compared to the analytical predictions.

The material tested in this program was 6061 aluminum reinforced with silicon carbide whiskers. Specimens of three different volume fractions were tested: 0, 15, and 25%, randomly oriented and having an extrusion ratio of 10:1. Specimens with 25 volume percent were also manufactured with an extrusion ratio of 5:1.

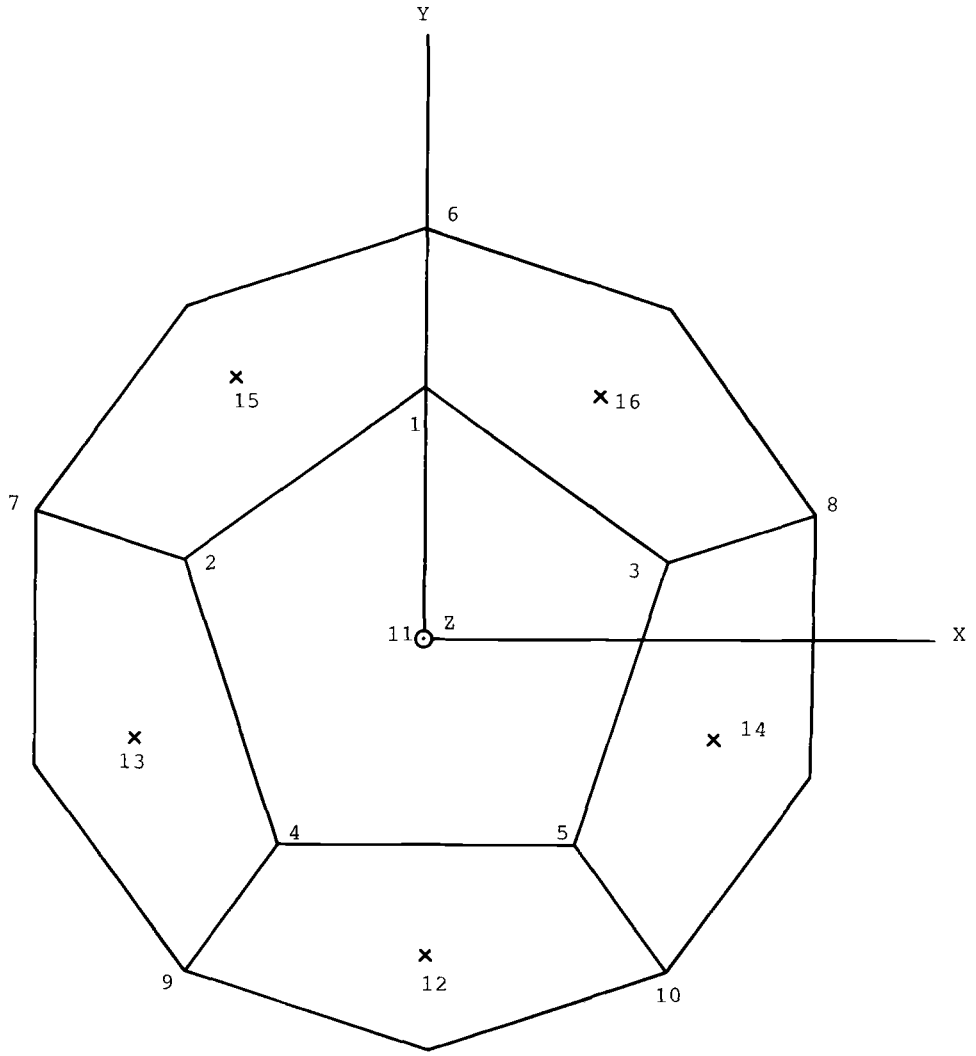

FIG. 3—*Dodecahedron showing verticies and face centers used to define bundle orientations for randomly oriented short-fiber composites.*

In order to determine the effect of fabrication on the mechanical properties of the aluminum matrix, commercial aluminum 6061-T6 was also purchased and machined. The data obtained with the commercial aluminum alloy were compared with those obtained with extruded aluminum, volume percent = 0%.

Quasi-static uniaxial tension tests and compression tests were performed on a closed loop servo hydraulic Instron testing machine (Model 1331). Specimens were loaded under stroke control mode at a rate of 0.07 mm/min (0.003 in./min). Each specimen was instrumented with an extensometer to obtain the "global" stress-strain curves. A selected number of specimens were strain-gaged to obtain the "local" stress-strain curves and to ensure that the extensometer data were reliable. Two gages (EA06-031DE-120) were applied along opposite sides of the specimens to minimize the effect of bending and to ensure axiality of

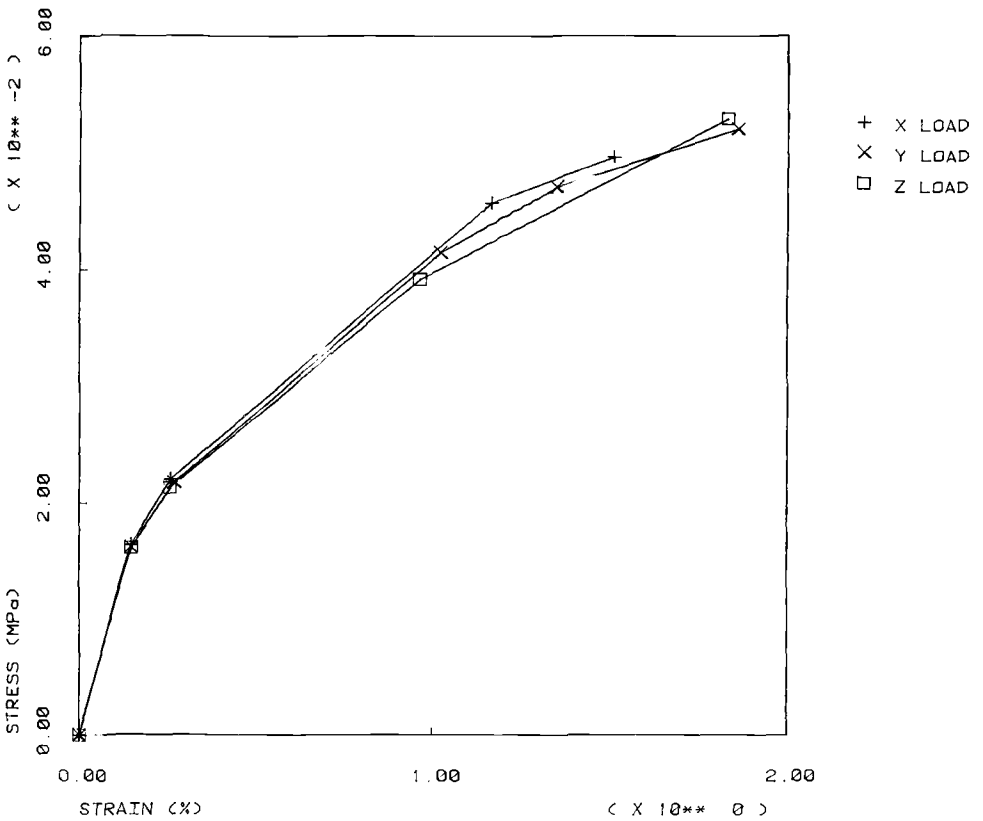

FIG. 4—*Stress-strain curves for orthogonal loadings on a SiC/Al composite modeled with bundle directions defined by a dodecahedron.*

loading. For all specimens tested, initial stiffness, stress-strain curves, and strength data were recorded.

Test results were recorded on X-Y-Y recorders to monitor the test progression in real time. The testing system was also interfaced with a data acquisition system (PDP 1103 Model MINC-11 of Digital Equipment Corporation). Post-test analyses provided complete load-displacement curves, stress-strain curves, and mechanical properties such as strength and stiffness. Printouts of stress-strain data in tabular form were also obtained. The experimental program is detailed in Ref *5*.

Data Correlation

Although this material model includes certain assumptions, it also allows a great deal of flexibility in analyzing whisker reinforced materials. For example, the properties of the unidirectional bundles depend upon the constituent properties, volume fractions, and aspect ratio. The properties of the RVE depend upon the bundle properties and orientation. Thus, the model is capable of examining the behavior of materials with different constituents, whisker contents, whisker aspect ratios, and extrusion ratios. Therefore, the basis for the analytical development includes not only a desire to develop a representative material model, but also a desire to create a useful analysis tool.

TABLE 1—*Constituent properties used in analysis of SiC/Al materials.*

Material	E, GPa	v	F_y^{tens}, MPa	F_y^{comp}, MPa	F_y^{shear}, MPa
Silicon carbide whisker[a]	448.2	0.20	689.5 to 6894.8	5515.8	...
6061 extruded aluminum	71.7	0.33	382.0	387.2	220.6

[a] Taken from Ref. *6*.

In order to compute SiC/Al properties, it was first necessary to calculate the stiffness of a unidirectional whisker reinforced bundle. The constituent properties used in this study are shown in Table 1. The SiC whisker properties are believed to be representative of the *in situ* SiC whisker behavior. The matrix properties were determined from the experimental stress-strain curves of extruded unreinforced aluminum shown in Fig. 5. Since the materials under investigation included composites with 15 or 25% whisker volume content, properties were computed for these reinforcement concentrations with whiskers of various aspect ratios.

The experimental material was all extruded to either a ratio of 10:1 or 5:1. Thus, it was necessary to determine bundle orientations that represented the whisker directions in an extruded material. To accomplish this, it was assumed that the reported extrusion ratio represented the change in cross-sectional area of a circular cylinder as it was extruded. To define the problem, it was assumed that the random material, represented by a 16 bundle composite, was extruded along its z-axis. It was further assumed that the projection of a

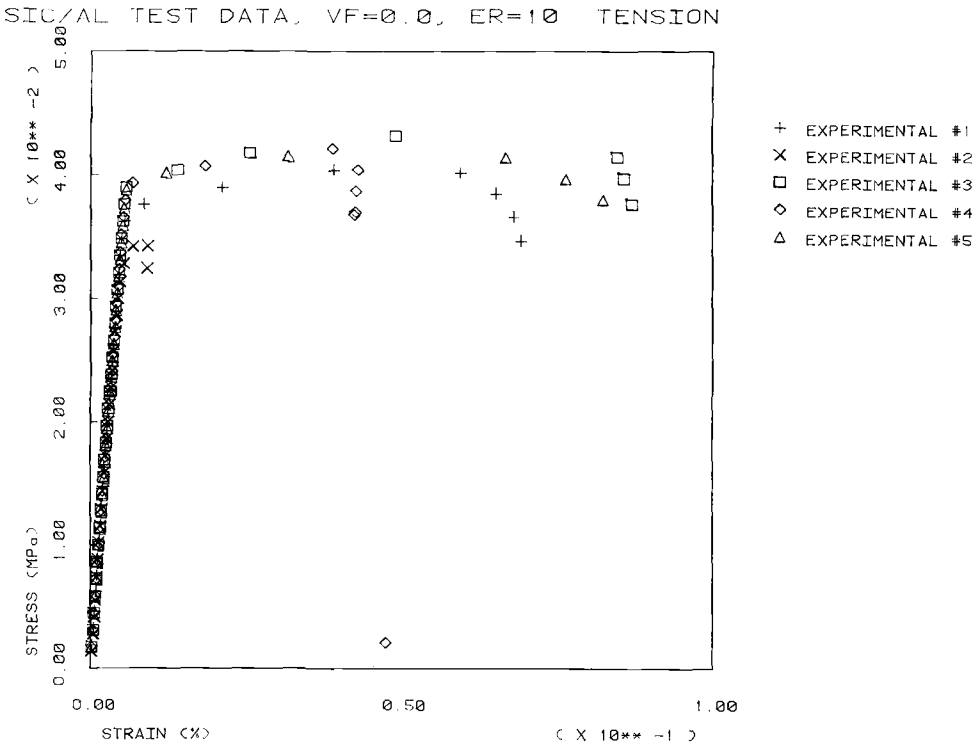

FIG. 5—*Measured stress-strain response for extruded unreinforced aluminum.*

whisker on the *x-y* plane would be shortened by the amount of the area reduction. The *z*-direction cosine was then computed by assuming that the whisker maintained its original length and did not elongate like the overall extruded material.

At this point, the bundle properties were defined and the bundle directions were known for the extruded materials. The remaining stiffness variable that was not yet fixed was the aspect ratio of the *in situ* whiskers. Although the actual material contains a distribution of whisker geometries, the model required only an average aspect ratio to represent the material behavior. The bundle properties were computed for typical aspect ratio of SiC whiskers, but it was necessary to determine the actual average as-fabricated whisker geometry within the composite.

This was done by comparing the analytical predictions to the experimental data. The moduli of composites with 5:1 and 10:1 extrusion ratios were computed as a function of whisker volume fraction and aspect ratio. Typical results for a material with a 5:1 extrusion ratio are shown in Fig. 6. The experimental moduli are also plotted on the curves. The comparisons showed that a 5:1 extruded material can be represented with an aspect ratio of 3, and the 10:1 extruded material is best modeled with an average whisker aspect ratio 2.5.

These values are lower than expected, however, they may explain data measured on previous SiC/Al programs. It has been reported that the extrusion process degrades the whiskers. Thus, whiskers with an average aspect ratio of 10 or 15 prior to extrusion may have a much lower aspect ratio after extrusion. This would explain why the aspect ratio of

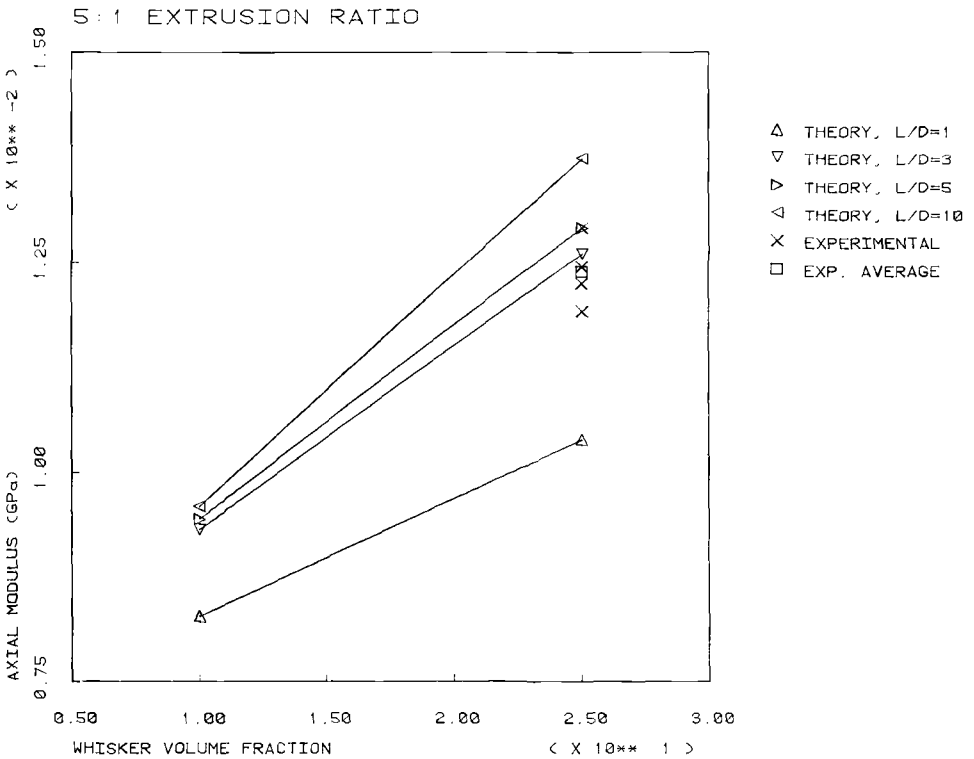

FIG. 6—*Comparison of experimental data to theoretical predictions for SiC/Al with 5:1 extrusion ratio.*

the 10:1 material is lower than that of the 5:1 material. It has been also reported that particle reinforced materials have essentially the same properties as whisker reinforced materials with equal reinforcement volume fractions. The data shown in Fig. 6 implies that the average whisker aspect ratio is so small that whiskers essentially behave as particles. That is, even though the extrusion process is believed to align the whisker which increases stiffness, it also shortens the average aspect ratio which decreases stiffness.

Based upon these comparisons, all further data correlations assumed that the 10:1 material had an average aspect ratio of 2.5 and the 5:1 material had an average aspect ratio of 3.

The remaining properties that were required to exercise the model were estimates of the local yield strengths of the unidirectional whisker reinforced bundles. This is probably best done by examining the local stresses that occur near a whisker through a detailed stress analysis. The solution to that problem, however, is quite complex and represents an analytical program of its own. For the purpose of this study, estimates were made of the limiting yield strengths of a whisker bundle based upon knowledge of particle and continuous fiber reinforced materials.

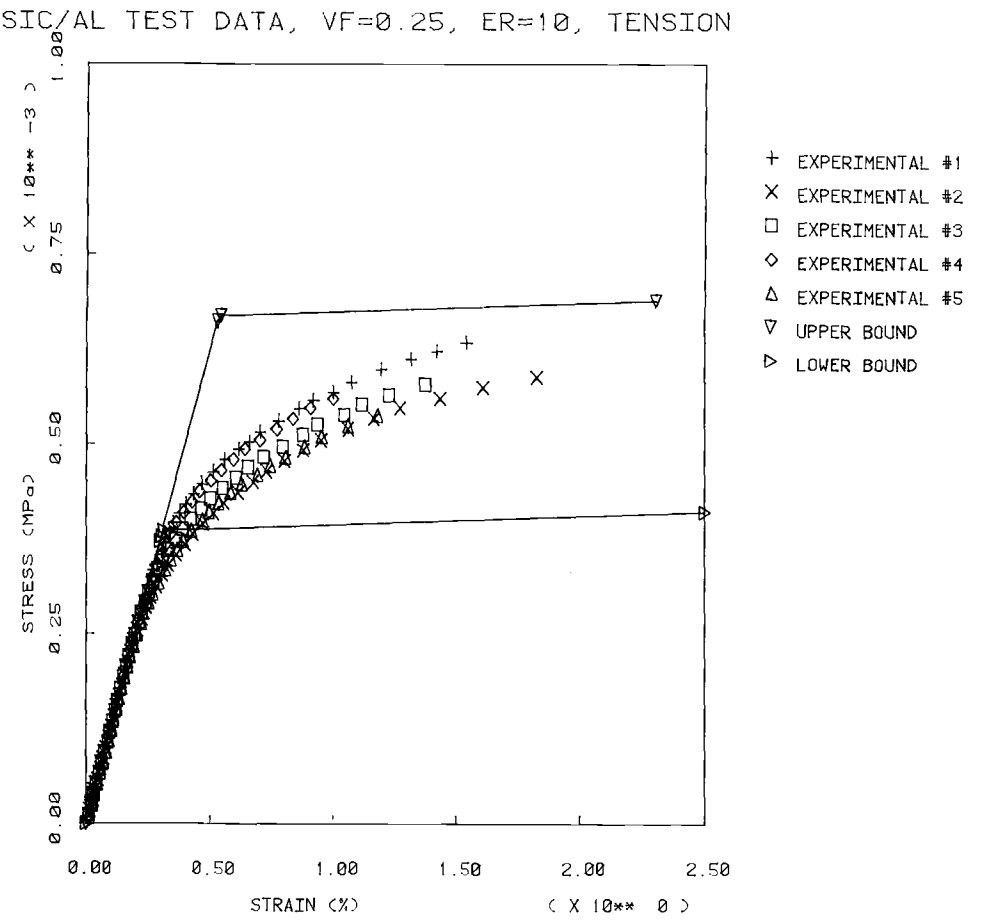

FIG. 7—*Comparison of predicted versus measured stress-strain response for 25% 10:1 SiC/Al tensile data.*

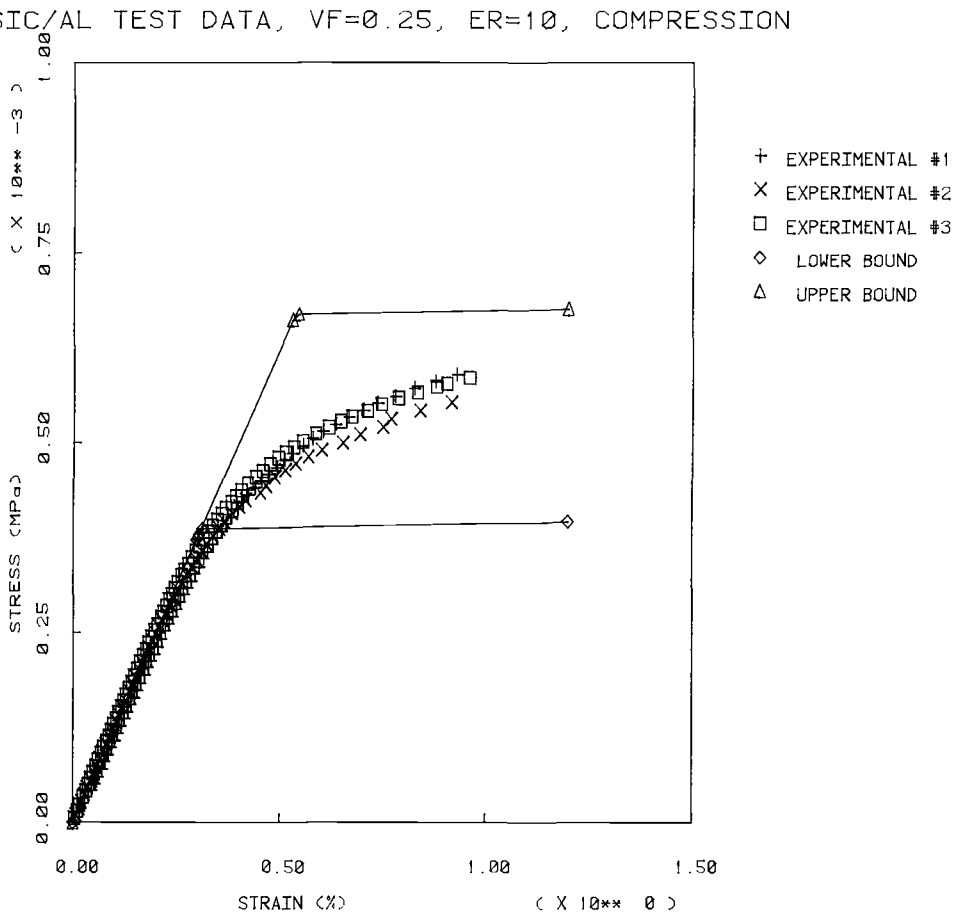

FIG. 8—*Comparison of predicted versus measured stress-strain response for 25% 10:1 SiC/Al compressive data.*

Strengths were then estimated in two ways. The upper limit on strength treated the whiskers as continuous fibers. Under this assumption, the whisker and matrix carry equal strains. The bundle will yield when it is strained to such a degree that the matrix reaches its yield strain. This will occur at a bundle stress which is much higher than the matrix yield stress since the bundle is stiffer than the matrix. The lower limit on bundle strength treats the whisker as spherical inclusions. Under this assumption, the whisker and matrix carry almost equal stress. Thus, the bundle will yield at a lower limit when the bundle stress reaches the matrix stress.

Typical comparisons between the model and the composite experimental data are shown in Figs. 7 and 8. Figure 7 shows the comparison for the tensile, 25%, 10:1 material. The corresponding comparison of the model and compressive data is shown in Fig. 8. The model shows good agreement with the initial stiffness. The analytically predicted limits on strength result in an envelope which contains the post yield experimental data. The lower limit prediction compares well with the yield strength, and the upper limit compares well with the ultimate strength.

Unfortunately, although the model was expected to show strain hardening through sequential bundle yielding, the predicted results are almost elastic-perfectly plastic. The bundle directions used to represent the extrusion process are aligned strongly with the loading axis so the composite is behaving as if it were almost unidirectional. Thus, there is very little difference between the initial bundle yield stress and final bundle yield stress. In other words, in terms of the model, all material fails at approximately the same stress.

The results also show that the bundles require a strain hardening law to represent the actual material behavior. Since the matrix is almost perfectly plastic, the effective strain hardening must be due to plastic flow around the whiskers. This can only be addressed through detailed stress analysis of a whisker reinforced bundle which was not attempted here but is recommended to gain further understanding of the material behavior.

Sensitivity Study

Once the material model was developed and the analytical predictions were compared to the experimental data, the model was further exercised by parametrically varying material parameters. This was done to determine the sensitivity of the analytical predictions to the input data and to investigate potential improved material constructions. Specifically, the material model was employed to examine the anisotropy of the material; to determine the effects of extrusion ratio; and to study the effects of whisker geometry.

The effects of varying the whisker content in the materials were studied analytically by examining the behavior of random materials containing whiskers with an average aspect ratio of 2.5. The material model was utilized to predict the elastic properties and the upper limit stress-strain curves for composites containing 0.15 and 25% whisker by volume. A comparison of the predicted stress-strain curves is shown in Fig. 9. Here, again it can be seen that an increase in the whisker content significantly increases the computed stiffness and strength of the material.

The effects of extrusion ratio on the resulting material properties were studied in a similar manner. In this case, a material containing 25 volume percent whiskers with an average aspect ratio of 2.5 was analyzed. Elastic properties and upper limit stress-strain curves were predicted for extrusion ratios of 1:1 (random), 5:1 and 10:1. The predicted stress-strain curves are compared in Fig. 10. Notice that the sequential bundle failure is very evident for the random materials, but the bundles fail within the extruded material almost simultaneously. The stress-strain curves show that moderate extrusion (5:1) significantly increases the axial stiffness and strength of a random material but further extrusion (10:1) has a much less noticeable effect.

The model was also utilized to examine the effects of whisker geometry on the material behavior. Specifically, the effects of increased whisker length on the predicted stress-strain response were examined. The material studied was a randomly oriented composite with 25% whisker content by volume.

Elastic properties, strengths, and post yield properties for unidirectional whisker bundles with aspect ratios ranging from 1 to 500 were calculated. These data were utilized to predict the stress-strain response, and the results are plotted in Fig. 11. The figure indicates that the initial elastic modulus and yield point are relatively insensitive to whisker geometry. However, the post yield behavior is strongly effected by whisker geometry. The results show that at aspect ratios of 100 or less the whiskers become inactive after the matrix yields and can carry very little additional stress. However, whiskers with aspect ratios of 500 or greater continue to carry stresses after the matrix has yielded and will theoretically result in much higher material ultimates. This implies that whiskers and particles should result in relatively

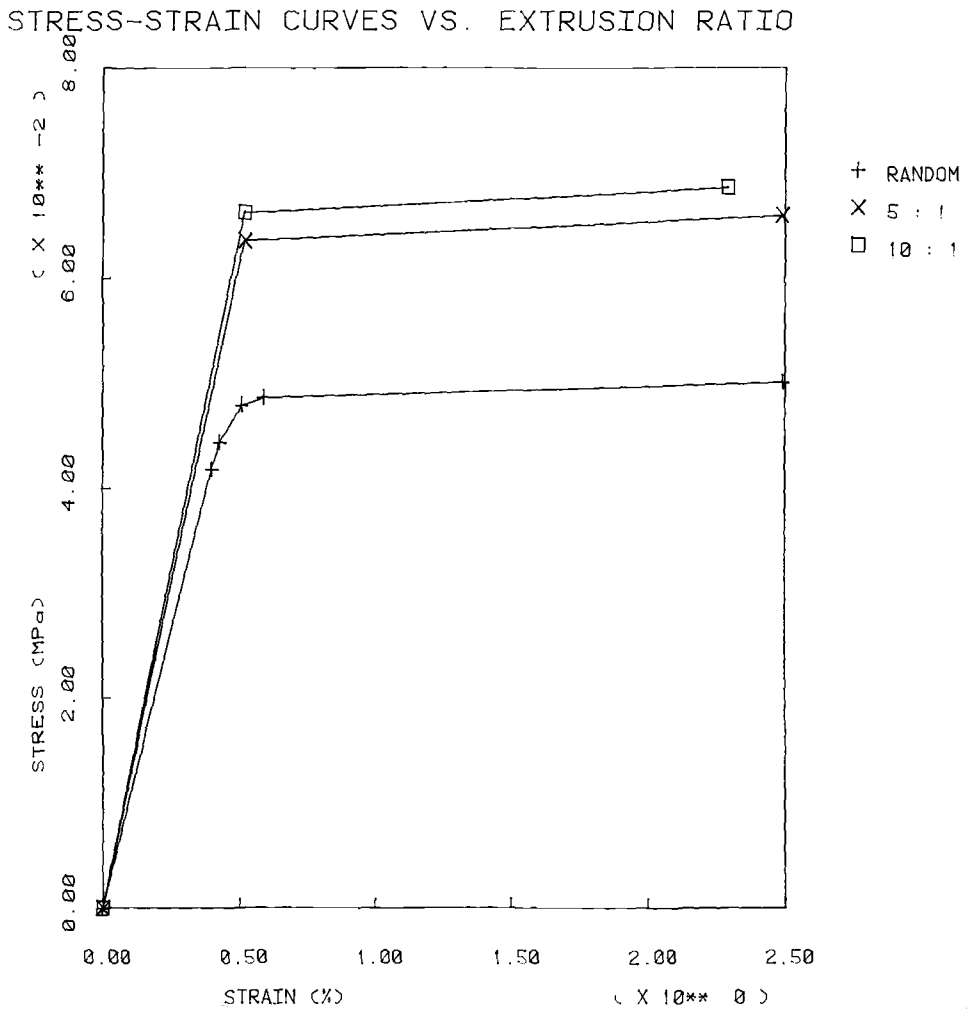

FIG. 9—*Analytically predicted stress-strain curves versus whisker content for SiC/Al materials (random,* L/D = *2.5).*

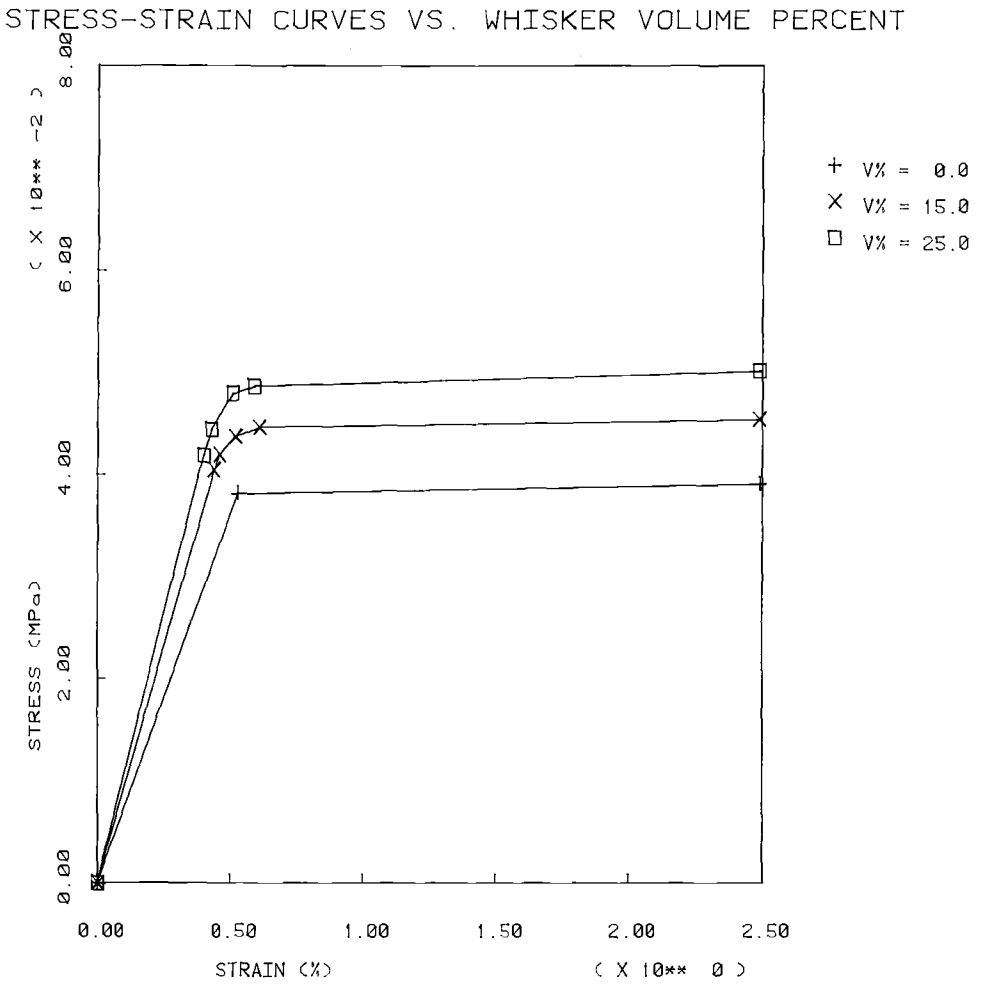

FIG. 10—*Analytically predicted stress-strain curves versus extrusion ratio for 25% SiC/Al materials* (L/D = 2.5).

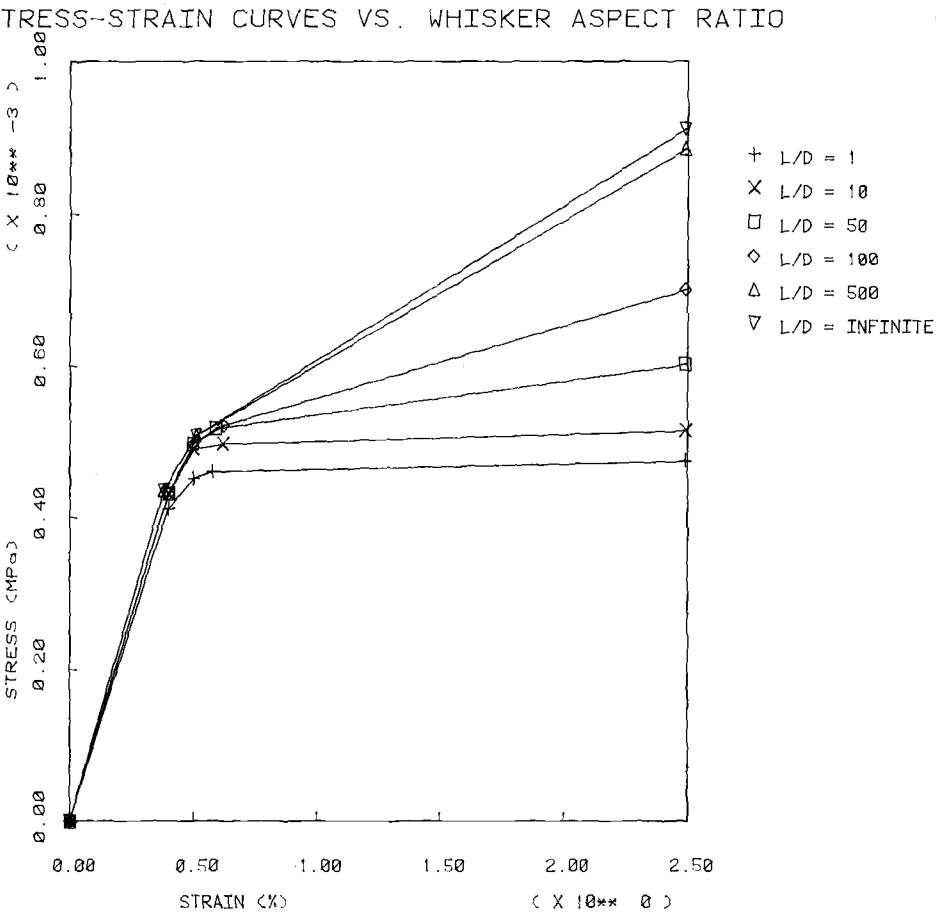

FIG. 11—Analytically predicted stress-strain curves versus whisker geometry for 25% Sic/Al material (random).

equivalent stress-strain response for typical state of the art whisker aspect ratios (1 to 10). It also appears that the material will improve dramatically only when whiskers of much higher aspect ratios (500 or greater) can be fabricated.

Conclusions

The results of this program have led to the refinement of a material model to compute the properties of a whisker reinforced metal matrix material. The model treats the material as a collection of unidirectional whisker reinforced bundles with special spatial orientations. The model has been exercised to determine that a randomly reinforced SiC/Al material can be analyzed by considering bundles in 16 directions. These directions are defined by vectors which run from the center to the vertices and face centers of a dodecahedron. A procedure has been developed to compute the whisker reorientations which occur during the extrusion process. Thus, the model is capable of predicting a stress-strain curve for SiC/Al materials as a function of whisker shape, whisker content, whisker properties, matrix properties, and extrusion ratio.

Comparisons of the material model predictions to the experimental data led to the following conclusions:

1. Comparisons of the predicted stiffnesses to the measured moduli show that the average whisker aspect ratio (l/d) is 3 for the 5:1 extruded material and 2.5 for the 10:1 extruded material. Thus, it appears that the *in situ* whiskers are very short and that the extrusion process reduces the whisker length.
2. The computed lower limit strength compares well with the measured yield strength and the computed upper limit strength compares well with the measured ultimate strength. The strain hardening measured for the composites is not a result of sequential bundle failure. It may be due to growth in the matrix plastic zone near the whiskers.

The results of a parametric sensitivity study have shown that:

1. The analytical model can be employed to compute realistic anisotropic properties for extruded SiC/Al materials. Increases in whisker volume fraction significantly increase the analytically predicted stiffness and strength. The calculated stress-strain curves are significantly altered by moderate extrusion (5:1). The effects of further extrusion (10:1) are much less significant.
2. Preliminary investigations of the effects of whisker geometry show that the post yield material behavior will be improved significantly only when whisker aspect ratios are of the order of 500 to 1. Typical whisker geometries (l/d ranging from 1 to 10) will behave very much like particles.

Acknowledgment

The authors wish to thank Drs. S. Fishman, C. Crowe, and J. Tydings of the Naval Surface Weapons Center (NSWC) for serving as technical monitors on this program. This work was supported by NSWC under Contract Number N60921-82-C-0133.

References

[1] Christensen, R. M. "Mechanics of Composite Materials," John Wiley & Sons, New York, 1979, pp. 89-99.
[2] Johnson, W. and Mellor, P. B., *Engineering Plasticity,* Van Nostrand Rheinhold, London, 1973, pp. 76-78.
[3] Rosen, B. W. and Shu, L. S., "On Some Symmetry Conditions for Three-Dimensional Fibrous Composites," *Journal of Composite Materials,* April 1971, p. 279.
[4] Dow, N. F., "Directions for 3-D Composite Reinforcement I. Intimations of Isotropy," Proceedings of 21st AIAA/ASME Structures, Structural Dynamics and Materials Conference, May 1980, pp. 318-323.
[5] Goering, J., Awerbuch, ., and Buesking, K., "Minimechanics Analysis and Testing of Short Fiber Composites," prepared for NSWC, MSC TFR 1401/1412, Materials Sciences Corporation, Spring House, PA, May 1983.
[6] "Engineering Property Data on Selected Ceramics, Vol. 2, Carbides," MCIC-HB-07, Vol. II, Battelle Laboratories, Columbus, OH, Aug. 1979.

APPENDIX A

The effective tangent stiffness of the RVE is defined as the matrix which relates an increment in composite strain to an increment in composite stress

$$\Delta\bar{\sigma} = C^* \Delta\bar{\epsilon} \tag{1}$$

where $\Delta\bar{\sigma}$ and $\Delta\bar{\epsilon}$ are stress and strain increments, respectively, C^* is the effective tangent stiffness, and overbar denote average values.

The average stress increment may be found by volume averaging the stress increment in each bundle due to a strain increment applied to the RVE

$$\Delta\bar{\sigma} = \sum_{i=1}^{n} v_i \Delta\bar{\sigma}_i \tag{2}$$

where $\Delta\bar{\sigma}_i$ is the stress increment in the i^{th} bundle and v_i is the volume fraction of bundle i in the RVE.

Since each bundle experiences the same strain increment, the stress increment in the i^{th} bundle is given by

$$\Delta\sigma_i = C_i \Delta\bar{\epsilon} \tag{3}$$

where C_i is the effective tangent stiffness of the i^{th} bundle. Substituting 3 into 2 gives

$$\Delta\bar{\sigma} = \left(\sum_{i=1}^{n} v_i C_i\right) \Delta\bar{\epsilon} \tag{4}$$

Equation 4 may now be cast in the form of 1 by defining

$$C^* = \sum_{i=1}^{n} v_i C_i \tag{5}$$

Inverting 1 and substituting into 3 then gives the increment in stress in the i^{th} bundle due to an increment is stress applied to the RVE

$$\Delta\sigma_i = C_i S^* \Delta\bar{\sigma} \tag{6}$$

where

$$S^* = C^{*-1} \tag{7}$$

The total stress in the i^{th} bundle after n global stress increments is then found using 6

$$\sigma_i^n = \sum_{j=1}^{n} C_i^j S_j^* \Delta\bar{\sigma}_j \tag{8}$$

where the stress dependent properties used to calculate the stiffness C_i^j and compliance S_j^* are determined from the total stress at the $(j-1)^{th}$ step.

Dale A. Hopkins[1] *and Christos C. Chamis*[1]

A Unique Set of Micromechanics Equations for High-Temperature Metal Matrix Composites

REFERENCE: Hopkins, D. A. and Chamis, C. C., "**A Unique Set of Micromechanics Equations for High-Temperature Metal Matrix Composites,**" *Testing Technology of Metal Matrix Composites, ASTM STP 964,* P. R. DiGiovanni and N. R. Adsit, Eds., American Society for Testing and Materials, Philadelphia, 1988, pp. 159–176.

ABSTRACT: A unique set of micromechanics equations is presented for high-temperature metal matrix composites. The set includes expressions to predict mechanical properties, thermal properties, and constituent microstresses for the unidirectional fiber reinforced ply. The equations are derived based on a mechanics of materials formulation assuming a square array unit cell model of a single fiber, surrounding matrix, and an interphase to account for the chemical reaction which commonly occurs between fiber and matrix. A preliminary validation of the equations was performed using three-dimensional finite element analysis. The results demonstrate excellent agreement between properties predicted using the micromechanics equations and properties simulated by the finite element analyses. Implementation of the micromechanics equations as part of an integrated computational capability for nonlinear structural analysis of high-temperature multilayered fiber composites is illustrated.

KEY WORDS: metal matrix composites, composite micromechanics, mechanical properties, thermal properties, uniaxial strengths, microstresses

The mechanical performance and structural integrity of fiber reinforced metal matrix composites are ultimately governed by the behavior of the constituent materials at a micromechanistic level. In general, the individual constituents behave quite differently relative to one another. Moreover, behavior of the constituents is dynamic, particularly in high-temperature applications, due to the various nonlinearities associated with, for example, (1) large local stress excursions, (2) temperature-dependent material properties, (3) time-dependent effects, and (4) constituent chemical reaction.

In the structural analysis of metal matrix composites, then, it is important to be able to describe and track this micromechanistic constituent behavior. Available methods for this purpose are limited. For example, techniques such as finite element analysis in principle, can be applied directly with the constituents modeled discretely. It becomes obvious, however, that for complex structures the resources (manpower and computer) necessary to define, conduct, and interpret such an analysis are prohibitive. Another approach is to employ composite micromechanics theory and derive simplified relationships which describe the three-dimensional anisotropic behavior of the simple composite (for example, unidirectional ply). The latter approach has been taken as part of a comprehensive research program to develop effective computational mechanics methodologies for high-temperature multilayered fiber composite structures.

[1] Aerospace structures engineer and senior research engineer, National Aeronautics and Space Administration, Lewis Research Center, Cleveland, OH 44135.

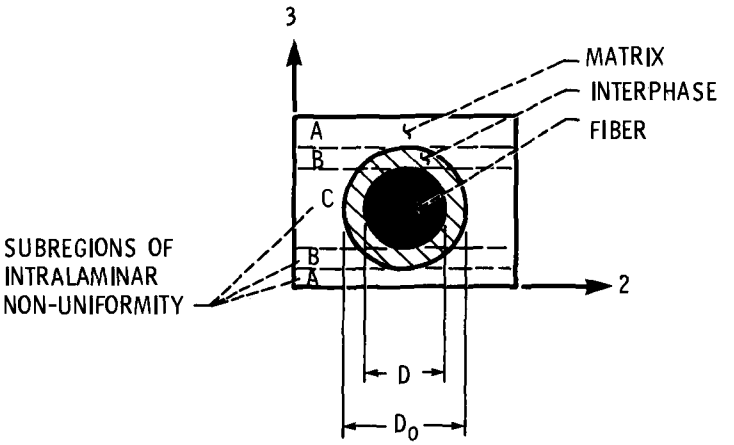

FIG. 1—*Micromechanics model; square array unit cell.*

As an essential part of the previously mentioned program, a unique set of micromechanics equations has been derived for high-temperature metal matrix composites. The set comprises closed-form expressions to predict equivalent "pseudo homogeneous" properties for the unidirectional fiber reinforced ply, including: (1) mechanical properties—moduli, Poisson's ratios, and uniaxial strengths; (2) thermal properties—conductivities, coefficients of expansion, and heat capacity; and (3) constituent microstresses.

The micromechanics equations presented here are derived based on a mechanics of materials formulation assuming a square array unit cell model of a single fiber, surrounding matrix and an interphase to account for the chemical reaction which commonly occurs between fiber and matrix. The basis of the formulation is summarized as part of the discussion next.

Concurrent with the derivation of equations, a study was conducted using three-dimensional finite element analysis. The purpose of the study was to assess the validity of the mechanics of materials formulation, in general, and to investigate the accuracy of the micromechanics equations for a specific composite material system. Results from this study are presented also as part of the discussion which follows.

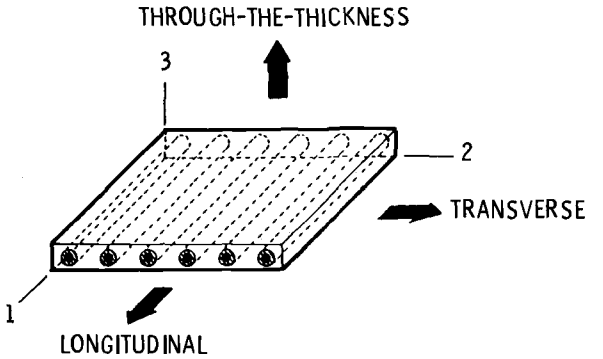

FIG. 2—*Unidirectional composite (ply) material coordinate system.*

Finally, a demonstration of the utility of this unique set of micromechanics equations is provided by illustrating their use as part of an integrated computational capability for the nonlinear structural analysis of high-temperature multilayered fiber composites. A few typical results are presented from the stress analysis of a hypothetical tungsten fiber reinforced superalloy turbine airfoil.

Composite Micromechanics Theory

Composite micromechanics theory refers to the collection of physical principles, mathematical models, assumptions, and approximations employed to relate the behavior of a simple composite unit (for example, lamina or ply) to the behavior of its individual con-

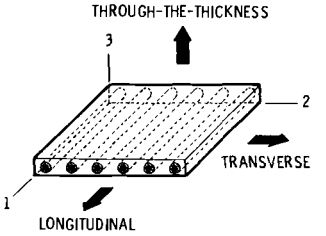

$$E_{\ell 11} = k_m E_{m11} + k_f \left\{ \left[1 - \left(\frac{D}{D_o} \right)^2 \right] E_{d11} + \left(\frac{D}{D_o} \right)^2 E_{f11} \right\}$$

$$E_{\ell 22} = E_{m22} \left\{ \left(1 - \sqrt{k_f} \right) + \frac{\sqrt{k_f} \left(1 - \frac{D}{D_o} \right)}{1 - \sqrt{k_f} \left(1 - \frac{E_{m22}}{E_{d22}} \right)} + \frac{\sqrt{k_f} \left(\frac{D}{D_o} \right)}{1 - \sqrt{k_f} \left[1 - \left(1 - \frac{D}{D_o} \right) \frac{E_{m22}}{E_{d22}} - \left(\frac{D}{D_o} \right) \frac{E_{m22}}{E_{f22}} \right]} \right\} = E_{\ell 33}$$

$$G_{\ell 12} = G_{m12} \left\{ \left(1 - \sqrt{k_f} \right) + \frac{\sqrt{k_f} \left(1 - \frac{D}{D_o} \right)}{1 - \sqrt{k_f} \left(1 - \frac{G_{m12}}{G_{d12}} \right)} + \frac{\sqrt{k_f} \left(\frac{D}{D_o} \right)}{1 - \sqrt{k_f} \left[1 - \left(1 - \frac{D}{D_o} \right) \frac{G_{m12}}{G_{d12}} - \left(\frac{D}{D_o} \right) \frac{G_{m12}}{G_{f12}} \right]} \right\} = G_{\ell 13}$$

$$G_{\ell 23} = G_{m23} \left\{ \left(1 - \sqrt{k_f} \right) + \frac{\sqrt{k_f} \left(1 - \frac{D}{D_o} \right)}{1 - \sqrt{k_f} \left(1 - \frac{G_{m23}}{G_{d23}} \right)} + \frac{\sqrt{k_f} \left(\frac{D}{D_o} \right)}{1 - \sqrt{k_f} \left[1 - \left(1 - \frac{D}{D_o} \right) \frac{G_{m23}}{G_{d23}} - \left(\frac{D}{D_o} \right) \frac{G_{m23}}{G_{f23}} \right]} \right\}$$

$$\upsilon_{\ell 12} = k_m \upsilon_{m12} + k_f \left\{ \left[1 - \left(\frac{D}{D_o} \right)^2 \right] \upsilon_{d12} + \left(\frac{D}{D_o} \right)^2 \upsilon_{f12} \right\} = \upsilon_{\ell 13}$$

$$\upsilon_{\ell 23} = \frac{E_{\ell 22}}{2 G_{\ell 23}} - 1$$

FIG. 3—*Micromechanics equations; ply mechanical properties.*

stituents. For example, a variety of approaches have been used in the past to predict equivalent thermoelastic material properties of unidirectional fiber composites [*1–6*]. More recently, simple equations have been derived [*7,8*] to predict mechanical, thermal, and strength properties for resin matrix composites using a mechanics of materials formulation. A similar approach was taken to derive the set of micromechanics equations presented here for high-temperature metal matrix composites.

The formal procedure of composite micromechanics theory relies on the principles of solid mechanics, thermodynamics, etc., at different levels of mathematical sophistication, together with certain assumptions (consistent with the physical situation) and approximations. In the approach taken here, application is made of the principles of displacement compatibility and force equilibrium as defined in elementary mechanics-of-materials theory and Fourier's law for heat conduction from thermodynamics. In addition, the assumptions

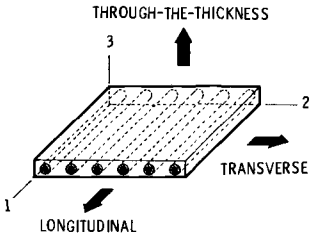

$$C_\ell = k_m\left(\frac{\rho_m}{\rho_\ell}\right)C_m + k_f\left\{\left[1-\left(\frac{D}{D_0}\right)^2\right]\left(\frac{\rho_d}{\rho_\ell}\right)C_d + \left(\frac{D}{D_0}\right)^2\left(\frac{\rho_f}{\rho_\ell}\right)C_f\right\}$$

$$K_{\ell 11} = k_m K_{m11} + k_f\left\{\left[1-\left(\frac{D}{D_0}\right)^2\right]K_{d11} + \left(\frac{D}{D_0}\right)^2 K_{f11}\right\}$$

$$K_{\ell 22} = K_{m22}\left\{\left(1-\sqrt{k_f}\right) + \frac{\sqrt{k_f}\left(1-\frac{D}{D_0}\right)}{1-\sqrt{k_f}\left(1-\frac{K_{m22}}{K_{d22}}\right)} + \frac{\sqrt{k_f}\left(\frac{D}{D_0}\right)}{1-\sqrt{k_f}\left[1-\left(1-\frac{D}{D_0}\right)\frac{K_{m22}}{K_{d22}}-\left(\frac{D}{D_0}\right)\frac{K_{m22}}{K_{22}}\right]}\right\} = K_{\ell 33}$$

$$\alpha_{\ell 11} = k_m\left(\frac{E_{m11}}{E_{\ell 11}}\right)\alpha_{m11} + k_f\left\{\left[1-\left(\frac{D}{D_0}\right)^2\right]\left(\frac{E_{d11}}{E_{\ell 11}}\right)\alpha_{d11} + \left(\frac{D}{D_0}\right)^2\left(\frac{E_{f11}}{E_{\ell 11}}\right)\alpha_{f11}\right\}$$

$$\alpha_{\ell 22} = \frac{E_{m22}}{E_{\ell 22}}\left\{\left(1-\sqrt{k_f}\right)\alpha_{m22} + \frac{\left(1-\frac{D}{D_0}\right)\left[\left(1-\sqrt{k_f}\right)\alpha_{m22}+\sqrt{k_f}\,\alpha_{d22}\right]}{1-\sqrt{k_f}\left(1-\frac{E_{m22}}{E_{d22}}\right)}\right.$$

$$\left. + \frac{\sqrt{k_f}\,\alpha_{m22} - k_f\left[\alpha_{m22}-\left(1-\frac{D}{D_0}\right)\alpha_{d22}-\left(\frac{D}{D_0}\right)\alpha_{f22}\right]}{1-\sqrt{k_f}\left[1-\left(1-\frac{D}{D_0}\right)\frac{E_{m22}}{E_{d22}}-\left(\frac{D}{D_0}\right)\frac{E_{m22}}{E_{f22}}\right]}\right\} = \alpha_{\ell 33}$$

FIG. 4—*Micromechanics equations; ply thermal properties.*

are made that: (1) fibers are continuous and parallel, (2) properties of all fibers are identical, and (3) complete bonding exists between constituents. No restrictions need be placed on the constitutive behavior or isotropy of the individual constituent materials. For generality, constituent material behavior can be taken as thermoviscoplastic, anisotropic, and three-dimensional. It is implied by this that the individual constituent material histories can be tracked independently as a function of time and represented as an instantaneous stress/strain state.

The periodic structure of a unidirectional metal matrix composite (ply) is approximated here by a square array unit cell model. The geometry of the model is illustrated in Fig. 1. It should be noted that the interphase growth is assumed to result from the degradation of fiber material and thus propagates inward causing a continuous decrease of the current (intact) fiber diameter (D) from the original (virgin) fiber diameter (D_0). With the existence of the interphase, three subregions (A, B, C) are distinguished to characterize the intra-

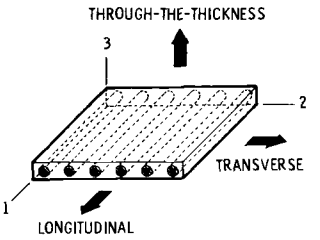

$$S_{\ell 11T} = S_{f11T}\left\{k_m\left(\frac{E_{m11}}{E_{f11}}\right) + k_f\left[\left(\frac{D}{D_0}\right)^2 + \left\{1 - \left(\frac{D}{D_0}\right)^2\right\}\frac{E_{d11}}{E_{f11}}\right]\right\}$$

$$S_{\ell 11C} = \text{MIN.}\begin{cases} S_{f11C}\left\{k_m\left(\frac{E_{m11}}{E_{f11}}\right) + k_f\left[\left(\frac{D}{D_0}\right)^2 + \left\{1 - \left(\frac{D}{D_0}\right)^2\right\}\frac{E_{d11}}{E_{f11}}\right]\right\} \\ S_{m11C}\left\{k_m + k_f\left[\left(\frac{D}{D_0}\right)^2\frac{E_{f11}}{E_{m11}} + \left\{1 - \left(\frac{D}{D_0}\right)^2\right\}\frac{E_{d11}}{E_{m11}}\right]\right\} \\ G_{m12}\left\{\frac{1}{k_m + k_f\left[\left(\frac{D}{D_0}\right)^2\frac{G_{m12}}{G_{f12}} + \left\{1 - \left(\frac{D}{D_0}\right)^2\right\}\frac{G_{m12}}{G_{d12}}\right]}\right\} \\ S_{m11C} + S_{\ell 12} \end{cases}$$

FIG. 5—*Micromechanics equations; ply uniaxial strengths, longitudinal.*

laminar (through-the-thickness) nonuniformity of the constituent (matrix and interphase) microstresses and material properties.

The definition of ply properties is with respect to the ply material coordinate system which is depicted in Fig. 2. The common terminology associated with each of the coordinate axis directions is also illustrated on the ply schematic. The micromechanics equations presented here are derived for the special case of a transversely isotropic (isotropic in the 2–3 plane) ply allowing for transversely isotropic constituents.

Composite Micromechanics Equations

The micromechanics equations to predict ply equivalent mechanical properties are summarized in Fig. 3. Included are expressions for normal (extensional) moduli ($E_{\ell 1}$, $E_{\ell 22}$), shear moduli ($G_{\ell 12}$, $G_{\ell 23}$), and Poisson's ratios ($\nu_{\ell 12}$, $\nu_{\ell 23}$). In the expressions k represents constituent original volume fraction (values prior to any interphase growth) and the subscripts f, m, d, and ℓ denote fiber, matrix, interphase, and ply quantity, respectively. The volume fraction of interphase is expressed in terms of the fiber original volume fraction and the virgin and intact (*in situ*) fiber diameters.

The equations for moduli are derived with modulus taken in the general context as simply

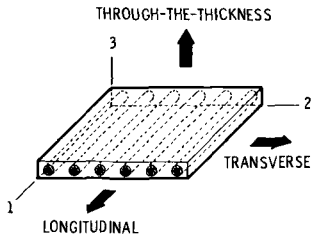

$$S_{\ell 22T,\,C} = \frac{S_{m22T,\,C}}{\left\{1 - \sqrt{k_f}\left[1 - \left(1 - \frac{D}{D_o}\right)\frac{E_{m22}}{E_{d22}} - \left(\frac{D}{D_o}\right)\frac{E_{m22}}{E_{f22}}\right]\right\}\left[1 + \Phi(\Phi - 1) + 1/3(\Phi - 1)^2\right]^{1/2}}$$

WHERE;

$$\Phi = \frac{1}{\sqrt{\frac{\pi}{4k_f}} - 1}\left\{\sqrt{\frac{\pi}{4k_f}} - \frac{\left(\frac{E_{m22}}{E_{f22}}\right)}{1 - \sqrt{k_f}\left[1 - \left(1 - \frac{D}{D_o}\right)\frac{E_{m22}}{E_{d22}} - \left(\frac{D}{D_o}\right)\frac{E_{m22}}{E_{f22}}\right]}\right\}$$

LOWER BOUND;

$$S_{\ell 22T,\,C} = \left(1 - \sqrt{\frac{4k_f}{\pi}}\right)S_{m22T,\,C}$$

EQUATIONS FOR INTRALAMINAR SHEAR STRENGTH ($S_{\ell 12}$) ARE ANALOGOUS TO ABOVE EQUATIONS WITH E AND $S_{m22T,\,C}$ REPLACED BY G AND S_{m12}, RESPECTIVELY

FIG. 6—*Micromechanics equations; ply uniaxial strengths, transverse and shear.*

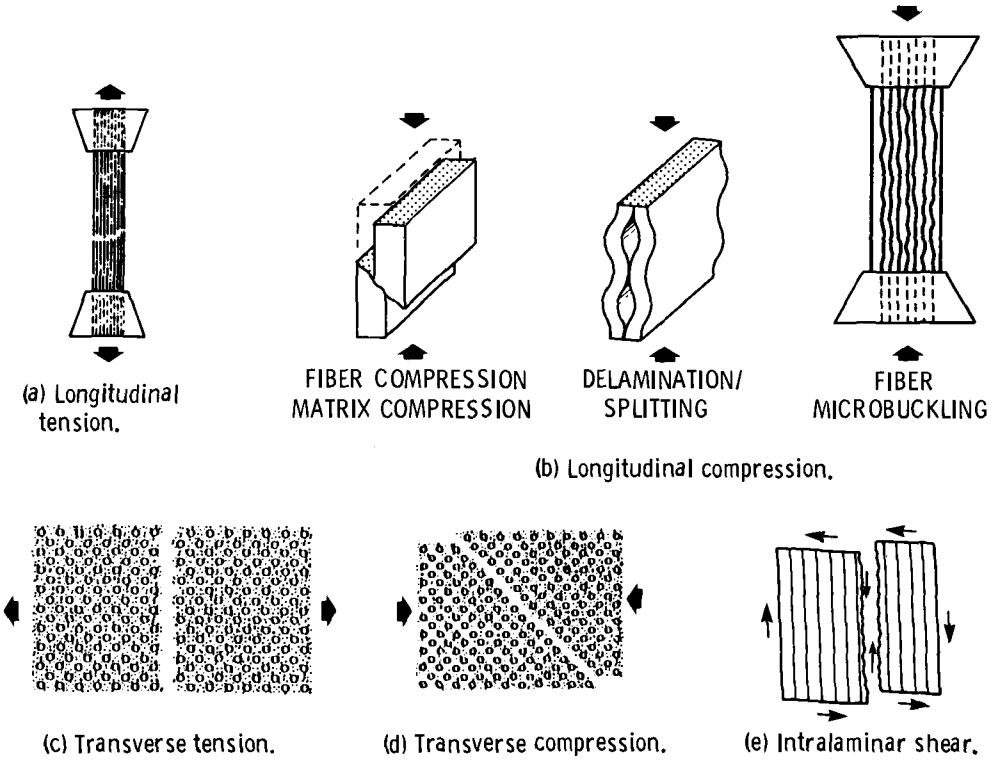

FIG. 7—*In-plane failure modes for unidirectional ply.*

the derivative of stress with respect to strain. As such, the expressions are applicable to the prediction of instantaneous or tangent moduli as well as elastic moduli. It should be noted that the expressions for transverse moduli do not account for the longitudinal Poisson restraining effect that the fiber imparts on the matrix. The restrained matrix effect is considered here to be negligible for metal matrix composites. The effect is generally more significant in resin matrix composites, for example, where the fiber/matrix relative stiffness ratio is much greater.

The ply equivalent thermal properties are predicted by the micromechanics equations summarized in Fig. 4. Included are expressions for heat capacity (C_i), thermal conductivities (K_{d1}, K_{d2}), and thermal expansion coefficients (α_{d1}, α_{d2}). In the expression for heat capacity the symbol ρ represents density.

The ply in-plane uniaxial strengths are predicted by the micromechanics equations summarized in Figs. 5 and 6. Included are expressions for tensile strength (S_{d1T}, S_{d2T}), compressive strength (S_{d1C}, S_{d2C}), and intralaminar shear strength (S_{d2S}). Each of the ply strengths is associated with a specific failure mode, as illustrated by the schematics in Fig. 7. In the case of longitudinal compressive strength, four different failure modes are considered. The four expressions in Fig. 5 for S_{d1C} correspond, respectively, to the four failure modes as follows; fiber compression mode, matrix compression mode, delamination/splitting mode, and fiber microbuckling mode. A more comprehensive treatment of micromechanics strength theories is given by Chamis [*9*].

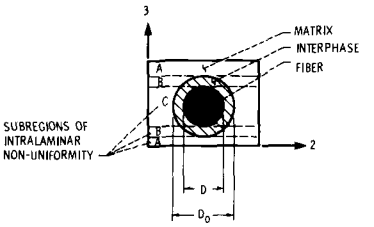

$$\sigma_{f11} = \left[\frac{\sigma_{\ell 11}}{E_{\ell 11}} + \Delta T\,(\alpha_{\ell 11} - \alpha_{f11})\right] E_{f11}$$

$$\sigma_{f22} = \frac{E_{f22}\left\{\frac{\sigma_{\ell 22}}{E_{\ell 22}} + \Delta T\left[\alpha_{\ell 22} - (1 - \sqrt{k_f})\,\alpha_{m22}^{(C)} - \sqrt{k_f}\left(1 - \frac{D}{D_0}\right)\alpha_{d22}^{(C)} - \sqrt{k_f}\left(\frac{D}{D_0}\right)\alpha_{f22}\right]\right\}}{1 - \sqrt{k_f}\left[1 - \left(1 - \frac{D}{D_0}\right)\frac{E_{m22}}{E_{d22}} - \left(\frac{D}{D_0}\right)\frac{E_{m22}}{E_{f22}}\right]}$$

$$\sigma_{f12} = \frac{\left(\frac{\sigma_{\ell 12}}{G_{\ell 12}}\right) G_{f12}}{1 - \sqrt{k_f}\left[1 - \left(1 - \frac{D}{D_0}\right)\frac{G_{m12}}{G_{d12}} - \left(\frac{D}{D_0}\right)\frac{G_{m12}}{G_{f12}}\right]}$$

EQUATION FOR σ_{f23} IS ANALOGOUS TO EQUATION FOR σ_{f12}

FIG. 8—*Micromechanics equations; fiber microstresses.*

The expressions to predict the thermomechanical microstress distribution in the ply constituents are summarized in Figs. 8 to 10. Included are expressions for fiber microstresses (σ_{f11}, σ_{f22}, σ_{f12}, σ_{f23}) interphase microstresses (σ_{d11}, $\sigma_{d22}^{B,C}$, $\sigma_{d12}^{B,C}$, $\sigma_{d23}^{B,C}$) and matrix microstresses (σ_{m11}, $\sigma_{m22}^{A,B,C}$, $\sigma_{m12}^{A,B,C}$, $\sigma_{m23}^{A,B,C}$). In the expressions ΔT represents an incremental change in temperature and the superscripts A, B, and C denote the intralaminar subregions illustrated in the accompanying schematics. It should be noted that these expressions for constituent microstresses are based on uniaxial behavior, that is, they do not incorporate any Poisson contributions.

The systematic procedure for deriving the micromechanics equations summarized previously is explicitly demonstrated in the Appendix with the derivations for normal moduli (E_{t11} and E_{t22}). Derivations of the other equations are omitted here solely for the sake of brevity. The selection of E_{t11} and E_{t22} for demonstration purposes was based on the authors' judgment that their derivations are sufficiently representative to adequately demonstrate the formal procedure.

Micromechanics/Finite Element Validation

In order to investigate the validity of the mechanics of materials formulation and assess the accuracy of the equations derived therefrom, a preliminary study was conducted using three-dimensional finite element analysis. The objective of the study was to compare the equivalent ply properties (E_{t11}, E_{t22}, G_{t12}, G_{t23}, ν_{t12}, ν_{t23}, α_{t11}, α_{t22}) predicted by the micromechanics equations with the average "pseudo homogeneous" ply properties simulated in the finite element analyses.

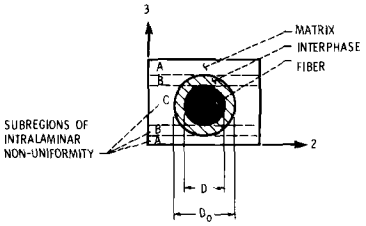

$$\sigma_{d11} = \left[\frac{\sigma_{\ell 11}}{E_{\ell 11}} + \Delta T\,(\alpha_{\ell 11} - \alpha_{d11})\right] E_{d11}$$

$$\sigma^{(B)}_{d22} = \frac{E^{(B)}_{d22}\left\{\frac{\sigma_{\ell 22}}{E_{\ell 22}} + \Delta T\left[\alpha_{\ell 22} - (1-\sqrt{k_f})\,\alpha^{(B)}_{m22} - \sqrt{k_f}\,\alpha^{(B)}_{d22}\right]\right\}}{1-\sqrt{k_f}\left(1-\frac{E_{m22}}{E_{d22}}\right)}$$

$$\sigma^{(C)}_{d22} = \frac{E^{(C)}_{d22}\left\{\frac{\sigma_{\ell 22}}{E_{\ell 22}} + \Delta T\left[\alpha_{\ell 22} - (1-\sqrt{k_f})\,\alpha^{(C)}_{m22} - \sqrt{k_f}\left(1-\frac{D}{D_o}\right)\alpha^{(C)}_{d22} - \sqrt{k_f}\left(\frac{D}{D_o}\right)\alpha_{f22}\right]\right\}}{1-\sqrt{k_f}\left[1-\left(1-\frac{D}{D_o}\right)\frac{E_{m22}}{E_{d22}} - \left(\frac{D}{D_o}\right)\frac{E_{m22}}{E_{f22}}\right]}$$

$$\sigma^{(B)}_{d12} = \frac{\left(\frac{\sigma_{\ell 12}}{G_{\ell 12}}\right)G^{(B)}_{d12}}{1-\sqrt{k_f}\left(1-\frac{G_{m12}}{G_{d12}}\right)}$$

$$\sigma^{(C)}_{d12} = \frac{\left(\frac{\sigma_{\ell 12}}{G_{\ell 12}}\right)G^{(C)}_{d12}}{1-\sqrt{k_f}\left[1-\left(1-\frac{D}{D_o}\right)\frac{G_{m12}}{G_{d12}} - \left(\frac{D}{D_o}\right)\frac{G_{m12}}{G_{f12}}\right]}$$

EQUATIONS FOR $\sigma^{(B,C)}_{d23}$ ARE ANALOGOUS TO EQUATIONS FOR $\sigma^{(B,C)}_{d12}$

FIG. 9—*Micromechanics equations; interphase microstresses.*

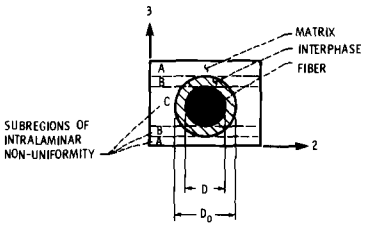

$$\sigma_{m11} = \left[\frac{\sigma_{\ell 11}}{E_{\ell 11}} + \Delta T\,(\alpha_{\ell 11} - \alpha_{m11})\right] E_{m11}$$

$$\sigma^{(A)}_{m22} = \left[\frac{\sigma_{\ell 22}}{E_{\ell 22}} + \Delta T\left(\alpha_{\ell 22} - \alpha^{(A)}_{m22}\right)\right] E^{(A)}_{m22}$$

$$\sigma^{(B)}_{m22} = \frac{E^{(B)}_{m22}\left\{\frac{\sigma_{\ell 22}}{E_{\ell 22}} + \Delta T\left[\alpha_{\ell 22} - (1-\sqrt{k_f})\,\alpha^{(B)}_{m22} - \sqrt{k_f}\,\alpha^{(B)}_{d22}\right]\right\}}{1-\sqrt{k_f}\left(1-\frac{E_{m22}}{E_{d22}}\right)}$$

$$\sigma^{(C)}_{m22} = \frac{E^{(C)}_{m22}\left\{\frac{\sigma_{\ell 22}}{E_{\ell 22}} + \Delta T\left[\alpha_{\ell 22} - (1-\sqrt{k_f})\,\alpha^{(C)}_{m22} - \sqrt{k_f}\left(1-\frac{D}{D_0}\right)\alpha^{(C)}_{d22} - \sqrt{k_f}\left(\frac{D}{D_0}\right)\alpha_{f22}\right]\right\}}{1-\sqrt{k_f}\left[1-\left(1-\frac{D}{D_0}\right)\frac{E_{m22}}{E_{d22}} - \left(\frac{D}{D_0}\right)\frac{E_{m22}}{E_{f22}}\right]}$$

$$\sigma^{(A)}_{m12} = \left(\frac{\sigma_{\ell 12}}{G_{\ell 12}}\right) G^{(A)}_{m12}$$

$$\sigma^{(B)}_{m12} = \frac{\left(\frac{\sigma_{\ell 12}}{G_{\ell 12}}\right) G^{(B)}_{m12}}{1-\sqrt{k_f}\left(1-\frac{G_{m12}}{G_{d12}}\right)}$$

$$\sigma^{(C)}_{m12} = \frac{\left(\frac{\sigma_{\ell 12}}{G_{\ell 12}}\right) G^{(C)}_{m12}}{1-\sqrt{k_f}\left[1-\left(1-\frac{D}{D_0}\right)\frac{G_{m12}}{G_{d12}} - \left(\frac{D}{D_0}\right)\frac{G_{m12}}{G_{f12}}\right]}$$

EQUATIONS FOR $\sigma^{(A,B,C)}_{m23}$ ARE ANALOGOUS TO EQUATIONS FOR $\sigma^{(A,B,C)}_{m12}$

FIG. 10—*Micromechanics equations; matrix microstresses.*

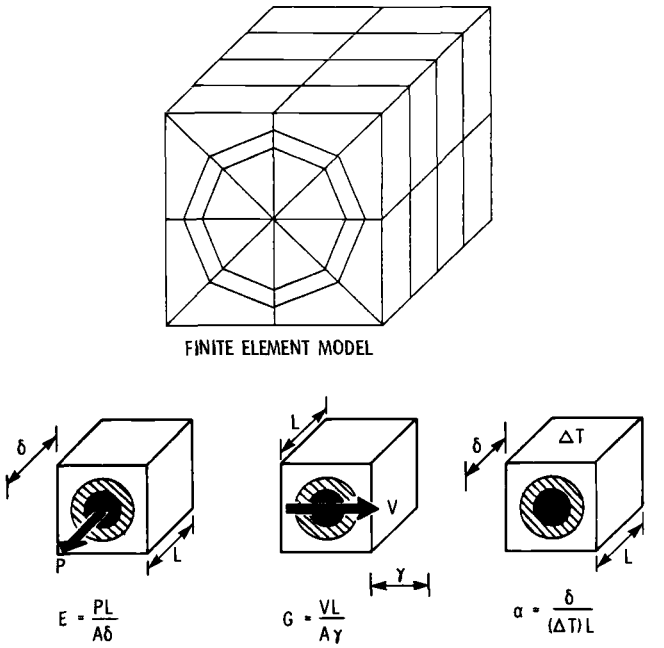

FIG. 11—*Micromechanics/finite element validation; finite element model and simple mechanics of materials expressions for idealized deformation modes.*

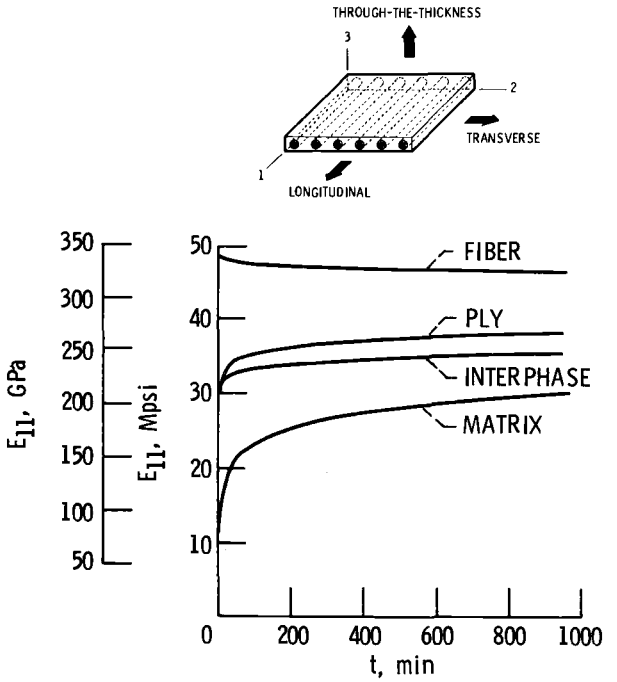

FIG. 12—*Fabrication cool-down transient; variation of* E_{11} *for constituents and ply.*

TABLE 1—*Micromechanics/finite element validation; comparison of property predictions/simulations.*

Property	P_{MEQ}/P_{FEM}
E_{f1}	1.00
$E_{\rho 22}$	1.01
G_{f12}	0.96
G_{f23}	0.98
ν_{f12}	1.00
ν_{f23}	1.08
α_{f11}	0.99
α_{f22}	1.15

NOTE—P_{MEQ} = property predicted by micromechanics equation.
P_{FEM} = property simulated by finite element analysis.

To conduct the analyses, a discrete model of the square array unit cell was constructed, as shown in Fig. 11, from isoparametric solid finite elements. The composite material system assumed for this study involved a thoriated tungsten (W-1.5ThO_2) fiber embedded in an iron-base superalloy (Fe-25Cr-4Al-1Y) matrix. Properties for the interphase were taken to be a simple average of the fiber and matrix properties.

The analyses entailed simulations of idealized modes of deformation such as simple elongation, pure shear, and unconstrained thermal expansion. These were achieved through the judicious application of the loading/boundary conditions on the model. The appropriate simple expressions from elementary mechanics of materials theory (see Fig. 11) were then applied in conjunction with the nodal displacement/force results of the finite element analyses to compute the simulated average properties of the discrete model as a "pseudo homogeneous" unit.

Results of the study are summarized in Table 1 which gives the ratios of property values determined from the micromechanics equations (P_{MEQ}) and by finite element simulation (P_{FEM}). As can be seen, excellent agreement was achieved overall. These results indicate that the mechanics of materials formulation is an effective approach to the micromechanical modeling of metal matrix composites. It is recognized, however, that additional investigation, both analytical and experimental, would be prudent before any final conclusions are made regarding the specific accuracy of these micromechanics equations.

Application of Micromechanics Equations

The primary impetus in deriving the set of micromechanics equations presented here was for implementation as part of an integrated computational capability for the nonlinear analysis of high-temperature multilayered fiber composites [*10*]. This particular utilization of the equations is demonstrated here with a few typical results taken from the nonlinear (quasi-static) stress analysis of a hypothetical turbine blade (airfoil only) model. The incremental/iterative analysis was conducted to investigate the thermally induced residual stresses developed during the cool-down transient of a typical fabrication process.

The airfoil is a hollow thin shell structure of constant thickness with walls comprising a four-ply $[\pm 45]_s$ laminate based on W-1.5ThO_2 fiber reinforced Fe-25Cr-4Al-1Y at a fiber volume fraction of 0.50. Since the purpose here is merely to illustrate the types of information provided by the micromechanics equations in this particular implementation, further details of the airfoil model and analysis are omitted.

Two examples of ply mechanical property predictions are given in Figs. 12 and 13 which show the variation during the cool-down transient of constituent and ply longitudinal and

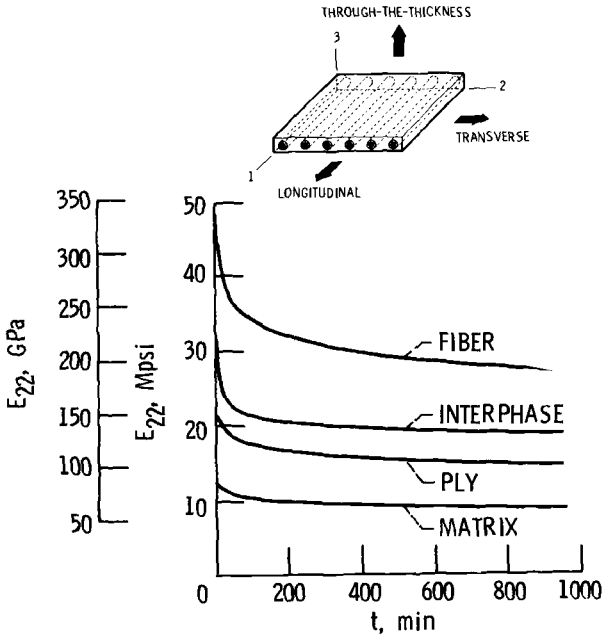

FIG. 13—*Fabrication cool-down transient; variation of* E_{22} *for constituents and ply.*

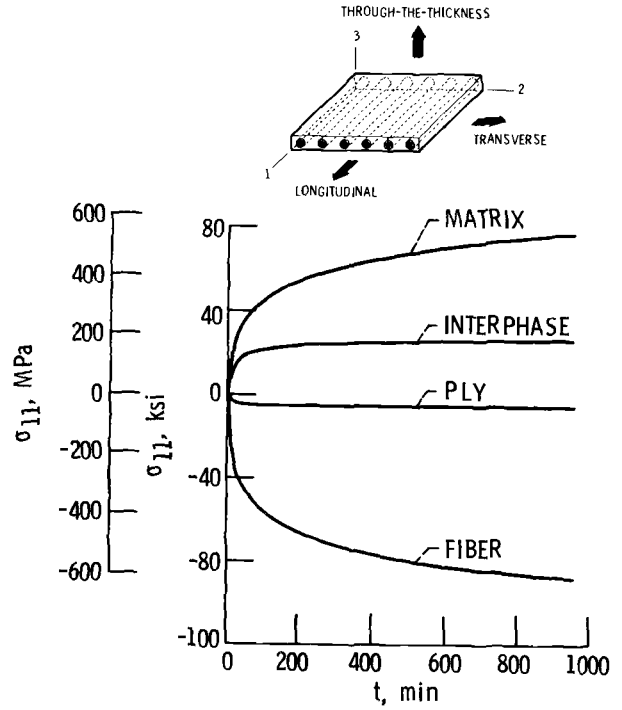

FIG. 14—*Fabrication cool-down transient; induced residual stress* (σ_{11}) *for ply and constituents.*

transverse moduli, respectively. The ply moduli are computed from the corresponding micromechanics equations. The results in Fig. 12 reflect the rule-of-mixtures relationship expressed by the equation for $E_{\sigma 11}$ while the results in Fig. 13 illustrate the dominance of the matrix modulus on the value for $E_{\sigma 22}$.

The development of residual stresses during the cool-down transient is illustrated in Figs. 14 and 15. The results are for the longitudinal and transverse normal components, respectively, of ply stress and constituent microstresses. The microstresses are computed from the corresponding micromechanics equations. The points to be noted from these results are the relative magnitudes and sense (tensile or compressive) of the constituent microstresses. In Fig. 14, for example, the opposite sense of the fiber and matrix microstresses results from the difference in thermal expansion coefficients between the two materials. The results in Fig. 15 illustrate the significant through-the-thickness nonuniformity of the matrix and interphase microstresses, as characterized in the different intralaminar subregions (A, B, C).

From just the few examples given, the utility of the micromechanics equations becomes more apparent. Considering the results of microstress distribution, for example, it becomes intuitively more clear how material failures might occur at a local level and prompt the initiation of a flaw. This type of information provides an insight into the behavior of composites at a micromechanistic level which undoubtedly influences their performance and integrity in a structural application.

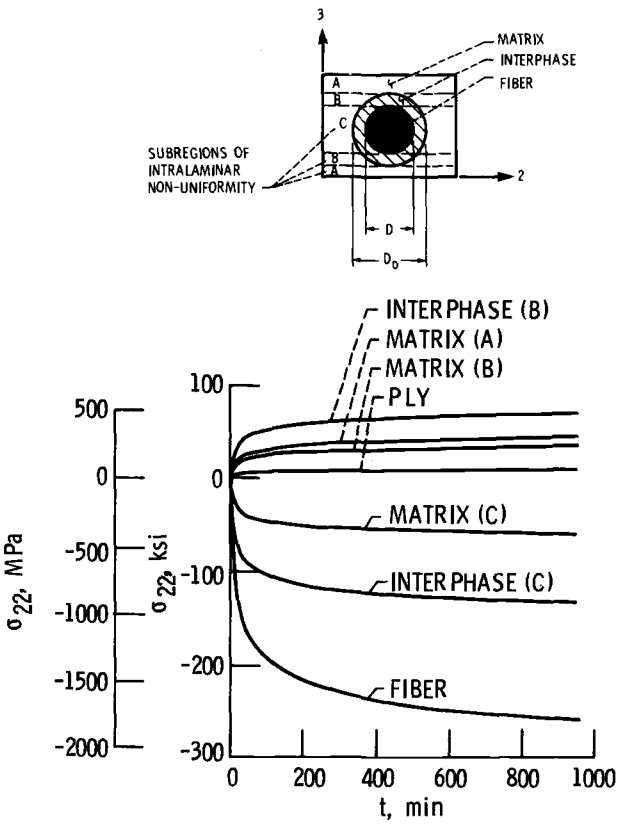

FIG. 15—*Fabrication cool-down transient; induced residual stress* (σ_{22}) *for ply and constituents.*

Summary

The set of micromechanics equations presented here for high-temperature metal matrix composites includes expressions to predict the mechanical properties, thermal properties, and constituent microstress distribution for a unidirectional fiber reinforced ply. The equations incorporate an interphase region at the fiber/matrix boundary in order to account for the chemical reaction which commonly occurs in high-temperature applications of these composites. The basis of the mechanics of materials formulation from which the equations are derived is described. The formulation is shown to be a valid and effective approach to micromechanical modeling of metal matrix composites, supported by the favorable results achieved in a comparison with three-dimensional finite element analysis. The utility of the micromechanics equations as part of an integrated composite structural analysis capability is illustrated with examples taken from the nonlinear stress analysis of a turbine airfoil. The results demonstrate the ability to describe and track behavior at a micromechanistic level which impacts the performance and integrity of these composites in structural applications.

APPENDIX

In order to demonstrate the formal procedure involved in the application of composite micromechanics theory, derivations of the equations for ply normal moduli (E_{t11} and E_{t22}) are explicitly developed next. The particular approach taken here relies on the principles of force equilibrium and displacement compatibility as defined from elementary mechanics-of-materials theory.

Longitudinal Normal Modulus

Consider the square array unit cell model (see Fig. 1) subjected to a uniaxial load in the longitudinal direction (see Fig. 2). The equivalent composite (ply) load is defined from force equilibrium to be the sum of the constituent loads as follows

$$P_t = P_f + P_d + P_m \tag{1}$$

In the integrated average sense, Eq. 1 is rewritten as

$$\sigma_t A_t = \sigma_f A_f + \sigma_d A_d + \sigma_m A_m \tag{2}$$

where A represents cross-sectional area. Dividing through by A_t and noting that because of a common longitudinal dimension the resulting area ratios are equivalent to actual volume fractions, Eq 2 reduces to

$$\sigma_t = \sigma_f k'_f + \sigma_d k'_d + \sigma_m k'_m \tag{3}$$

Because compatibility of longitudinal displacement requires equal strains for the composite and constituents ($\epsilon_t = \epsilon_f = \epsilon_d = \epsilon_m$), Eq 3 can be differentiated with respect to strain to give

$$\left(\frac{d\sigma_t}{d\epsilon}\right) = \left(\frac{d\sigma_f}{d\epsilon}\right) k'_f + \left(\frac{d\sigma_d}{d\epsilon}\right) k'_d + \left(\frac{d\sigma_m}{d\epsilon}\right) k'_m \tag{4}$$

The quantities $(d\sigma/d\epsilon)$ represent the slopes of the corresponding stress-strain curves for the composite and constituents and in this context define instantaneous or "tangent" moduli. Hence, Eq 4 becomes

$$E_t = E_f k'_f + E_d k'_d + E_m k'_m \tag{5}$$

Expressing actual volume fractions in terms of original fiber and matrix volume fractions (before interphase growth) and original and intact fiber diameters, Eq 5 is rewritten as

$$E_t = k_f \left\{ \left(\frac{D}{D_0}\right)^2 E_f + \left[1 - \left(\frac{D}{D_0}\right)^2\right] E_d \right\} + k_m E_m \tag{6}$$

Equation 6 is the desired form and is the same as that given in Fig. 3.

Transverse Normal Modulus

Consider the square array unit cell model again except that the fiber and interphase are of equivalent square cross section such that linear dimensions (in the plane of cross section) can be defined as follows

$$a_f = \left(\frac{\pi}{4}\right)^{1/2} D, \; a_d = \left(\frac{\pi}{4}\right)^{1/2} D_0, \; a_t = \left(\frac{\pi}{4k_f}\right)^{1/2} D_0 \tag{7}$$

and

$$s_f = a_f, \; s_d = a_d - a_f, \qquad s_m = a_t - a_d, \; s_t = a_t \tag{8}$$

Assume a uniaxial load in the transverse direction and neglect Poisson effects. For subregion C displacement compatibility yields

$$s_t \epsilon_t = s_f \epsilon_f + s_d \epsilon_d + s_m \epsilon_m \tag{9}$$

and force equilibrium results in equal stresses for the composite and constituents ($\sigma_t = \sigma_f = \sigma_d = \sigma_m$). Hence, Eq 9 can be differentiated with respect to stress to give

$$\left(\frac{d\epsilon_t}{d\sigma}\right) s_t = \left(\frac{d\epsilon_f}{d\sigma}\right) s_f + \left(\frac{d\epsilon_d}{d\sigma}\right) s_d + \left(\frac{d\epsilon_m}{d\sigma}\right) s_m \tag{10}$$

The quantities $(d\epsilon/d\sigma)$ represent reciprocals of the slopes of the corresponding stress-strain curves for the composite and constituents and in the same context as before define reciprocals of instantaneous or "tangent" moduli. Hence, with some rearranging Eq 10 becomes

$$E_t^C = \frac{E_m}{\left[\left(\frac{s_m}{s_t}\right) + \left(\frac{s_d}{s_t}\right)\left(\frac{E_m}{E_d}\right) + \left(\frac{s_f}{s_t}\right)\left(\frac{E_m}{E_f}\right)\right]} \tag{11}$$

Substituting the definitions in Eqs 7 and 8 into Eq 11 and rearranging gives

$$E_t^C = \frac{E_m}{\left\{1 - \sqrt{k_f}\left[1 - \left(1 - \frac{D}{D_0}\right)\left(\frac{E_m}{E_d}\right) - \left(\frac{D}{D_0}\right)\left(\frac{E_m}{E_f}\right)\right]\right\}} \tag{12}$$

which defines an equivalent modulus for subregion C. The equivalent modulus for subregion

B is deduced from Eq 12 by letting D/D_0 equal zero. The result is

$$E_t^B = \frac{E_m}{\left\{1 - \sqrt{k_f}\left[1 - \left(\frac{E_m}{E_d}\right)\right]\right\}} \tag{13}$$

The equivalent modulus for subregion A is simply the matrix modulus or

$$E_t^A = E_m \tag{14}$$

The ply transverse modulus (E_{t22}), then, is defined by assuming that subregions A, B, and C act as parallel elements when subjected to a transverse load. This is analogous to the case for E_{t11} where the constituents are assumed to act in parallel. Hence, from Eq 5 it is deduced that

$$E_t s_t = E_t^C s_f + E_t^B s_d + E_t^A s_m \tag{15}$$

Dividing through by s_t, substituting the definitions from Eqs 7 and 8 and the results from Eqs 12 through 14, and rearranging gives

$$E_t = E_m \left\{ (1 - k_f) + \frac{\sqrt{k_f}\left[1 - \left(\frac{D}{D_0}\right)\right]}{1 - \sqrt{k_f}\left[1 - \left(\frac{E_m}{E_d}\right)\right]} + \frac{\sqrt{k_f}\left(\frac{D}{D_0}\right)}{1 - \sqrt{k_f}\left[1 - \left(1 - \frac{D}{D_0}\right)\left(\frac{E_m}{E_d}\right) - \left(\frac{D}{D_0}\right)\left(\frac{E_m}{E_f}\right)\right]} \right\} \tag{16}$$

Equation 16 is the desired form and is the same as that given in Fig. 3.

References

[1] Chamis, C. C. and Sendeckyj, G. P., *Journal of Composite Materials*, Vol. 2, No. 3, July 1968, pp. 332–358.

[2] Ekvall, J. C., "Elastic Properties of Orthotropic Monofilament Laminates," ASME Paper 61-AV-56, ASME Aviation Conference, Los Angeles, CA, 1961.

[3] Abolin'sh, D. S., *Polymer Mechanics*, Vol. 1, No. 4, July-Aug. 1965, pp. 28–32.

[4] Springer, G. S. and Tsai, S. W., *Journal of Composite Materials*, Vol. 1, No. 2, April 1967, pp. 166–173.

[5] Agarwal, B. D. and Broutman, L. J., *Analysis and Performance of Fiber Composites*, Wiley, New York, 1980.

[6] Halpin, J. C., *Primer on Composite Materials: Analysis*, 1st ed. revised, Technomic, Lancaster, PA, 1984.

[7] Chamis, C. C., *SAMPE Quarterly*, Society for the Advancement of Materials and Process Engineers, Vol. 15, No. 3, April 1984, pp. 14–23.

[8] Chamis, C. C., *SAMPE Quarterly*, Society for the Advancement of Materials and Process Engineers, Vol. 15, No. 4, July 1984, pp. 41–55.

[9] Chamis, C. C., in *Fracture and Fatigue*, L. J. Broutman, Ed., Academic Press, New York, 1974, pp. 94–148.

[10] Hopkins, D. A., "Nonlinear Analysis for High Temperature Multilayered Fiber Composite Structures," NASA TM-83754, National Aeronautics and Space Administration, Washington, DC, 1984.

DISCUSSION

Muzaffer Sutcu[1] (*written discussion*)—(1) Does your unit cell finite element allow relative slippage between the fiber and the matrix? (2) Is the tensile strain of the fiber and the matrix the same?

D. A. Hopkins and C. C. Chamis (*authors' closure*)—(1) In the finite element model of the square array unit cell, no special provisions are made to directly allow relative slippage between fiber and matrix (such as the use of duplicate nodes to relax continuity or the use of gap elements). However, the existence of incomplete bonding could be simulated by assigning essentially "zero" stiffness properties to one or more of the elements representing the interphase zone. (2) In the theoretical development of the micromechanics equations the assumption is made that complete bonding exists between fiber and matrix. Enforcing displacement compatibility in the *longitudinal* (parallel to the fiber) direction, then, results in equal strains for the constituents and ply.

[1] General Electric R&D, Schenectady, NY, 2301.

Christos C. Chamis[1] *and Dale A. Hopkins*[1]

Thermoviscoplastic Nonlinear Constitutive Relationships for Structural Analysis of High-Temperature Metal Matrix Composites

REFERENCE: Chamis, C. C. and Hopkins, D. A., **"Thermoviscoplastic Nonlinear Constitutive Relationships for Structural Analysis of High-Temperature Metal Matrix Composites,"** *Testing Technology of Metal Matrix Composites, ASTM STP 964,* P. R. DiGiovanni and N. R. Adsit, Eds., American Society for Testing and Materials, Philadelphia, 1988, pp. 177–196.

ABSTRACT: A set of thermoviscoplastic nonlinear constitutive relationships (TVP-NCR) is presented. This set is unique and has been developed mainly for application to high-temperature metal matrix composites (HT-MMC) and is applicable to thermal and mechanical properties. Formulation of the TVP-NCR is based at the micromechanics level. The TVP-NCR are of simple form and readily integrated into nonlinear composite structural analysis. Results show that this unique set of TVP-NCR is computationally effective. It provides a direct means for predicting complex materials behavior at all levels of the composite simulation; that is, from the constituent materials, through the several levels of composite mechanics, and up to the global response of complex HT-MMC structural components.

KEY WORDS: metal matrix composites, thermal properties, mechanical properties, thermoviscoplastic behavior, nonlinear composites

High temperature metal matrix composites (HT-MMC) are emerging as materials with potentially high payoffs in structural applications. Realization of these payoffs depends on the parallel and synergistic development of (1) a technology base for fabricating HT-MMC structures and components, (2) experimental techniques for measuring their thermal and mechanical characteristics, and (3) computational methodologies for predicting their nonlinear thermoviscoplastic (TVP) behavior in complex service environments. In fact, development of computational methodologies should precede the other two because the structural integrity and durability of HT-MMC can be numerically assessed, and the potential payoff for the specific application can be closely estimated. In this way, it is possible to minimize the costly and time consuming experimental effort that would otherwise be required in the absence of a predictive capability.

Recent research at the National Aeronautics and Space Administration (NASA), Lewis Research Center is directed towards the development of a computational capability to predict the nonlinear TVP behavior of HT-MMC. This capability is schematically depicted in Fig. 1. As can be seen in this figure, the capability consists of several computational modules encompassing the material TVP behavior (bottom), composite mechanics (sides), and the finite element analysis of structural components (top). The TVP computational module

[1] Senior research engineer, Aerospace Structures/Composites, and aerospace structures engineer, National Aeronautics and Space Administration, Lewis Research Center, Cleveland, OH 44135.

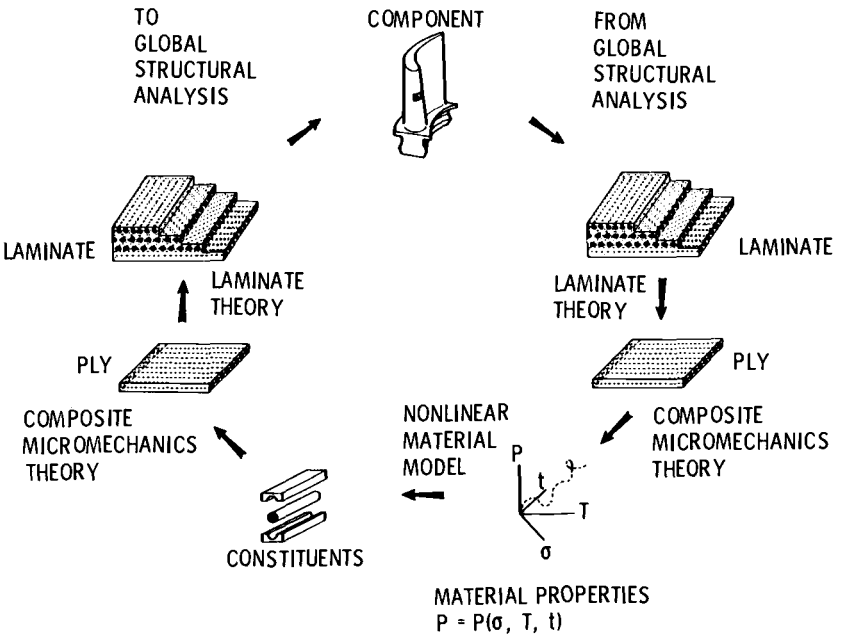

FIG. 1—*Integrated nonlinear composite structural analysis.*

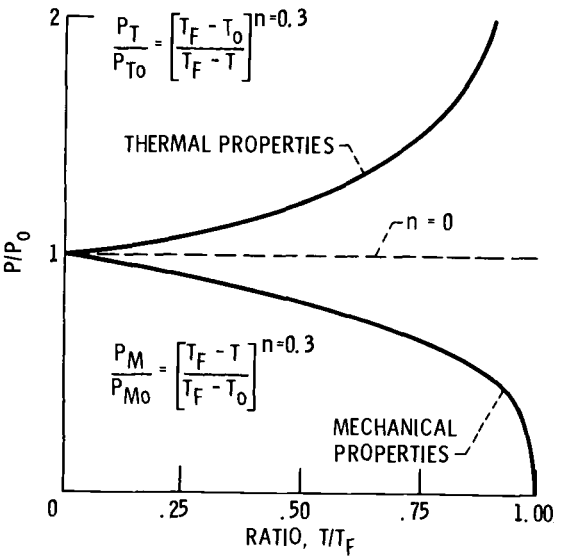

FIG. 2—*Thermoviscoplastic nonlinear constitutive relationships—typical behavior for a given exponent.*

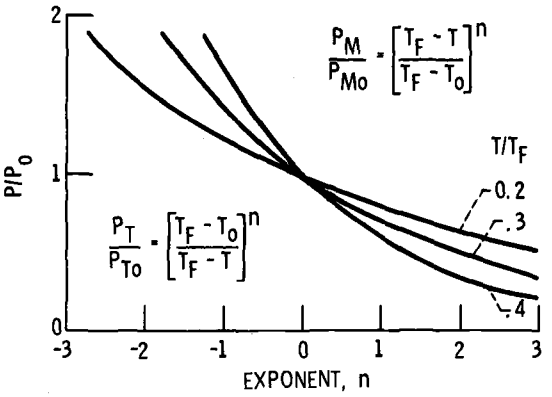

FIG. 3—*Thermoviscoplastic nonlinear constitutive relationships typical behavior for given* T/T_F *ratio.*

consists of mathematical models which formally and explicitly relate the dependence of the constituent material properties on (1) temperature, (2) stress, and (3) time. These mathematical models are collectively called thermoviscoplastic nonlinear constitutive relationships (TVP-NCR). The objective of this report is to present the TVP-NCR developed as a part of the computational capability for HT-MMC structures.

The TVP-NCR to be described were developed with an emphasis on computational effectiveness and are unique in their following features: (1) generic form—they are applicable to all constituent material properties (thermal, mechanical, including strength), (2) evolutionary—they are easily extended/modified to accommodate additional effects such as strain rate and material degradation, (3) isomorphic—they have similar structure for all the properties, (4) unified—they are fully coupled at both the increment and cumulative levels, (5) universal—they are applicable to any of the three constituent materials (fibers, matrix, and the interphase), and (6) nondimensional—they are normalized with respect to initial, reference, and ultimate states.

This unique set of TVP-NCR consists of products of terms with unknown exponents. The exponents are determined for the specific material and type of nonlinear dependence. For

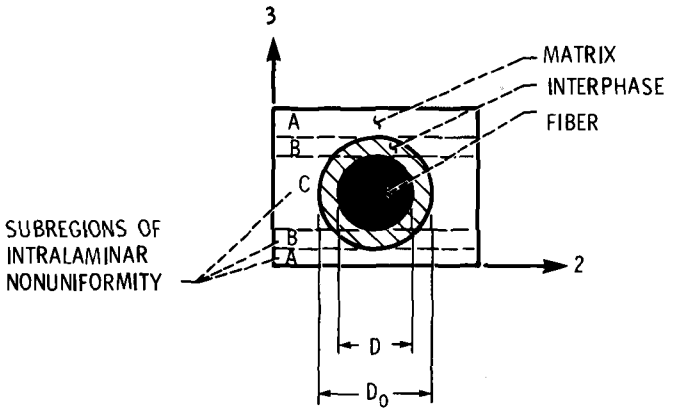

FIG. 4—*Typical interconstituent regions for composite micromechanics.*

example, three product terms are required in one TVP-NCR equation to account for: (1) temperature dependence, (2) stress level, and (3) stress rate. Three exponents need to be determined to completely describe this equation. These exponents are determined from available experimental data or estimated from anticipated behavior of the particular product term.

The computational effectiveness of this unique set of TVP-NCR is evaluated using the computational capability depicted schematically in Fig. 1. The structural response of a turbine blade, made from fiber reinforced superalloy HT-MMC and subject to representative mission loading conditions, is determined. The effectiveness of the TVP-NCR to represent the physical behavior of the material is computationally assessed by perturbing the exponents and comparing the structural response of the blade to the unperturbed case.

Equation Form/Features

The generic form selected for the TVP-NCR for the constituents of HT-MMC is as follows:

1. Mechanical property (moduli, strength) P_M

$$\frac{P_M}{P_{Mo}} = \left[\frac{T_M - T}{T_M - T_o}\right]^n \left[\frac{S_F - \sigma}{S_F - \sigma_o}\right]^m \left[\frac{\dot{S}_F - \dot{\sigma}_o}{\dot{S}_F - \dot{\sigma}}\right]^l \tag{1}$$

2. Thermal property (expansion coefficients, thermal conductivity, heat capacity) P_T

$$\frac{P_T}{P_{To}} = \left[\frac{T_M - T_o}{T_M - T}\right]^n \left[\frac{S_F - \sigma_o}{S_F - \sigma}\right]^m \left[\frac{\dot{S}_F - \dot{\sigma}}{\dot{S}_F - \dot{\sigma}_o}\right]^l \tag{2}$$

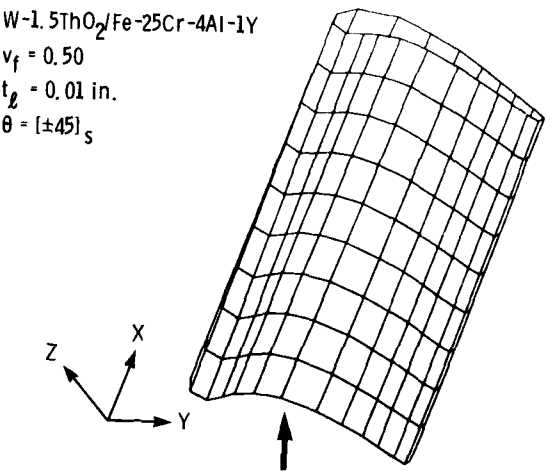

FIG. 5—*Finite-element model for hollow turbine blade airfoil of high-temperature metal matrix composite.*

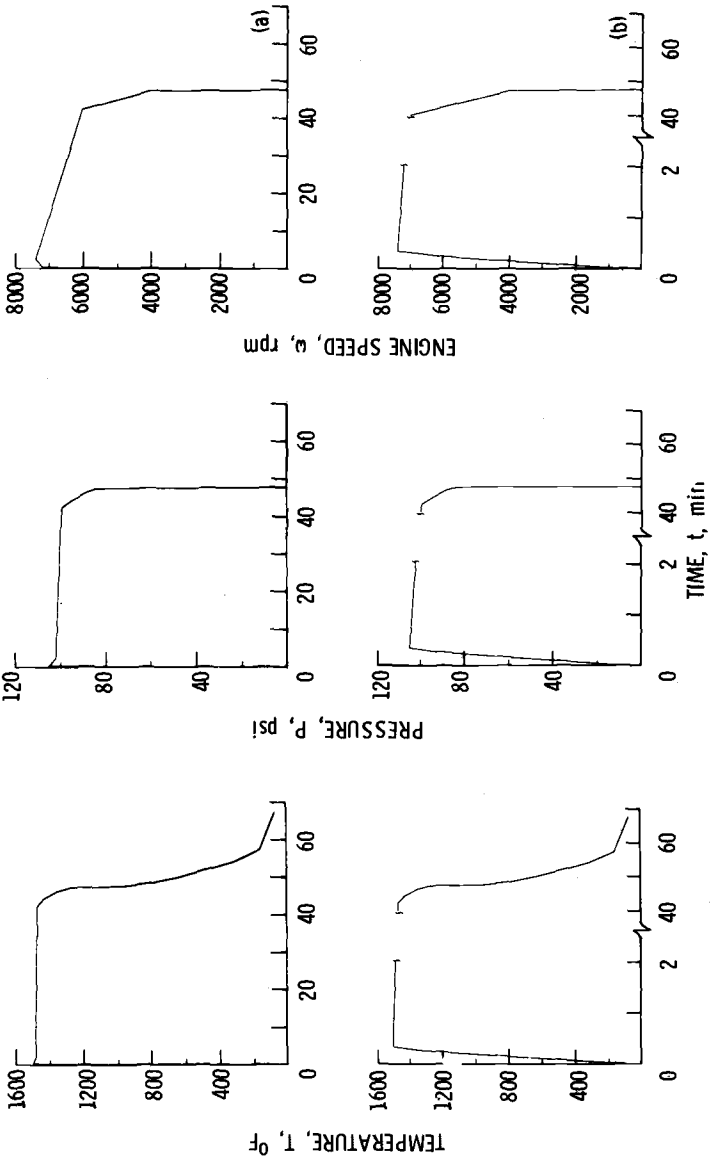

FIG. 6—*Flight mission profile for turbine blade structural analysis. Node 6; Ply 4.*

TABLE 1—*Exponent perturbation effects on structural response.*

Case	Constituent	Property	Change	Exponent			Structural Response						Percent Frequency and Cruise/Residual
							Cruise Conditions			Residual			
				N	M	L	Displacement	Unt't	Frequency	Displacement	Unt't	Frequency	
1	Fiber	P_M	R	0.3	0.6	0.1	0.015	−0.22	3650	0.00016	−0.04	4380	0/0
		P_T	R	0.6	0.1	0.05							
	Matrix	P_M	R	0.8	2.8	0.1							
		P_T	R	0.2	0.1	0.05							
2	Fiber	P_M	R	0.3	0.6	0.1	0.015	−0.16	3840	0.00016	−0.03	4550	+5/+4
		P_T	R	0.6	0.1	0.05							
	Matrix	P_M	I	0.4	2.0	0.1							
		P_T	D	0.1	0.05	0.05							
3	Fiber	P_M	R	0.3	0.6	0.1	0.017	−0.31	4230	0.00012	−0.05	4650	+16/+6
		P_T	R	0.6	0.1	0.05							
	Matrix	P_M	D	1.2	4.0	0.1							
		P_T	I	0.6	0.2	0.05							
4	Fiber	P_M	I	0.1	0.2	0.1	0.014	−0.20	3470	0.00010	−0.04	4370	−5/~
		P_T	D	0.2	0.05	0.05							

	Matrix	P_M	R	0.8	2.8	0.1							
		P_T	R	0.2	0.1	0.05							
5	Fiber	P_M	D	0.5	1.0	0.1	0.016	−0.23	4050	0.00020	−0.02	4540	+11/+4
		P_T	I	1.0	0.2	0.05							
	Matrix	P_M	R	0.8	2.8	0.1							
		P_T	R	0.2	0.1	0.05							
6	Fiber	P_M	I	0.1	0.2	0.1	0.015	−0.29	3660	0.00021	−0.06	4580	~/+6
		P_T	D	0.2	0.05	0.05							
	Matrix	P_M	D	1.2	4.0	0.1							
		P_T	I	0.6	0.2	0.05							
7	Fiber	P_M	D	0.5	1.0	0.1	0.016	−0.17	4040	0.00018	−0.02	4350	+11/+6
		P_T	I	1.0	0.2	0.05							
	Matrix	P_M	I	0.4	2.0	0.1							
		P_T	D	0.1	0.05	0.05							

NOTES:
P_M = mechanical properties.
P_I = thermal properties.
R = reference.
I = increase.
D = decrease.
Units: Displacement, inches; Unt't, degree; frequency, hertz.

TABLE 2—*Exponent perturbation effects on ply stresses.*

Case	Constituent	Property	Change	Exponent			Ply Stresses: Cruise Conditions			Ply Stresses: Residual			Percent $\Delta\sigma l_{11}$ and Cruise/Residual
				N	M	L	σl_{11}	σl_{22}	σl_{12}	σl_{11}	σl_{22}	σl_{12}	
1	Fiber	P_M	R	0.3	0.6	0.1	29.2	8.4	−13.7	0.4	−0.6	~	0
		P_T	R	0.6	0.1	0.05							
	Matrix	P_M	R	0.8	2.8	0.1							
		P_T	R	0.2	0.1	0.05							
2	Fiber	P_M	R	0.3	0.6	0.1	27.6	10.2	−13.6	0.5	−0.4	~	−5
		P_T	R	0.6	0.1	0.05							
	Matrix	P_M	I	0.4	2.0	0.1							
		P_T	D	0.1	0.05	0.05							
3	Fiber	P_M	R	0.3	0.6	0.1	32.1	6.0	−13.7	0.5	−0.7	~	+10
		P_T	R	0.6	0.1	0.05							
	Matrix	P_M	D	1.2	4.0	0.1							
		P_T	I	0.6	0.2	0.05							
4	Fiber	P_M	I	0.1	0.2	0.1	30.8	7.1	−13.9	1.9	−1.8	~	+5
		P_T	D	0.2	0.05	0.05							

	Matrix	P_M	R	0.8	2.8	0.1							
		P_T	R	0.2	0.1	0.05							
5	Fiber	P_M	D	0.5	1.0	0.1	33.2	10.4	−16.1	5.2	−1.4	−2.8	+14
		P_T	I	1.0	0.2	0.05							
	Matrix	P_M	R	0.8	2.8	0.1							
		P_T	R	0.2	0.1	0.05							
6	Fiber	P_M	I	0.1	0.2	0.1	33.7	4.5	−13.7	1.4	−1.4	−0.2	+15
		P_T	D	0.2	0.05	0.05							
	Matrix	P_M	D	1.2	4.0	0.1							
		P_T	I	0.6	0.2	0.05							
7	Fiber	P_M	D	0.5	1.0	0.1	26.7	11.1	−13.7	0.1	~	−0.2	−9
		P_T	I	1.0	0.2	0.05							
	Matrix	P_M	I	0.4	2.0	0.1							
		P_T	D	0.1	0.05	0.05							

NOTES:
P_M = mechanical properties.
P_I = thermal properties.
R = reference.
I = increase.
D = decrease.

The notation used in Eqs 1 and 2 is as follows:

$p_{M,T}$ = denotes the current property of interest
P_o = corresponding property at reference conditions,
T_M = melting temperature,
T = current temperature,
T_o = reference temperature at which P_o is determined,
S_F = fracture stress determined at T_o conditions,
σ_o = reference stress at which P_o is determined,
$\dot{S}_F$ = an appropriately selected stress rate, for example, the stress rate at which penetration occurs during impact,
σ_o = stress rate at which P_o is determined, and
σ = current stress rate.

The exponents n, m, and l are empirical parameters which are determined from available experimental data or estimated from the anticipated behavior of the particular product term.

The first term on the right side of Eq 1 represents the temperature dependence, the second

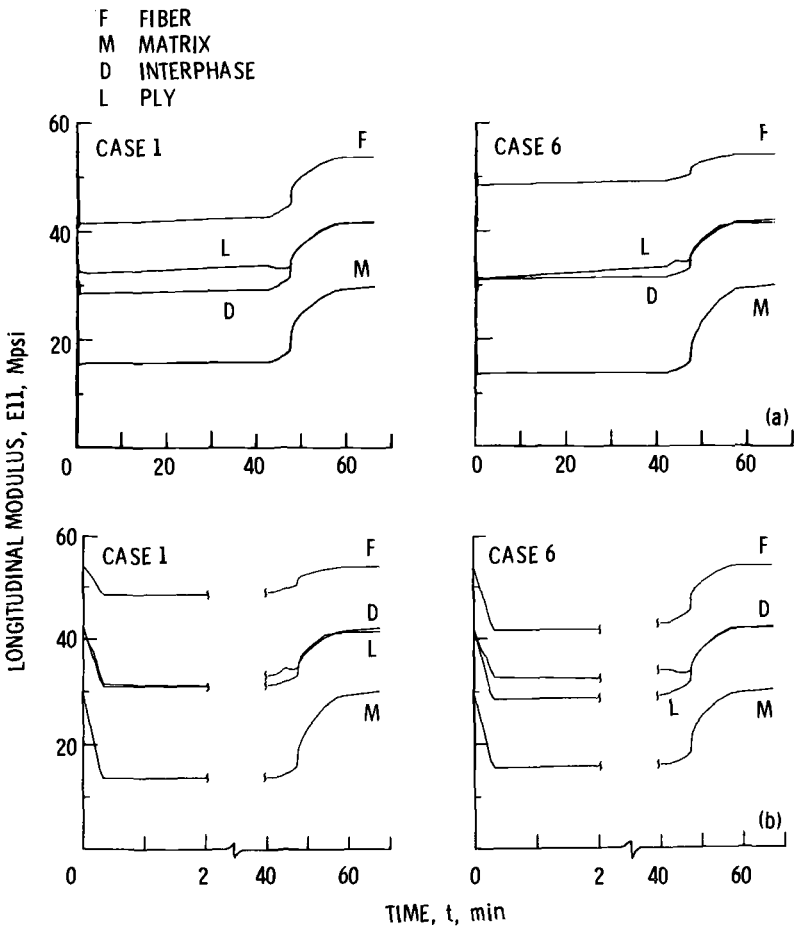

FIG. 7—*Longitudinal modulus behavior during flight mission. Node 6; Ply 4.*

represents the stress dependence, and the third represents the rate dependence or the time dependence, in part. The other part of the time dependence is through the direct time integration as will be described later. Equations 1 and 2 describe, then, material behavior in the temperature-stress-time space.

Each term on the right side of Eqs 1 and 2 describes a monotonic functional dependence of P/P_o from some initial property value to a terminal or ultimate material state. The specific shape of the function depends on the exponent as is shown in Fig. 2 for a fixed exponent and in Fig. 3 for a fixed T/T_F ratio. By judicious selection of the exponent and the initial and terminal values, a variety of functional dependences can be simulated using Eqs 1 and 2.

The form of Eqs 1 and 2 makes it convenient (provides direct feedback) to select the various parameters so that the functional dependence described is consistent with the physical considerations. For example, is is well known that the melting temperature (T_M) is a fundamental parameter in metals and that the mechanical properties are "zero" at T_M. Also, the stress at fracture for some reference condition is readily determined by simple experiments. In addition, the ultimate value of the stress rate may be determined from high-velocity impact penetration tests. It can be seen from Fig. 2 that the P/P_o increases/decreases very rapidly as the melting temperature (or any terminal value) is approached. Furthermore, the form of the equations make it convenient to evaluate the exponents from available data since each term is "isolated" from the others, that is, the other terms can be taken at

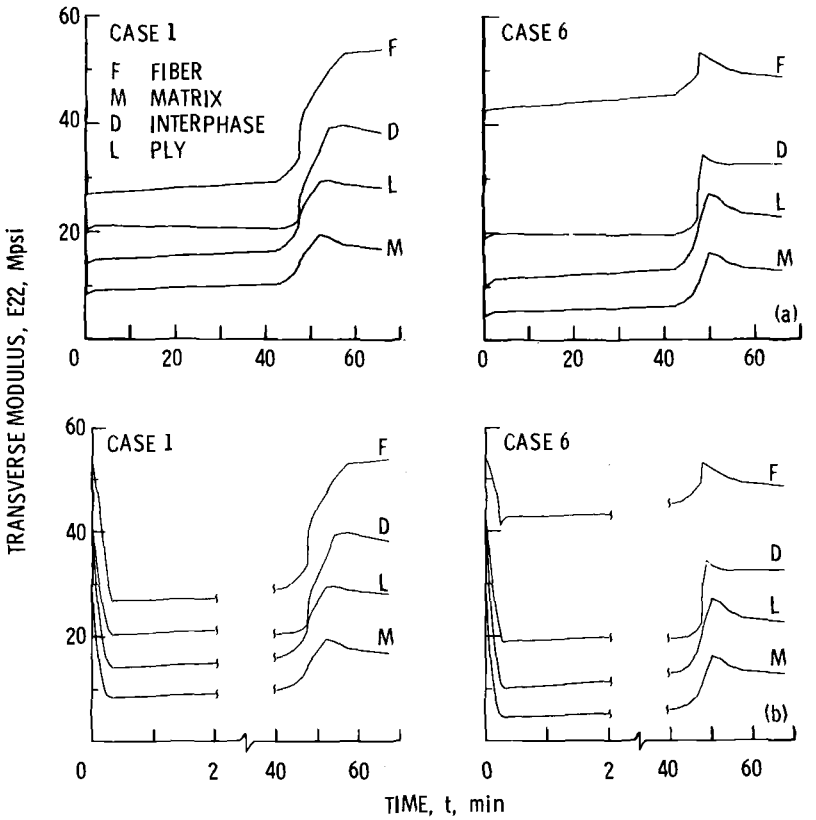

FIG. 8—*Transverse modulus behavior during flight mission. Node 6; Ply 4.*

reference conditions and will be unity. The equations are computationally effective since each term requires simple substitution of values and one exponentiation.

The form of the TVP-NCR selected has all the desirable features mentioned in the introduction. These features can be conveniently summarized into three groups: (1) physical, (2) fundamental, and (3) computational, as follows:

1. *Physical*—The constitutive relationships describe dependence on: temperature, time, stress, stress rate, and complete property degradation as the ultimate value is approached.
2. *Fundamental*—The constitutive relationships are:
   (*a*) generic—they are applicable to all constituent material properties (Fig. 4);
   (*b*) evolutionary—they are easily extended to include additional dependence, for example cyclic (mechanical, thermal);
   (*c*) isomorphic—they have the same form for all the properties;
   (*d*) unified—they are fully coupled from the initial to the terminal material state;
   (*e*) universal—they are equally applicable to any three constituents (fibers, matrix, interphase); and
   (*f*) nondimensional—they are normalizable with respect to reference and ultimate values.
3. *Computational*—the constitutive relationships are:
   (*a*) computationally effective—they only require simple substitution and exponentiation; and
   (*b*) easily integrated into nonlinear composite mechanics and structural analysis codes—they can be fully integrated using only a few programming statements.

Application

The TVP-NCR were integrated into a special-purpose computer code for structural analysis of turbine blades made from HT-MMC [*1*]. This code is depicted schematically in Fig. 1. The TVP-NCR describe the constituent material properties in the material space as shown at the bottom of the figure. Note that the cumulative time, temperature, and stress at the current state are tracked through the integrated computational process as shown in the figure. Once the current properties for the constituent materials have been determined, they are used in the various levels of composite mechanics to generate the quantities required for the global structural analysis. [*1*].

The finite element model of the component (HT-MMC hollow turbine blade airfoil), selected to demonstrate the computational effectiveness of the TVP-NCR, is shown in Fig. 5. For the analysis, typical engine mission loads were simulated including temperature, pressure, and rotor speeds as shown in Figs. 6*a* and *b* expanded to show start-up and shutdown details. The airfoil was assumed to be made from tungsten-fiber/superalloy HT-MMC. The volume ratio of the fiber was 0.5. The laminate configuration in the airfoil was a four-ply $(\pm 45)_s$ angle-plied laminate. The airfoil structure is a thin-wall hollow shell. The hollow structure is required for internal cooling and minimum weight. Some of the constituent material properties are available in the literature. Others (especially temperature, stress, and strain-rate-dependent properties) are estimated or deduced from other relevant data.

The structural analyses were performed to determine global and local structural response. The global structural response variables are tip displacement, untwist, and frequencies. The local response variables are ply stresses and constituent stresses at the various nodes. The examples presented next on local response correspond to the outermost ply (Ply 4) at the nodal point identified by the arrow in Fig. 5 (Node 6). Two sets of structural analyses were

performed. The first set was performed to determine the global and local structural response at the baseline properties condition. The second set was performed to determine the sensitivity of the structural response to arbitrary perturbations of the TVP-NCR exponents. The second set of analyses demonstrates the importance of computational simulation since it provides an assessment of the accuracy of the data required to experimentally determine the parameters in the TVP-NCR.

The results obtained from both structural analyses are summarized in Table 1 for the global variables (cruise and residual state) and in Table 2 for the local variables (cruise state only). The results are grouped into Cases 1 to 7. Case 1 is the baseline case and has the "best" values for the parameters in the TVP-NCR. Cases 2 to 7 constitute the sensitivity analyses. The perturbed values of the exponents and their contribution (increase (I)/decrease (D)) to the particular constituent material property (P_M or P_T) are listed next to the case. The percent change with respect to the baseline case is listed in the last column of the tables.

It can be seen from the results in Tables 1 and 2 that the changes in the global and local structural response variables, due to the perturbations in the exponents, are about 15% or less. This is a very significant result as it implies that very careful experiments would be

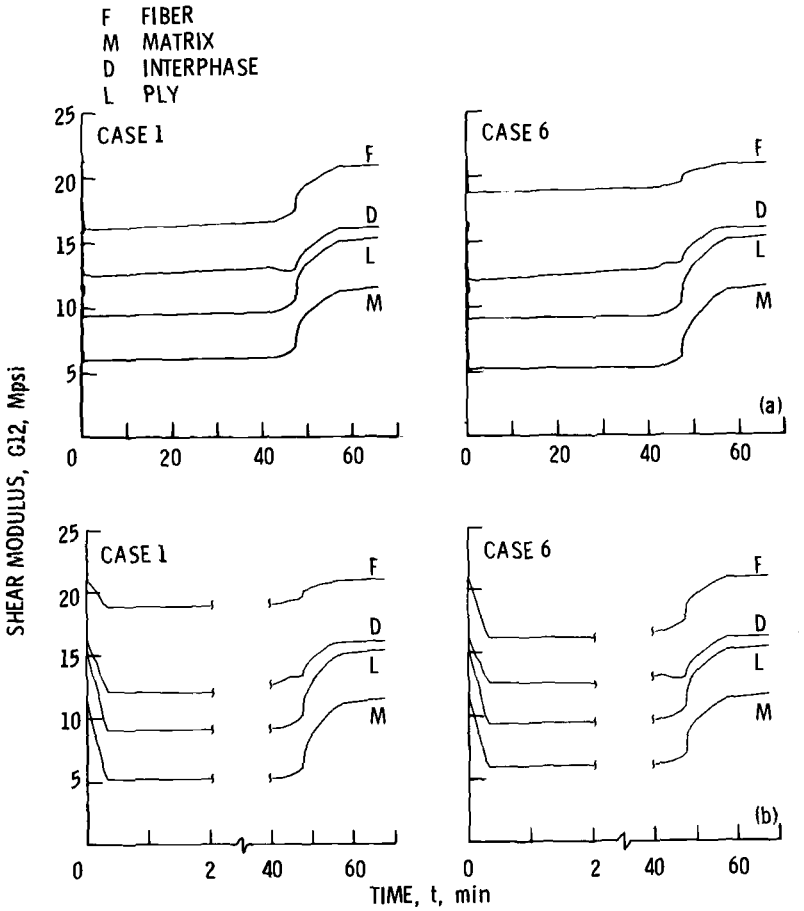

FIG. 9—*Intralaminar shear modulus behavior during flight mission. Node 6; Ply 4.*

necessary to obtain data for these exponents which is accurate to within 15% especially in these high-temperature ranges.

The greatest change (16%) in the frequency occurs in Case 3 (Table 1) where the perturbations in the exponents decrease the mechanical properties and increase the thermal properties of the matrix. The greatest change (15%) in the ply stress occurs in Case 6 (Table 2) where the perturbations in the exponents (1) increase the fiber mechanical properties but decrease those of the matrix, and conversely (2) decrease the thermal properties of the fiber but increase those of the matrix. The residual state ply stresses for all cases are negligible for all practical purposes.

The integrated analysis generates properties at all levels of the composite behavior simulation. Behavior of the longitudinal (fiber direction) modulus (E_{11}) of the constituents and ply are shown graphically in Figs. 7*a* and *b* for Cases 1 and 6 throughout the mission duration. The modulus decreases initially during the start-up and climb part of the mission. The modulus levels off during the steady state (cruise) part of the mission. Finally, the modulus increases during the landing and engine cutoff part of the mission. The significant point is

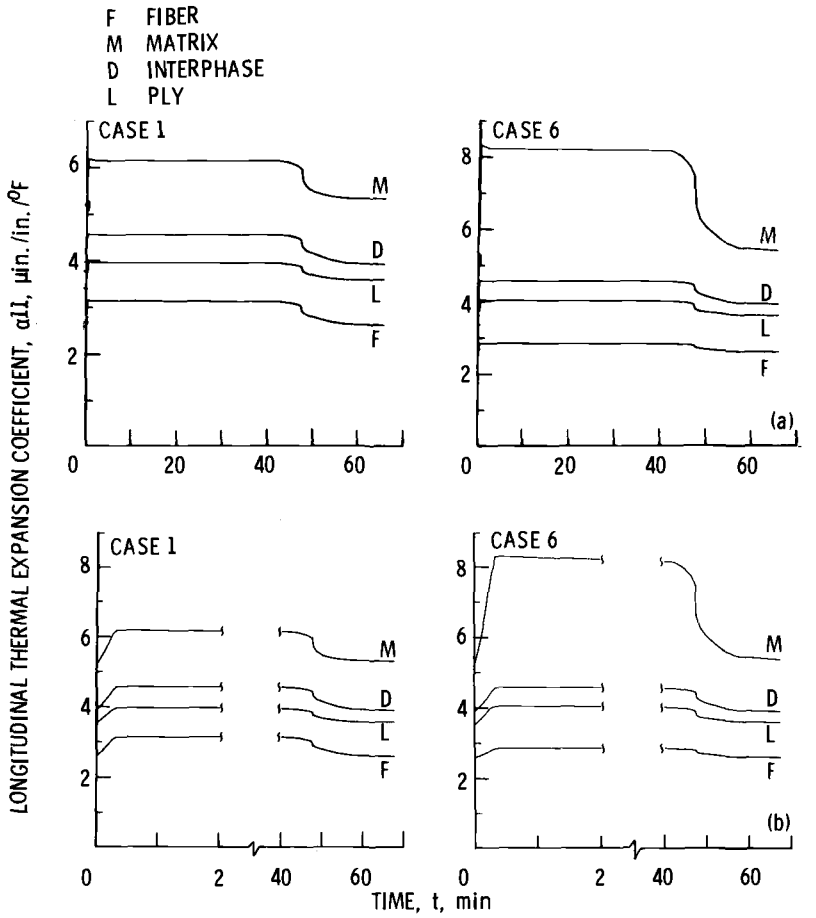

FIG. 10—*Longitudinal thermal expansion coefficient behavior during flight mission. Node 6; Ply 4.*

that the TVP-NCR appear to represent the material behavior as would be intuitively anticipated for this type of flight mission.

The corresponding behavior for the transverse (perpendicular to fiber) modulus (E_{22}) is shown in Figs. 8*a* and *b* and for the in-plane shear modulus (G_{12}) in Figs. 9*a* and *b*. The behavior of these moduli is about the same as that for the longitudinal modulus (E_{11}).

The behavior of the longitudinal thermal expansion coefficient (α_{11}) throughout the mission is shown in Figs. 10*a* and *b* for Cases 1 and 6. This coefficient initially increases rapidly (during climb), levels off during cruise, and slowly decreases to about its initial value during landing. This type of behavior is to be expected since the thermal expansion coefficients increase with increasing temperature. Note that even though α_{11} for the matrix for Case 6 is about 30% smaller than for Case 1, the coefficients for the ply and the interphase are about the same. This illustrates, in part, the restraining influence of the fibers in the HT-MMC behavior and in addition the importance of having TVP-NCR defined at the micromechanics level. The corresponding behavior for the transverse thermal expansion coefficient (α_{22}) is shown in Figs. 11*a* and *b*. The behavior of α_{22} is similar to that of α_{11}.

The behavior of the three lowest natural frequencies of the airfoil throughout the flight

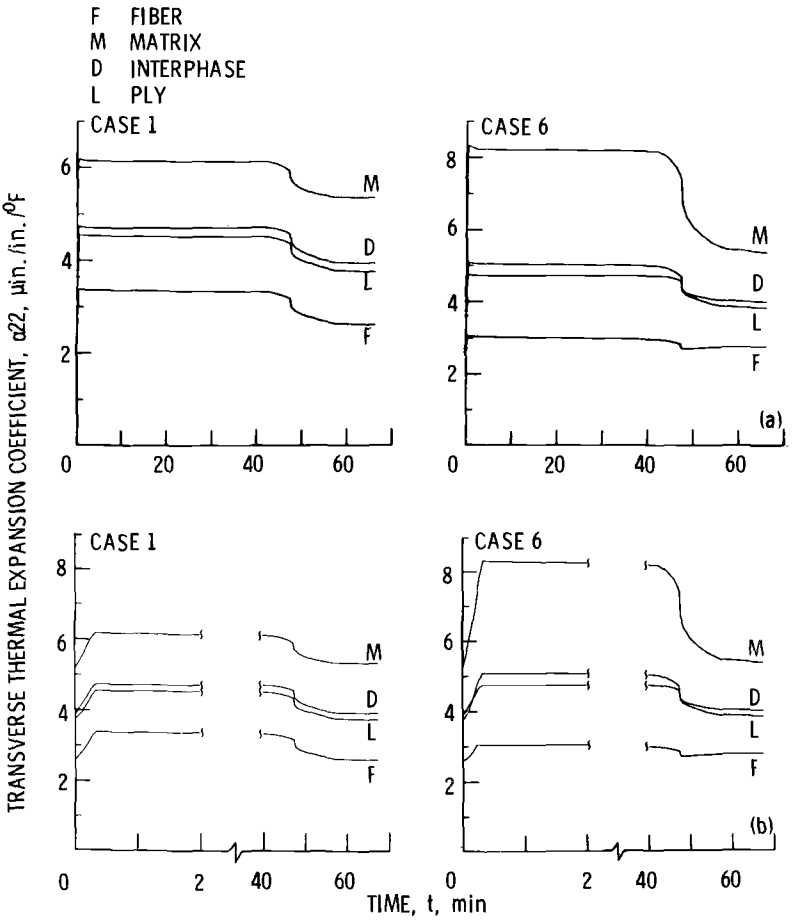

FIG. 11—*Transverse thermal expansion coefficient behavior during flight mission.*

mission is shown in Figs. 12*a* and *b* for Cases 1 and 6. Note that each frequency behaves somewhat differently. This is expected since each frequency is influenced differently by the centrifugal force. The second and third frequencies decrease during climb, increase during the early part of cruise, remain constant during the major portion of the cruise, and increase gradually to about their initial value during landing and engine cutoff. On the other hand, the first frequency increases sharply during climb (due to centrifugal force stiffening), levels off during cruise, increases slightly during landing (cooling but speed retained), and gradually decreases to approximately its initial value (zero speed). The coupled behavior of these three frequencies throughout the flight mission further demonstrates the computational effectiveness of the TVP-NCR to represent the physics of the HT-MMC from the constituent materials level to the component global structure response.

The longitudinal stress (σ_{11}) behavior throughout the mission in the constituents and in the ply is shown in Figs. 13*a* and *b* for Cases 1 and 6. The stress in the fiber increases very rapidly during climb, decreases gradually during cruise, decreases rapidly during landing, and decreases gradually to a small residual compressive stress at engine cutoff. The ply stress exhibits the same behavior as the fiber stress but its much lower in magnitude. The stress in the matrix increases (compressively) very rapidly during climb, remains compressive during cruise, and decreases gradually to a residual tensile value during landing and engine cutoff.

The corresponding behavior for the transverse stress (σ_{22}) is shown in Figs. 14*a* and *b* and

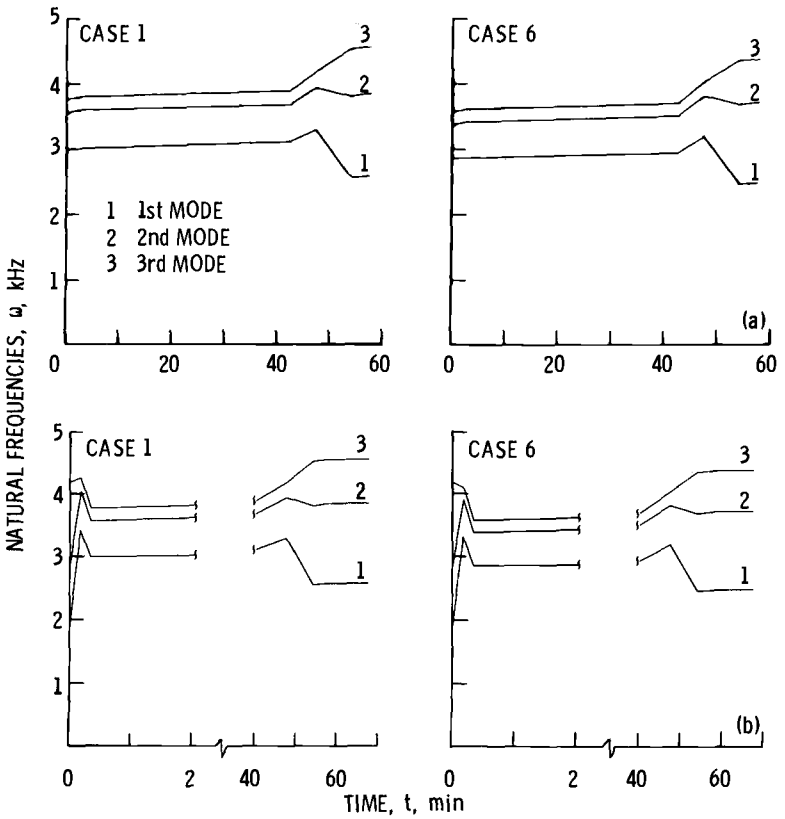

FIG. 12—*Turbine airfoil frequencies behavior during flight mission.*

that for the intralaminar shear stress (σ_{12}) in Figs. 15*a* and *b*. Note there are three different regions (A, B, and C) for the matrix and two different regions (B and C) for the interphase in which σ_{22} and σ_{12} are computed. These regions correspond to the intralaminar regions shown in Fig. 4. The interesting points to note are: (1) the matrix in the different regions is subjected to both tensile and compressive transverse stresses which can be of substantial magnitude, (2) the interphase can be subjected to relatively high transverse tensile stresses which may cause interfacial damage, (3) the fiber is subjected to very high transverse tensile stresses which could cause fiber splitting, and (4) the transverse ply stress is relatively small compared to the stress distribution in the constituents.

Collectively, the local stress behavior demonstrates the computational effectiveness of the TVP-NCR to predict the instantaneous behavior of the constituents at the micromechanics level as well as at the ply (macromechanics) level. Determination of the stress behavior in the constituents is possible because the TVP-NCR are referred to the constituent material space, and the formulation is based at the composite micromechanics level. The gradual decrease indicated for all the stresses during cruise is caused by the material thermoviscoplastic behavior and may be thought of as a form of creep.

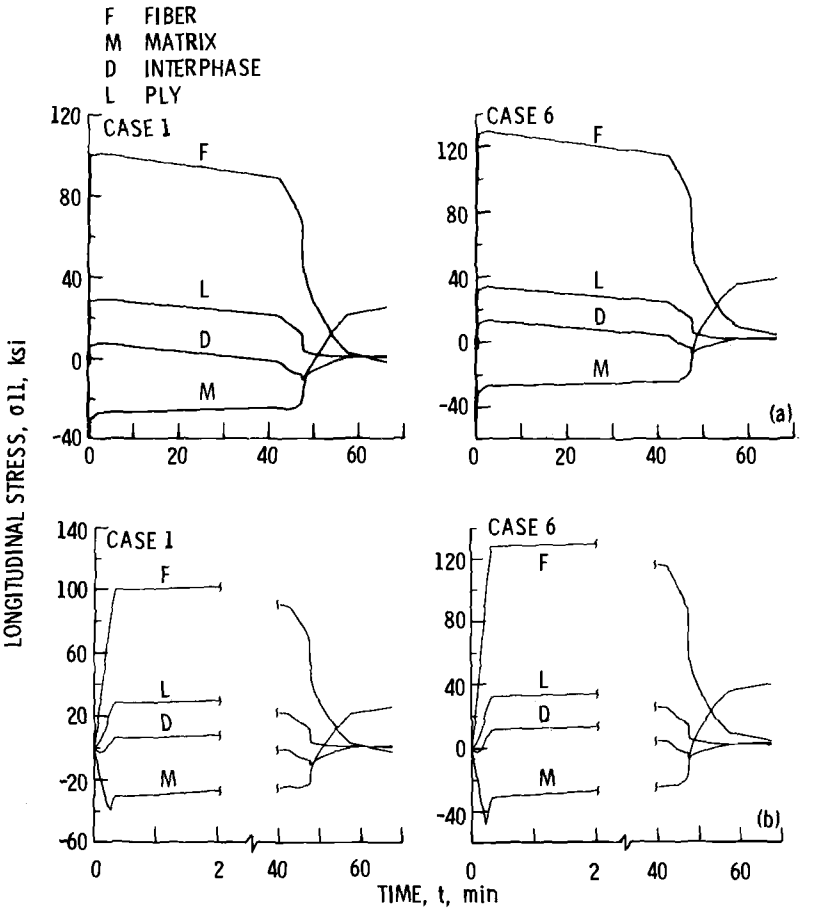

FIG. 13—*Longitudinal stress variation during flight mission. Node 6; Ply 4.*

Possible Extensions/Limitations

The TVP-NCR can be extended to include thermal cycle and mechanical cycle effects, diffusion, other material degradation effects, as well as time directly. Though terms for these factors are easily added since they will be of similar form, it is not necessarily clear which of these will contribute to independent material behavior.

In the direct time integration analysis, the effects of temperature are accounted for directly. Any ratchetting, for example, will be part of the residual displacements. Also, residual thermal stresses and other stresses are known and constitute a part of the cumulative stress history. On the other hand, vibratory stress effects are not accounted for in the direct time integration of the structural analysis. Though these effects can be accounted for through the stress rate, vibratory stress effects may indeed contribute to independent behavior. Diffusion or any other material degradation can be incorporated once the type of degradation has been defined. Other extensions will become self evident as HT-MMC start being extensively applied in enviroments where limited or no property data are available.

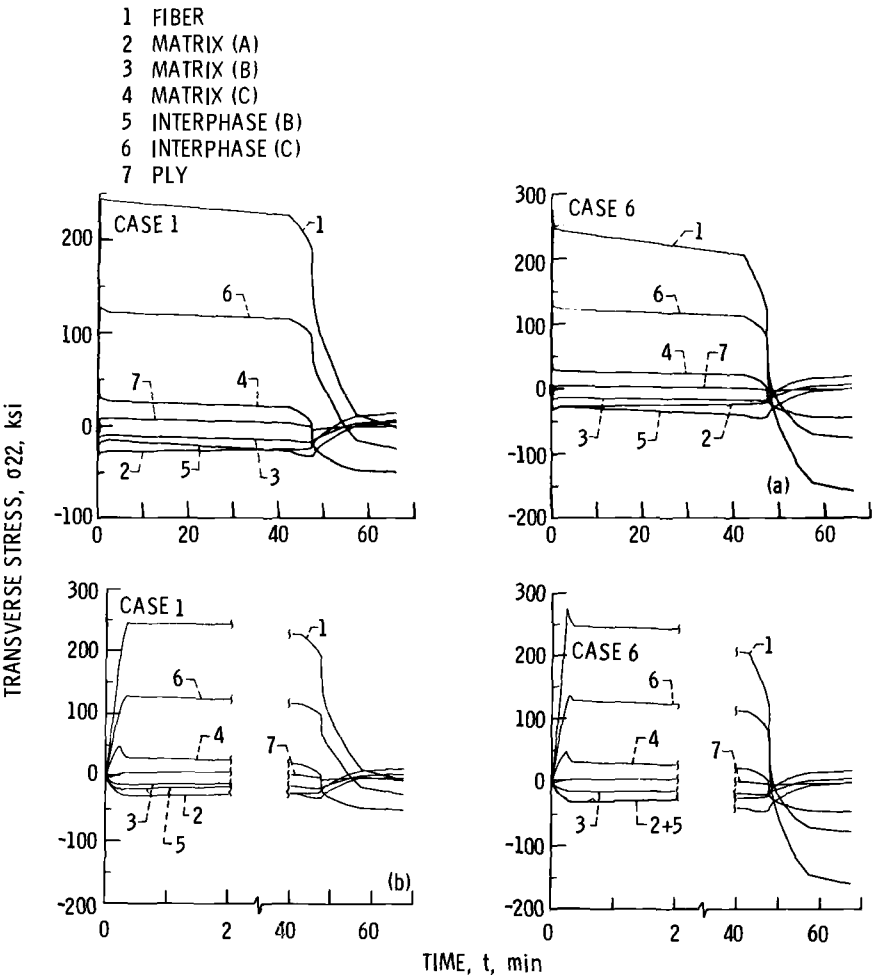

FIG. 14—*Transverse stress variation during flight mission. Node 6; Ply 4.*

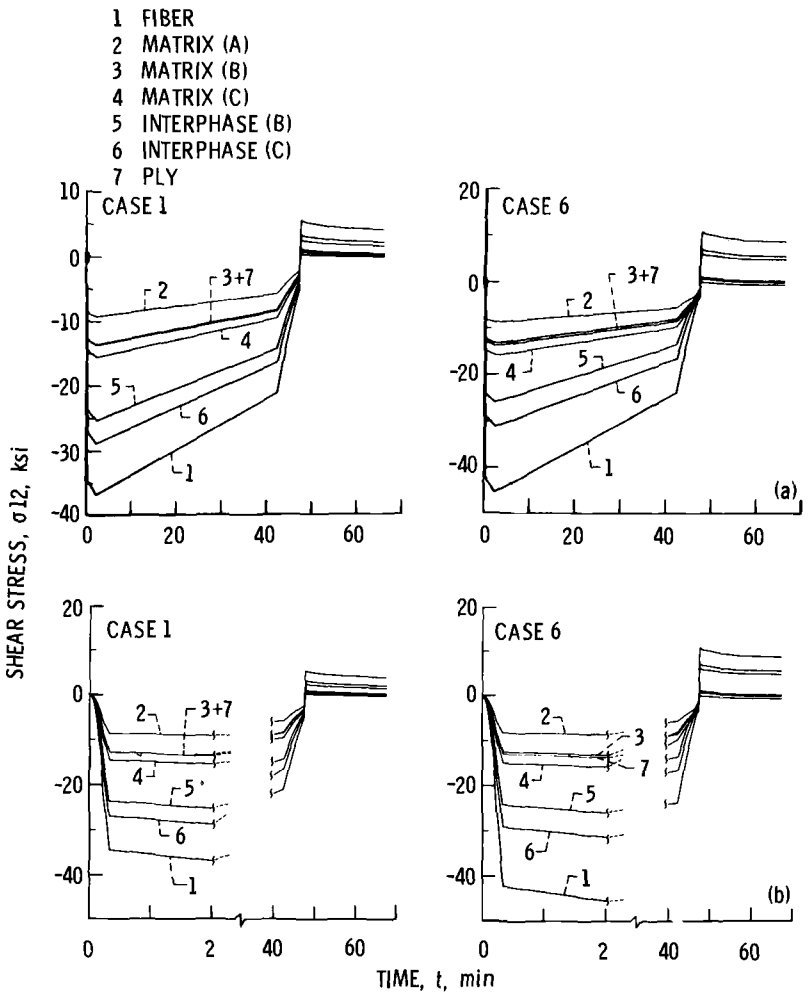

FIG. 15—*Intralaminar shear stress variation during flight mission. Node 6; Ply 4.*

Some limitations of the TVP-NCR described herein are that they: (1) must be used at the current instant of time, (2) must be used with a direct time integration nonlinear composite structural analysis, (3) cannot be verified experimentally at all levels of the composite mechanics analysis and at the very high temperatures, and (4) do not incorporate initial tangent unloading or possible shakedown in the classical plasticity sense. Whether (3) and (4) are serious limitations is yet to be determined. At this stage of the development it is prudent to say that these TVP-NCR must be used judiciously in design studies relying mainly on sensitivity analyses and other judgement factors that are appropriate for the specific case.

Conclusions

A unique set of thermoviscoplastic nonlinear constitutive relationships (TVP-NCR) for high-temperature metal matrix composites (HT-MMC) has been developed and is presented. This set of TVP-NCR is of simple form, is applicable to all thermomechanical properties,

is fully coupled, is readily integrated into nonlinear composite structural analyses, and is computationally effective. Applicability and computational efficiency were demonstrated through an application to a HT-MMC turbine blade structural analysis. Sensitivity analyses indicated that substantial perturbations in the TVP-NCR exponents have rather minimal effect on the global and local response of the structure. These TVP-NCR make it possible to trace the history of HT-MMC structural components from fabrication through service and from the composite micromechanics to global composite structural response. The TVP-NCR are suitable for preliminary designs and parametric studies. They should be judiciously used in design applications since they have not been experimentally verified as yet.

References

[1] Hopkins, D. A., "Nonlinear Analysis of High-Temperature Multilayered Fiber Composite Structures," NASA TM-83754, National Aeronautics and Space Administration, Washington, DC, 1984.

DISCUSSION

D. J. Chang (written discussion)—One of the weakness in the subject paper is that all the nonlinear property behaviors are based on strictly nonlinear mathematical expressions. The author did not substantiate the nonlinear expressions associated with the physical. In my opinion, such an approach will severely limit the validity, credibility and applicability if the basic constitutive equations are not based on actual physical observations. I suggest that Dr. Chamis can provide explanation to his assumptions of all the equations that were used.

C. C. Chamis and D. A. Hopkins (authors' closure)—The authors presented and discussed the assumptions for the nonlinear constitutive relationship equation in the text. The equation is of generic form, and the exponents can be selected to fit known or anticipated data (presently nonexisting) or material behavior at these high temperatures. Furthermore, the authors do not consider uniaxial data appropriate for the 3-D analysis required. The credibility of the constitutive relationship will be established as data of service-environment mission cycles becomes available. Its applicability was already demonstrated in the results summarized in Tables 1 and 2 of the paper. Though we share Dr. Chang's concerns we do not know of any nonlinear constitutive relationships of equal generality for all the properties.

[1] The Aerospace Corporation, El Segundo CA.

Clayton L. Harmsworth[1]

Development of Design Allowables for Metal Matrix Materials

REFERENCE: Harmsworth, C. L., **"Development of Design Allowables for Metal Matrix Materials,"** *Testing Technology of Metal Matrix Composites, ASTM STP 964*, P. R. DiGiovanni and N. R. Adsit, Eds., American Society for Testing and Materials, Philadelphia, 1988, pp. 197–204.

ABSTRACT: One of the most critical elements in the transition of a structural material from the development stage to an aerospace application is the existence of reliable design allowables. The Department of Defense (DOD) and the Federal Aviation Administration (FAA) require the use of MIL-HDBK-5 (for metals) and MIL-HDBK-17 (for composites) allowables unless alternate values are approved by these organizations. The major benefit of handbook allowables is not, however, the automatic approval of a material for use. It is the reliability and confidence that comes to the designer in being able to use a material with predictable property values. The end result is a design that is safe yet not overly burdened with excess structure. This article reviews the requirements for the development of allowables and some of the potential problems which may be encountered in developing allowables for metal matrix composites.

KEY WORDS: mechanical properties (basic data), statistical data, specifications, metal particle composites

The design allowables in MIL-HDBK-5 and data in MIL-HDBK-17 are used in the design of both military and civilian aerospace structures. Thus, it is exceedingly important that the design values presented represent as accurately as possible the mechanical properties of production material. In order to ensure this accuracy, exact requirements have been established for data appearing in these documents. These requirements include the number of test specimens, the number of lots of material, and the existence of an industry wide or government specification controlling the consistency of the material. Obviously, the best defined set of allowables would be of little value unless there were a specification to ensure that future material would be similar to the material on which the allowables were based.

MIL-HDBK-5

MIL-HDBK-5, "Metallic Materials and Elements for Aerospace Structures," was originally printed in 1938 as ANC-5 Bulletin to standardize the requirements of various government agencies in the design of aircraft structure. The original document contained the allowables for metal elements, fasteners, joints, and other aircraft structural members of the day including wood. Wood was subsequently removed from the handbook in 1946.

[1] Technical manager, AFWAL Materials Laboratory, Wright-Patterson Air Force Base, OH 45433.

Data in MIL-HDBK-5 are presented in the form of "A" allowables "B" allowables, "S" values, and typical values. These values are defined as follows:

"A" Allowables

The values above which 99% of the population is expected to fall with a 95% confidence.

"B" Allowables

The values above which 90% of the population is expected fall with a 95% confidence.

"S" Values

A minimum value from a government or industry specification. (The statistical assurance is unknown.)

Typical Values

Average values with individually stated statistical requirements.

Table 1 shows the different mechanical property values in MIL-HDBK-5. Only the tensile, compressive, bearing, and shear data which are presented as allowables are considered compulsory data, although the inclusion of the other property data is highly desirable. For material to be used in damage tolerant design, both fracture toughness and crack growth data are essential. For materials which may be used at elevated temperatures, the effect of temperature and creep curves are needed.

Number of Specimens

To ensure the reproducibility of allowables in the Handbook, a minimum number of test specimens and a minimum number of production lots of materials are required. Detailed guidance on the statistical specimens needed and its analysis are specified in the "Guidelines" chapter in MIL-HDBK-5. In essence, a minimum of 100 tensile strength observations spec-

TABLE 1—*Types of data presented in MIL-HDBK-5.*

Property	Basis	Test Method
Tensile (TUS, TYS, AND E)	allowables	ASTM E 8[a]
Compression (CYS)	allowables	ASTM E 9[b]
Shear (SUS)	allowables	proposed ASTM pending
Bearing (BUS AND BYS)	allowables	ASTM E 238[c]
Stress-strain	typical	...
Fatigue	typical	ASTM E 466[d]
Crack-growth	typical	per ASTM recommendations
Creep and stress rupture	typical	per ASTM recommendations
Low and elevated temperature data for tensile, compression, shear, and bearing	% of RT allowables	...

[a] Methods of Tension Testing of Metallic Materials.
[b] Compression Testing of Metallic Materials at Room Temperature.
[c] Method for Pin-Type Bearing Test of Metallic Materials.
[d] Recommended Practice for Presentation of Constant Amplitude Fatigue Tests of Metallic Materials.

imens are necessary if the sample population can be described by a normal or 3-parameter Weibull distribution. If the assumption of a normal or Weibull distribution is rejected, then a minimum of 300 tensile observations are required to compute allowables nonparametrically. Guidance for the statistical evaluation of normality or "Weibullness" by the Anderson-Darling Goodness of Fit test is also described in the Handbook. It is important that the data be uncensored (all outliers included) even though some values may be below specification requirements. Uncensored data are necessary to ensure an accurate representation of the population. While the shape of the distribution can be nonnormal, it should be a single population. Biomodal or multi-populations indicate the producer's process may be out of control. In such a case the scatter in properties will produce such low "A" and "B" values that the material may be unattractive. To encourage the submission of all observations, raw data are kept confidential within the MIL-HDBK-5 files.

Once the "A" allowables are established they are compared with the "S" (specification tensile) values. If the "S" values are higher, the "A" values are presented as the design values. If the "S" values are lower, the "S" values are listed in lieu of the "A" values with a footnote indicating the higher "A" values. When the "S" value is significantly different from the "A" value, an effort is made to obtain a specification revision to change the specification value to the "A" value.

Ten lots of material are required to ensure that the tensile strength data include any lot-to-lot variance that will occur in normal production. Past experience on metal alloys has shown that 10 lots are sufficient, and generally the variance from lot to lot at a consistent location is less than the variation in properties from different locations within a single product. This behavior is undoubtly due to differences in the amount of working during processing and quenching effects which may vary from the edge to the center of a product.

Derived Properties

Typically, when considering a new material for an aerospace structural application, the designer first looks at tensile strength, fracture toughness, and fatigue or crack growth properties. However, when actually sizing a part for final design, compression, bearing, and shear properties may play an equal if not greater role. It is not uncommon for at least 50% of an aerospace structure to be designed to compressive yield strength or stiffness criteria.

Fortunately, for conventional alloys, once the tensile allowables for a given grain direction are computed it may not be necessary to directly compute the remaining allowables using the full complement of from 100 to 300 specimens. Instead, by using a paired ratio technique compression, shear, and bearing strength allowables can be indirectly computed with as few as 10 test specimens if certain requirements are met. This method involves the pairing of compression, shear, and bearing measurements with mean tensile yield or ultimate strength measurements for which an allowable has been already established. These paired measurements are required for each significant test direction, representing at least ten lots of material obtained from at least two production heats for each product form and heat-treat condition. For a single form and thickness, data from no more than one heat-treat lot per heat may be used to meet the ten lot requirement. Test specimens for paired measurements shall be located in close proximity. If coupons or specimens are machined prior to heat treatment, the coupons or specimens representing paired measurements must be heat treated simultaneously in the same heat-treat load through all heat-treating operations. Data for the ten lots of material should represent the thickness range covered by the material specification.

The derived ratio process is based on the pairing of mean compression, shear, and bearing measurements with mean tensile yield or ultimate strength measurements for which an allowable has been already established. It can be also used to establish tensile yield and

ultimate strength allowables in alternate testing directions. The technique is based on the premise that the mean ratio of paired observations provides an estimate of the ratio of their allowables. The steps in this process are detailed in the MIL-HDBK-5 guidelines as follows.

Determine the ratios of paired observations for each lot of material by dividing the measurement of the property to be obtained (for example, CYS (LT) mean compressive yield strength) by the measurement for the established property (for example, TYS LT) mean tensile yield strength). The ratio of the two population means should exceed the lower confidence limit defined as

$$\bar{r} - t_{1-a}s/\sqrt{n}$$

where

n = number of ratios,
r = the average of ratios,
s = the standard deviation of the ratios, and
t_{1-a} = the 1-a fractile of the t distribution for $n - 1$ degrees of freedom. At a risk level of $a = 0.05$, the appropriate t value is $t_{0.95}$

Since the lower confidence interval estimate is used as the ratio between the design allowable properties, the reduced ratio, R, may be defined as

$$R = r - t_{0.95}s/\sqrt{n}$$

Values of $t_{0.95}$ for various degrees of freedom, $n - 1$, are tabulated in MIL-HDBK-5 and various statistical references.

The reduced ratio may now be used to establish the design allowable for the property to be derived.

$$R = \frac{E_{cy}(LT)}{F_{ty}(LT)} = \frac{\text{allowable to be derived}}{\text{established allowable in specified test direction.}}$$

The preceding is a summary of the derived ratio process which has been shown to be reliable for application to wrought alloys. The more detailed description in MIL-HDBK-5 should be reviewed before making any actual calculations. In addition, it is emphasized that this ratioing technique has not been proven for use with metal matrix composites or for properties other than tension, compression, bearing, and shear. Its applicability to metal matrix composites would have to be proven by comparison with compression, bearing, and shear allowables obtained through direct computation using the full 100 to 300 specimen sample. However, this comparison is necessary and should be a part of the first allowables development program for a metal matrix product.

These analysis requirements were established and are constantly reviewed by a coordination group consisting of members from most of the aerospace companies and aerospace material producers along with representatives from the DOD and the FAA. As a result, the statistical requirements reflect a balance of what is needed for design, what can be actually produced, and what the customer can live with. In addition, the values in MIL-HDBK-5 are reviewed on an intermittent basis to ensure that any minor changes in material processing (within the limits of the processing specification) have not affected the published allowables.

MIL-HDBK-17

MIL-HDBK-17 (Plastic for Aerospace Vehicles) was originally published in 1955. Fiberglass reinforced materials were incorporated into the handbook in the mid-1960s. In the past, MIL-HDBK-17 has been different than MIL-HDBK-5 in that typical rather than minimum values have been presented. This has been due to the lack of adequate government or industry wide processing specifications to control quality and the complex relationships between unidirectional composite specimen properties and the strength of a laminated composite component consisting of many layers of different fiber orientations. As a result, MIL-HDBK-17 has not been updated or reissued in over 10 years.

However, the MIL-HDBK-17 coordination activity has been reactivated in recent years and the Handbook is under major revision. The new Handbook will be titled, "Composite Materials for Aircraft and Aerospace Applications." The development of new analytical techniques, and guidelines is in progress. The current goal is to obtain sufficient data from at least five prepreg batches of each composite system to be able to demonstrate that the material and fabrication process is under control and that statistically based "B" design values can be established. These design minimum values are being or will be generated on several resin matrix composite materials having fiberglass, Kevlar, and carbon (graphite) fibers.

Differences and Similarities

The goals for MIL-HDBK-5 and MIL-HDBK-17 are similar; however, due to differences in the product characteristics, the approaches to obtain these goals are somewhat different. Normally "B" values are not published in MIL-HDBK-5 without "A" values. Only "B" values are being proposed for MIL-HDBK-17. From the design standpoint "B" values are generally used for redundant or multi-load path structure while "A" values are used for critical single load path structure. As composites are generally limited to fail safe structure the development of "B" values for MIL-HDBK-17 is the current goal.

The test methods for metals and composites are considerably different. Those commonly used by the two handbooks are shown in Table 2. In MIL-HDBK-5, emphasis is on tension, compression, bearing, and shear allowables with statistically valid fracture toughness, fatigue, and crack growth data needed for damage tolerant and durability analysis.

In MIL-HDBK-17 emphasis is currently on tension (0 and 90° lay-ups), compression (0°) and inplane shear (±45°) with secondary emphasis on bolt bearing. The angle lay-up refers to the angle between the fiber orientation and the specimen's length dimension. An approved damage tolerant analysis has not been developed for composites although most proposed approaches relate to a strain limiting criteria rather than an effective flaw size.

TABLE 2—*Types of data proposed for MIL-HDBK-17.*

Property	Basis	Test Method
Tensile	"B" allowables	ASTM D 3039[a]
Compression	"B" allowables	ASTM D 3410[b]
Bolt bearing	"B" allowables	new test proposal
In-plane shear	"B" allowables	ASTM D 3518[c]

[a] Test Method for Tensile Properties of Fiber-Resin Composites.
[b] Test Method for Compressure Properties of Unidirectional or Crossply Fiber-Resin Composites.
[c] Practice of In-Plane Shear Stress-Strain Response of Unidirectional Reinforced Plastics.

Metal matrix composites, by definition, involve both metals and composites and as a result may present some unique allowables problems. Such problems should not be compounded, however, by arbitrary decision to characterize the material as a metal or a composite. Rather, the allowables approach should relate to the basic structure of the material and how it will be used in design. In general, it appears that discontinuous or short fiber reinforced materials will display somewhat the same behavior and require the same properties as metals, making them more amenable to the MIL-HDBK-5 approach. Continuous filament metal matrix materials appear more related to resin matrix composites, and their test methods and analysis should be more amenable to the MIL-HDBK-17 approach. Obviously any unique fabrication process or configurations such as three dimensional weaves will require rather specialized analysis and will be treated best on an individually approved basis.

Specifications

An effective material processing specification is essential prior to the development of allowables on metals or composites and will be equally necessary for metal matrix composites. Government or industry specifications are generally acceptable for MIL-HDBK-5. Company specifications are not acceptable (except for fasteners) without special approval. Acceptable processing specifications are a more difficult problem for composite systems in MIL-HDBK-17. This is due to the less precise and more proprietary nature of the resin and the more tenuous relationship between the strength of a unidirectional composite specimen and the strength of a built-up laminated composite structure. A highly promising approach involves the use of a prepreg specification utilizing chromatographic fingerprinting techniques to define chemical compositions. The premise is that it does not matter what proprietary process was used to obtain a given prepreg, as long as one can match fingerprints and other physical and chemical properties throughout the production process.

The importance of an adequate materials processing specification prior to allowables development can not be overemphasized. For many years attempts to develop allowables on castings for MIL-HDBK-5 were thwarted due to the wide variance in properties from lot to lot of castings even though the material was well within existing specification limits. This variation was primarily due to inconsistencies in foundary practice involving location of casting chills, risers, mold orientation etc.; all of which affect cooling rate which in-turn influence properties. When casting strength values obtained from different suppliers on material produced under the same specification were combined, the calculated allowable values were so low as to make the material noncompetitive. These same general types of problems may develop for metal matrix composites if adequate materials processing specifications are not developed.

Increased quality can not be inspected into a part. Increasing minimum property values in a specification will not improve the strength of parts; it will only increase the rejection rate of material produced. This is true unless the specification changes lead to significant processing or fabrication changes. In the case of high-performance aluminum castings a better inspection process was needed. A metallographic analysis of dendritic arm spacing or cell size was incorporated into a proposed specification along with tighter chemistry of several elements. The impact of this new specification has not yet been fully established; however, preliminary evaluation has indicated that casting tensile property data from different suppliers may constitute or more nearly constitute a single population. Relative to metal matrix composites, the message is that industry wide processing specifications are extremely important and should be developed as soon as possible. In addition, it may be necessary to include in these specifications new and innovative inspection techniques to control reinforcement distribution, spacing, volume percent, etc.

Initial Material Application

As with many other new materials, the of allowables for metal matrix composites may be delayed while sufficient number of production lots are produced. This is very frustrating to material producers who feel they are caught in a chicken and egg dilemma. How can a product be accepted for commercial production until it is documented in MIL-HDBK-5 or MIL-HDBK-17, and, conversely, how can a material be included in a handbook until an adequate number or production lots or batches are produced?

One approach is to limit a new material to nonflight critical secondary structure until some production experience is obtained. Ideally, such an application, should be easily inspectable and easily replaceable. Speed brakes, vertical fin sections, landing gear doors, and seat track fittings are some of the components that have been selected in the past. A side benefit of a gradual transition is that as material is produced for noncritical applications, quality control tensile property data sufficient to meet MIL-HDBK-5 or MIL-HDBK-17 requirements can be automatically obtained. With appropriate foresight, sufficient material located adjacent to the quality control tension specimens can be set aside and subsequently be used to obtain the paired measurements for a complete MIL-HDBK-5 or MIL-HDBK-17 analysis at a relatively low cost.

A second approach that has been used to obtain allowables for MIL-HDBK-5 when time is of the absolute essence is to simply pay for the production of ten commercial lots of material for an allowables test program. Unfortunately, this approach can become quite expensive, particularly when a production lot could be a 9072 kg (20 000 lb) ingot. Accepting an order for test material may be of particular concern to the supplier if there is no assurance of a market for the remaining portion of each lot of material. With much smaller production lots for metal matrix materials, this approach may be more viable.

A third approach or consideration is that it is not absolutely necessary to have allowables in MIL-HDBK-5 or MIL-HDBK-17 to use a material in primary structure. For the most part, the FAA will approve such exceptions for commercial application when the proposing organization has obtained allowables using the approved military handbook guidelines, and when a company specification which meets AMS or MIL specification requirements is available. This approach is most often used when the material is highly proprietary in nature. For military applications, the terms of acceptance are more open to negotiation between manufacturer and the procuring organization. Many new materials are introduced in this manner when temperature or corrosion considerations are a priority factor in material selection.

Relative to metal matrix materials, there are sufficient nonflight critical applications on both manned and nonmanned systems that the first of the three approaches mentioned seems the most desirable.

Summary

The existence of military handbook approved design allowables for any new material is a critical step in the widespread acceptance of that material in aerospace structure. Both the Department of Defense (DOD) and the Federal Aviation Administration (FAA) require the use of MIL-HDBK-5 (metals) and MIL-HDBK-17 (composites) allowables unless alternate values are specifically approved by these agencies. To ensure the reliability of such allowables a statistically valid quantity of data are needed from various grain orientations and thicknesses on several lots of materials. In addition, an industry or government specification must be developed to describe the material and to ensure that material produced in the future will have predictable property values. Although the statistical goals are the same for both handbooks, the approach to reach these goals is different. Metals exhibit a

higher degree of isotropy than composites, and industry wide processing specifications are available. For metals, emphasis is on tensile, compression, bearing, and shear allowables with statistically valid fracture toughness, fatigue, and crack growth data needed for damage tolerant and durability analyses. For resin matrix advanced composites emphasis is on tension (0 and 90° lay-ups), compression (0°), and inplane shear (±45°) properties with a secondary emphasis on bolt bearing properties. A damage tolerant analysis for composites is not yet finalized although most proposals relate to a strain limiting criteria rather than an effective flaw size. Metal matrix composites will present some unique allowables problems. The problem should not be compounded, however, by any arbitrary decision to characterize the material as a metal or a composite. Rather, the allowables analysis should relate to the basic structure of the material. In general, the MIL-HDBK-5 or metals approach appears more amenable to discontinuous fiber and particulate composites while the MIL-HDBK-17 approach may be more appropriate for continuous filament structures.

Nondestructive Evaluation and Physical Tests

Alan Wolfenden,[1] *Mahmoud R. Harmouche,*[1] *and Steven V. Hayes*[2]

Anelastic and Elastic Measurements in Aluminum Metal Matrix Composites

REFERENCE: Wolfenden, A. Harmouche, M. R., and Hayes, S. V., **"Anelastic and Elastic Measurements in Aluminum Metal Matrix Composites,"** *Testing Technology of Metal Matrix Composites, ASTM STP 964,* P. R. DiGiovanni and N. R. Adsit, Eds., American Society for Testing and Materials, Philadelphia, 1988, pp. 207–215.

ABSTRACT: The piezoelectric ultrasonic composite oscillator technique (PUCOT) has been used at temperatures up to 638 K and at 80 kHz to measure dynamic Young's modulus E, mechanical damping or internal friction Q^{-1} and strain amplitude ϵ in Al/SiC_w and Al/Sic_p. For four adjacent specimens from one sheet of 6061 Al/SiC_p E-values varied in the range 114–119 GPa at room temperature. The composition dependence of the modulus followed $E = 68.6 + 2.2X$ with $R \approx 0.95$ (E is in GPa and X in volume percent SiC). The temperature dependence of the dynamic modulus followed $E = 138.7 - 0.11T$ with $R = 0.98$ (E is in GPa and T in Kelvin). The amplitude dependence of Q^{-1} for 6061 Al/SiC_w revealed a damping peak at $\epsilon = 10^{-6}$. An analysis of the internal friction data in terms of a damping theory yielded values for the minor pinning length of dislocation lines and the density of mobile dislocations. The results are discussed in terms of the microstructure.

KEY WORDS: dynamic modulus, damping, internal friction, temperature, composition, aluminum, silicon carbide, metal matrix composites, composites, dislocations, whiskers, particles, mechanical properties, anelasticity, elasticity

Relatively soft metals, along with their alloys, and engineering polymers show remarkable ductility, but their stiffness remains inferior to that of other materials such as iron- and nickel-based alloys. In space and subsea applications, the use of light-weight materials has been of economic and engineering advantage. Thus, efforts have been directed towards improving the stiffness of light weight materials rather than seeking other alternatives. The recent boost in the introduction of low density brittle materials such as silicon carbide and boron in the form of whiskers and fibers embedded in a ductile matrix of light weight materials continues. These relatively new materials are properly called composites. Research has led to improvements of strength while ductility remains satisfactory, and composites show stiffnesses far superior to those of the materials making up the matrix. Since stiffness has been shown [*1,2*] to depend largely on the distribution, quality, quantity, and direction of the fibers or particles, and on interface bonding, it must be measured accordingly. Moreover, composite materials have been used in thermally fluctuating environments. Thus the stiffness dependence on temperature cannot be ignored.

In this paper on anelastic and elastic measurements, we present some experimental results on dynamic Young's modulus E in the temperature interval 300 to 638 K for aluminum metal matrix composites (MMCs) reinforced with silicon carbide (SiC) whiskers or particles.

[1] Professor and lecturer, respectively, Mechanical Engineering Department and Advanced Materials Laboratory, Texas A&M University, College Station, TX 77843.
[2] Lead engineer, LTV Aerospace and Defense Company, Dallas, TX 75265.

Also, Young's modulus dependence on the homogeneity of particles distributed across a plate by means of measuring E for small longitudinal segments is reported for room temperature only. Finally, the strain amplitude dependence of the mechanical damping or internal friction is reported and leads to estimations of mobile dislocation densities and minor pinning lengths of dislocation lines.

Experimental Procedures

The technique used to measure the reported values for Young's modulus E, internal friction Q^{-1}, and strain amplitude ϵ is the piezoelectric ultrasonic composite oscillator technique (PUCOT). A brief description of the apparatus and its operation is given in the following paragraph. Full details can be found elsewhere [*3–5*].

Test specimens with a variety of cross-sectional areas and lengths of approximately 40 mm were supplied to us and are listed in Table 1. All the specimens from the University of Maryland were annealed for 12 h at 530°C and furnace cooled to room temperature. The specimen from Arizona State University was hot extruded to a thickness of 12.7 mm, hot rolled perpendicular to the extrusion direction, solutionized at 493°C for 1 h, water quenched, and then aged at 160°C for 24 h. This heat treatment is the one normally used to produce a T6 condition in the unreinforced 2124 aluminum alloy. The PUCOT experimental arrangement consists of two piezoelectric quartz drive and gage crystals to excite longitudinal ultrasonic resonant stress waves in a specimen of appropriate resonant length. For higher temperature measurements, a fused quartz spacer rod joins the specimen and the quartz crystals. The addition of the spacer rod allows insertion of the specimen in the furnace while keeping the crystals at about room temperature. In either case we have a resonant system driven by a closed-looped oscillator which maintains a constant (preselected) gage crystal

TABLE 1—*Results of the modulus measurements for the materials studied with the PUCOT.*

ID No.	Material[a]	Temperature/Kelvin	Modulus/GPa	Source[b]
1	6061 aluminum + 0 volume percent SiC	300	70	A
2	1100 aluminum + 0 volume percent	300	67	A
3	6061 aluminum + 5 volume percent (w)	300	85	A
4	1100 aluminum + 5 volume percent (p)	300	78	B
5	2124 aluminum + 15 volume percent (w)	300	91	C
6	6061 aluminum + 20 volume percent (w)	300	123	A
7	1100 aluminum + 20 volume percent (p)	300	105	B
8	6061 aluminum + 20 volume percent (p)	300	114	D
9	6061 aluminum + 20 volume percent (p)	300	119	D
10	6061 aluminum + 20 volume percent (p)	300	117	D
11	6061 aluminum + 20 volume percent (p)	300	115	D
12a	6061 aluminum + 20 volume percent (w)	300	109	E
12b	6061 aluminum + 20 volume percent (w)	473	85	E
12c	6061 aluminum + 20 volume percent (w)	638	67	E
13a	6061 aluminum + 20 volume percent (w)	300	105	E
13b	6061 aluminum + 20 volume percent (w)	473	84	E
13c	6061 aluminum + 20 volume percent (w)	638	73	E

[a] w = whisker; p = particulate.
[b] A = SILAG via University of Maryland.
B = DWA via University of Maryland.
C = ARCO via Arizona State University.
D = Science Applications International Corporation via LTV Aerospace and Defense Company.
E = Science Applications International Corporation via LTV Aerospace and Defense Company and Air Force Flight Dynamics Laboratory.

voltage and hence a constant maximum stress or strain amplitude in the specimen. During a test, the gage and drive voltages, the period, and temperature are recorded and appropriate equations are employed to yield experimental values for E, Q^{-1}, and ϵ.

Results and Discussion

A total of 17 specimens were tested. All specimens are aluminum alloy matrices containing randomly oriented SiC whiskers or particulates in the range 0 to 20 volume percent. The measured Young's moduli are discussed first, followed by discussion of the internal friction.

Young's Modulus

The measured Young's moduli, materials specifications, temperature and source of materials appear in Table 1. The precision for a single measurement of modulus E is $\pm 0.7\%$. Looking at the data, one notices three variables affecting the modulus. The first one is the addition of the SiC. This increased E from about 70 GPa at 0 volume percent SiC to about 120 GPa at 20 volume percent SiC. This substantial increase is attributed to the existence of the second phase in the matrix. The data points for E are plotted as a function of volume percent SiC in Fig. 1 and then pooled together to yield the following correlation

$$E = 68.6 + 2.2X$$

with $SE = 6.4$ GPa and $R = 0.95$, where X is the volume percent SiC, SE is the standard error of estimate, and R is the correlation coefficient. The second variable effecting E is the homogeneity of the materials. Perhaps this effect is most noticeable in specimens 8 to

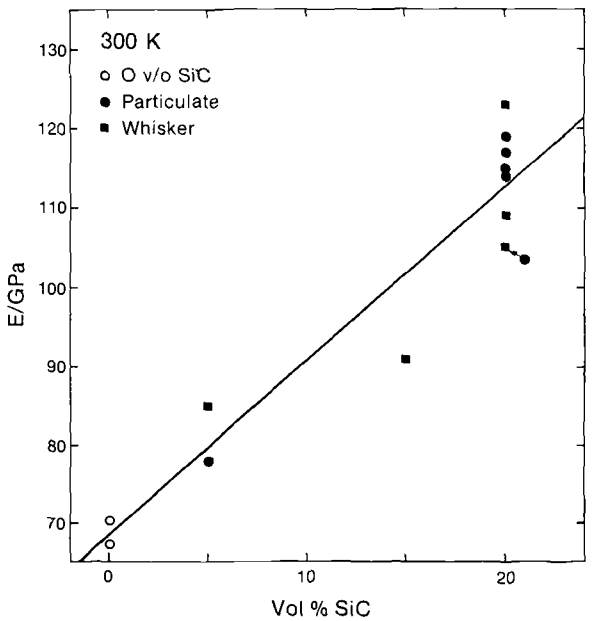

FIG. 1—*Dynamic Young's modulus* E *as a function of volume percent SiC for metal matrix composites tested at 300 K.*

11. These four specimens were cut from the same plate. However their E-values vary from 114 to 119 GPa. Since we used longtitudinal wave stresses, we believe this variation is due to variations in the distribution of the SiC particles in the specimens. The third effect is that of temperature. This effect is shown for specimens 12 and 13 only. Figure 2 shows a plot of E as a function of temperature T where E decreases linearly with increasing T. Here E decreases from about 106 to 70 GPa as T increases from 473 to 638 K. Again, we pooled the data points for both specimens to obtain the following correlation between E and T

$$E = 138.7 - 0.11T$$

where E is in GPa and T is in Kelvin (SE = 3.3 GPa and R = 0.98). One should point up that different slopes can be obtained for each specimen separately, but, as can be seen from Fig. 2, the expected difference is rather minor.

Internal Friction

The results of the measurements of internal friction or mechanical damping for 6061 aluminum + 20 volume percent SiC_w and 2124 aluminum + 15 volume percent SiC_w are presented as a function of strain amplitude in Figs. 3 and 4. The internal friction is clearly amplitude dependent, rising to a peak and then dininishing (Fig. 3), or showing the classical break away behavior (Fig. 4). The reason for the peak in Fig. 3 is not clear but could be connected with the relative concentrations of precipitates in the microstrucutres of the 6061 and 2124 aluminum alloys. This possible explanation of the peak is elucidated further in the later part of the discussion. The curves are of the form $Q^{-1} = Q_I^{-1} + Q_H^{-1}$, where Q_I^{-1} is the amplitude independent part of the internal friction (horizontal parts of the curves) and Q_H^{-1} is the amplitude dependent part (the parts of the curves that curve upwards). These curves are now analyzed in terms of the Granato-Lucke (G-L) [6] theory of amplitude dependent damping due to dislocation lines and their break away from pinning points at high strain amplitude. The theory recommends a plot (a G-L plot) of ϵQ_H^{-1} versus ϵ^{-1} to

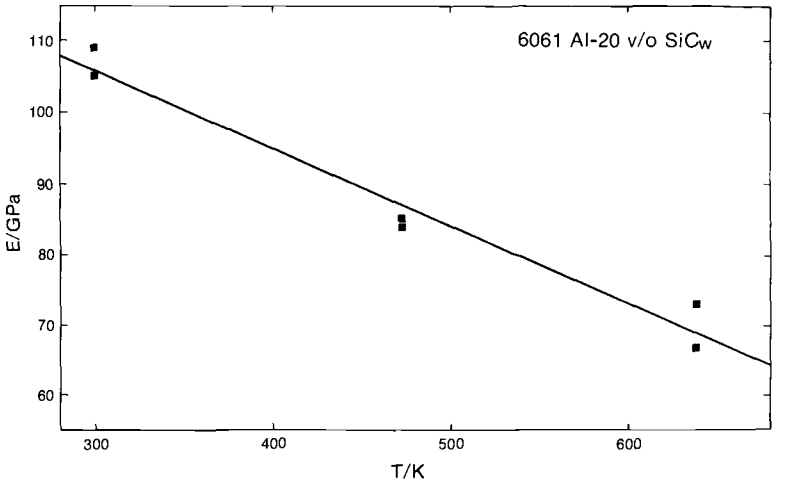

FIG. 2—*Temperature dependence of dynamic Young's modulus for 6061 aluminum + 20 volume percent SiC_w.*

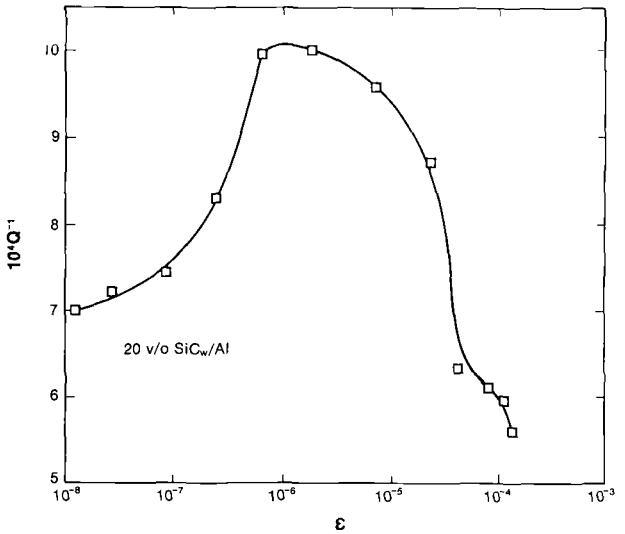

FIG. 3—*Strain amplitude dependence of mechanical damping or internal friction for 6061 aluminum + 20 volume percent SiC_w at 300 K.*

obtain estimates of the minor pinning length of dislocation lines L_c and the mobile dislocation density Λ. Such plots are shown in Figs. 5 and 6. Most of the data points in Fig. 6 fall on a straight line on the log-linear plot as predicted by the theory. In Fig. 5 we see that the expected straight line is not evident. Such curvature has been noted previously [6] for some materials. To proceed with the G-L analysis, one refers to the slope of the curve at the

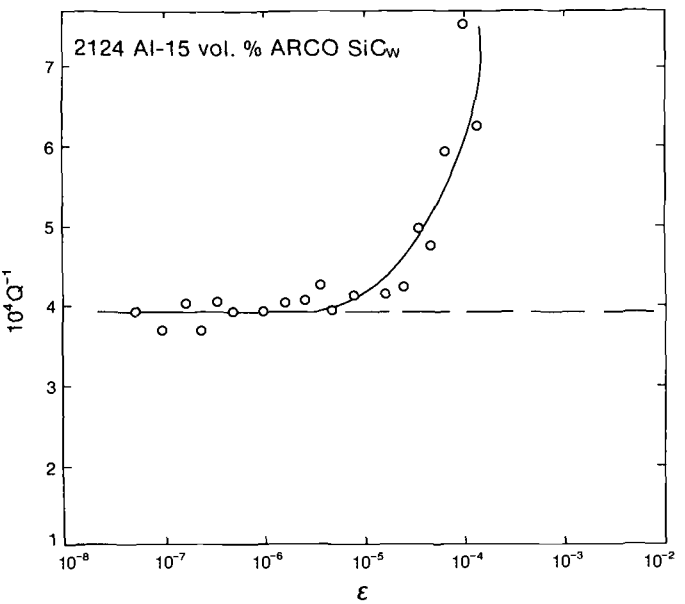

FIG. 4—*Strain amplitude dependence of mechanical damping or internal friction for 2124 aluminum + 15 volume percent SiC_w at 300 K.*

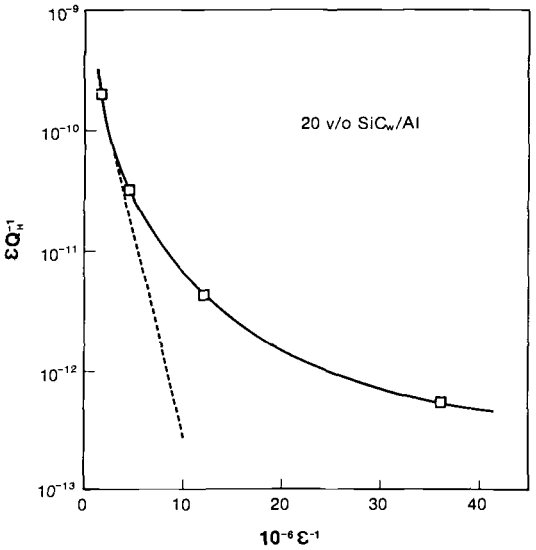

FIG. 5—*Granato-Lucke plot for 6061 aluminum + 20 volume percent SiC_w.*

smallest values of $1/\epsilon$. The slope and intercept of the G-L plot are given by Ref *6*

$$\text{Slope} = C_2 = -K\epsilon^1 \, a/L_c$$
$$\text{Intercept} = I = \Lambda\Omega\Delta_0 \, LN^3N \, K\epsilon^1 \, A/\pi^2 \, L_c^2$$

where

$K = 32G/\pi^2 p^2 RE$,
ϵ^1 = misfit parameter,
a = lattice parameter,
$\Omega = \omega/\omega_0$ = frequency/resonant frequency = 1,
$\Delta_0 = 4/(1-\nu)/\pi = \frac{1}{4}$,
ν = Poisson's ratio,
$A = \pi\rho(a^1)^2$,
ρ = mass density,
a^1 = Burgers vector of dislocation,
G = shear modulus,
p = number between 2 and 3,
R = resolved shear stress factor, and
E = Young's modulus.
L_N = dislocation network length

For the analysis we have set $\epsilon^1 = 10^{-2}$ as suggested in Ref *6*, $p = 2.5$, $R = 0.5$, $G/E = 1/2.66$, $a = 4.05 \times 10^{-10}$ m, $a^1 = 2.86 \times 10^{-10}$ m, $\rho = 2700$ kg/m^3, and $L_N = 10^{-6}$m (the approximate interfiber spacing). The results of the calculation for L_c and Λ are given in Table 2. The minor pinning lengths are found to be 2 and 0.02 μm, and the mobile dislocation densities 10^8 and 10^{10} cm^{-2}, for the 6061 and 2124 MMCs, respectively.

The results of the G-L analysis suggest that, since the minor pinning lengths differ in the two materials, the mechanism controlling the yield stress operates on a finer scale in the 2124 MMC than in the 6061 MMC. This will be influenced undoubtedly by the details of

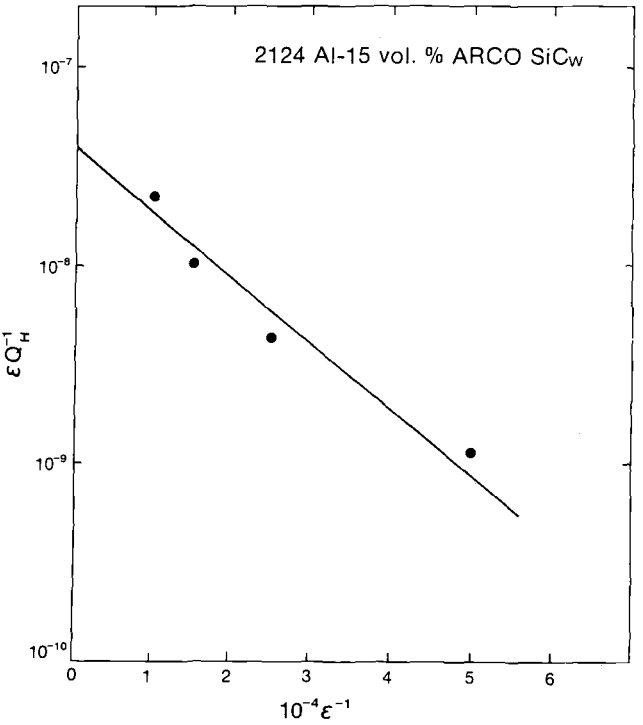

FIG. 6—*Granato-Lucke plot for 2124 aluminum + 15 volume percent SiC_w.*

the heat treatment of the aluminum alloys and by the processing to introduce the SiC. Fine scale precipitates (such as GP zones) may be pinning the dislocations in the 2124 aluminum. The relative concentrations of pinning points (given by L_c^{-2}) seem to offer an explanation for the peak in Fig. 3 and the classical break away in Fig. 4. In the 2124 aluminum MMC the minor pinning length (0.02 μm) is very small, representing a high concentration of pinning points (3×10^{15} m^{-2}). The scale of the pinning points in the 2124 aluminum MMC is thus much finer than that of the SiC whiskers (typically 1 μm; corresponding concentration is 10^{12} m^{-2}). For this material with abundant pinning points for the dislocations the break away strain would be expected to be relatively high and was measured as approximately 10^{-5} (Fig. 4). On the other hand, in the 6061 aluminum MMC the minor pinning length is 2 μm, the concentration of pinning points is therefore 3×10^{11} m^{-2}, the spacing of the SiC whiskers is typically 1 μm, the concentration of the whiskers is typically 10^{12} m^{-2}, and the expected break away strain for this material with relatively few pinning points is therefore low (measured as approximately 5×10^{-8}, see Fig. 3).

TABLE 2—*Results of Granato-Lucke analysis for the 6061 and 2124 metal matrix composites.*

Material	Minor Pinning Length, L_c (μm)	Mobile Dislocation Density, Λ (cm^{-2})
6061 + 20 volume percent SiC_w	2	10^8
2124 + 15 volume percent SiC_w	0.02	10^{10}

After break away, dislocations will continue to move and at higher strain amplitudes will become pinned again on new pinning points. Thus the damping level will decrease again at high strain amplitudes. This situation occurred for the 6061 aluminum MMC within the range of strain amplitudes obtainable with the PUCOT (10^{-8} to 3×10^{-4}) (Fig. 3) but did not occur for the 2124 aluminum MMC (Fig. 4). At higher strain amplitudes (say 10^{-3}) the curve in Fig. 4 would pass through a peak and then be reduced to low values of damping again. The mobile dislocation densities listed in Table 2 appear to be high for nominally annealed material. However, these values (up to 10^{10} cm^{-2}) are comparable with those observed by Arsenault and Fisher [7] using TEM on 6061 aluminum + 20 volume percent SiC (whiskers and particles). Their micrographs show high densities of dislocations clustered around the SiC fibers. These dislocations were presumed to be generated by stresses resulting from differential contraction (on cooling) between SiC and the 6061 aluminum matrix.

Conclusions

This study of the anelastic and elastic properties of MMCs using the PUCOT leads to the following conclusions:

1. The addition of SiC to the aluminum alloys studied raises dynamic Young's modulus by up to 60%.
2. The following general correlation was found for the composition dependence of dynamic Young's modulus:

$$E = 68.6 + 2.2X \ (E \text{ in GPa}, X \text{ in volume percent SiC}).$$

3. In adjacent specimens of 6061 aluminum + 20 volume percent SiC_p cut from the same plate there was a 4% variation in dynamic Young's modulus.
4. The temperature dependence of dynamic Young's modulus shows a linear decrease for 6061 aluminum + 20 volume percent SiC_w according to this correlation:

$$E = 138.7 - 0.11T \ (E \text{ in GPa}, T \text{ in Kelvin}).$$

5. The mechanical damping or internal friction in the MMCs studied is strain amplitude dependent.
6. The damping data, analyzed in terms of the Granato-Lucke theory, yield values for the minor pinning lengths of dislocation lines of 2 and 0.02 μm, and for the mobile dislocation densities of 10^8 and 10^{10} cm^{-2}, for the 6061 and 2124 MMCs, respectively.
7. Macroscopic (bulk) measurements of mechanical damping, when analyzed in terms of an appropriate theory of dislocation damping, allow information on the microscopic features of MMCs to be extracted.

Acknowledgments

The authors would like to express their thanks to Frank Boensch of the Air Force Flight Dynamics Laboratory and the Air Force in providing the material and sponsorship for a portion of this work. (Contract No. F33615-81-C-3234) and to LTVAD/VMAPD for their assistance and support.

References

[1] Ledbetter, H. M. and Datta, S. K., *Materials Science and Engineering,* Vol. 67, 1984, pp. 25–30.
[2] Ledbetter, H. M., Datta, S. K. and Kriz, R. D., *Acta Metallurgica,* Vol. 32, 1984, pp. 2225–2231.
[3] Marx, J., *Review of Scientific Instruments,* Vol. 22, 1951, pp. 503–509.
[4] Robinson, W. H. and Edgar A., *IEEE Transactions on Sonics and Ultrasonics,* Vol. SU-21, 1974, pp. 98–105.
[5] Wolfenden, A. and Harmouche, M. R., *Journal of Materials Science,* Vol. 20, 1985, pp. 654–660.
[6] Granato, A. and Lucke, K., *Journal of Applied Physics,* Vol. 27, 1956, pp. 583–593 and 789–805.
[7] Arsenault, R. J. and Fisher, R. M., *Scripta Metallurgica,* Vol. 17, 1983, pp. 67–71.

Robert W. Reed[1]

Noncontact Ultrasonic Evaluation of Metal Matrix Composite Plates and Tubes

REFERENCE: Reed, R. W., **"Noncontact Ultrasonic Evaluation of Metal Matrix Composite Plates and Tubes,"** *Testing Technology of Metal Matrix Composites, ASTM STP 964*, P. R. DiGiovanni and N. R. Adsit, Eds., American Society for Testing and Materials, Philadelphia, 1988, pp. 216–226.

ABSTRACT: Noncontacting electromagnetic acoustic transducers (EMATs) are used to generate and receive wideband pulses of ultrasound in graphite/aluminum (Gr/Al) plates and tubes. High precision velocity and attenuation measurements are used to locate defects and to determine elastic moduli. Both static global and scanned local values of the attenuation and velocity are measured by using large or small receiver EMAT separations, respectively. Nondispersive, shear horizontal, and lowest order symmetric Lamb waves are employed along with a four-transducer method which eliminates measurement uncertainties associated with EMAT lift-off variations. Elastic moduli of Gr/Al plates are determined from ultrasonic data.

KEY WORDS: metal matrix composites, graphite/aluminum, nondestructive evaluation, electromagnetic acoustic transducers (EMATs), elastic moduli evaluation

The development of reliable and cost effective methods for the nondestructive evaluation (NDE) of metal matrix composite (MMC) parts and structures is essential to permit the use of these materials in critical applications. In many of the envisioned applications, the structures will be manufactured with only one or several plys of precursor wires. The resulting structure will have thin (less than 1 mm) walls which are difficult to inspect using conventional ultrasonic immersion methods. In addition, immersion of some of the candidate MMC systems in water could lead to undesirable corrosion of the matrix metal.

This paper represents the status of an ongoing effort to develop noncontact ultrasonic methods for the NDE of thin MMC structures. The approach utilizes the generation and reception of ultrasonic propagation modes that exist only in thin plates or plate-like structures, namely, plate or Lamb waves. Electromagnetic acoustic transducers (EMATs) are used to generate these ultrasonic waves.

Measurement Methods

The two ultrasonic propagation modes that are used in this investigation are the lowest order symmetric Lamb (SL) mode and the shear horizontal (SH) mode. Wideband pulses with center frequencies in the 200 kHz to 1 MHz range are used so that the wavelength is greater than the plate thickness of the structures inspected. Both attenuation and velocity are measured for these propagation modes. These parameters permit the evaluation of structural variations or flaws, as well as a determination of the elastic constants which characterize the material. An essential feature of the use of these particular propagation

[1] Senior research engineer, United Technologies Research Center, East Hartford, CT 06108.

modes is that the entire propagation path is accessible to interrogation by receiver transducers placed on the surface of the plate (or plate-like structure.)

EMATs are used to generate and receive the ultrasonic signals. They permit ultrasonic measurements without the use of any acoustic coupling fluid between the transducer and the part. This facilitates scanning the transducers over the surface of the structure. By using appropriately designed coils and magnetic field orientations, the EMATs can be constructed to generate and receive the desired SL or SH waves. A wideband, single element construction is used for the EMATs designed for this work. The wideband construction permits the use of single, half cycle, sine wave sound pulses which, in turn, permit the use of time interval counting techniques for the measurement of the sound velocity even in a scanning mode of operation. The wideband design does suffer from a lower conversion efficiency than the narrow band, multielement EMATs more commonly used. However, the use of special low-noise electronics, coupled with careful matching of the transducers to the circuitry, gives signal-to-noise ratios typically in excess of 20 dB.

The wideband EMATs used in this investigation are placed on the surface of the plate being evaluated. (The EMAT coils are typically within about 0.5 mm of the surface with the housing resting on the surface.) Access to the edges of the plate is unnecessary. In addition, the EMATs are bidirectional so that they are equally sensitive to waves traveling to the right or to the left as schematically illustrated in Fig. 1. This would not be true for typical piezoelectric transducers used with wedges or in immersion to generate the same propagation modes. The fact that the EMATs are bidirectional and can be positioned on the surface of the plate, permits the use of a 4-transducer measurement technique for making accurate attenuation measurements in the presence of large, random variations in the acoustic coupling of the acoustically generated radio frequency field to the transducers. These variations are caused by changes in the lift-off distances betweeen the EMAT coil elements and the surface of the plate. As a part is scanned, lift-off variations may cause signal variations as large as 10 dB. These variations would obscure relevant attenuation variations in an MMC plate which may be as small as 1 dB. The four-transducer arrangement of two receivers located between two transmitters, as shown in Fig. 1, permits the complete rejection of the unwanted lift-off errors so that accurate measurement of the absolute attenuation in the plate is possible.

By referring to Fig. 1, it is seen that variations in the transmitter coupling efficiency equally affect the signal levels seen by both receiver EMATs. Hence, signal voltage ratios computed for the two receivers are independent of transmitter coupling variations. Variations in receiver coupling efficiency will have a large effect on this voltage ratio. The receiver coupling problem is overcome by use of a second transmitter. This can be seen by considering the following algebra. The apparent attenuation, α'_{12}, when transmitter 1 is pulsed

$$\alpha'_{12} = \frac{1}{\Delta x} \log \left(\frac{V_{11}}{V_{12}} \right) = \alpha + G_{R_1} - G_{R_2} \tag{1}$$

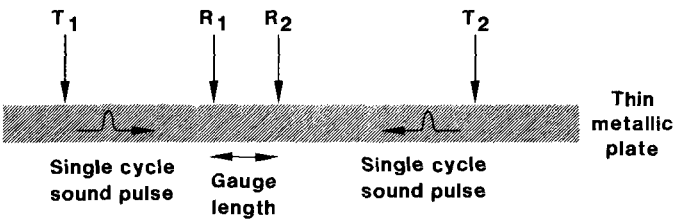

FIG. 1—*Schematic representation of the four-transducer method for measuring attenuation with EMATs.*

includes the actual attenuation, α, and an error term, G_R, for each receiver caused by liftoff or transducer sensitivity differences. The first subscript on the V's indicates the transmitter and the second subscript indicates the receiver in Fig. 1 for which the voltage, V, is measured. Δx is the distance or gage length between the receivers. When transmitter 2 is excited, the apparent attenuation is given by

$$\alpha'_{21} = \frac{1}{\Delta x} \log \left(\frac{V_{22}}{V_{21}} \right) = \alpha - G_{R_1} + G_{R_2} \tag{2}$$

Adding Eqs 1 and 2 eliminates the error terms and yields

$$\alpha = \frac{1}{2\Delta x} \left[\log \left(\frac{V_{11}}{V_{12}} \right) + \log \left(\frac{V_{22}}{V_{21}} \right) \right] \tag{3}$$

Hence, by the measurement of four voltages, the absolute attenuation can be calculated using Eq 3.

The voltages shown in Eq 3 are determined using a novel, four-channel, gated peak detector developed for this application. The peak detector unit performs the indicated calculations and outputs the attenuation [*1,2*]. The resultant attenuation is accurate to 0.5 dB with a typical repeatability of 0.25 dB. A unique feature of the gated peak detector is that a computing, gain control, feedback loop is used to maintain the peak voltage of the single half cycle waveform at a fixed level. Hence, time delay intervals between the pulses in the individual channels can be measured between fixed phase points on the waveforms. Time intervals accurate to 10 ns on a single shot basis are typically achieved independent of the normal amplitude variations observed during a scanning operation. Multiple time interval measurements may be averaged to improve the resolution. The time interval and attenuation data are simultaneously output by the four-channel, gated peak detector.

The EMATs and the interrogating SL waves can be also used to observe the reflections of the wideband ultrasonic pulses from cracks or other discontinuities in a scanned part. If a crack in the plate is located between the receiver EMATs, R_1 and R_2, in Fig. 1, then when a sound wave travels toward the right from EMAT transmitter T_1, a pulse reflected back from the crack should be observed at R_1 immediately following the arrival of the direct SL wave pulse. Only the direct SL wave pulse, attenuated by the crack, will be observed at R_2. If the crack is to the right of R_2, the reflected pulses will be detected by both R_1 and R_2. Unfortunately, the transmitter EMATs are bidirectional and send pulses in both directions (both to the right and left in Fig. 1). Hence, a crack located to the left of T_1 will also send relected pulses toward the right to both R_1 and R_2. These reflected pulses will also arrive after the arrival of the direct pulse (sent directly to the right) at R_1 and R_2. If the 4-transducer array is scanned over a plate and a gated peak detector is set to record pulses occurring in time just after the arrival of the direct pulse, an image of the cracks in the plate can be created. However, a double image will result from the fact that an echo will be seen when the crack is located just to the right of R_1 and just to the left of T_1. Efforts are underway to use computer processing of the data from various receivers, using the two transmitters, to eliminate the double image.

C-Scans in MMC Plates

A 4-transducer array of EMATs may be used to evaluate local variations in the properties of a unidirectional graphite (P55)/aluminum (6061) plate 33 cm long in the fiber direction and 50 cm wide. The resolution or detail in the resultant display depends on the gage length

between the two receiver transducers. The data presented in this section were obtained with a receiver gage length of 1.0 cm and with the transmitters located 6.0 cm from the receivers. The four EMATs were rigidly attached together and connected to the end of the manipulator of a computer-controlled scanning system. The transmitter EMATs were excited with unipolar, 250 A, 1 μs wide pulses at a 1 kHz repetition rate. The lowest order SL mode was used for the measurements made in the single-ply graphite/aluminum (Gr/Al) plate approximately 1 mm thick. Attenuation, pulse-echo, and velocity data, as a function of receiver location on the plate surface, were digitally recorded and used to create C-scan images. The data were obtained every 0.125 cm along the scan direction, and the scan lines were separated by 0.125 cm. The scan direction was always coincident with the sound propagation direction.

Figure 2 is a gray scale image of the SL wave attenuation for the center, 24.8 cm (fiber direction) by 31.5 cm, portion of the plate. The scan direction is perpendicular to the fiber direction and is the low speed propagation direction. The original image on the computer screen contained 16 levels of gray (or color). The darkest level in the image corresponds to an attenuation of 0 dB/cm and the lightest level corresponds to 10.4 dB/cm. The bright vertical band in the upper right hand corner results from the attenuation caused by a crack in the plate. The crack image appears to be wide because of the 1 cm gage length between the receiver EMATs. This crack is perpendicular to the sound propagation direction so that a large sound attenuation results as the SL wave passes through the crack. Flaw resolution

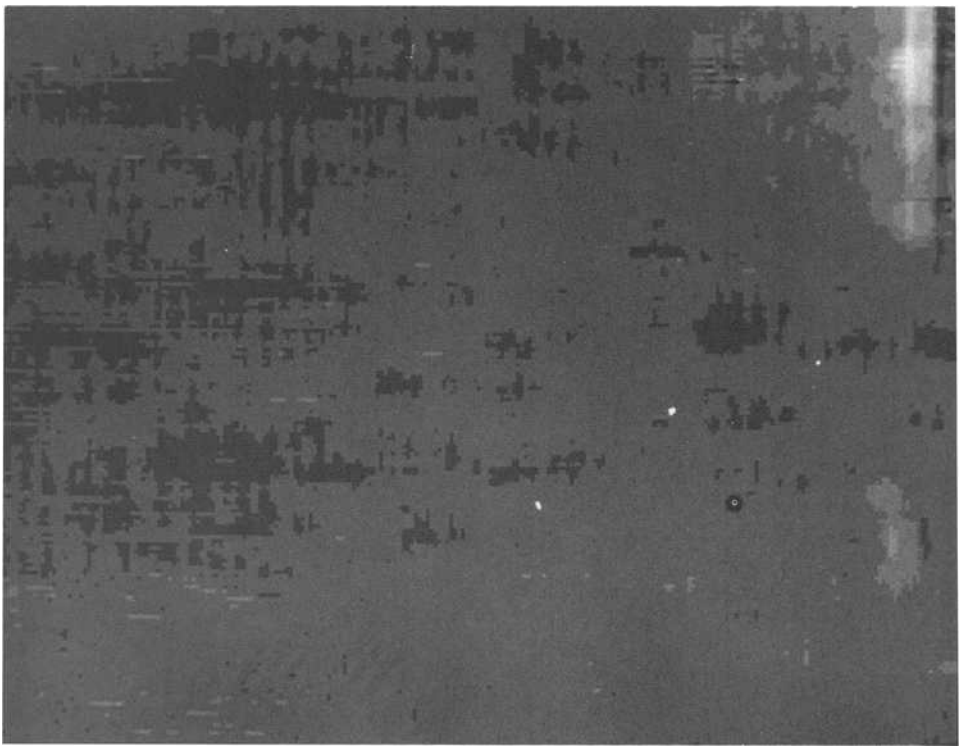

FIG. 2—*Attenuation image of Gr(P55)/Al(6061) plate. The darkest level corresponds to 0 db/cm and the lightest level to 10.4 dB/cm. The sound propagation direction is perpendicular to the graphite fibers.*

will be improved in future scans when the ability to use shorter receiver gage lengths is available.

Figure 3 is a pulse-echo image of the same portion of the plate as displayed in Fig. 2. In this case, back reflected pulses, detected by receiver R_1 immediately after the passage of the direct pulse, are recorded by a separate gated peak detector. The brightest levels correspond to the biggest reflections. These data are simultaneously recorded along with the attenuation and velocity for a single scan of the plate. The general precursor lay-up pattern is now observable in the image. The crack is again located in the upper right hand corner. Unfortunately, a second image of the crack appears about one quarter of the way across the plate to the left. This is consistent with the description of this method previously given. The light band along much of the top of the image results from an off-angle reflection from the plate edge. When a computer algorithm becomes available for eliminating the double image, the method will provide excellent images of flaws which act as acoustic reflectors. The amplitude of the reflections from individual precursor wires may provide information concerning the quality of the interwire bonding.

Figure 4 is the attenuation image obtained by scanning the transducer array along the fiber or high propagation speed direction. The image area corresponds to a 13.5 cm (along the fibers) by 39.4 cm section of the plate. The center of this image is approximately at the same position on the plate as that for Fig. 2 and 3. The attenuation range for this scan is 1.2 to 2.9 dB/cm with the brightest level corresponding to the highest value. The amount

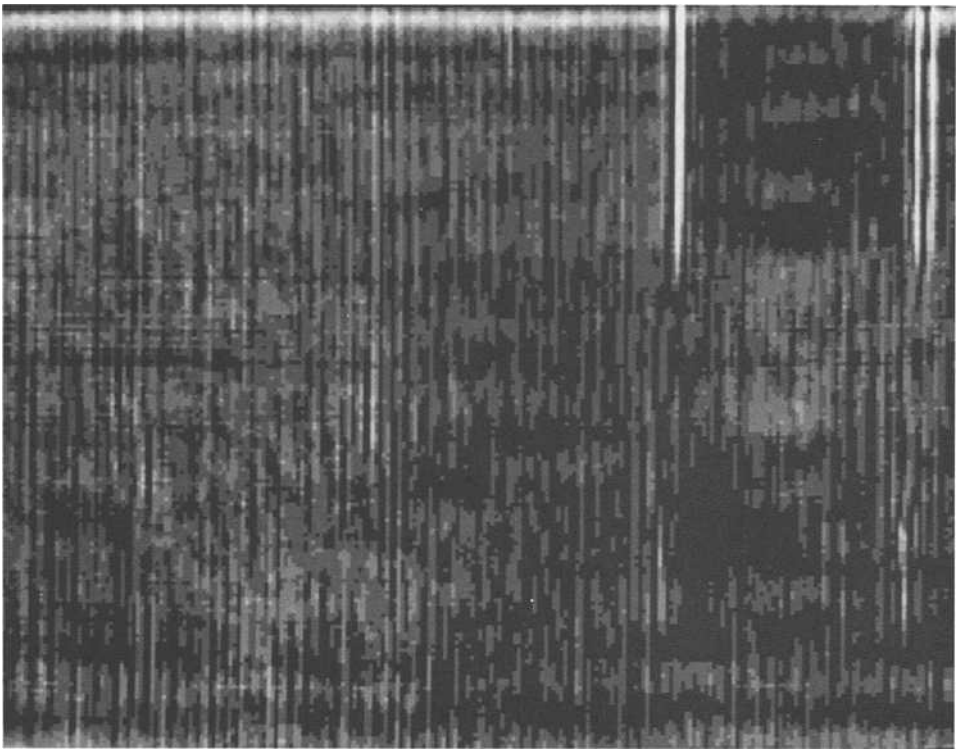

FIG. 3—*Pulse-echo image of Gr(P55)/Al(6061) plate. The brightest levels are from the strongest reflections. The sound propagation direction is perpendicular to the graphite fibers.*

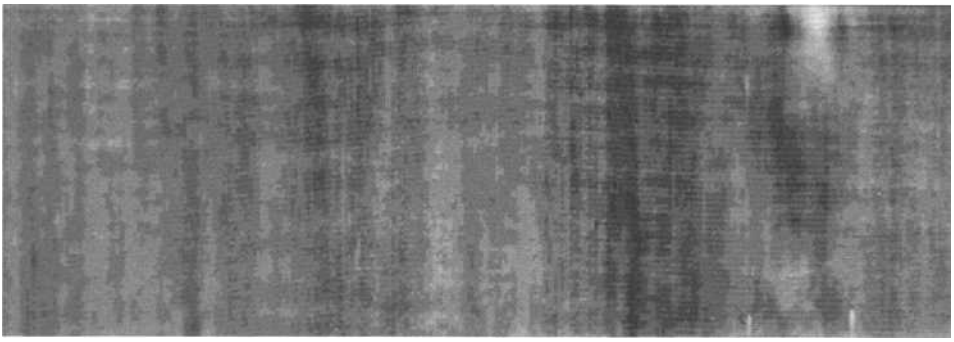

FIG. 4—*Attenuation image of Gr(P55)/Al(6061) plate. The darkest level corresponds to 1.2 dB/cm and the lightest level to 2.9 dB/cm. The sound propagation direction is parallel to the graphite fibers.*

of the crack length scanned (Fig. 4) is much shorter than for the scan in the other direction (Fig. 2). The bright spot in the upper right of this image results from the end of the crack seen in Fig. 2. The general level of attenuation is lower for this scan direction since the prominent discontinuities are parallel to the sound propagation direction and as a result they reflect very little energy out of the sound beam.

Figure 5 is a velocity image obtained from the same scan as used for Fig. 4. The velocity range in this image is from 8920 to 9600 m/s with the brightest level corresponding to the highest value. The higher value areas on the image probably result from areas where the precursor wire packing density is higher with a resulting increase in fiber volume fraction. The higher velocity areas in this figure generally are located where the lower (darker) attenuation areas are found in Fig. 4. It is expected that more tightly packed precursor wires would have a lower attenuation.

The pulse-echo image for the same scan direction as for Figs. 4 and 5 shows considerably less detail than for the other direction, and it is not reproduced here. It is expected that this should be the case since the sound scattering discontinuities are parallel rather than perpendicular to the propagation direction.

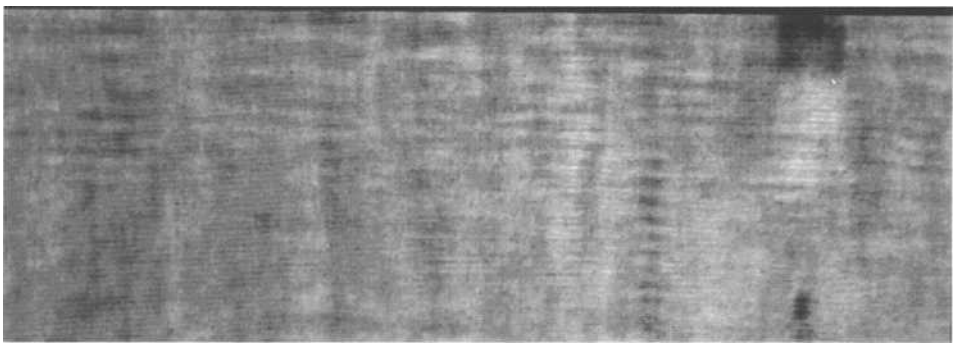

FIG. 5—*Velocity image of Gr(P55)/Al(6061) plate. The darkest level corresponds to 8920 m/s and the lightest level to 9600 m/s. The sound propagation direction is parallel to the graphite fibers.*

SL Wave Velocity Measurements in Tubes

Transmitter and receiver EMATs were constructed to allow measurements on MMC tubes. The EMAT coils were constructed to be conformal to the tube and to provide sound propagation in the tubular axial direction. In the present case, the Gr/Al tubes have an outside diameter of 5.1 cm. The propagation mode generated is the lowest order, pseudosymmetric Lamb (SL) mode.

These EMATs were employed to measure the SL wave velocity in a 2-ply graphite (P100)/aluminum (6061) tube with a ±23° lay-up. The tube is 30.5 cm long with a 5.1 cm outside diameter. The layup is designed to provide a minimum coefficient of thermal expansion (CTE). Velocity measurements were made every 45° around the circumference and at 2.5, 7.6, 12.7, 17.8, 22.9, and 27.9 cm from one end of the tube. The receiver EMATs had apertures of 1 cm and were seperated by 1 cm. The measured velocity values are tabulated in Table 1.

The average velocity value was determined to be 8860 m/s with a standard deviation of 380 m/s. If the theoretical values of the major and minor Poisson's ratios of 1.1 and 0.17 are used, the axial Young's modulus can be computed from the velocity data and the density which was taken as 2.5 g/cm^3. The resultant average modulus is 160 GPa. It is not yet known if the observed variations in the velocity value shown in the table are indications of local variations in the CTE of the tube. However, the parameters which can affect the velocity, that is, density, fiber volume fraction, matrix microstructure, etc., all can affect CTE.

Elastic Moduli Evaluations

Foltz, Bertram, and Anderson [*3*] have developed the necessary equations for determining the in-plane elastic moduli from a set of plate wave velocity measurements. Under the assumption that a unidirectional MMC plate may be considered to be an orthotropic plate, the dispersion relation is given by the determinant

$$\begin{vmatrix} (A_{11} - \rho v^2) & A_{12} \\ A_{12} & (A_{22} - \rho v^2) \end{vmatrix} = 0 \tag{4}$$

In Eq 4 ρ is the plate density and v is the wave phase velocity. The A_{ij} are related to the

TABLE 1—*Symmetric Lamb wave velocities for MMC tube.*

	Velocity in m/s					
	Axial Location					
Angle, deg	2.5 cm	7.6 cm	12.7 cm	17.8 cm	22.9 cm	27.9 cm
0	9070	9450	8710	9040	9310	9360
45	8580	8840	9210	8590	9070	8550
90	9010	8600	8860	8300	8750	9100
135	8730	8900	8500	8680	9420	9310
180	9760	9320	9050	9270	9230	9790
225	8910	8320	8490	8340	8340	8560
270	8870	8490	8620	8540	8630	8640
315	8630	8860	8520	8370	8680	9040

plate stiffness coefficients, Q_{ij}, by

$$\begin{aligned} A_{11} &= Q_{11}\cos^2\theta + Q_{66}\sin^2\theta \\ A_{22} &= Q_{66}\cos^2\theta + Q_{22}\sin^2\theta \\ A_{12} &= (Q_{12} + Q_{66})\sin\theta\cos\theta \end{aligned} \tag{5}$$

where θ is the angle between the propagation direction and the X-axis which is taken along the fiber direction. Equation 4 has two roots for each angle θ. These correspond to fast and slow plate modes of propagation. Along the X- and Y-axes, the fast and slow modes correspond to the SL and SH modes, respectively. For off-angle directions, the propagating modes are not purely longitudinal or shear in character. In this case, the fast and slow modes are referred to as pseudo-SL or pseudo-SH waves. The stiffness coefficients are related to the velocities, v_{SL} and v_{SH}, for the 0 and 90° propagation directions by

$$\begin{aligned} v_{SL}(0°) &= (Q_{11}/\rho)^{1/2} \\ v_{SL}(90°) &= (Q_{22}/\rho)^{1/2} \\ v_{SH}(0°) &= v_{SH}(90°) = (Q_{66}/\rho)^{1/2} \end{aligned} \tag{6}$$

The stiffness coefficients are related to the engineering elastic moduli by

$$\begin{aligned} Q_{11} &= E_{11}/(1 - \nu_{12}\nu_{21}) \\ Q_{22} &= E_{22}/(1 - \nu_{12}\nu_{21}) \\ Q_{12} &= \nu_{12}Q_{22} \\ Q_{66} &= G_{12} \\ \nu_{21}E_{11} &= \nu_{12}E_{22} \end{aligned} \tag{7}$$

Here E_{11} and E_{22} are Young's like moduli along the X- and Y-axes, respectively. G_{12} is the shear modulus and ν_{12} and ν_{21} are the major and minor Poisson's ratios.

Equations 4 through 7 may be used along with measurements of v_{SL} and v_{SH} to find E_{11}, E_{22}, G_{12}, and ν_{12}. Typically, the ν's are measured along the X- and Y-axes, but at least one measurement at an off-angle direction is required to permit the calculation of all the unknown parameters. The value of the plate density is assumed to be available from an independent measurement.

Foltz et al. [3] also have shown that, for all propagation directions except 0 and 90 deg, the group and phase velocity vectors are not colinear. As a result, the propagating wave front is not perpendicular to the propagation direction. Hence, extreme care must be exercised in making off-axis measurements in order to insure that the appropriate phase velocity is determined. This problem may cause difficulties when contact type piezoelectric transducers are applied to the specimen edges for generating and receiving the sound waves. The result is that the parallel reflecting specimen edges to which the transducers are bonded are

not oppositely located across the sample from each other. This problem is sufficiently severe that it is typically impossible to make all of the velocity measurements in the same part of the specimen. These problems are all largely eliminated by using EMATs which can simply be located appropriately on the specimen surface. Only the reciever gage length is important in terms of the material being evaluated; the rest of the propagation path may be conveniently located to provide for the best overlap in the gage length region of the specimen. This point is particularly important in view of the fact that velocity variations may typically exceed 10% at different locations in a Gr/Al plate as is evidenced in the C-scan data shown previously. EMATs are also ideal for use in time delay (velocity) measurements, in that there are no acoustic bond effects to generate time interval errors.

The calculation of the elastic moduli and Poisson's ratio from the velocity data can often lead to anomalous results for ν_{12} because of extreme sensitivity to small errors in the velocity data. Better results are typically obtained by making additional velocity measurements along a number of off-axis angles. The resultant, overly determined data set is then least squares fitted to theoretically determined velocities by making small iterations of the stiffness parameters. In the present case, the uncertainties in the velocity values contribute the smallest error with an accuracy typically better than 0.5%. The determination of the propagation angles is no better than ±2°. The largest uncertainty comes from the normal variation of the elastic moduli at different locations in the plate and the fact that the measurement gage lengths, for different propagation directions, do not include exactly the same portion of the plate.

The elastic moduli values were determined from SL and SH wave data taken in the same large, unidirectional single-ply Gr(P55)/Al(6061) plate for which scan data were presented in Figs. 2 through 5. Phase velocity angles of 0, 30, 45, 60, and 90° were used. The SH and SL data were taken with 1.0 and 4.25 cm gage lengths, respectively, so that the 10 ns time interval uncertainty contributes approximately the same error to the two velocities. For each angle, the orientations of the transmitter and twin receiver EMATs were carefully laid out on the plate, along with the computed propagation path (group velocity) directions as calculated using representative elastic moduli. The resultant velocities are given in Table 2 for two locations on the plate.

The resultant SL and SH wave velocities for the 0° direction are in excellent agreement with those previously reported for longitudinal and torsional (shear) waves in Gr(P55)/Al(6061) precursor wires with approximately 40 to 43% graphite [2].

The resultant elastic moduli, calculated using the notation presented previously are for location 1: E_{11} = 182 GPa, E_{22} = 34.2 GPa, G_{12} = 22.3 GPa, ν_{12} = 0.626, and ν_{21} = 0.118; and for location 2: E_{11} = 177 GPa, E_{22} = 34.0 GPa, G_{12} = 21.6 GPa, ν_{12} = 0.571, and ν_{21} = 0.11.

SL wave velocities were also measured in a 4-ply, Gr(P100)/Al(6061) plate with a ±23° lay-up that was designed for a low CTE. The plate was 15.2 cm square at the time of the

TABLE 2—*Measured phase velocities for SL and SH waves in Gr/Al plate.*

	Location 1		Location 2	
Angle, deg	v (m/s) SL	v (m/s) SH	v (m/s) SL	v (m/s) SH
0	8807	2807	8725	2790
30	7880	3023	7600	2990
45	6957	3175	6768	3129
60	5445	3220	5412	3196
90	3735	2925	3722	2930

TABLE 3—*Measured phase velocities for SL waves in four-ply Gr/Al plate.*

Prior to Heat Treatment		After Heat Treatment	
Location	v (m/s) SL	Location	v (m/s) SL
1	8980	1	7400
2	8500	2	7900
3	9360		
4	9250		
5	9440		
6	9420		

initial measurements which were made in the "as received" condition. The plate was then heat-treated for one hour at 530°C in an argon atmosphere. This was followed by a water quench and a subsequent aging for 18 h at 163°C. The purpose of the heat treatment was to put the 6061 aluminum matrix into a T6 temper. The plate was then cut up for mechanical testing. One of the cut off pieces was provided for SL wave measurements before mechanical tests were run. Velocity measurements could only be made at two locations on that small piece. The velocity data for both conditions are provided in Table 3. All of the velocities are for the high-speed symmetry axis.

The average velocity before heat treatment was 9160 m/s, and after treatment it was reduced to 7650 m/s. These velocities yield computed values of E_{11} of 171 and 119 GPa, respectively. For this particular specimen, the heat treatment lead to a substantial reduction in the modulus.

The observed loss of stiffness with heat treatment may be related to the loss of shear modulus in Gr(P55)/Al(6061) precursor wires to which similar heat treatment was supplied as reported by Reed and Bertram [*2*]. In that study, only the shear modulus underwent a significant reduction, while the Young's modulus remained nearly unchanged. The results of that study imply that the E_{11} modulus, along the fiber direction, would not change significantly in a unidirectional plate which had undergone a T6 heat treatment. However, in a cross-plied plate, such as the one studied here, the high symmetry Young's modulus will be affected by the precursor shear modulus. Hence, any heat treatment which affects the shear modulus and Poisson's ratio in a unidirectional plate will be expected to cause changes in the high symmetry Young's modulus of the cross-plied plate which has individual layers with a similar construction.

Conclusions

Methods are under development for using EMATs in the noncontact ultrasonic evaluation of metal matrix composite structures. Data have been obtained from MMC plates and tubes which show that these methods offer considerable promise. The SL wave velocity and attenuation measurements are used to produce C-scans that produce images of variations in the properties of a plate. The SL and SH wave velocity data are used in the determination of the in-plane elastic moduli of a MMC plate.

Acknowledgments

Dr. John Foltz and Mr. Albert Bertram of the Naval Surface Weapons Center made many helpful suggestions and supplied the 1-ply and 2-ply Gr/Al plates. Dr. James Strife of the United Technologies Research Center supplied the 4-ply, low CTE plates, along with the theoretical values of ν_{12}. This work was supported by the Naval Surface Weapons Center under Contract No. N60921-84-C-0112 and the United Technologies Research Center.

References

[1] Reed, R. W., "Quantitative Attenuation and Velocity Measurements in Metal Matrix Precursor Wires," *Review of Progress in Quantitative Nondestructive Evaluation*, Vol. 2A, D. O. Thompson and D. E. Chimenti, Eds., Plenum Press, New York, p. 695.

[2] Reed, R. W. and Bertram, A. L., "Ultrasonic Measurements of Elastic Moduli of Thermally Cycled Metal Matrix Composite Precursor Wires," *Nondestructive Methods for Material Property Determination*, C. O. Ruud and R. E. Green, Jr., Eds., Plenum Press, New York, 1984, p. 327.

[3] Foltz, J. V., Bertram, A. L., and Anderson, C. W., "A Method to Determine Dynamic Elastic Constants of Thin Shell Composites by Guided Ultrasonic Waves," NSWC TR 85-186, Naval Surface Weapons Center.

Joyce E. Widrig,[1] *Duncan D. McCabe,*[1] *and Ralph L. Conner*[1]

Nondestructive Evaluation of Fiber FP Reinforced Metal Matrix Composites

REFERENCE: Widrig, J. E., McCabe, D. D., and Conner, R. L., **"Nondestructive Evaluation of Fiber FP Reinforced Metal Matrix Composites,"** *Testing Technology of Metal Matrix Composites, ASTM STP 964*, P. R. DiGiovanni and N. R. Adsit, Eds., American Society for Testing and Materials, Philadelphia, 1988, pp. 227–247.

ABSTRACT: Fiber FP is a continuous polycrystalline alumina fiber suited for reinforcement of metals, plastics, and ceramics. Fiber FP/metal composites are very attractive for weight and stiffness critical applications. In order for these materials to be accepted in the marketplace, quality control methods needed to be developed. In this study, we developed methods based on computed tomography (CT) and ultrasonic scanning to identify porosity, delamination, and other discontinuities in Fiber FP reinforced composites.

Prior to this work, Fiber FP/metal plates and coupons were inspected using a combination of X-ray and ultrasonic methods—both with significant limitations. The ultrasonic evaluation utilized a defect threshold technique with inherent sensitivity uncertainties of defects close to the threshold level. This study demonstrated that defect intensity level scanning was superior to threshold scanning for Fiber FP reinforced composites. We developed color indicators for the various intensity levels to facilitate data interpretation.

The ultrasonic technology was also limited to simple flat shapes. Fiber FP development programs have recently shifted to fabrication of more complex prototype components such as connecting rods and helicopter transmission housings. CT offers several advantages over traditional radiographic techniques. Standard radiography creates an obscure 2-D image of a 3-D body by superimposing defect indications. A CT scanner has the ability to look at 2-D slices of a 3-D component. A series of 2-D images can be taken, and then interfaced with a computer to show the 3-D nature of the object. This technique has been demonstrated for prototype connecting rods and confirmed via destructive testing.

KEY WORDS: nondestructive tests, ultrasonic scanning system, through-transmission, FP/magnesium, FP/aluminum, computed tomography, composite materials, attenuation

There is considerable interest in reinforcing metals with high-modulus fibers to improve mechanical and high-temperature properties. Some of the fibers under evaluation are graphite, silicon carbide, alumina, and boron. These materials can offer superior weight and design advantages, but are often overlooked because reliable ways of nondestructively determining the quality of the final composite have not been available. During fabrication and processing of a fiber reinforced metal composite component, defects, such as delamination, porosity, nonhomogeneous fiber distribution, may be introduced. Nondestructive test procedures are needed to determine material quality, to develop accept/reject criteria and to predict service performance. Fiber reinforced metal matrix composites are complex materials and offer major challenges for nondestructive evaluation. The difficulties are compounded when specimens of irregular geometry are to be evaluated. This paper reviews our work in

[1] Section engineer, section engineer, and research technician, respectively, Experimental Station, Du Pont Company, Wilmington, DE 19898.

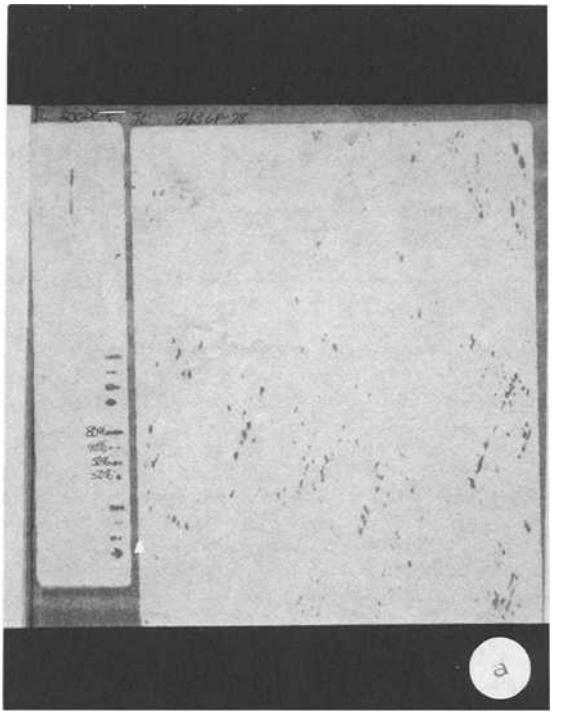

(*a*) May 1984

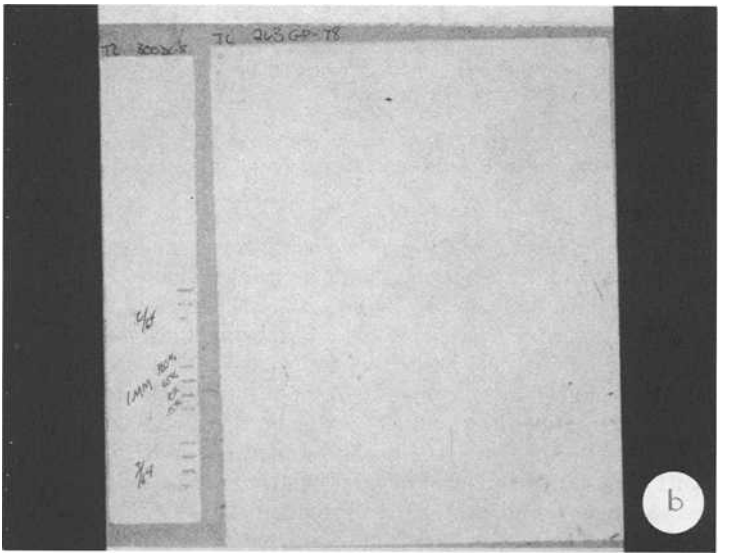

(*b*) July 1984

FIG. 1—*Pulse echo threshold ultrasonic scans of the same plate on three occasions showing various degrees of defect indications.*

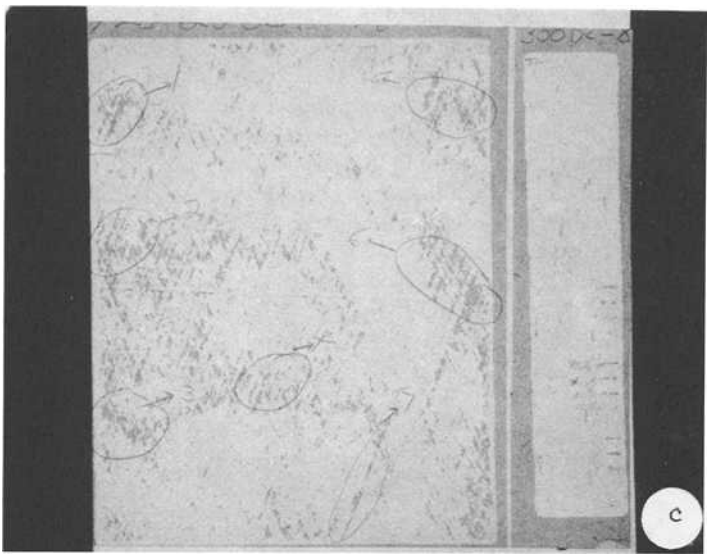

(c) September 1984

FIG. 1—*Continued.*

developing nondestructive evaluation techniques for alumina fiber reinforced aluminum and magnesium composites.

Fiber FP, a continuous polycrystalline alumina fiber being developed by Du Pont, is well suited for reinforcing nonferrous metals such as aluminum and magnesium to form composite parts such as test bars, flat plates, connecting rods, and other components. Nondestructive testing techniques are necessary to assess the quality of these components. A combination

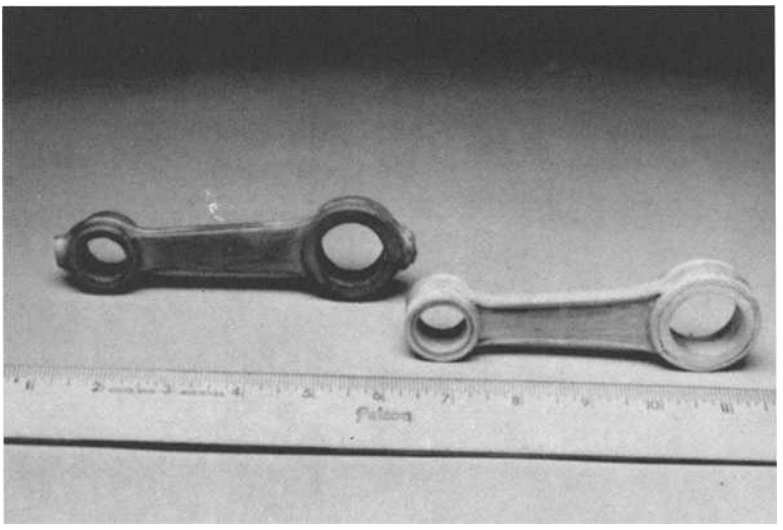

FIG. 2—*Fiber FP wax preform and FP reinforced aluminum connecting rod.*

of ultrasonic and X-ray radiography techniques have been used for analysis of flat shapes. Threshold ultrasonic inspection using a pulse-echo technique consists of concurrent scanning of a specimen and a calibration standard. The criteria for assigning defects in the test specimen is based on comparing the attenuation of the ultrasonic beam caused by a 0.1-cm (0.04-in.)-diameter hole drilled in the side of the calibration standard to the test specimen. A problem with using a defect threshold is the lack of reproducibility. The appearance of material discontinuities close to the threshold level depend upon arbitrary operator testing procedures. Figure 1 shows three scans of the same FP/Al plate inspected on three different occasions using the pulse-echo technique. Dark regions indicate "defects." The different results are not acceptable. Obviously, as the shape of the composite becomes more complex, these testing deficiencies are magnified. Figure 2 shows a Fiber FP wax preform and Fiber FP/Al connecting rod. The ultrasonic scans did not give reliable information on the quality of connecting rods due to reflection and refraction of the beam at the curved surfaces and the varying thickness of the rod. Standard radiography indicated possible defect regions, but it was not possible to quantify the magnitude or location of the defects. Therefore, improved ultrasonic and tomography techniques were investigated as means to characterize defects in Fiber FP reinforced components.

Operation of a Tomographic Scanner

The use of tomography [*1,2,3*] was pioneered in the medical X-ray field where these systems are commonly known as CAT (Computerized Axial Tomography) scanners. In

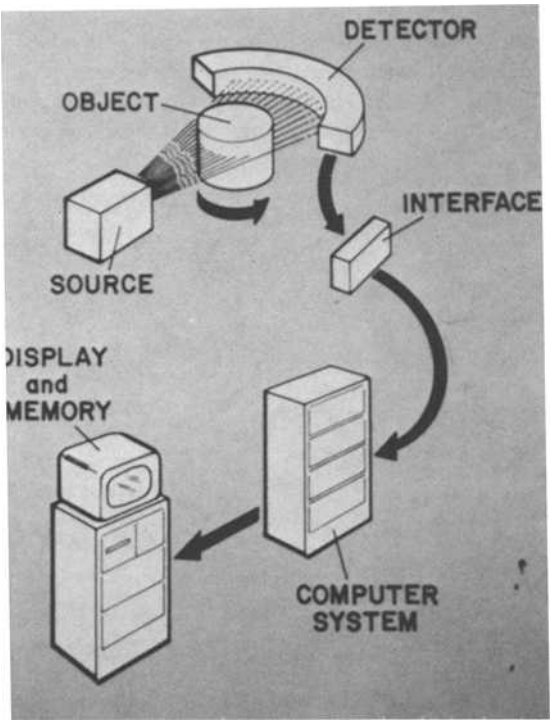

FIG. 3—*Schematic of CT scanner operation.*

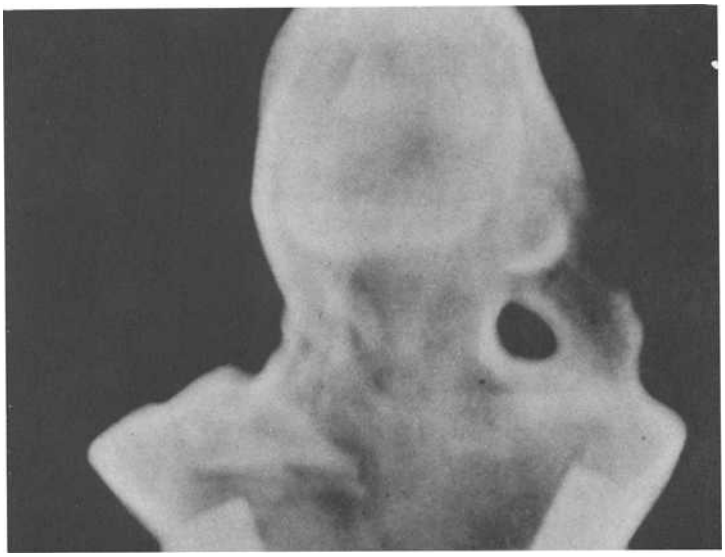

FIG. 4*a*—*Gamma-ray radiograph of Remington bronze Indian bust.*

medical applications, the intensity of the X-rays is normally in the 60 to 100 KeV range whereas 100 to 650 KeV is required for industrial applications. A computer assisted tomographic (CT) scanner operates by combining the power of a computer with traditional radiography techniques. Figure 3 illustrates the operation of a CT scanner. Flaws are detected by rotating the object relative to a radiation source and a set of detectors. The source consists of either a gamma ray emitting isotope, such as iridium 192 or cobalt 60, or a high intensity

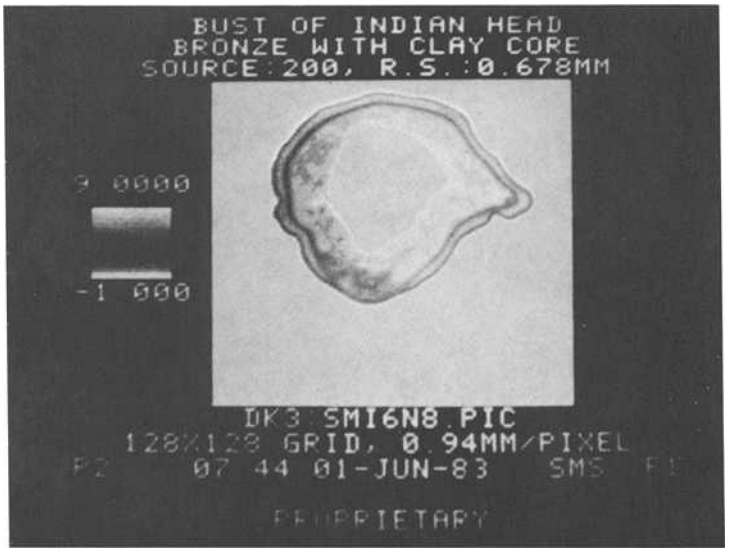

FIG. 4*b*—*CT tomograph through the chin of the Indian bust. Distinguishes the defect as a thin-wall in casting with slag material embedded in the clay mold.*

X-ray tube. The detectors obtain transmission data from the object at a number of different angles. This information is transformed by the computer into a two-dimensional density map of the desired cross section. By taking multiple scans of the object a three dimensional picture can be synthesized by the computer. Defects as small as 0.0025 cm (0.01 in.) can be resolved. Traditional radiography compresses a 3-D body into a 2-D image; therefore, 3-D information is lost. However, CT scans preserve the 3D nature of the body. Figures 4*a* and *b* illustrate one of the distinguishing differences between radiography and tomography. Figure 4*a* is a gamma-ray radiograph of a Remington bronze Indian bust. It was suspected to have porosity or defects in the chin region. A tomographic slice plane of 0.1 cm (0.04 in.) thick was taken through the suspect region. Figure 4*b* shows the tomographic cross section which indicates the bronze casting, the clay mold, air, and voids in the mold. By tomography the defect is shown to be a thin-wall in the casting with slag material embedded in the clay mold behind the thin wall.

Ultrasonics

Ultrasonic inspection [*4*] consists of directing a beam of ultrasonic energy into a specimen and then measuring either the energy transmitted through the specimen, or the energy reflected from a discontinuity or a defect in the specimen. This measurement is possible because the ultrasonic beam travels with little loss of energy through homogeneous material and is only intercepted and reflected by discontinuities in the material. Pulse-echo and through-transmission are the two basic methods of ultrasonic testing. The pulse-echo method measures the energy reflected from discontinuities or defects in the material. The through-transmission method measures the energy which traverses the composite specimen. Figure 5 illustrates the method of through-transmission ultrasonic testing.

Materials and Procedures

The materials evaluated were magnesium and aluminum plates and connecting rods reinforced with DuPont's continuous alumina fiber (Fiber FP). Standard plates were approxi-

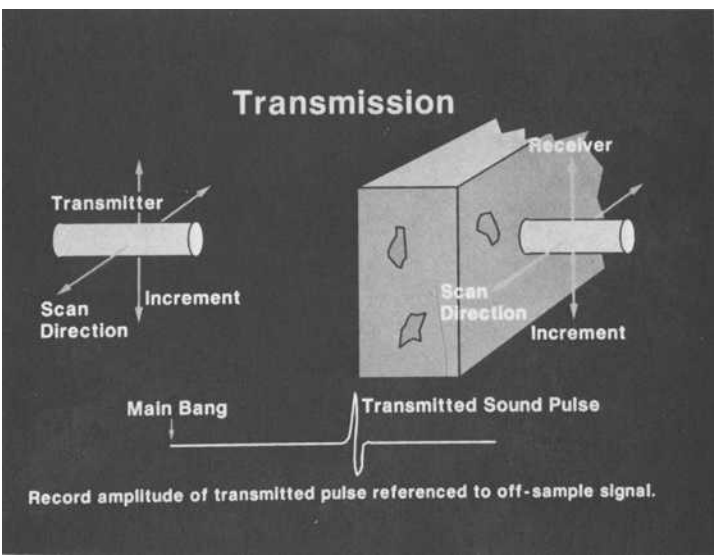

FIG. 5—*Schematic of through transmission ultrasonic technique.*

mately 15.2 by 15.2 by 1.3 cm (6 by 6 by 1/2 in.). These components were fabricated via molten metal infiltration [5,6]. The matrix in the magnesium components was ZE41A alloy which contains 4% zinc, 1% rare earths, and zirconium as a grain refiner. Since aluminum does not wet alumina at atmospheric pressure, the alumina/aluminum matrix composites utilized an Al-2.5Li alloy which promotes bonding between the alumina fiber and the aluminum.

The evaluation of CT scanning was conducted in cooperation with Scientific Measurement Systems, Inc. of Austin, Texas, who design and manufacture industrial tomographic systems. The SMS Model 101 High resolution Tomograph (Fig. 6) was used to develop tomographic techniques for inspecting Fiber FP reinforced components. The 200 Curie IR-192 source emits gamma rays collimated to a fan beam of 30 deg. An array of 63 detectors count individual gamma rays at rates of 1 MHz. The data are collected and analyzed with a PDP-11/730 minicomputer. The computer controls the scanning functions, collects the tomographic data, and by means of a proprietary collection of algorithms and analytical programs, provides detailed analysis of the test object.

The development of intensity level ultrasonic inspection was conducted at Du Pont's Engineering Physics Laboratory. The system (Fig. 7) consists of two Dec 11/23+ computers, a Testech LS 86 Scanner with two transducers which have computer controlled 3-dimensional coordinates and a 1 Mbyte high-speed image memory. The software and hardware for the high speed memory was developed at Du Pont. The system contains a color graphics terminal which provides a color hardcopy. The image is painted in real time. The system operates at very rapid scan speeds of up to 38.1 cm/s (15 in./s). Through transmission was selected as the ultrasonic scanning mode for the evaluation and development of ultrasonic testing for Fiber FP/metal composites. The intensity level technique uses shades of grey or pseudocolors to represent attenuation levels. All of our research was done using pseudocolor, but because of the necessity of reprinting in black and white, shades of grey are shown in this paper. The color scale or grey scale are shaded by the decibel (dB) scale which enhances testing reproducibility because it is referred to an off-sample signal. There is an impedance

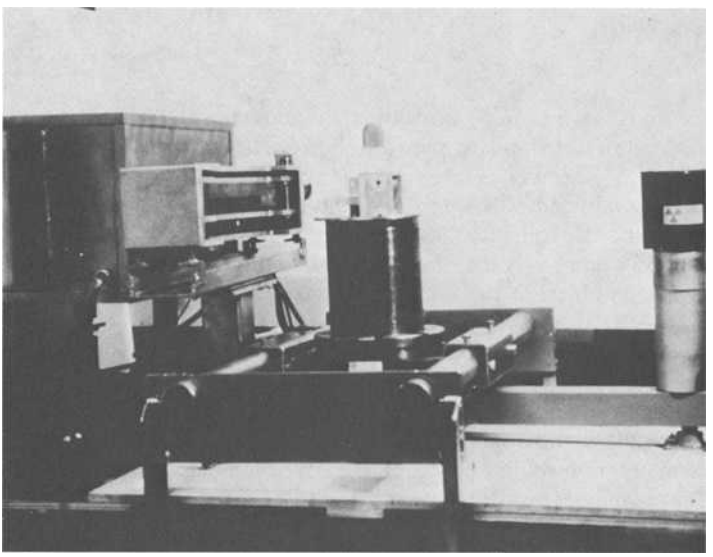

FIG. 6—*SMS Model 101 High Resolution Tomograph.*

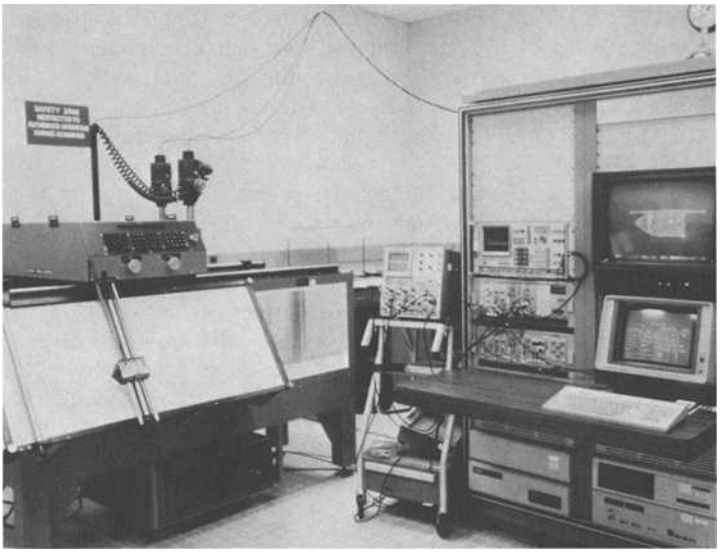

FIG. 7—*Ultrasonic system.*

mismatch at the specimen surface caused in part by the difference in the velocity of sound in water (1500 m/s) and in the FP/Al specimen (6500 m/s). This makes setting the focal point difficult because of refraction at the specimen surface. The transmitting transducer had a focal length of 3.81-cm (1.5-in.) and was focused on the specimen surface. The effect of refraction at the specimen surface is illustrated in Fig. 8. Most of the evaluation was conducted using a focused 15-MHz transducer with an unfocused receiver.

Results and Discussion

CT Scans

A feasibility study was begun by evaluating a unidirectional 35 volume percent Fiber FP reinforced magnesium test standard shown in Fig. 9*a*. This calibration standard is used for ultrasonic evaluation. The standard has the same matrix metal, fiber content and thickness as the part being evaluated plus side drilled holes of various sizes arranged at different depths. Figure 9*b* shows a tomographic slice at a depth of 0.32 cm (1/8 in.) through the long dimension of the 35 volume percent Fiber FP/Mg standard which clearly shows the magnitude of all the side drilled holes. In the lower left hand corner of the Fiber FP/Mg specimen is a shiny spot in the 0.119 cm (3/64 in.) diameter hole. This is a piece of the drill bit that had broken off during machining. At the top of Fig. 9*b* a 0.079-cm (1/32-in.)-diameter hole can be clearly seen indicating that defects of this size can be easily found. Another technique which can be used is to display the subtractive difference between the tomographic scan of the hole in the standard and a tomographic scan of the good region of the standard. Figure 9*c* is a tomogram of the 55 volume percent Fiber FP/Al standard which shows this subtractive difference. These analyses confirm the practicality of CT scanning for the nondestructive testing of Fiber FP reinforced magnesium and aluminum.

The next step was to prove the viability of this technqiue on a complex item such as a

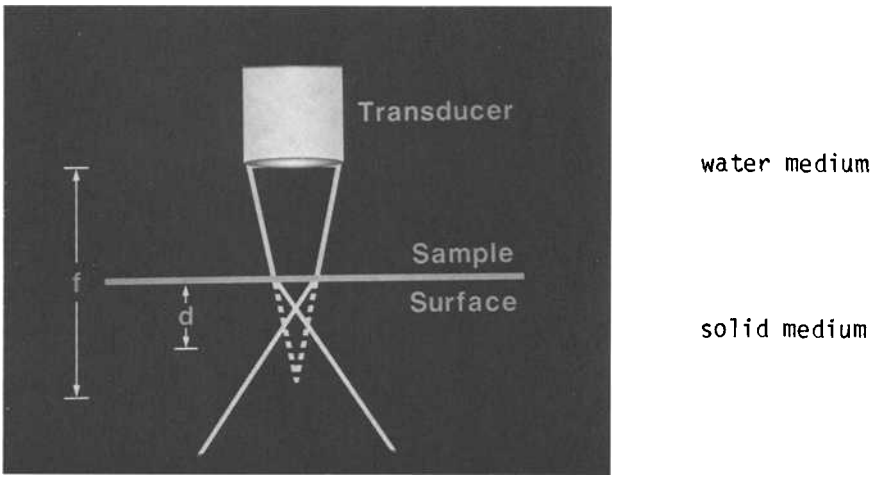

FIG. 8—*Refraction of sound at specimen surface.*

motorcycle connecting rod. Figure 10*a* is a tomogram of a Fiber FP reinforced aluminum motorcycle connecting rod taken through the long dimension of the rod. The slice plane is 0.1 cm (0.04 in.) thick. The defects are shown in this scan as regions of low density. At the side of the rod the density is displayed in terms of a grey scale. This scan clearly shows several probable strength limiting defects in this rod. To determine defect size, a cross section was taken through the shank of the connecting rod. The tomogram on the right in

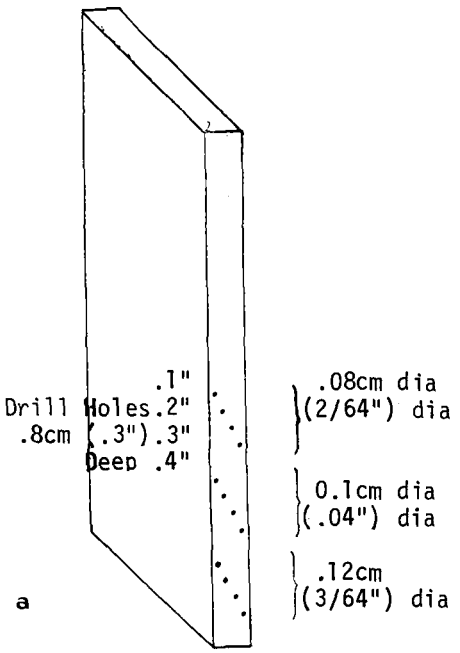

FIG. 9*a*—*Calibration standard, 35 volume percent FP/Mg.*

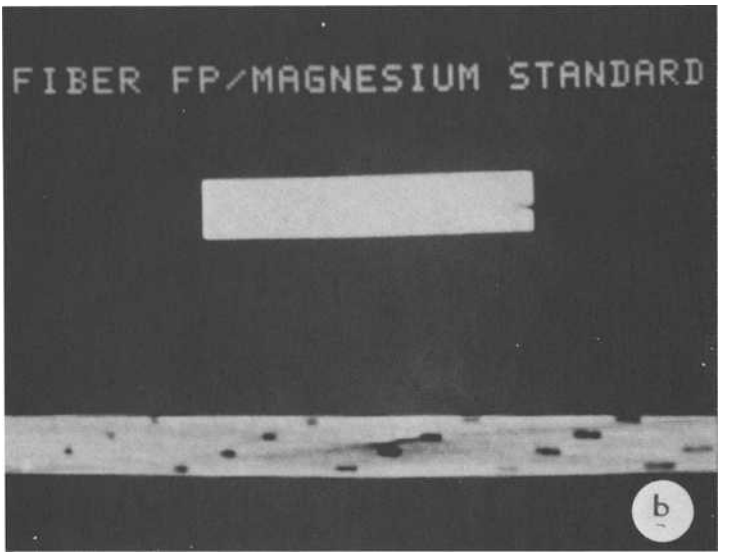

FIG. 9*b*—*Tomogram of 35 volume percent FP/MG calibration standard.*

Fig. 10*b* shows the magnitude and location of the defect within the connecting rod. Also shown in this figure on the left is a tomogram of the junction at the piston end of the connecting rod. Again, we see evidence of porosity and voids. The system reliability was confirmed by physically cross sectioning the rod at the indicated defect areas. Figure 10*c* shows the defects present in the motorcycle connecting rod.

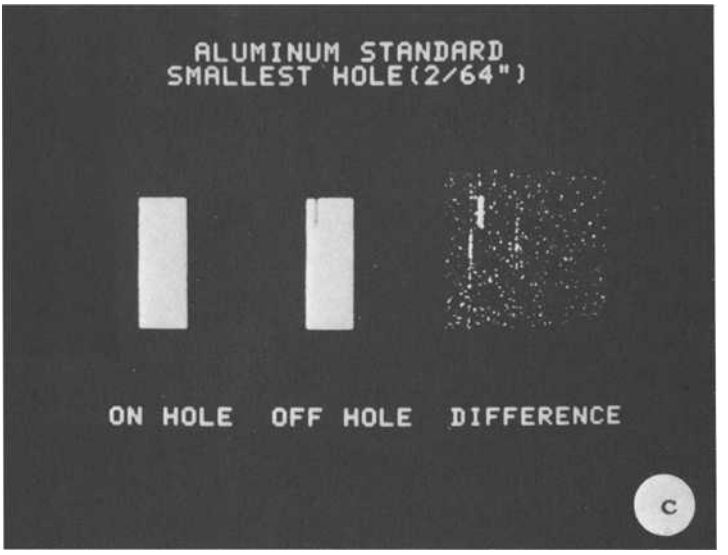

FIG. 9*c*—*Tomogram of subtractive difference in 55 volume percnt FP/Al standard.*

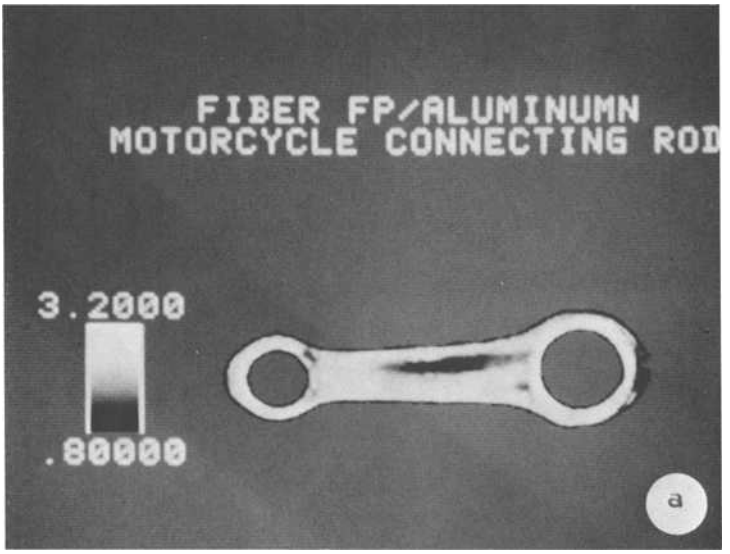

FIG. 10*a*—*Tomogram of FP/Al motorcycle connecting rod. Dark regions indicate low density (defects).*

CT scanning was initially used for casting process development and later as a quality control tool for connecting rods. The quality needed was determined by bench fatigue testing a connecting rod at 75% of the static ultimate load for 10^7 cycles and then CT scanning. Each rod released for outside testing had a CT scan as good as or better than the test rod. Figure 11*a* shows a tomogram of a standard connecting rod which could be used for testing.

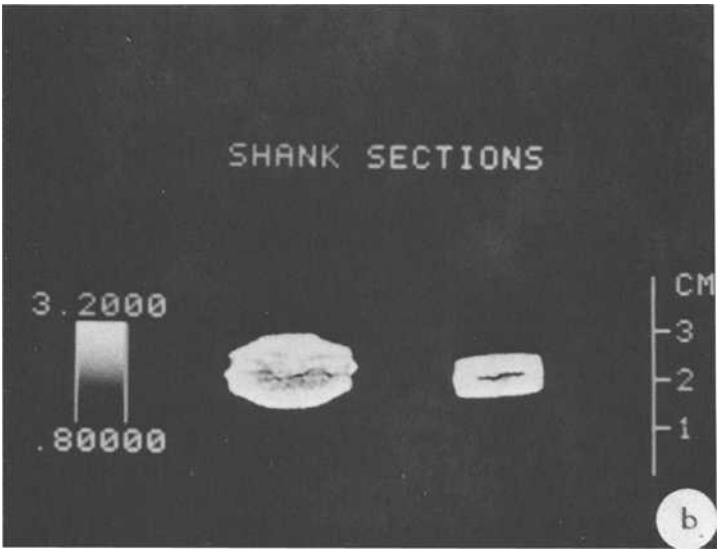

FIG. 10*b*—*Tomogram of shank of motorcycle connecting rod.*

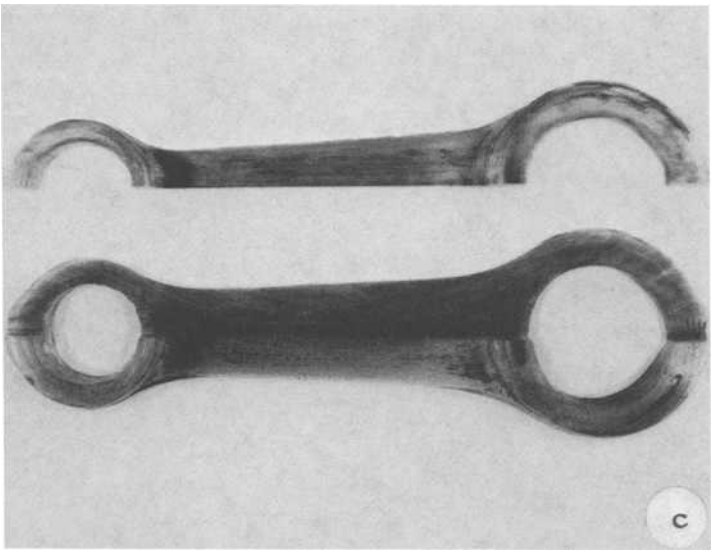

FIG. 10*c*—*Defects confirmed by destructive evaluation.*

The bright area along the center of the connecting rod is a stainless steel insert which was cast into the rod as an oil passage. Figure 11*b* shows the tomographic slices near the ends of the shank. The selection of scan regions is based on areas known most likely to contain defects and areas which are highly stressed.

Other interesting information can be obtained by this technique by comparing specimen density against a standard. A cursor is moved to the area of interest and the density calculated by comparing against a known standard. Figure 12 shows a density profile taken from several key areas within the connecting rod. This procedure makes it possible to calculate fiber volume fraction and porosity from the density profile. This technique was also used on a standard unidirectional 50 volume percent FP/Al plate. Figure 13 shows the analysis of density in several areas of interest. The density of Area 2 is 3.15 g/cm^3 and represents a void free region. The density in area 1 is 2.72 g/cm^3 with the density in area 3 being 2.79 g/cm^3. Another tomographic slice was taken through area 1 to determine depth of the defect in the plate. This information is shown in Fig. 14.

Intensity Level Ultrasonic Evaluation

The development of the intensity level ultrasonic evaluation began with the evaluation of a 55 volume percent Fiber FP/Al test standard shown in Fig. 15. Figure 16 shows the ultrasonic scan of this standard which clearly delineates the side drilled holes. The light region of the scale at the bottom (left side) represents good transmission of sound or high quality material while the darker regions (right side) represents poor transmission of sound or defective regions. The grey scale is shaded by the decibel (dB) scale in this specimen. A dB scale is more quantitative than a voltage scale as it is referenced to the signal off the specimen, which normalizes the system each time, allowing comparisons between different specimens. From this standard we selected an appropriate dB range for scanning all 55 volume percent 1.27-cm (1/2-in.)-thick FP/Al plates. Figures 17*a* and 17*b* show the additional

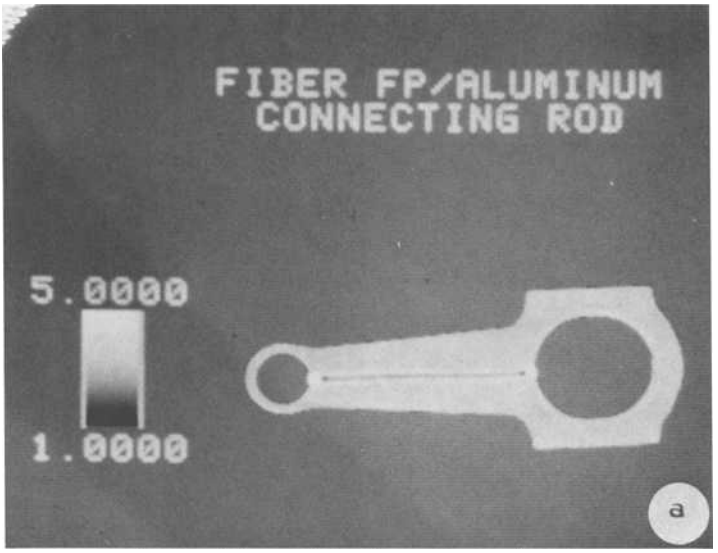

FIG. 11*a*—*Tomogram of FP/Al automotive connecting rod.*

information that can be gained from using an intensity level scan as opposed to a defect threshold scan. In the center of this plate the intensity level clearly shows that the defect runs the length of the plate while the defect threshold level scan only shows several questionable spots. This loss of data is due to the defect being close to the threshold level. Metallographic examination of this area indicates that the defect is actually a metal rich

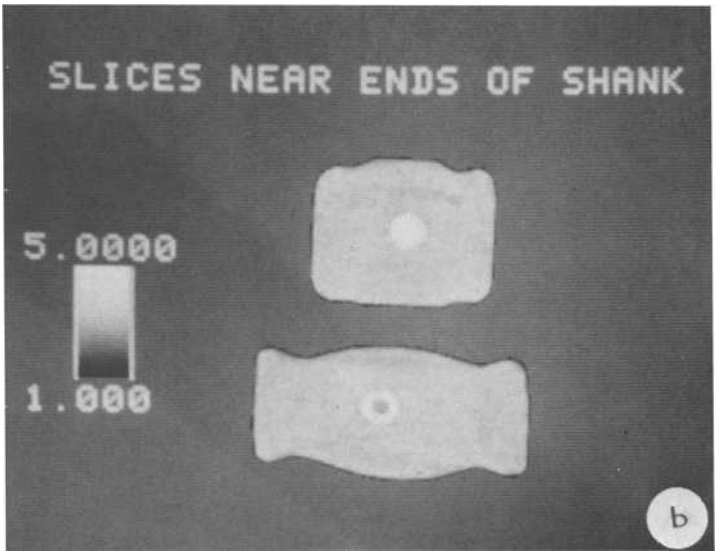

FIG. 11*b*—*Tomogram of shank of automotive connecting rod.*

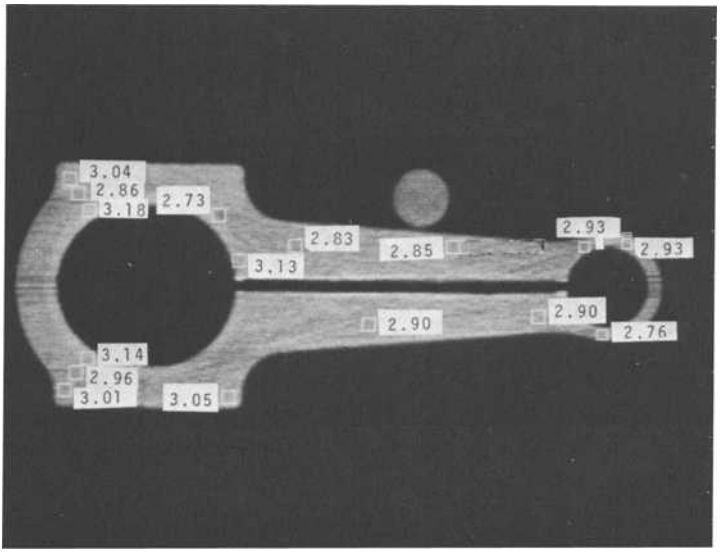

FIG. 12—*Density profile of FP/Al connecting rod* (*g*/cm³).

region (Fig. 17*c*). This would have little effect on mechanical properties in the longitudinal direction, but in the transverse direction metal rich regions can initiate failure. However, this onset of transverse failure is usually above the level of properties required for takeout due to the excellent bond between the fiber and the matrix.

One of the goals of this research effort is to be able to predict mechanical properties from

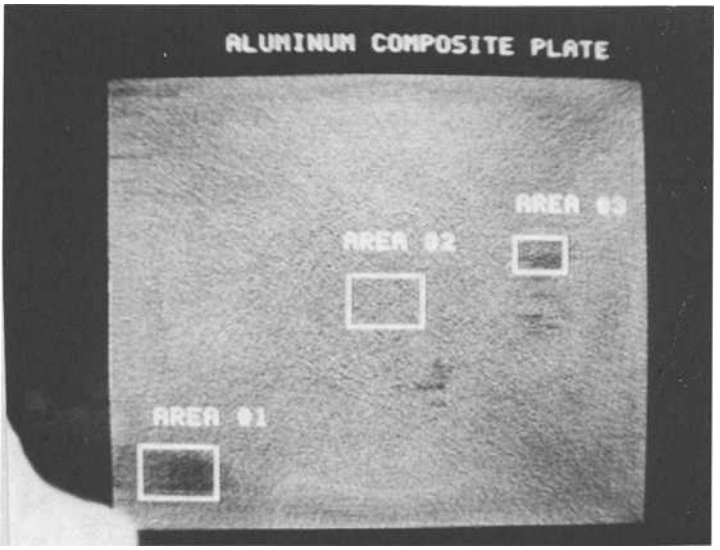

FIG. 13—*Density measurements in areas of interest in a 50 volume percent FP/Al plate. Area 1 has a density of 2.72 g/cm³, area 2 had a density of 3.15 g/cm³, and area 3 has a density of 2.79 g/cm³.*

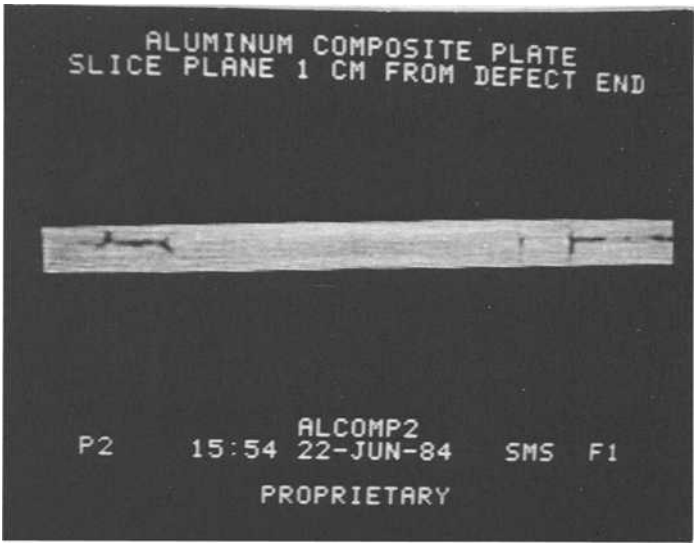

FIG. 14—*Tomograph through area 1 to determine magnitude of defective region.*

the ultrasonic scans. Initial efforts in this area have not been particularly successful. The threshold ultrasonic scans of two different 35 volume percent FP/Al plates show no difference in quality, but using an intensity level scan with color enhancement shows that the plates are consistently 6 DB different in their scan quality. Figures 18*a* and *b* show the intensity level scans in a grey scale. The scan on the right has a 50% higher transmission of sound which indicates a more homogeneous plate. Pseudocolor shows this difference much more clearly. Tensile properties from these two plates are given in Table 1. Statistically, there is

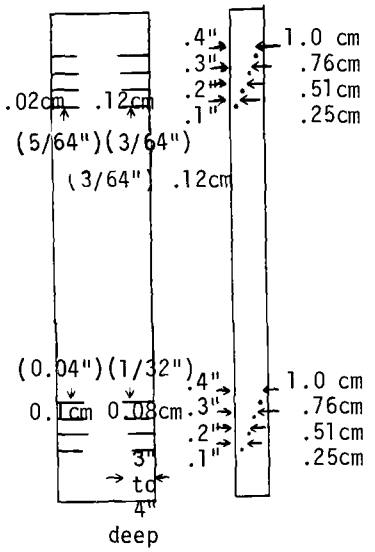

FIG. 15—*Calibration standard 55 volume percent FP/Al.*

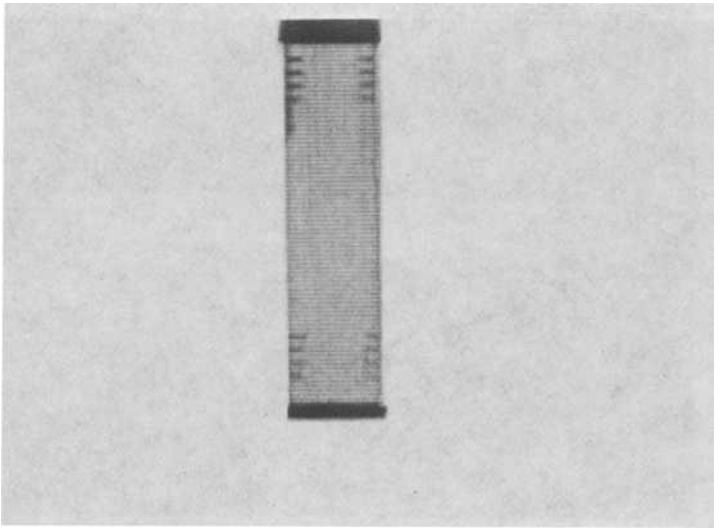

FIG. 16—*Ultrasonic scan of FP/Al calibration standard showing side drilled holes.*

little or no difference between these plates. This was not surprising because the properties of the specimens tested in the longitudinal direction are fiber dominated. Figures 18*c* and *d* show micrographs taken from the plates which indicate that the plate with poorer transmission of sound has more generalized porosity, but it does not appear to be serious enough to affect tensile properties.

More information can be gained by looking at the distribution of ultrasonic signal intensities in a histogram which plots counts versus voltage level. Figure 19 shows a graphical

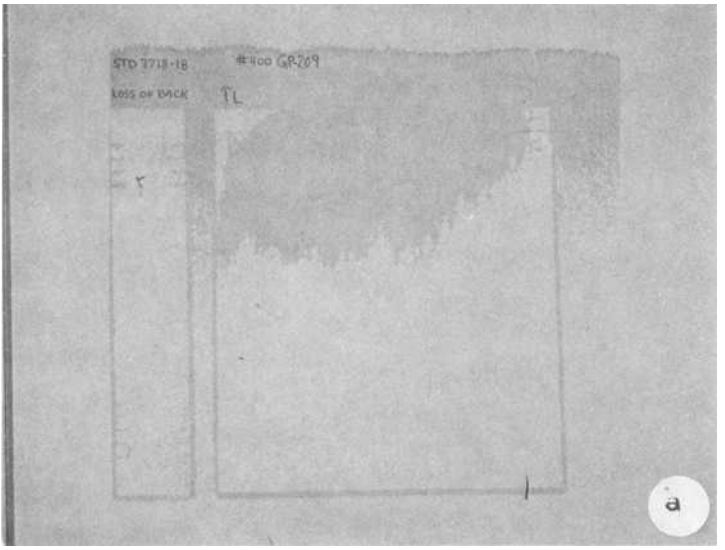

FIG. 17*a*—*Threshold ultrasonic scan of FP/Al plate.*

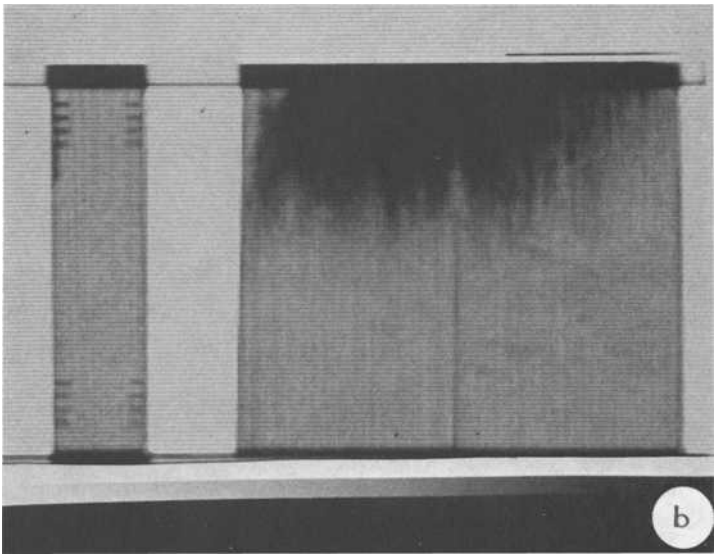

FIG. 17*b*—*Intensity level scan of same FP/Al plate showing the defect runs the length of the plate.*

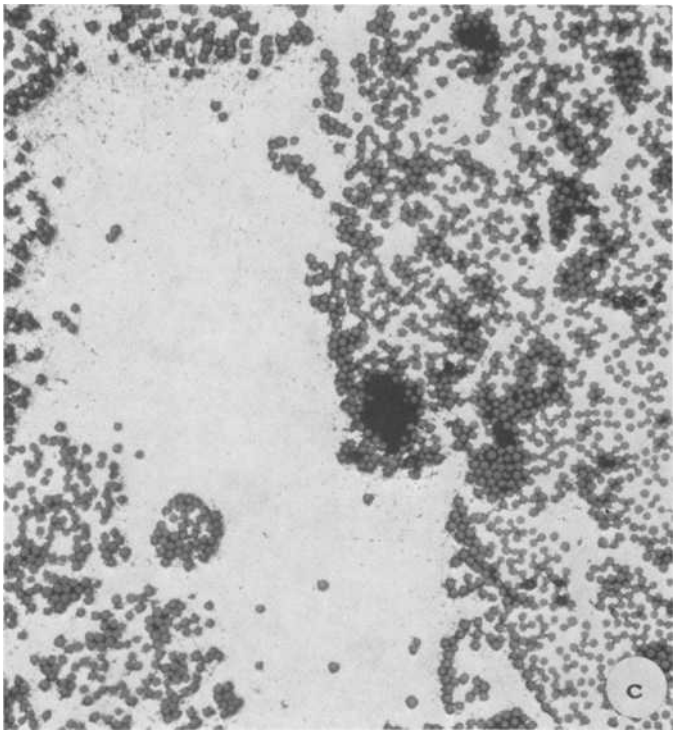

FIG. 17*c*—*Micrograph of area running length of plate indicates defect is a metal rich region.*

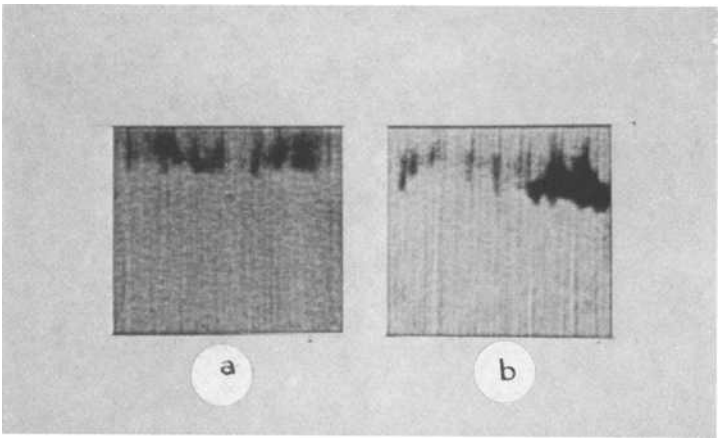

FIG. 18—*Intensity level scan* (a) *poorer transmission and* (b) *good transmission.*

representation of the FP/Al calibration standard (see Fig. 15) uniformity. This specimen shows individual spikes in the distribution instead of a general tail and is indicative of discrete flaws instead of generalized porosity. Transforming the data into a histogram can be very useful for providing information on the type of characteristic flaws present.

Concurrent with development of the intensity level technique for flat shapes, we are

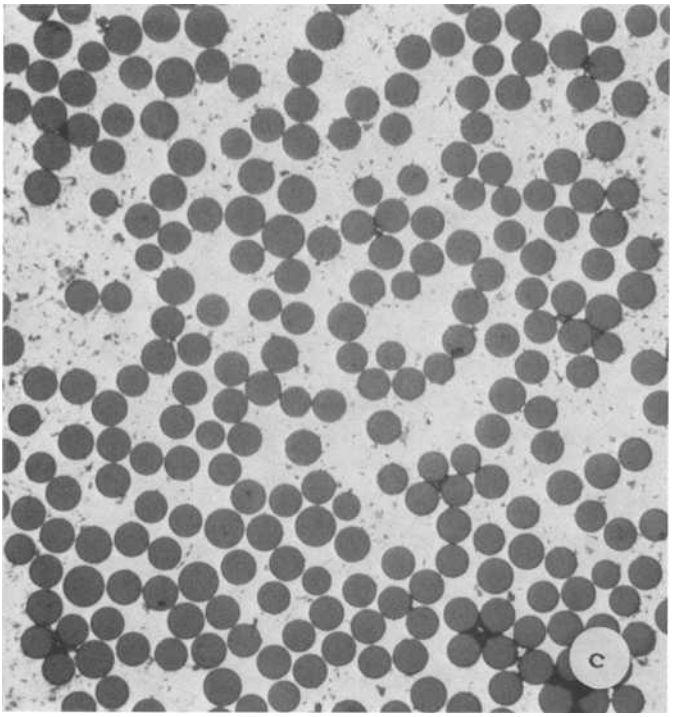

FIG. 18*c*—*Micrograph—good transmission.*

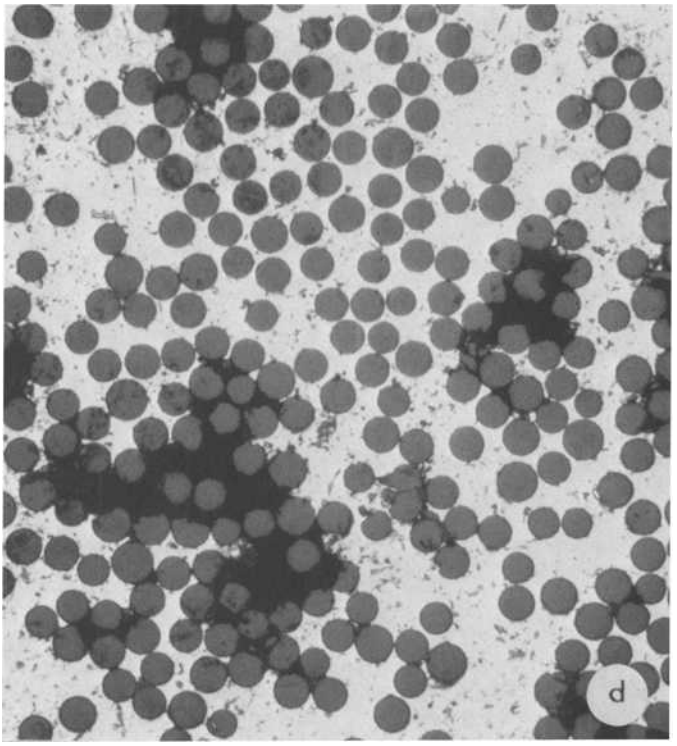

FIG. 18*d*—*Micrograph—poorer transmission.*

developing improved methods for ultrasonic inspection of complex shapes. Figure 20 is an intensity level ultrasonic scan of a FP/Al motorcycle connecting rod similar to the one used for CT evaluation. The scanning information from the white areas at the connection of the rod shank with the rod eyes was lost due to nonperpendicular beam reflection caused by the curved rod surface. Preliminary work has shown that these areas can be inspected using offset transducers. By using computerized specimen dimension information and a stored "library" of standards, the varying material thickness throughout the specimen can be compensated for.

Conclusions

Computed tomography is a reliable nondestructive test method for the inspection of Fiber FP metal prototype components. This technique is very useful for flaw detection and characterization of complex components containing varying thicknesses and curved surfaces. CT offers several advantages over ultrasonic inspection for complex components since the gamma

TABLE 1—*Tensile properties of two FP/Al plates.*

	Longitudinal Tensile Properties	Transverse Tensile Properties
High quality plate	446.1 MPa (64.7 ksi)	146.9 MPa (21.3 ksi)
Poorer quality plate	470.9 MPa (68.3 ksi)	155.1 MPa (22.5 ksi)

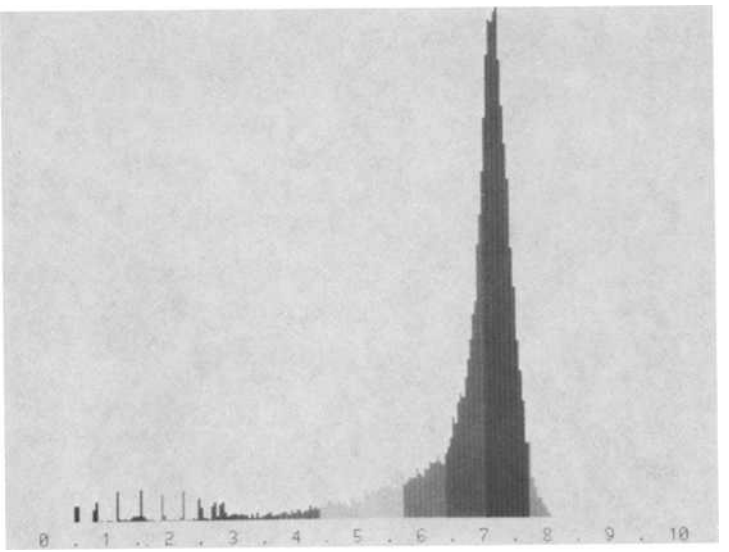

FIG. 19—*Histogram of FP/Al standard which show discrete peaks which represent discrete defects.*

rays are not reflected or refracted. CT offers advantages over traditional radiography as it takes individual slice planes from multiple directions making it possible to not only locate the flaw but to characterize the flaw size. CT scans are particularly useful when only selected regions need analysis.

Intensity level ultrasonic scans give more information about the overall quality of the

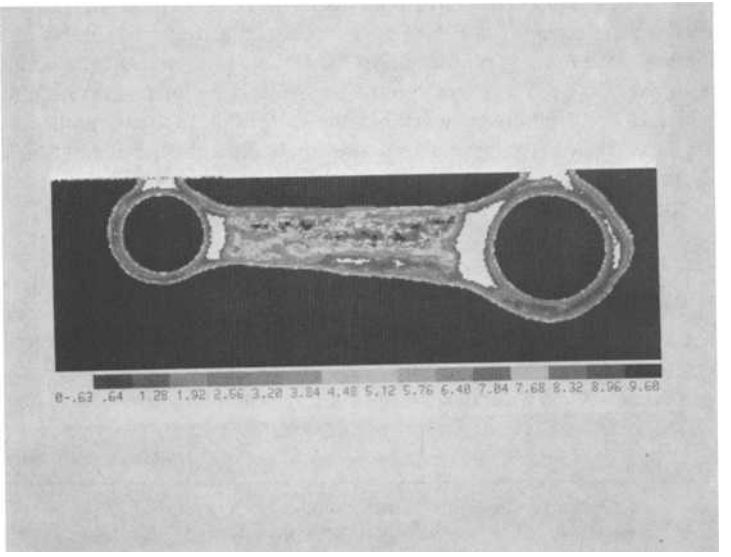

FIG. 20—*Intensity level ultrasonic scan of FP/Al connecting rod. White regions indicate loss of signal due to reflection at the curved surfaces.*

specimen than do threshold ultrasonic scans. The use of pseudocolor to represent various intensity levels facilitates data interpretation. The use of a decibel loss scale gives more quantitative information about specimen quality than does a voltage scale. Through-transmission ultrasonic scanning is a useful tool for analysis of flat shapes and with further development of offset transducers, complex shapes may be analyzed. Ultrasonic scans are cheaper than CT scans for a complete dimensional analysis, but do not provide as much information.

More work needs to be done to develop the relationship between material flaws, as measured by ultrasonics or CT scans, and mechanical properties. Minor porosity and metal rich regions appear to have little effect on longitudinal tensile properties, but other mechanical properties have not been investigated. Research has been initiated to develop this needed correlation.

Acknowledgment

The authors wish to thank Dr. Ira Lon Morgan of Scientific Measurement Systems and Dr. Pete Mrozinski and Dr. Tom Harding of Du Pont for their valuable advice and technical support.

References

[*1*] Hopkins, F. F., Morgan, I. L., Ellinger, H., and Klinksiek, R., "Tomographic Image Analysis," *Materials Evaluation*, Vol. 40, No. 12, 1982, pp. 1226–1228.

[*2*] Morgan, I. L., Ellinger, H., Klinksiek, R., and Thompson, J., "Examination of Concrete by Computerized Tomography," *American Concrete Institute Journal*, No. 1, *Proceedings*, Vol. 77, 1980.

[*3*] Chiang, B., Gautam, S. R., Hopkins, F. F., and Morgan, I. L., "Spatial Resolution in Industrial Tomography," *IEEE Transactions on Nuclear Science*, Vol. NS-30, No. 2, April 1983, pp. 1671–1676.

[*4*] Metals Handbook, Volume 11, "Nondestructive Inspection and Quality Control," American Society for Metals, 1976.

[*5*] Champion, A. R. et al., "Fiber FP Reinforced Metal Matrix Composites," *Proceedings*, 1978 International Conference on Composite Materials, Metallurgical Society of the American Institute of Mining, Metallurgical, and Petroleum Engineers, 1978, p. 883.

[*6*] Dhingra, A. K. and Krueger, W. H., "New Engineering Material—Magnesium Castings Reinforced with Du Pont Continuous Alumina Fiber FP," *Proceedings*, 36th World Conference on Magnesium, sponsored by the International Magnesium Association, 1979.

Stephen S. Tompkins[1] *and Gregory A. Dries*[2]

Thermal Expansion Measurements of Metal Matrix Composites

REFERENCE: Tompkins, S. S. and Dries, G. A., **"Thermal Expansion Measurements of Metal Matrix Composites,"** *Testing Technology of Metal Matrix Composites, ASTM STP 964*, P. R. DiGiovanni and N. R. Adsit, Eds., American Society for Testing and Materials, Philadelphia, 1988, pp. 248–258.

ABSTRACT: A high-precision Fizeau type, laser interferometric dilatometer has been developed and used to measure the thermal expansion of metal matrix composites. The strain resolution of this dilatometer system is about 1×10^{-6}. The thermal expansion of graphite/magnesium and graphite/aluminum composite laminates were measured over the temperature range of 117 to 394 K. The expansion of a P100 graphite/6061 aluminum (P100 Gr/6061 Al) unidirectional laminate was measured and compared with an approximate nonlinear analysis. The good agreement obtained between analytical and experimental results was further improved when temperature dependent properties were included in the analysis. Data showed that the behavior of the specimen at the end of the first thermal cycle was path dependent during the cycle. Test data on a P100 Gr/AZ91C Mg unidirectional laminate indicated a lower coefficient of thermal expansion and smaller residual strain than P100 Gr/6061 Al after thermal cycling between about 117 and 394 K.

KEY WORDS: thermal expansion, metal-matrix composites, composite materials, graphite/aluminum, graphite/magnesium, dimensional stability

Precision space structures which have very strict tolerances on dimensional control require structural materials that possess a high specific stiffness and low coefficient of thermal expansion (CTE). Graphite-fiber reinforced composites can be designed to meet these requirements by proper selection of the type of reinforcement fiber and matrix, number of plies, and the ply orientation. Both metal- and resin-matrix composite materials are leading candidates for use in future space structures. Fiber reinforced metal matrix composites (MMC), although more expensive, offer many advantages over the resin-matrix composites, such as higher electrical and thermal conductivities, better radiation resistance, and no outgassing. The primary MMC material systems considered for space structures are continuous graphite-fiber reinforced aluminum (Gr/Al), and magnesium (Gr/Mg).

Recognizing the need to characterize the thermal expansion behavior of these low expansion composite materials, an effort was undertaken to develop a high-precision dilatometer to measure thermal strains on the order of 1 to 10×10^{-6}. A comprehensive survey and discussion of available techniques to measure small displacements are given in Refs *1* and *2*. These techniques can be divided into three categories: electromechanical, optical noninterferometric, and optical interferometric. The application of electromechanical techniques, such as the push rod dilatometer, to composites is discussed in Ref *3*. In general,

[1] Senior researcher, NASA Langley Research Center, Hampton, VA 23665–5225.
[2] Senior materials engineer, PRC Kentron Aerospace Technologies Division, Hampton, VA 23665–5225.

the measurement of the ultrasmall displacements, such as those associated with low expansion materials for space structures requires the resolution achievable only with interferometric techniques. The application of two of these techniques, the Michelson and Moiré interferometers, to composites is discussed in Refs *4* and *5* respectively.

The anisotropic characteristics of composite materials introduce additional requirements on the measurement method. Test specimens must be large enough not to be influenced by edge effects or local inhomogeneities. For example, a specimen with chamfered ends must be at least 5.08 cm (2-in.) long to ensure an induced error in the CTE, due to end effects, of 1% or less [*6*]. The method should be also capable of measuring a wide range of CTE and a variety of specimen configurations. Specimen preparation must be minimal because the material must be characterized before, after, and during exposure to environmental parameters. Laser interferometry was selected as the method which best meets these requirements.

This paper describes the laser-interferometric-dilatometer system developed and currently in use at the NASA Langley Research Center, to characterize metal matrix composites [*7*]. The salient features of the system include: (1) high precision, (2) automated data acquisition, and (3) capability to test a wide variety of specimen geometries over temperature ranges within 89 to 422 K. Typical thermal-expansion measurement data for a Gr/Al rod, Gr/Al, and Gr/Mg unidirectional laminates and a Gr/Mg $[\pm 8]_s$ laminate are presented and discussed. The thermal expansion of the unidirectional Gr/Al laminate is compared with results from an approximate analytical model.

Experimental Method

Test System

A schematic diagram of the interferometer is shown in Fig. 1. A detailed description of this interferometer and the associated equipment is given in Ref. *7*; a synopsis follows. The specimen and two reference rods are oriented vertically. The two reference rods are located on the opposite side of a pedestal from the specimen and form a triangle on which an optical flat is supported. The base, pedestal, and the optical flat are made with an ultralow expansion glass. The pedestal and a mechanical spring system are used to maintain both the specimen

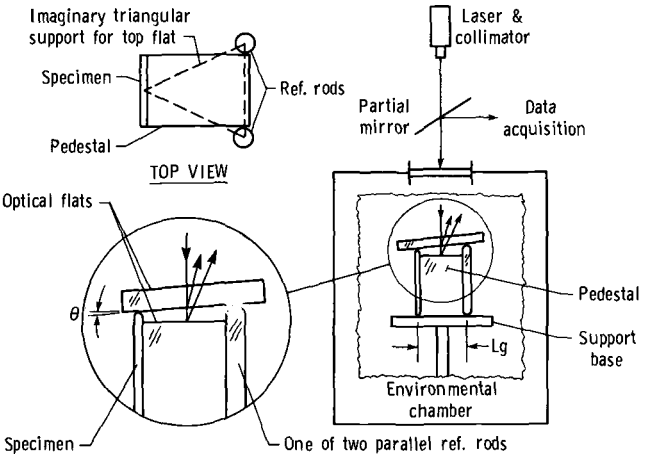

FIG. 1—*Schematic diagram of Fizeau type interferometer.*

and reference rods in a vertical position. The top of the pedestal serves as the second optical flat. The lengths of the reference rods are approximately equal but are different from the specimen length. This results in a small angle, θ, between the two flats. The incident laser beam reflects from the top and bottom surfaces of the top flat and from the top of the pedestal. The reflections from the bottom of the flat and the pedestal form an interference pattern which consists of a series of parallel fringes. The number of fringes over the gage length, L_g, is directly proportional to θ (Fig. 1). As the lengths of the reference rods or specimen change or both, the angle θ will also change. For small angles, the change in θ is given by

$$\Delta\theta = \frac{\Delta n\,\lambda}{2\,L_g} \tag{1}$$

where Δn is the change in the fringe count over the gage length, L_g, and λ is the laser wavelength. The relative strain, ϵ_r, for a specimen of length L_s, is given by

$$\epsilon_r = \frac{\Delta n\,\lambda}{2\,L_s} = \frac{\Delta N\,\lambda\,L_g}{2\,L_s} \tag{2}$$

where ΔN is the change in fringe density (fringes/meter) over any arbitrary gage length. Since the thermal expansion of the reference rods, ϵ_R, is known very precisely, the total strain of the specimen ϵ_T is given by

$$\epsilon_T = \epsilon_r + \epsilon_R \tag{3}$$

A schematic diagram of the dilatometer system is shown in Fig. 2. The system consists of: (1) the Fizeau type interferometer, (2) an environmental chamber, (3) an optical train, (4) a He-Ne laser, (5) a camera, (6) a photodiode array, (7) a wave analyzer, and (8) a computer. The environmental chamber is controlled by the computer which also activates the camera and records test temperatures. A photodiode array and wave analyzer have been also integrated into the system and serve as an alternate method for data acquisition and real time data reduction.

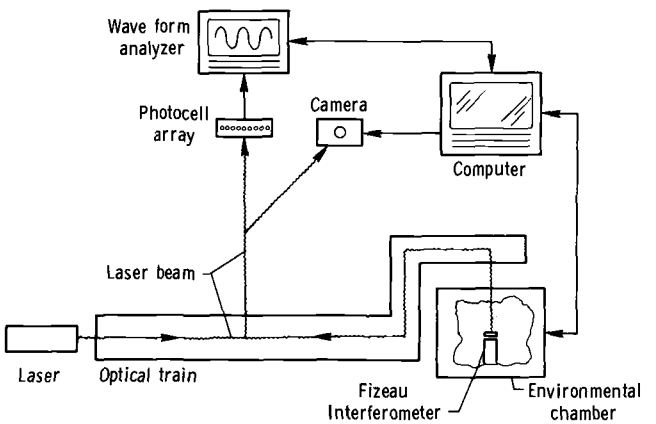

FIG. 2—*Schematic diagram of laser interfermometric dilatometer system.*

The environmental chamber is an air circulating, insulated chamber which can achieve closely controlled temperatures between 89 and 700 K. The chamber is heated with resistance heaters and cooled by liquid nitrogen. The optical train, which consists of various lenses, a beam splitter, colimator, and several mirrors, provides a colimated monochromatic source for the interferometer and images the fringe pattern onto both the photodiode array and camera. A 5 mW, He-Ne laser is used for the light source.

The fringe pattern is recorded at specified time intervals on 35 mm film. The chamber temperature, data acquisition interval, and test time are controlled by the computer. The specimen temperature is monitored by a calibrated 30-gage Chromel-Alumel thermocouple in contact with the specimen. Temperature surveys of the chamber, using matched thermocouples, have shown that 45 min after the temperature was changed, the temperature gradient along the length of a graphite reinforced epoxy composite specimen was approximately zero. The temperature gradient along the length of the National Bureau of Standards (NBS) Standard Reference Material (SRM) 739 quartz reference rods was less than 0.25 K/cm above room temperature and about 0.5 K/cm below room temperature. The two reference rods were within ±1 K of each other. The maximum difference between the average temperatures of the specimen and reference rods over the temperature range 117 to 422 K was about 1 K.

Test Procedure

Specimen preparation is an important first step in the test procedure. Specimens, about 2.5 cm wide and 7.6 cm long, are first machined to near final length with the ends rounded (Fig. 3) to provide single point contact with both the top flat and interferometer base. After machining, slight modifications to the specimen length are generally necessary to obtain practical fringe densities over the test temperature range. This is accomplished by very light polishing with 600 grit paper. The edges of the specimen ends are also beveled to minimize end effects. The surfaces of the interferometer in contact with the reference rods and specimen are thoroughly cleaned with alcohol before each test.

The cleaned interferometer, with reference rods and specimen installed, is placed in the chamber and the test is started. The initial fringe data are taken after the chamber has equilibrated. The set point on the temperature controller is changed in 22 K steps every 45 min. The rate of specimen temperature change never exceeds 2 K/min. Data, including the fringe pattern, are recorded at the end of each step.

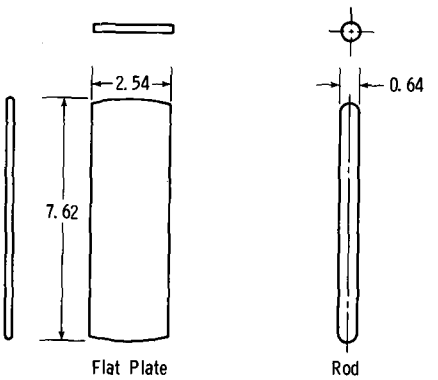

FIG. 3—*Typical interferometer specimen geometries. Dimension in centimeters.*

At the conclusion of a test, magnified images of the 35 mm negatives are viewed in a microfiche reader, and the number of fringes is visually counted over a defined gage length. Data to the nearest 1/4 fringe, which results in a strain resolution of approximately 1×10^{-6} for a 7.6-cm specimen, can be obtained with this technique.

The measurement of specimen length changes resulting from some environmental conditioning outside of the interferometer chamber, for example thermal cycling, can be also made using this test procedure. For this approach, the initial length of a specimen is measured with the interferometer. Then the specimen is cycled a specified amount, reinserted in the interferometer, and the final length is measured. Tests at room temperature have indicated that a specimen can be reinserted into the interferometer with no more than 4×10^{-6} cm/cm difference in the length measurement.

Analysis

An approximate analysis, called the phase average stress model, was used to predict the nonlinear thermal expansion of unidirectional Gr/Al during thermal cycling. The mathematical development for this analysis is described in Ref *8*. In the analysis, the average stress and strain in a composite laminate are defined and are used to compute the average stresses in the fiber and matrix. Based on the constituent properties, the composite properties and the average states of stress in the fiber and matrix for a given incremental load on the composite are computed. The incremental composite load can be due to a temperature change or changes in any of the six composite-stress components. The computed matrix stresses are used in a von Mises yield condition to determine the yield point of the composite. Once the matrix has yielded, the matrix-plastic strains are computed based upon the assumption of kinematic linear hardening in the matrix material. This is a good assumption for an aluminum matrix. The matrix elastic and plastic compliances are utilized to define an effective matrix compliance which is then employed to compute a new composite stiffness for the next load increment. If the composite load increment causes the matrix to unload, the matrix is assumed to exhibit linear elastic behavior, and no plastic strains are computed. The analysis has been verified by correlations with experimental data [*8*].

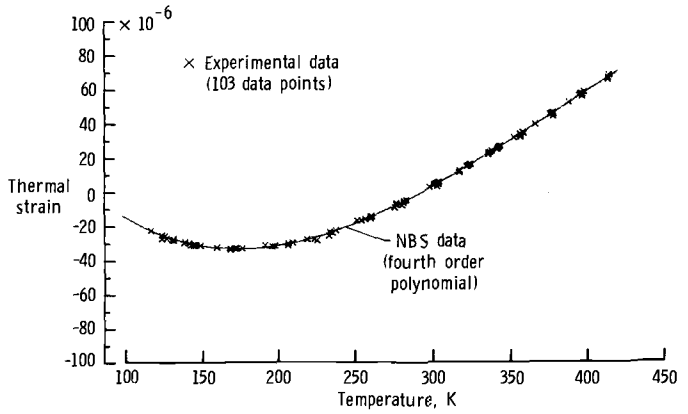

FIG. 4—*Thermal expansion of NBS SRM 739 fused silica.*

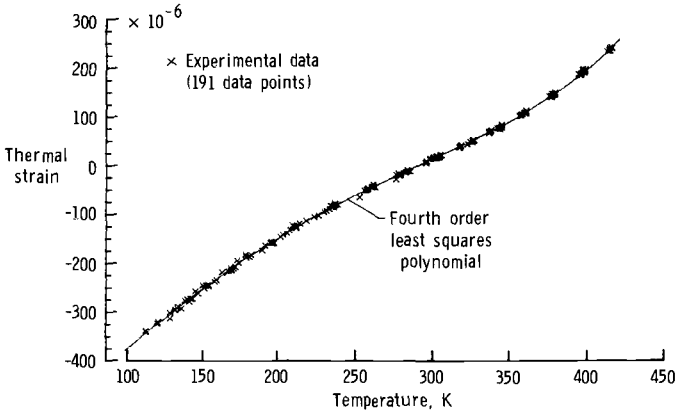

FIG. 5—*Thermal expansion of Invar 36.*

Results and Discussion

Precision of Measurement Technique

The precision of the measurement technique was established by repeated tests of the same specimen, using both NBS SRM 739 fused-silica and Invar. All of these tests were run using NBS SRM 739 as the reference material. All of the data have been adjusted to zero strain at 293 K. Data from 4 tests (a total of 103 data points) were collected on a specimen of NBS SRM 739 fused silica, and are shown in Fig. 4. Ideally, the relative strain, ϵ, for these tests should be zero, and therefore the total strain equal to the strain of the reference material. This is because both the specimen and reference are the same material. However, some slight scatter in the measured total strain is shown in Fig. 4. This scatter may be attributed to differences in the thermal expansion of the reference material and specimen or measurement errors or both. The root mean square (RMS) error in total strain for the fused-silica data was 0.85×10^{-6} [7].

Data were also collected from seven tests (a total of 191 points) of an annealed Invar 36 specimen. These data, together with a fourth order least squares polynominal fit to the data

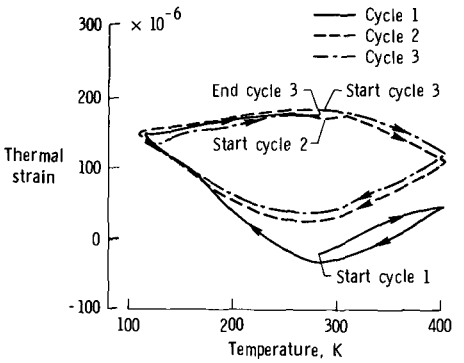

FIG. 6—*Thermal expansion of P100 Gr/6061 Al composite rod.*

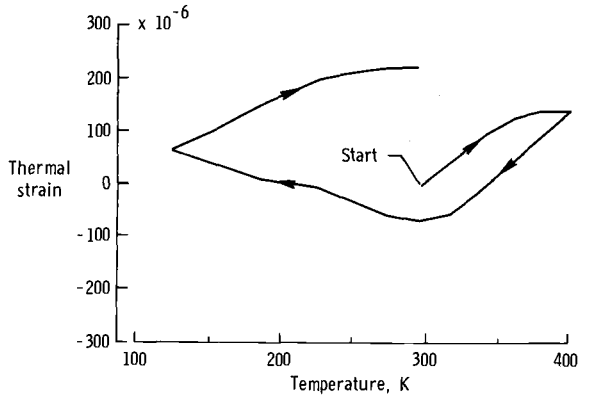

FIG. 7—*Thermal expansion of P100 Gr/6061 Al single-ply unidirectional composite laminate.*

are shown in Fig. 5. The RMS error in total strain for these data was 2.67 × 10^{-6}. The larger scatter for the Invar data as compared to the fused-silica data is attributed to the higher fringe densities in the Invar tests. At very high fringe densities (26 fringes/centimeters or higher) fringes can be only counted to the nearest one half fringe as compared to the nearest one quarter of a fringe for modest fringe densities. Data from both the fused silica and Invar indicate a precision of about 1 to 3 × 10^{-6} m/m.

Thermal Expansion of Graphite/Aluminum

If a material will be subjected to thermal cycling in its service environment, the response of the material during these cycles must be defined and understood. The present interferometer system has been used for expansion measurements, *in situ*, during continuous thermal cycling. The thermal expansion of a Gr/Al composite rod during three continuous cycles between 117 and 394 K is shown in Fig. 6. The rod was composed of seven wires of 6061 aluminum reinforced with the high modulus pitch fiber P100 with six of the wires forming a hexagon around the seventh wire. The composite wire had a nominal fiber volume fraction (V_f) of 0.45. For this test, the rod specimen rested in a V-groove cut in the pedestal of the interferometer. The specimen was first heated from room temperature to 394 K, then cooled to 117 K, and then reheated to room temperature during each cycle. The expansion is characterized by large hysteresis loops and a large positive residual strain after the first cycle, which is typical of Gr/Al. This behavior may be explained, qualitatively, by the following series of events. During the initial heat up from room temperature, the matrix expands while the graphite fibers (which have a negative CTE) contract. At higher temperatures the matrix yields under compression, the expansion of the rod becomes strongly influenced by the fiber, and the composite CTE decreases. The matrix continues to yield to maximum temperature in the cycle. On cool down from the maximum temperature the fiber expands while the matrix contracts; this leads to a reversal of thermal strains until the matrix yields under tension. As the matrix yields the rod again follows the fiber response. On heat up from the coldest temperature the matrix expands while the fiber contracts and the rod CTE is similar to the CTE during the initial heat up from room temperature. The difference in the expansion behavior between the first and subsequent thermal cycles is

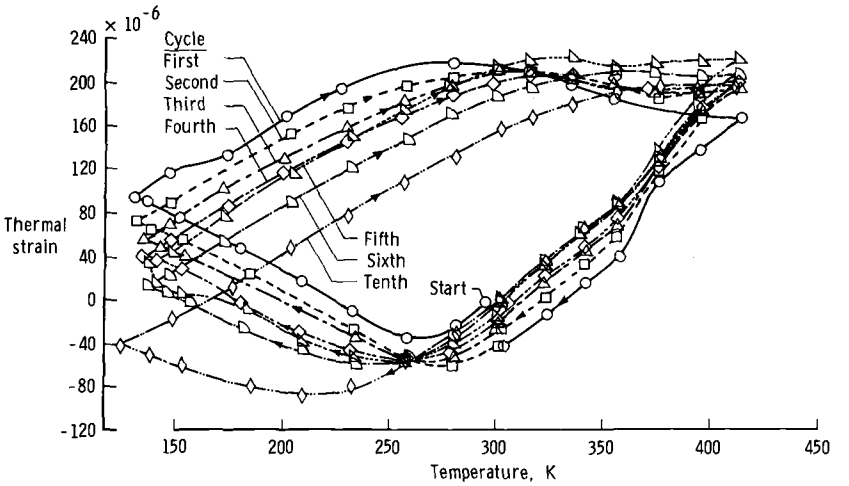

FIG. 8—*Thermal expansion of P100 Gr/6061 Al two-ply unidirectional composite laminate.*

attributed to the reduction in the fabrication residual stresses by plastic deformation during the first thermal cycle.

The thermal expansion during one thermal cycle of a single-ply, unidirectional P100 graphite/6061 aluminum (P100 Gr/6061 Al) flat laminate specimen with a V_f of about 0.40, is shown in Fig. 7. The specimen was first heated to maximum temperature, then cooled to the minimum temperature, and then reheated to room temperature. The response is very similar to the rod which is not surprising since both materials are made with the same constituents, that is, P100 Gr/6061 Al wire.

The thermal expansion of a two-ply, unidirectional P100 Gr/6061 Al flat laminate specimen with a V_f of about 0.37, between about 130 and 408 K during 10 continuous cycles is shown in Fig. 8. The response is characterized by a large hysteresis loop which becomes smaller

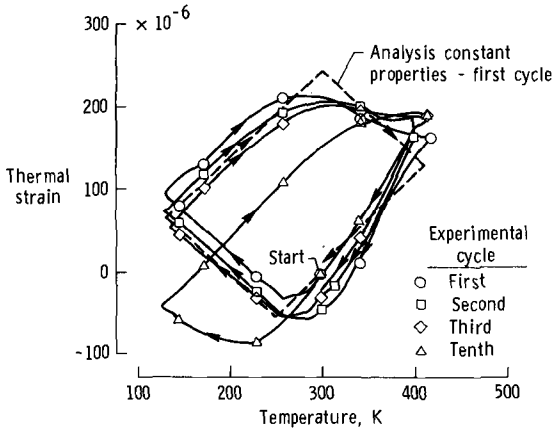

FIG. 9—*Comparison of experimental data with analytical prediction of the thermal expansion of P100 Gr/6061 Al two-ply unidirectional laminate.*

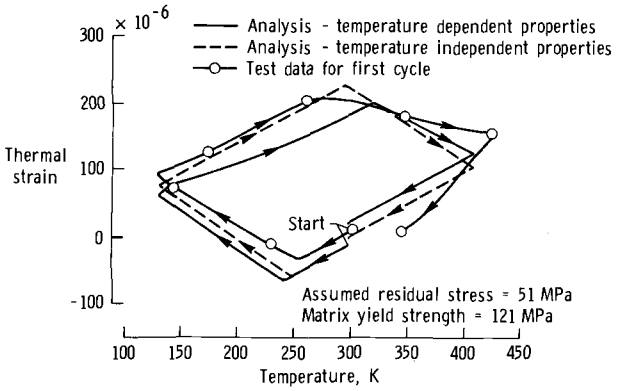

FIG. 10—*Thermal expansion of Gr/Al unidirectional laminate as predicted by the phase average stress model with and without temperature dependent properties.*

as the material is cycled but does not close. After the first cycle, the specimen's length decreased about 40 × 10^{-6} m/m but returned to its original length after the tenth cycle. The overall elastic-plastic behavior of this laminate is similar to the behavior of the rod (Fig. 6) and the single-ply laminate (Fig. 7). Note, however, that for this specimen (Fig. 8) the direction of the cycle was reversed from the other two specimens. That is, the specimen was first cooled from room temperature to the minimum temperature, then heated to the maximum temperature, and then cooled to room temperature. The data in Fig. 7 show that the CTE of Gr/Al at the end of a cycle, (297 K), which began with a heating period, was about zero or slightly negative. The data also show that the specimen had a positive residual strain. However, the data in Fig. 8 show that the CTE of Gr/Al at the end of a cycle which began with a cool-down period was about 0.45 × $10^{-6}K^{-1}$, and the specimen was shorter. Therefore, in one case, an increase in temperature after the first thermal cycle would cause the specimen to grow while in the other case the specimen would not change length or may even shrink. Together these data show that the initial direction of temperature change can

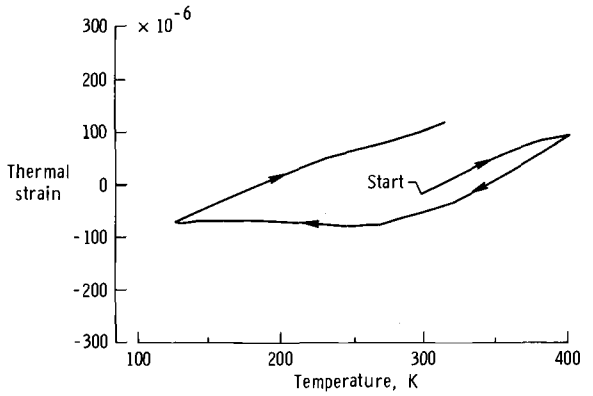

FIG. 11—*Thermal expansion of P100 Gr/AZ91C Mg one-ply unidirectional laminate.*

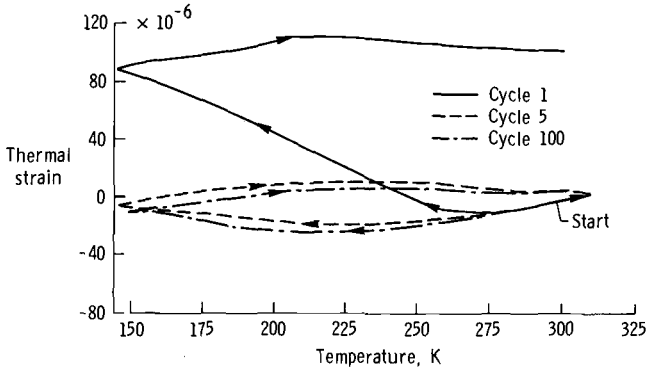

FIG. 12—*Thermal expansion of* $(\pm 8)_s$ *P100 Gr/AZ91C Mg laminate in the longitudinal directional.*

have a significant effect on the state of Gr/Al after the first thermal cycle. These data are consistant with predictions using the phase average stress model [8].

Comparisons of Experimental and Analytical Data for Gr/Al

A comparison of the thermal expansion data for Gr/Al, Fig. 8, and results from the phase average stress model are shown in Fig. 9. The theoretical analysis of the first cycle used temperature independent properties. In general the analysis is in satisfactory agreement with the first cycle data except in the region near the maximum temperature. The comparison in Fig. 10 shows that a qualitative improvement was made in the agreement when temperature dependent properties were used. The temperature dependent solution results in some curvature near 150 K and also a less abrupt change in the slope during heating near 300 K.

Thermal Expansion of Graphite/Magnesium

The thermal expansion of a single-ply unidirectional laminate of P100 Gr/AZ91C Mg with a V_f of about 0.37, between 117 and 394 K is shown in Fig. 11. The general response, the elastic/plastic behavior of the material and the resultant residual strain, is similar to the response of the Gr/Al. The residual strain of the Gr/Mg, about 100×10^{-6} after one thermal cycle, is about half the residual strain for the Gr/Al over the same approximate temperature range, Fig. 7. This difference may result from a lower residual stress due to the lower elastic modulus of the magnesium.

The thermal expansion of a $[\pm 8]_s$ Gr/Mg laminate with a V_f of about 0.47, during 1 and 5 continuous cycles and during the 100th cycle between 144 and 373 K is shown in Fig. 12. (This specimen was cycled 94 times in another chamber, then reinserted in the interferometer for the 100th cycle.) A large residual strain is shown after the first cycle, which is similar to the expansion of the unidirectional laminate between a larger temperature range (Fig. 11). However, the size of the hysteresis loop and the residual strain is significantly smaller after 5 cycles. Thermal expansion during the 100th cycle is about the same as during the 5th cycle. The reduced hysteresis and residual strain is due to the reduction of the internal residual fabrication stresses by plastic deformation induced through cooling to cryogenic

temperatures. The apparent stability in the thermal expansion behavior after 5 cycles is likely due to the stability of the microstructure of the matrix alloy.

Concluding Remarks

A high precision Fizeau type, laser interferometric dilatometer has been developed and used to measure the thermal expansion of metal matrix composites. The strain resolution is about 1×10^{-6}. Data from an NBS standard reference material and low expansion Invar indicate a precision of about 1 to 3×10^{-6}. The thermal expansion of a Gr/Al composite has been measured and compared with an approximate nonlinear analysis. The good agreement between the analytical and experimental results was further improved when temperature dependent properties were included in the analysis. The data showed that the behavior of the specimen at the end of the first thermal cycle was path dependent during the cycle. Test data on a Gr/Mg composite indicated lower CTE and much smaller residual strain than Gr/Al after the initial thermal cycling between about 117 and 394 K.

References

[1] Wolff, E., "Measurement Techniques for Low Expansion Materials," Vol. 9, National SAMPE Technical Conference Series, Society for the Advancement of Materials and Process Engineers, October 1977.

[2] Johnson, R. R., Kural, M. H., and Mackey, G. B., "Thermal Expansion Properties of Composite Materials," NASA CR-165632, National Aeronautics and Space Administration, Washington, DC, July 1981.

[3] Freeman, W. T. and Campbell, M. D., "Thermal Expansion Characteristics of Graphite Reinforced Composite Materials," *Composite Materials: Testing and Design ASTM STP 497*, American Society for Testing and Materials, Philadelphia, 1972, pp. 121–142.

[4] Eselun, S. A., Neubert, H. D., and Wolff, E. G., "Microcracking Effects on Dimensional Stability," Vol. 24, SAMPE Technical Conference Series, Society for the Advancement of Materials and Process Engineering, May 1979.

[5] Bowles, D. E., Post, D., Herokovich, C. T., and Tenney, D. R., "Moiré Interferometry for Thermal Expansion of Composites," *Experimental Mechanics,* Vol. 21, No. 12, Dec. 1981, pp. 441–448.

[6] Kural, M. H. and Ellison, A. M., "Induced Errors During Thermal Expansion Testing of Graphite Fiber Reinforced Metal-Matrix Composites," *SAMPE Journal,* Society for the Advancement of Materials and Process Engineering, Sept.–Oct., 1980, pp. 20–26.

[7] Tompkins, S. S., Bowles, D. E., and Kennedy, W. R., "A Laser Interferometer for Thermal Expansion Measurement of Composites," *Experimental Mechanics*, Vol. 26, No. 1, March 1986, pp. 1–6.

[8] Buesking, K. W., "Nonlinear Unidirectional Metal-Matrix Composite Behavior," *Proceedings*, Mechanics of Composite Review, Dayton, OH, 15–17 Oct., 1984, pp. 221–230.

Craig M. Browne[1]

Alternative Methods for the Determination of Shear Modulus in a Composite Material

REFERENCE: Browne, C. M., **"Alternative Methods for the Determination of Shear Modulus in a Composite Material,"** *Testing Technology of Metal Matrix Composites, ASTM STP 964,* P. R. DiGiovanni and N. R. Adsit, Eds., American Society for Testing and Materials, Philadelphia, 1988, pp. 259–274.

ABSTRACT: The off-axis and ±45° axial tests are not only effective but also low cost methods for the determination of in-plane shear modulus in individual unindirectional lamina, because they avoid the difficulties of producing a pure state of shear stress experimentally. Possible test approaches for more general composites, including multidirectional laminates, are developed from an investigation into the transformation equations for orthotropic mechanical properties, laminate theory, and the mechanical advantages of the ±45° test. Other possible test approaches for the indirect determination of shear modulus in laminates and pultrusions are developed from the formulas used to correct for shear deformation in flexural test. The proposed tests should be more economical to perform than tube torsion or rail shear tests. They should also provide relatively uniform shear stresses over larger portions of the specimens than the notched specimen type tests.

KEY WORDS: shear modulus, shear testing, off-axis testing, flexural modulus, flexural testing

Because the shear modulus of an orthotropic composite material is independent of its axial elastic moduli, it must be determined from experimental measurements. Many techniques have been developed and used to determine the shear modulus; some of these techniques produce a state of shear stress in a portion of or throughout a specimen. Other testing procedures, such as the ASTM standard off-axis and ±45° tests, rely on the phenomenon of shear coupling in orthotropic materials to produce a state of combined stress in an axially loaded coupon [*1*]. These techniques are either costly, have problems with stress concentrations, require specially prepared specimens, or are limited to the characterization of individual lamina, as shown in Fig. 1.

When parts are manufactured from composite materials, the resulting material could be a laminate of unidirectional plies oriented in several directions, a unidirectional pultrusion, or a complex three-dimensional weave. The measured shear modulus of these fabricated composites may be required for engineering analyses of the manufactured part or for process quality control. Test methods used to characterize individual lamina or which require a specially prepared specimen would not be applicable, because the specimen should be as cut or trimmed from the manufactured part in order to obtain a representative sample.

Alternative methods for the experimental determination of shear modulus in more general laminates, were determined from an investigation into the mechanics of the simpler test methods. The simplest tests to perform and analyze appear to be the off-axis and ±45° axial tests as well as the three or four-point bending tests. The axial tests have been used to

[1] Staff member, The BDM Corporation, Albuquerque, NM 87106.

CRITERIA \ EXISTING PROCEDURES	TUBE TORSION	BIAXIAL TUBE	RAIL SHEAR	PICTURE FRAME	BLOCK SHEAR	IOSIPESCU	NOTCHED TENSILE COUPON	OFF-AXIS	± 45°	FLEXURAL
TEST GENERAL LAMINATES OR PULTRUSIONS SUCH AS QC COUPONS			•	•	•	•	•			
MINIMUM STRESS CONCENTRATIONS	?	?						•	•	
UNIFORM SHEAR OVER A SIGNIFICANT REGION	•	•	•	•				•	•	
LOW COST			?	?	?	?	•	•	•	

FIG. 1—*Evaluation of existing procedures.*

characterize the shear modulus and other properties of individual unidirectional plies: the flexural tests have been used to determine the interlaminar shear strength and tensile strength of deep beam sections or flexural modulus of slender specimens. Because these are the least complicated tests to perform, they have a relatively lower cost than other test techniques.

The investigation into the mechanics of the axial tests indicated a testing principle that could be used to determine the shear modulus of more general plies, such as chopped fiber composites, as well as fabricated laminates. The investigation into the mechanics of flexural tests indicated another testing principle, because the shear deformation of a composite material beam has a significant effect on the deflection of the beam in bending.

Although the principles described were originally derived for orthotropic materials in general, the metal matrix composite testing community may benefit the most from their application, due to the special nature and test requirements of metal matrix composite materials. Because these materials are costly to produce in sample quantities, specimens are restricted in size and limited to simpler shapes. Because the matrix material exhibits a ductile rather than brittle failure, measurements in the range of nonlinear response are more important. Finally, because metal matrix composites are often planned for critical structures, simple and cost-effective testing methods for quality control/quality assurance will be required.

Discussion

Direct measurement of a material's shear modulus is complicated and costly, because of the difficulties associated with producing a pure state of shear stress experimentally [*2*]. Shear stress is a biaxial stress state that exists when the principal stresses on a structural element are unequal. This occurs primarily under conditions of structural bending and torsion. Pure shear represents a special condition in which the principal stresses are of equal magnitude but opposite in sign.

The biaxial tube test is the most widely accepted biaxial test. The combination of internal pressure and axial load can produce a complete range of biaxial conditions including those of pure shear. But, the test is expensive and has problems with stress concentrations [*3*]. The tube torsion test is also capable of producing a range of biaxial conditions, but it has the same drawbacks.

Both of these tests require preparation of special tubular specimens in a specific geometry. Even though the specimens may be multi-directional laminates, they must be specially fabricated rather than cut or trimmed from manufactured parts. This limits the usefulness

of these tests to the characterization of individual lamina or the laminate of the prepared tubular specimen. The off-axis and ±45° tests are much simpler to perform and evaluate, but current procedures limit their use to specimens prepared from individual unidirectional lamina [*4*].

To measure the shear modulus of individual lamina as well as composite laminates, several specimen shapes and loading fixtures are used. The rail shear and picture frame test fixtures produce fairly uniform shear stresses over large regions of a specimen but have problems with stress concentrations, data analysis, and cost [*5*]. Finite-element studies of other more complex specimens and fixtures have indicated not only the presence of potentially severe stress concentrations, but also that the maximum shear in some cases is produced over just a localized region of the specimen [*6*]. Even though the axial and flexural test techniques discussed in the following paragraphs do not produce pure shear, they do produce large regions of combined stress without severe stress concentrations and are relatively simple to perform, instrument, and evaluate.

Axial Test Methods

The shear modulus (G) of a homogeneous isotropic material may be determined, in the elastic range, indirectly from measurements of its two independent engineering constraints: the Young's modulus (E) and the Poisson's ratio (μ). The equation used to determine the shear modulus from these other properties is

$$G = \frac{E}{2(1 + \nu)} \tag{1}$$

Because the shear modulus can be determined from a calculation based on measurements made in relatively simple axial tests, the costs and difficulties associated with a direct shear test may be avoided.

The elastic properties in a given plane of an orthotropic material, such as a fiber-reinforced composite, are characterized with four independent engineering constants: the longitudinal Young's modulus (E_{11}) in a direction parallel to the fibers, the transverse Young's modulus (E_{22}) perpendicular to the fibers, a Poisson's ratio (ν_{12}), and a shear modulus (G_{12}) [*7*]. The shear modulus is independent of the material's other three elastic constants. The material's axial modulus (E_{xx}), shear modulus (G_{xy}), and Poisson's ratio (ν_{xy}) at orientations (Θ) other than the orthotropic axes (1 and 2), however, are dependent on all four elastic constants, as shown by the following orthotropic transformation equations

$$\frac{1}{E_{xx}} = \frac{\cos^4 \Theta}{E_{11}} + \left[\frac{1}{G_{12}} - \frac{2\nu_{12}}{E_{11}}\right] \cos^2 \Theta \sin^2 \Theta + \frac{\sin^4 \Theta}{E_{22}} \tag{2}$$

$$\frac{1}{G_{xy}} = \frac{\sin^2 2\Theta[E_{11} + E_{22}(1 + 2\nu_{12})]}{E_{11} + E_{22}} + \frac{\cos^2 2\Theta}{G_{12}} \tag{3}$$

$$\frac{-\nu_{xy}}{E_{xx}} = \left[\frac{1}{E_{11}} + \frac{1}{E_{22}} - \frac{1}{G_{12}}\right] \cos^2 \Theta \sin^2 \Theta + \frac{\nu_{11}}{E_{11}} (\cos^4 \Theta + \sin^4 \Theta) \tag{4}$$

The shear strain (η_{xy}), exhibited by composites loaded at orientations other than their

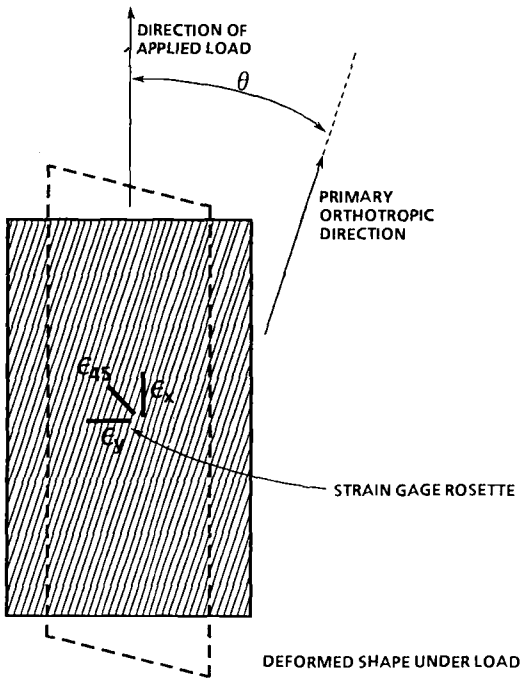

FIG. 2—*Composite off-axis shear coupling.*

orthotropic axes, is also dependent on the four elastic constants, as shown by this equation

$$\frac{\eta_{xy}}{E_{xx}} = \sin 2\Theta \left[\frac{\cos^2 \Theta}{E_{11}} - \frac{\sin^2 \Theta}{E_{22}} + \left(\frac{1}{2G_{12}} + \frac{\nu_{12}}{E_{11}} \right) \cos 2\Theta \right] \tag{5}$$

These transformation equations form the basis for the ASTM standard off-axis and ±45° tests that use measurements of axial modulus and Poisson's ratio in a lamina at orientations other than the orthotropic axes to determine the on-axis shear modulus.

When a composite specimen is loaded at an angle to its orthotropic axes, it exhibits a shear strain as well as strain parallel to and perpendicular to the load direction, as shown in Fig. 2. This is called shear coupling. If the ends of the specimen are prevented from rotating, as in the off-axis test, a combined stress state is produced in the specimen. Measurements from a strain gage rosette on the specimen (ϵ_x,ϵ_y,ϵ_{45}) and a load cell (σ_x) provide the means to determine the on-axis shear modulus according to the following equation

$$G_{12} = \frac{E_{xx}}{2(1 + \nu_{xy}) - 2\eta_{xy} \cot 2\Theta} \tag{6}$$

where

$E_{xx} = \sigma_x/\epsilon_x$,
$\nu_{xy} = \epsilon_y/\epsilon_x$, and
$\eta_{xy} = (2\epsilon_{45} - \epsilon_x - \epsilon_y)/\epsilon_x$.

Note that Eq 6 reduces to a form similar to Eq 1 for off-axis specimens tested at 45° from the orthotropic axes, because the trigonometric coefficient in the denominator's shear coupling term becomes zero.

If a composite laminate axial test specimen were prepared such that alternate plies were oriented at angles of equal magnitude but opposite sign to the load direction, as shown in Fig. 3, the shear coupling in each layer from the axial load would be of equal magnitude but opposite sign, so that the laminate shear coupling in that specific load direction would be zero. The laminate would be in a uniaxial stress state, but the individual lamina would be a combined stress state.

In this case, Eq 5 reduces to a form similar to Eq 1, because the shear coupling term itself is zero. The simplification of Eq 5 is independent of the ply orientations, as long as the lamina orientations are balanced with respect to the load direction. These are the conditions of the ±45° test, but as shown, the angle of the alternating plies to the load direction may vary from 45° without affecting the test mechanics.

Because there is no shear coupling, only two strain gages are required to acquire the data for the on-axis shear modulus measurement. Equation 6 may be rewritten as [*9*]

$$G_{12} = \frac{\sigma_x}{2(\epsilon_x - \epsilon_y)} \tag{7}$$

Some researchers have reported a better correlation of shear properties with the ±45° test than with the off-axis test, even well into the inelastic range [*10,11*]. This may be due to the lack of shear coupling in the ±45° specimen.

As an approach to determining the shear modulus in more general laminates, consider

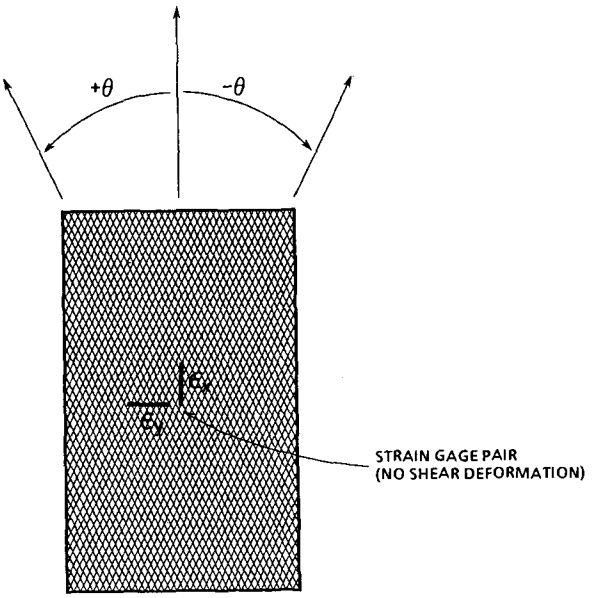

FIG. 3—*Angle-ply specimen.*

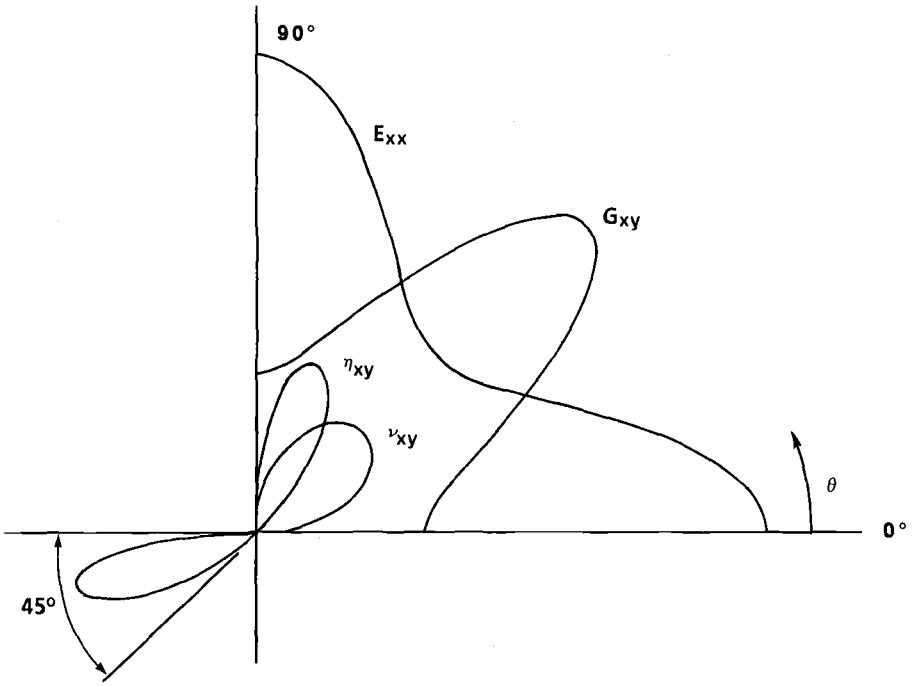

FIG. 4—*Off-axis properties of a graphite/aluminum composite [0/90] laminate.*

the ±45° test as an off-axis test of a [0/90] laminate with the load direction at 45° off the orthotropic axis of this square symmetric material. Figure 4 shows the off-axis properties of a graphite/aluminum [0/90] laminate with equal proportions of plies oriented at 0 and 90°. Note that at the 45° load orientation, the calculated shear coupling coefficient of the laminate is zero, giving the same configuration as in the ±45° test. Therefore the instrumentation, data reduction, and reliability of results for this laminate in this orientation should be the same as for the shear modulus of individual lamina in the ±45° test.

The on-axis shear modulus of more general composite laminates could be determined in the same manner with the same reliability, if an off-axis laminate test orientation with a zero shear coupling coefficient existed and could be determined. To determine whether more general laminates would have off-axis orientations with zero shear coupling, the shear coupling coefficients, for several graphite/aluminum composite ($0_A/90_B$) laminates with varying percentages of 0 and 90° plies, were calculated at angles ranging between 0 and 90° from the orthotropic axis. Figure 5 shows a plot of the calculated coefficients which indicates that the desired condition may occur, depending on the elastic properties of the laminate. Note that as the volume fraction of 90° plies increases, the angle at which the shear coupling coefficient intercepts the origin approaches 45°.

When the transformation equation for the shear coupling coefficient (Eq 5) is solved for angles at which it is zero, the following equation is derived

$$\Theta = \tfrac{1}{2} \cos^{-1} \left[\frac{G_{12}(E_{22} - E_{11})}{G_{12}[E_{11} + E_{22}(1 - 2\nu_{12})] + E_{11}E_{22}} \right] \tag{8}$$

where the orthotropic engineering constants are those of the laminate. The use of this relationship is limited to those laminates or plies that meet the criteria in this equation

$$E_{22} > \frac{2E_{11}G_{12}}{2\nu_{12}G_{12} + E_{11}} \tag{9}$$

due to the inverse cosine function of Eq 7. Another drawback to its use is that the shear modulus is required in order to determine the angle to perform the test to determine the shear modulus.

On the other hand, in the manufacturing environment, the shear modulus of the individual plies should be known from characterization tests of the unidirectional material. Then the laminate shear modulus could be predicted from laminate theory and used in Eq 8 to determine the zero shear coupling load orientation in material of a manufactured composite part. A specimen cut from the part at this orientation could be tested axially to determine the material's shear modulus.

Because the shear coupling is eliminated, the only instrumentation required would be two strain gages: parallel and perpendicular to the load direction. As with the ±45° test, a specimen tested at this zero coupling orientation should produce more accurate results well into the nonlinear range than an axial specimen orientation with shear coupling. This could be especially important when the ductile nature of the metal matrix is considered.

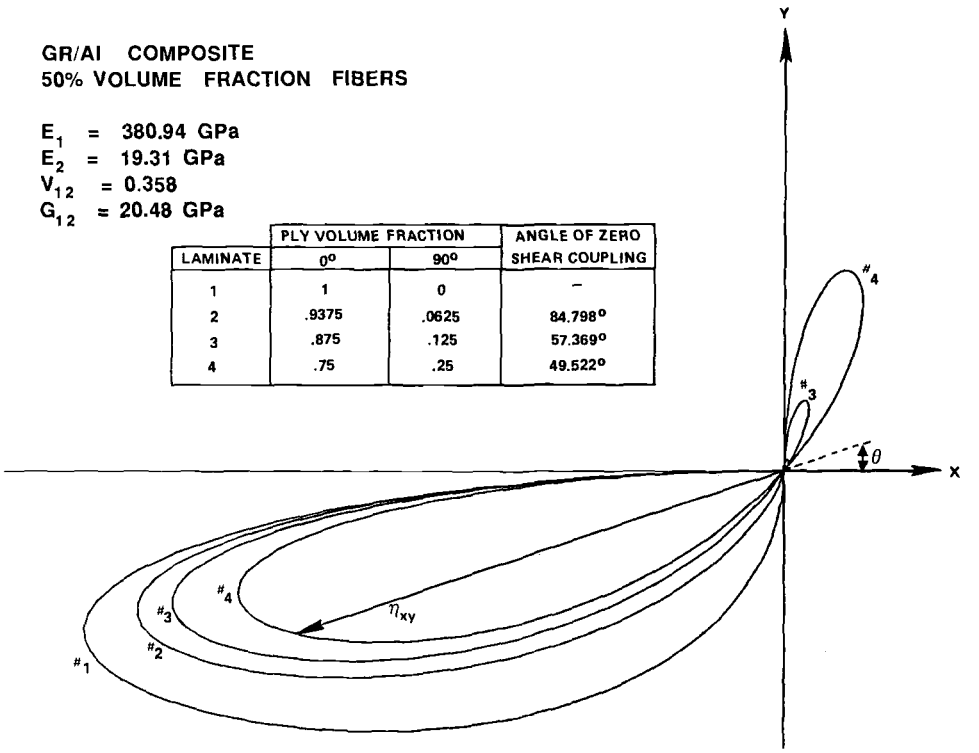

FIG. 5—*Shear coupling coefficients in cross-ply laminates.*

Flexural Tests

Flexural tests appear to have been limited to the determination of interlaminar shear strength, tensile strength, or flexural modulus [*12*]. Samples are generally configured with the plane of bending perpendicular to the plane of the composite lamina. Because the shear deformation of a flexure specimen may add significantly to its bending deformation, one of the first steps in analyzing the force-deformation data from these tests is to correct for the effect of the shear modulus, as shown in Fig. 6. For a three-point bending test this correction is the last term in parentheses of the equation

$$E = \frac{mL^3}{48I}\left(1 + \frac{12IFE}{AL^2G}\right) \tag{10}$$

where

m = slope of the force-deformation curve,
L = beam length,
E = its Young's modulus,
I = its moment-of-inertia,
A = its area,
F = a factor based on cross-sectional geometry, and
G = its shear modulus [*13*].

Although other equations have been derived from shear deformation in other loading configurations, this discussion is limited to the one for three-point bending for simplification and because the shear deformation has the greatest effect in this configuration.

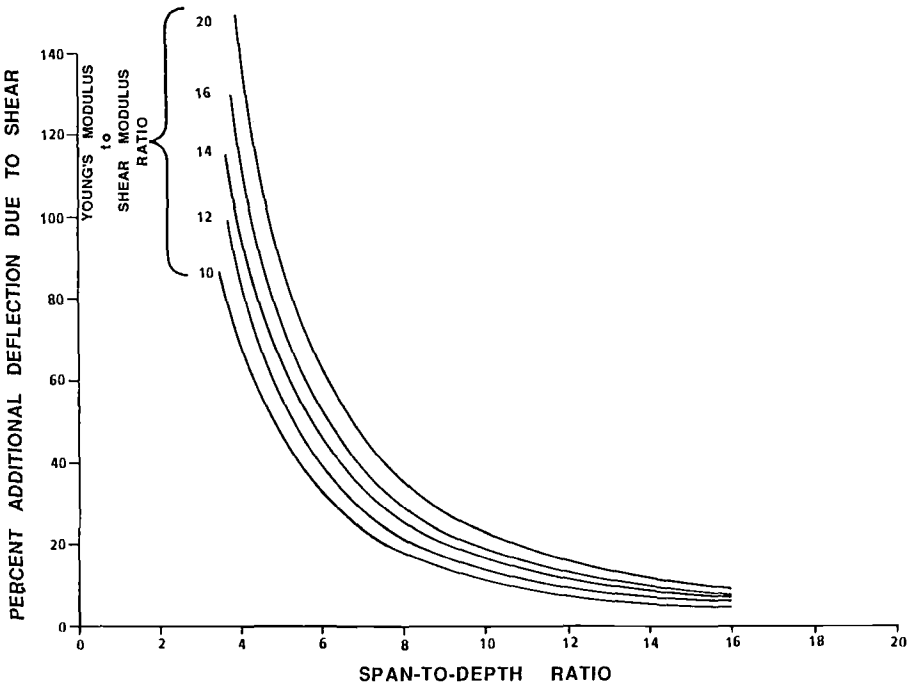

FIG. 6—*Effect of shear deformation in three point flexure.*

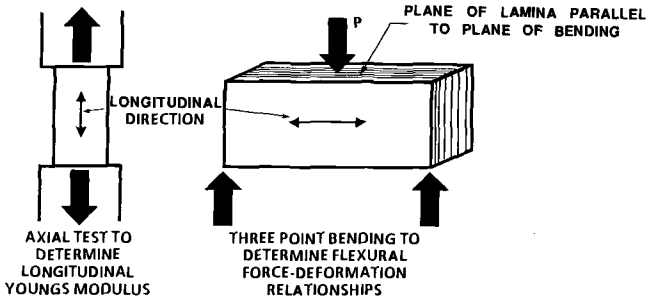

FIG. 7—*Shear modulus from axial and flexure tests combined.*

With this relationship, the shear modulus is required to perform this correction and calculate the Young's modulus from the flexural data. The recommended procedure assumes that the ratio between the Young's modulus and shear modulus is constant for a material, so that the shear modulus is no longer a variable in the equation [*14*]. Another procedure recommends the measurement of specimens with gradually increasing length until the difference in Young's modulus without the correction is insignificant [*15*].

This same relationship, however, could be used to determine the shear modulus of pultruded parts or specimens. If the Young's modulus were determined by other methods, such as an axial test, then flexure test measurements, as shown in Fig. 7, would supply data necessary to solve Eq 10 for shear modulus, yielding the following equation

$$G = \frac{12mLEIF}{A(48EI\text{-}mL^3)} \tag{11}$$

This approach could be used to determine shear modulus in pultrusions or laminates, and demonstrates how the shear deformation of a flexure specimen may be used to determine the shear modulus. But, it would be more cost-effective if the axial test could be avoided, and both the shear and Young's moduli were determined from the flexural test.

There are two unknown variables in Eq 10: the Young's modulus and the shear modulus. By configuring a pair of flexural tests so that some of the other parameters—force-deformation slope, moment-of-inertia, or length—are varied, test data may be acquired to rewrite Eq 10 as a pair of simultaneous equations to be solved for the two moduli. The following paragraphs discuss two possible approaches based on this principle.

In pultruded composites, the Young's and shear moduli should be the same in all planes parallel to the pultrusion's longitudinal axis. Fig. 8 shows a few of these planes. If a pultruded part had a solid rectangular cross section, and the applied loads were limited to the elastic range, then a pair of flexural tests could be performed on the same specimen: one on each of the principal axes, as shown in Fig. 9. Because the moment of inertia is different on each axis ($I_1 \neq I_2$), then the force-deformation slope of each flexural test will be different ($m_1 \neq m_2$). This pair of tests could then provide the data required to rewrite Eq 10 as the following two equations

$$E = \frac{m_1L^3}{48I_1}\left(1 + \frac{12I_1FE}{AL^2G}\right) \tag{12}$$

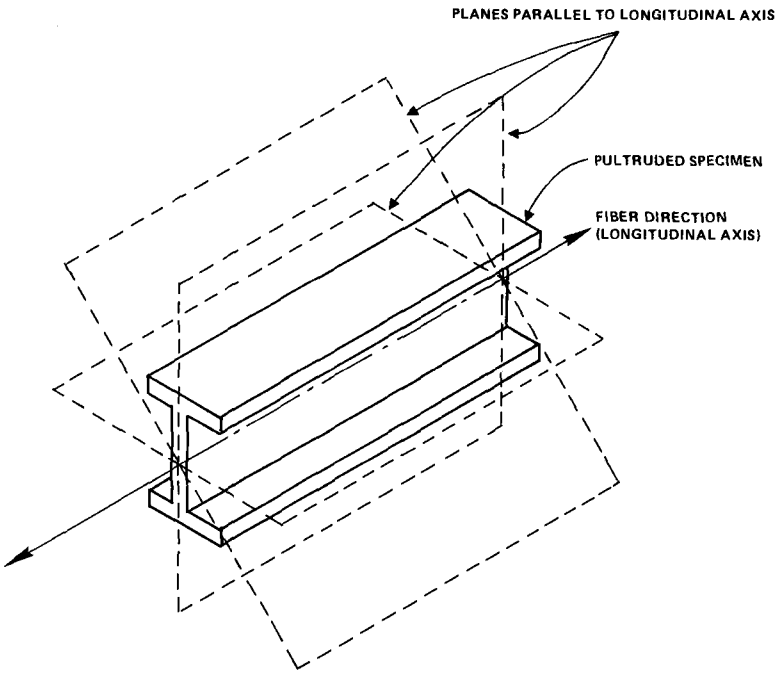

FIG. 8—*Geometry of longitudinal planes in a pultruded composite.*

$$E = \frac{m_2 L^3}{48 I_2}\left(1 + \frac{12 I_2 FE}{AL^2 G}\right) \tag{13}$$

Solving these two equations simultaneously for the Young's and shear moduli yields the following

$$E = \frac{m_1 m_2 L^3 (I_1 - I_2)}{48\, I_1 I_2 (m_1 - m_2)} \tag{14}$$

$$G = \frac{m_1 m_2 LF\,(I_1 - I_2)}{4A(I_1 m_2 - I_2 m_1)} \tag{15}$$

For a solid rectangular beam, the shape factor $F = 1.2$ and the beam's breadth (b) and depth (h) can be substituted into formulas for the area and the moments of inertia, so that Eqs 14 and 15 can be rewritten as

$$E = \frac{m_1 m_2 L^3 (h^2 - b^2)}{4\, b^3 h^3 (m_1 - m_2)} \tag{16}$$

$$G = \frac{3 m_1 m_2 L\,(h^2 - b^2)}{10bh\,(h^2 m_2 - b^2 m_1)} \tag{17}$$

Therefore, it may be possible to determine both the Young's and shear moduli from a

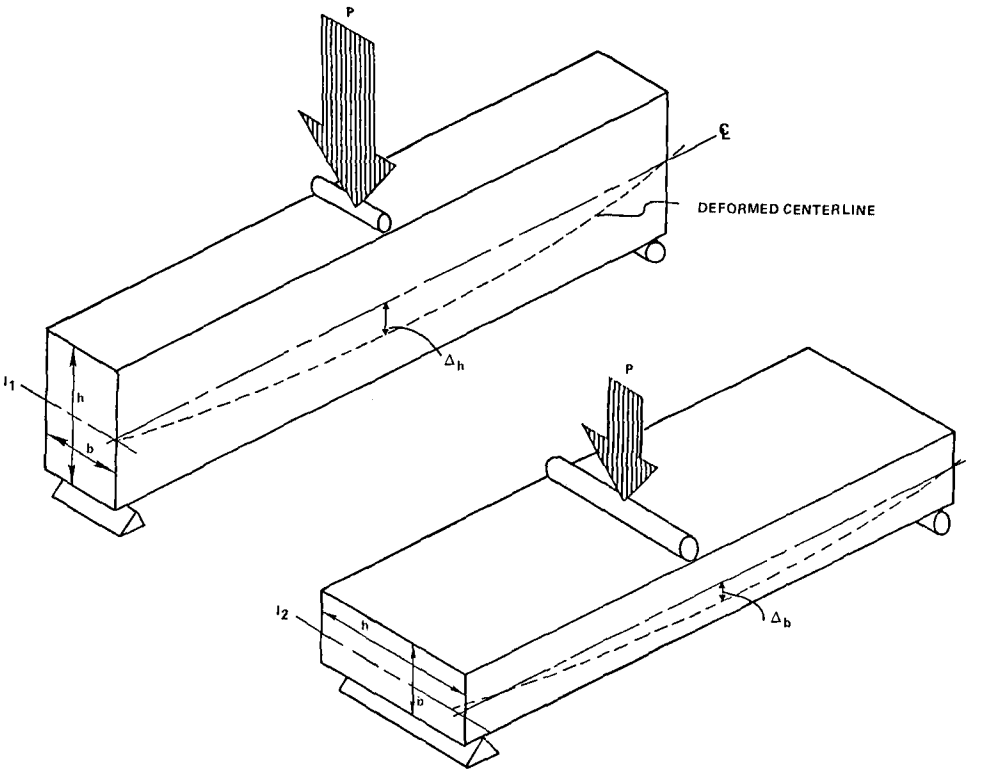

FIG. 9—*Bending tests on both axes of a rectangular beam.*

pair of flexural tests on a single specimen. Note that the pultruded part need not have a solid rectangular cross section as long as it has two longitudinal planes with different moments of inertia. Some of the sections appropriate for this approach might include elliptical sections, rectangular box beams, I-beams, angles, or T-sections.

For specimens that cannot be tested on two axes or do not have different moments of inertia on different axes—such as square or circular sections—the test fixture might be configured so that specimens could be tested over two different spans, as shown in Fig. 10. Because the support spans are different, the force-deformation slope of the two flexural tests will be different. When Eq 10 is rewritten as a pair of equations with two span lengths and two force-deformation slopes, and they are solved simultaneously for the Young's and shear moduli, the following two equations are derived

$$E = \frac{m_1 m_2 L_1 L_2 (L_1^2 - L_2^2)}{48I(m_2 L_2 - m_1 L_1)} \tag{18}$$

$$G = \frac{F m_1 m_2 L_1 L_2 (L_1^2 - L_2^2)}{4A(m_1 L_1^3 - m_2 L_2^3)} \tag{19}$$

Therefore it may be possible to develop a flexural testing approach to determine both Young's and shear moduli for pultrusions of any shape. Because testing on only one axis is required, the approach might even be useful for laminates if the difficulties of buckling can

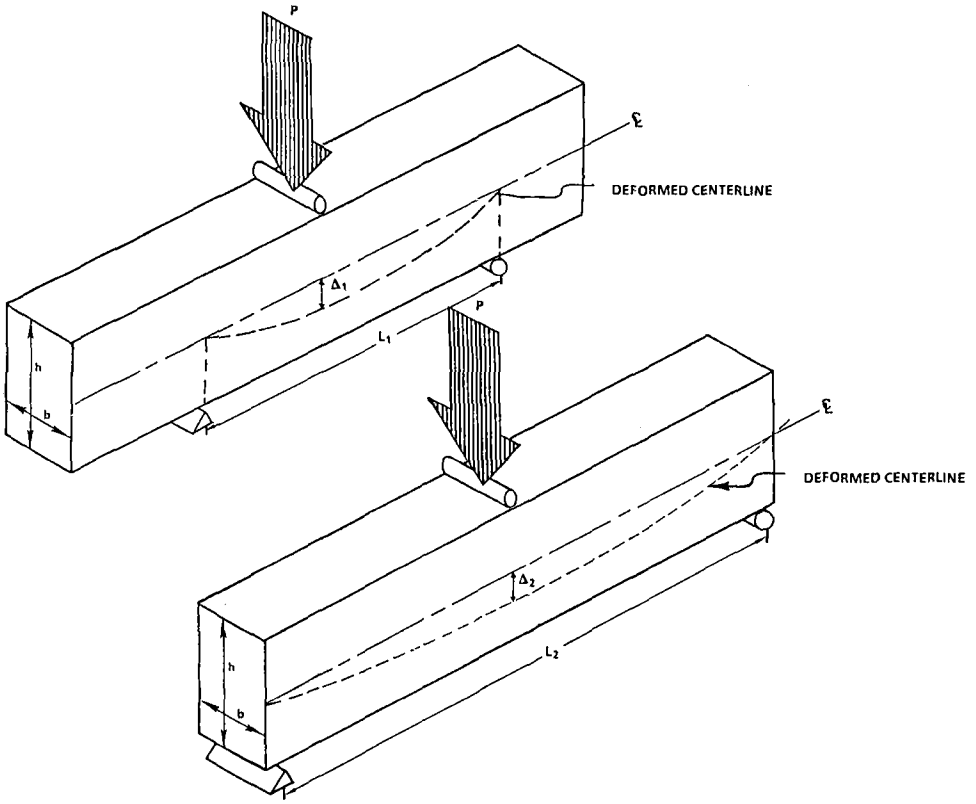

FIG. 10—*Bending tests on beams of different spans.*

be overcome when these composites are loaded in such a way that the plane of bending is parallel to the lamina.

A possible test configuration for this approach is envisioned as using a three-point loading fixture with a load cell to measure the applied force and a deflectometers to measure the center point deflection. Because a form of difference between force-deformation slopes occurs in the denominators of all the equations used to calculate Young's and shear moduli from this approach (Eqs 14 through 19), the precision of the deflection measurements and their relative magnitudes are important to the accuracy of the moduli determination. Therefore, the specimen's span-to-depth ratio, the difference between moments of inertia for the two-axis approach, and the difference between the lengths in the two-length approach, as well as the deflection precision, are all important to the measurement.

To determine, in a rough way, an appropriate set of specimen dimensions for this approach, a sensitivity study was performed. The graphite/aluminum composite selected had the following properties

$$E = 310.3 \text{ GPa}$$
$$G = 27.58 \text{ GPa}$$

The deflectometer used to measure the specimen's center point deflection was assumed to have a precision of ±0.025 mm. The applied load was limited so that the maximum fiber

stress was less than 50% of the failure stress to ensure linear response. For the two-axis approach, the possible specimens investigated were rectangular in section with spans varying from 100 to 300 mm on 50 mm intervals. For some composites, the shear deformation has been shown to be significant at span-to-depth ratio $L/h = 32$. For this study the span-to-depth ratios were varied from 4 to 20. The breadth-to-depth ratios were varied from 0.5 to 0.9. For each span, span to depth, and breadth to depth, the specimen dimensions were determined and then used to accurately calculate the two deflections from the flexural tests. The deflections were then reounded to the nearest 0.025 mm and used in Eq 15 and 16 to calculate the Young's and shear moduli that would be observed as a result of the test limitations. The computer program to perform the study is listed in Appendix I.

Because the relative error in the deflection decreases as the magnitude of the deflection increases, the longer specimens generally gave more accurate readings. The accuracy also tended to improve as the breadth-to-depth and span-to-depth ratios decreased. Any variation, however, from the longest specimen, with the smallest breadth-to-depth and span-to-depth ratio, introduced an error as large as 5% in the Young's modulus and 20% in the shear modulus. But, the 300 mm long specimen with a depth of 75 mm and breadth of 37.5 mm showed an observed Young's and shear moduli each within 2%. Increasing the deflectometer precision to ±0.0025 mm gave the same accuracy on a 150 mm long specimen with a proportionate breadth and depth.

A similar study was performed on the two-length test approach using square sections varying over the same range of spans and span-to-depth ratios. Instead of a breadth-to-depth ratio, however, a span ratio for the two different spans in the test was varied from 1.1 to 2.0 at 0.1 intervals. The computer program to perform this study is listed in Appendix II. A review of the resulting data indicated that span lengths of at least 300 and 510 mm on a specimen with a depth of 75 mm were required to determine the Young's and shear moduli within 2%, if the deflectometer measured to within ±0.025 mm. As with the two-axis approach, a deflectometer precision of ±0.0025 mm allowed the use of much shorter specimens if the span-to-depth and span-to-span ratios were maintained.

In actual flexural tests, the accuracy would be much greater with smaller specimens, because the force-deformation slope would be developed statistically from a series of measurements, rather than a single one. To examine the capabilities of smaller specimens, data from flexural specimens of a graphite/aluminum plate [*16*] were evaluated using a form of Eqs 18 and 19. In this case, the flexure test was conducted in four-point bending, and the span-to-depth ratio was changed by varying the specimen depth rather than the support span. Due to the nature of these tests and the variation of modulus in the plates, only two of the specimens were suitable for determination of shear modulus.

The data used to determine the shear modulus from these specimens are shown in Table 1. The flexural modulus had been calculated using a force-deformation slope and the following equation [ASTM Test Methods for Flexural Properties Unreinforced and Reinforced Plastics and Electrical Insulating Materials D 790-84]

$$E_b = 0.21L^3m/bh^3 \tag{20}$$

TABLE 1—*Data for the determination of shear modulus.*

Specimen	Depth,d	Width,w	Span,s	Load Span	Modulus,E
1	2.24 mm	12.57 mm	37.5 mm	12.5 mm	115.83 GPa
2	1.55 mm	12.73 mm	37.5 mm	12.5 mm	119.97 GPa

This equation was used to obtain the force-deformation slope which was then used with the breadth, depth, and support span data of the two specimens in the following two equations

$$E = \frac{23L^3m_1m_2(h_1^2 - h_2^2)}{103h_1^2h_2^2(m_1b_2h_2 - m_2b_1h_1)} \tag{21}$$

$$G = \frac{21.6Lm_1m_2(h_2^2 - h_1^2)}{103(b_2h_2^3m_1 - b_1h_1^3m_2)} \tag{22}$$

Evaluating the test data in this manner gave a Young's modulus of 131.93 GPa and a shear modulus of 6.00 GPa. The shear modulus of the specimen had not been determined in any other way, so no comparison could be made. But, note that the Young's modulus determined in this way is greater than the flexural modulus and conforms to the rule that the flexural modulus is approximately 0.8 times the axial modulus [*17*].

The ultimate usefulness of these flexural test approaches will depend on the accuracy of the deflection measurement and the selection of appropriate specimen dimensions. Other studies may indicate limits to the ratio between the Young's and shear moduli for which the test is useful. The possible cost advantages of a flexural test, as opposed to an axial test, should provide the incentive for more comprehensive studies and tests to make the approach practical.

Conclusion

Several potential alternative approaches for the experimental determination of shear modulus in fiber-reinforced composites are indicated from an investigation into the mechanics of existing axial and flexural tests. At the present time, these approaches are only theoretical in nature. More comprehensive studies and tests will be required to develop practical testing procedures from these approaches. But, the incentive to develop these procedures should exist, because they are simpler to perform on a wider range of specimens than are existing tests.

Acknowledgments

The author would like to express his gratitude and sincere appreciation to Dr. Stewart W. Johnson for his guidance and encouragement, Mr. William C. Harrigan for the graphite/aluminum flexural data, and The BDM Corporation who funded the preparation of this manuscript.

References

[*1*] Whitney, J. M., Daniel, I. M., and Pipes, R. B., "Experimental Mechanics of Fiber-Reinforced Materials," The Society for Experimental Stress Analysis, Nomograph No. 4, 1982, p. 171.

[*2*] Bodig, J. and Jayne, B. A., *Mechanics of Wood and Wood Composites*, Van Nostrand Rheinhold, New York, 1982.

[*3*] Zweben, C., "Test Methods for Fibrous Composite Materials," presented at the UCLA Metal Matrix Composites short course, University of California at Los Angeles, 14–18 June 1982.

[*4*] Adams, D. F., "Iosipescu Method for Determination of Shear Modulus in Composite Materials," *Composite Materials: Testing and Design (Sixth Conference), ASTM STP 787*, I. N. Daniel, Ed., American Society for Testing and Materials, Philadelphia, 1982, p. 20.

[*5*] Zweben, C., "Test Methods for Fibrous Composite Materials," presented at the UCLA Metal Composite short course, University of California at Los Angeles, 14–18 June 1982.

[6] Herakovich, C. T., Bergner, H. W., and Bowles, D. E., "A Comparative Study of Composite Shear Specimens Using the Finite-Element Method," *Test Methods and Design Allowables for Fibrous Composites, ASTM STP 734,* C. C. Chamis, Ed., American Society for Testing and Materials, Philadelphia, 1981, pp. 129–151.
[7] Tsai, S. W. and Hahn, T. T., *Introduction to Composite Materials,* Technomic Publishing, Stamford, CT, 1980.
[8] Whitney, J. M., Daniel, I. M., and Pipes, R. B., "Experimental Mechanics of Fiber-Reinforced Materials," The Society of Experimental Stress Analysis, Monograph No. 4, 1982, pp. 173–174.
[9] Whitney, J. M., Daniel, I. M., and Pipes, R. B., "Experimental Mechanical Fiber-Reinforced Materials," The Society of Experimental Stress Analysis, Monograph No. 4, 1982, p. 188.
[10] Yeow, Y. T., "In-Plane Behavior of a Ribbon-Reinforced Composite," *Composite Materials: Testing and Design (Sixth Conference), ASTM STP 787,* I. M. Daniel, Ed., American Society for Testing and Materials, Philadelphia, 1982, pp. 101–123.
[11] McKague, L., Reynolds, J. D., and Fruit, J., "Mechanical Characteristics of T300-6k/V378A Graphite/Polyimide," *Composite Materials: Testing and Design (Sixth Conference), ASTM STP 787,* I. M. Daniel, Ed., American Society for Testing and Materials, Philadelphia, 1982, pp. 73–84.
[12] Whitney, J. M., Daniel, I. M., and Pipes, R. B., "Experimental Mechanics of Fiber-Reinforced Materials," The Society of Experimental Stress Analysis, Monograph 4, 1982, pp. 165 & 199.
[13] Roark, R. J. and Young, W. C., *Formulas for Stress and Strain, 5th Edition,* McGraw-Hill, New York, 1982, pp. 185.
[14] Whitney, J. M., Daniel, I. M., and Pipes, R. B., "Experimental Mechanics of Fiber-Reinforced Materials," The Society for Experimental Stress Analysis, Monograph No. 4, 1982, pp. 167–168.
[15] Whitney, J. M., Daniel, I. M., and Pipes, R. B., "Experimental Mechanics of Fiber-Reinforced Materials," The Society for Experimental Stress Analysis, Monograph No. 4, 1982, p. 168.
[16] Padilla, F. J., "Flexural Strength and Modulus of Elasticity in Aluminum-Graphite Composites," The Aerospace Corporation, Interoffice Correspondence, 23 Aug. 1974.
[17] Padilla, F. J., "Flexural Strength and Modulus of Elasticity in Aluminum-Graphite Composites," The Aerospace Corporation, Interoffice Correspondence, 23 Aug. 1974.

APPENDIX I

Computer Program for Data Analysis of Two-Axis Flexure Test

```
10  DIM E(2),G(2)
20  E=4.5E7
30  G=4E6
40  FOR L=4 TO 12 STEP 2
50  FOR Hl=4 to 20 STEP 2
60  H=L=Hl
70  PRINT "L=";L,"H=";H
80  PRINT
90  PRINT "    B    P    Dh       Db       E1       G1       E2       G2"
100 FOR Bh=.5 to .9 STEP .1
110 B=H*Bh
120 P=DROUND(7.0E4*2*B*B*H/3/L,1)
130 Dh=P*L 3*(1+1.2*(H/L) 2*E/G)/4/E/B/H 3
140 Db=P*L 3*(1+1.2*(B/L) 2*E/G)/4/E/H/B 3
150 FOR Q=-3 TO -4 STEP -1
160 X=PROUND(Db,Q)-PROUND(Dh,Q)
170 IF X=0 THEN GOTO 200
180 E(Q+5)=(P*L 3*(H*H-B*B)/H 3/B 3/4/X/E-1)*100
190 GOTO 210
200 E(Q+5)=99.999
```

```
210 X=PROUND(Dh,Q)*H*H-PROUND(Db,Q)*B*B
220 IF X=0 THEN GOTO 250
230 G(Q+5)=(.3*P*L*(H*H-B*B)/B/H/X/G-1)*100
240 GOTO 260
250 G(Q+5)=99.999
260 NEXT Q
270 PRINT USING "DD.DDD,DDDDDD,2(DD.DDDDDD),4(DDDD.DDD)";
      B,P,Dh, Db,E(2)G(2),E(1),G(1)
280 NEXT Bh
290 PRINT
300 NEXT Hl
310 PRINT
320 NEXT L
330 END
```

APPENDIX II

Computer Program for Data Analysis of Two-Length Flexure Test

```
10  DIM E(2),G(2)
20  E=4.5E7
30  G=4E6
40  FOR L=4 TO 12 STEP 2
50  FOR Ll=1.1 TO 2 STEP .1
60  L2=L*Ll
70  PRINT "L1=";L,"L2=";L2
80  PRINT
90  PRINT "    B    P    Dh   Db      E1      G1      E2      G2"
100 FOR Hl=4 TO 20 STEP 2
110 H=L/Hl:B=.5*M
120 P=DROUND(7.0E4*2*B*B*H/3/L2,1)
130 D1=P*L 3*(1+1.2*(H/L) 2*E/G)/4/E/B/H 3
140 D2=P*L2 3*(1+1.2*(H/L2) 2*E/G)/4/E/B/H 3
150 FOR Q=-3 TO -4 STEP -1
160 X=PROUND(D1,Q)*L2-PROUND(D2,Q)*L
170 IF X=0 THEN GOTO 200
180 E(Q+5)=(P*L*L2*(L*L-L2*L2)/H 3/B/4/X/E-1)*100
190 GOTO 210
200 E(Q+5)=99.999
210 X=PROUND(D2,Q)*L 3-PROUND(D1,Q)*L2 3
220 IF X=0 THEN GOTO 250
230 G(Q+5)=(.3*P*L*L2*(L*L-L2*L2)/B/H/X/G-1)*100
240 GOTO 260
250 G(Q+5)=99.999
260 NEXT Q

270 PRINT USING "DD.DDD,DDDDDD,2(DD.DDDDDD),4(DDDD.DDD)";
      B,P,Dh,Db,E(2),G(2),E(1),G(1)
280 NEXT Hl
290 PRINT
300 NEXT Ll
310 PRINT
320 NEXT L
330 END
```

Fracture Behavior and Nondestructive Evaluation

Louis Raymond[1] *and James A. Jennings*[2]

Fracture Toughness of Thin-Walled Cylinders Fabricated from Discontinuous Silicon Carbide Whiskers/Aluminum Metal Matrix Composites

REFERENCE: Raymond, L. and Jennings, J. A., **"Fracture Toughness of Thin-Walled Cylinders Fabricated from Discontinuous Silicon Carbide Whiskers/Aluminum Metal Matrix Composites,"** *Testing Technology of Metal Matrix Composites, ASTM STP 964,* P. R. DiGiovanni and N. R. Adsit, Eds., American Society for Testing and Materials, Philadelphia, 1988, pp. 277–284.

ABSTRACT: Six cylinders (16 cm diameter with 6 mm wall thickness) were manufactured from two unreinforced aluminum alloy and four silicon carbide (SiC) whisker reinforced aluminum composites. Curved, subthickness, Charpy sized specimens were used to measure the fracture toughness, K_{Ic} in accordance with ASTM E 399. For the more ductile, unreinforced alloys, the British crack opening displacement (COD) method was used as an elastic-plastic approximation of the fracture toughness. The results rank the relative toughness of the aluminum alloy metal matrix composite (MMC) materials.

The test program was successful in demonstrating the changes in fracture toughness due to the addition of SiC whiskers, notch acuity, and prior hydrostatic straining. A new procedure was developed by which materials can be successfully fatigue precracked (FPC) by utilizing the notched strength ratio in bending. This procedure eliminates the cost of the excessive waste commonly generated in attempting to fatigue precrack fracture toughness specimens by conventional techniques.

KEY WORDS: fracture toughness testing, silicon carbide whiskers/aluminum cylinders, hydrostatic strain, notch acuity effects, matrix effects

Background

Six cylinders, measuring about 16 cm in diameter and having a wall thickness of 6 mm, were manufactured from two unreinforced and four discontinuous silicon carbide whiskers (SiCw)-reinforced aluminum composites. This program was designed to measure the resulting fracture toughness of cylinders hydrostatically tested to failure, being aware of the large range of toughness represented by this group of materials and the difficulties encountered in attempting to measure the fracture toughness in accordance with ASTM Test Method for Plane-Strain Fracture Toughness of Metallic Materials (E 399), which require fatigue precracking. Because specimens had to be machined from the wall of a cylinder, curved specimens had to be used in conducting the fracture toughness tests.

[1] President, L. Raymond & Associated, Irvine, CA 92714.
[2] Materials engineer, Naval Oceans Systems Center, San Diego, CA 92152.

TABLE 1—*Composite materials tested as fabricated cylinders.*

Item No.	Composite	Thickness, mm	Identification
(3)	SiCw/6061-T6,	4	(coded C)
(4)	SiCw/6061-T6,	6	(coded B)
(5)	SiCw/6061-T6,[a]	6	(coded F)
(6)	SiCw/7090-T6,	6	(coded A)

[a] Hydrostatically strained.

Materials

A total of six cylinders, representing six different materials were tested. The two unreinforced aluminum alloy cylinders were manufactured from: (1) 6061-T6, 4 mm thick (coded E) and (2) 7075-T6, 4 mm thick (coded D). The four SiCw-reinforced aluminum composite cylinders are listed in Table 1. The nominal tensile properties of these alloys are given in Table 2 [*1*]. The nominal tensile properties of these metal matrix composite materials (MMC) materials are in Table 3.

Aluminum Alloy 7090 is a powder metallurgy alloy containing about 1.5% cobalt. The 7090 alloy is claimed to have typical strength levels similar to, or greater than, those of alloy 7075, presumably with much improved stress corrosion resistance and fracture toughness properties.

Testing Procedure

In order that the corrosion-fatigue behavior of these cylinders can be further evaluated by LRA Labs' (formerly METTEK) rapid, inexpensive, modular (RIM) fracture testing system that uses Charpy-sized specimens [*2,3*], the test specimens were machined to 4 to 6 by 10 by 55 mm; that is, a curved, subthickness Charpy-sized specimen. The tests described in this report were performed with Instron closed loop hydraulic fatigue machine.

The root radius of the notch was 0.12 mm (127 μm) and the initial, machined depth-to-width ratio (a/W) was 0.35. The length of the specimen was oriented parallel to the axis of the cylinders. The contour of the cylinder was maintained, with the faces of the specimen cut parallel to the radius drawn to the centerline of the specimen as shown in Fig. 1.

One specimen from each cylinder or a set of six notched specimens was loaded to failure on a 3-point bend fixture, in order to measure the maximum bending load and to calculate the *notched* strength ratio in bending (NSRb) in the same manner as the *specimen* strength ratio in bending (Rsb) is calculated according to ASTM E 399. For Charpy size specimens, this ratio is given as

$$\text{Rsb} = 6\,P_{max}/\text{YS} \times \text{BW}^2(1\text{-}a/W)^2 \quad (1)$$

TABLE 2—*Tensile properties of matrix alloys.*

Material	Elastic Modulus, GPa	Yield Strength/Tensile Strength, MPa	Elongation, %	Ref
6061-T6	69	276/310	17	*1*
7075-T6	72	503/572	11	*1*
7090-T6	70	600/641	10	...

TABLE 3—*Tensile properties of composites.*

Material	Elastic Modulus, GPa	Form	Yield Strength/ Tensile Strength, MPa	Elongation, %	Ref
20 volume % SiCw/6061-T6	122	plate	443/584	1.8	4
20 volume % SiCw/6061-T6	96	plate	321/423	6.7	1
20 volume % SiCw/6061-T6	108	tube	374/520	2.7	4
20 volume % SiCw/6061-T6	110	tube	392/...	...	...[a]
20 volume % SiCw/7090-T6	121	tube	689/...	...	...[a]

[a] Compression data from cylinders after hydrostatically testing to failure.

where

P_{max} = maximum breaking load,
B = thickness;
W = width; and
a/W = crack depth ratio.

The maximum breaking loads of each alloy is then used in conjunction with the notched strength ratio to estimate the loads required to fatigue precrack the remaining test specimens.

The fatigue precrack extended the crack length to between 0.45 to 0.55 a/W. The maximum fatigue precrack load, according to ASTM E 399 was such that the maximum stress intensity of the terminal (25%) stage of fatigue crack growth did not exceed 60% of the K_{Ic}-value of the material; however, since MMC materials are notoriously difficult to fatigue precrack, a methodology was developed during the course of this work that quickly estimates the con-

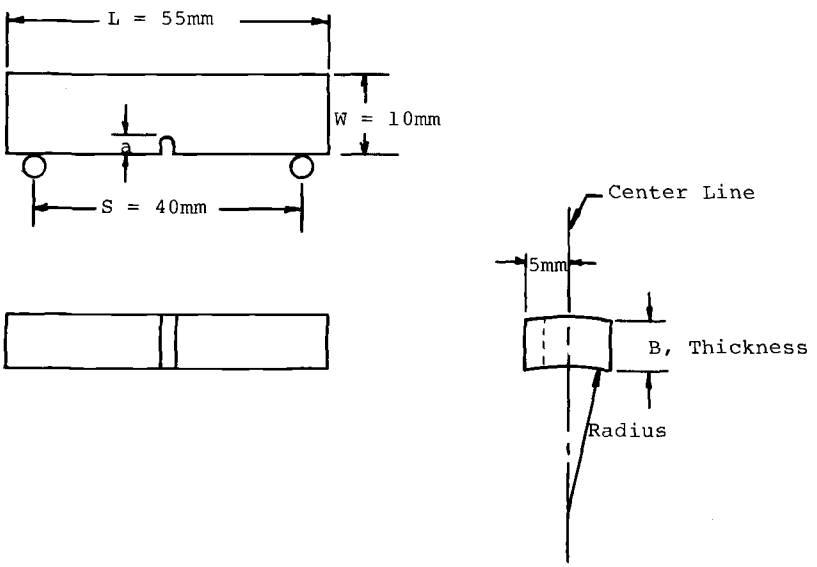

FIG. 1—*Specimen shape and dimensions taken from SiC_w/Aluminum cylinders.*

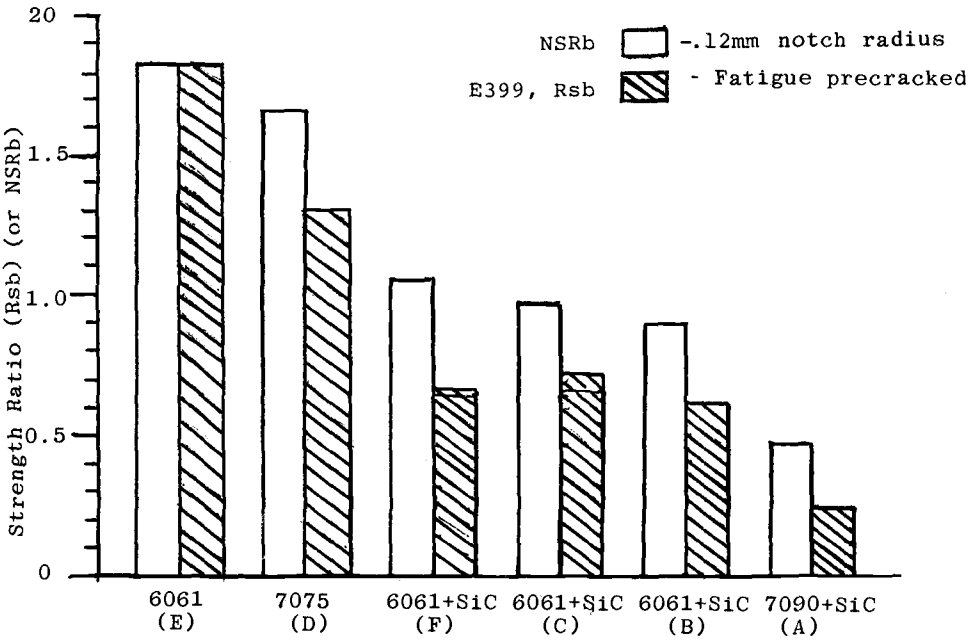

FIG. 2—*Specimen strength ratio (Rsb) per ASTM E 399 for 3-point bend for both fatigue precracked and 0.12 mm root radius specimens.*

ditions for successfully precracking test specimens, even for the low toughness MMC materials.

Test Results

Figure 2 is a bar chart of NSRb and Rsb per ASTM E 399 plotted to rank the relative fracture toughness of the six different materials listed in Table 4 in descending order. Also to be noted is that as NSRb decreases, the ratio of Rsb/NSRb decreases. This information will be used to generate an empirically based fatigue precracking (FPC) methodology;

Figure 3 is a plot of the calculated fracture toughness using linear elastic analysis per

TABLE 4—*Relative ranking of fracture toughness with most ductile material at top of list.*

Material	Code	Comments[a]
6061-T6, 4 mm	E	HTF
7075-T6, 4 mm	D	HTF
20 volume % SiCw/6061-T6, 4 mm	C	HTF
20 volume % SiCw-HS/6061-T6, 6 mm	F	HS prior to HTF
20 volume % SiCw/6061-T6, 6 mm	B	HTF
20 volume % SiCw/7090-T6, 6 mm	A	HTF

[a] HS = hydrostatically strained.
HTF = hydrostatically tested to failure.

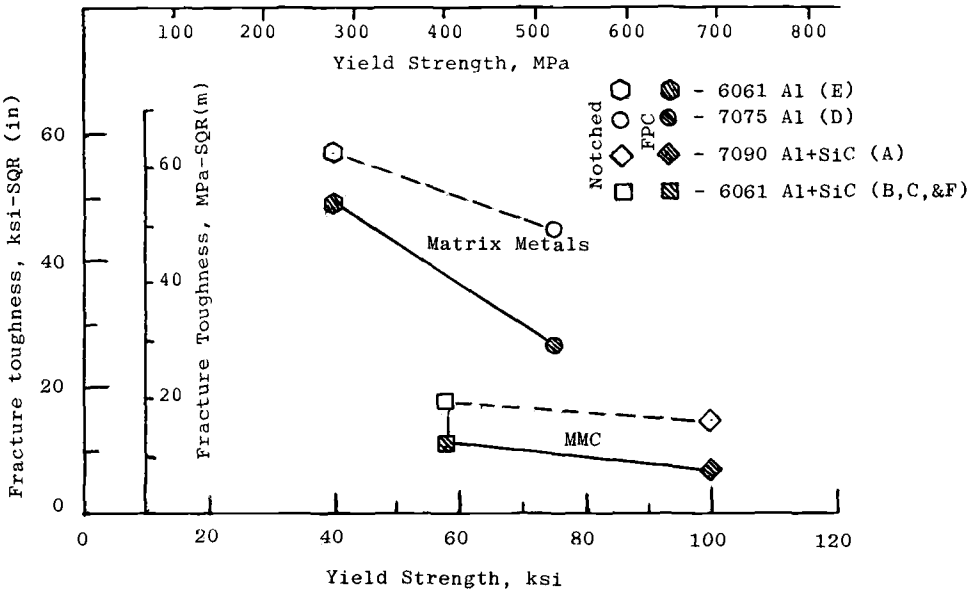

FIG. 3—*Fracture toughness as a function of yield strength for both the wrought aluminum alloys and silicon carbide metal matrix composite materials.*

ASTM E 399 for the MMC materials and elastic-plastic crack opening displacement (COD) analysis for the wrought aluminum alloys. A single specimen, load-unloading compliance technique was used to identify the point of crack extension necessary to calculate the K_{COD}-values. The fracture toughness is tabulated in Table 5. It should be noted that the results are a single data point and do not represent statistical sampling.

Figure 4 is a photograph of a metallographic section showing the root radius to be about 0.12 mm. Figure 5 is a photograph of the fracture faces, illustrating the difference in two topographical features and thickness dimensions. To be noted is the fact that the MMC materials have no shear lip, which is apparent in the wrought aluminum alloys.

Description of FPC Methodology

Figure 6 is a plot of the ratio of Rsb/NSRb versus NSRb. As noted, an increase in the ratio occurs as NSRb increases or the material becomes more ductile; in fact, as NSRb

TABLE 5—*Quantitative estimates of fracture toughness.*

Code	Material	K_{Ic} or K_{COD}[a]
E	6061-T6, 4 mm	53.7 (48.9)
D	7075-T6, 4 mm	31.3 (28.5)
C	20 volume % SiCw/6061-T6, 4 mm	17.0 (15.5)
F	20 volume % SiCw-HS/6061-T6, 6 mm	11.6 (10.6)
B	20 volume % SiCw/6061-T6, 6 mm	11.3 (10.3)
A	20 volume % SiCw/7090-T6, 6 mm	7.9 (07.2)

[a] Units of MPa-SQR(m) and ksi-SQR(in.) in parenthesis.

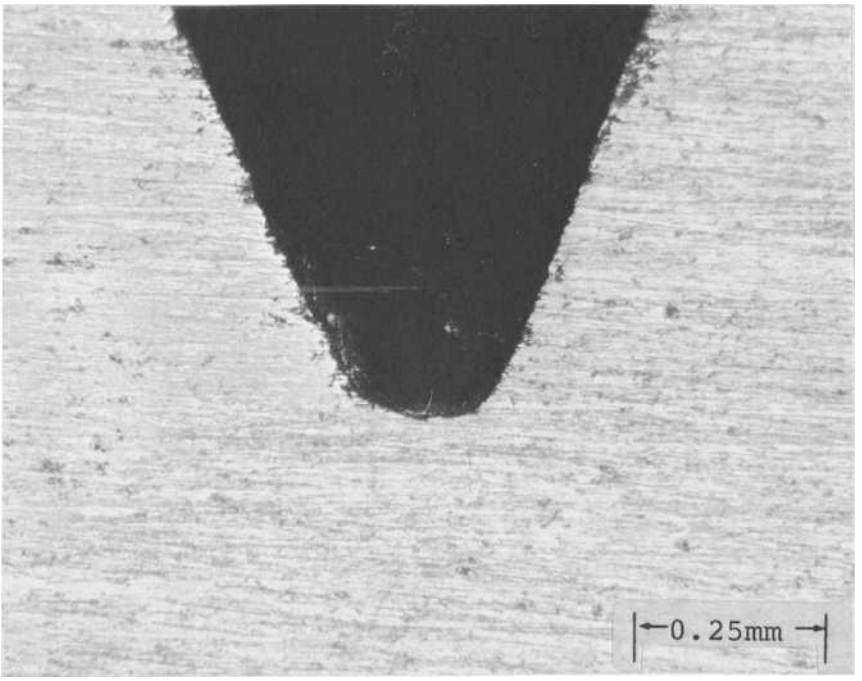

FIG. 4—*Transverse section through 125 μm (5 mil) notch radius of Charpy V-notch.*

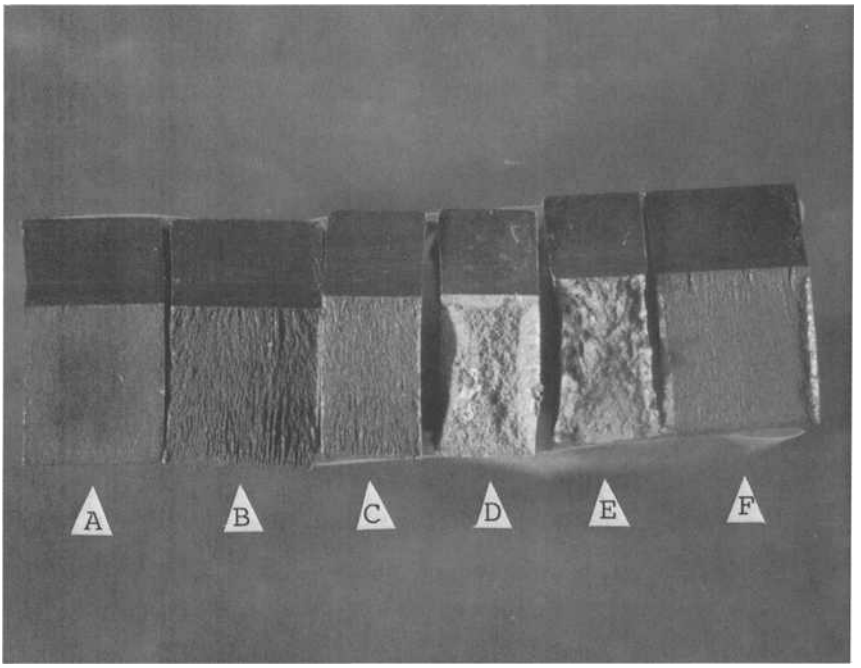

FIG. 5—*Fracture faces of test coupons from six different aluminum/silicon carbide and aluminum alloy cylinder fragments.*

approaches the theoretical limit of 2.2, the ratio approaches unity; that is, the maximum fracture load is not a function of notch acuity.

Figure 6 can be used for aluminum matrix composite materials, and might well apply for other metals and alloys because the trend would be similar, but no data to this affect has been generated to date.

Figure 6 allows the maximum load for precracking to be estimated from the maximum load required to fracture a notched specimen and the calculated value of NSRb. The maximum load for FPC is estimated as 60% of the ratio NSRb/Rsb. These calculated values are plotted along the right side of Fig. 6. Therefore, with only the value of NSRb, the FPC maximum load is given as a fraction of the maximum load to break the notched specimen or P_{max}.

Mathematically, the relationship can be reduced to

$$P_{FPC} = (0.16\,\text{NSRb} + 0.175)P_{max} \tag{2}$$

This empirically derived equation prescribes the load for fatigue precracking a Charpy size specimen with a root radius of 125 μm (5 mil) with 85% confidence. The procedure would involve breaking one machine notched specimen, calculating NSRb, and using Eq. 2 to establish the load for fatigue precracking other specimen from the same lot. It is advisable to do the precracking under displacement control in 3-point bending.

Conclusions

1. The fracture toughness of aluminum MMC materials decreases with notch acuity from a radius of 0.12 mm to a fatigue precrack. The decrease implies a critical root radius of

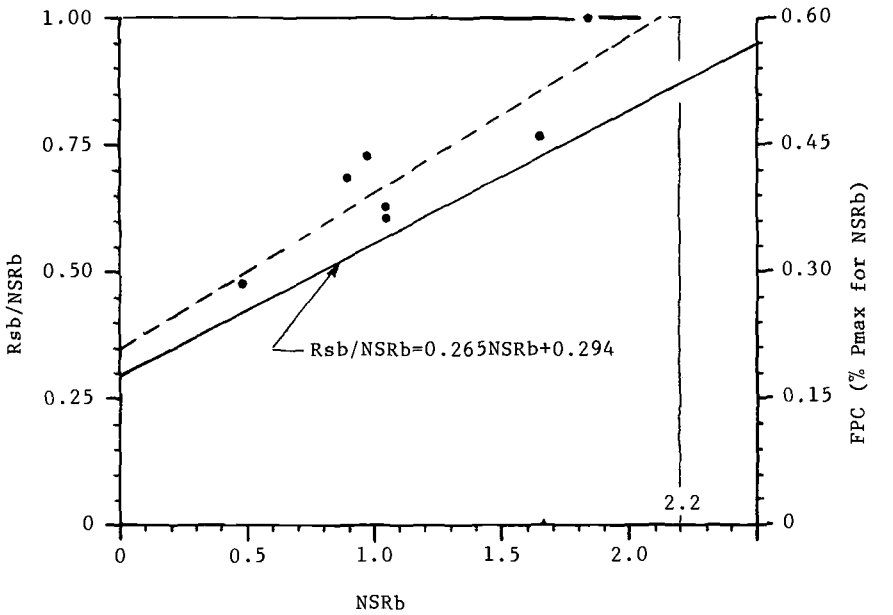

FIG. 6—*A method of estimating the maximum load for fatigue precracking based on fractured load of notched test specimen.*

about 50 μm for an invariant measurement of K_{Ic}, assuming a proportional relationship between K and rho (SQR).

2. The prior hydrostatic straining or cold work did not decrease the fracture toughness.

3. The high-strength SiCw/7090 aluminum MMC has lower toughness than the SiCw/6061-T6 aluminum MMC.

4. The fracture toughness of the wrought aluminum matrix materials is significantly decreased by the addition of SiC whiskers.

Recommendations

The use of the notched strength ratio in bending, NSRb, of a fracture toughness specimen in accordance with the calculations of the specimen strength ratio, Rsb, per ASTM E 399 is recommended as a method of estimating the maximum loads for fatigue precracking fracture toughness specimens. The root radius of the starting notch should be standardized. The 125 μm (5 mil) root radius utilized in this program is recommended because it was found to be successful in achieving the goals of the program in measuring a large range of fracture toughness values.

References

[1] Hoffman, C. and McDanels, D., "Microstructure and Orientation Effects on Properties of Discontinuous Silicon Carbide/Aluminum Composites," National Aeronautics and Space Administration, Washington, DC, 1984.

[2] Coates, D. J., Raymond, L., "Development and Use of a Modular, Subsize Specimen Test Procedure for HEM and SCC Failure Analysis," International Society of Testing and Failure Analysis, 1985.

[3] Raymond, L., "Small Specimen Corrosion Testing Techniques for Failure Analysis," National Association of Corrosion Engineers, 1985.

[4] Crowe, C. R., Gray, R. A., and Hesson, D. F., "The Effect of Notch Activity in the Fracture Toughness of Silicon Carbide/Aluminum Metal Matrix Composites," NRL Memorandum Report 5417, Naval Research Laboratory, 27 Feb. 1985.

Madhu S. Madhukar,[1] *Jonathan Awerbuch,*[1] *and Michael J. Koczak*[1]

Deformation and Failure Characteristics of Center-Notched Unidirectional Boron/Aluminum at Room and Elevated Temperatures

REFERENCE: Madhukar, M. S, Awerbuch, J, and Koczak, M. J., **"Deformation and Failure Characteristics of Center-Notched Unidirectional Boron/Aluminum at Room and Elevated Temperatures,"** *Testing Technology of Metal Matrix Composites, ASTM STP 964,* P. R. DiGiovanni and N. R. Adsit, Eds., American Society for Testing and Materials, Philadelphia, 1988, pp. 285–304.

ABSTRACT: The global and local deformation characteristics of center-notched unidirectional B/Al composites were examined both in the elastic and inelastic regions of the load-displacement curves. The global deformation was measured at room temperature by applying the conventional compliance gage, while the local deformation was measured by means of the interferometric displacement gage (IDG) technique at room and elevated temperatures. The effects of notch length and test temperature on the deformation characteristics and on damage initiation and progression were determined. The local compliance calibration curves, obtained with the IDG technique, were found to be highly sensitive to notch length. With increasing load, significant nonlinearity in the load-crack-opening displacement (COD) and jumps in COD have been observed, resulting from the crack-tip damage progression in the form of fiber breakage, matrix inelastic (plastic) shear deformation, and matrix cracking. The results obtained with the IDG technique were qualitatively correlated with high magnification ($\times 150$) visual observations in real-time via a closed circuit television. The IDG technique could be easily applied at elevated temperatures. Results from the IDG indicate that significant changes in the deformation characteristics occur at temperatures above 204°C (400°F). The experimental global and local compliance calibration curves were compared with predictions and an excellent agreement has been established. The predictions of COD were made by applying an existing analytical model which assumes the existence of a zone of longitudinal inelastic shear deformation emanating from the notch-tip. Good agreement between prediction and experiment could be established. The comparison provided a simple procedure to evaluate the *in situ* matrix shear yield stress. The experimental results indicate that the analytical modeling for the inelastic deformation of the subject material should incorporate both the matrix strain hardening and the mechanism of sequential failure.

KEY WORDS: metal-matrix composites, boron/aluminum, compliance, fracture

Metal-matrix composites are currently being considered for the so-called "primary" structural applications in a variety of aircraft and aerospace structures. In several aspects they are superior to most resin-matrix composites, for example, in elevated temperature per-

[1] Research assistant, associate professor, Department of Mechanical Engineering and Mechanics, and professor, Department of Materials Engineering, Drexel University, Philadelphia, PA 19104.

formance, transverse and shear strengths, impact resistance, and susceptibility to the potential problem of moisture absorption.

Among the variety of metal-matrix composites available, the boron/aluminum (B/Al) system has received most of the attention in the research and application studies. However, in spite of the recognized advantages of this material system under larger operating temperature ranges, very little information is available regarding the effects of temperature on the deformation, damage progression, and failure mechanisms. In characterizing the fracture behavior of these composites, emphasis has been given primarily to the notched strength and fracture toughness [*1,2*]. These ultimate values (at failure) are of concern for design purposes. However, in order to obtain an insight into the deformation characteristics, crack-tip damage growth, thermal response, etc., a better understanding of the load-deformation characteristics is also required. Detailed load-deformation curves will also aid in establishing the validity of any proposed analytical model for predicting the deformation characteristics of composites and thus will ultimately provide criteria for identifying the material variables that dominate in specific applications.

The ability to detect damage initiation and progression through the examination of the load-displacement curves strongly depends on the experimental procedure employed. In the case of notched B/Al, the crack-tip damage is localized. It appears primarily in the form of longitudinal inelastic shear deformation of the matrix, fiber breakage, and matrix cracking [*3*]. Slow crack-tip damage growth has been observed, and a sequential failure process of these three major failure modes usually occurs. The first indication of crack-tip damage is seen in the nonlinearity of the load-deformation curve. The deviation from stress-displacement linearity depends on crack length, temperature, and the variety of intrinsic material variables. Due to the localized nature of the crack-tip damage, the application of a highly sensitive experimental procedure for monitoring the failure process is essential. In this manner the conditions under which damage initiates and progresses can be identified.

In this study the interferometric displacement gage (IDG) technique [*4–7*] has been applied in order to obtain accurate and sensitive measurements of crack opening displacements (COD) at room and elevated temperatures. The effect of crack length and temperature on the "local" compliance calibration curves (obtained with the IDG) have been determined. The "global" compliance calibration curves (obtained with the conventional compliance gage) were determined at room temperature, and the results were compared with those obtained with the more sensitive IDG technique. Far-field load-displacement curves and "local" load-COD curves to failure were also obtained. The load-COD curves were examined in detail for detecting damage initiation, crack length effects, and temperature effects on the degree of nonlinearity. The comparisons between experiments and predictions for both the elastic and inelastic regions are also discussed.

Experimental Procedure

The boron/aluminum (B/Al) material tested in this study is 142 μm (5.6 mil) B/Al-6061F, 45 to 50% volume fraction, manufactured by DWA Composite Specialities. Unidirectional specimen coupons having dimensions of 200 by 25.4 mm (8.0 by 1.0 in.) were machined from 200 by 200 mm (8.0 by 8.0 in.) plates. Center notches of approximately 1.27, 2.54, 5.10, 7.60, 10.20, and 12.70 mm (0.05, 0.10, 0.20, 0.30, 0.40, and 0.50 in.) long and 0.37 mm (0.015 in.) wide were introduced. All machining was performed by means of the Electrical Discharge Machining (EDM) technique. Aluminum end tabs, 25.4 by 25.4 by 1.3 mm (1.0 by 1.0 by 0.05 in.) were applied to all specimens using epoxy resin.

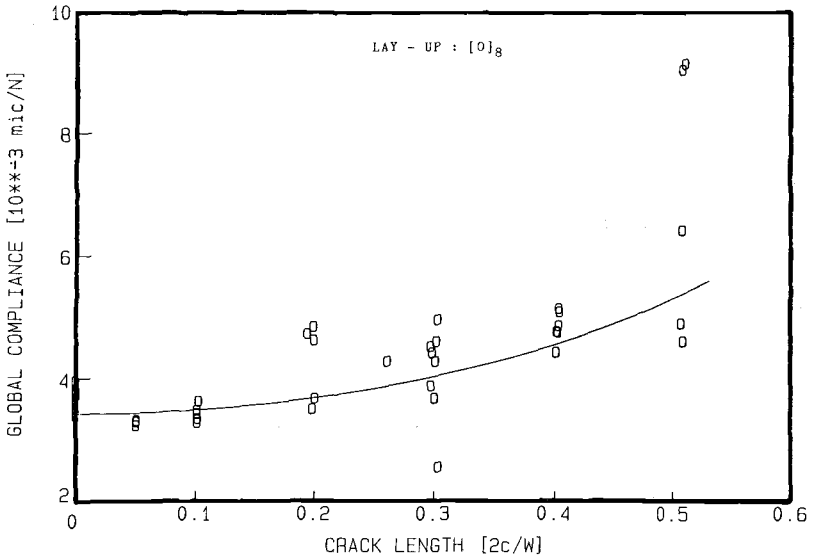

FIG. 1—*Prediction of global compliance calibration curve (Eq 1) and comparison with experiments for center-notched* $[0]_8$ *B/Al. There is a large scatter in the experimental data and the global compliance is not very sensitive to crack length.*

All specimens were tested on a closed loop servohydraulic Instron testing machine (Model 1331). The tension tests were performed under stroke control mode at a rate of approximately 0.07 mm/min (0.003 in./min). Steps were taken to ensure loading axiality which was confirmed by applying pairs of strain gages along the specimen's edges.

The global deformation curves were obtained at room temperature by means of a standard compliance gage (gage length = 25.4 mm (1.0 in.)). The local load-COD curves were obtained at room and elevated temperatures (up to 371°C (700°F)) by means of Laser Interferometric Displacement Gage (IDG) technique. The details of the IDG technique can be found in Ref *4–7*. This technique has been shown to be very accurate, highly sensitive (in the submicron scale), simple to utilize, and can be applied over a wide range of operating temperatures [*6,8*]. Elevated temperature tests were performed by enclosing the specimens in a custom-made furnace with a temperature capability of 538°C (1000°F).

All five elastic moduli were determined at room temperature by means of an extensometer (25.4 mm (1.0 in.) gage length), attached to the specimen surface. In order to verify the extensometer results and ensure load axiality, selected room temperature specimens were also strain gaged. The longitudinal stiffness, E_L, and the major Poisson's ratio, ν_{LT}, were determined by testing $[0]_8$ specimens; the transverse stiffness, E_T, and the minor Poisson's ratio, ν_{TL}, by testing $[90]_8$ specimens; and the longitudinal shear stiffness, G_{LT}, by testing

TABLE 1—*Average elastic moduli at room temperature.*

	E_L	E_T	ν_{LT}	ν_{TL}	G_{LT}
Average, GPa	205.21	134.59	0.252	0.150	115.10
Number of specimen	23	7	5	3	2
Standard deviation, GPa	20.14	22.87	0.024	0.078	61.10

$[\pm 45]_{2s}$ laminates. The longitudinal shear stiffness was calculated using the procedure proposed in [*9*]. Fiber strength was determined by testing representative fibers used in the fabrication of each B/Al plate.

The five elastic moduli were determined at elevated temperatures by means of strain gages (type: Micromeasurement WK-06-062TT-350, gage length = 1.57 mm, grid width = 1.91 mm). Tests were performed in the temperature range of 38°C (100°F) to 371°C (700°F) and in increments of 38°C (100°F). In order to ensure the data reliability, each specimen was loaded three to ten times within the elastic region, and the average values have been used in the data reduction and analysis.

Fracture surfaces of notched and unnotched specimens subjected to various elevated temperatures were examined through the scanning electron microscope (SEM). Three-dimensional, or stereo, views of the fracture surfaces were prepared from which the different microfailure modes could be easily identified. Several specimens were loaded to a predetermined load level, unloaded, and the matrix was dissolved in order to reveal crack extension and damage progression. Notch-tip damage extension and the number of broken fibers were inspected optically and via the SEM. Damage progression was also monitored in real time via a closed-circuit television (CCTV) system which provided a clear view of the notch-tip region at the specimen surface at magnifications up to $\times 150$.

Results and Discussion

Elastic Behavior

The elastic behavior of center-notched B/Al has been characterized by the compliance calibration curves of the subject material. Both the far-field displacement and actual crack opening displacement (COD) were measured using the conventional compliance gage and the interferometric displacement gage (IDG) techniques, respectively. From these two respective experimental procedures the "global," C_g, and the "local," C_l, compliance calibration curves were recorded [*8*]. The global compliance was determined at room temperature only, while the local compliance was determined at temperatures ranging from 21°C (70°F) to 371°C (700°F) in 38°C (100°F) increments. Following is a summary of the results:

1. Global Compliance Calibration Curves—A summary of the global compliance as a function of crack length is shown in Fig. 1. Clearly the compliance increases with increasing crack length; however, the sensitivity of the global compliance to crack length is not very pronounced. Also, assessment of the sensitivity is made more difficult by the large scatter in the data points. The prediction of the global compliance can be made from the analysis based on the energy release rate due to crack extension [*7,10*]. The following closed-form expression for the global compliance can thus be derived, for example [*7*]

$$C_g = \pi\alpha/(E_L B)\int Y^2 2c/W \, \mathrm{d}(2c/W) + L/(BWE_L) \tag{1}$$

where

W = specimen width,
B = specimen thickness,
L = gage length of the compliance gage,
c = half crack length, and
Y = Width Correction Factor (WCF), and

the orthotropic correction factor, α, is given by

$$\alpha = 1/\sqrt{2}\,[(E_L/E_T)^{1/2} - \nu_{LT} + E_L/(2G_{LT})]^{1/2} \quad (2)$$

where E_L, E_T, and G_{LT} are the longitudinal, transverse, and shear moduli, respectively, and ν_{LT} is the major Poisson's ratio.

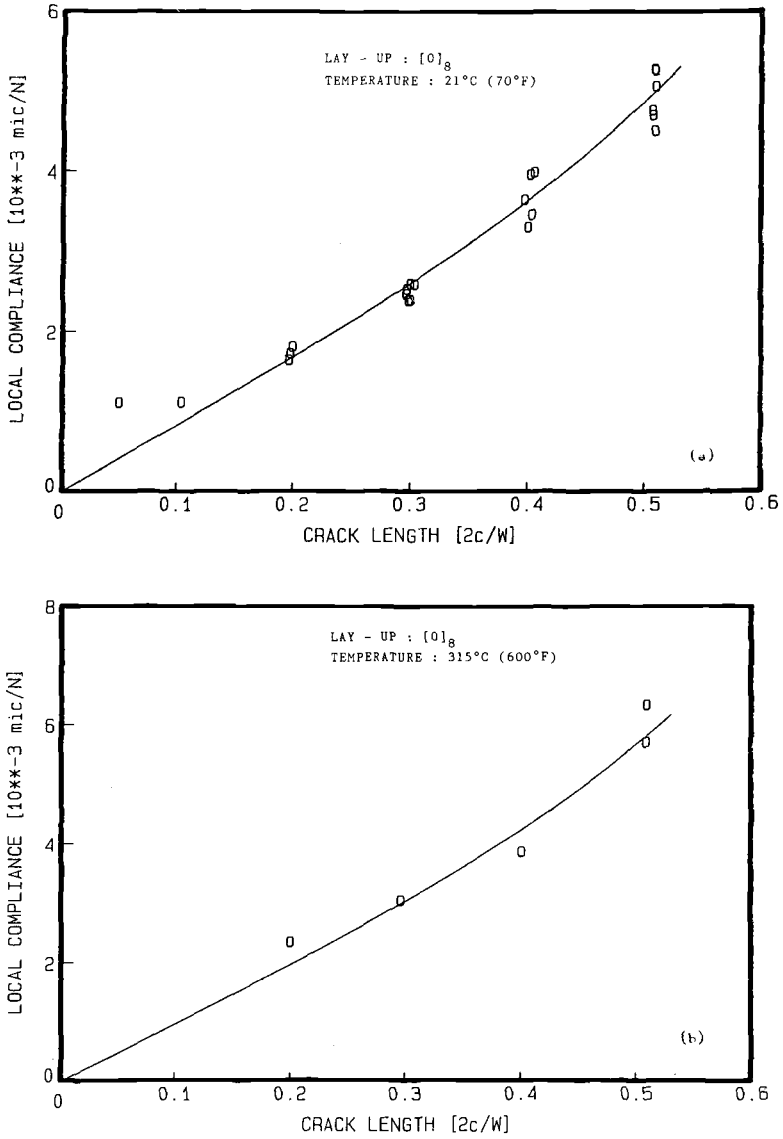

FIG. 2—*Prediction of local compliance calibration curves (Eq 4) and comparison with experiments for center-notched* $[0]_8$ *B/Al at:* (a) *21°C (70°F) and* (b) *315 °C (600°F). The local compliance is much more sensitive to crack length and the results are highly reproducible.*

It has been shown in Ref 7 that the isotropic value of Y can be applied for orthotropic unidirectional B/Al composites as well. The following expression of Y has been chosen [7,11]

$$Y = 1 + 0.1282(2c/W) - 0.2881(2c/W)^2 + 1.5254(2c/W)^3 \quad (3)$$

Utilizing Eqs 1 to 3, the global compliance can then be predicted. Based on the elastic moduli obtained experimentally, the value of $\alpha \simeq 1.0$ was calculated from Eq 2. This value is lower than expected (for example, $\alpha = 1.3$ in. [7]). However, it should be noted that significant scatter in the experimental values of all four elastic moduli has been recorded in this study. The average values of these moduli obtained from all the specimens tested at room temperature are given in Table 1. Similar Tables were obtained at all the temperatures applied in this study. Based on the previous results, for example [7], the value of $\alpha = 1.20$ was selected for the purpose of comparison between prediction and analysis. The predicted global compliance is shown by the solid line in Fig. 1. There is a general agreement between the prediction and the experiments. However, as mentioned earlier, due the poor sensitivity of the global compliance to crack length and the large scatter in the data, the global compliance calibration curves may not be sufficiently accurate for determining the "effective" crack-tip damage size.

2. Local Compliance Calibration Curves—The local compliance calibration curves obtained by the IDG technique were determined for all crack lengths and at a wide range of temperatures. In order to obtain accurate and reliable results, each specimen was loaded/unloaded 3 to 10 times within the elastic region (to approximately 10% of ultimate). The average of these compliances has been used in the data analysis. Very good reproducibility in the local compliance was recorded from these repeated quasi-static loadings/unloadings.

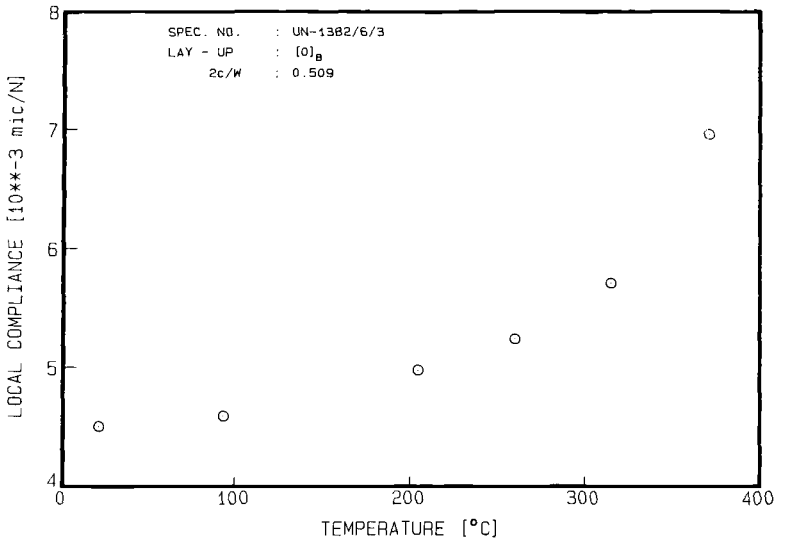

FIG. 3—*The experimental values of local compliance as a function of temperature for center-notched $[0]_8$ B/Al. The compliance is sensitive to temperature and it increases significantly at temperatures greater than 204°C (400°F).*

For example, the average local compliance recorded in seven loading/unloading tests at 315°C (600°F) for $2c/W = 0.4$ was $3.87 \times 10^{-3}\mu/N$ with standard deviation of $7.0 \times 10^{-5}\mu/N$. Similar reproducibility has been recorded in most tests.

The experimental values of the local compliance as a function of crack length at room and at elevated temperature are shown in Fig. 2. The solid lines shown in Fig. 2 are the predictions to be discussed later. In comparison with the global compliance, Fig. 1, the local compliance is much more sensitive to crack length and the experimental results are highly reproducible, Fig. 2. It is clear, therefore, that the estimation of the "effective" damage size made through the change in compliance will be much more accurate if the local compliance values are used.

The change in the local compliance with temperature is shown in Fig. 3 for a single specimen. It is interesting to note that the increase in compliance becomes quite significant at approximately 204°C (400°F). In regard to the effects of temperature on the properties of the constituents, that is, boron fibers and aluminum matrix, it has been reported that the boron fibers show little change in their properties up to 400°C (752°F) [*12*]. The aluminum matrix, on the other hand, undergoes a significant change at approximately 204°C (400°F) in mechanical properties such as stiffness and strength [*13*]. Therefore, it can be concluded that the significant degradation in the stiffness of aluminum beyond 204°C (400°F) is the primary cause of the increased compliance of B/Al composites at these temperatures.

For the prediction of the local elastic behavior the existing solutions for an orthotropic plate containing an elliptical opening [*14*] were applied. The expression for the local compliance can be derived as [*7*]

$$C_1 = (2c/W)\,\alpha/(BE_L)\,Y \tag{4}$$

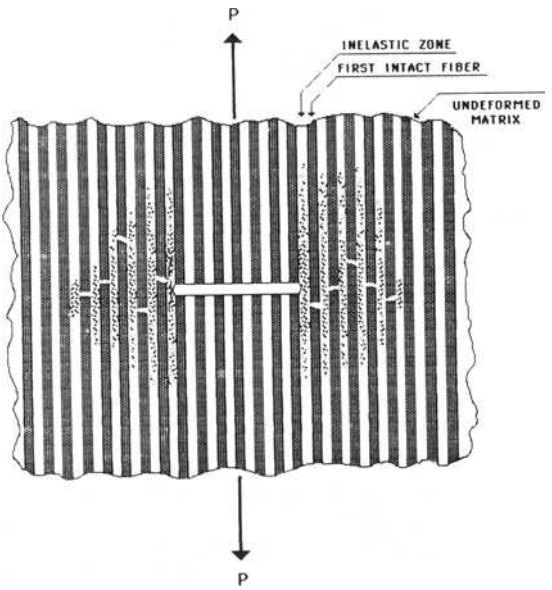

FIG. 4—*Schematic of crack-tip damage progression in center-notched* $[0]_8$ *B/Al.*

In order to predict the local compliance calibration curves at room and elevated temperatures, the variation of α with temperature was determined from Eq 2. For this purpose the elastic modulii (E_L, E_T, ν_{LT}, and G_{LT}) were determined experimentally for the entire range of temperatures applied in this study. The resulting values of α, calculated from Eq 2, varied between 1.0 to 1.14 for the entire temperature range. It should be noted that there was large scatter in the experimental values of the elastic moduli at elevated temperatures, as there was at room temperature. For this reason the values of the orthotropic correction factor, α, were adjusted to best fit the experimental data. The purpose of this study was not to determine the values of α, but rather to establish the trend and compare the prediction

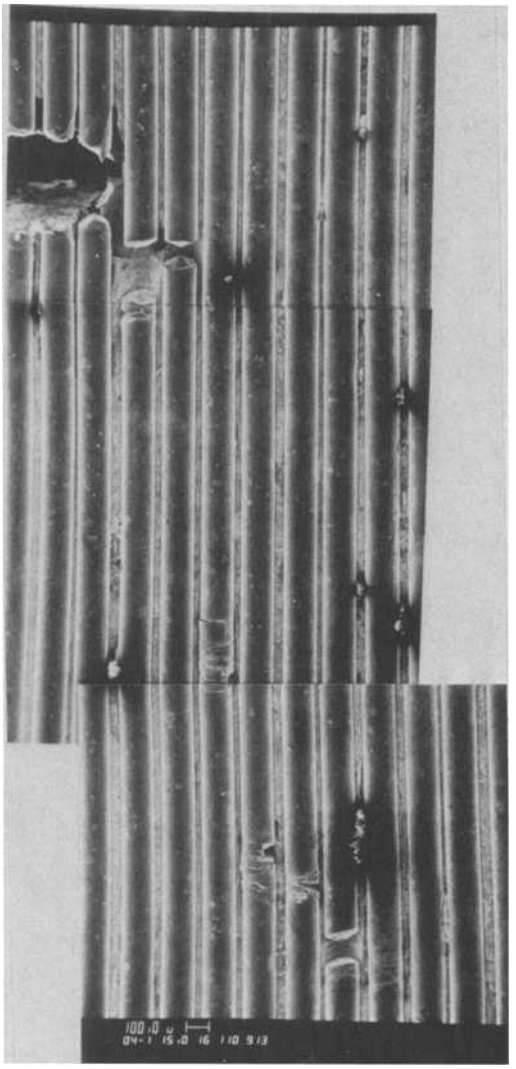

FIG. 5—*Crack-tip damage extension in unidirectional B/Al; aluminum matrix is dissolved exposing broken fibers.*

with experiments. The values of α used were 1.2 for the predictions of the local compliance calibration curves at room temperature, Fig. 2*a*, and 1.4 for elevated temperature, Fig. 2*b*. Clearly the predictions are in an excellent agreement with experiments. It can be concluded that the analysis correctly describes the local elastic deformation characteristics of center-notched unidirectional B/Al composites, and the local compliance calibration curves obtained through this analysis can be more accurately used to determine the "effective" crack-tip damage size in these composites.

Failure Mechanisms and Processes

For notched unidirectional B/Al it has been observed through Closed Circuit Television (CCTV) that the first damage occurs in the form of matrix-plastic deformation at the crack tip. With increasing applied stress, this plastic zone grows parallel to the fibers and is confined between the crack tip and the first intact fiber, Fig. 4. At sufficiently high stress levels (approximately 40 to 50% of ultimate), the first intact fiber (next to the crack tip) fails and crack extension occurs. Upon the breakage of the first intact fiber, load transfer occurs and the second plastic zone develops. With increasing load this plastic region grows along the adjacent intact fiber until the second intact fiber breaks. This process repeats itself approximately four to six times before a catastrophic fracture of the specimen occurs. This early occurrence of damage and the initial slow crack growth have been also verified by monitoring acoustic emission (AE) during quasi-static loading [*15*]. It is demonstrated in the following discussion that the global load-deformation curves obtained by means of a standard compliance gage give little indication of this early damage. On the other hand, the local load-COD curves obtained by means of the IDG technique do indicate damage initiation and progression at early stages of loading. Consequently, a significant effort has been directed in this study toward determining the load-COD curves at a wide range of temperatures. The appropriate analytical procedure is also identified, and the predictions of the local deformation characteristics are compared with the experimental load-COD curves.

The sequential failure process described previously can be seen in the SEM micrographs, Fig. 5. Following loading to approximately 80% of ultimate load, the specimen was unloaded, and the outer layer of the aluminum was dissolved. The crack-tip damage includes seven broken fibers. The number of broken fibers, revealed by this procedure, depends on the applied stress. As seen in Fig. 5 the fibers fractured at different locations, that is, at some weak spots along their length, resulting in an irregular fracture surface. Multiple cracks at the fibers' fracture sites can be clearly seen, resulting in fragmentation of the fiber. This is most probably due to the high elastic energy released during fiber fracture. The gaps that are seen in the fibers resulted from the extensive dissolution of the matrix which caused the fragments to fall away. When the matrix is sufficiently intact (for example, the third and seventh fibers to the right of the crack tip) all the fiber fragments are held in place. Matrix etching and dissolution is increased by the degree of local inelastic deformation. Consequently a large degree of matrix removal occurs in the region of the inelastic zone. The effect of the matrix dissolution diminishes (that is, dissolving less material) as one moves away from the crack tip, which corresponds with the decrease of the plastic deformation. Thus, from the photographs shown in Fig. 5, it is clear that the bay between each pair of broken fibers has been plastically deformed, illustrating again the sequential nature of crack-tip damage progression.

Examination of the fracture surfaces indicates good fiber/matrix bonding and matrix consolidation. The photographs shown in Fig. 6 are paired to be viewed under a stereo viewer. These fracture surfaces reveal shattering of most fibers, both at room and elevated temperatures. The fragmented pieces of the boron fibers are well bonded to the aluminum

SPEC. NO. UN-1401/4/5
2c/W = 0.299

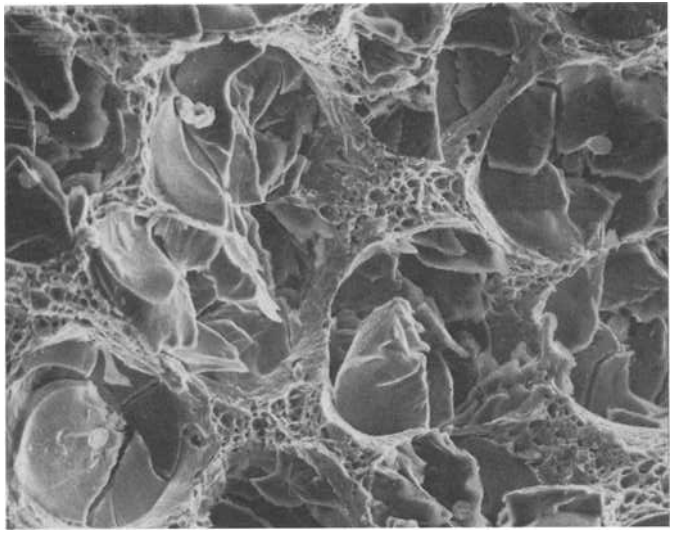

T = 21°C (70°F)
σ_f = 742.4 MPa

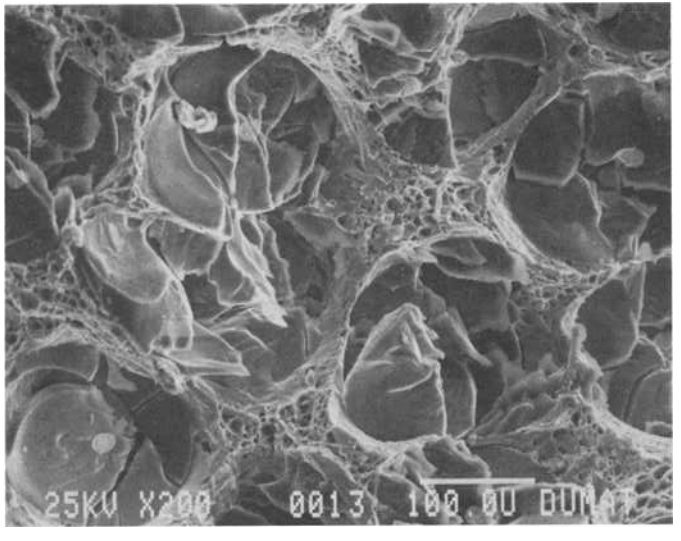

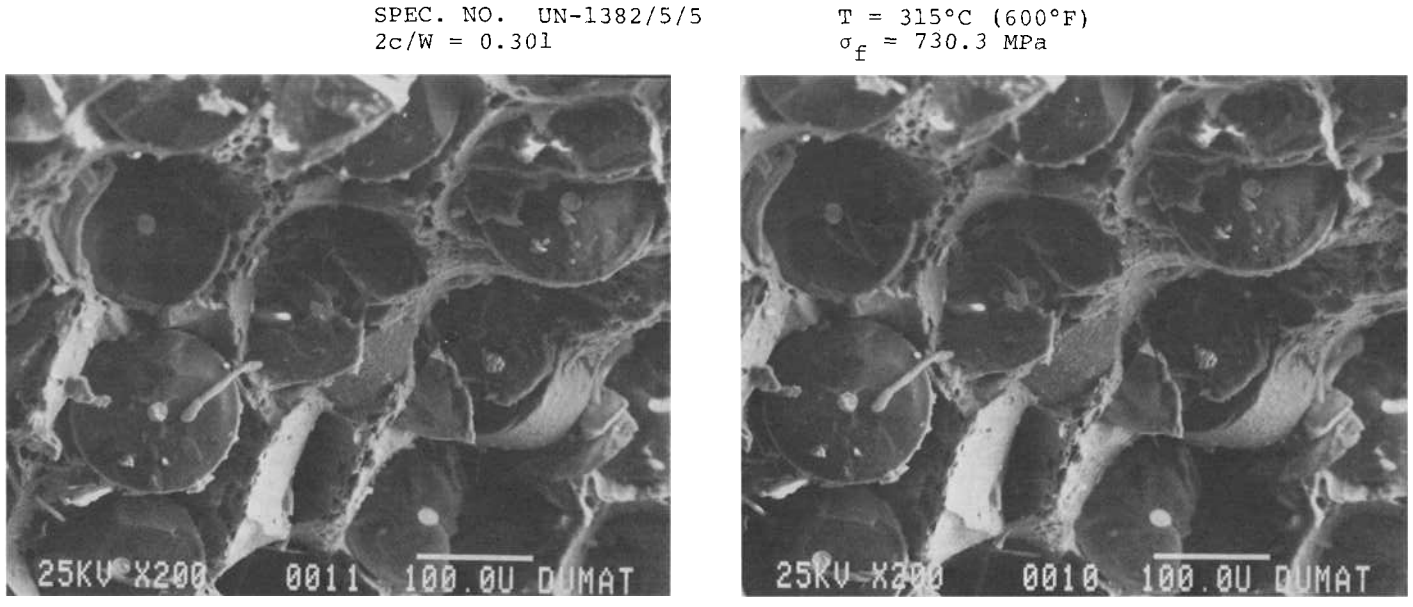

FIG. 6—*Scanning electron micrographs and stereo views of the fracture surfaces of unidirectional B/Al at room and elevated temperatures.*

matrix at different depths along the fibers, indicating a good fiber/matrix bonding. X-ray examination of the fiber's surface, using an energy dispersive x-ray analyzer on the SEM, demonstrated the presence of the aluminum 6061 matrix on the fiber's surface, for example, the aluminum, silicon, and magnesium lines. No splitting, that is, interfacial fracture, has been observed during the loading.

The significant plastic deformation of the aluminum matrix, seen in the photomicrographs of Fig. 6, is manifested by the large amount of microvoid coalescence. A comparison between the specimens tested at room and elevated temperatures does not show significant differences in the various microfailures associated with the fracture. However, the specimen loaded at elevated temperature has been subjected to an increased amount of plastic deformation, as expected.

Far-Field Load-Displacement Curves (Global Deformation)

The representative far-field stress-displacement curves for several center-notched unidirectional B/Al composites are shown in Fig. 7. Clearly the deformation characteristics depend on the crack length. The curves are fairly linear for most crack lengths. Only for the longer crack lengths and when the applied load approaches ultimate levels can a slight nonlinearity be detected. The lack of sensitivity of the global displacements to crack-tip damage (as detected through the CCTV) at low load levels is expected, considering that the damage is initially highly localized at the crack tip. Only as the applied stress approaches the ultimate value, where several fibers are broken and the longitudinal inelastic zone is no longer confined to the crack-tip region, Fig. 4, do the stress-displacement curves deviate from linearity, Fig. 7. It is concluded, therefore, that the global deformation measured across the crack by means of a conventional compliance gage (having a 25.4 mm gage length) is not sufficiently sensitive to detect such localized damage.

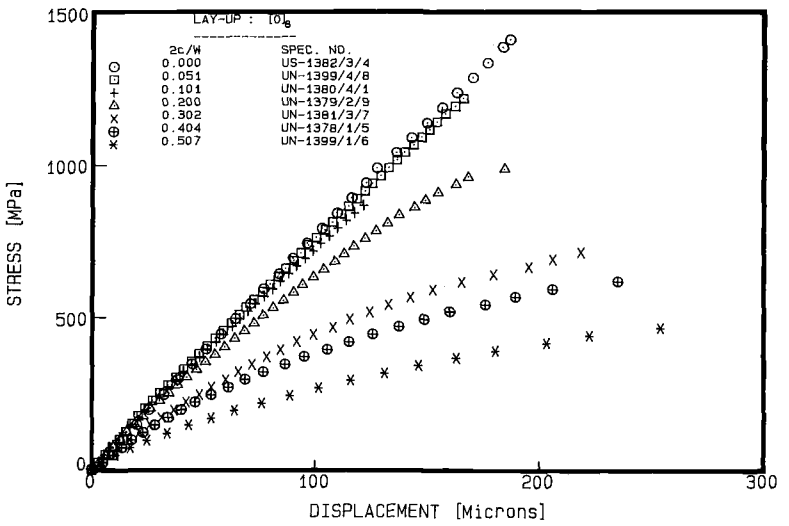

FIG. 7—*Effect of notch length on the global stress-displacement curves for center-notched* $[0]_8$ *B/Al. The nonlinearity in the curves is detected only when* $2c/W > 0.3$.

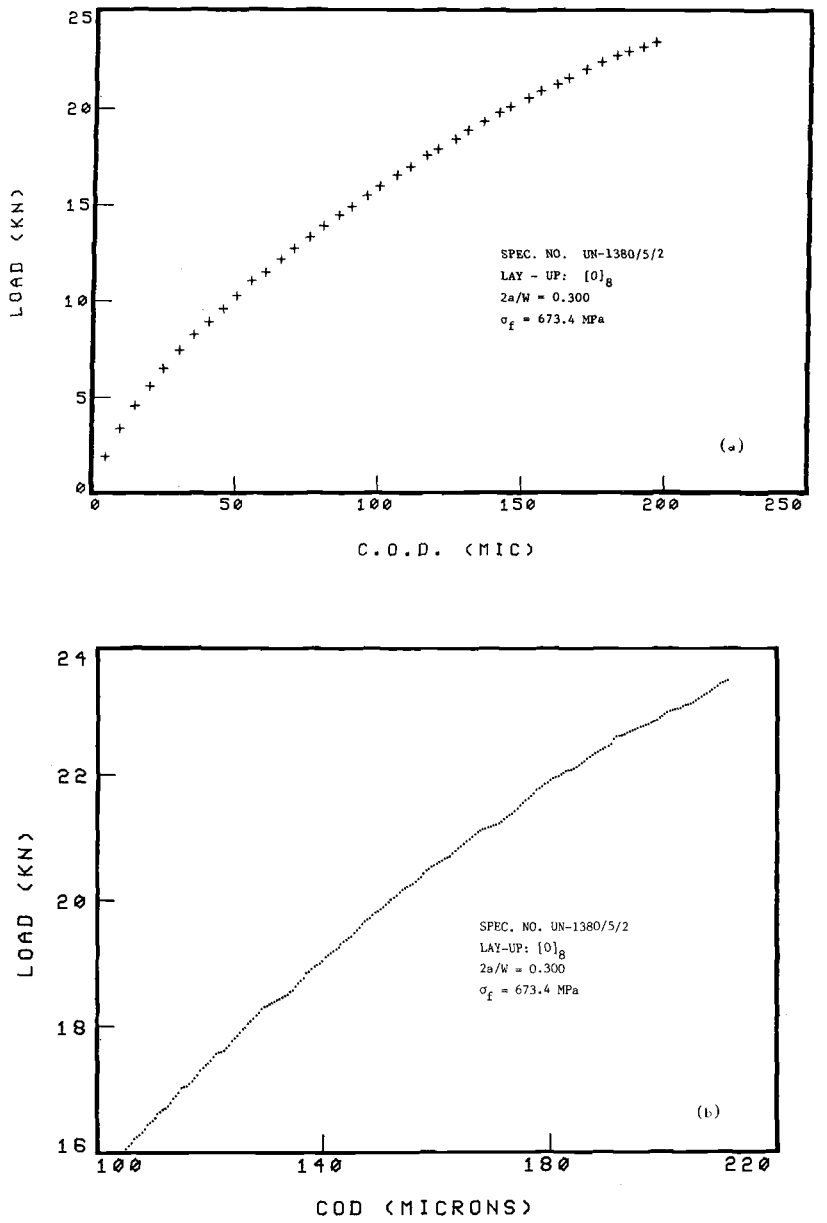

FIG. 8—*Experimental load-COD curves for center-notched* $[0]_8$ *B/Al at room temperature:* (a) *complete load-COD curve;* (b) *upper part of the load-COD curve. Notch-tip damage growth is clearly indicated by the jumps in COD.*

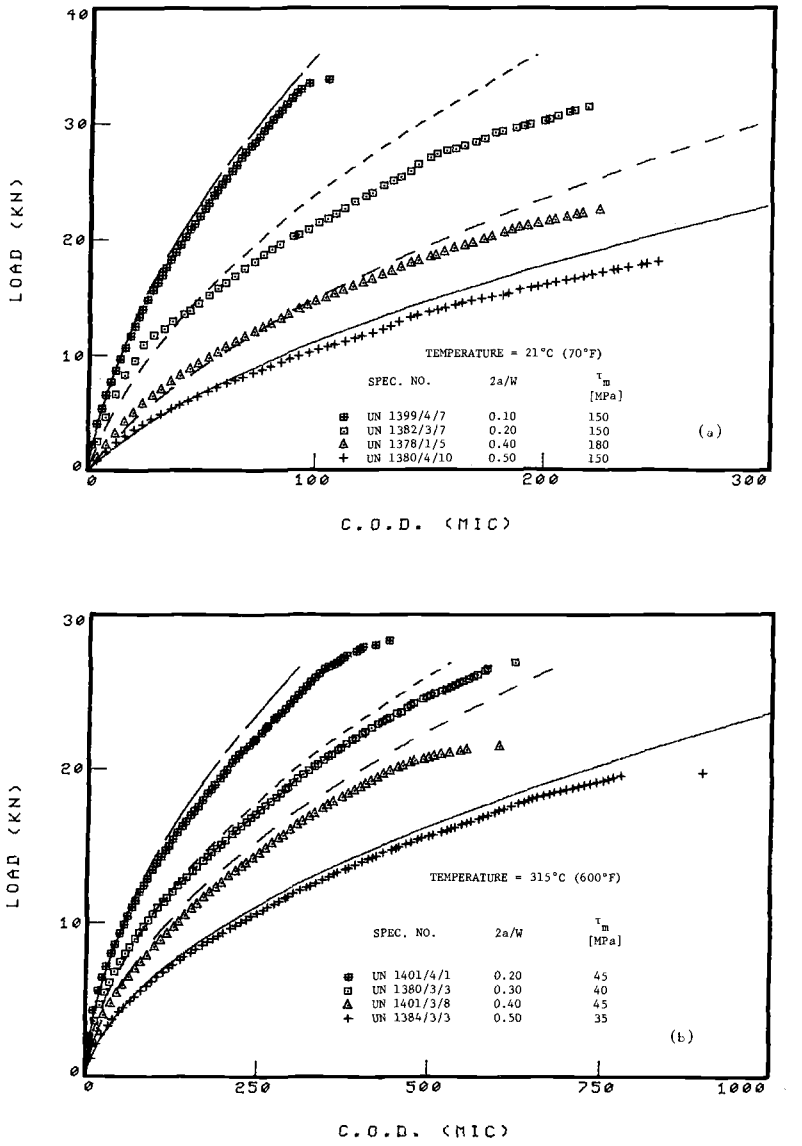

FIG. 9—*Comparison between predicted (Eq 6) and experimental load-COD curves for several center-notched B/Al composites at:* (a) *21°C (70F) and* (b) *315°C (600°F). There is an excellent agreement between the theory and experiments and the empirically determined values of* τ_m *are independent of notch length.*

An examination of these curves also reveals that the degree of nonlinearity increases with crack length. This is due primarily to the experimental procedure employed, that is, for the shorter cracks the knives of the conventional compliance gage are wider than the crack length. Thus the displacement recording system may not detect the effect of crack-tip damage initiation and progression. For larger crack lengths, the degree of nonlinearity can be clearly seen, Fig. 7.

Load-Crack Opening Displacement Curves (Local Deformation)

1. Crack-Tip Damage Growth—A typical load-COD curve for a center-notched unidirectional B/Al specimen is shown in Fig. 8*a*. Nonlinearity in the load-COD curve is indicated, resulting from the multiplicity of the failure modes described previously. Additional features of the load-COD curve are revealed when it is plotted at a higher resolution. For example, a portion of the load-COD curve shown in Fig. 8*a* is plotted in Fig. 8*b*, showing discontinuities in the form of jumps in the COD. These jumps occur randomly with increasing applied stress. Correlation of the load-COD curves with the results of other experimental techniques, for example, AE [*15*] and visual observation through the CCTV indicates that the jumps in COD, as detected by the IDG, are caused by fiber breakage at the crack tip. It can be concluded that the catastrophic fracture of the composite is preceded by a sequence of several fiber breaks at the crack tip, and this is indicated by the sudden jumps in the COD. Also these jumps occur at a relatively early stage of loading. In other words, the local load-COD curves indicate a slow crack-tip damage growth rather than a rapid fracture.

2. Effect of Crack Length—The effect of crack length on load-COD curves is shown in Figs. 9*a* and 9*b* obtained at room temperature and at 315°C (600°F), respectively. The lines shown in the figures are the predictions, to be discussed later. For all crack lengths the curves are highly nonlinear, and with increasing applied stress, the curves approach a plateau. This occurs when significant damage has been already accumulated at the crack tip, and the applied stress approaches the maximum load-carrying capacity of the laminate. At this stage a rapid increase in COD occurs with increasing load. The stresses at which the load-COD curves reach a plateau depend strongly on crack length. The degree of nonlinearity in the load-COD curves is affected by the number of fibers broken, and the number and the extent of the inelastic zones developed at the crack tip. In comparison with the global deformation curves, Figs. 7, the load-COD curves are more spacially separated, Fig. 9, demonstrating a more pronounced sensitivity of local deformations to the crack length.

The deviation from linearity is noticeable at load levels as low as 10 to 20% of ultimate, indicating early initiation of damage at the crack tip primarily in the form of matrix inelastic deformation in the bay between the crack tip and the first intact fiber. Similar results were obtained by applying the AE technique [*15*]. In comparison with visual observations through the CCTV discussed previously, the application of the IDG and the AE techniques reveal crack-tip damage growth at much lower load levels. Consequently, the reliance on visual observation of crack-tip damage growth, frequently applied in fatigue studies of metals, may not be appropriate in the case of composites. Through visual observation, only the extent of surface damage can be identified. In composites, however, internal nonvisual damage (for example, broken fibers) can be critical. Using the IDG technique for an accurate determination of COD (and local compliance) results in a direct measure of the "effective" crack-tip damage growth.

3. Effect of Temperature—The load-COD curves were obtained at room and elevated temperatures for all crack lengths. The representative examples in Figs. 10*a* and 10*b* for

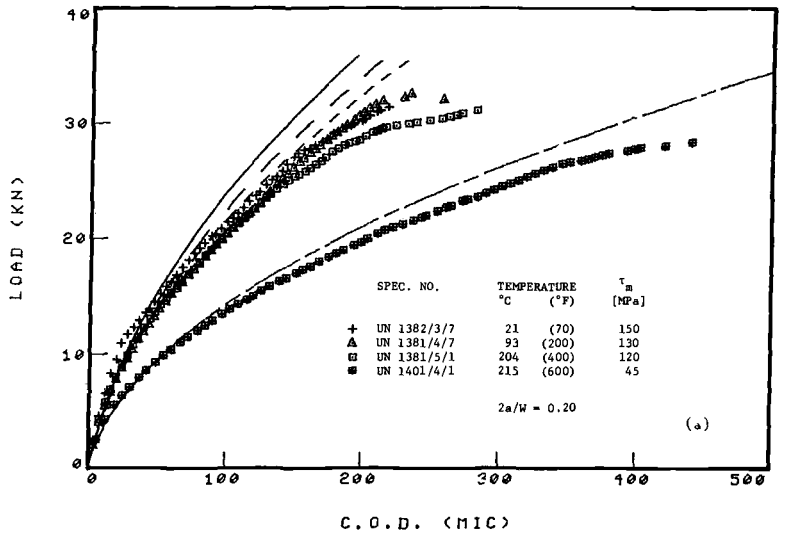

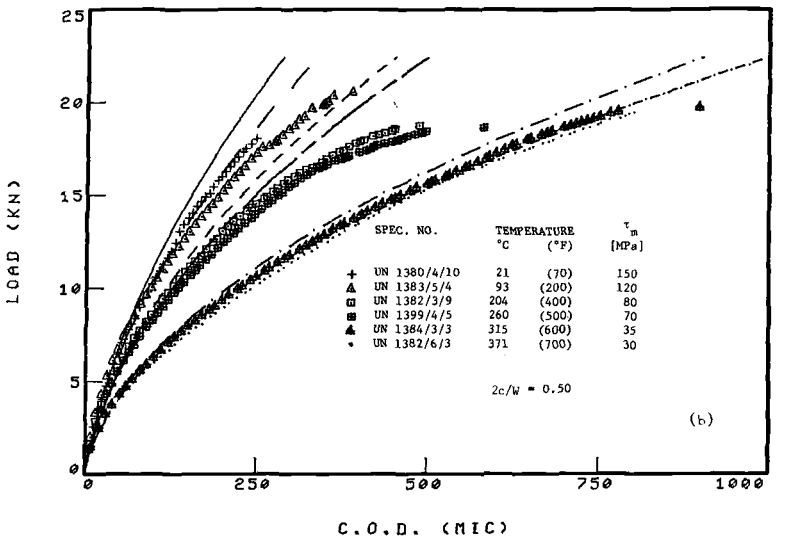

FIG. 10—*Comparison between predicted (Eq 6) and experimental load-COD curves at various temperatures for several center-notched* $[0]_8$ *B/Al containing* 2c/W = : (a) *0.20 and* (b) *0.50. Empirically determined values of* τ_m *decrease significantly at temperatures greater than 204°C (400°F).*

two different crack lengths are shown with the analytical predictions. Clearly a strong influence of temperature on the local deformation characteristics is indicated. It is seen that with increasing temperature the nonlinearity in the load-COD curves is much more significant and the crack opens more rapidly with applied stress. Also, the effect of temperature is more pronounced beyond 204°C (400°F). It should be recalled that a similar effect of temperature was observed in the case of local compliance, Fig. 3. For both regions, elastic and inelastic, the increased deformation is attributed to the significant degradation in properties of the aluminum matrix at that temperature.

Predictions of Load-COD Curves

The first indication of damage in notched unidirectional composites appears near the crack tip in the form of matrix shear deformation parallel to the fibers, Fig. 4. With increasing applied stress, the length of the yield zone, R_p, increases and the crack tip is blunted, improving the overall toughness of the composite. There have been several attempts to model this longitudinal damage through a variety of approaches [*16–20*]. In this research, an approximate mechanistic model proposed by McClintock [*16,17*] has been extensively applied and the predictions are compared with the experimental load-COD curves at room and elevated temperatures.

McClintock [*16*], used a mathematical analogy between a rectilinear antisotropic body in a tensile mode and an isotropic body in an antiplane shear mode. This model was used by Tirosh in Ref *17*. For simplicity in the solution, matrix shear stress in the yield zone was assumed to be constant and equal to the matrix yield shear stress. In other words, linear elastic-perfectly plastic material has been assumed. With this analogy Tirosh obtained the following closed-form solutions for the length of the longitudinal plastic zone, R_p, in the bay between the crack tip and the first intact fiber [*17*]

$$R_p = \pi^2/16\ (G_{LT}/E_L)^{1/2}\ cY^2P^2/(\tau_m WB)^2 \tag{5}$$

where τ_m is the yield shear stress of the matrix.

Having obtained the plastic zone size, the corresponding permanent opening of the crack tip can be derived by integrating the shear strain γ^p along the contour of the plastic zone [*17*]. Details of the analytical model are given in Ref *3* and are not repeated here for the sake of conciseness. The resulting total crack-tip opening displacement (CTOD) is the sum of the elastic and the inelastic CTOD

$$\text{CTOD} = Y/(BE_L)\ (2c/W)\ [2\alpha + \pi\ Y/(4\tau_m WB)P]\ P \tag{6}$$

Comparison between predicted and experimental load-COD curves are shown in Figs. 9 and 10. The comparison between the predicted CTOD and the experimental COD (measured with the IDG at the crack center) is based upon the observation (through the CCTV) that the crack surfaces do not deform. It should be noted that the material property which is mostly affected by temperature is the matrix yield shear stress, τ_m, [*13*]. In correlating the predictions with the experimental results, the value of τ_m was chosen to best fit the predictions with experiments at each temperature. The selected values of τ_m at a given temperature are also indicated in Figs. 9 and 10. The comparison indicates that the values selected yield good agreement between the predicted and experimental load-COD curves for all crack

lengths, Fig 9. That is, the yield shear stress, τ_m, is for all practical purposes not a function of crack length. It should be also noted that τ_m decreases with temperature, Fig. 10. The decrease in τ_m is significant at approximately 204°C (400°F). Again, the matrix properties play a significant role in determining the local crack-tip deformations.

The comparison between an approximate mechanistic model, such as that employed in this study, and experimental load-COD curves can serve as a basis for determining the *in situ* yield shear stress, τ_m, of the matrix. Following the procedure described previously, the *in situ* yield shear stress as a function of temperature can be determined as well. Furthermore, the derived value of τ_m may serve for comparing the performance of several material systems, and may ultimately serve as a guideline for determining fabrication quality with regard to interfacial bonding and the effect of fabrication procedure on performance.

The good agreement between the predictions and the experiments holds for the early stages of the applied load only. For increasing loads the measured COD is higher than that predicted by the analysis. This is expected considering the fact that at higher loads, multiple inelastic zones are developed (four to six zones were observed through the CCTV), Fig. 4, while the analysis incorporates only a single inelastic zone throughout loading to failure. Therefore, the predicted COD should be smaller than the actual at high load levels.

Conclusions

In this paper we have presented and analyzed experimental results on the global and local load-displacement curves for center-notched unidirectional B/Al at room and elevated temperatures. Results were obtained for crack length-to-width ratios varying from 0.05 to 0.50 at temperatures ranging from 21°C (70°F) to 371°C (700°F). Emphasis has been placed on both the elastic and inelastic regions of the load-deformation curves.

The laser interferometric displacement gage (IDG) was successfully employed to measure the actual (local) crack opening displacement (COD), that is, at the crack surfaces, for the entire temperature range studied.

Global compliance calibration curves were found to be insensitive to crack length, with significant scatter. Local compliance calibration curves were found to be highly sensitive to crack length, and results were highly reproducible both at room and at elevated temperatures. Thus, they can serve as a reliable measurement of crack-tip damage growth during quasi-static and fatigue loading. Variation of the local compliance with temperature is pronounced beyond 204°C (400°F). Good correlation has been established between predictions and experiments for both global and local compliance curves.

Visual observations of the failure process at the crack tip, via a closed circuit television (CCTV), which allows magnifications of ×150, revealed a slow crack-tip damage growth in the form of matrix inelastic deformation along the fibers direction followed by fiber breakage. A sequential failure process has been observed with approximately four to six such inelastic zones appearing prior to catastrophic fracture.

The global far-field load-displacement curves are essentially linear to failure. The nonlinearity associated with the crack-tip damage growth can not be detected through the global measurements of deformation.

The resulting load-COD curves, obtained with the IDG, are highly nonlinear with rapid increases and jumps in COD as the load approaches ultimate. These characteristics were successfully correlated in real time with visual observations of the failure process through high magnification (×150) CCTV. Crack-tip damage initiation could be detected at load levels as low as 10% of ultimate. At elevated temperatures the nonlinearity of the load-COD curves is much more pronounced, primarily beyond 204°C (400°F), resulting from the reduced matrix shear yield stress.

Experimental load-COD curves for unidirectional specimens at room and elevated temperatures correlate well with predictions based on an existing approximate mechanistic model which is operationally simple to use. The model accounts for the matrix shear deformation along the fiber direction and assumes the matrix to be elastic-perfectly plastic. Based on the load-COD curves, and employing such a mechanistic analytical model, the *in situ* shear yield stress of the aluminum matrix could be determined. Further modifications of such mechanistic model, such as incorporating the actual shear stress-strain curve of the matrix, multiple inelastic zones at the crack tip, and observed sequential failure process, will lead to a better agreement with experiments.

Acknowledgments

The research work has been sponsored in part by the Air Force Office of Scientific Research (AFOSR) under contract No. 79-0079. The support of the AFOSR is greatly appreciated. In particular we would like to express our thanks to Dr. D. Glasgow, the program monitor, for his encouragement and many technical discussions we had.

References

[1] Awerbuch, J. and Madhukar, M. S., "Notched Strength of Composite Laminates: Predictions and Experiments—A Review," *Journal of Reinforced Plastics and Composites,* Vol. 4, No. 1, Jan. 1985, pp. 3–159.

[2] Jones, W. F. and Goree, J. C., "Experimental Determination of Internal Damage Growth in Unidirectional Boron/Aluminum Composite Laminates," *Mechanics of Composite Materials,* AMD Vol. 58, 1983, pp. 171–178.

[3] Awerbuch, J. and Hahn, H. T., "Crack-Tip Damage and Fracture Toughness of Boron/Aluminum Composites," *Journal of Composite Materials,* Vol. 13, 1979, pp. 82–107.

[4] Macha, D. E., Sharpe, W. N., Jr., and Grant, A. F., Jr., "A Laser Interferometry Method for Experimental Stress Intensity Factor Calibration," *Cracks and Fracture, ASTM STP 601,* American Society for Testing and Materials, Philadelphia, 1976, p. 490.

[5] Sharpe, W. N., Jr., "Interferometric Surface Strain Measurements," *International Journal of Nondestructive Testing,* Vol. 3, 1971, p. 56.

[6] Sharpe, W. N., Jr., "Preliminary Development of an Interferometric Strain Gage for use on Nosetip Materials Subjected to Thermal Shock," AFML-TR-76-63, Air Force Materials Laboratory, 1976.

[7] Awerbuch, J. and Hahn, H. T., "K Calibration of Unidirectional Metal Matrix Composites," *Journal of Composite Materials,* Vol. 12, 1978, pp. 222–237.

[8] Madhukar, M. S., "*Fracture Behavior of Boron/Aluminum Laminates at Room and Elevated Temperatures,*" Ph.D. dissertation, Drexel University, Philadelphia, PA, Oct., 1985.

[9] Rosen, B. W., "A Simple Procedure for Experimental Determination of the Longitudinal Shear Modulus of Unidirectional Composites," *Journal of Composite Materials,* Vol. 6, Oct. 1972, pp. 552–554.

[10] Paris, P. C. and Sih, G. C., "Stress Analysis of Cracks," *Fracture Toughness Testing, ASTM STP 381,* American Society for Testing and Materials, Philadelphia, 1965, p. 30.

[11] Brown, W. F. and Srawley, T. E., *Plane Strain Crack Toughness Testing of High Strength Metallic Materials, ASTM STP 410,* American Society of Testing and Materials, Philadelphia, 1966.

[12] Erasov, V. S., Pirogov, E. N., Konoplenko, V. P., Akimkin, V. A. Marukhin, A. P., Tsirlin, A. M., Shchetilina, E. A., and Balagurova, N. M., "Temperature Dependence of Mechanical Properties of Boron Fibers," *Mechanics of Composite Materials,* Vol. 18, No. 2, March–April 1982, pp. 127–130.

[13] Mondolfo, L. F., "*Aluminum Alloys: Structures and Properties,*" Butterworths, Boston, MA, 1979.

[14] Lekhnitskii, S. G., *Anisotropic Plates,* Translated from the Second Russian Edition by S. W. Tsai and T. Cheron, Gordon and Breach Science Publishers, New York, 1968.

[15] Madhukar, M. S. and Awerbuch, J., "Monitoring Damage Progression in Center-Notched Boron/Aluminum Laminates Through Acoustic Emission," *Composite Materials: Testing and Design (Seventh Conference), ASTM STP-893,* J. M. Whitney, Ed., American Society for Testing and Materials, Philadelphia, 1986, pp. 337–363.

[16] McClintock, F. A., "Problems in the Fracture of Composites With Plastic Matrices," presented at the Fourth Symposium on High Performance Composites at St. Louis, MO, Monsanto Co. and Washington University, 1969.

[17] Tirosh, J., "The Effect of Plasticity and Crack Blunting of the Stress Distribution in Orthotropic Composite Materials," *Journal of Applied Mechanics*, ASME Applied Mechanics Division, Oct. 1971, pp. 1–6.

[18] Dharani, L. R., Jones, W. F., and Goree, J. G., "Mathematical Modeling of Damage in Unidirectional Composites," *Engineering Fracture Mechanics*, Vol. 17, No. 6, 1983, pp. 555–573.

[19] Reedy, E. D., "Analysis of Center-Notched Monolayers With Application to Boron/Aluminum Composites," *Journal of Mechanics and Physics of Solids*, Vol. 28, Jan. 1980, pp. 265–286.

[20] Zweben, C., "An Approximate Method of Analysis for Notched Unidirectional Composites," *Engineering Fracture Mechanics*, Vol. 6, 1974, pp. 1–10.

Shun-Chin Chou,[1] *John L. Green,*[1] *and Ronald A. Swanson*[1]

Mechanical Behavior of Silicon Carbide/ 2014 Aluminum Composite

REFERENCE: Chou, S.-C., Green, J. L., and Swanson, R. A., **"Mechanical Behavior of Silicon Carbide/2014 Aluminum Composite,"** *Testing Technology of Metal Matrix Composites, ASTM STP 964*, P. R. DiGiovanni and N. R. Adsit, Eds., American Society for Testing and Materials, Philadelphia, 1988, pp. 305–316.

ABSTRACT: The composite material consists of 25 volume percent of silicon carbide whiskers in 2014-T4 aluminum matrix. Specimens were taken from hot-isostatically-pressed cylindrical billets and tested at various loading conditions and strain rates. Tension and compression tests were performed at strain rates of 10^{-4} and 5 s^{-1} to determine the effect of strain rate. Bauschinger effect was investigated by precompressing specimens to two strain levels followed by reversing load to tension until fracture occurred. Torsion tests were carried out to determine the relationship between torque and twist angle. The K_{Ic}-value was determined by testing short-rod specimens. The tensile properties and K_{Ic} were compared with those of 2014-T4 aluminum to demonstrate the effect of silicon carbide whisker reinforcement on the properties of matrix materials.

KEY WORDS: metal matrix composite, whiskers, elastic modulus, fracture toughness, Bauschinger effect, strain rate, 2014-T4 aluminum, silicon carbide

The demand of light-weight and high-stiffness materials in space application provides an impetus for developing many new materials, particularly metal-matrix composite materials. There are many parameters which affect the mechanical properties of composite materials. Therefore, there is a need to generate a data base for these materials. The results presented here are a part of the whole effort.

In this paper the attention is focused on silicon carbide (SiC)/2014-T4 aluminum. The blended powder of 2014 aluminum and SiC whisker was hot-isostatically-pressed into various sizes of cylindrical billets. Various test specimens were machined from the billets. Specimens were tested in tension, compression, and torsion. Bauschinger effect was studied by precompressing specimens to two strain levels followed by reversing load to tension until fracture occurred. The Mode I fracture toughness value, K_{Ic}, was measured by employing the small cylinder technique developed by Barker [*1*]. Comparisons were made in tensile properties and fracture toughness values of SiC/2014-T4 aluminum and the 2014-T4 aluminum alloy to demonstrate the effect of SiC whisker reinforcement.

Material Description and Specimen Configuration

The metal-matrix composite material investigated in this study was 25 volume percent silicon carbide (SiC) whiskers in a 2014 aluminum alloy matrix. The mixture was hot-isostatically-pressed (HIP) into a form of various sizes of cylinders. Before specimens were

[1] Mechanical engineer, mechanical engineer, and engineering technician, respectfully, Army Materials Technology Laboratory, Watertown, MA 02172–0001.

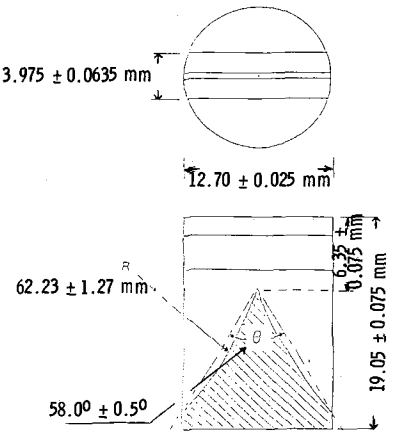

FIG. 1—*Short rod fracture toughness specimen.*

taken from these cylindrical billets, the HIP material was given the conventional heat treatment which brought 2014 aluminum to T4 condition. The whiskers were 0.2 to 0.5 μm in diameter and had an initial length-to-diameter ratio between 50 and 80. The ratio after HIP is unknown. It was expected that the whiskers were randomly oriented and dispersed in the matrix so that the mechanical properties would be isotropic. The isotropy of the HIP cylindrical billets was verified by testing specimens taken from those billets in both axial and radial directions.

Specimens were tested in tension, compression, and torsion. The Bauschinger effect was investigated by precompressing specimens to a prescribed strain level then reversing the load direction to tension until specimens fractured. Fracture toughness K_{Ic} was measured by using the small cylinder technique developed by Barker [*1*]. The geometry and dimensions of the test specimens are shown in Figs. 1 through 5.

Experimental Procedures

The test conditions in this study were quite diversified. Not only were specimens subjected to various loading conditions, but also to a range of strain rates. Three test apparatus were used to cover all the test conditions. One of the apparatus is a specially designed test machine incorporated with gage condition units and a fast data acquisition system. The test machine has two operating modes: one is servohydraulic control mode or closed-loop mode, and the

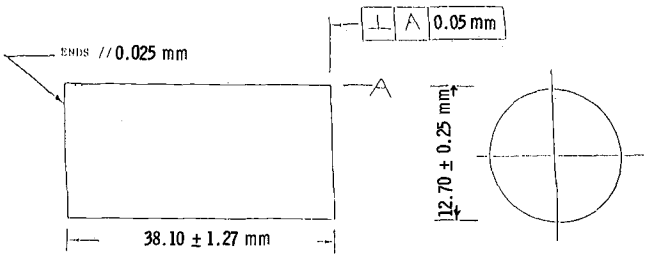

FIG. 2—*Compression specimen.*

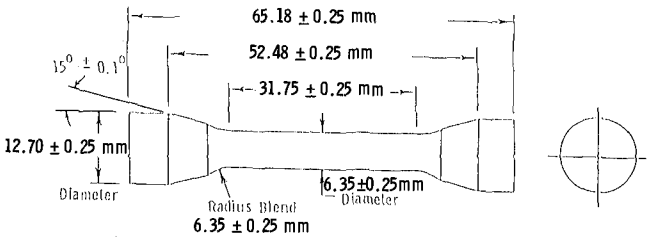

FIG. 3—*Tension specimen.*

other is a pneumatic operating mode or open-loop mode. The closed-loop mode covers the range of strain/load/displacement rates from quasi static to 10^{-1} s^{-1}, while the open-loop mode covers the range approximately from 10^{-1} to 50 s^{-1} depending on the ductility of the specimen being tested. In the closed-loop mode the rate can be precisely controlled. However, in the open-loop mode, only a nominal rate can be achieved by adjusting the gas pressure, stroke, and size of release orifice in the fast-acting valve. This machine was used to complete the tension, compression, and Bauschinger effect tests. All spcimens were instrumented with strain gages, and load and strain were recorded for analysis.

Torsion tests were carried out in a standard Instron machine. Torque and twist angle were measured.

The Mode I fracture toughness value, K_{Ic}, was measured with a fractometer manufactured by the Terra Tek, Inc. The specimen was a short rod with a length-to-diameter ratio equal to 1.5. A curved chevron notch was machined at one end of the specimen, and no fatigue crack was required before testing. A specially designed set of grips applied the load at the end of the chevron notch. The load and the displacement at the load points were measured. The K_{Ic} was calculated by following the manufacturer's procedure (for details see Ref *2*).

Test Results and Discussion

The metal-matrix composite material SiC/2014 aluminum was characterized at the following conditions: tension, compression, and torsion. Bauschinger effect was investigated, and fracture toughness value K_{Ic} was measured. The effect of reinforcement with SiC whiskers was investigated by comparing test results of SiC/2014 aluminum with those of 2014-T4 aluminum alloy tested at the same conditions. Results from each test condition will be discussed separately in the following sections.

Tension

Tension tests were performed at two strain rates, 10^{-4} and 5 s^{-1}. Results are shown in Figs. 6 to 7 for SiC/2014 aluminum and 2014-T4 aluminum, respectively. It is noticed that

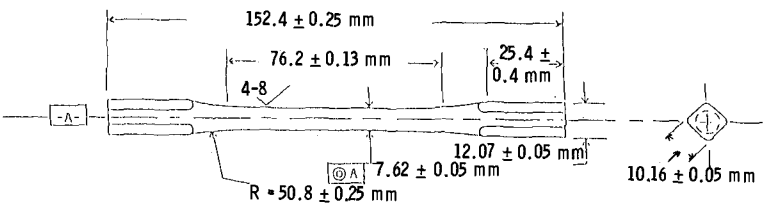

FIG. 4—*Torsion specimen.*

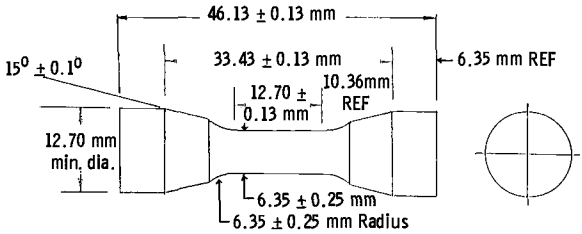

FIG. 5—*Bauschinger effect specimen.*

neither material is strain-rate sensitive in the range of strain rates tested. The average value of elastic modulus for SiC/2014 aluminum is 120.7 GPa, which is more than 60% higher than that for the 2014-T4 aluminum. Strength data are not presented; the reasons are explained as follows. Tests were performed in the closed-loop mode with strain as a feed back controlling parameter to ensure a constant strain rate condition. Ths constant strain rate condition was maintained as long as the strain gage on the specimen was functional. If

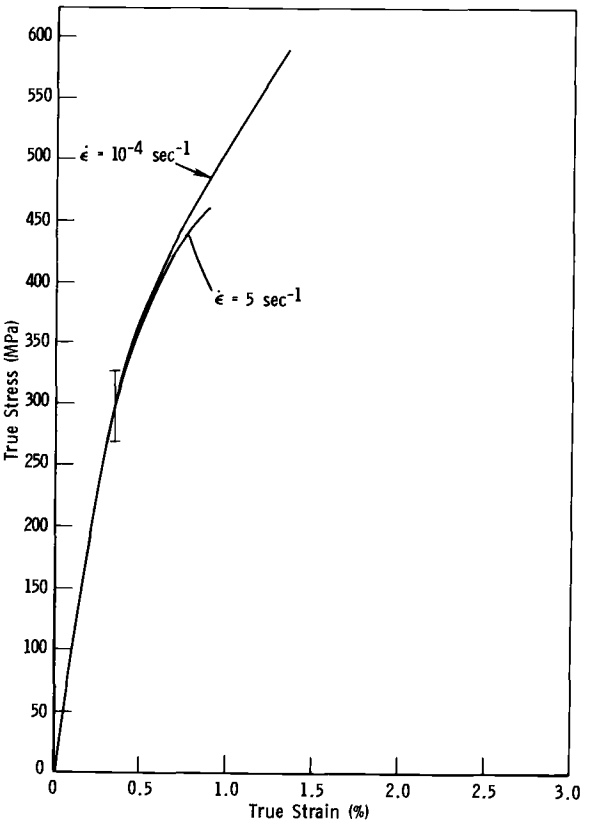

FIG. 6—*Tension test of SiC/2014-T4 aluminum at room temperature and strain rates of* 10^{-4} *and* 5 s^{-1}.

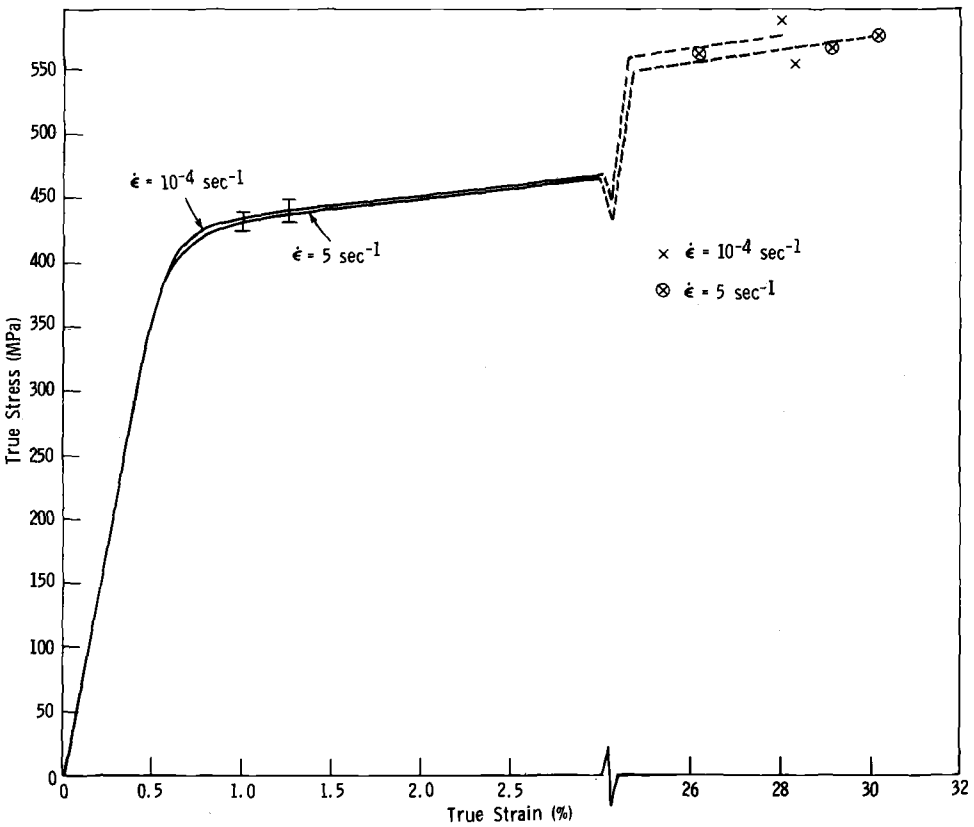

FIG. 7—*Tension test of 2014-T4 aluminum at room temperature and strain rates of* 10^{-4} *and* 5 s^{-1}.

the strain gage, for some reason, failed before the end of the test, the test machine would be uncontrollable, and the specimen would be fractured in tension immediately. Since the strain, load, and displacement data must be sampled at a rate corresponding to the rate of testing due to the finite number of core memory available in the data acquisition system, the response of the test machine was so rapid after the gage failed that the specimen was fractured within a sampling interval. Therefore, the last data points were not the ultimate strength and strain; rather they were the data points just before the gage failure. This explanation was proved to be true by post-mortem examination of specimens and conducting tension tests in closed-loop mode with the displacement as a controlling parameter. At this mode the test results indicated that the ultimate strength of SiC/2014 aluminum under investigation is consistently higher than 586 MPa.

The location of a strain gage on the specimen very often did not coincide with the location of failure. This occurrence will not affect the interpretation of test results for SiC/Al because of the brittle nature of the material. However, the same comment cannot be applied to test results of 2014-T4 aluminum which exhibited necking before fracture took place. In this situation the recorded maximum strain value is not the strain at failure, if the strain gage is not at the location where fracture and necking of the specimen take place. A correction was made in the analysis of test results. The diameter of the necked section where fracture

occurred was measured after the test, and the ultimate strength was calculated based on the measured necked area rather than the original area. The strain at failure was calculated by assuming that the volume of material remained constant during the plastic deformation which yields the expression for the true strain, e

$$e = \ln (L/L_0) = \ln(A_0/A)$$

where A_0 and L_0 are original area and length, while A and L are those in the deformed state. The stress-strain curves shown in Fig. 7 include the interpretation discussed previously, and the axes are labelled as "true stress" and "true strain" to reflect this correction.

The tensile results indicate that the whisker reinforcement has increased the modulus by approximately 60% and the ultimate strength slightly, but the ductility has been drastically reduced in comparison with those of matrix alloys.

Compression

The compression specimens were machined according to the ASTM standards with the ratio of length-to-diameter equal to three. Tests were performed at two strain rates, 10^{-4} and $\approx 5\ s^{-1}$, and results are shown in Fig. 8. There is no indication of strain rate sensitivity in the range of interest. The average elastic modulus is about the same as that in tension, 120.7 GPa. Specimens were slightly buckled before failed in shear, that is, the failure surface had an inclination of about 45° from the direction of the load. The stress levels at failure were indicated by crosses in Fig. 8.

Torsion

The torque and twist angle were measured during torsion tests. Results are shown in Fig. 9. The initial linear relationship between torque and twist angle can be used to calculate the shear modulus of the specimen. The calculated shear modulus is approximately 44.8 GPa, which, combining with the elastic modulus measured in tension tests yields the Poisson's ratio about 0.3.

The maximum torque may be also estimated by assuming that the material behaves elastic-perfect plastically. The expression for torque is (see Ref *3*)

$$M = 2/3\ \pi k\ (a^3 - 1/4\ c^3)$$

where

M = torque,
k = $Y/\sqrt{3}$ for von Mises criterion,
a = radius of specimen, and
c = elastic-plastic boundary.

The estimated torque required to cause complete yielding of the specimen (that is, to set $c = 0$ and $Y = 586$ MPa) falls within the range of measured values. This implies that the material is a work-hardening material which is also observed in tension test results.

Bauschinger Effect

The Bauschinger effect was investigated by precompressing specimens to two strain levels, 1 and 2%, then reversing the load direction to tension until specimens fractured. Results

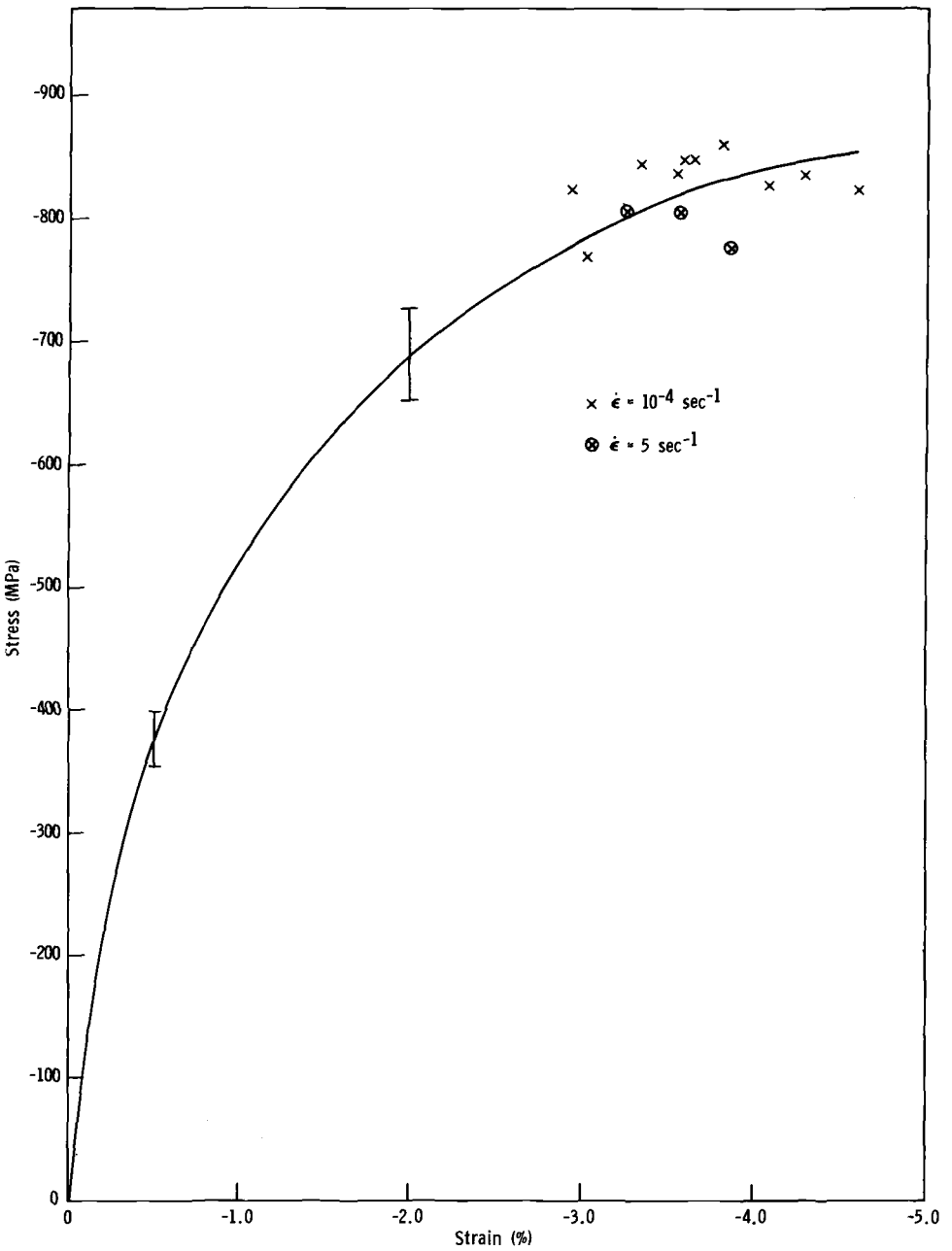

FIG. 8—*Compression test of SiC/2014-T4 aluminum at room temperature and strain rates of* 10^{-4} *and* 5 s^{-1}

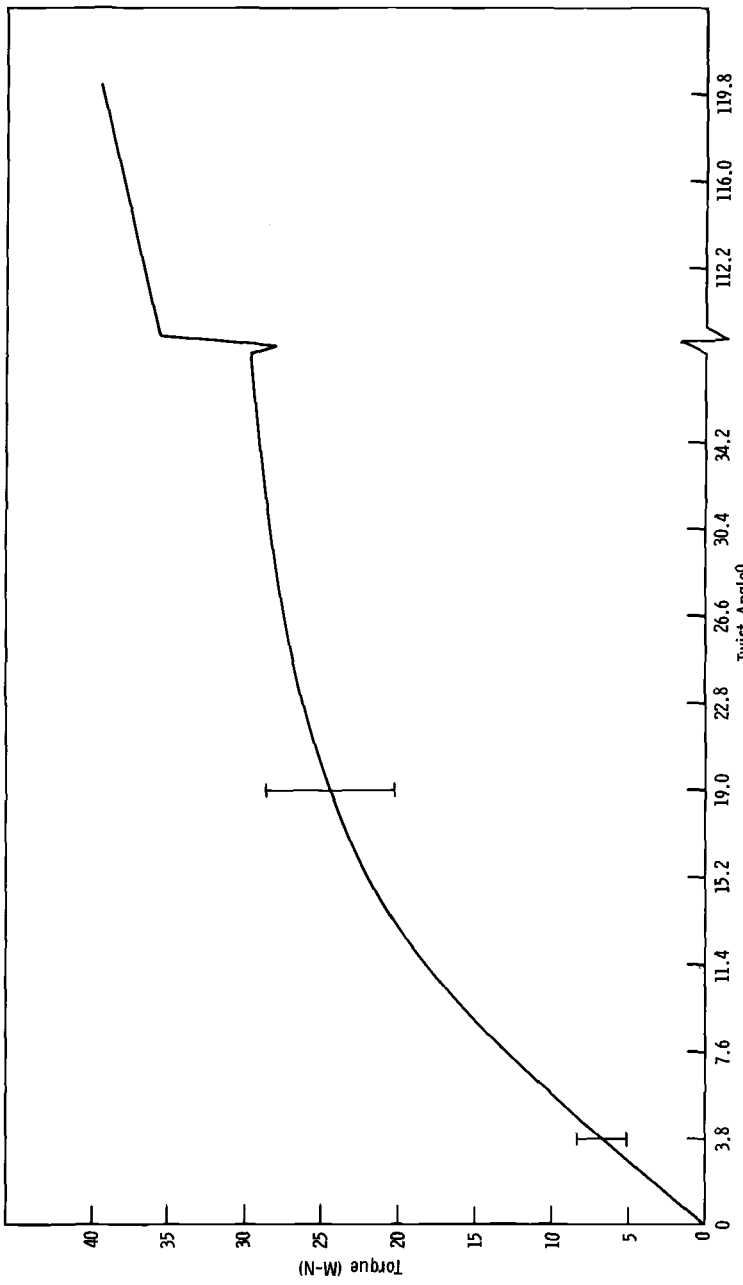

FIG. 9—*Torsion test result of SiC/2014-T4 aluminum at room temperature.*

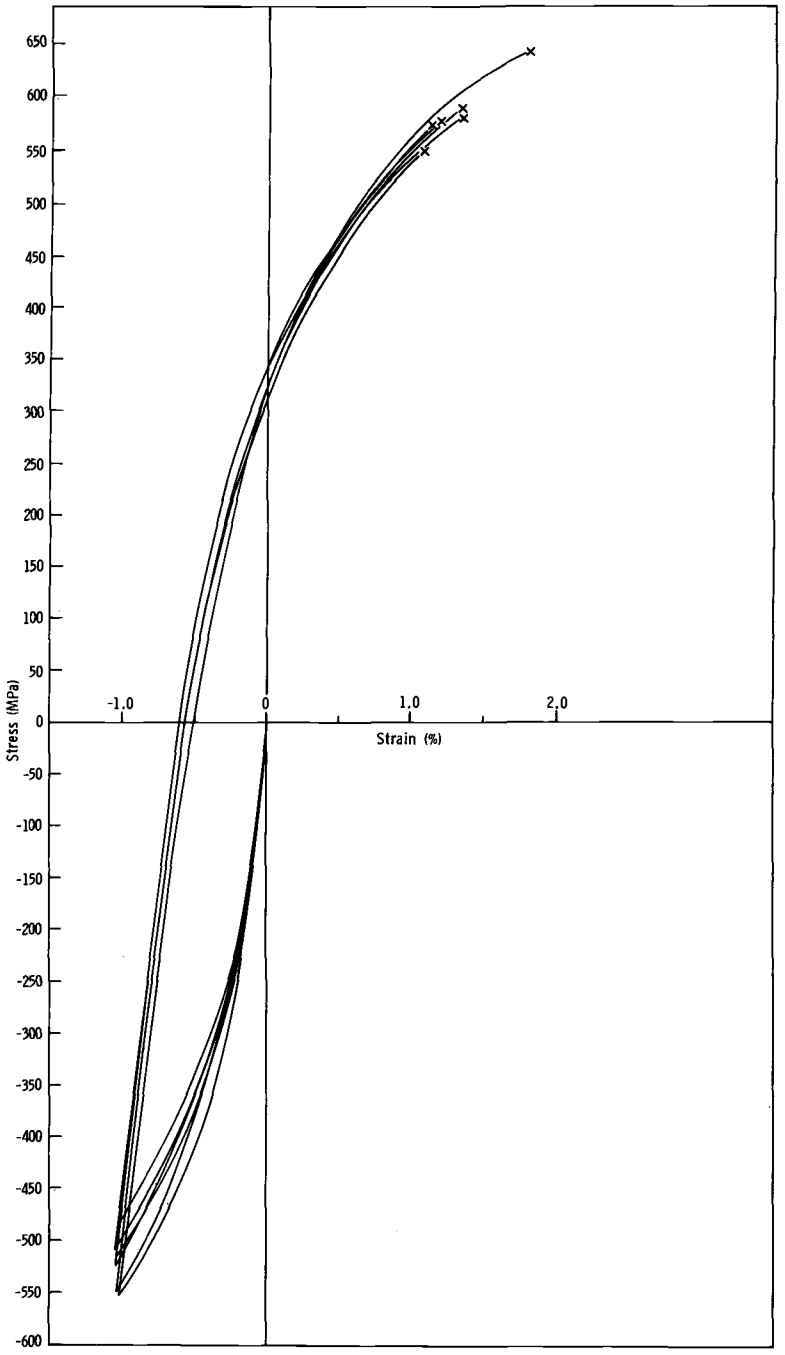

FIG. 10—*Bauschinger effect test with precompression to 1% strain of SiC/2014-T4 aluminum at room temperature.*

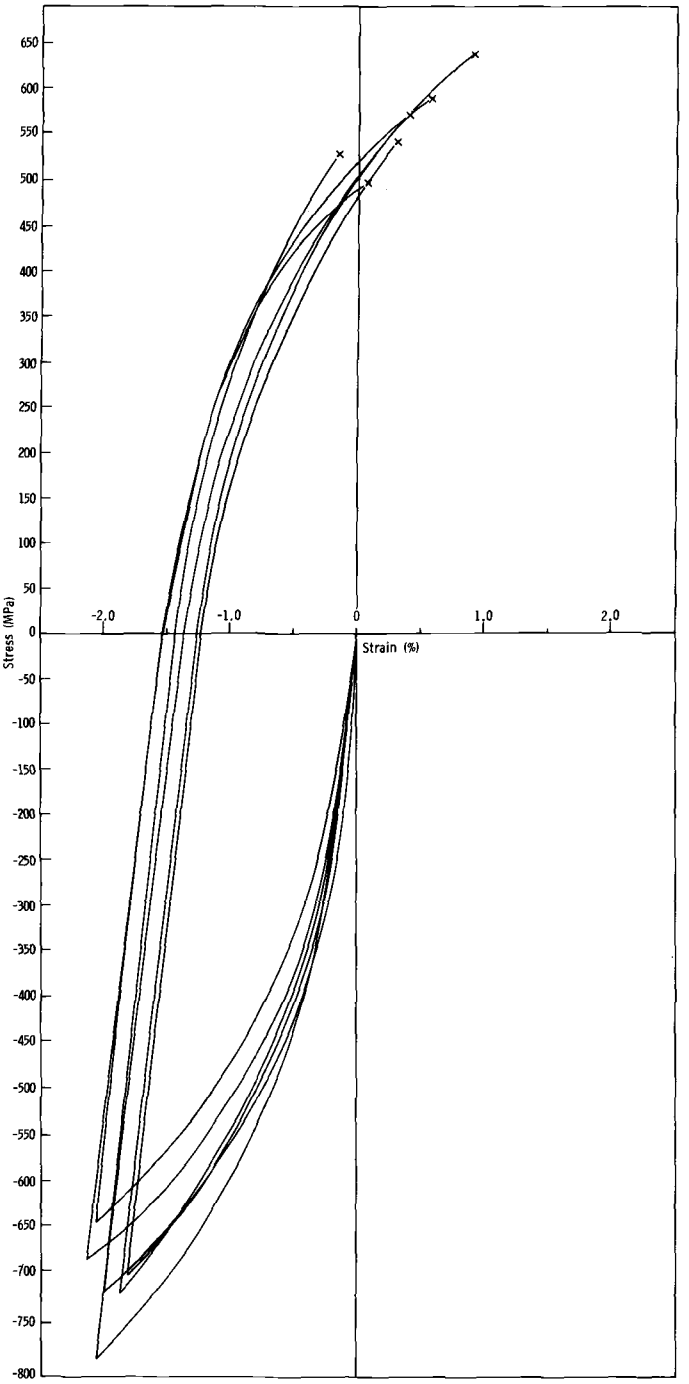

FIG. 11—*Bauschinger effect test with precompression to 2% strain of SiC/2014-T4 aluminum at room temperature.*

are shown in Figs. 10 and 11, respectively. It is noticed in Fig. 10 that the precompression to 1% strain seems to have no deteriorating effect on tensile properties such as modulus, ultimate strength, and ductility. The results show that there is approximately 0.5% residual strain in the specimen at the completion of unloading. The specimens are stretched to their original length when the tensile stress reaches approximately 310.3 MPa. Finally the specimens were fractured at stress equal to approximately 586 MPa and strain around 1.5% which are the same as those from the monotonic tension tests.

In the case of specimens precompressed to 2% strain (Fig. 11), the residual strain at zero stress level is about 1.5%. The elastic modulus and ultimate strength seem to be not affected by the precompression; however, the specimens barely return to their original length before fracture.

Based on the results of Bauschinger effect and tension tests, it seems that the material has a total available tensile strain of approximately 1.5% which is not affected by preworking conditions investigated in this study.

Since there are only limited data available, there is no attempt to formulate a work hardening model for this material.

Fracture Toughness Measurements

The Mode I fracture toughness value, K_{Ic}, was measured by using a Terra Tek Fractometer II testing machine. The specimen was a short rod with a diameter of 1.27 cm and length-to-diameter ratio of 1.5. The advantage of using this method is that no fatigue crack was needed to ensure the sharpness of the crack tip. K_{Ic}-values of many commonly used metals have been measured by using this method, and results agree very well with those obtained by employing a standard ASTM method.

The K_{Ic}-value of 2014-T6 aluminum rolled rod was measured which agrees very well with the value listed in Ref *4*. It is known that the mechanical behavior of 2014-T4 and -T6 alloys are very similar. Hence, the measured 2014-T6 fracture toughness may be used to compare with those of SiC/2014 aluminum to demonstrate the effect of whisker reinforcement. Table I shows the measured K_{Ic}-values for both 2014-T6 aluminum alloy and SiC/2014 aluminum composite. The first character in the orientation indicated the load direction and the second character for the direction of crack propagation. The average value of K_{Ic} for 2014-T6 aluminum is 19.3 MPa$\sqrt{m}$ which agrees with the handbook value [*4*]. The average value of K_{Ic} for SiC/Al in the *Z-R* orientation is 13.7 MPa$\sqrt{m}$, while the K_{Ic} in *R-Z* orientation if 13.3 MPa$\sqrt{m}$. This is further evidence indicating that HIP process produces an isotropic material. The low value of K_{Ic} for SiC/Al indicates the brittle behavior of the material which is consistent with the low ductility exhibited in tension tests.

Summary

The metal matrix composite material, consisting of randomly dispersed and oriented 25 volume percent silicon carbide whiskers in a 2014-T4 aluminum alloy matrix, was tested at various conditions. It was found that the elastic modulus was increased by 60% to 120.7 GPa in comparison with that of the matrix material. However, the ductility was significantly reduced to less than 2% of strain.

Torsion test of a circular rod gave the relationship between torque and twist angle from which the shear modulus was calculated to be approximately 44.8 GPa. The maximum twist angle per unit length around 1.57 deg/mm also indicated the brittle nature of the material.

The Bauschinger effect was investigated by precompressing the specimens to two strain

TABLE 1—*SiC/Al and 2014-T6 aluminum fracture toughness test results.*

Material	Specimen No.	Diameter, mm	Orientation	K_{Ic} SR, MPa$\sqrt{m}$	Test Temperature, °C	Relative Humidity, %
SiC/Al	R-1	12.726	Z-R	13.1	22.2	50.0
	R-2	12.713	Z-R	14.4	22.2	50.0
	R-3	12.703	Z-R	13.1	22.2	50.0
	R-4	12.713	Z-R	14.0	22.2	50.0
	R-5	12.700	Z-R	14.0		
SiC/Al	Z-1	12.713	R-Z	12.0	22.2	50.0
	Z-2	12.713	R-Z	12.7	22.2	50.0
	Z-3	12.687	R-Z	13.8	22.2	50.0
	Z-4	12.662	R-Z	14.5	22.2	50.0
	Z-5	12.680	R-Z	13.3	22.2	50.0
2014-T6 Al	L-1	12.700	R-L	19.6	22.2	50.0
	L-2	12.700	R-L	19.1	22.2	50.0
	L-3	12.687	R-L	19.1	22.2	50.0
	L-4	12.700	R-L	19.2	22.2	50.0
	L-5	12.700	R-L	19.7	22.2	50.0

NOTE—Terra Tek Fractometer II testing machine was used to obtain fracture toughness values. Specimen type used was the short rod with curved chevron slot.

levels before reversing the load to tension and fracturing the specimens. Results indicated that the material possesses a fixed total available tensile strain of approximately 1.5% which was not affected by precompression levels used in this study.

The Mode I fracture toughness value, K_{Ic}, was measured with an average value of 13.5 MPa$\sqrt{m}$ which was consistent with the low ductility exhibited in tension tests.

References

[1] Barker, L. M., "Theory for Determining K_{Ic} from Small Non-LEFM Specimens, Supported by Experiments on Aluminum," *Internal Journal of Fracture,* Vol. 15, No. 6, Dec. 1979, pp. 515–536.
[2] *FRACTOMETER System 4202 Owner's Manual,* Terra Tek, Inc., Salt Lake City, UT.
[3] Hill, R., *The Mathematical Theory of Plasticity,* Oxford, 1950.
[4] "Typical Values of Room Temperature Plane-Strain Fracture Toughness of Aluminum Alloys," MIL-HDBK-5D, 1 June 1983, p. 3–11.

Mechanical Test Methods and Material Characterization

Wayne M. Bethoney,[1] *John Nunes,*[1] *and James A. Kidd*[1]

Compressive Testing of Metal Matrix Composites

REFERENCE: Bethoney, W. M., Nunes, J., and Kidd, J. A., **"Compressive Testing of Metal Matrix Composites,"** *Testing Technology of Metal Matrix Composites, ASTM STP 964*, P. R. DiGiovanni and N. R. Adsit, Eds., American Society for Testing and Materials, Philadelphia, 1988, pp. 319–328.

ABSTRACT: A newly developed direct compressive test fixture for metal matrix composites is described and evaluated in this paper. This fixture was designed to be reusable, provide accurate and reproducible data, and to eliminate premature "brooming" failures. A comparative analysis between this test method and ASTM D 3410 for compressive properties of unidirectional or cross-ply fiber-resin composites using the Illinois Institute of Technology Research Institute (IITRI) indirect compression test method was also investigated.

In utilizing the direct compressive test method, the affects of specimen size and geometry were studied on a uniaxially oriented FP-alumina fiber reinforced magnesium composite. Cylindrical specimens 6.35, 9.53, and 12.7 mm in diameter, and a 9.53-mm-square specimen were tested at a constant 1/d ratio of 2.0. The tabbed specimen size and geometry that was employed in the IITRI test method was 2.54 mm thick by 6.35 mm wide by 152.4 mm long with a 12.7 mm untabbed gage length. All IITRI test specimens were tabbed by employing an improved method for bonding the aluminum tabs to the FP-alumina/magnesium surface. This tabbing procedure was developed to overcome earlier difficulties that were encountered in obtaining sufficient tabbed bond strength.

All of the test specimens investigated were from a single plate of as-cast composite material that contained a fiber volume fraction of 55%.

Tests were conducted with the applied load parallel to the fiber axis. Each specimen was strain gaged to provide a continuous load-strain curve to failure, to determine various materials properties, and to monitor any bending of the specimen. Data obtained included the ultimate compressive strength, the tangent modulus, the apparent proportional strain, strain to failure, and Poisson's ratio. Results from both the direct and the indirect compressive test methods were statistically compared. Finally, post test metallographic and fractographic examinations were performed to determine the principal failure modes.

Final results indicate that the cylindrical specimens, regardless of their respective diameters, display the least scatter in their ultimate compressive strengths (UCS). Also, higher stress values for the cylindrical specimens was obtained; as compared to the IITRI specimens.

KEY WORDS: direct compression, modified compressive fixture, metal matrix composites, fixturing, shape factor, brooming

In the compression testing of metal matrix composites material, the Illinois Institute of Technology Research Institute (IITRI) test method, also known as the indirect compressive test, is currently the most widely used test method available. Misuse of this testing procedure can lead to significant scatter in the data due to variables associated with the test fixturing and specimen design. If the IITRI test fixturing tolerances are not maintained, excessive friction can occur, or the specimen will display significant bending. Specimen tabbing is

[1] Mechanical engineer, materials research engineer, and mechanical engineer, respectively, Materials Technology Laboratory, Watertown, MA 02172–00001.

necessary when using the IITRI test fixture, because the compressive load that is transmitted to the IITRI specimen is brought about by a side load applied to the tabbing which is then translated to the specimen by a shearing action between the adhesive bond and the metal matrix composite. Specimen tabbing poses a significant problem if the adhesive bonding between the tab material and the metal matrix composite fail.

In earlier studies [*1,2*], it was shown that axial compressive testing of metal matrix composites with a 0° fiber orientation along the loading axis could be successfully accomplished without brooming failures at the ends of the specimens. It was also shown [*2*] that a reusable fixture could be designed to provide reliable and reproducible data. An equally important emphasis was placed on a simple geometric specimen design that would allow samples to be fabricated from any orientation of composite plate material one centimeter or greater in thickness.

This paper represents a continuation of the previous work [*2*] on axial compressive testing with the primary emphasis on cylindrical specimens of various diameters and a constant aspect ratio of 2. Also included in this study was the testing of a square specimen with the same aspect ratio. These results were compared to test data obtained from IITRI tests performed on the same material.

Specimen Material and Preparation

Material Description

The candidate material chosen for this program was FP alumina/magnesium with a volume fraction of 55%. All specimens (IITRI and axial compression) were cut from a 152.4-mm by 152.4-mm by 19.05 mm (6-in. by 6-in. by 3/4-in.) plate. Fiber orientation was uniaxial. Material was purchased from Du Pont.

Axial Compressive Specimens

The axial compressive specimens were broken down into two geometric shapes. The first shape was cylindrical (12.7, 9.53, and 6.35-mm-diameter specimens). The second shape was square (9.53 by 9.53 mm). Machining tolerance was ±0.05 mm. The 12.7 and 9.53-mm-diameter specimens were strain gaged with two 90° rosette strain gages. The 6.35-mm-diameter specimens were gaged with two single element rosettes. The aspect ratio is defined in this report as the gage-length divided by the diameter for the round specimens and the gage length divided by the length of one side for the square specimens. All axial compressive specimens had an aspect ratio of 2.

The IITRI Specimens

The IITRI specimens were machined to the same tolerances as the axial compressive specimens. Overall specimen length was 13.97 cm (5 1/2 in.) in length. Tabbing material was 6061 T6 aluminum 6.35 cm (2 1/2 in.) in length. Bonding between the metal maxtix composite and the (MMC) aluminum tabbing was achieved by using Hysol EA-934 adhesive and a modified version of Hysol's bonding procedure. Each specimen was strain gaged with two axial strain gages that were placed on opposite sides of the specimen. The aspect ratio for the IITRI specimen is the gage length divided by the thickness of the gage section; the aspect ratio for the IITRI specimens was 5. Specimen dimensions are shown in Table 1.

TABLE 1—*Specimen dimensions.*

ROUND SPECIMENS

DIAMETER		OVERALL LENGTH		GAGE SECTION		ASPECT RATIO (r)
mm	in.	mm	in.	mm	in.	
12.70	1/2	31.75	1 1/4	25.40	1.0	2.0
9.53	3/8	25.40	1.0	19.05	3/4	2.0
6.35	1/4	19.05	3/4	12.70	1/2	2.0

SQUARE SPECIMEN

THICKNESS		WIDTH		OVERALL LENGTH		GAGE SECTION		ASPECT RATIO (r)
mm	in.	mm	in.	mm	in.	mm	in.	
9.53	3/8	9.53	3/8	25.40	1.0	19.05	3/4	2.0

IITRI

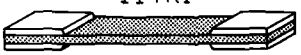

THICKNESS		WIDTH		OVERALL LENGTH		GAGE SECTION	
mm	in.	mm	in.	mm	in.	mm	in.
2.54	0.10	6.35	1/4	139.7	5 1/2	12.70	1/2

Experimental Procedure

Axial Test Method

The fixture used for the axial test was a modified version of the previous axial test fixture [*2*]. The addition of two tungsten carbide inserts constituted the major modification (Fig. 1). The previous fixture relied on hardened steel anvils, which were inadequate in strength and hardness because they yielded under load.

The retaining collars for the modified fixture were fabricated with a 5° taper on the top side. Because the fixture was intended to be reusable, different collars were fabricated to facilitate the compressive testing of specimens with different geometric configurations.

The axial stress loading was performed on a 300 kip open-loop hydraulic test machine at approximately 25 cm/min. Careful alignment was maintained between the fixturing and the anvils of the test machine. Two 0.013-mm-brass shims were placed between the tungsten carbide anvils and the specimen. Each strain gage was monitored on separate X-Y recorders. All specimens were loaded until failure occurred. Failure was indicated by an audible snap and a slight decrease in load. The failed specimen was removed from the fixture, and the mode of failure was examined metallographically. Mechanical properties obtained from the test include the ultimate compressive strength, compressive modulus, Poisson's ratio, strain to the elastic limit, and strain to failure. Poisson's ratio was not obtained for the 6.35-mm-round specimens due to limited surface area.

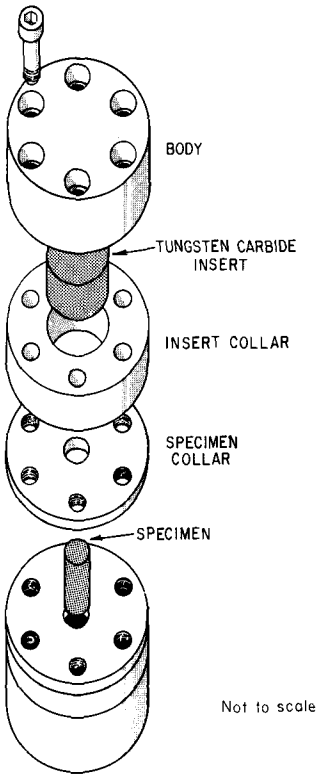

MODIFIED AXIAL COMPRESSION FIXTURE

FIG. 1—*Modified axial compression fixture.*

Indirect Compressive Test

The IITRI test fixture was used for the indirect compression test. The test fixture was carefully aligned between the cross heads of a 20 kip electro-mechanical Instron. Testing speed was 0.25 cm/min. Load versus strain was recorded on separate X-Y recorders.

The indirect compressive specimens were fabricated in accordance with ASTM Test Method for Tensile Properties of Fiber-Resin Composites (D 3039 76 (1982)). Each specimen was tabbed individually using 6061-T6 aluminum tabs. A gage section of 12.70 mm (1/2 in.) between tabs was maintained. Each specimen was strain gaged with two longitudinal strain gages. As in the case for the axial compressive specimens, the specimens were loaded until an audible snap was heard, followed by a decrease in load. The mode of failure was also determined using metallographic techniques. Mechanical properties obtained were ultimate compressive stress, compressive modulus, elastic strain, and strain to failure.

Separate X-Y recorders were used in each test to monitor alignment of the specimen and to determine if significant bending of the specimen was occurring during loading.

Results and Discussion

Compressive stress-strain curves obtained by the axial test method were essentially linear up to a strain of approximately 1 %. Beyond one percent strain the curves became slightly

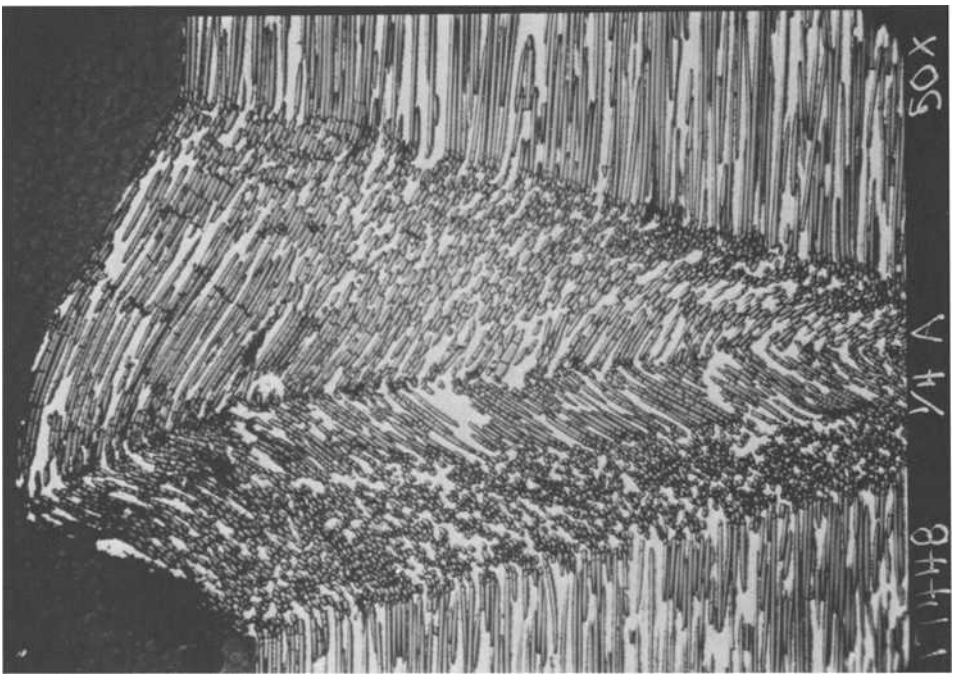

FIG. 2—*Formation of multiple kink bands; in and out of the midsection plane of a 0.635-cm-diameter FP/Mg cylinder specimen.*

nonlinear up to failure which occurred at about 1.4% strain. A slight bulging that developed in the gage section of the specimen may have been the cause of this nonlinearity. The test was terminated once a sharp snapping sound was heard and before any appreciable drop in load was observed. Interruption of the failure process in this manner suppressed extensive localized damage usually found to take the form of one or more kink bands [*1,2*] as shown in Fig. 2.

Post failure metallographic examination of the cylindrical specimens revealed no signs of kink band formations in those cases where failure was terminated in the early stages of development. The failure origin sites were easily located and were found to consist of local fiber bending fractures (Fig. 3) that developed at the free surface near the stabilizing collars. Axial stress concentrations probably developed at these areas due to the constraint introduced by the collars.

The results of this study indicate that the compressive deformation and failure behavior consist of at least four separate stages as shown in Fig. 4. The first stage, (*a*), is purely elastic deformation exhibiting a linear compressive stress-strain curve. The second stage, (*b*), consists of localized elastic bending of the fibers which is most intense at the free surface of the specimen.

Plastic deformation of the matrix accompanies the fiber bending resulting in a nonlinear stress-strain curve. When the second stage is unloaded, however, it also exhibits fully reversible deformation characterized by the closed hysterisis loop with no evidence of permanent set. If the fiber/matrix interface was weak, longitudinal splitting would occur in this second stage. On the other hand, it has been shown that the Fp/Mg composite studied here has a very strong fiber/matrix interfacial bond that is capable of supporting stress levels

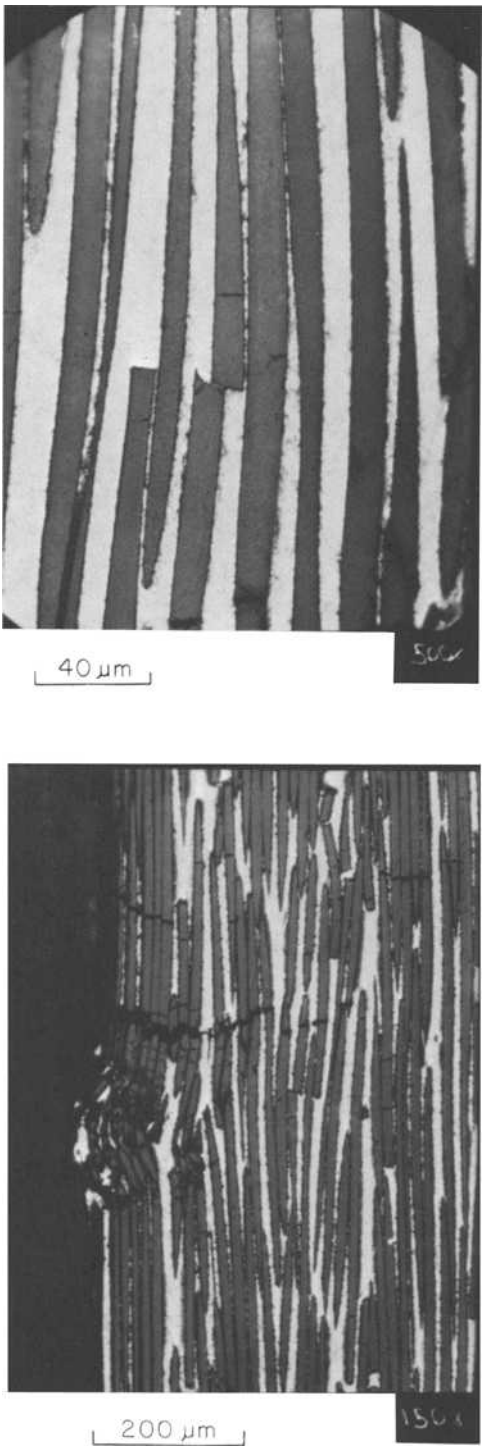

FIG. 3—*Failure origin site of 0.635-cm-diameter FP/Mg cylindrical specimen showing local bending fracture of the free surface prior to kink band formation.*

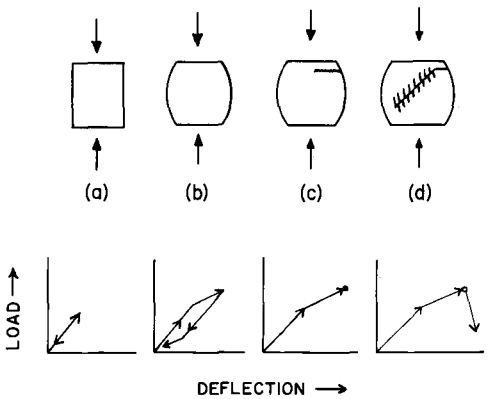

FIG. 4—*Schematic of proposed compressive deformation and failure behavior of uniaxially fiber oriented metal matrix composites.*

well above that of the matrix itself [*3*]. The third stage, (*c*), develops when fracture is initiated by the breaking of fibers at or near the free surface and in an area of high stress concentration, for example, at the constraining collars. The fourth and final stage, (*d*), occurs when the fiber and matrix cracking near the free surface transforms into localized deformation kink bands.

Although the stabilizing collars eliminated premature brooming, failure on the axially loaded cylindrical specimens, the compressive failure stresses measured may still not be the true compressive strengths for these composites. On the other hand, they are the highest recorded data obtained with any other test method to date. These and other test results are summarized in Table 2.

Unlike the cylindrical specimen results, the axially loaded square specimens exhibited brooming and correspondingly lower failure stresses most likely due to excessive lateral movement of material at the corners (Fig. 5). Both axially loaded geometries exhibited reproducible results with little scatter. The maximal scatter (percent variation of an individual value from the mean) of the data for ultimate compressive strength (Table 2) ranges from 1.6% (12.7-mm-diameter specimens) to 6.9% (6.35-mm-diameter specimens).

Of all the specimens tested, the IITRI test gave the greatest amount of scatter which was probably due to eccentric loading affects. Except for one case, the relative eccentricity varied from 15.7 to 18.8%. Values for relative eccentricity were obtained from the following expression

$$R = \frac{|\epsilon_1 - \epsilon_2|}{\bar{\epsilon}} \times 100 \tag{1}$$

where, ϵ_1 and ϵ_2 are strains obtained at the same load from back to back gages and $\bar{\epsilon}$ is the average of ϵ_1 and ϵ_2. The values of ϵ_1 and ϵ_2 were found by drawing the modulus line over the primary elastic portion of the load strain curve from 0 load to the maximal load scale for that specimen. For example, if the load scale for the 6.35 mm (1/4 in.) specimens was 1420 kg (50 lbs), then the modulus line would extend from 0 to 1420 kg (0 to 50 lb). The strain was then taken over this region of the curve. ϵ_1 was obtained from one of the longitudinal gages, while ϵ_2 was obtained from the other longitudinal gage which was placed on the same specimen except 180° opposite the strain gage from which ϵ_1 was obtained.

Because the IITRI fixture applies an indirect compressive load through shear, greater care must be used when aligning the IITRI specimens. Although considerable care was taken to visually align the specimen in the fixture, a more objective procedure is required.

TABLE 2—*Summary of compressive properties obtained on axial and shear load specimen.*

Specimen	Ultimate Compressive Strength (MPa)	E_c (GPa)	Eccentricity, R(%)	Poisson's Ratio, v	Strain at Bending, ϵ_B (%)	Strain at Failure, ϵ_f (%)
6.35 mm Dia. (average of 4 specimens)	3198 ± 191	226.2 ± 4.8	2.43	N/A	1.23	1.46
9.53 mm Dia. (average of 3 specimens)	3110.0 ± 50	226.8 ± 3.6	2.87	0.287	1.12	1.39
12.7 mm Dia. (average of 3 specimens)	3271.0 ± 50	233.5 ± 2.2	4.37	0.306	0.95	1.42
9.53 mm Sq. (average of 3 specimens)	2919.0 ± 60	218.8 ± 0.8	N/A[a]	0.279	1.14	1.37
IITRI	2951.0 ± 196.0	220.6 ± 5.6	12.0	N/A	N/A	1.40

[a] NA = not available

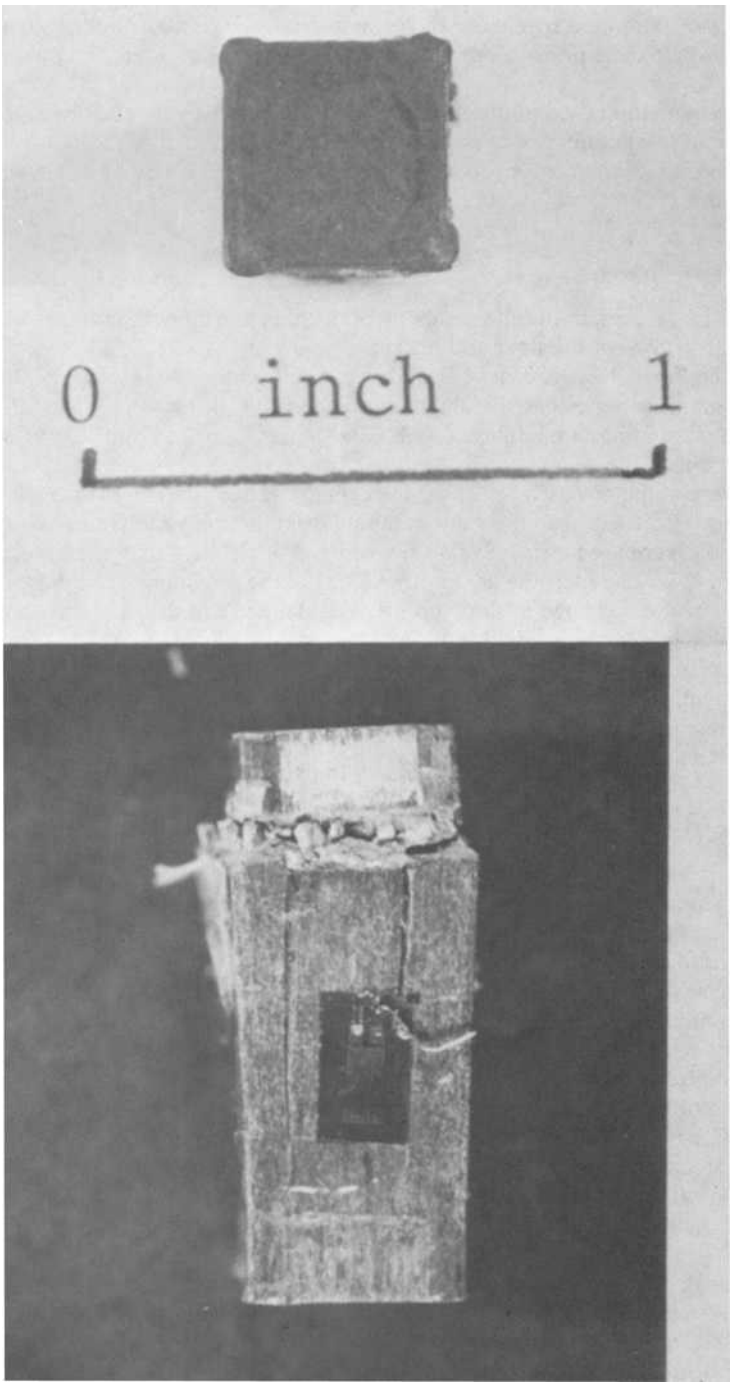

FIG. 5—*Failed square axial compression specimen.*

For example, a calibrated specimen whose dimensions would allow better alignment could be placed in the fixture prior to each test in order to ensure accurate fixture and specimen alignment.

The tabbing method used in this investigation proved to be very effective and resulted in no evidence of tab failure as was encountered in an earlier study [2].

The prediction of the compressive elastic modulus, E_c, is based on the formula for the rule of mixtures

$$E_c = V_f E_f + V_m E_m \tag{2}$$

where E_f and E_m represent the elastic moduli of the fiber and matrix, and V_f and V_m represent the volume fractions of the fiber and matrix.

The Textile Fibers Department of E. I. du Pont de Nemours and Company, Inc. indicates that FP fiber, which is essentially aluminum oxide (Al_2O_3), has a modulus of 379.2 GPa, and the magnesium has a modulus of 45.0 GPa. Using $V_f = 0.55$ and $V_m = 0.45$ produces $E_c = 228.8$ GPa.

The average value of E_c (Table 2) for the cylindrical and IITRI specimens is 228.3 GPa, which is only 0.22% less than the value resulting from the rule of mixtures. The mean value of E_c for the square specimen is 218.8 GPa which is 4.37% less than the predicted value.

The strain ϵ_B is defined as that strain originating at the origin up to the point on the load-strain curve where a change in slope occurs. ϵ_f is defined as the strain to specimen failure where any additional strain would result in a decrease in load. In all the tests, ϵ_f was shown to be higher in value than ϵ_B.

Poisson's ratio was obtained for the 9.53, 12.70, and 9.53-mm-square specimens. The range for these values was 0.28 to 0.31. Previous values published indicated a Poisson's ratio of approximately 0.28.

Conclusion

The axial compression test fixture has proven to be reliable in reproducing data for all the MMC geometric specimens tested with the square specimen being the exception. Although the square specimen failed by premature brooming, the cause of the failure was directly attributed to a poorly machined collar.

This nonconformity was evident when comparing the resulting lower average stresses and average modulus with those of the cylindrical and IITRI specimens.

Although an adequate method for obtaining well bonded tabbed specimens was utilized, indirect compressive testing such as the IITRI method proved that the IITRI test fixture required a more diligent alignment procedure. Although the Material Technology Laboratory (MTL) followed a careful alignment procedure in setting up the IITRI fixture, a significant amount of scatter occurred in the compressive strength data as shown by the standard deviation in Table 2. The relative eccentricity (R) for the IITRI specimens was greater (12.0) than those for the cylindrical specimens (4.37 maximum for the 12.7 mm diameter).

Even though the 9.53-mm-square specimens did not display a high average ultimate compressive strength as did the cylindrical specimen, the scatter was still considerably less than the IITRI specimens.

The ease of manufacturing the axial compressive specimens proved worthwhile in terms of cost. Also, specimens could be cut out of actual components to be tested for their compressive properties.

Robert S. Frankle[1] *and Jay G. Baetz*[2]

Elevated Temperature Testing of Metal Matrix Composites Under Rapid Heating Conditions

REFERENCE: Frankle, R. S. and Baetz, J. G., **"Elevated Temerature Testing of Metal Matrix Composites Under Rapid Heating Conditions,"** *Testing Technology of Metal Matrix Composites, ASTM STP 964*, P. R. DiGiovanni and N. R. Adsit, Eds., American Society for Testing and Materials, Philadelphia, 1988, pp. 329–345.

ABSTRACT: The Atlantic Research Corporation has designed and built facilities for testing metal matrix composites at elevated temperatures. The facilities are capable of performing tension or compression tests of sheet-type specimens to 1927°C (3500°F) at heating rates in excess of 38°C/s (100°F/s). Tension tests were performed on unidirectional and cross-ply graphite/aluminum, unidirectional graphite/copper, and discontinuous silica carbide/aluminum materials. The continuously reinforced materials exhibited superior room temperature properties and elevated temperature property retention when compared with the matrix metals alone. The elevated temperature response of the discontinuously reinforced SiC/Al was comparable to that of aluminum. These test results indicate the potential advantages of using metal matrix composites in rapid heating, elevated temperature applications, where the temperature may approach the melting point of the matrix material.

KEY WORDS: composite materials, metal matrix composites, mechanical properties, test, elevated temperature, test method

As metal matrix composites technology matures, new applications for these materials arise. One example is the use of metal matrix composites at elevated temperatures that may approach the melting point of the matrix. In these applications, metal matrix composites would substitute for strategic materials, such as superalloys. Superalloys have high densities which impose severe penalties on structures which may be weight critical. At elevated temperatures, even these high-temperature metals lose a significant portion of their room temperature properties. Metal matrix composites present an attractive alternative because they are lower density, nonstrategic materials. Prior to 1982, when this work was performed, the properties of metal matrix composites at elevated temperatures were largely unknown. Therefore, tests were conducted to measure the properties of a variety of materials over a range of temperatures.

An added consideration in this evaluation was the effect of heating rate on the response of metal matrix composites. Some of the applications postulated included heating conditions in which the temperature would increase from room temperature to near the matrix melting point in a matter of seconds. It was hypothesized that, for a continuously reinforced composite, the properties in the reinforcement direction would maintain a sufficient fraction of their room temperature values as long as the matrix remained solid. Even for discontinuous

[1] Managing engineer, Failure Analysis Associates, Palo Alto, CA 94303.
[2] Manager, Materials Technology Department, Atlantic Research Corporation, Alexandria, VA 22312.

composites, potentially acceptable elevated-temperature properties were theorized for high heating rates and short exposure times. For the rapid heating rates of greatest interest, few, if any, facilities were available to perform the required tests. Therefore, beginning in 1981, the Materials Technology Department of Atlantic Research Corporation designed and fabricated such a facility under IR&D funding. The high-heating rate, elevated-temperature test facility was configured for tension testing of sheet-type specimens. The success of this initial test facility led to the development in 1985 of a second facility, which incorporated improved and expanded testing capability. The paper describes both of these test facilities, their application to metal matrix composites, and selected test results.

Experimental Procedure

Equipment

The first test facility was designed to conduct tension tests on sheet specimens to 1927°C (3500°F) at a heating rate of 38°C/s (100°F/s). Other design goals included:

1. The ability to test a broad range of materials, including metals, continuous and discontinuous reinforced metal matrix composites, and carbonaceous composites.
2. Programmable, flexible, independent control of temperature, load, displacement, and strain as a function of time.
3. Compatibility with existing specimen designs, with specimen sizes up to 25.4 cm (10 in.) long by 3.18 cm (1.25 in.) wide by 0.64 cm (0.25 in.) thick.
4. An inert gas environment.
5. Highly automated data acquisition, reduction, and storage.
6. Cyclic loading capability.
7. Continuous, real-time measurement of load, strain, displacement, and temperature.
8. The capability to observe the specimen during the test.

During the preliminary design phase, alternative approaches to meeting these goals were evaluated. A fundamental decision was the selection of a heating technique. Several techniques were considered, including induction, resistance, laser, and radiation heating. Direct resistance heating was ultimately selected because it provided the required heating capability and left the specimen accessible for instrumentation and observation.

The resulting tension test facility is shown in Fig. 1. The facility utilizes an MTS servohydraulic, closed loop materials testing system, which produces monotonic and cyclic loading. The load train, the grips, and the test chamber make up the remainder of the loading system. The load train incorporates an insulating coupler to isolate the direct resistance heating current. The grips are Instron tension grips with modified water-cooled inserts which provide both the conductive path for the direct resistance heating and the serrated surfaces for gripping the specimen. The test chamber provides an inert gas environment surrounding the grips and the specimen. The front and back of the chamber are transparent for observing the specimen during the test. The chamber also provides access and support for the laser extensometer system.

Specimen heating is achieved via a closed loop system, including a transformer, a programmable controller, and thermocouples. The power for the direct resistance heating is provided by a transformer, which was fabricated to meet the specific requirements of this facility. The transformer operates in response to a programmable controller, which defines the required power-time conditions to achieve the desired time-temperature response. The specimen temperature is measured using thermocouples, which provide the feedback signal for temperature control. The thermocouples are bonded to the specimen surface with ceramic

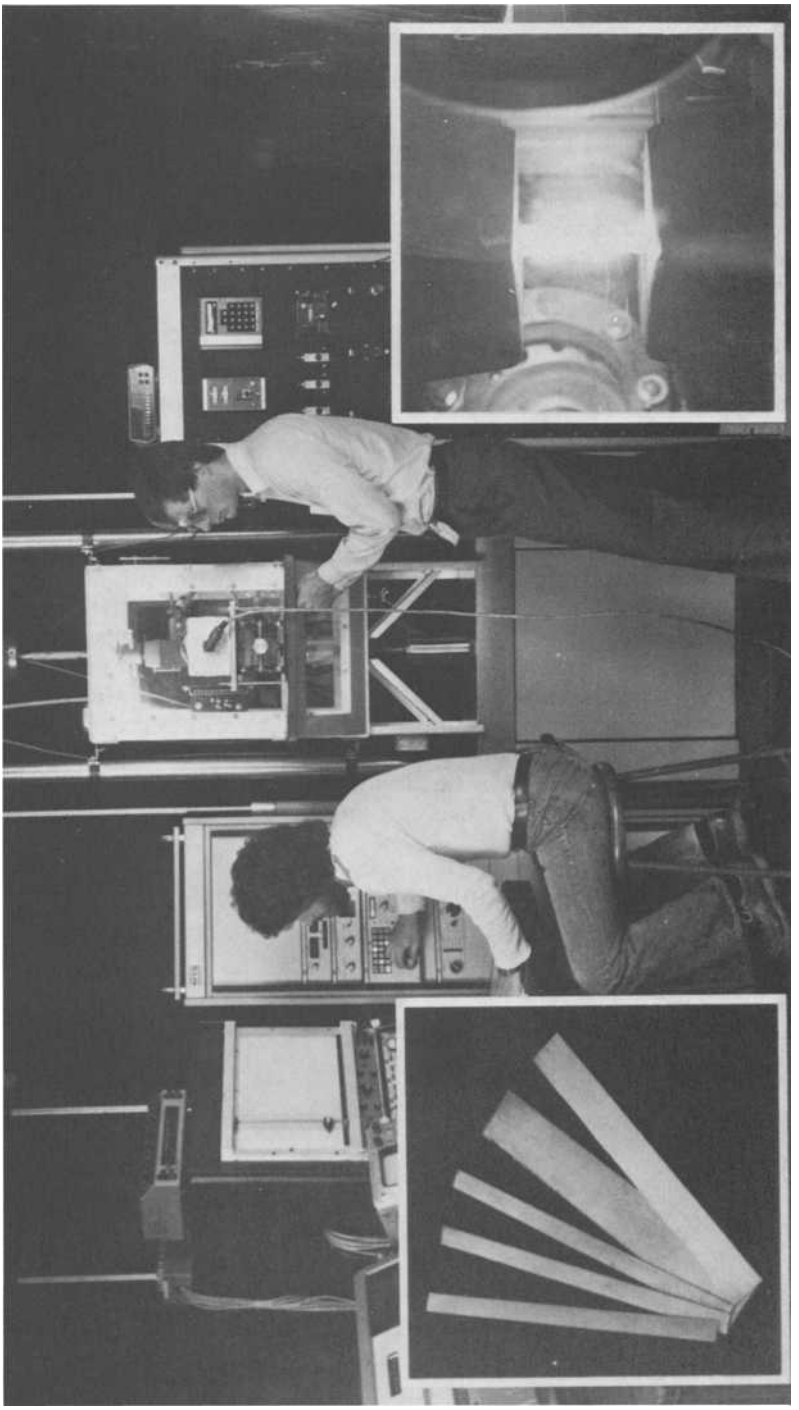

FIG. 1—*Elevated-temperature tension test facility.*

adhesive. One of the improvements incorporated in the subsequent test facility was to use remote temperature measurement instead of thermocouples. Test results demonstrated that the closed loop heating system does permit precise control of specimen heating and accurate reproduction of the desired time-temperature response.

Strain is measured using a Zygo Model 120 laser extensometer, in conjunction with flags bonded to the test specimen. The Zygo's transmitter and receiver are mounted on opposite sides of the test chamber. A vertical planar laser field is transmitted, passes by the specimen, and is sensed by the receiver. The laser field is interrupted by the two flags, which are ceramic tubes bonded to the specimen. The extensometer senses change in the distance between the flags, from which strain is calculated. The output appears on the Zygo controller and is also fed directly to the computer. The accuracy of the Zygo laser extensometer is ±0.0005 cm (±0.0002 in.). The gage length, which is defined by the distance between the two flags, can be varied as long as the specimen deformation is such that the flags remain within the 4.57 cm (1.8 in.) planar laser field. The capability of this strain measurement system is illustrated in Fig. 2, a room temperature stress-strain curve for 7075-T6 aluminum. This approach proved to be a practical solution to the requirement for continuous, real-time strain measurement at elevated temperature.

Data acquisition instruments include a microcomputer, *x-y* plotters, and a strip chart recorder. All test data are recorded and stored in the computer. The data can be then reduced automatically and presented in tabular and graphical formats. Real-time load, extension, and temperature data are displayed by the *x-y* plotters and the strip chart recorder.

A second test facility, shown in Fig. 3, was subsequently developed in 1985 to incorporate greater capability than the tension test facility, including tension and compression testing of sheet-type specimens, improved strain measurement accuracy, measurement of Poisson's ratio, and remote temperature sensing. Specially designed hydraulic grips permit tension and compression testing of sheet-type specimens. Improved strain measurement is achieved by employing a Zygo Model 121F laser extensometer, which is 10 times more accurate than the Zygo Model 120 used in the tension test facility. Poisson's ratio is obtained by adding a second Zygo laser extensometer and monitoring the change in the specimen width in the

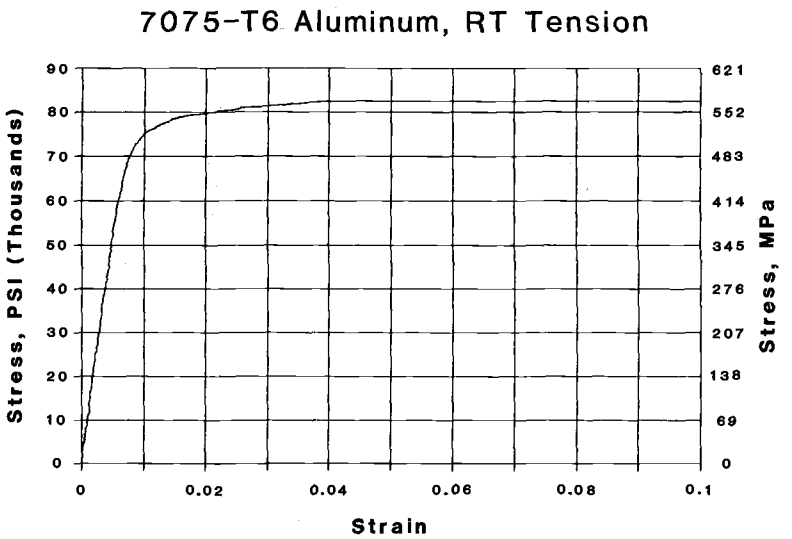

FIG. 2—*Measured stress-strain curve for 7075-T6 aluminum.*

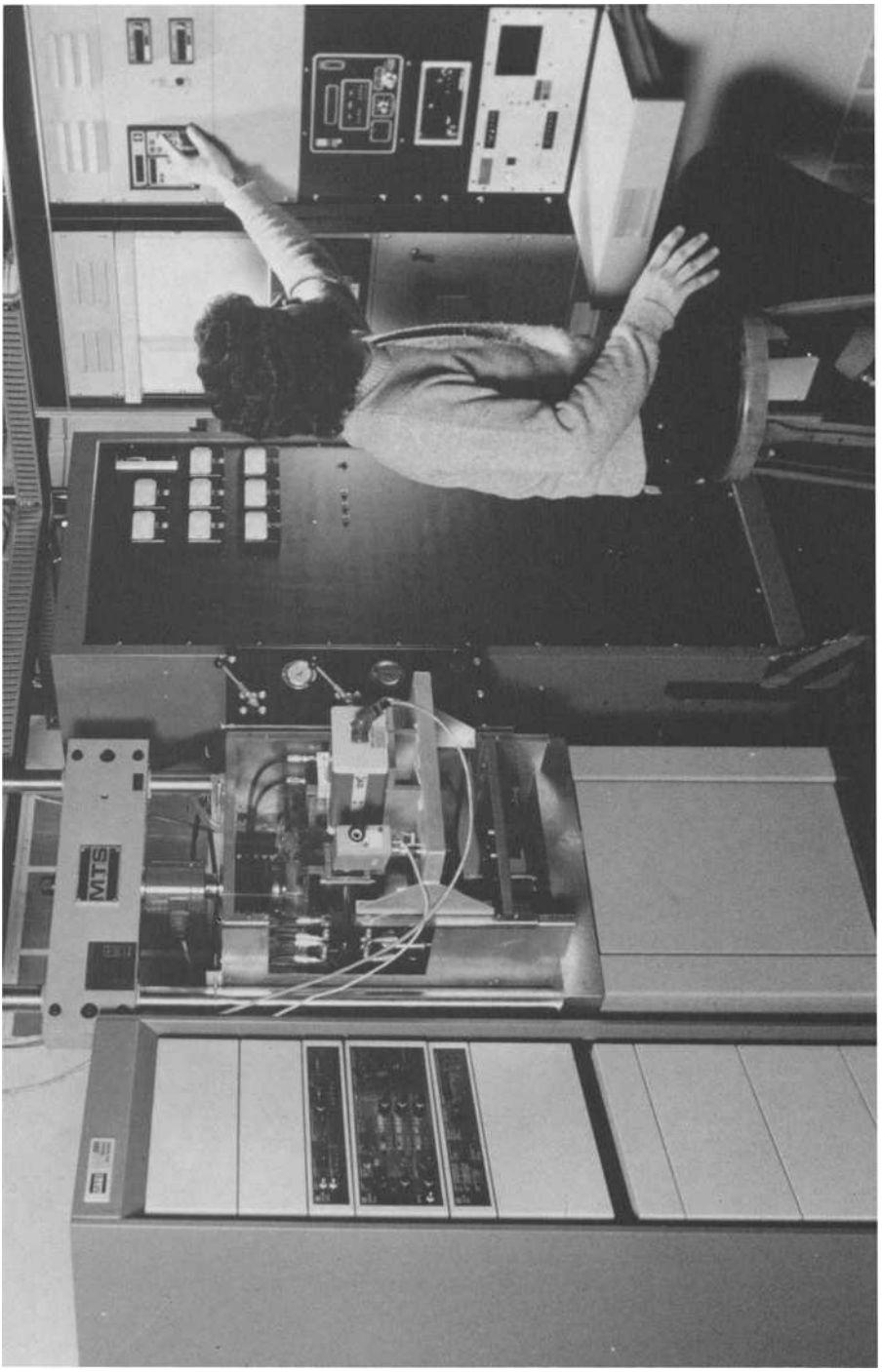

FIG. 3—*Improved elevated-temperature test facility.*

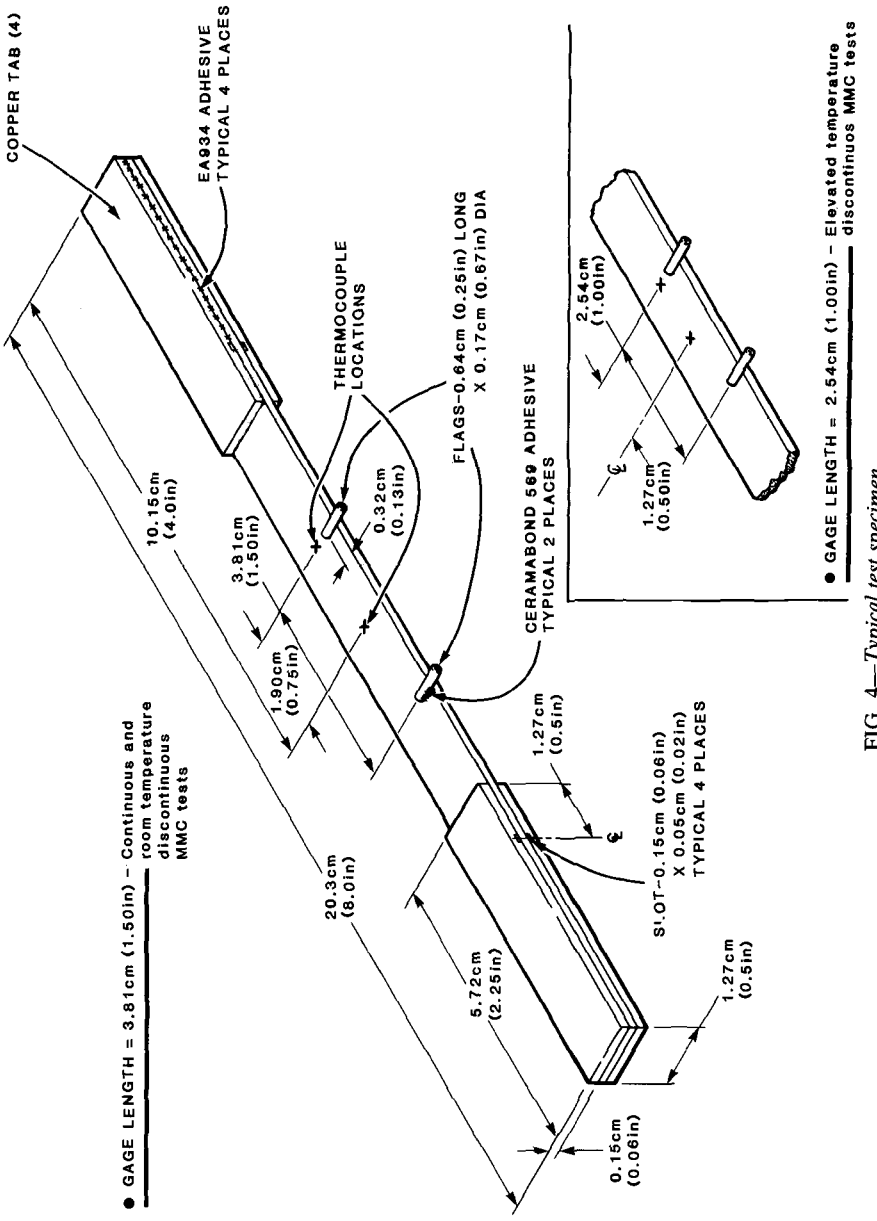

FIG. 4—*Typical test specimen.*

gage section. Rather than thermocouples, optical pyrometers are used to measure temperature remotely. This improved facility provides greater capability to evaluate the response of metal matrix composites, as well as other materials, at temperatures up to 1027°C (3500°F) and heating rates beyond 38°C/s (100°F/s). The work reported on in this paper was performed using the original tension test facility.

Specimen Preparation

The test specimens were machined from sheet stock supplied to the program. The specimens were nominally 20.3 cm (8.0 in.) long by 1.27 cm (0.5 in.) wide by the thickness of the sheet. Four copper tabs 5.72 cm (2.25 in.) by 1.27 cm (0.5 in.) by 0.15 cm (0.060 in.) were bonded to the ends of the specimen using EA934 epoxy adhesive. The tabs were designed to incorporate an area adjacent to the gage section without adhesive to ensure a conductive path for the direct resistance heating. The strain measurement flags were bonded to the gage section with Ceramabond 569 ceramic adhesive. Both the tab and flag bonding procedures utilized specially designed fixtures to enhance proper placement and adhesion. A 93°C (200°F) cure was used for both adhesives. Because the grips were water cooled, the tabbed region of the specimen remained at or near room temperature throughout the test. Two thermocouples were bonded to one side of the specimen, one at the center and one at the edge of the gage section. Figure 4 presents a drawing of an instrumented specimen.

Procedure

The tension test facility was used to perform these metal matrix composites tests. A standard test procedure, which includes specimen preparation, testing, and data reduction, was followed for each test to promote reproducibility. Following specimen preparation, the test specimen is placed between the grips. The thermocouples are bonded to the specimen surface, and the laser extensometer is aligned with respect to the flags. The test facility parameters are set to provide the prescribed time-temperature and load-time conditions.

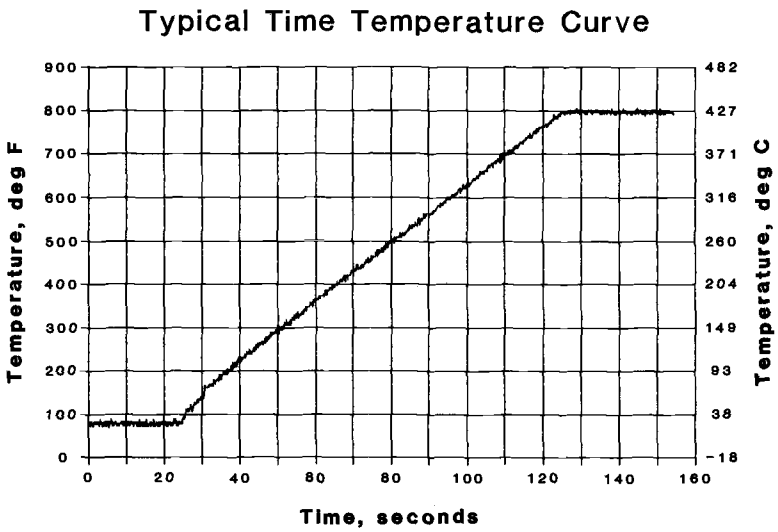

FIG. 5—*Typical time-temperature curve.*

The parameters will change with test conditions, materials, and specimen configurations. Prior to testing, all systems are checked, and the test chamber is purged with nitrogen for 30 min.

Testing begins by initiating the heating system controller program, and it continues automatically to failure of the specimen. For these tests, the specimen is heated to a standard 24°C (75°F) for 1 min, followed by heating at a constant rate of 10°C/s (50°F/s) to the specified test temperature. After a specified hold time at temperature, the specimen is loaded at a constant displacement rate of 0.013 cm/s (0.005 in./s) to failure. A standard hold time of 2 s was employed, with some specimens tested after hold times of 2 and 5 min. During the test, the strip chart recorder plots time versus temperature, as shown in Fig. 5. One *x-y* plotter presents the temperature gradient along the gage length, which will vary depending upon the material, specimen geometry, and test temperature. Typical gradients are less than 5%. At 427°C (800°F), a temperature variation of less than 14°C (25°F) is common. A second *x-y* plotter displays load versus extension.

Results and Discussion

The elevated-temperature test facility has been used to test a variety of composite materials. These materials and the test temperatures at which they were tested are summarized in Table 1. Generally, the test conditions were controlled in order to provide heating conditions representative of a projected rapid heating application and a maximum test temperature approaching the material melting point. In addition to the composite materials shown in Table 1, various metals, including aluminum and copper, have been also tested. Figure 6 shows an example of a test specimen at elevated temperature, in this case, carbon-carbon at 1649°C (3000°F).

The metal matrix composite materials tested in this study are described in Table 2. The materials include VSB32/6061-T6 graphite/aluminum (Gr/Al) from three manufacturers: DWA, Composite Specialties, Inc., of Chatsworth, California; Material Concepts, Inc. (MCI), of Columbus, Ohio; and Amercom, Inc., of Chatsworth, California; particulate and whisker-reinforced silicon carbide/6061-T6 aluminum (SiC/Al) from DWA and ARCO Advanced Materials Operations of Greer, South Carolina; and a DWA VSB32/Cu113 graphite/copper (Gr/Cu). The aluminum matrix composites were tested to 427°C (800°F) and the copper matrix materials to 982°C (1800°F).

TABLE 1—*Composite materials tested in elevated-temperature facility.*

Material	Reinforcement	Maximum Temperature °C	Maximum Temperature °F
Graphite/copper	unidirectional, 2 ply	982	1800
Graphite/aluminum	unidirectional 0/90/0	427	800
SiC_w/aluminum	whisker	427	800
SiC_p/aluminum	particulate	427	800
SiC_p/aluminum Ti clad	particulate	260	500
SiC/aluminum	unidirectional 0/90/0	482	900
Borsic/aluminum	unidirectional cross ply	482	900
SiC/Ti René 41 clad	unidirectional	982	1800
3-D carbon-carbon		1927	3500
2-D carbon phenolic		260	500

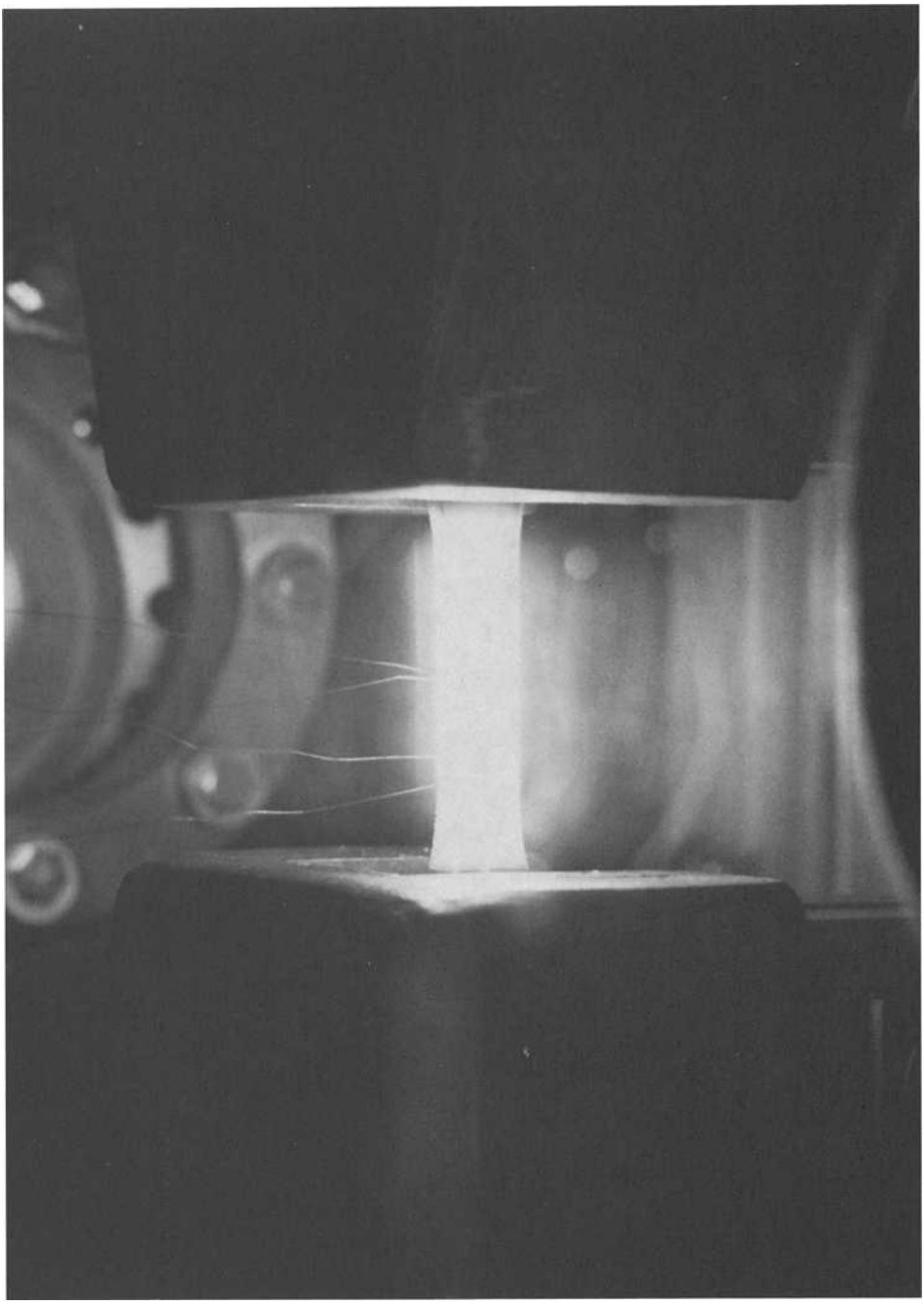

FIG. 6—*Test specimen at elevated temperature.*

TABLE 2—*Material description.*

Material	No. of Plies	Design	Fiber	Matrix	Supplier	Fiber Volume, %	Nominal Thickness, cm	(in.)
Gr/Al	2	0-0	VSB32	6061-T6	DWA	41.0 to 43.5	0.114	(0.045)
					MCI	44.0	0.124	(0.049)
	3	0-90-0	VSB32	6061-T6	DWA	40.9 to 43.3	0.170	(0.067)
					Amercom	33.9	0.229	(0.090)
Gr/Cu	2	0-0	VSB32	Cu113	DWA	50.0 to 51.0	0.112	(0.044)
SiC/Al	...	...	SiCp	6061-T6	DWA	25.0	0.274	(0.108)
			SiCw	6061-T6	ARCO	25.0	0.251	(0.099)

TABLE 3—*Test results summary.*

Material	Design	Supplier	Test Temperature °C	Test Temperature °F	Test Direction	No. of Tests	Tensile Strength, % Avg	Tensile Strength, % S	Failure Strain, % Avg	Failure Strain, % S	Modulus, % Avg	Modulus, % S
Gr/Al	0-0	DWA	260	500	0	3	109	5	95	6	110	3
			427	800	0	3	93[1]	1	100[1]	6	91[1]	7
		MCI	427	800	0	3	101	8	95	9	105	2
	0-90-0	DWA	260	500	0	3	112	4	103	9	108	9
					90	2	104	6	89	11	107	0
			427	800	0	3	100	4	106	17	94	9
					90	3	96	4	100	12	89	6
		Amercom	260	500	0	3	95	5	93	4	103	3
					90	3	83	1	60	8	128	12
Gr/Cu	0-0	DWA	427	800	0	3	100	4	105[1]	18	84[1]	8
			538	1000	0	3	88	13	93	23	91	8
			649	1200	0	4	65	5	60	4	90	5
			871	1600	0	3	63	9	83	40	87	24
			871	1600[2]	0	3	71	3	93	16	79	3
			982	1800	0	3	62	6	80	3	67	7
SiCp/Al	...	DWA	260	500	L	3	54	1	805[1]	7	83[1]	13
					LT	3	50	1	307	10	81	22
			260	500[3]	L	3	49	1	415[1]	92	87[1]	1
					LT	3	48	2	341	26	66	11
			427	800	L	3	9	2	112	158	83	22
SiCw/Al	...	ARCO	260	500	L	3	40	4	124	77	44	9
					LT	3	34	2	167	3	40	6
			427	800	LT	1	7	...	318	...	29	...

NOTE:
All tests conducted at 10°C/s (50°F/s) and 2 s ho ld at test temperature except as noted.
(1) 1 data point not included in statistics due to testing problems.
(2) 5 min hold at test temperature.
(3) 2 min hold at test temperature.

The test results are summarized in Table 3, in which the elevated-temperature test results are presented in terms of the extent of room-temperature property retention. Average and standard deviation values are shown for ultimate tensile strength, failure strain, and tensile elastic modulus. In general, all three test replicates were used to calculate these quantities. In a few tests, where testing problems were identified, the data were not used in the statistical computations. Typically, one observes a higher standard deviation for the failure strain and modulus data than for the strength data. This is attributed to the greater difficulty inherent in strain measurement, as compared to load measurement. In addition, the identification of a failure strain for the discontinuous SiC/Al specimens was complicated by the very large strains at elevated temperature and the lack of a well-defined failure event. These specimens tended to deform gradually with extreme reduction in areas. The modulus determination was made difficult by the lack of an ideal initial linear segment of the stress-strain curve, especially for the elevated-temperature SiC/Al specimens. Because a tangent modulus was used, this stress-strain behavior contributed to the observed scatter in the modulus data.

The test results presented in Table 3 are illustrated graphically in Figs. 7 through 14. All of the plots represent measured response after a 2 s hold at the specified test temperature. Figures 7 through 10 display the variation of ultimate tensile strength with temperature, where strength is expressed in terms of a percentage of the measured room temperature value. The four figures each address a separate type of material, the unidirectional graphite/aluminum (Gr/Al), cross-ply Gr/Al, discontinuous Gr/Al, and unidirectional graphite copper (Gr/Cu). In addition, curves for unreinforced 6061-T6 aluminum and Cu113 copper are also shown. The aluminum curve was derived from Military Handbook 5 [*1*] and the copper curve from *Materials and Design Engineering, Materials and Process Manual* [*2*]. An identical form of presentation is used in Figs. 11 through 14, which display the elastic modulus results. In all cases, curves have been drawn between the data points to indicate the possible temperature variation.

An examination of the ultimate tension strength results (Figs. 7 through 10) reveals some overall trends. Perhaps most apparent is that the elevated temperature properties of the

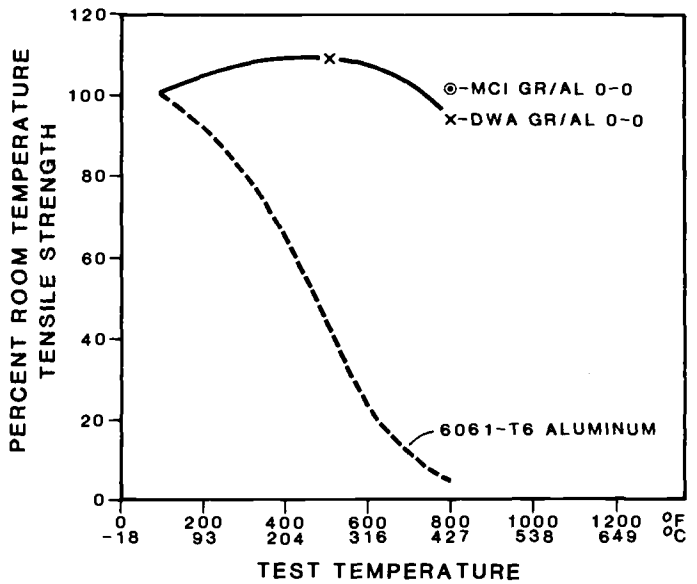

FIG. 7—*Ultimate tensile strength versus temperature Gr/Al (0,0).*

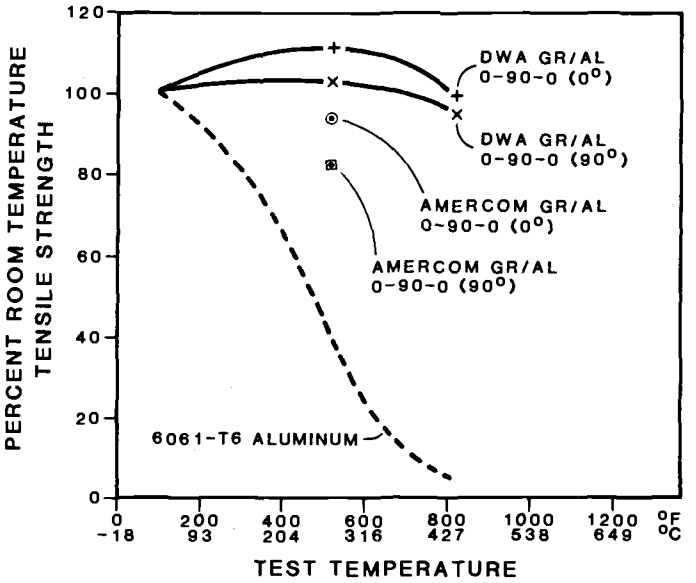

FIG. 8—*Ultimate tensile strength versus temperature Gr/Al (0,90,0).*

continuously reinforced composites are vastly superior to those of the matrix material alone, either aluminum or copper. At 427°C (800°F), which is approximately 75% of its melting point, aluminum has an ultimate tensile strength equivalent to 4% of its room-temperature value. In comparison, the graphite/aluminum composites tested retain a minimum of 93% of their room-temperature tensile strength at 427°C (800°F). The results were similar for the copper matrix composites. At 649°C (1200°F), the graphite/copper specimens exhibited 65° of their room temperature tensile strength, as compared to 24% for unreinforced copper.

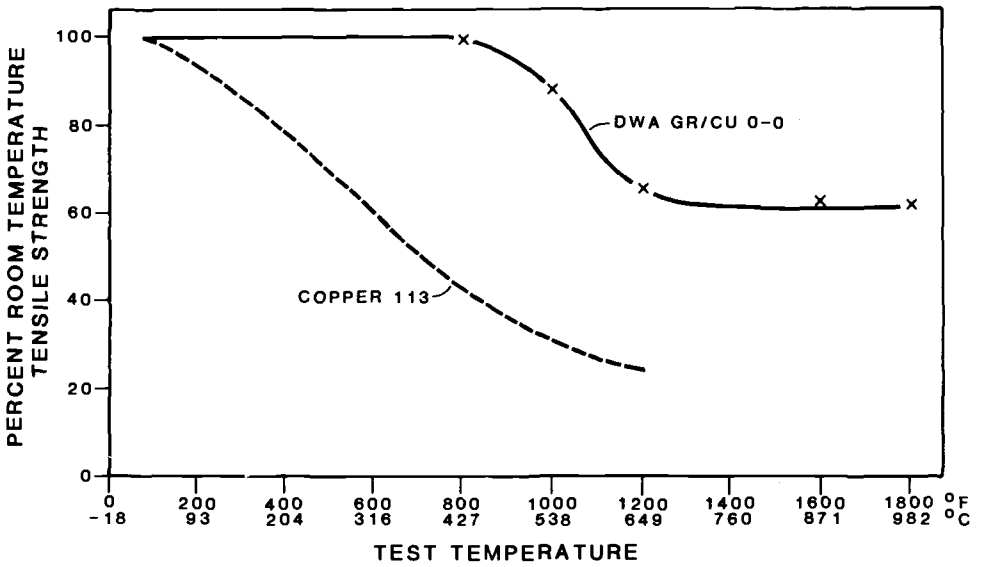

FIG. 9—*Ultimate tensile strength versus temperature Gr/Cu (0,0).*

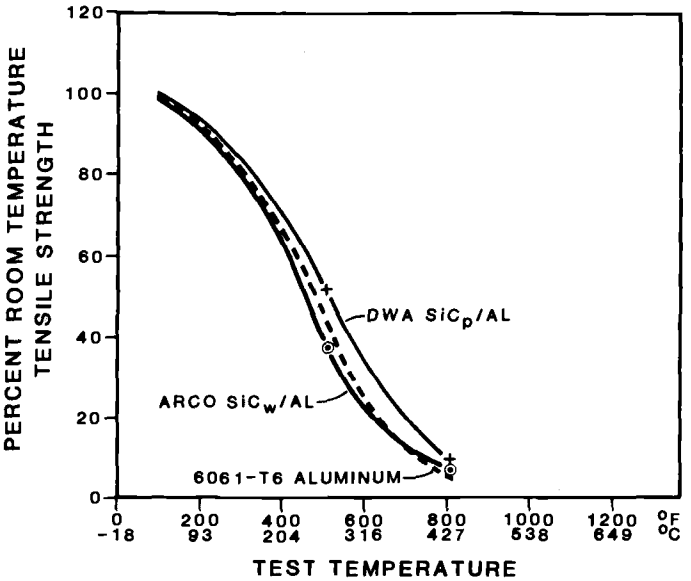

FIG. 10—*Ultimate tensile strength versus temperature SiC/Al.*

The retained strength of graphite/copper only dropped to 62% of the room temperature value at 982°C (1800°F), which is approximately 90% of the melting point for copper. The lower values for graphite/copper, as compared to graphite/aluminum, at the same fraction of the matrix melting point may be due in part to the fact that the graphite/copper was a relatively new product at the time of this study. As a result, the immature material quality may have adversely affected the elevated temperature property retention.

For the tensile elastic modulus data, the results are similar, in that the continuous metal

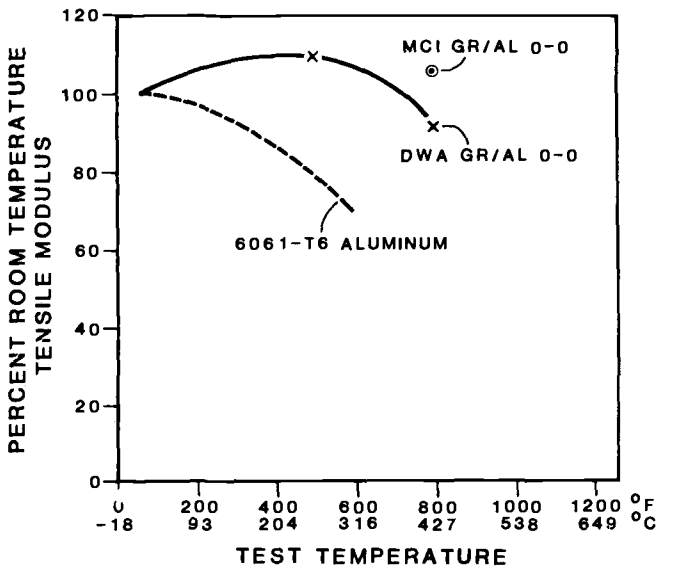

FIG. 11—*Tensile elastic modulus versus temperature Gr/Al (0,0).*

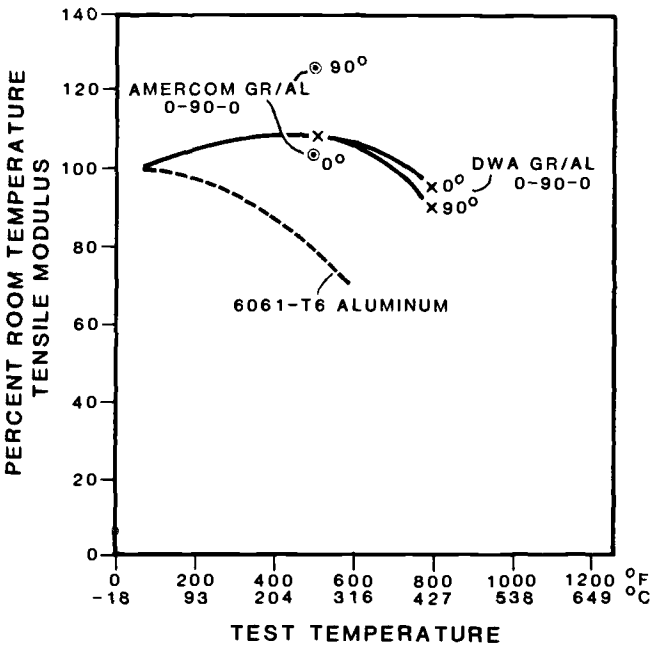

FIG. 12—*Tensile elastic modulus versus temperature Gr/Al (0,90,0).*

matrix composites retain a greater portion of their room temperature stiffness at elevated temperature. However, because the stiffness degradation for aluminum and copper is less severe than the strength degradation, the composites display a less dramatic advantage. For example, at 427°C (800°F), the stiffness of the graphite/aluminum composites was 89% of the room-temperature value, as compared to 70% for aluminum alone. The graphite/copper material retained 66% of its room temperature stiffness at 982°C (1800°F). For copper alone

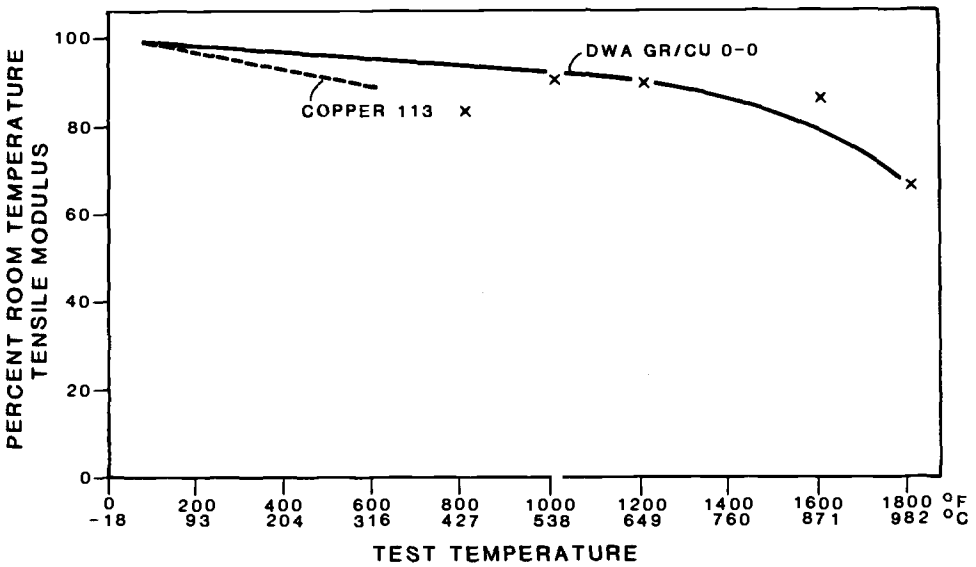

FIG. 13—*Tensile elastic modulus versus temperature Gr/Cu (0,0).*

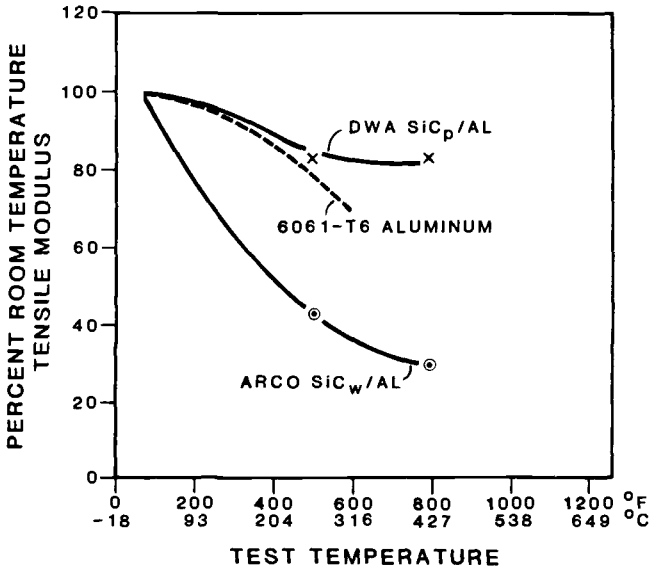

FIG. 14—*Tensile elastic modulus versus temperature SiC/Al.*

at 316°C (600°F), the highest temperature data available, the stiffness was 88% of the room temperature value.

Based on retained tensile strength and stiffness, the clear superiority of the continuous reinforced metal matrix composites over the unreinforced metal at elevated temperatures has an added advantage not readily apparent from the data presented. The elevated temperature property retention is based on the measured room temperature values for the metal matrix composites and the handbook values for the matrix metals. The continuous metal matrix composites exhibit a higher room temperature tensile strength and modulus in the reinforcement direction than the metals. The combination of superior room temperature properties and elevated temperature property retention makes the continuous metal matrix composites even more attractive for potential elevated temperature applications. Of course, other properties, such as elongation and transverse strength, must be considered when evaluating such applications.

For the Gr/Al materials, the test results illustrated in the figures contain a characteristic increase in both tensile strength and modulus at 260°C (500°F). The repetitive nature of this response for the various materials and specimens tested leads one to believe that, in fact, it is real. In some cases, the property increase exceeds 10%. One possible explanation for this behavior is the realignment of the fibers to provide a more well aligned, more effective load carrying structure. At this warm temperature for the aluminum matrix, the matrix is such that it can likely accommodate this realignment and redistribution of load. This behavior certainly deserves further study, so that if it is, in fact, material based, then full advantage can be taken in the application of structures in this temperature regime.

For the cross-plied (0-90-0) Gr/Al materials, the strength retention in the two test directions (0° and 90°) is illustrated in Fig. 8. As shown in the figure, the 0° properties retain a greater proportion of their room temperature values. This may be due to the greater fiber volume fraction in the 0° direction. The difference between 0° and 90° retention is greater in the Amercom material than the DWA material. In addition to the greater strength retention in the 0° material direction, the actual elevated temperature properties at 0° and 90° will also differ due to the significantly lower 90° strength at room temperature.

In the case of the discontinuous silica carbide/aluminum (SiC/Al) composites, the results are very different, as shown in Figs. 10 and 14. The temperature dependency of the tensile strength for both SiC/Al materials tested was comparable to that of 6061-T6 aluminum (Fig 10). For the elastic modulus (Fig. 14), the DWA particulate material exhibited a comparable temperature dependency, but the response of the ARCO whisker material was significantly worse than aluminum. No analysis was performed to evaluate this result, but the consistency of the data appears to indicate a material cause, as opposed to a test method effect. Both the DWA and ARCO materials produced room temperature properties significantly greater than 6061-T6 aluminum. Therefore, with this higher room temperature base, the comparable variation with temperature will still provide higher elevated temperature properties than aluminum, but lower than the continuously reinforced metal matrix composites tested.

Referring to Table 3, one additional observation is that the effect of hold time at temperature appears to be minimal. Most of the specimens were held for 2 s prior to applying the load. The time was also increased to either 2 min, in the case of the DWA SiC_p/Al at 260°C (500°F), or to 5 mins, for the Gr/Cu at 871°C (1600°F). The differences between the two sets of data, short and long hold times, was on the order of 10%. This result may be unique to the direct resistance heating, which produces a rapid temperature response in the thin specimens used. Hold time would be expected to have a greater effect for a thicker section or a different heating technique, such as heat lamps, where the bulk response is slower.

Conclusions

The results from these tests indicate that metal matrix composites may be suitable for applications in which the material is exposed to rapid heating and elevated temperatures, including temperatures approaching the melting point of the matrix material. For the continuously reinforced composites, elevated temperature properties in the reinforcement direction were shown to be superior to those of either aluminum or copper matrix materials alone. Continuous metal matrix composites retained a greater portion of their room temperature tensile strength and stiffness at elevated temperatures and exhibited a higher room temperature strength and modulus than did the metals. Testing also indicated that discontinuous silica carbide/aluminum composites are suitable for application at higher elevated temperatures than would be possible with aluminum, but lower than possible with the continuous matrix composites.

In addition to verifying the hypothesized elevated temperature response of metal matrix composites, the consistency of these test results indicates that the test methods employed can indeed be used to accurately and reproducibly measure and evaluate material responses at elevated temperatures up to 982°C (1800°F) and heating rates of 10°C/s (50°F/s). Subsequent testing, not reported here, yielded similar results over a wider range of temperatures and heating rates. In addition, these initial tests revealed needed test facility improvements, such as greater strain measurement accuracy, simultaneous transverse strain measurement, and compression testing capability. These improvements were incorporated in the subsequent test facility.

References

[1] *Military Standardization Handbook: Metallic Materials and Elements for Aerospace Vehicle Structures,* MIL-HDBK-5D, Notice 1, Department of Defense, Washington, DC.

[2] *Materials and Design Engineering, Materials and Process Manual,* No. 226, Reinhold Publishing, New York, Dec. 1964.

Peter L. Boland,[1] *Peter R. DiGiovanni,*[1] *and Larry Franceschi*[1]

Short-Term High-Temperature Properties of Reinforced Metal Matrix Composites

REFERENCE: Boland, P. L., DiGiovanni, P. R., and Franceschi, L., **"Short-Term High-Temperature Properties of Reinforced Metal Matrix Composites,"** *Testing Technology of Metal Matrix Composites, ASTM STP 964,* P. R. DiGiovanni and N. R. Adsit, Eds., American Society for Testing and Materials, Philadelphia, 1988, pp. 346–375.

ABSTRACT: While the Department of Defense initiated Metal Matrix Composite Information Analysis Center (MMCIAC) has been charged with providing centralized information dealing with metal matrix composites (MMCs), test procedures for obtaining primary MMC properties have evolved from ASTM standards. These standards in turn have evolved from polymeric matrix composite (PMC) test procedures and have not yet been established as appropriate for MMC applications. Methods for obtaining short-term high-temperature tensile, flexural, and pin bearing data for reinforced MMC are presented. In addition, coupon design and fabrication, instrumentation, measurement techniques, and some lessons learned are discussed.

Rapid heating, typical of tactical missile aerodynamic heating, can be suitably simulated using infrared quartz lamps. In fact, this type of furnace facilitates longer term baseline testing since temperatures can be reached more quickly, and test fixtures and equipment can be easily cooled. For short-term high-temperature strain measurements, extensometers were utilized. A computerized, digital data acquisition and control system is necessary to maximize data retrieval and minimize test errors during rapidly changing test conditions. Results show that while tensile strength of MMCs subjected to rapid heating greatly exceed those strengths obtained for long-term heating, flexure and pin bearing strength exhibit only moderate increases. Furthermore, differences are observed for specimens fabricated from thin versus thick panels.

KEY WORDS: metal matrix composites, missile aerodynamic heating, quartz lamps, extensometers, tensile strength

Some of the advantages and disadvantages of metal matrix composites (MMCs) compared to polymeric reinforced composites (PRCs) have been discussed in Ref *1*, as well as the role of the Metal Matrix Composite Information Analysis Center (MMCIAC) in acquiring, storing, and disseminating MMC technical data. However, very little data are available from MMCIAC or other technical sources on strengths of MMCs when subjected to short-term elevated heating, particularly its relations to long-term heating. In addition to lack of standard experimental procedures for evaluating short-term high-temperature strengths, it is important to note that no ASTM standard exists for MMC coupon preparation and short-term high-temperature testing procedures for either MMCs or PRCs.

No standard test specimen exists for tension testing of discontinuous and continuous metal matrix reinforced materials.[2] Reviews of existing literature, test reports, symposia proceed-

[1] Manager and principal engineer, Advanced Materials, and program manager, respectively, Raytheon Company, Missile Systems Laboratories, Tewksbury, MA 01876-0901.

[2] ASTM Standard D 3552, "Tensile Properties of Fiber-Reinforced Metal Matrix Composites," is presently under ASTM Committee D-30 review and has not been established as an appropriate test standard for elevated temperature tests.

ings, and ASTM D-30 committee and subcommittee meeting minutes indicate that significant deviations exist among tension test coupons used for continuously reinforced polymeric matrix composites and the recommended ASTM Test Method for Tensile Properties of Fiber-Resin Composites (D 3039) test coupon. Issues such as tab angle, tab to coupon width and thickness, tab to test material stiffness ratio, tab bonding procedures, and test machine gripping procedures continue to be debated.

Test coupon designs used in the present study evolved from Raytheon test experience and are consistent with those used in similar high-temperature composite experimental studies.

Tension tests were conducted for both short-term high-temperature (<60-s exposure) conditions and baseline high temperature (15-min exposure) conditions. Baseline tests were also conducted for flexure and pin bearing tests. The temperatures ranged from room temperature to 398°C (750°F) for baseline tests and 204 to 537°C (400 to 1000°F) for short-term tests.

Detailed descriptions of coupon design, tool requirements, instrumentation, and test procedures are found in Ref *2*.

Specimen Panel Tests

Materials tested and reported on herein were as follows:

SiC_w/2124-T4	(20% V/O)
SiC_p/7090-T6	(25% V/O)
P55/6061-0	(43% V/O)

Here, V/O, refers to volume fraction of reinforcing material.

The P55/6061-0 was a continuously reinforced, unidirectional material. Materials were received in panel form and were fabricated using the fabrication processes indicated in Table 1. These materials are similar to those reported in Ref *2*; however, the reinforcement/matrix ratios are slightly different for the first two materials.

All incoming discontinuously reinforced silicon carbide aluminum (SiC_D/Al) material was subjected to hardness testing (Rockwell B) to check for proper heat treatment. Hardness results are shown in Table 2 for Raytheon and vendor tests.

Discontinuously Reinforced Coupons

Dogbone coupons 203.2 mm (8 in.) were used for all tension tests for the SiC_p/Al materials according to ASTM methods of Tension Testing of Metallic Materials (E.8). All coupons

TABLE 1—*Test materials.*

Material	Fabrication Method	Material Supplier	Thickness, in.[a]
SiC_w/2124-T4 (20% V/O)	hot rolled	ARCO Metals	0.1
SiC_p/7090-T6 (25% V/O)	hot rolled	DWA Composites Specialties, Inc.	0.1
P55/6061-0 (43% V/O)	Rapi-Press[b] process	Material Concepts, Inc.	0.1

[a] 1 in. = 25.4 mm.

[b] MCI patented process—precursor wire vacuum pressed @ 585 to 600°C followed by isothermal rolling. Five-ply panels with 0.005-in. 6061 cladding.

TABLE 2—*Rockwell hardness test results* (R_B).

Material	Raytheon Results	Vendor Results
SiC_p/7090-T6 (25% V/O)	97	
	100	
	>100	
	92	85 to 90[a]
	91	
	95	
	$\bar{R}_B$ = 95.8	
SiC_w/2124-T4 (20% V/O)	86	89.7
	84	89.6
	86	90.4
	87	89.9
	100	$\bar{R}_B$ = 89.9
	92	
	92	
	$\bar{R}_B$ = 89.6	

[a] DWA Composites Specialties, Inc. results verbal.

were identified according to their location within each of the composite panels so that the origin of all test coupon fractures could be traced to a specific region on the original panel. Examination of failed MMC coupons and test results showed a consistent failure pattern within the gage section and reasonable uniformity of failure stress.

Continuously Reinforced Coupons

The test coupon used for the continuously reinforced graphite aluminum composite was a 152.4 mm (6-in.) tabbed coupon with a 12.7 by 50.8 mm (1/2 by 2 in.) gage section and is shown in Fig. 1. Both glass/polyimide and graphite/polyimide tabbing material were used. Both tabbing materials were adequate and are recommended for both short-term and long-term high-temperature testing. Tabs were bonded to the graphite aluminum panels.

All tabbing material was bonded to the test panels using HT-424F (film) adhesive obtained from American Cyanamid, Aerospace Products Dept., Wayne, New Jersey. The premachined tabbing material was bonded to the specimen panels using a precision bonding fixture [2]. Assembly alignment pins are used to maintain the panel in a fixed position, and end pins are fitted through each end of the prepared tabbing material to hold the entire panel and tabbing material in place during bonding. After the film adhesive was layed in place and the tabs fully assembled, the cover plate was installed, and the entire assembly was placed in a hot press. Thickness of both the test panel and end tabs are limited solely by the height of the removable dowel pins. Several sets of pins are available to accommodate a wide variety of panel and tab material thicknesses. Thermocouples were installed in the bond line to ensure that the proper HT-424F cure schedule was maintained. The cure schedule used for HT-424F was: starting at room temperature, increase bond line temperature to 176°C (350°F) in 1 h, then hold at 176°C (350°F) for 90 min, and cool in the press to room temperature. Slightly higher than contact pressure was maintained by the press on the tab bonding assembly coverplate during cure and cooldown. Nominal bond line thickness was 0.009 in.

In these tests bevelling of the tabs were found to result in higher measured tensile strengths as reported in Ref 2. A series of tension tests with and without bevels were conducted at

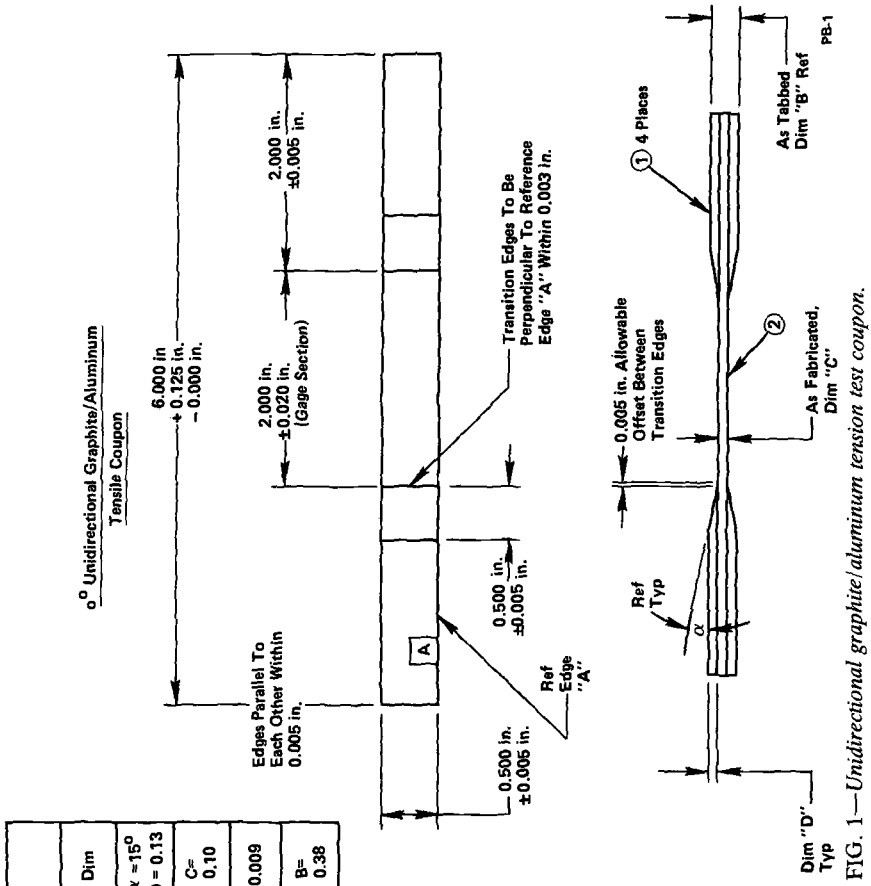

FIG. 1—*Unidirectional graphite/aluminum tension test coupon.*

room temperature on the 152.4-mm 6-in. coupons. Those with the bevel had an average measured tensile strength 31% greater than those without the bevel. Thus all tabbing for this testing was bevelled.

Heating Techniques

Two methods of heating were used. The first was limited to baseline high-temperature tests up to 315°C (600°F) and 15 min exposure prior to coupon loading. This method used a controlled closed oven (BEMCO model FTU 3.2). Two type K (028 gage) thermocouples were used during the tests. One monitored and controlled the oven temperature while the second was clipped to the test specimen to ensure the specimen and oven were at the same temperature subsequent to initial transient variances. The coupon temperature control was monitored on a strip chart recorder (Gould Model 110) from oven start-up to coupon fracture.

For baseline temperatures at 398°C (750°F) and all short-term high-temperature tests, radiant quartz heat lamps consisting of two Research Inc. (RI) AV 612 reflectors and an RI MICRISTAR based power controller were used to develop steady-state and short-term temperature profiles. Total available radiant power was 2000/watts per lamp. Eight lamps were mounted in each reflector, and one reflector was placed per coupon side. The area of each reflector was 390 cm^2 (60.5 in.). Closed loop radiant heating was found in earlier studies on methodology described in Ref. *2* to be an effective method of rapidly increasing the temperature of tension test coupons and holding maximum temperatures to predetermined levels. New control microprocessors and computers now allow for more complex temperature profiles to be preprogrammed for testing purposes.

Baseline Tests

Baseline tension tests were performed on all three MMC materials, SiC_w/2124-T4 (20% V/O), SiC_p/7090-T6 (25% V/O), and unidirectional P55/6061-0 (43% V/O). Tests were conducted at room temperature, 204, 315, and 398°C (400, 600, and 750°F). For the elevated temperture cases the test coupons were held at temperature for 15 min after reaching the prescribed maximum temperature (within several minutes). For 204 and 315°C (400, and 600°F) a closed controlled convective oven was used with the test grips enclosed within the oven. The 398°C (750°F) baseline tests were performed using quartz radiant lamps.

Biaxial strains were measured at room temperature 204°C (400°F), and 315°C (600°F) using dual-sensor strain transducer (DSST), Model DSST-GP-BI-1.00-BL02, manufactured by Measurements Technology Inc., Roswell, Georgia. While the results obtained using the extensometer are encouraging for temperatures up to 315°C (600°F) several cautionary comments are necessary lest the reader be given the impression that all which is required to obtain these results is to clamp the extensometer in place, heat the specimens, and begin recording readings. At 204 and 315°C (400 and 600°F) it was found necessary, based on past experience, to recalibrate the extensometer following a series of six 204°C (400°F) tests and three 315°C (600°F) tests. Also, great difficulty in determining transverse strain (so that Poisson's ratio could be calculated) was experienced. Virtually all transverse strains measured at 315°C (600°F) are considered unreliable. However, in spite of these difficulties, with proper handling and care the extensometer was found to substantially reduce the time necessary to obtain strain readings compared with using high-temperature strain gages.

Spring loaded quartz rod high-temperature transducers appear to be an attractive method of increasing the temperature range for which strains can be measured to at least 537°C (1000°F). They were utilized for tests reported on later in this paper.

Short-Term Tests

Short-term tension testing consisted of providing a rapid heating thermal environment and load application. Procedures for these tests are described in Ref *2*.

Maximum temperatures (typically reached in less than 20 s) of the materials for short-term strengths were: 204, 315, 398, 482, and 537°C (400, 600, 750, 900, and 1000°F). No moduli were measured during the short-term tests. It is assumed that no significant difference between static and dynamic moduli exists for the loading rates used.

TABLE 3—*Tension test results for SiC_w/2124 T4 (20% V/O).*

NOTE: All material hot rolled and tested in whisker direction.
(SS) = steady-state temperature exposure (15 min).
(ST) = short-term temperature exposure (25 to 60 s).

Coupon Nos.	Temperature, °F[a]	Ultimate Stress, ksi[b]	Modulus, Msi	Poisson's Ratio	Elongation, %
AW28	75	87.6	16.0	0.27	
AW32	75	89.0	16.3	0.28	3.4
AW33	75	90.4	14.6	0.28	3.6
AW18	400 (SS)	[d]	12.8	0.29	[d]
AW19	400 (SS)	67.0	12.8	0.32	3.8
AW20	400 (SS)	67.0	12.8	0.32	3.6
AW31	400 (SS)	66.5	...	...	3.7
AW21	600 (SS)	13.7	9.5	not reliable	12.0
AW22	600 (SS)	13.4	10.9	not reliable	14.0
AW23	600 (SS)	13.7	10.5	not reliable	14.5
AW24	750 (SS)	7.1		...[e]	...[e]
AW25	750 (SS)	8.7	...	...	...
AW26	750 (SS)	7.9	...	...	...
AW3	400 (ST)	73.6	...	...	...
AW17	400 (ST)	73.1	...	...	...
AW36	400 (ST)	71.3	...	...	...
AW4	600 (ST)	31.4	...	...	...
AW5	600 (ST)	32.9	...	...	...
AW6	600 (ST)	32.2	...	...	...
AW7	750 (ST)	13.9	...	...	...
AW9	750 (ST)	13.0	...	...	...
AW10	750 (ST)	13.2	...	...	...
AW11	900 (ST)	4.3	...	...	...
AW12	900 (ST)	4.7	...	...	...
AW13	900 (ST)	4.5	...	...	...
AW14	1000 (ST)	1.9	...	...	...
AW15	1000 (ST)	2.2	...	...	...
AW16	1000 (ST)	2.6	...	...	...

[a] °C = 5/9 (°F − 32).
[b] 1 in. = 25.4 mm.
[c] Extensometer disconnected prior to coupon fracture.
[d] Coupon failed in test grip.
[e] Not measured.

Although the test grips are insulated and protected from direct radiation by high-emissivity foil plates, the test grips do become heated after a number of experiments are conducted. However, the initial temperature of the test coupon in the gage region never exceeded 37 to 51°C (100 to 125°F).

Specimen Panel Test Results

Tension test results are given in Tables 3 to 5, and short-term versus baseline data strength are plotted in Fig. 2. At moderate and high temperatures very little data scatter exists for the discontinuously reinforced aluminum. At least three tests were conducted at each test

TABLE 4—*Tension test results for SiC_p/7090 T6 (25% V/O).*

NOTE: All material hot rolled and tested in final roll direction.
(SS) = Steady-state temperature exposure (15 min).
(ST) = Short-term temperature exposure (25 to 60 s).

Coupon Nos.	Temperature, °F[a]	Ultimate Stress, ksi[b]	Modulus, Msi	Poisson's Ratio	Elongation, %
XA1	75	111.1	15.5	−(1)	1.7
XA2	75	110.3	15.5	0.24	2.0
XA3	75	110.5	15.5	0.26	2.0
XA4	400 (SS)	45.4	13.0	0.25	9.2
XA5	400 (SS)	45.1	14.0	0.28	8.5
XA6	400 (SS)	45.8	13.5	0.27	11.2
XA7	600 (SS)	7.7	9.5	...[c]	13.0
XA8	600 (SS)	8.1	7.5	...	15.0
XA9	600 (SS)	8.0	10.5	...	15.5
XA10	750 (SS)	4.8	...[c]	...	...[c]
XA11	750 (SS)	4.9	...	...	...
XA12	750 (SS)	6.1	...	...	...
XA16	400 (ST)	73.1	...	...	...
XA17	400 (ST)	74.0	...	...	...
XA18	400 (ST)	68.0	...	...	...
XA13	600 (ST)	26.4	...	...	...
XA14	600 (ST)	26.9	...	...	...
XA15	600 (ST)	24.7	...	...	...
XA19	750 (ST)	11.2	...[c]	...	...[c]
XA20	750 (ST)	11.9	...	...	...
XA21	750 (ST)	10.9	...	...	...
XA22	900 (ST)	5.1	...	...	...
XA23	900 (ST)	5.1	...	...	...
XA24	900 (ST)	5.1	...	...	...
XA25	1000 (ST)	3.6	...	...	...
XA26	1000 (ST)	3.2	...	...	...
XA27	1000 (ST)	3.3	...	...	...

[a] °C = 5/9 (°F − 32).
[b] 1 in. = 25.4 mm.
[c] Not measured.

TABLE 5—*Tension test results for P55/6061-0 (43% V/O).*

NOTE: Unidirectional graphite/aluminum—5 plies.
All material: 0.005 in. surface clad with 6061.
Tested in fiber direction
(SS) = Steady-state temperature exposure (15 min).
(ST) = Short-term temperature exposure (25 to 60 s).

Coupon Nos.	Temperature, °F[a]	Ultimate Stress, ksi[b]	Modulus, Msi	Poisson's Ratio	Elongation, %
P1[c]	75	77.1	24.4	0.41	0.32
P2	75	74.3	24.2	[c]	0.31
P3	75	77.1	22.7	0.31	0.34
P4	400 (SS)	73.9	26.5	0.42	0.29
P5	400 (SS)	70.6	28.6	0.48	0.25
Q1	400 (SS)	79.2	26.3	0.45	0.29
XX-1[e]	400 (SS)	73.6	...[d]	...[d]	...
XX-2	400 (SS)	74.0	...	...	...
XX-3	400 (SS)	78.6	...	...	...
Q2	600 (SS)	67.1	24.5	0.50	0.27
Q3	600 (SS)	73.2	24.0	0.51	0.30
Q4	600 (SS)	70.0	24.6	0.53	0.29
VV-1	600 (ST)	83.2	...[d]	...[d]	...[d]
XX-4	600 (ST)	72.8	...	...	...
XX-5	600 (ST)	74.9	...	...	...
UU-1	750 (SS)	72.6	...	...	...
UU-2	750 (SS)	74.6	...	...	...
UU-3	750 (SS)	75.0	...	...	...
VV-2	750 (ST)	83.9	...	...	...[c]
VV-3	750 (ST)	85.2	...	...	...
VV-4	750 (ST)	82.8	...	...	...
WW-1	900 (ST)	70.3	...	...	...
WW-2	900 (ST)	69.4	...	...	...
VV-5	900 (ST)	78.1	...	...	...
WW-3	1000 (ST)	52.1	...	...	...
WW-4	1000 (ST)	50.1	...	...	...
WW-5	1000 (ST)	50.1	...	...	...

[a] °C = 5/9 (°F − 32).
[b] 1 in. = 25.4 mm.
[c] Coupons P1 to P5, Q1 to Q4: bevelled (nominal tab thickness = 0.15 in.).
[d] Not measured.
[e] All UU, VV, WW, XX coupons: bevelled 20-ply unidirectional Hy E 1678°F (Celion 6000/Larc 160) tabs (nominal tab thickness = 0.13 in.).

condition. Moderate to significant increases in short-term strength are evident for the discontinuously reinforced aluminum at a given temperature while this phenomenon is far less pronounced for the graphite/aluminum.

While the average value of the room-temperature ultimate strength of SiC_w/2124/T4 (20% V/O) is less than the corresponding strength of SiC_p/7090-T6 (25% V/O), 89 ksi compared

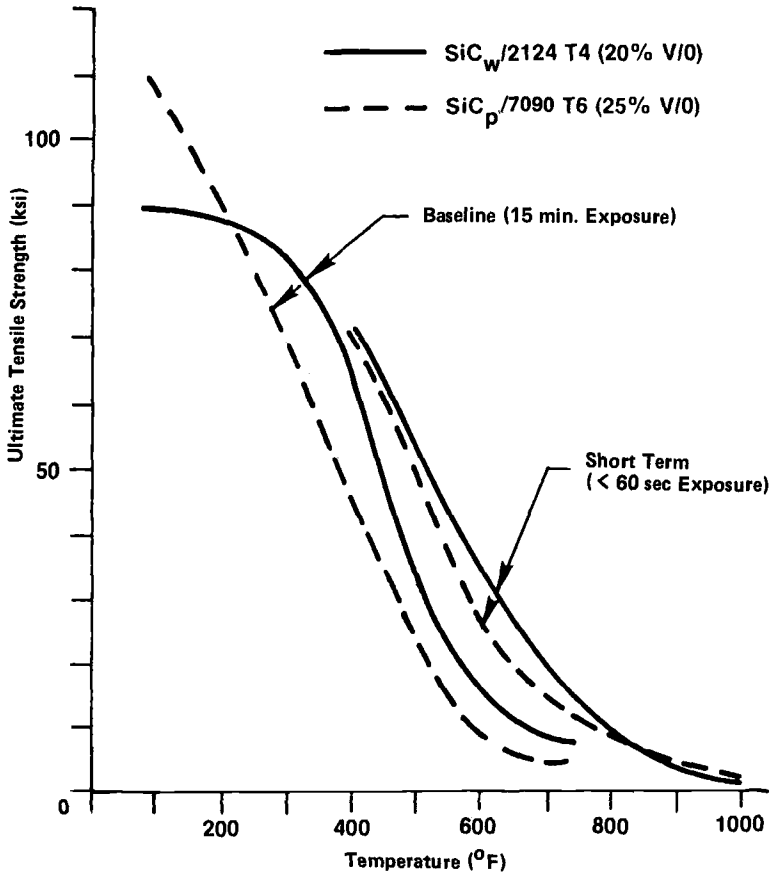

FIG. 2—*Baseline and short-term high-temperature strengths of SiC$_w$/2124-T4 (20% V/O) and SiC$_p$/7090-T6 (25% V/O).*

to 110 ksi, the latter material strength decreases more rapidly with temperature. This is primarily a function of the alloy rather than the reinforcement type.

The baseline test results are in general agreement with those reported in the literature for discontinuously reinforced aluminum. The average strength of the graphite/aluminum material at room temperature is low for the 43% V/O reported at Material Concept, Inc. (MCI). However, in information transmitted verbally from MCI to Raytheon this was stated to be MCI's first attempt at fabricating 5-ply unidirectional graphite/aluminum using the Rapi-Press process. No conclusions can be drawn regarding strength as a function of ply thickness from the tests conducted during this program.

Short-term strength increases were the least for the continuously reinforced graphite/aluminum material. However, since the material tested was fiber dominant such measurements do not characterize the material nearly as fully as tests conducted with more matrix-dominated lay-ups likely to be used in structural components.

Significant stiffness increases (compared to unreinforced aluminum) were measured for the discontinuously reinforced aluminum composites. The room temperature increase was 60% greater for discontinuously reinforced aluminum compared to unreinforced aluminum.

Although the particulate reinforced aluminum contained 25% reinforcement compared to 20% reinforcement for the whisker aluminum, stiffness increases were not evidenced by the corresponding increase in reinforcement levels. The experiments performed were limited to one reinforcement level, different for each material and with different matrices. Therefore, it is difficult to make a direct comparison between whisker and particulate reinforced aluminum. The original program intent was to test particulate reinforced aluminum in 2124 aluminum. However, at the time material was being ordered optimization of the SiC_p/2124 rolling process had not been completed resulting in lack of availability of this MMC for the present test program.

Typical stress-strain curves at various temperatures for discontinuously reinforced material are shown in Figs. 3–5 for room temperature, 204 and 315°C (400 and 600°F) baseline conditions, respectively. These results were obtained using the DSST biaxial extensometer. For 315°C (600°F), the transverse extensometer strain is unreliable and has been omitted.

Typical fractured coupons are shown in Fig. 6 for SiC_w/2124-T4 (20% V/O) Coupon No. AW-32, P55/6061-0 (43% V/O) Coupon No. VV-5, and SiC_p/7090-T6 (25% V/O) Coupon No. XA-1. Coupons AW-32 and XA-1 were tested at room temperature, while Coupon VV-5 was tested at 482°C (900°F) (short term). Note that all coupons failed within the gage section and those shown in Fig. 6 are typical of all coupon failures.

Parent Panel Material Tests

MMC material obtained from parent panels of SiC_w/2124-T6 (20% V/O) and SiC_p/2124-T4 (25% V/O), which were used to fabricate hardware, was used for additional material tests. Originally it was intended that this material be used for the following tests:

1. Flexural—baseline high temperature.
2. Pin Bearing—baseline high temperature.
3. Tension—baseline and short term high temperature.

However, since only a limited amount of material was available, only tension tests were conducted using the parent panels. Flexural and pin bearing tests utilized thin-rolled sheet stock.

Engineering drawings of the flexural and pin bearing test coupons are shown in Figs. 7 and 8. ASTM Test Method for Flexual Properties of Unreinforced and Reinforced Plastics and Electrical Insulating Materials (D 790) was developed for determining flexural strength of plastics, but it has been used throughout the industry for isotropic metals and in many cases for continuously reinforced polymerics and metallic composites.

Flexural and bearing test coupons were laid out and numbered on each panel so that each coupon could be located with respect to panels identified by the SiC_D/Al suppliers. All flexural and bearing coupons were configured to be loaded in the final roll direction.

The tension test coupons were machined from full thickness panels subsequently used to fabricate hardware. The nominal thickness of the SiC_w/Al panel was 1.42 cm (0.56 in.) and was 1.09 to 1.43 cm (0.43 to 0.45 in.) for the SiC_p/Al panel. The directions of the tensile coupons with respect to the final roll direction were 20° for the SiC_w/Al and 45° for the SiC_p/Al. The inplane orientation of the coupons corresponded to the inplane orientation of the full-thickness panels. The purpose of the tension tests was to determine whether material originating from as fabricated thick stock was characterized by different strengths and stiffnesses as compared with the similar material in the thin rolled condition.

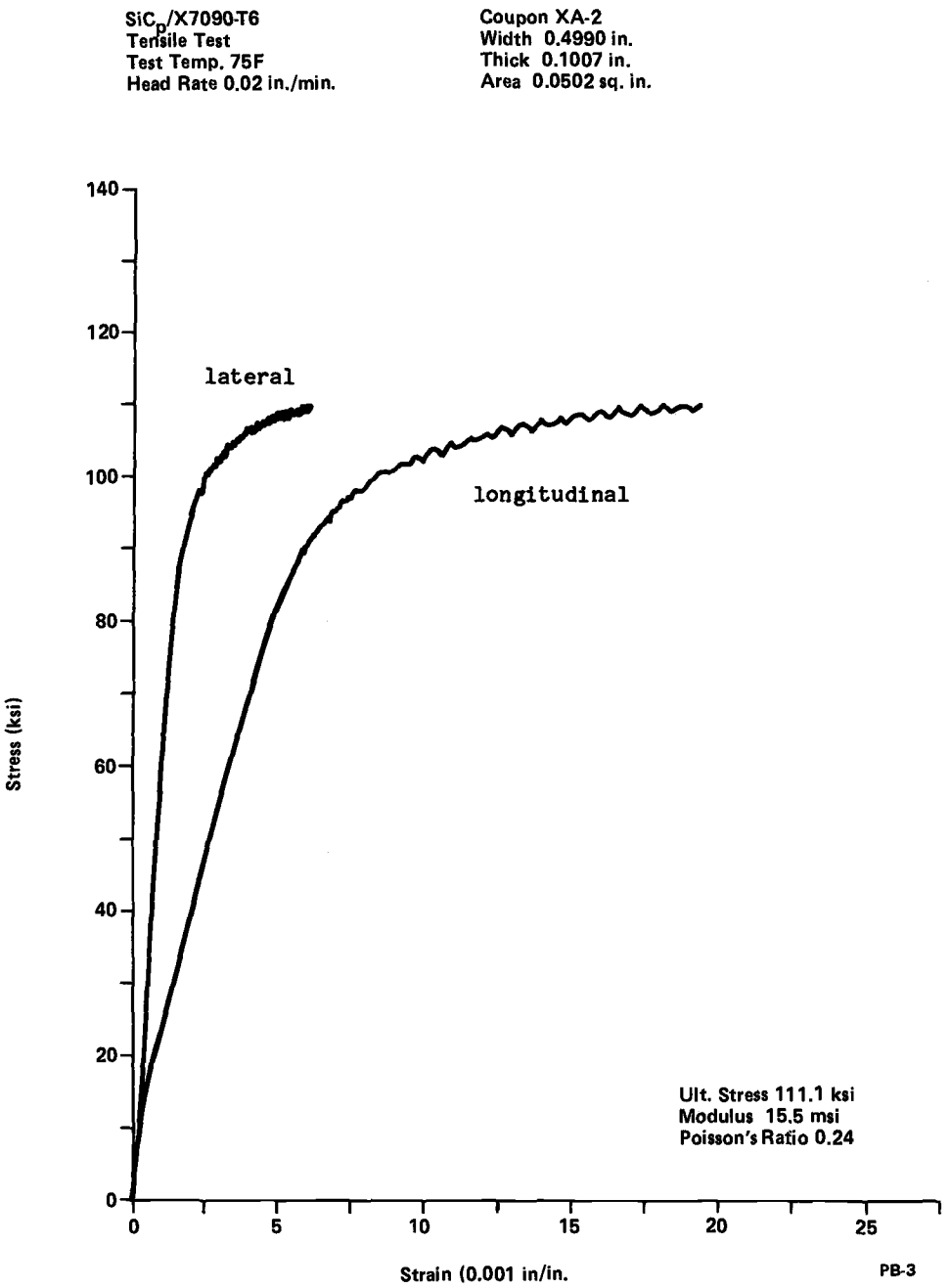

FIG. 3—*Stress-strain curves: SiC_p/7090-T6 (25% V/O)—room temperature.*

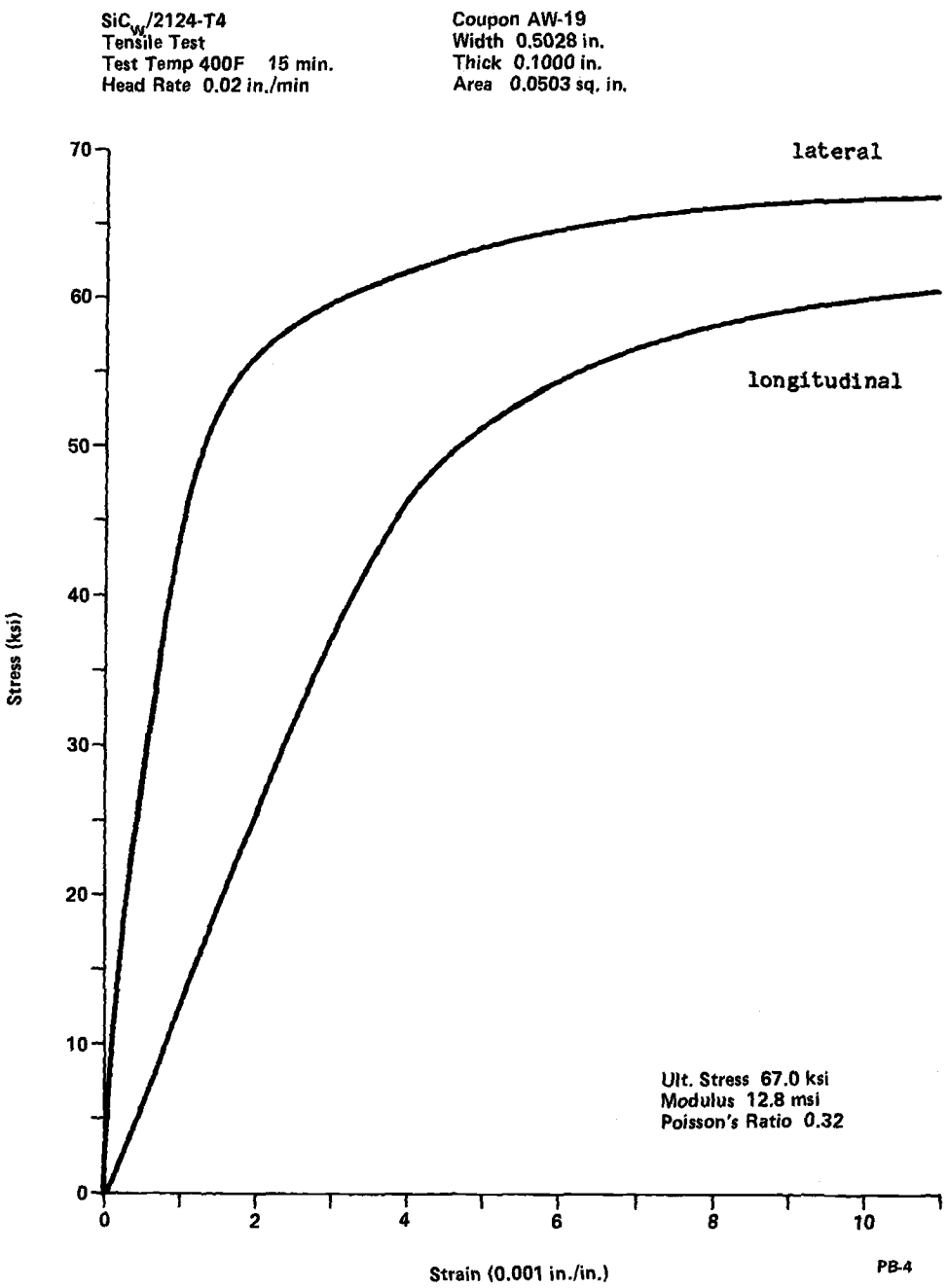

FIG. 4—Stress-strain curves: SiC$_w$/2124-T4 (25% V/O)—204°C (400°F).

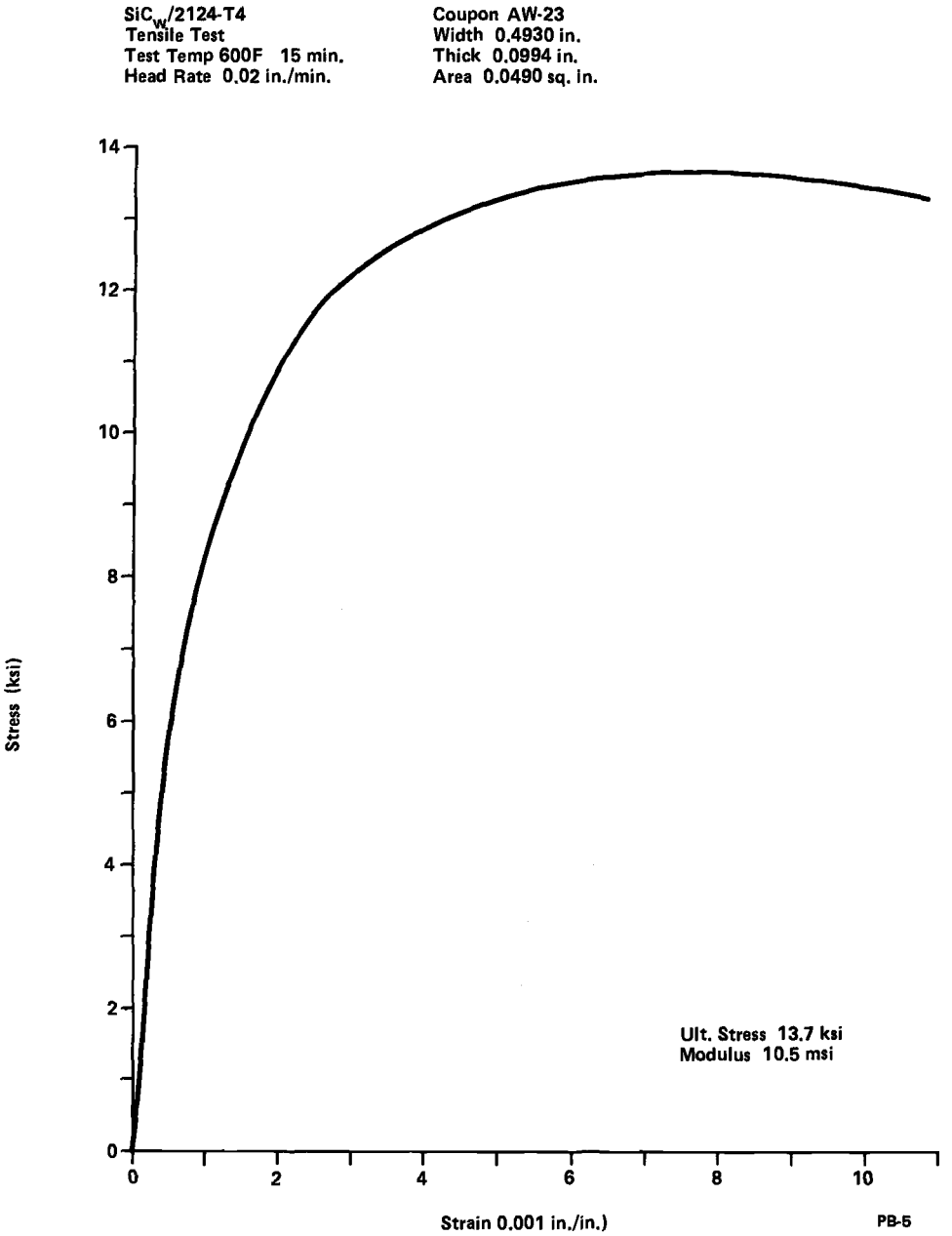

FIG. 5—*Stress-strain curve: SiC$_w$/2124-T4 (20% V/O)—315°C (600°F).*

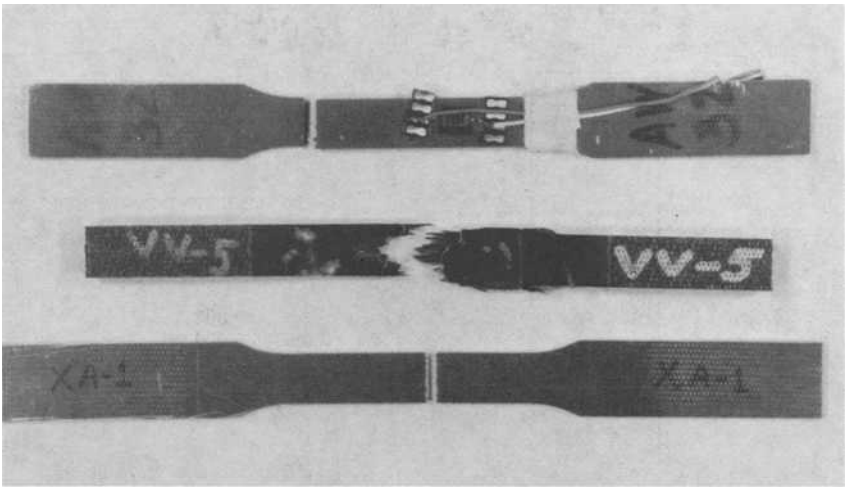

FIG. 6—*Typical tensile fractured metal matrix composite coupons: AW-32: SiC_w/2124-T4 (20% V/O)—room temperature; VV-5: P55/6061-0 (43% V/O)—482°C (900°F) (short term); XA-1: SiC_p/7090-T6 (25% V/O)—room temperature.*

Flexural Tests

Flexural tests were performed on the as rolled SiC_w/2124-T4 (20% V/O) and SiC_p/2124-T4 (25% V/O) material. The four-point bending fixture, adjustable for variable load and span distances and also easily convertible to three-point bending, is shown in Fig. 9 together with a SiC_D/Al test coupon. The distance between load points was 2.54 cm (1 in.) while the

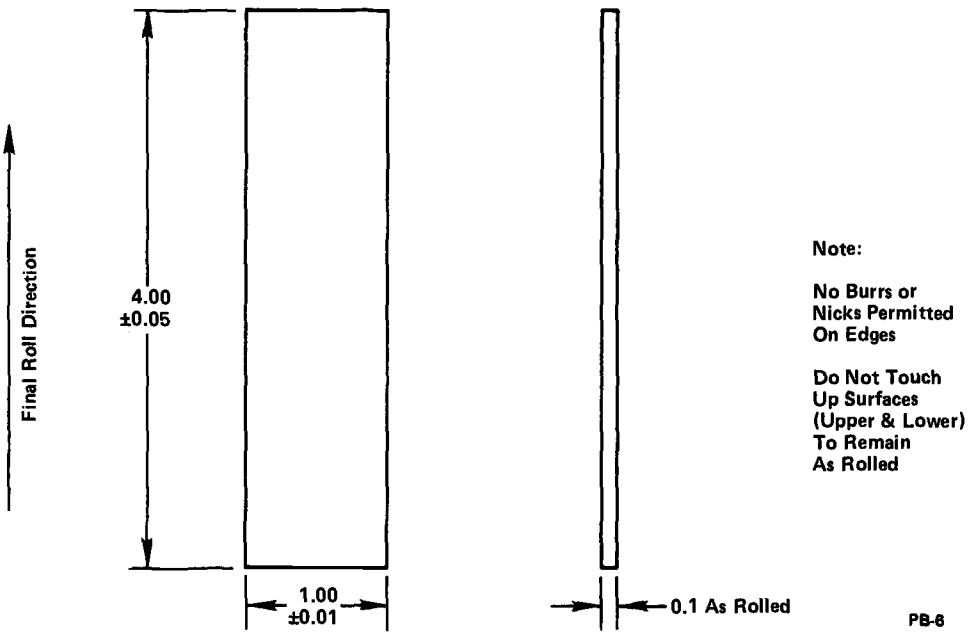

FIG. 7—*Flexural test coupon (D 790).*

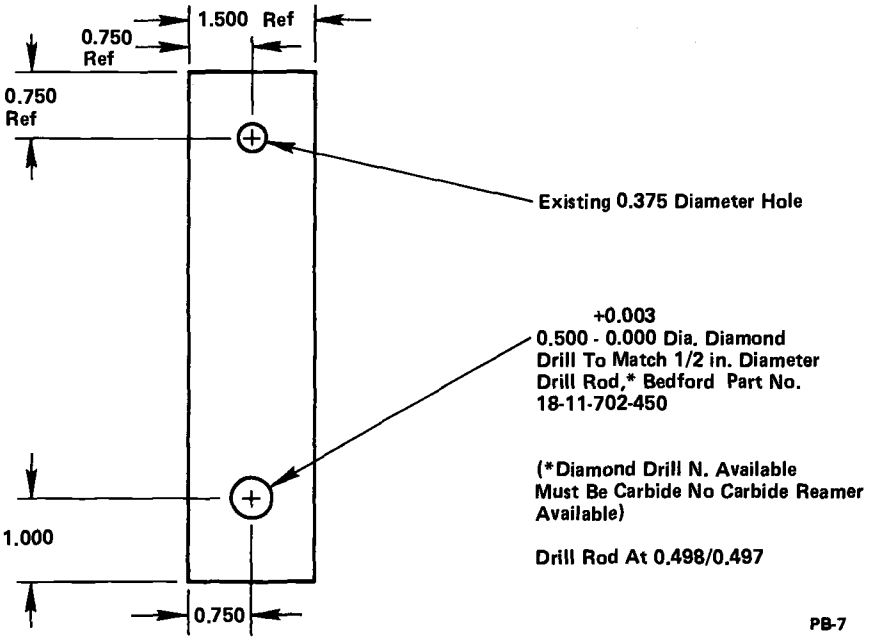

FIG. 8—*Pin bearing test coupon (ASTM E 238).*

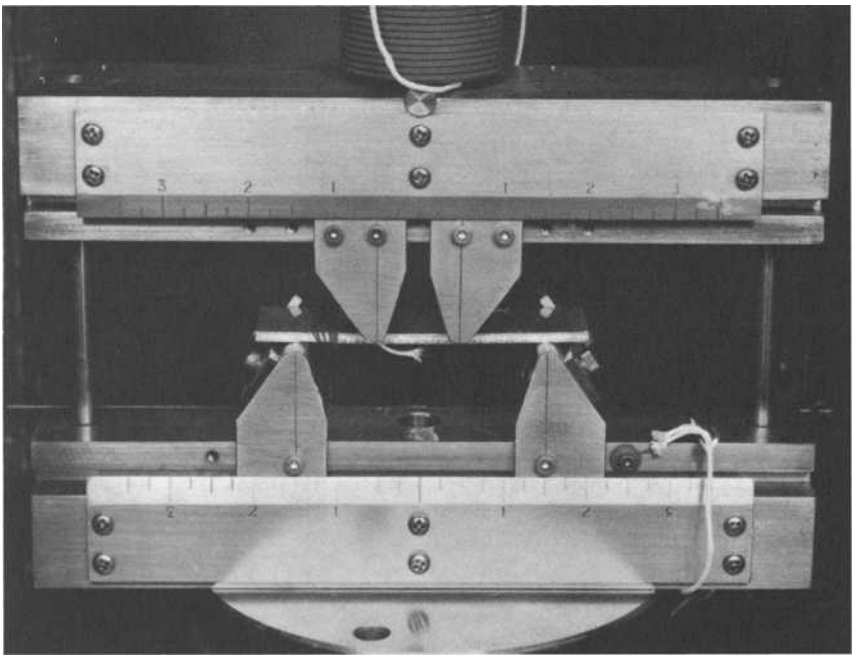

FIG. 9—*Adjustable four-point bending fixture.*

TABLE 6—*Flexural test results SiC_w/2124-T4 (20% V/O).*

Coupon No.	Temperature,[a,b] °F	Crosshead Speed, in./min[c]	Flexural Strength, ultimate	Flexural Modulus, 10^6 psi
FW-1	RT[d]	0.02	135.1	17.3
FW-2	RT	0.02	127.9	16.7
FW-3	RT	0.02	135.1	16.9
FW-4	400	0.02	127.0	...
FW-5	400	0.02	119.4	...
FW-6	400	0.02	118.1	...
FW-7	600	0.1	30.3	...
FW-8	600	0.2	35.1	...
FW-9	600	0.2	35.0	...
FW-10	750	0.2	19.9	...
FW-11	750	0.2	18.4	...
FW-12	750	0.2	18.8	...

[a] Exposure time = 15 min.
[b] °C = 5/9 (°F − 32).
[c] 1 in. = 25.4 mm.
[d] RT = room temperature.

distance between supports was 7.62 cm (3 in.). Three tests were conducted for each material at each of the following temperatures: room temperature, 204°C (400°F), 315°C (600°F), and 398°C (750°F). The coupons were held at temperature for 15 min and then loaded. The SiC_p/Al coupons were loaded at a machine crosshead rate of 0.05 cm (0.02 in./min). The SiC_w/Al tests were conducted at crosshead rates from 0.05 to 0.5 cm (0.02 to 0.2 in./min). All room temperature test coupons were strain gaged to obtain flexural moduli. Flexural test results and associated data are presented in Tables 6 and 7.

Flexural strengths versus temperature are plotted for both MMC materials on Fig. 10. As was observed for tensile strengths and will be demonstrated for bearing strengths, primary

TABLE 7—*Flexural results SiC_p/2124-T4 (25% V/O).*

Coupon No.	Temperature,[a,b] °F	Crosshead Speed, in./min[c]	Flexural Strength, ultimate	Flexural Modulus, 10^6 psi
FP-1	RT[d]	0.02	138.6	17.7
FP-2	RT	0.02	140.6	17.8
FP-3	RT	0.02	...[e]	...
FP-4	400	0.02	121.6	...
FP-5	400	0.02	127.6	...
FP-6	400	0.02	127.3	...
FP-7	600	0.02	32.6	...
FP-8	600	0.02	45.5	...
FP-9	600	0.02	46.0	...
FP-10	750	0.02	15.7	...
FP-11	750	0.02	17.7	...
FP-12	750	0.02	17.8	...

[a] Exposure time = 15 min.
[b] °C = 5/9 (°F − 32).
[c] 1 in. = 25.4 mm.
[d] RT = room temperature.
[e] Invalid data.

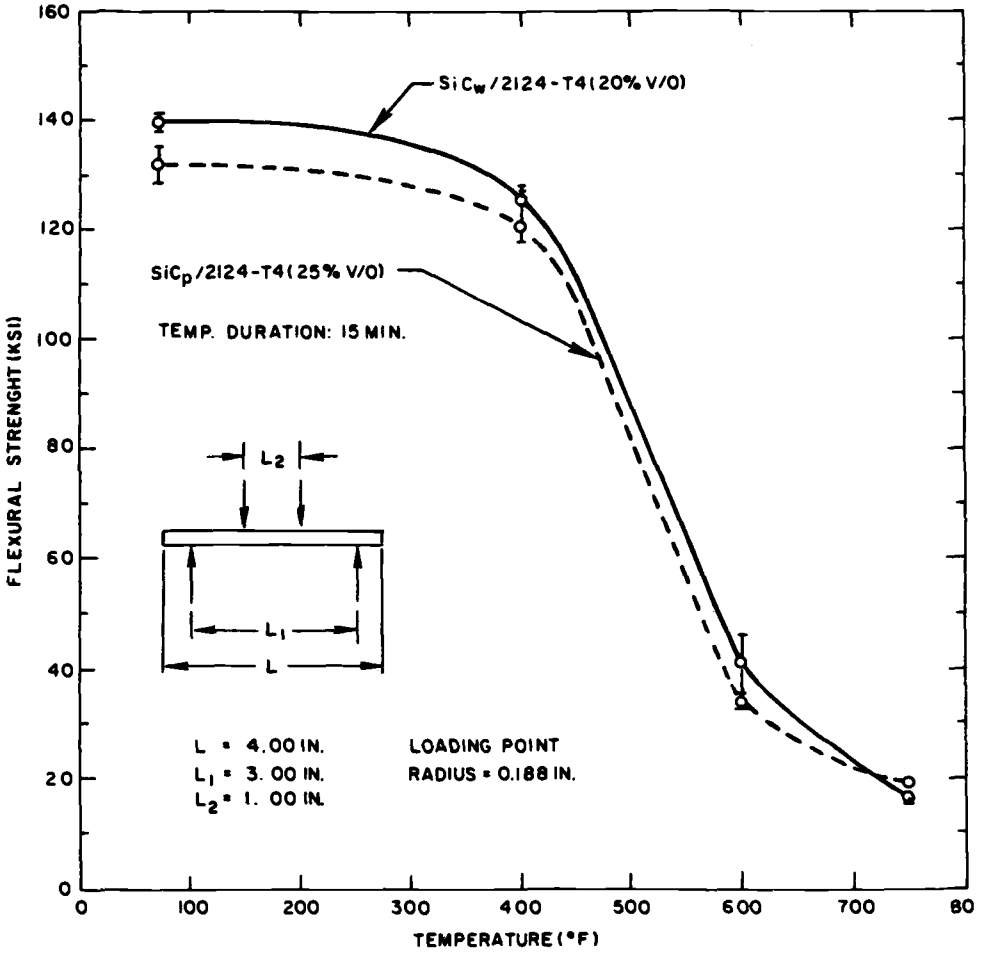

FIG. 10—*Flexural strength versus temperature for SiC_w/2124-T4 (20% V/O) and SiC_p/2124-T4 (25% V/O)—15 min exposure.*

strength decrease occurs between 204 and 315°C (400 and 600°F). Also, while the affect of particulate and whisker reinforcement results in approximately 50% tensile stress increase compared to unreinforced material the strength increase in flexure is only 10 to 15%.

Pin Bearing Tests

Bearing tests were performed on the as-rolled SiC_w/2124-T4 (20% V/O) and SiC_p/2124-T4 (25% V/O) material. The pin bearing hole was 9.5 min (3/8 in.) and loading hole was 12.7 mm (1/2 in.). Precision drill rod stock was used to load the bearing coupon. The coupon installed in the test fixture and Bemco oven is shown in Fig. 11.

Bearing test data were developed for temperature exposures of 7 min instead of the usual 15 min exposure time. This occurred since the bearing tests, which were the first series of tests performed, used a control thermocouple in the oven cavity rather than on the specimen. Midway through the test series for SiC_p/Al a dummy aluminum coupon was thermocoupled

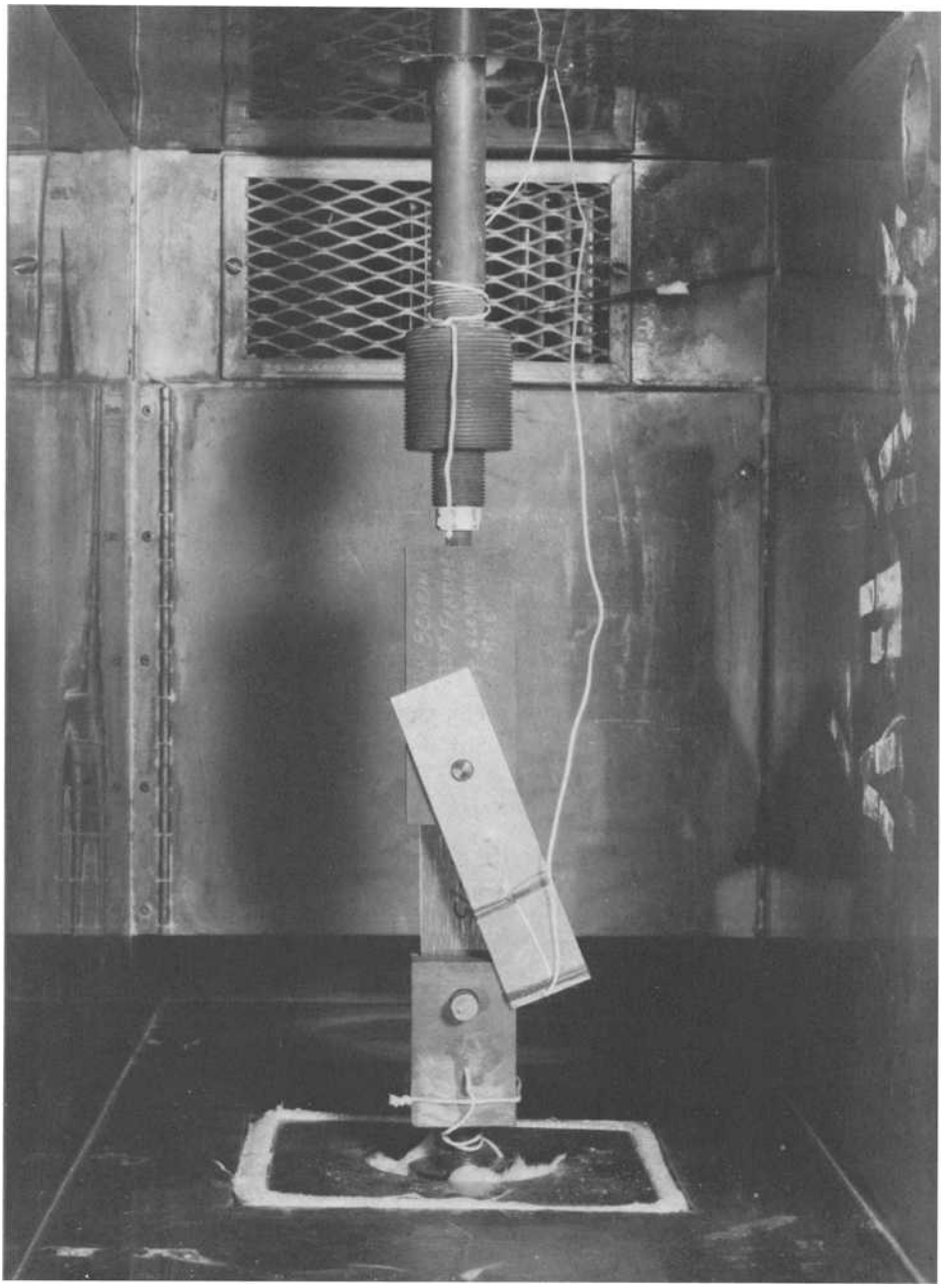

FIG. 11—*Pin bearing test arrangement.*

TABLE 8—*Pin bearing test results SiC_w/2124-T4 (20% V/O).*

Coupon No.	Temperature,[a,b] °F	Crosshead Speed, in./min[c]	Bearing Strength, ultimate, ksi
PBW-1	RT[d]	0.02	92.2[e]
PBW-2	RT	0.02	135.7
PBW-3	RT	0.02	130.6
PBW-4	400	0.02	125.1
PBW-5	400	0.02	121.8
PBW-6	400	0.02	123.1
PBW-7	600	0.02	24.1
PBW-8	600	0.05	27.8
PBW-9	600	0.05	28.2
PBW-10	750	0.05	11.0
PBW-11	750	0.05	10.5
PBW-12	750	0.05	11.2

[a] Exposure time 7 min (PBW-9 exposure time 10 min).
[b] °C = 5/9 (°F − 32).
[c] 1 in. = 25.4 mm.
[d] RT = room temperature.
[e] Failed at support hole.

and hung off the protruding drill rod on the test fixture. It was deduced that the time the test coupon was at maximum temperature was 7 min.

In order that data for bearing be obtained for consistent temperature exposure times the change to 15 min. exposure at maximum temperature was not made. In future tests, it is recommended that the thermocouple be clip mounted directly to the test specimen to monitor temperature as was done on all previous tests.

Bearing strength versus temperature for both SiC_D/Al materials are shown in Tables 8 and 9 and compared in the plots of Fig. 12 which show bearing strength versus temperature for 15 min exposure.

Note that the particulate material (25% V/O) displayed higher bearing strength at 315°C (600°F) than whisker material (20% V/O).

TABLE 9—*Pin bearing test results SiC_p/2124-T4 (25% V/O).*

Coupon No.	Temperature,[a,b] °F	Crosshead Speed, in./min[c]	Bearing Strength, ultimate, ksi
PBW-1	RT[d]	0.02	125.6[e]
PBW-2	RT	0.02	135.0
PBW-3	RT	0.02	126.9
PBW-4	400	0.02	121.9
PBW-5	400	0.02	123.8
PBW-6	400	0.02	119.8
PBW-7	600	0.02	35.2
PBW-8	600	0.05	42.4
PBW-9	600	0.05	42.5
PBW-10	750	0.05	14.8
PBW-11	750	0.05	15.0
PBW-12	750	0.05	15.0

[a] Exposure time 7 min.
[b] °C = 5/9 (°F − 32).
[c] 1 in. = 25.4 mm.
[d] RT = room temperature.

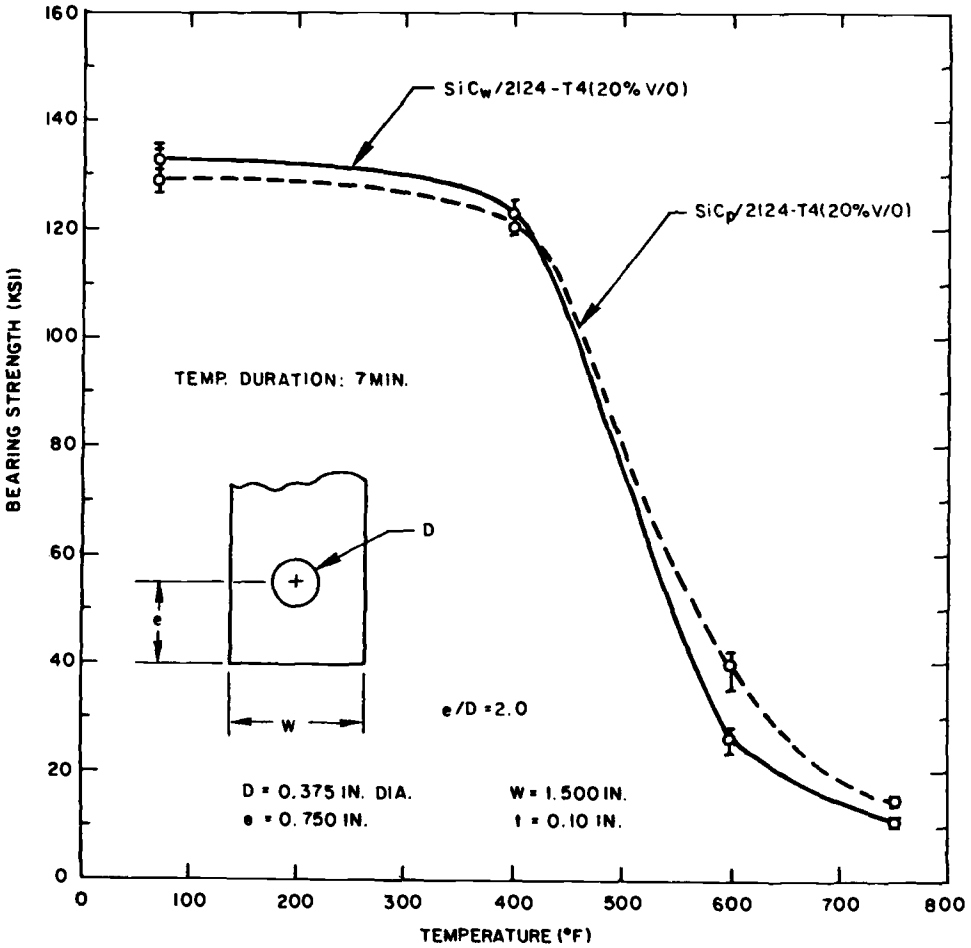

FIG. 12—*Bearing strength versus temperature for SiC_w/2124-T4 (20% V/O) and SiC_p/2124-T4 (25% V/O)—7 min exposure.*

Tension Tests

The purpose of these tests was to better understand what changes, if any, exist in material obtained from thick panels (from which hardware was fabricated) and MMC material in thin-rolled sheet form. All test coupon dimensions were identical except for thickness as noted.

Baseline Tests

Tests were conducted at room temperature and after 15 min exposure to high temperature. An MTS 810 servohydraulic universal testing machine capable of both crosshead motion rate and load rate control was used to develop preprogrammed tensile loads. Instron wedge locking mechanical grips with 25 teeth/in. provided grip loads on the dogbone specimens. A compact microprocessor controlled quartz lamp (Research Inc.) was used to heat the test coupons.

The test coupons were instrumented with two type K thermocouples, one on each side of the coupon and supported during the tests with thin steel wire wrapped around the coupons. A spot of AREMCO 568 high-temperature, high-thermal conductivity adhesive was used to maintain direct thermocouple contact at its junction to the side face of the test coupon in the gage section. Each coupon was pre-marked with 25.4 mm (1 in.) lines about the center of the gage section to serve as a base for confirming strain deduced elongation, as necessary.

Baseline strength data for the tested SiC_w/2124-T6 (20% V/O) and SiC_p/2124-T4 (25% V/O) thick material are shown in Table 10, where such data are compared with earlier obtained tension strength data for thin-stock SiC_w/2124-T4 (20% V/O) and SiC_p/2124-T4 (30% V/O). During that time 25% V/O particulate reinforced 2124 material could not be obtained from DWA Composites Specialties, Inc. within schedule so that the 30% V/O material which was available had been tested. Also, note that the heat treat of the whisker material tested was a T6 condition, while that tested earlier was T4. The new heat treat schedule was used to increase strength of the hardware.

The significant findings regarding tensile strengths of rolled stock versus thick panel stock are as follows:

1. SiC_w/Al: significantly greater strength of the thick material (T6) was observed at 315°C (600°F).
2. SiC_p/Al: significantly greater strength of the thick stock (30% V/O) was observed at 315°C (600°F).

While those coupons having higher strength at 315°C (600°F) were thicker than the lower strength coupons, scale effects do not explain the strength increase. For example, at room temperature the trend is slightly reversed (with respect to coupon thickness) for both types of reinforced material. The T6 heat treat condition seems to clearly benefit tensile strength for the SiC_w/Al at elevated temperatures. For the SiC_p/Al material room temperature strengths are approximately the same for 30 and 25% V/O, while the 5% V/O increase appears to substantially increase strength at elevated temperatures. However, since the thick material was fabricated by the vendor over one year after the thin-rolled material, other effects not obvious may be present. Until substantially more test points are obtained for both materials with controlled heat treat schedule and fabrication sequences, the baseline data do not reveal any significant distinction between the particulate and whisker reinforced material, at least at high temperatures. The baseline tensile data versus temperature are shown in Fig. 13 where estimated local trends are shown for the SiC_p/Al material.

Modulus measurements were made at room temperature, 204°C (400°F), and 315°C (600°F) using an MTS 25.4 mm (1 in.) gage length water-cooled high-temperature quartz rod extensometer system, Model No. 632-50B-02, which was mounted to the external load frame. This extensometer significantly out performed and is recommended over the DSST strain transducer used earlier. During high-temperature tests a dab of high-temperature strain gage adhesive, Micromeasurement M Bond 610, was applied at the tip of each quartz rod to minimize any tendency for the conically pointed extensometer rods to slip with respect to the coupon.

Moduli and elongation ranges for the tests are shown in Table 11. No significant stiffness or elongation differences were attributed to material extruded in thick-plate form compared to thin-rolled material.

TABLE 10—*Comparison of tensile strength of thick-panel stock and thin-rolled stock for various SiC_D/Al MMCs.*
(Ultimate Stress, ksi)

	Baseline Test Results 15 min Exposure			
Temperature,[a] °F	SiC_w/2124-T4, 20% V/O,[b,c] specimen thickness 0.10 in.	SiC_w/2124-T6, 20% V/O,[d,e] specimen thickness 0.15 in.	SiC_p/2124-T4, 30% V/O,[b] specimen thickness 0.15 in.	SiC_p/2124-T4, 25% V/O,[d] specimen thickness 0.10 in.
75	87.6	87.8	82.8	79.8
75	89.0	82.6	77.6	79.7
75	90.4	83.2	71.3[f]	81.2
400	67.0	76.2	...[g]	...[g]
400	67.0	73.5	...[g]	...[g]
400	66.5	72.5	...[g]	...[g]
600	13.7	33.1	37.2	17.1
600	13.4	33.8	30.7	16.9
600	13.7	23.7	27.9	16.4
Method of Heating	closed oven	radiant heat lamps	closed oven	radiant heat lamps

NOTE—(*a*) All coupons machined from master ASTM E 8 dogbone (8 in.); see text.
(*b*) SiC_p/2124-T4 (30% V/O): Raytheon IR&D results.

[a] °C = 5/9 (°F − 32).
[b] Rolled sheet stock.
[c] 1 in. = 25.4 mm.
[d] 20° to final roll direction, all others in roll direction.
[e] Thick-panel stock.
[f] Flaw observed in specimen within gage section.
[g] No test.

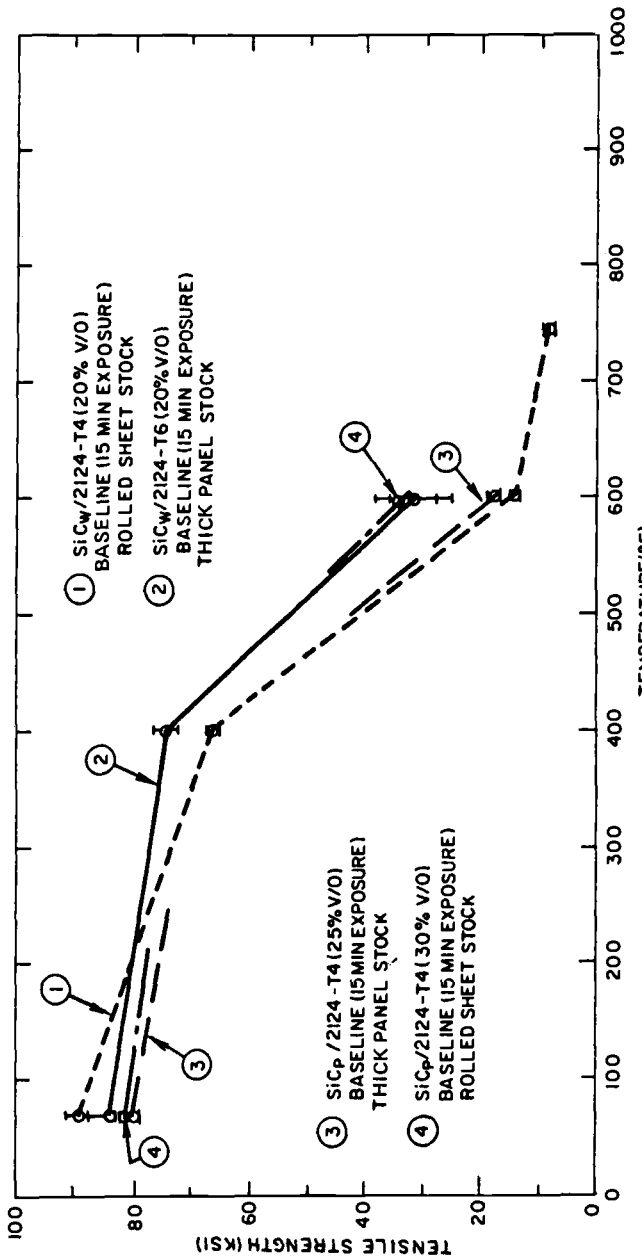

FIG. 13—*MMC baseline tension strength versus temperature.*

TABLE 11—*Comparison of moduli and elongations of thick-panel stock and thin-rolled stock for various SiC_D/Al MMCs.*

	SiC_w/2124-T4 (20% V/O)[b]		SiC_w/2124-T6 (20% V/O)[c]		SiC_p/2124-T4 (30%)[b]		SiC_p/2124-T4 (25% V/O)[c]	
Temperature,[a] °F	Moduli,[d] Msi	Elongation, %	Moduli, Msi	Elongation, %	Moduli, Msi	Elongation, %	Moduli, Msi	Elongation, %
75	14.6–16.0	3.4–3.6	15.0–15.6	1.83–2.54	...[e]	0.89–1.8	16.5–16.7	1.64–1.90
400	12.8	3.6–3.8	12.8–12.9	2.80–4.67	...[e]	...[e]	...[f]	...[f]
600	9.5–10.9	12.0–14.5	9.6–10.2	>10	...[e]	...[e]	9.5–10.6	12.9–13.0

NOTE—All SiC_p/2124-T4 (30% V/O): Raytheon IR&D results.
[a] °C = 5/9 (°F − 32).
[b] Rolled sheet stock.
[c] Thick-panel stock.
[d] 1 in. = 25.4 mm.
[e] Data unreliable.
[f] No test performed.

Short-Term Tension Tests

Short-term testing was performed using radiant heat lamps and the thermocouple feedback controller described earlier. Short-term tests were performed on SiC_w/2124-T6 (20% V/O) thick-panel material at 315, 482, and 537°C (600, 900, and 1000°F). No tests were performed on the SiC_p/2124-T4 (25% V/O) material. The results of the short-term tests are shown in Table 12.

For the SiC_w/Al, the thick panel stock (T6) exhibits slightly higher strength than the rolled sheet stock (T4). The SiC_p/Al sheet stock displayed the highest short-term tensile strength above 315°C (600°F).

Short-term tension test results are plotted versus temperature in Fig. 14.

Failure Modes

A basic characteristic of failures in tension, flexure, and bearing is the transition from relatively brittle failures at temperatures below approximately 260°C (500°F) to ductile type failures at temperatures greater than 260°C (500°F). This is supported by the increased elongation measured at 315°C (600°F) compared to elongation at 204°C (400°F) and lower. This phenomenon is displayed rather clearly in Figs. 15 and 16.

Tension failures at room temperature and 204°C (400°F) were brittle-like with little necking resulting from low elongation, while failures at 315°C (600°F) and higher showed more pronounced necking. Flexural failures also displayed brittle transverse cracking at relatively low curvatures and strains for room temperature and 204°C (400°F) conditions, while curvatures were very large and ductile-like at 315°C (600°F) and above. These observations were similar for both the whisker and particulate reinforced aluminum. Failures of pin bearing coupons were more complex. An examination of Fig. 16 shows that final failure in bearing at room temperature conditions (also for 204°C (400°F) conditions) was net tension

TABLE 12—*Comparison of short-term tensile strength of thick-panel stock and thin-rolled stock for various SiC_p/Al MMCs.*

Temperature,[a] °F	SiC_w/2124-T4, 20% V/O[b]	SiC_w/2124-T6, 20% V/O[c]	SiC_p/2124-T4, 30%[b]
400	73.6	...[d]	71.1
400	73.1	...[d]	65.9
400	71.3	...[d]	65.7
600	31.4	35.1	45.7
600	32.9	37.0	44.9
600	32.2	37.8	35.5
750	13.9	...[d]	15.3
750	13.0	...[d]	15.3
750	13.2	...[d]	15.6
900	4.3	5.8	10.3
900	4.7	7.6	7.7
900	4.5	7.4	8.5
1000	1.9	1.7	...[d]
1000	2.2	3.0	...[d]
1000	2.6	5.9	...[d]

[a] °C = 5/9 (°F − 32).
[b] Rolled sheet stock.
[c] Thick-panel stock (see Table 10 for thickness).
[d] No test.

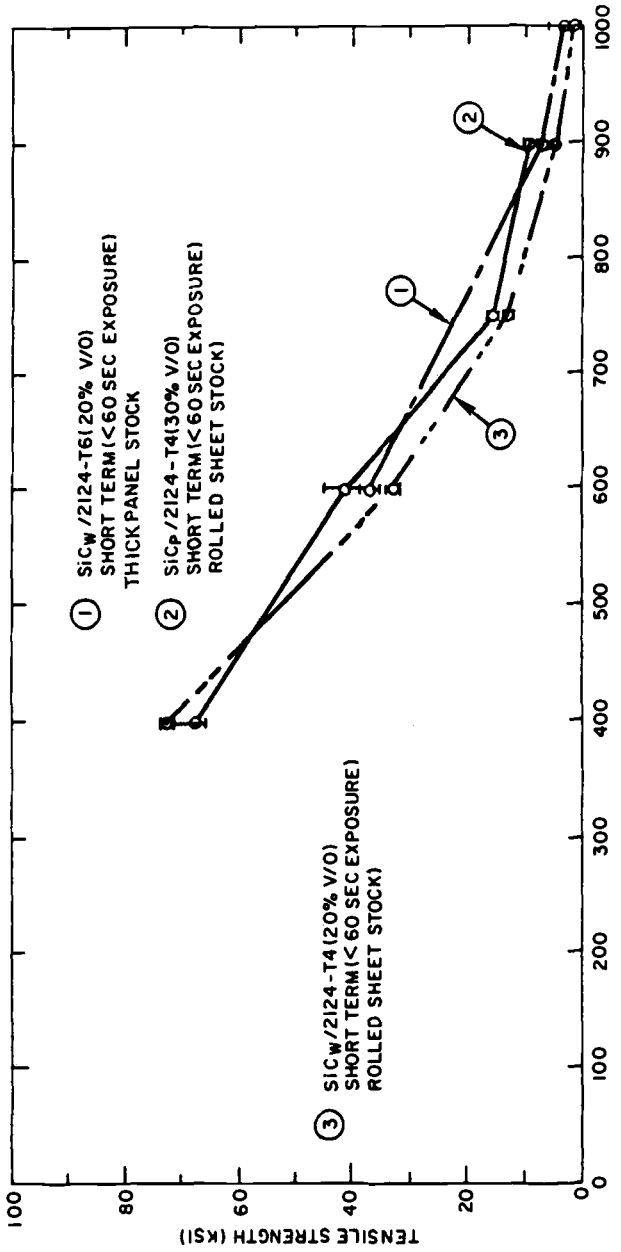

FIG. 14—*Short-term high-temperature tensile strengths of three SiC_D/Al MMCs.*

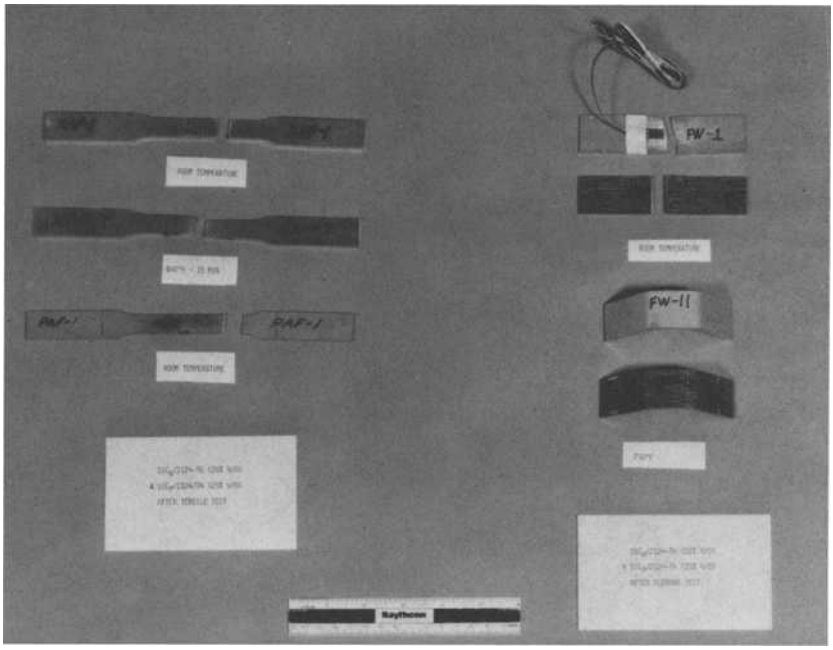

FIG. 15—*Tensile and flexural coupon failures at room temperature and 398°C (750°F).*

across the test section indicating a wider coupon should be used in the future at these test temperatures. At 315 and 398°C (600 and 750°F) conditions, however, as the material became more ductile, combined net tension and bearing predominated the failures with some evidence of shear out beginning.

Summary and Conclusions

Tensile strengths of silicon carbide particulate and whisker reinforced aluminum at temperature after exposure to 60 s (maximum) of heating were significantly greater than strengths subsequent to 15 min exposure to the same maximum temperatures. Short-term strengths were measured for maximum temperatures to 537°C (1000°F) while baseline (15 min exposure) were measured to 398°C (750°F). For example, at 204°C (400°F) the increases in average strength of SiC_w/2124/T4 (20% V/O) and SiC_p/7090-T6 (25% V/O) were 9 and 58%, respectively. At 315 and 398°C (600 and 750°F) the increases in average strength were 137 and 70% for the whisker material and 230 and 113° for the particulate material. For unidirectional graphite aluminum the increase in strength was far less pronounced and more difficult to assess because of the brittle nature of the graphite fibers and its associated strength data scatter.

Until significant increases in graphite/aluminum unidirectional tensile and compressive, transverse, and shear strengths are realized only specialized local application of this MMC to achieve thermal stability (near zero CTE) appears feasible for highly loaded structures.

Increased stiffness of SiC_D/Al was evident for all temperatures tested. At room temperature the increase in stiffness of both SiC_p/7090-T6 (25% V/O) and SiC_w/2124-T4 (20% V/O) was 57% compared to the unreinforced aluminum alloys. At 204 and 315°C (400 and 600°F), the increases were 64 and 77% at each of the respective temperatures for particulate

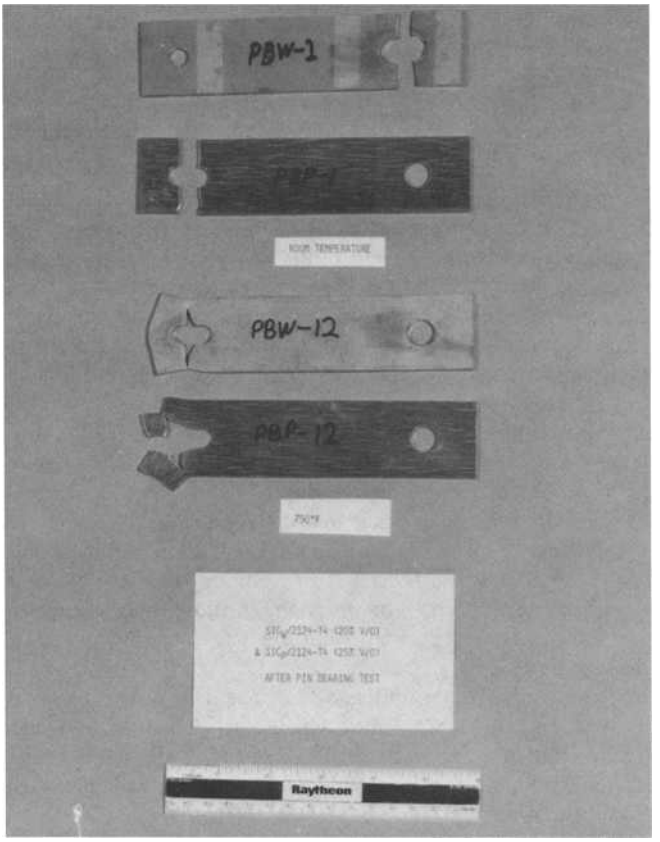

FIG. 16—*Pin bearing failures at room temperature and 398°C (750°F).*

reinforced aluminum compared to 7000 series unreinforced aluminum, while the increases were 44 and 49% for whisker reinforced aluminum compared to 2000 series aluminum at the same respective temperatures.

Standard metallic 203.2 mm (8 in.) dogbone coupons (ASTM E 8) were found to satisfy all testing requirements for SiC_D/Al MMCs. Tabbing is not required since all coupons of this type failed within the 12.7 by 50.8 mm (1/2 by 2 in.) gage section. The "bow tie," streamline, double radii, and other more complex coupon designs provide no improvement upon the present design. Continuously reinforced MMCs require some type of stress relief at the grips [*2*]. The most popular forms are bonded tabs with or without bevels. The present study indicates bevelling is required. However, other studies and discussions with other users indicate that no significant effect of tab bevel can be established. Furthermore, use of a soft unbonded tabbing material, such as Lexan, together with hydraulically acutated grips appear to be as satisfactory as bonded tabs [*2*].

No ASTM standards exist for SiC_D/Al tensile coupon design. Presently, ASTM Committee D-30 on High Performance Fibers and Composites has formed a task group to rewrite the outdated MMC tension testing standard. This task group is being chaired by one of the authors. The first task will be to separate continous and discontinuous MMC testing procedures and rewrite them accordingly.

A review of high-temperature baseline testing procedures indicates the use of temperature

controllable ovens or radiant heat lamps adequate for performing tests at elevated temperature exposure of 15 min or more or both. Dual thermocouples, one attached to the coupon and the other located randomly inside the oven, should be continuously monitored to reveal significant differences between oven and test specimen temperatures.

Short time heating (<60 s) and high-temperature strain measurements >315°C (>600°F) represent more difficult experimental tasks. Radiant heat lamps together with a preprogrammed microprocessor with thermocouple feedback from the test coupon is a reliable and repeatable procedure. Direct resistance heating of the test specimen has been reviewed and found less desirable than use of radiant heating. The use of radiant heat lamps which can be water cooled would provide greater flexibility for use with various coupon dimensions. Together with the use of water-cooled grips this would provide an improved method for short-term, high-temperature testing. These systems are moderately priced and can be adapted directly to standard servomechanical loading systems, either hydraulic or screw driven. If fatigue testing is envisioned, hydraulic servomechanical systems are required.

One interesting observation is that strength increases of reinforced aluminum at all temperatures for flexure and bearing are not nearly as pronounced when compared to unreinforced aluminum as are increases in tensile strength. The strengthening mechanism at work in tension is not translated to flexure and bearing (and possibly shear). While this might appear reasonable for bearing it is difficult to explain why flexural strength increase with reinforcement does not follow the tensile strengthening since the bending stress state is predominantly uniaxial tension and compression. Although compression tests were not conducted during this program, reported data indicate strength increases comparable to those measured for tension.

These phenomena must be better understood in hardware design since both flexure and bearing are often predominant stress states which exist at failure. Indeed, examination of the high-temperature statically tested hardware failed in combined bending and bearing.

During the present study, laser and equivalent light sensing strain measuring systems were reviewed. When review of turnkey systems was completed, the available resolution was not adequate to accurately develop stress-strain curves at high temperature.

Several systems have been reported to have capabilities for measuring strain in the 1% maximum range with an accuracy of ±5% full range. However, consistent data showing this capability could not be obtained. Based on the present study the following methods or devices or both for developing stress-strain curves at high temperature are recommended:

1. Water cooled quartz rod (spring loaded) extensometers: These devices are off-the-shelf items and easily adapted to radiant (nonclam shell enclosed) quartz heating systems. They are good to 537 to 648°C (1000 to 1200°F) and capable of use for fatigue testing.
2. High-temperature extensometers (both single axis and biaxial): These provide good to excellent strain measuring capability. However, they must be handled with extreme care, calibrated frequently for use at the upper limits of the rated temperature [315°C (600°F)], and are "operator" sensitive.
3. Capacitance type transducers: These sense changes in gap spacing and are available off the shelf. However, because of their shadowing effect on the test coupon and their mounting requirements, they present greater difficulties for measuring more than several coupons, and thus represent a costly excercise when making numerous measurements.
4. Strain gaging: This technique is effective for obtaining moduli at temperatures to 426°C (800°F) and are limited mainly by the gage adhesive system. Further, because of

adhesive high-temperature bonding times [1 to 2 h at 10°C (50°F) greater than use temperature] specimen heat treat conditions are altered during bond affecting material strength. Therefore, high-temperature strain gaged coupons are useful only for modulus measurements. High-temperature strain gaging is time consuming and tedious, therefore, is costly and subject to frequent faults.

Test techniques and standards must be advanced by ASTM to evaluate reinforced MMCs under different environmental conditions. The present situation of numerous and vaguely described test procedures for developing a MMC data base does not provide designers with the confidence required to consider MMCs among the first choice for structural application. Independent evaluation of MMC capabilities must be accelerated to develop design confidence and ensure that the most promising of these materials are introduced into production.

Finally, with the expanding role of lightweight, high-temperature, high-strength polymeric reinforced composites, MMCs should be traded off with the former composites rather than solely with traditional isotropic metals.

References

[1] Bradstreet, S. W. and Davis, L. W., "The Technical Information Requirements of Inorganic Matrix Composites," *Metal Matrix Composites II,* NASA Conference Publication 2252, Proceedings of Joint NASA/DoD Conference, Cocoa Beach, Florida, Jan. 1982, pp. 43–53.

[2] DiGiovanni, P., Franceschi, L., Boland, P., and Paterson, D., "Metal Matrix Composite Test Data Requirements for Design Applications," *Proceedings,* DoD/NASA 9th Conference on Composite Materials, Cocoa Beach, Florida, Jan. 1985.

Philip L. Blue[1]

Ultrasonic Inspection of Silicon Carbide Reinforced Aluminum Metal Matrix Composite Billets and Secondary Fabricated Products

REFERENCE: Blue, P. L., **"Ultrasonic Inspection of Silicon Carbide Reinforced Aluminum Metal Matrix Composite Billets and Secondary Fabricated Products,"** *Testing Technology of Metal Matrix Composites, ASTM STP 964,* P. R. DiGiovanni and N. R. Adsit, Eds., American Society for Testing and Materials, Philadelphia, 1988, pp. 376–382.

ABSTRACT: This work describes the ultrasonic inspection of silicon carbide whisker and particulate reinforced aluminum metal matrix composite billets, extrusions, forgings, and rolled plate and sheet. Inspection techniques will be described and results discussed including metallographic analysis of flaws. A correlation will be made between billet attributes and extrusion results.

KEY WORDS: nondestructive evaluation, ultrasonic inspection, aluminum alloys, silicon carbide, whiskers, particulate, discontinuous, metal matrix composite, composite

Advanced Composite Materials Corporation (ACMC) is a producer of aluminum-silicon carbide discontinuous metal matrix composites (MMC). These composites, comprising a range of matrix alloys and both whisker and particulate reinforcement have been under continuous development by the ACMC group for approximately six years. This paper will discuss the roll of ultrasonic inspection and characterization in transitioning Al-SiC from a "best effort" to one which meets critical quality standards.

ACMC produces a family of MMCs under the SXA® trademark which comprise primarily 2124 and 6061 aluminum alloys as the matrix and silicon carbide whiskers or particulate in volume fractions ranging from 15 to 40%, as the reinforcement. Billet sizes range from approximately 7.5 to 60 cm in diameter and 7.5 to 60 cm in length.

The composites are formed by vacuum hot pressing a billet from a powder blend then machining or hot forming to the final shape. The ultrasonic work with SXA® materials to be reported here involves the characterization of billets for the effects of porosity and discontinuities and the inspectability of subsequently processed shapes such as extrusion and rolled plate.

Procedure

A variety of ultrasonic tests were performed on SXA® materials, primarily billets. Since March 1984, all billets produced by ACMC have been ultrasonically inspected to determine

[1] Manager, Quality Control and Testing, Advanced Composite Materials Corporation, Greer, SC 29651.

what conditions are deleterious to extruding the billet successfully or degrading physical properties.

Billets are inspected for internal flaws by conventional pulse-echo methods using either immersion or contact techniques. The billets are machined right circular cylinders and are inspected by scanning across the flat faces. The hot pressing method causes flaws to generally be planar in shape and lying orthogonal to the pressing direction, that is, parallel with the flat faces of the cylinder. This orientation offers the best opportunity for detection by ultrasonic inspection.

When immersion testing was employed, the billet was scanned either by rotating the billet on a turntable and making a polar scan or indexing the transducer in a rectilinear scan by means of a bridge (Fig. 1). Records were made of the output of the ultrasonic analyzer in conventional C-scan orientation.

Contact testing was done by making a numbered grid on the billet face which coincided with a grid on the inspection form. The billet was inspected section by section and the form marked appropriately if any flaws were detected.

For all billet inspection, flat 5 MHz transducers 1.3 cm in diameter were used. The ultrasonic analyzer was calibrated using a set of reference blocks fabricated of SXA® material. Billets were inspected from one face then inverted and inspected from the other face. Standards were used which contained 0.20-cm-diameter flat bottom holes according to ASTM Fabricating and Checking Aluminum Alloy Ultrasonic Standard Reference Blocks (E 127). The maximum metal path for a particular standard was selected to be approximately one half the billet height. Two more standards, as near to one quarter and one half billet height were also used. The recorder trigger level was set by maximizing the signal from the longest standard, adjusting the analyzer gain so the signal was 80% of the fill CRT scale, then setting the threshold trigger at 20% of full scale. Recordings were made of all three standards.

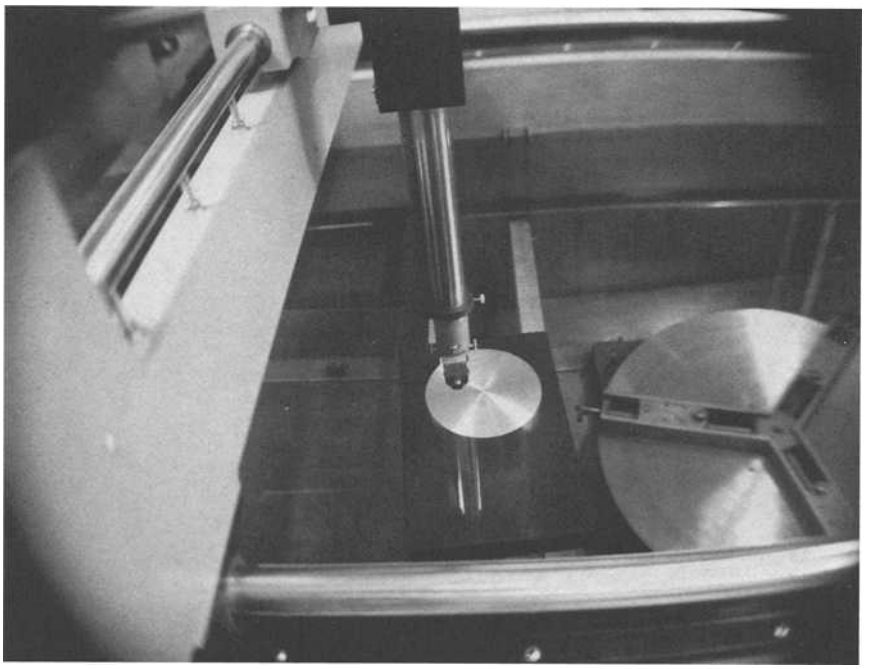

FIG. 1—*Scan setup for small billet. Turntable is used for large billet inspection.*

Extrusions, forgings, and plate were inspected similarly. Standards were fabricated as needed by producing flat bottom holes in representative material by drilling with tungsten carbide tooling.

Sonic velocity measurements were made on a wide range of SXA® compositions in billet and extruded form to determine the ultrasonic characteristics of the material. Those results have been reported elsewhere [*1*] and will not be discussed in this work except to the extent they were useful in determining the sensitivity of an inspection technique to certain flaw types in billet material. The velocity measurements were made by the pulse-echo overlap method using both longitudinal and shear wave transducers.

Results

Billets

Sound billets, extruded properly, produce extrusions which yield 85 to 90% useful material. When a billet contains a large flaw for porosity, a defective extrusion will result. From a commercial aspect then, nondestructive evaluation of billets can result in improved quality by direction process modifications.

Porosity is observed as a "grassy" echo during billet inspection, and the recording appears as a vaguely defined area (Fig. 2). Careful sectioning and inspection of a porous billet showed the minimum porosity level which can be detected by backscattered ultrasonic waves to be 1.0% by volume.

Discrete flaws appear as distinct round areas in a C-scan recording. Two types generally observed were related to processing problems. The first was believed due to outgassing of

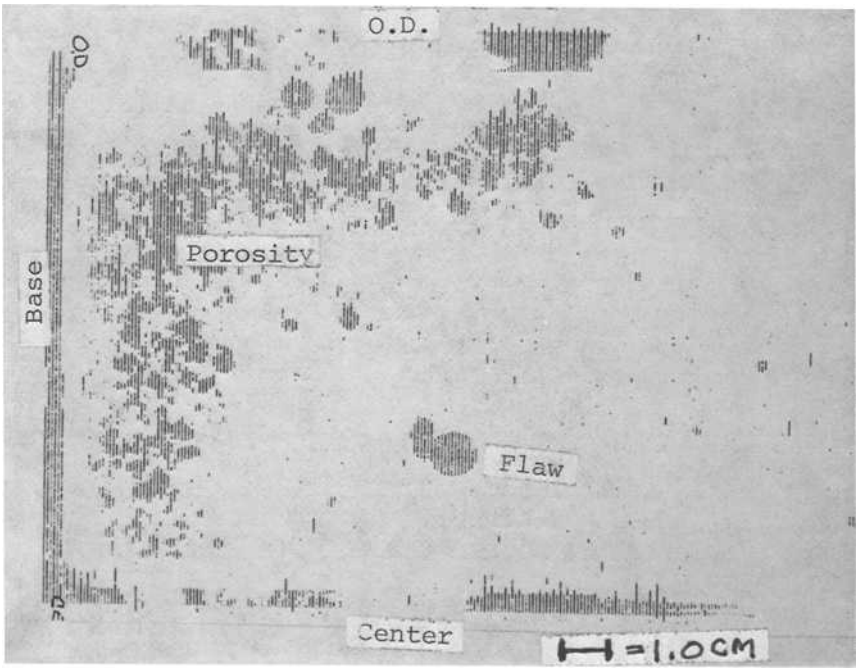

FIG. 2—*Portion of an ultrasonic recording showing porosity in an SXA® billet section.*

the aluminum during consolidation resulting in a void surrounded by porosity (Fig. 3) while the second appeared to be caused by a lack of aluminum infiltration due to non-uniform blending of the aluminum and silicon carbide (Fig. 4). A third flaw type is associated with an impurity in the billet (Fig. 5). This flaw appeared to be caused by a piece of paper or plastic in the powder blend.

A 30.5 cm diameter by 30 cm tall billet which exhibited porosity and discrete flaws was machined to provide a 4-cm-thick slab of billet length providing a cross section of the billet from center to outer surface. This slab was inspected and provided a recording (Fig. 2) which showed the distribution of porosity in the billet. This information coupled with microscopic examination of discrete flaws in the billet provided guidance for improving billet quality. The porosity distribution in the billet and heater construction in the hot press indicated the nonisothermal conditions during pressing. The isolated porosity around voids indicated the need for improved outgassing cycles during the die heat up and pump down.

The conditions were corrected by several process changes and improved controls. The operation of the pressing-heating-vacuum cycle was placed under the control of a microprocessor. The melting characteristics of the aluminum powder were observed using the differential thermal analysis while the outgassing characteristics were determined by residual gas analysis and experimentation with thermal cycles. A bottom plug heater was designed for the die assembly which, with the microprocessor control, allowed uniform heating of the powder mass. Mixing and blending technology were modified and equipment installed to remove impurities from whiskers resulting in reduced impurity content. The overall result of these changes was a decrease in defective billets, improved extrusion yields and more uniform mechanical properties.

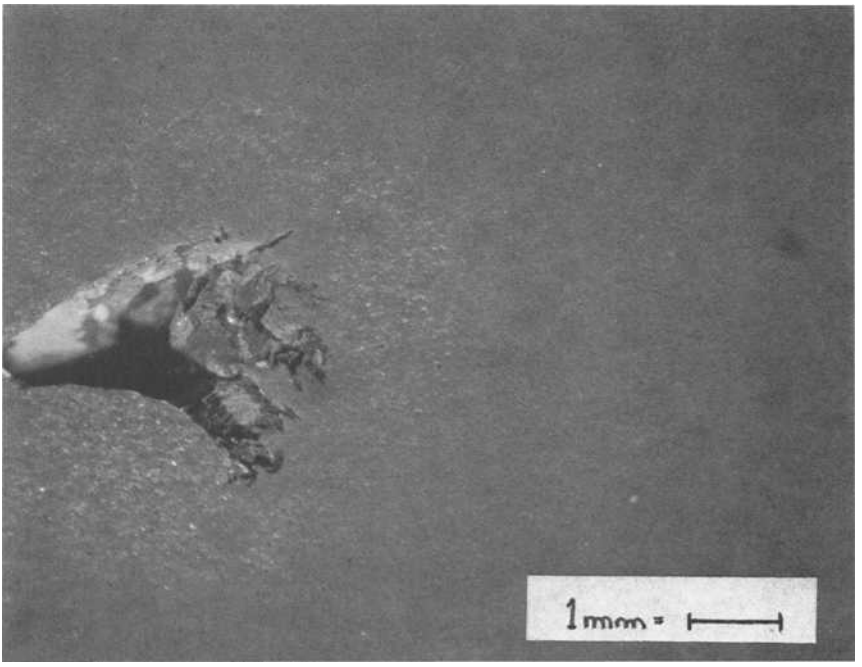

FIG. 3—*Void in SXA® billet possibly caused by insufficient outgassing of powder blend during vacuum hot pressing.*

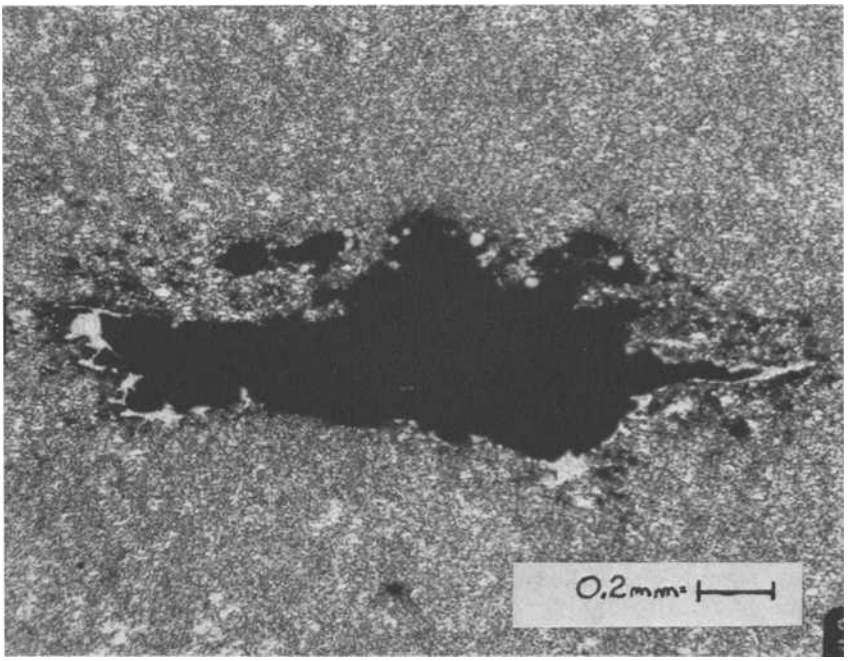

FIG. 4—*Flaw possibly caused by insufficient blending of aluminum alloy powder and silicon carbide whiskers.*

Extrusions

As stated earlier a billet which is not dense will not densify in the extrusion process but will tear and result in scrap material. The effect of small discrete flaw is less clear. These flaws cannot be easily followed through extrusion because favorable orientation to the sound beam is lost unless the reduction is sufficiently high so as to reorient the flaw in a manner amenable to detection. This condition appears to be met in the extrusion of round billets to high aspect ratio rectangles such as a 15.25 cm diameter round billed to a 1.27 by 12.70 cm cross section, a cross sectional reduction ratio of 11.3 to 1. Back extrusion of billets to form large diameter tubes also results in favorable orientation. A flaw detected in a tube formed by back extrusion of a 30.5-cm-diameter billet appeared to be an unbonded area caused by a silicon carbide rich area (Fig. 6).

The fabrication of sheet and plate begins with the extrusion of a billet. Generally, a 30.5 cm diameter billet is extruded to 6.35 by 17.78 cm then forged to a 2.54 cm thick by 53.34 cm by 71.12 cm plate. Forged plate of that thickness was amenable to ultrasonic inspection and sufficient working of the material occurred to orient flaws favorably for detection. When a forged plate containing known flaws was rolled to a thinner gage, the flaws were still detectable, and their size did not appear to change appreciably although their spatial relationship was altered by the rolling process. Metallographic examination showed such flaws to be the result of silicon carbide rich areas not infiltrated or mixed with aluminum.

Discussion

The successful ultrasonic inspection of SXA® metal matrix composites relies heavily on the determination of the types of flaws which can occur due to processing and how those

flaws can be detected sonically. ACMC is inspecting billets 15.25 cm to 45.72 cm in diameter and 2 cm to 61 cm in length and is attempting to characterize flaw types, their source, and to determine corrective action. Sufficient experience has been gained to generate the internal quality specification for billets to establish whether further processing is possible. The action has resulted in higher extrusion yields and more uniform mechanical properties.

Inspection of billets does not improve quality unless their manufacture is modified in response to the detection of systematic flaws. The manufacturing group at ACMC, apprised of ultrasonic test and metallographic results, caused significant improvements to be made.

The ultrasonic inspection of extrusions must be approached with caution. Conventional pulse-echo methods can cause flaws to be missed; alternative approaches have not yet been developed.

Flat heavily worked product forms can be ultrasonically inspected with reliable results. Currently ACMC applies Aluminum Association Standards to sheet and plate quality. As forging and rolling of sheet and plate continue to be developed, ultrasonic inspection will be relied upon to monitor the quality of the products.

Conclusions

The ultrasonic inspection of SXA® billets provided information which allowed process changes that resulted in improved quality. The level of detection of porosity by back scattered ultrasound was established, and internal flaws were evaluated to determine their source. Significant increases in extrusion yields were realized when discrimination was used in selecting only billets which were ultrasonically defect free. The satisfactory inspection of extrusions was found to be dependent on the extrusion shape and amount of reduction. Low extrusion ratio products did not have suitably oriented flaws for detection while increasing the ratio improved the inspectability.

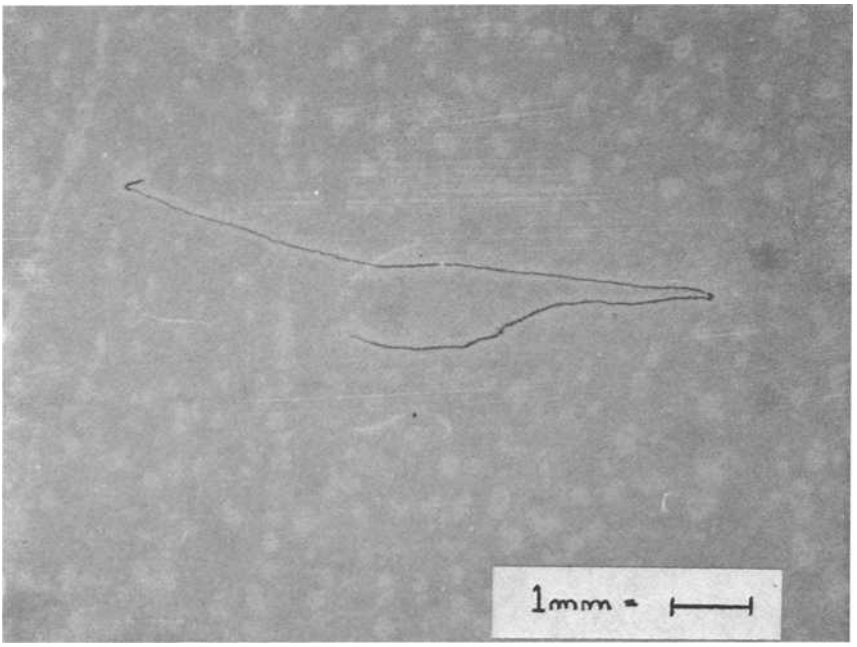

FIG. 5—*Flaw due to impurity in the powder blend, possibly a piece of paper.*

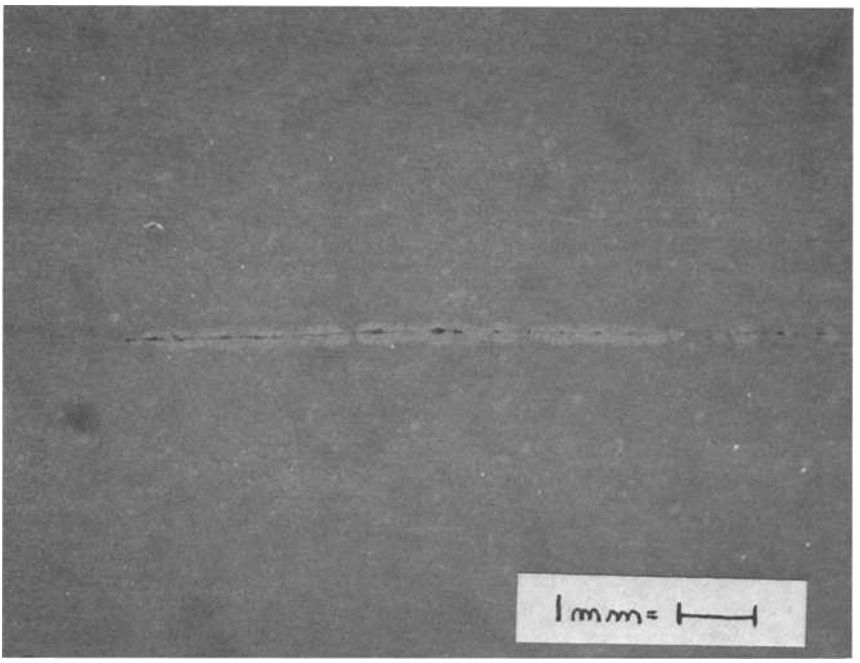

FIG. 6—*Discontinuity caused by silicon carbide rich area not being fused during hot pressing.*

Forged and rolled plate are readily inspectable by conventional means. Flaws in these products were able to be traced through process and appeared to be caused by silicon carbide rich areas forming an interface.

A final important conclusion of this work is the determination that flaws are not eliminated by hot mechanical working such as extrusion or rolling. Flaws which exist in the billet are carried through to the final product unless removed by trimming in intermediate processing.

Reference

[*1*] Blue, P. L., "Some Ultrasonic Characteristics of Silicon Carbide Whisker and Particulate Reinforced Aluminum Alloy Composites," *Proceedings,* Review of Progress in Quantitative Nondestructive Evaluation, 23–28 June 1985, to be published.

J. Heritier,[1] *P. Balladon,*[1] *J. Rambaud,*[2] *F. Chevet,*[2] *and M. De Coquereaumont*[2]

Influence of Heat Treatments and Working on Mechanical Properties of Silicon Carbide Reinforced Aluminum Alloys

REFERENCE: Heritier, J., Balladon, P., Rambaud, J., Chevet, F., and De Coquereaumont, M., **"Influence of Heat Treatments and Working on Mechanical Properties of Silicon Carbide Reinforced Aluminum Alloys,"** *Testing Technology of Metal Matrix Composites, ASTM STP 964,* P. R. DiGiovanni and N. R. Adsit, Eds., American Society for Testing and Materials, Philadelphia, 1988, pp. 383–395.

ABSTRACT: Three grades of silicon carbide (SiC) reinforced aluminium alloys are studied: one grade fabricated by powder metallurgy and reinforced by ≈25% volume fraction (vf) SiC particulates; two grades produced by casting and reinforced by ≈15% vf SiC whiskers.

Their behavior during hot working is simulated using unloading and holding times during high temperature tension testing. The three grades are also worked by extrusion and forging and the defects appearing on the wrought pieces are observed.

Mechanical properties of the three grades are represented versus temperature in the as received state, in the annealed state and in some cases after forging and annealing.

Microstructure is observed and its influence on mechanical properties is discussed.

KEY WORDS: metal matrix composite, working, mechanical properties, microstructure

Low weight or inertia, a high elastic modulus, high tensile properties at elevated temperatures and improved wear resistance make metal matrix composites high interest materials for military, aircraft, spatial, and automotive components.

The use of metal matrix composite materials which may be produced by different ways [*1–4*] depends on their ability to be formed by working. The conditions of their forming may be very accurate, and their physical and mechanical properties are strongly dependant on these forming conditions (working and heat treatment).

The aim of this work is to study for industrial application the forming conditions of metal matrix composites fabricated by two different ways and to determine the physical and mechanical characteristics of these materials after working and heat treatment; an attempt of correlation is done with microstructure.

Materials and Experimental Techniques

Materials

Tests have been performed on three grades fabricated by two differents ways:

1. A 25% volume fraction (vf) silicon carbide (SiC) particulates reinforced 2124 aluminium alloy fabricated by powder metallurgy (grade A).

[1] Research engineers, Department of Mechanics and composites, UNIREC, Groupe USINOR, Centre de Recherches d'Unieux, 42701 Firminy, France.

[2] Engineers, Groupe USINOR-SACILOR, France.

2. A 15% vf SiC whiskers reinforced 2024 aluminium alloy fabricated by squeeze-casting (grade B).
3. A 15% vf SiC whiskers reinforced AC8A aluminium alloy fabricated by squeeze casting (grade C).

Table 1 gives, respectively, for each grade, the type of product matrix and reinforcement initially used, the nominal chemical analysis, and SiC content.

Experimental Techniques

Transformation

The three grades were formed using following steps: extrusion (370°C), forging (455°C), and heat treatment (490°C), 1 h, water quenched and 120°C, 2 h, aircooled).

Tests for simulation of hot working were performed using tension testing apparatus; successive deformations of samples separated by holding times were used for predicting the behavior of the materials during forging.

Micrographic Examination

Scanning electron microscopy was used in conjunction with optical microscopy and electron microprobe analysis to determine the distribution and morphology of SiC particulates and whiskers and for evaluation of the quantity, shape size, and distribution of microvoids before and after transformation.

Mechanical Properties

Following mechanical properties were measured:

Elastic Properties—Tensile modulus was determined by vibration on specimens of dimensions 100 by 10 by 4 mm. Same specimens were used to determine flexural modulus by bending tests.

Flexural Strength—Flexural strength and modulus were determined by bending tests on specimen of dimensions 100 by 10 by 4 mm. Roller pin diameter was 4 mm and distance between pins 80 mm. Loading rate was 1 mm/min.

Tensile Strength and Ductility at Room and Elevated Temperature—Tension tests were performed on round specimens of diameter 5 mm. Loading rate was 1.5 mm/min at room temperature and 0.75 mm at high temperature. Ductility was measured by total elongation at fracture.

TABLE 1—*Type of products, nominal chemical analysis, and SiC content.*

	Type of Product	Reinforcement	Matrix
Grade A	powder metallurgy billet	particulate (25% vf Sic)	aluminium alloy 2124
Grade B	cast billet	whisker (15% vf SiC)	aluminium alloy 2024
Grade C	cast billet	whisker (15% vf SiC)	aluminium alloy with 12% Si

Hardness—Hardness measurements have been done on various specimens according to ASTM Standard Test Methods for Rockwell Hardness and Rockwell Superficial Hardness of Metallic Materials (E 18), with an applied load of 981 nitrogen and a diameter of ball of 1.588 mm.

Results

Hot Working

Extrusion was performed at 370°C as preparation before forging. 16-mm-diameter bars were transformed in 10-mm-diameter bars in several steps. This first forming procedure does not make all voids disappear.

Bars were forged at 455°C after extrusion from 16 to 14 mm diameter. Cracks begin to appear for a reduction rate greater than 38% (height reduction).

The reasons of such cracks may be due to the choice of the forming conditions (temperature, reduction rate, holding time, etc . . .). In order to determine the most appropriate forging conditions, preliminary tension tests were performed at high temperature. Tests were done for Grade A at first with monotonically increasing loading and then with interrupted loading periods (Fig. 1). Results appear on Fig. 2 and show the existence of a maximum ductility about 520°C. This ductility is also improved at this temperature by increasing the time of interrupted loading periods.

Mechanical Properties

The mechanical properties of the three grades before hot working appear in Table 2; properties in the as-received state and after heat treatment (490°C, 1 h, water quenched, and 120°C, 2 h, air cooled) are compared. The variation of ultimate strength, ductillity, and Young's modulus versus temperature are given on Fig. 3 for Grade A. Some values after forging appear also on that figure.

Density (Table 3)

SiC content is measured by dissolving the aluminium alloy matrix as following:

(*a*) sampling (500 mg of chips),
(*b*) dissolving with 2.5 g sodium hydroxide (NaOH) and 30 mL water (H_2O),
(*c*) dissolving hydroxides with 30 ml hydrochloric acid (HCl),
(*d*) filtering,
(*e*) burning at 1000°C,
(*f*) blowing hydrofluoric acid (HF) to eliminate silicon dioxide (SiO_2),
(*g*) burning, and
(*h*) weighing SiC.

Density measurement is done on specimens of weight 2 or 3 g by immersion.

Microscopic Examination

Figures 4, 5, and 6 show the size, shape, and distribution of SiC particulates or whiskers in different orientations in the aluminium alloy matrix before hot working. Voids (diameter between 5 and 10 μm) due to incomplete compaction before hot working can be found. A few of them may remain after extrusion.

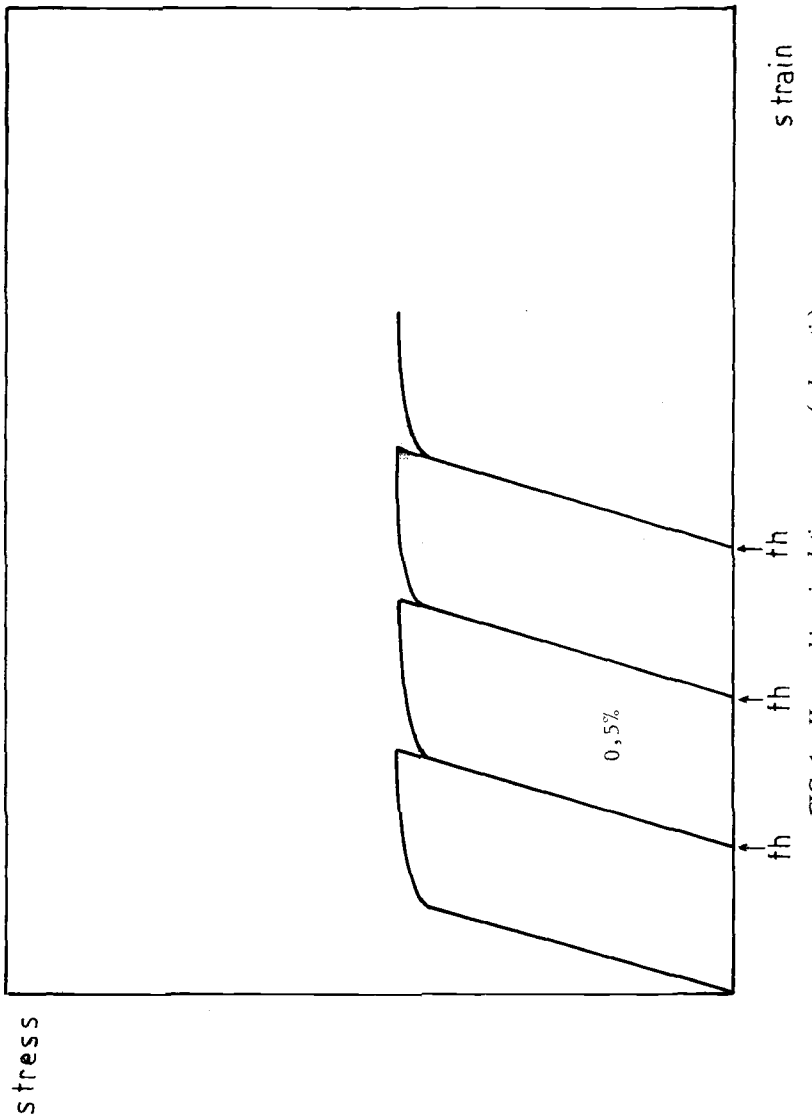

FIG. 1—*Hot-working simulation program (schematic).*

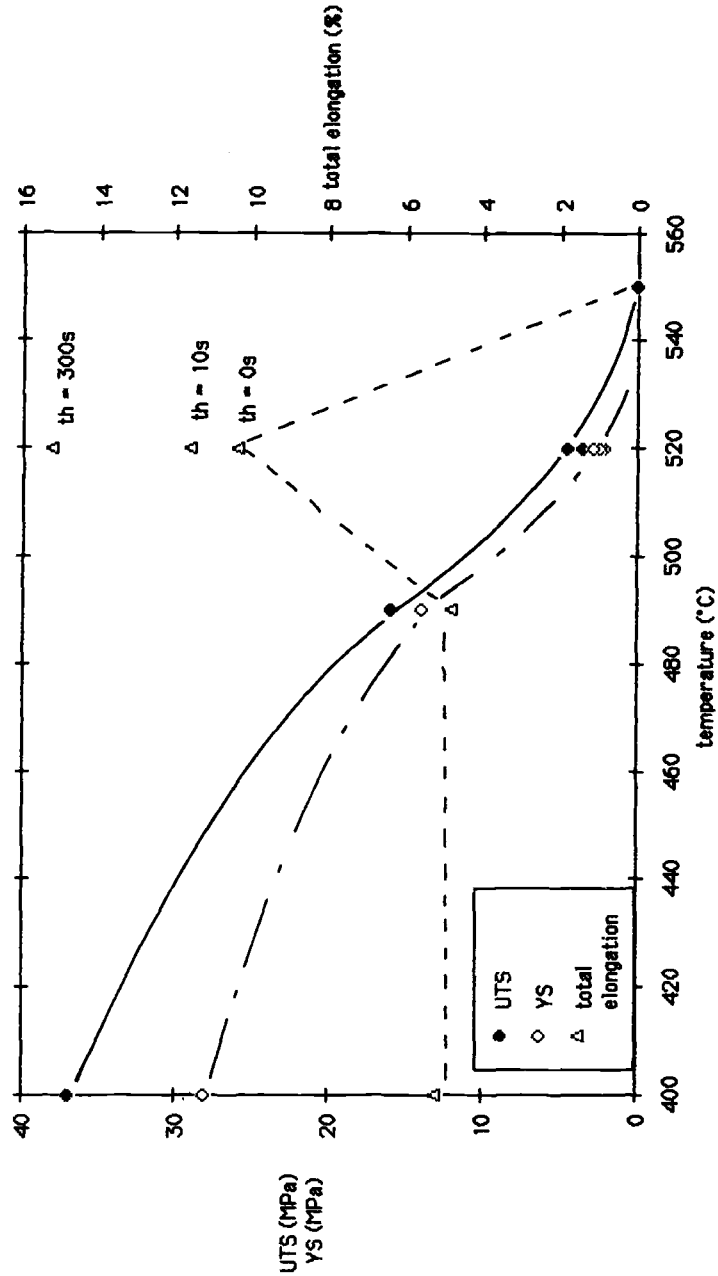

FIG. 2—*High-temperature tensile properties and hot-working simulation.*

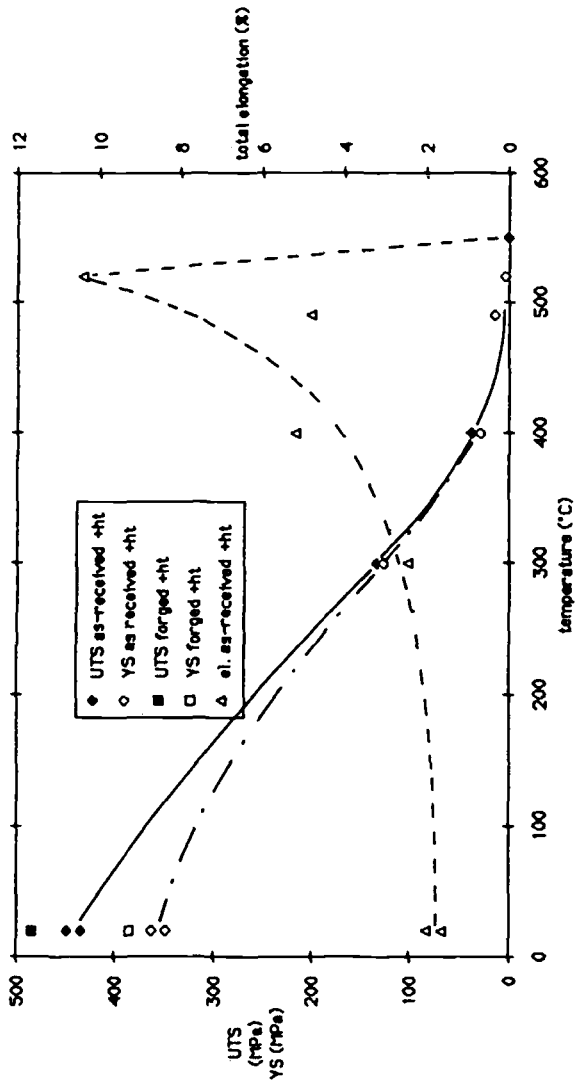

FIG. 3—*Tensile properties versus temperature (Grade A).*

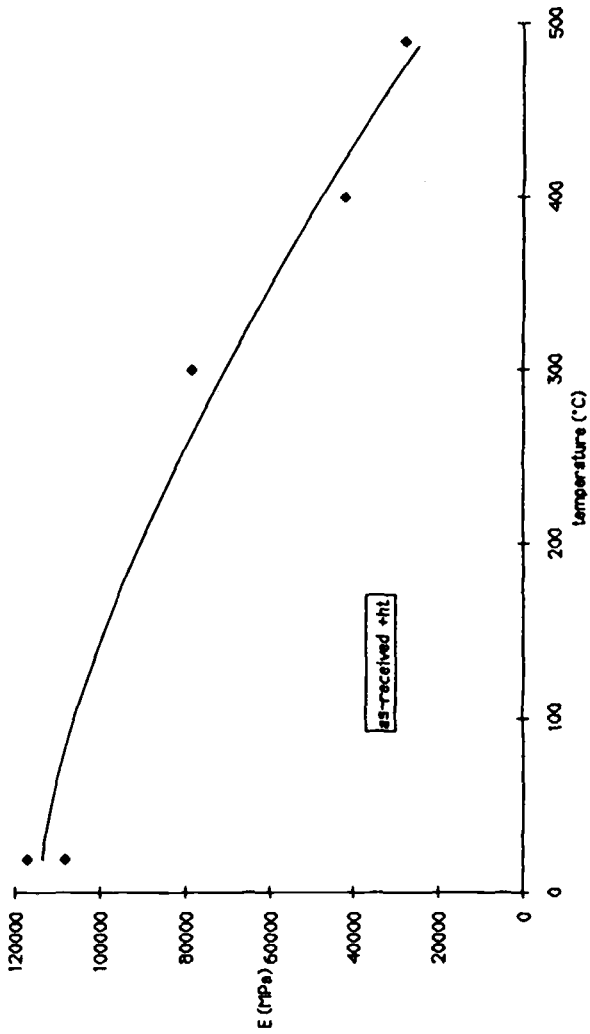

FIG. 3—*Continued*

TABLE 2—*Mechanical properties.*

Grade	State Orientation	Test Temperature[a]	σ_{YS}, MPa	σ_{UTS}, MPa	Total Elongation, %	Young's Modulus, MPa	Flexural Strength, MPa	Flexural Modulus, MPa
A	as received	RT	193	193	0.2	114 400/115 300	496	105 718
	as received	RT	206	283	1.85			
	as treated	RT	347	434	2	115 800	744	110 459
	as treated	RT	361	448	1.6			
	forged and treated (low reduction rate)	RT	384	485	1.6			
	extruded and treated	RT	270	365	2.4			
		RT	307	416	4			
	as treated	300°C	126	132	2.4			
		400°C	28	37	5.2			
		490°C	14	16	4.8			
		520°C	2 2	4 6	10.4			
B	as received							
	long	RT	214	387	2.8	92 400/92 900		
	transverse	RT	198	336	1.2			
	as treated							
	long	RT	328	458	2.4	89 800		
	transverse	RT	305	408	0.8			
C	as received					100 070/99 700		
	long	RT	158	269	1.6			
	transverse	RT	156	283	1.6			
	as treated							
	long	RT	271	332	1.2	98 500		
	transverse	RT	276	336	0.8			

[a]RT = room temperature.

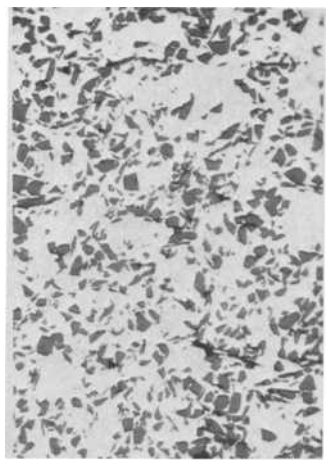

as received (x 400)
(section perpendicular to the axis of the billet)

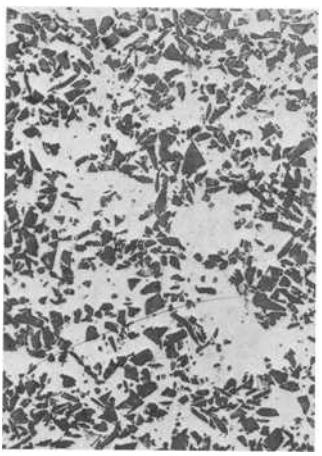

after extrusion (x 400)

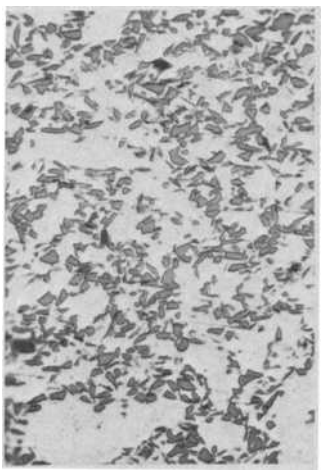

as-received (x 400)
(section parallel to the axis of the billet)

as received (x 1310)
examples of voids

FIG. 4—*Microstructure: Grade A as received and after extrusion.*

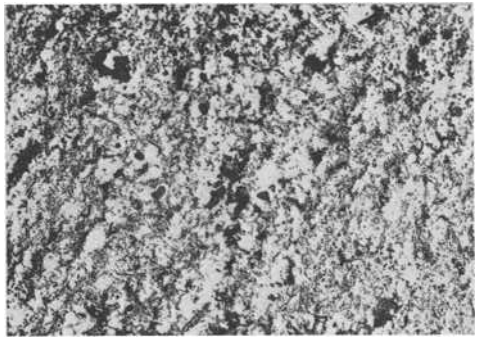

as received : face 1 (x200)

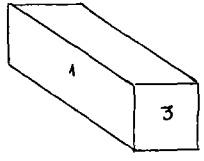

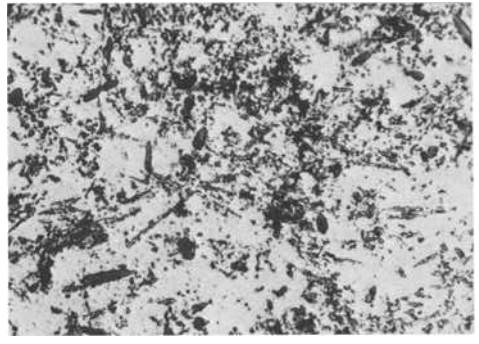

as received : face 1 (x 1000)

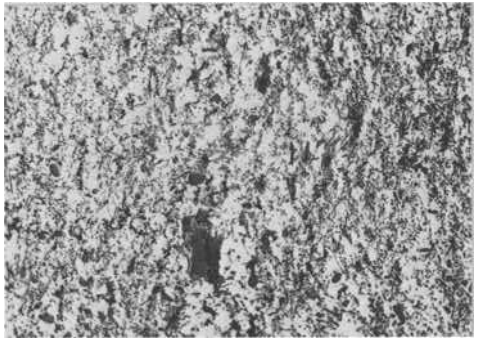

as received : face 3 (x200)

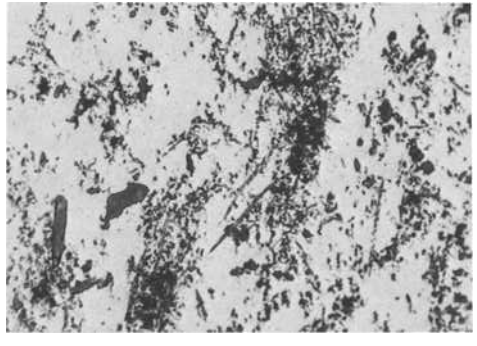

as received : face 3 (x 1000)

FIG. 5—*Microstructure: Grade B*

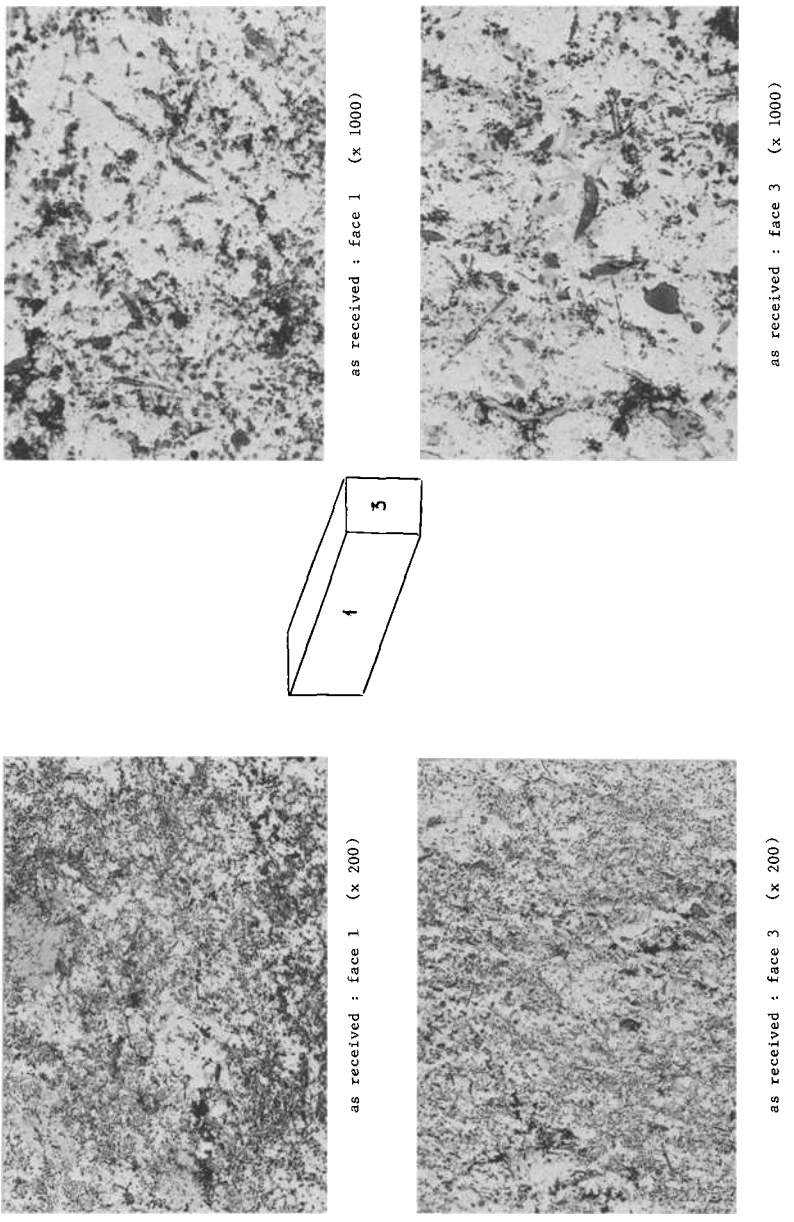

FIG. 6—*Microstructure: Grade C.*

Discussion

A comparison of the two grades A and B (whose matrixes are very similar) shows the following:

1. Ultimate tensile strength at room temperature on as received materials is lower for Grade A despite the higher percentage of SiC.
2. Heat treatment however improves significantly mechanical properties at room temperature for both grades, and both Grades A and B.
3. Young's modulus is nevertheless not significantly changed by heat treatment and is 25% higher at room temperature for Grade A than for Grade B and its value is near 100 000 MPa.
4. Micrographic examinations as well as tension testing show an isotropic behavior for Grade A. On the contrary for Grade B a difference of about 10% for yield strength and ultimate tensile strength and of more than 50% for ductility appears between long and transverse orientations. This anisotropy is due to a preferential orientation of SiC whiskers as appears on Fig. 5.
5. Yield strength and ultimate tensile strength for Grade A at 300°C in the as heat-treated state have respective values of 126 and 132 MPa.
6. Ductility of the three grades is very low for any state studied; one of the reasons seem to be the presence of microvoids, but their suppression (uncomplete) by extrusion and forging does not give a significant improvement of ductility.
7. The simulation of the behavior of Grade A during hot working allows to define conditions of forging (temperature, deformation, holding times) which could reduce the number of defects.
8. Tensile properties are higher for Grade B than for Grade C despite a similar SiC content. Young's modulus is on the contrary ≈10% higher for Grade C.

Conclusion

The comparison of three grades (A, B, C) of SiC reinforced aluminium alloys shows the improvement of tensile and flexural properties due to SiC particulates or whiskers (at room and elevated temperature).

Grades B and C reinforced with whiskers show a larger anisotropy of yield strength and ultimate tensile strength on ductility than Grade A reinforced with particulates, and this anisotropy may be explained by a preferential orientation of whiskers.

TABLE 3—*Density and SiC content.*

	Density		SiC, vf		
				Measured By	
	Nominal	Measured	Nominal	Si and C Concentration Measurement	Matrix Dissolution
Grade A	2.88	2.91	25	24.7	24.6
Grade B		2.83/2.85	15	14.4	
Grade C		2.72/2.76	15	13.4	

Hot working conditions of these grades must be defined with accuracy because of the very low ductility values, and successive reduction separated by holding times at elevated temperature can be used to improve hot workability.

The comparison of the three grades does not show a significant difference for mechanical properties of Grade A, reinforced by 25% vf SiC particulates and Grade B reinforced by 15% vf SiC particulates.

References

[1] Chai, T. W., Kelly A., and Okura, A. in *Composites*, Vol. 16, No. 3, July 1985, pp. 187–206.
[2] Kohara, S. and Muto, N., in *Recent Advances in Composites in the United States and Japan, ASTM STP 864*, J. R. Vinson and M. Taya, Eds., American Society for Testing and Materials, Philadelphia, 1985, pp. 456–464.
[3] Rocher, J. P., et al., in *Memoires scientifiques de la revue de métallurgie*, Feb. 1986, p. 69.
[4] Noir, S. U., Tien, J. K., and Bates, R. C., *International Metals Reviews*, Vol. 30, No. 6, 1985.

Robert B. Francini[1]

Characterization of Thin-Wall Graphite/Metal Pultruded Tubing

REFERENCE: Francini, R. B., "**Characterization of Thin-Wall Graphite/Metal Pultruded Tubing,**" *Testing Technology of Metal Matrix Composites, ASTM STP 964,* P. R. DiGiovanni and N. R. Adsit, Eds., American Society for Testing and Materials, Philadelphia, 1988, pp. 396–408.

ABSTRACT: The characterization of graphite/metal tubing will be discussed. Both destructive and nondestructive testing will be addressed. Test procedures to be discussed will include nondestructive (ultrasonic) modulus determination, longitudinal tension testing, short column compression testing, the hydrostatic burst (transverse) test, and thin-wall tube torsion test. The test fixtures and techniques used for these tests will be described, and typical test results for pultruded graphite/metal tubing will be presented. The use of these procedures to determine four of the five elastic constants and failure strengths necessary to characterize a transversely isotropic material in plane stress laminate analysis will be also discussed. Directions for future research in the testing area will be presented.

KEY WORDS: metal matrix composites, shear testing, compression testing, tension testing, bursting test

This paper is concerned with the development of suitable testing techniques to obtain tension, compressive, transverse bursting, and torsional test data on longitudinally reinforced graphite/aluminum (Gr/Al) seamless metal matrix composite tubing. Problems unique to the testing of metal matrix composites were encountered in the design of suitable test fixtures and techniques. These are discussed, along with results for P55 and P100 reinforced Gr/Al tubes.

The P55 tube consisted of two plies of P55/6061 precursor wire with an outside diameter of 2.748 cm and wall thickness of 0.122 cm. The P100 tube consisted of two plies of P100/6061 precursor wire with an outside diameter of 2.738 cm and wall thickness of 0.119 cm.

Test Procedures

These test procedures were developed in order to be able to test thin-walled graphite aluminum composite tubes whose diameters are too small to obtain straight sided specimens. By far the most difficult design problem was development of suitable grips for room temperature tension testing of Gr/Al tubing. This development is discussed briefly in the next section. Following are descriptions of the testing setups for the different tests listed previously.

[1] Engineer, Material Concepts Inc., Columbus, OH 43204.

Tension Test Grip Development

The tension testing of unidirectional graphite/metal tubing has presented some unique problems. These composites are too delicate to be tested in wedge type v-grips. The low transverse strength of the composite crushes the tube if it is not reinforced on the inside diameter, and, if it is reinforced, the low shear strength causes the grip area to fail prematurely.

A conical wedge-type grip thus was developed (Fig. 1). This allows a more uniform contact area between grip and tube. The inside of the tube in the grips was filled with a rigid material for reinforcement. With this type of fixture, tensile failures were generated. Unfortunately, most of the failures were in the grips, and the tensile strengths obtained were much lower than predicted values or past testing history dictated. The shortcoming of this grip design

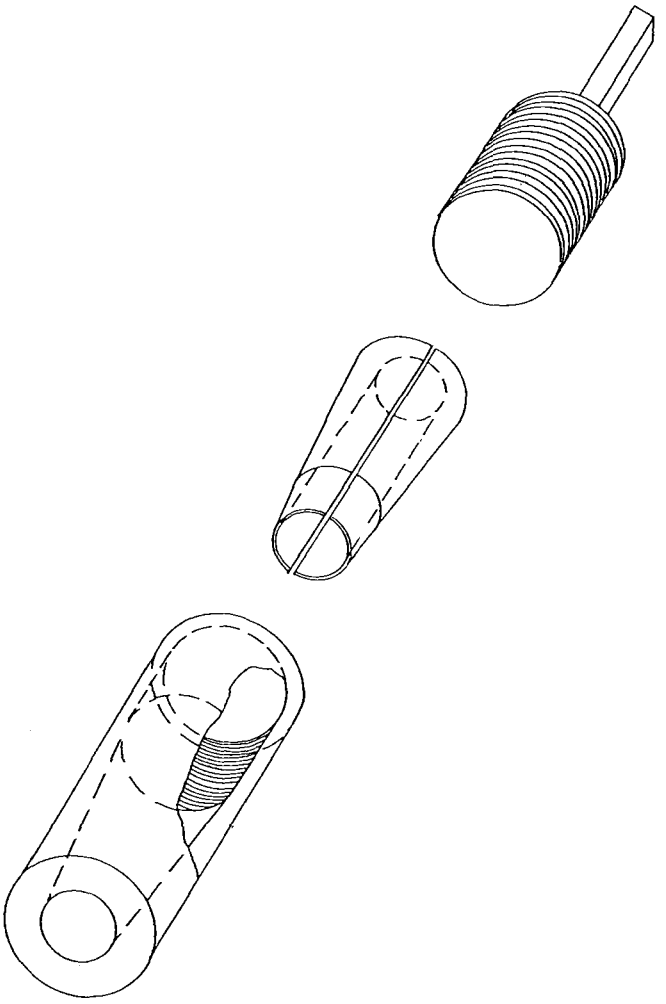

FIG. 1—*Original tension grip design.*

is that the edge of the inner reinforcement causes a biaxial state of stress in the composite, which, due to the low composite transverse strength, causes failure at lower values than are encountered under uniaxial tension.

The tension grip design used in these studies is shown in Fig. 2. The tube is potted into the grip using a high viscosity epoxy. There is no reinforcement on the inside and the slits in the grip allow the tube to strain radially. This puts almost no transverse stress on the tube, with the resulting stress being uniaxial.

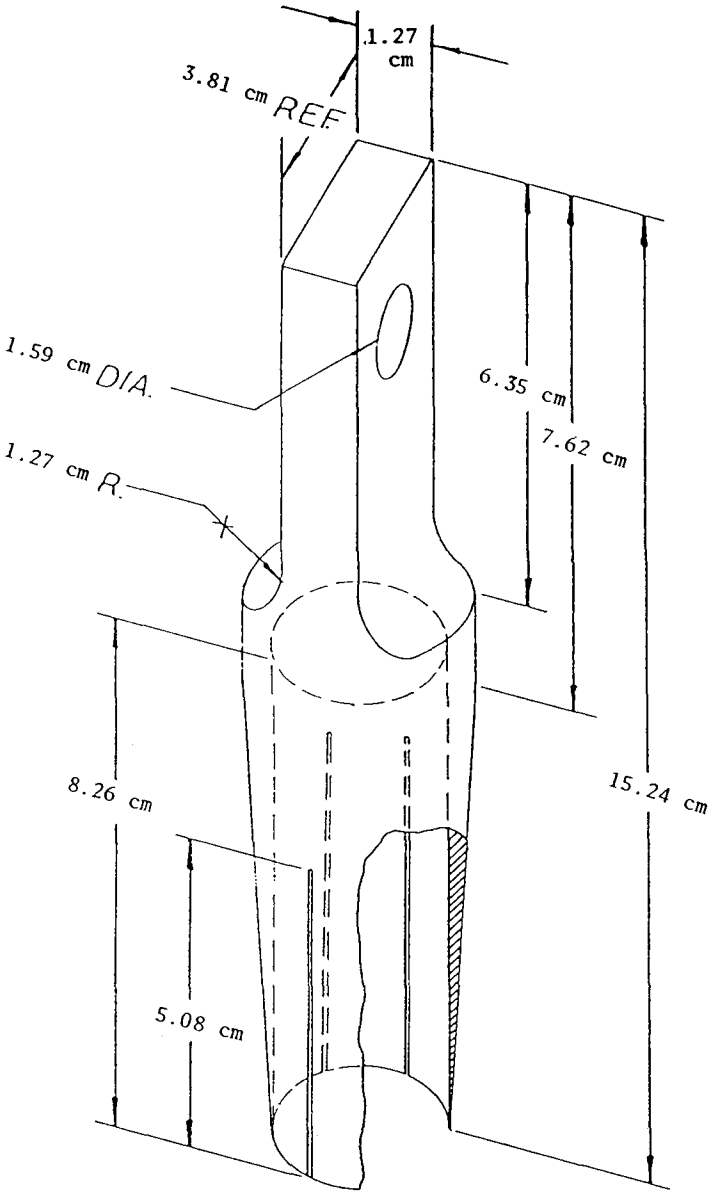

FIG. 2—*Tube tension grips.*

Tension Test Configuration

The setup for a typical tension test is shown in Fig. 3. At least 0.076 m of each end of a 0.25-m tube are sanded and the surface prepared for epoxy bonding. The inside of the grips are similarly prepared. A suitable two-part epoxy is then applied to the inside of the grips, and the prepared outside surface of the tube (Fusor 304 epoxy manufactured by Lord Chemical Products has been successfully used). The tube is then inserted into the grips and any excess epoxy removed with a clean cloth. The epoxy is cured at 49°C for 1 h. When the epoxy has hardened, two two-element 90° "tee" rosette strain gages are bonded to the

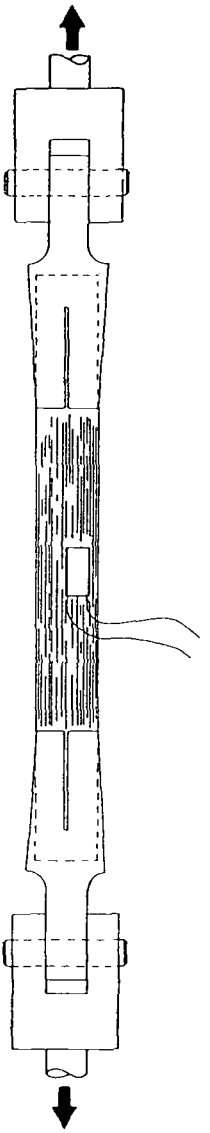

FIG. 3—*Tension test setup.*

surface 180° apart. Micro Measurements CEA-00-125UT-12 gages were used. The axes of the gages are aligned with the geometric axis of the tube. The tube is then placed in a tension tester which has a machined yoke to accept the tensile grips via pin loading. The specimen is loaded to failure with strain measurements taken at fixed intervals, or the load-strain curve is continuously recorded on an *X-Y* recorder.

Compression Test Configuration

The compression test fixture is shown in Fig. 4, and the setup is shown in Fig. 5. The specimen used is 0.089 m long for a 0.025-m-diameter tube with the ends machined flat and parallel to within 2.5×10^{-5} m in order to prevent buckling. The surface of 0.013 m of each end is then prepared for epoxy bonding. A small amount of epoxy is then placed in the hold in each grip, and the tube is inserted. A fixture is necessary to hold the ends of the grips flat and parallel while the epoxy is curing.

When the epoxy has cured, a pair of strain gages are bonded to the tube surface 180° apart along its geometric axis. The tube is then placed in a compressive test machine and loaded to failure with strain gage readings being made at fixed intervals.

Transverse Bursting Test Configuration

The grips used for a transverse test are shown in Fig. 6, and the setup is shown in Fig. 7. One tenth of a meter (0.10 m) on the outside diameter of each end of a 0.31-m-tube is prepared for epoxy bonding. The inside of the grips is prepared similarly. Both the inside of the grips and the end of the tube are coated with epoxy and joined. A uniform coating of epoxy (allowing the tube to be pressurized) is important.

The specimen is strain gaged with either a single element gage perpendicular to the tube axis or a two element 90° "tee" element gage if determination of Poisson's ratio is desired. Micro Measurements CEA-00-125UT-12 is the "tee" element that may be used, and their CEA-00-125UW-12 is the single element.

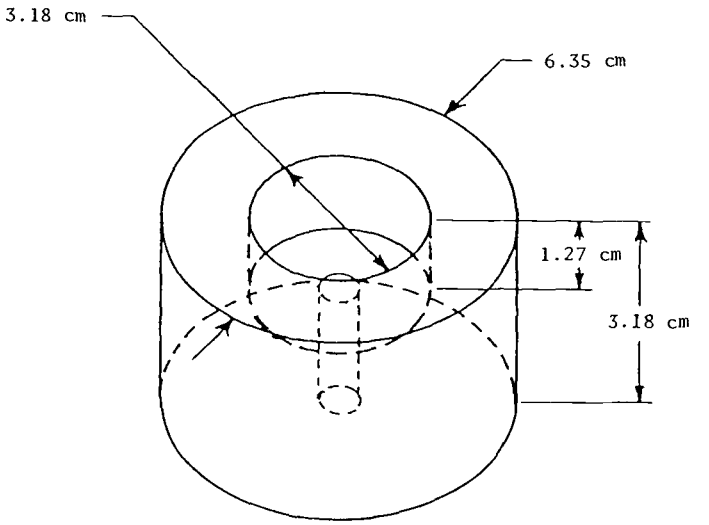

FIG. 4—*Compression grips.*

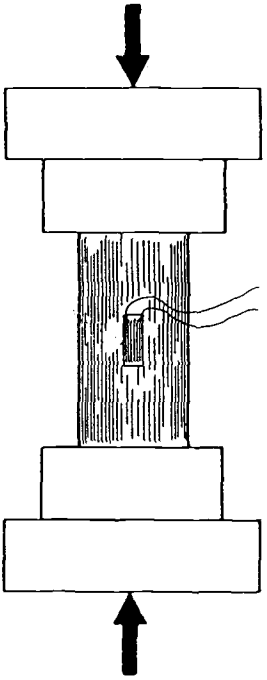

FIG. 5—*Compression test setup.*

The tube is then filled with hydraulic fluid and a pump attached to one of the holding fixtures. A pressure readout is attached in line with the system. The system is pressurized, and strain readings made at fixed pressure intervals until the tube bursts.

Torsion Test Configuration

The grips used for a torsion test are shown in Fig. 8, and the test setup in Fig. 9. A 0.25-m-tube is used for the test. A 0.038-m-area on each end is prepared for bonding with epoxy. The epoxy is smoothed over the prepared ends of the tube and the inside of the grips and the tube slipped into the grips. Any excess epoxy is cleaned off and the epoxy allowed to cure.

Two strain gages are then placed at ±45° to the tube axis and wired to form a shear gage. Micro Measurements CEA-00-125UT-12 strain gages were used. The tube is placed in a standard low-range torsion testing fixture and torqued to failure, with the shear strain being read out at fixed intervals.

Discussion of Results

Table 1 lists the results of the testing of a P55/6061 tube along with the stiffness values predicted by the Halpin-Tsai equations [*1*], while Table 2 lists corresponding values for a P100/6061 tube. At this time there is no similar set of equations for the prediction of strength values.

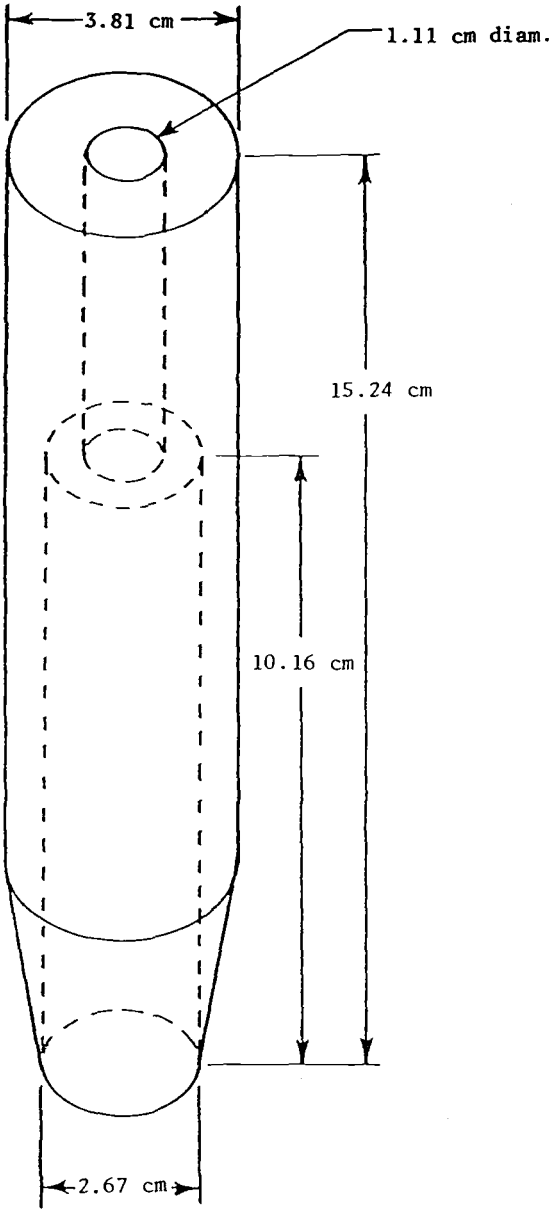

FIG. 6—*Transverse test grips.*

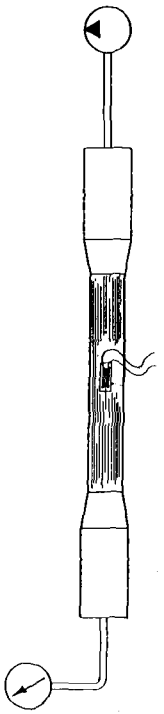

FIG. 7—*Transverse test setup.*

Tension Tests

The data from this test allows calculation of the longitudinal modulus, Poisson's ratio, and the ultimate tensile strength of the tube. Typical results for a P55/6061 tube are shown in Table 1 and for a P100/6061 tube in Table 2.

The results of the longitudinal tension test are 88% of those predicted by the Halpin-Tsai

TABLE 1—*Properties of pultruded P55/6061 GR/AL tube with 39.5 volume percent fiber.*

	Destructive Test Results	Ultrasonically Determined	Halpin-Tsai Prediction
Elastic modulus (longitudinal, tension)	...[a]	148 GPa	191.7 GPa
Ultimate tensile strength (longitudinal, tension)	485.0 MPa	...	...
Elastic modulus (longitudinal, compression)	120.7 GPa	102 GPa	191.7 GPa
Ultimate compressive strength	282.2 MPa	...	...
Elastic modulus (transverse)	37.9 GPa	...	37.2 GPa
Ultimate tensile strength (transverse)	12.4 MPa	...	...
Shear modulus (longitudinal, transverse)	29.6 GPa	...	23.4 GPa
Ultimate shear strength	24.1 MPa	...	...
Poisson's ratio (longitudinal, transverse)	...[a]	...	0.36

[a]Not measured due to strain gage problems.

NOTE—

(*a*) One example per test was performed.

(*b*) The moduli were determined from the initial straight line portion of the stress-strain curve. For elastic modulus (longitudinal tension) and elastic modulus (longitudinal compression) these curves are linear to failure, whereas for elastic modulus (transverse) and shear modulus (longitudinal transverse) they become nonlinear.

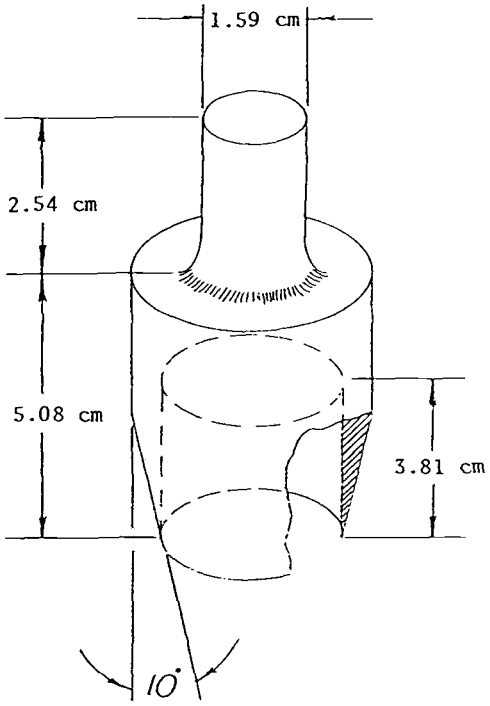

FIG. 8—*Torsion grip.*

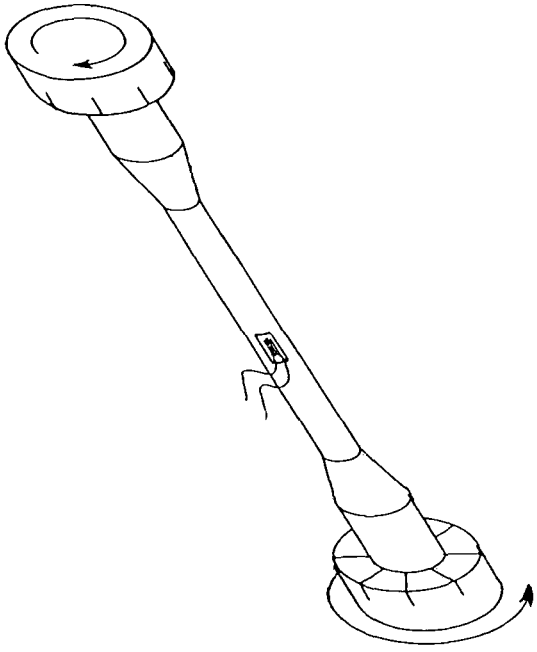

FIG. 9—*Torsion test setup.*

TABLE 2—*Properties of pultruded P100/6061 GR/AL tube with 43.5 volume percent fiber.*

	Destructive Test Results	Ultrasonically Determined	Halpin-Tsai Prediction
Elastic modulus (longitudinal, tension)	300.6 GPa	269 GPa	339.2 GPa
Ultimate tensile strength (longitudinal, tension)	543.0 MPa	...	...
Elastic modulus (longitudinal, compression)	289.6 GPa	170 GPa	339.2 GPa
Ultimate compressive strength	263.6 MPa	...	...
Elastic modulus (transverse)	48.0 GPa	...	35.2 GPa
Ultimate tensile strength (transverse)	13.0 MPa	...	...
Shear modulus (longitudinal, transverse)	11.7 GPa	...	23.4 GPa
Ultimate shear strength	28.3 MPa	...	...
Poisson's ratio (longitudinal, transverse)	0.29	...	0.36

NOTE—
(*a*) One example per test was performed.
(*b*) The moduli were determined from the initial straight line portion of the stress-strain curve. For elastic modulus (longitudinal tension) and elastic modulus (longitudinal compression) these curves are linear to failure, whereas for elastic modulus (transverse) and shear modulus (longitudinal transverse) they become nonlinear.

equation for P100/6061. This is in line with values obtained for other pultruded Gr/Al tubes, with most values falling in the range of 85 to 90% of that predicted by Halpin-Tsai. The strength values for Gr/Al tubing made from either P55 or P100 fiber generally fall into the 482 to 551 MPa range in the as-fabricated condition. Both of the tubes tested fall into this range. The value for Poisson's ratio is 80% of that predicted by the Halpin-Tsai equations.

The tension test is by far the most highly developed test for metal matrix composite tubes. It is used extensively at Material Concepts, Inc. (MCI) in the quality control and development of graphite/metal tubes. As a result of the low scatter of tension results for similarly processed tubes observed in duplicate tests at Material Concepts Inc., it is suggested that this design may be suitable for adoption as the standard for tension testing of these composites in the tubular configuration.

In addition, preliminary investigations were conducted to evaluate the uniformity of the state of stress in the subject grip design. Two tests were performed. In the first, a brittle coating was applied to a tube and the tube incrementally loaded. The cracks that developed in the brittle coating when the coating threshold strength was reached were uniform over the entire gage length. In the second test, the tube was strain gaged at the grips and at the center of the gage section. There was no significant difference in the strain measurements obtained from either gage. Further work in this area is necessary using methods that are more sensitive to a biaxial state of stress in order to establish the uniformity of the stress state in this procedure.

Compressive Tests

The data from this test allows measurement of the longitudinal modulus in compression and tube ultimate compressive strength. Results for P55/6061 and P100/6061 tubes are shown in Tables 1 and 2, respectively.

The low compressive values (relative to tensile) may be attributed to microbuckling of the fiber due to the twist in the tow or shift misalignment of the specimen in the test fixture or both. The modulus determined in compression is close to that obtained for tension test specimens, as would be expected in the absence of bending.

There is considerable room for improvement in this test. Work needs to be performed on the effects of end conditions as well as the optimum tube length to be used. Studies also need to be performed in order to ensure the uniformity of the stress state during the test.

Transverse Bursting Tests

The equation used to convert the pressure to a stress is

$$\sigma = PD/2t$$

where

σ = transverse stress,
P = applied pressure,
D = mean diameter of the tube, and
t = wall thickness of the tube.

With these data, the transverse modulus and the transverse strength of the tube can be measured. Data for P55/6061 and P100/6061 tubes are shown in Tables 1 and 2, respectively.

The transverse modulus results for the P55 specimen were well in line with the Halpin-Tsai predictions. The high results for the P100 tube cannot be explained at the present time, given the small number of tests that have been performed. The low strength values in the transverse direction are typical for Gr/Al, which usually exhibits a range of from 10 to 23 MPa.

Due to the nature of the test, the introduction of a biaxial state of stress is unavoidable, and the effects of this stress state on bursting strength should be studied. The edge effects of the constraint of the grips should be also studied in order to optimize the grip design.

Torsional Tests

The torque is converted to shear stress through the formula

$$\tau = Tr/J$$

where

τ = shear stress,
T = applied torque,
r = mean radius of the tube, and
J = momemt of inertia of the tube.

With these data, the shear modulus and the ultimate shear strength of the tube can be measured. Preliminary results for P55/6061 and P100/6061 tubes are shown in Tables 1 and 2, respectively.

The grips were designed to be accommodated by existing test equipment. There is much room for improvement in this test configuration, particularly with regard to the length and degree of taper in the grips.

The P55 tube is well in line with the Halpin-Tsai prediction for stiffness. The P100 tube is low and was rerun with the same results. One possible explanation for this is that there might have been an area of poor bonding along the length of one side of the tube. The strength results have been rather consistent for the few tests done with metal matrix composite tubes.

Nondestructive Evaluation of Composite Tubes

The complete destructive testing of a composite tube is time consuming and requires a large amount of material. This, combined with the fact that many of the defects found in composites can be highly localized, makes the development of nondestructive testing and evaluation procedures of paramount importance in the field of metal matrix composites.

The ability to accurately determine the longitudinal modulus of a tube using ultrasonics has been already shown [*2*]. This technique requires access to the ends of the tube and is only suitable for the determination of the longitudinal modulus. This method gives an average stiffness value. Work is also being done on the development of contactless electromagnetic methods for the ultrasonic evaluation of metal matrix composites [*3*]. This method allows for the measurement of both the longitudinal and transverse moduli both over local areas and average values for the whole tube. A suitable method does not exist at present to accurately determine the shear modulus of metal matrix tubes.

The nondestructive procedure used for the longitudinal moduli in Tables 1 and 2 is that described previously. The procedure is as follows: a sending transducer is placed at one end of the tube and a receiving transducer at the other end. The time delay of the first arrival signal is then measured. This value is used with the length of the tube to obtain a velocity which, if the distance is sufficiently short, will be a phase velocity. This, in conjunction with the density and Poisson's ratio for the composite (usually assumed to be 0.30), allows a good estimate of the longitudinal modulus.

Methods for the nondestructive evaluation for strength are not as straightforward as those for the determination of stiffness. Correlation of stress wave factor with the tensile strength of flat graphite/polyimide composites has been studied [*4*]. Recent work has extended this method into the frequency domain, and it is logical to assume that these methods can be extended to metal matrix composites.

Conclusions

As mentioned previously, there is much room for improvement in the development of testing procedures for graphite/metal composite tubing. Particular attention is needed to develop acceptable procedures for burst and torsion testing. Based on experience with the longitudinal test procedures described, it is recommended that this test be considered as a standard. The compression test described has been used many times. However, information needs to be obtained as to the nature of the end constraints and their effect on test results.

The development of testing for graphite/metal tubes is important in two areas. First, it serves to develop a data base that may be used by designers for the utilization of composite tubing in structures. Second, it is necessary to check the accuracy and reliability of nondestructive evaluation procedures on these composite materials.

It is apparent that although much work has been done in the area of the nondestructive evaluation of metal matrix composites, there are still many areas where research would be beneficial.

References

[*1*] Jones, R. M., "Mechanics of Composite Materials," McGraw-Hill, New York, 1975, p. 114.
[*2*] "Metal Matrix Composites for Naval Systems," Foltz, J. V. and Bertram, A. L., Eds., MP 84-108, Naval Surface Weapons Center, April 1984.

[3] Reed, R. W., "Development of Non-Contact Ultrasonic Nondestructive Evaluation Methods for Metal Matrix Composites," United Technologies Research Center Interim Technical Report, 18 June 1985.

[4] Bowles, V. J. and Vary, A., "Ultrasonic Evaluation of the Strength of Unidirectional Graphite-Polyimide Composites," NASA TM X-73646, National Aeronautics and Space Administration, Washington, DC, April 1977.

T. Kyono,[1] *I. W. Hall,*[2] *and M. Taya*[3]

On the Longitudinal and Transverse Tensile Strength and Work of Fracture of a Continuous Fiber Metal Matrix Composite Subjected to Thermal Exposure

REFERENCE: Kyono, T., Hall, I. W., and Taya, M., **"On the Longitudinal and Transverse Tensile Strength and Work of Fracture of a Continuous Fiber Metal Matrix Composite Subjected to Thermal Exposure,"** *Testing Technology of Metal Matrix Composites, ASTM STP 964,* P. R. DiGiovanni and N. R. Adsit, Eds., American Society for Testing and Materials, Philadelphia, 1988, pp. 409–431.

ABSTRACT: The mechanical properties of many metal matrix composites are known to be degraded when the metal matrix composite is subjected to thermal exposure. We have studied the effect of thermal exposure on the mechanical properties, namely, longitudinal and transverse strength and work of fracture of a boron fiber reinforced 1100 aluminum composite. It is found in this study that as the thermal exposure time increases, the longitudinal strength and work of fracture decrease, whereas the transverse strength increases slightly. The above experimental results are explained by analytical models, with reasonably good agreement between the experimental and analytical results.

KEY WORDS: longitudinal strength, transverse strength, work of fracture, thermal exposure, interface reaction

Metal matrix composites (MMCs) are superior to polymer matrix composites in demanding environments, particularly at elevated temperature. Thus, the maintenance of undegraded mechanical properties in a MMC that undergoes temperature excursions is vitally important if the MMC is to be used as a high-temperature material. Temperature excursions include not only the thermal loading which the MMC is designed to suffer in use, but also the past thermal history that the MMC has undergone during its fabrication. It is known that temperature excursions affect the condition of the fiber/matrix interface and, thus, the longitudinal strength, σ_{UL}, [*1–7*] of the composite.

DiCarlo [7] recently developed a theoretical model to predict the longitudinal strength of continuous fiber MMCs subjected to isothermal exposure. In DiCarlo's model, the formation of a brittle reaction product at the fiber/matrix interface plays a very important role.

Though the longitudinal strength and stiffness of MMCs have been always focused on as primary properties, the transverse strength, σ_{UT}, as well as toughness of MMCs must be also

[1] Mr. Kyono is on leave from Pioneering R&D Laboratories, Toray Industries, Inc., 2-1, 3-Chome, Sonoyama, Otsu, Shiga 520, Japan.

[2] Associate professor, Department of Mechanical Engineering, University of Delaware, Newark, DE 19716.

[3] Associate professor, Department of Mechanical Engineering, University of Washington, Seattle, WA 98195.

considered to be equally important for some applications. Unfortunately, these properties often conflict with each other.

Several studies have been reported on the transverse properties of MMCs [*1,8–15*]. However, no attempt has been made to formulate a correlation between the transverse tensile properties and the reaction at the fiber/matrix interface at elevated temperature except for the work of Amateau et al. [*15*]. As regards toughness of MMCs, it has been reported [*16–23*] that the concept of stress intensity factor, K_{Ic}, based on linear fracture mechanics, can not be applicable to most composites, particularly continuous fiber composites. Taya and his co-workers [*24–28*] have recently used three-point bending test to measure the work of fracture, γ_F, for various types of MMCs which are as-fabricated [*24–26*] and subjected to isothermal exposure [*27*]. They have also constructed a theoretical model to predict γ_F. A good agreement between experimental, and theoretical γ_F has led them to propose that γ_F can be used as a measure of the toughness of MMCs.

In this paper we will report on the results of the room temperature values of σ_{UL} and σ_{UT} of continuous fiber MMCs that were subjected to exposure to elevated temperature. Based on the previous results of γ_F [*27*] and the present reults of σ_{UL} and σ_{UT}, we will discuss the correlation among these three properties. An attempt is also made to predict the transverse tensile stress-strain curve of the isothermally exposed MMC.

Since the detailed results of γ_F have been described in our previous paper [*27*], only a summary of the case of γ_F will be presented here, outlining the main steps and conclusions of the derivation.

Experimental Procedures

Materials

Boron fiber reinforced 1100 aluminum (B/Al composites), supplied by AVCO Specialty Materials Division, Lowell, Massachusetts, were selected for our study, and two different volume fractions of the fiber, V_f = 0.3 and 0.5, were used. The mechanical properties of boron fiber and 1100 aluminum are given as

Boron fiber

$$d = 1.02 \times 10^{-4}\text{m}$$

$$\sigma_{fu} = 3520 \text{ MPa}$$

$$E_f = 400 \text{ GPa}$$

$$\nu_f = 0.18 \text{ [10]}$$

1100 aluminum

$$\sigma_{mu} = 90 \text{ MPa}$$

$$E_m = 69 \text{ GPa}$$

$$\tau_y = 20 \text{ MPa}$$

$$\nu_m = 0.33$$

1100 aluminum was selected as the matrix metal in order to avoid as far as possible the presence of any second phase or precipitate particles in the matrix which might affect σ_{UL}, σ_{UT}, and γ_F, particularly σ_{UT}, after isothermal exposure. The B/Al composite plates were fabricated by a diffusion bonding method, and two different plies were used, 8 plies for tension tests and 42 plies for three-point bending tests.

Isothermal Exposure

B/Al composite specimens were exposed at 500°C in argon for times, t, of 1, 8, 24, or 72 h. Although 500°C is considerably higher than any conceivable temperature which might be met in service, this temperature was specified because it is known to be sufficient to cause drastic changes in the tensile properties of B/Al composites and should allow rapid formation of reaction products at the fiber/matrix interface.

Tension Tests of Composites

Both longitudinal and transverse tension tests were carried out on as-fabricated as well as isothermally exposed composites. Specimens for longitudinal tests were 152.4 mm long, 12.7 mm wide, and 1.27 mm thick for $V_f = 0.3$ and 0.88 mm thick for $V_f = 0.5$, respectively, and those for transverse tension tests differ only in that they had a width of 25.4 mm. Strain gages were mounted to the middle of the gage length (76.2 mm), and aluminum end tabs were adhesively bonded to each side of the specimen in the grip area. All tests were conducted at room temperature on a standard Instron machine at a strain rate of 6.7×10^{-3} min^{-1}, deduced from the crosshead speed, and data acquisition was by means of an X-Y recorder.

Tension Tests of Fibers

In order to obtain the ultimate tensile strength, σ_{fu}, and Weibull modulus, ω, of isothermally exposed fibers, boron fibers were extracted from the composites with 10% sodium hydroxide (NaOH). Tension tests were conducted on 50 fibers for each isothermally exposed condition by using a standard Instron machine with pneumatic action grips. The fibers were held between papers to prevent breakage in the grips. Tests were conducted at constant crosshead speed and an initial strain rate of 5×10^{-3} min^{-1}. These tests provided data concerning the distribution of fiber strengths, from which the Weibull modulus was computed.

Three-Point Bending Tests

Three-point bending tests were conducted on both as-fabricated and isothermally exposed composites in order to measure γ_F. The configuration of the three-point bending tests and a typical load versus deflection record are shown schematically in Fig. 1. Specimens were 76.2 mm long, 6.10 mm wide, and 6.10 mm thick for $V_f = 0.3$, and 4.06 mm thick for $V_f = 0.5$. The ligament in the center is an isosceles triangle, and slits were cut using an 0.864-mm-thick diamond wheel. The slit plane is parallel to the plane of the triangular section. Specimens were mounted in a three-point bending fixture with a span length of 63.5 mm and were loaded to failure by using a standard Instron testing machine at a crosshead speed of 1.27 mm/min. Upon loading, a crack was initiated at the apex of the triangular section and propagated in a well-controlled manner until complete fracture of the specimen. The area under the load, P, versus deflection, δ, curve, which is considered to be equal to the total energy absorbed during the whole fracture process (shaded area in Fig. 1), W_F, was measured: δ is taken to be equal to the displacement of the crosshead. The

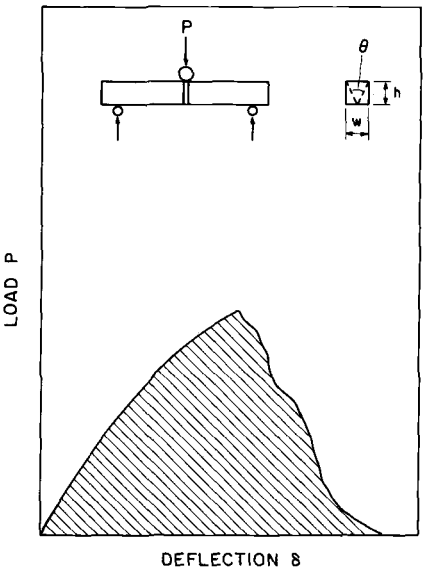

FIG. 1—*Three-point bending test and load,* P, *versus displacement,* δ, *curve used to obtain the fracture energy,* W_F.

work of fracture, γ_F, was computed as $\gamma_F = W_F/2A$, where A is the area of the triangular section. Tests were conducted on three specimens of isothermally exposed composite for each exposure time.

Experimental Results and Discussion

Tension Tests of Composites

The experimental results of the longitudinal, σ_{UL}, and transverse strength, σ_{UT}, are plotted as a function of exposure time, t, in Figs. 2 and 3, respectively, where the open symbols and vertical lines denote the mean values of three tests and the band of scattered data, respectively. It follows from Figs. 2 and 3 that σ_{UL} decreases beyond $t \simeq 8$ h, while σ_{UT} increases gradually with t. In order to find some clues for this observation, we have examined the fracture surfaces of both longitudinally and transversely tested specimens, the scanning electron microscope (SEM) pictures of which are shown in Figs. 4 and 5, respectively, where (*a*), (*b*), and (*c*) denote the fracture surface of samples as-fabricated and exposed at 500°C for 8 and 72 h, respectively. Figure 4 indicates that at longer exposure time the fracture surface tends to be flatter with less fiber pull-out, while Fig. 5 reveals that at longer exposure the mode of fiber splitting is more likely to occur in the transversely tested specimen. This SEM observation indicates that the fiber/matrix bond strength increases at longer exposure time due to the chemical reaction. For the longitudinally tested specimens, circumferential cracks can form in the brittle reaction layer, due to the high tensile stress there along the fiber axis [*28*], resulting in reduced longitudinal strength [*1*]. By contrast, in the transversely tested specimen, the high circumferential stress in the reaction layer can cause a splitting type crack [*28*]. Once the splitting type crack in the reaction layer occurs, it can propagate further into the fiber; consequently, fiber splitting is more likely to occur than interfacial debonding particularly for thermally exposed composites in which interfacial reaction occurs.

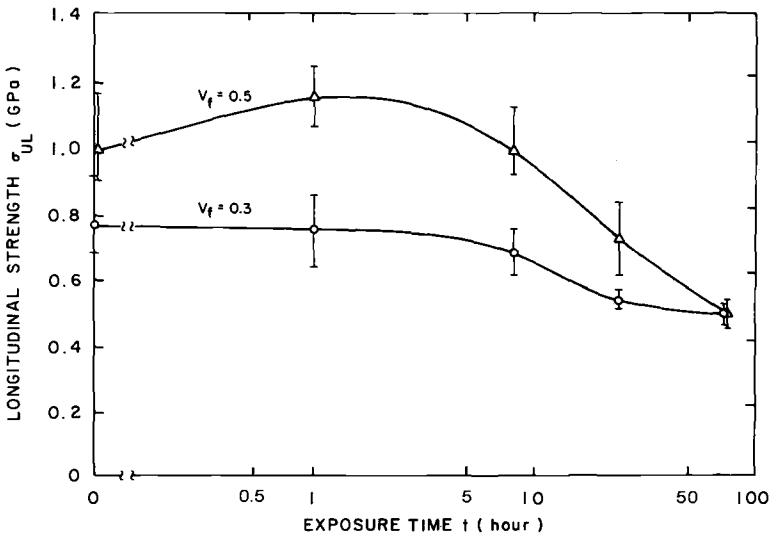

FIG. 2—*Longitudinal strength of thermally exposed B/Al as a function of exposure time* t, *at 500°C.*

Tensile Tests of Fibers

The results of the tension tests on as-fabricated and as-exposed fibers are shown as a solid curve with experimental error band in Fig. 6. As-exposed fibers were extracted from the composites that were subjected to isothermal exposure of T = 500°C. In the same figure the results of fiber strengths predicted by DiCarlo's model [7] are also plotted as a dashed curve. DiCarlo's formula to predict the fiber strength, σ_{fu} (in GPa), is given by

$$\sigma_{fu} = 3.5 \times 10^{-4} t^{-1/4} \exp\left[\frac{7060}{T}\right] \tag{1}$$

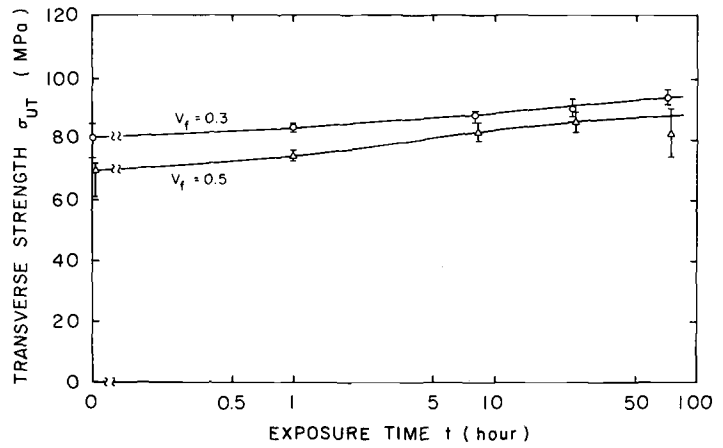

FIG. 3—*Transverse strength of thermally exposed B/Al as a function of exposure time,* t, *at 500°C.*

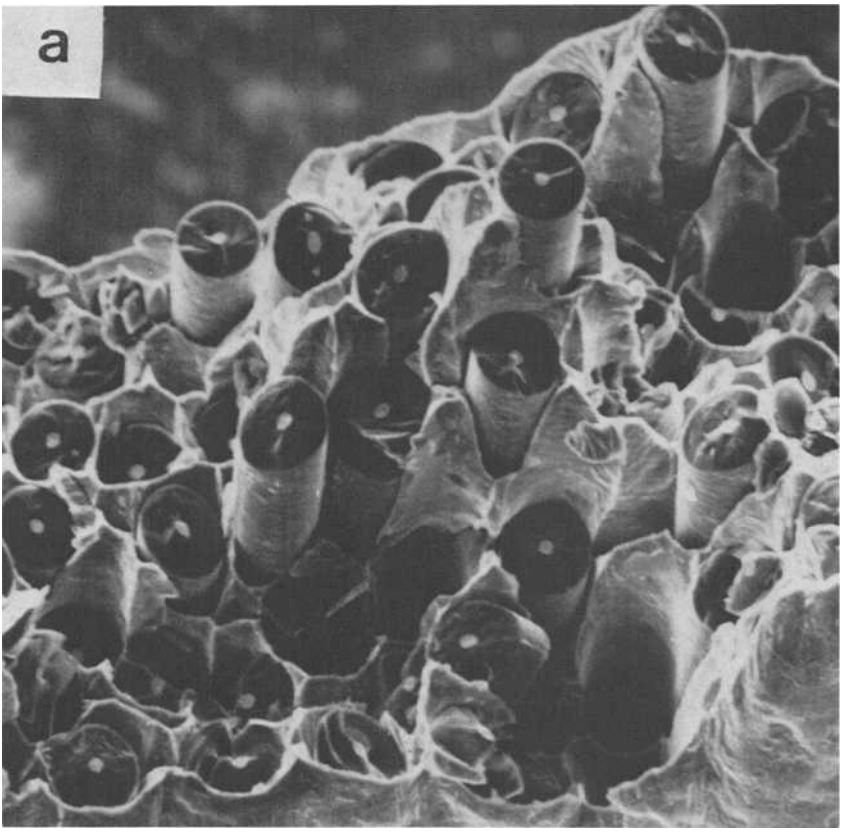

FIG. 4—*SEM photographs of the fracture surfaces of the longitudinally tensile tested B/Al of,* (a) *as-fabricated; exposed at 500°C for* (b) *8 h and* (c) *72 h.*

where

t = exposure time [hour], and
T = exposure temperature [K].

It is clear from Fig. 6 that the fiber strength decreases with increasing exposure time, t, and this can be ascribed to the formation of the fiber/matrix reaction product which has been identified previously as aluminum boride (AlB_2) by X-ray diffraction technique [*1,29*]. However, the reduction in the fiber strength measured as t increases is less than the theoretically predicted value. The discrepancy between the experimental and theoretical results is considered to be partly due to the difference of the interface condition between the present experiment and DiCarlo's idealized experiment [*7*]. The details are described in our recent paper [*27*], but, briefly, it appears that the pre-existing oxide layer on the surface of the aluminum acts as a diffusion barrier and reduces the extent of the reaction.

The SEM photographs of the surfaces of fibers extracted from as-fabricated and as-thermally exposed composites are shown in Fig. 7. No significant differences were observed in surface appearance of fibers from as-fabricated composite or material exposed for times

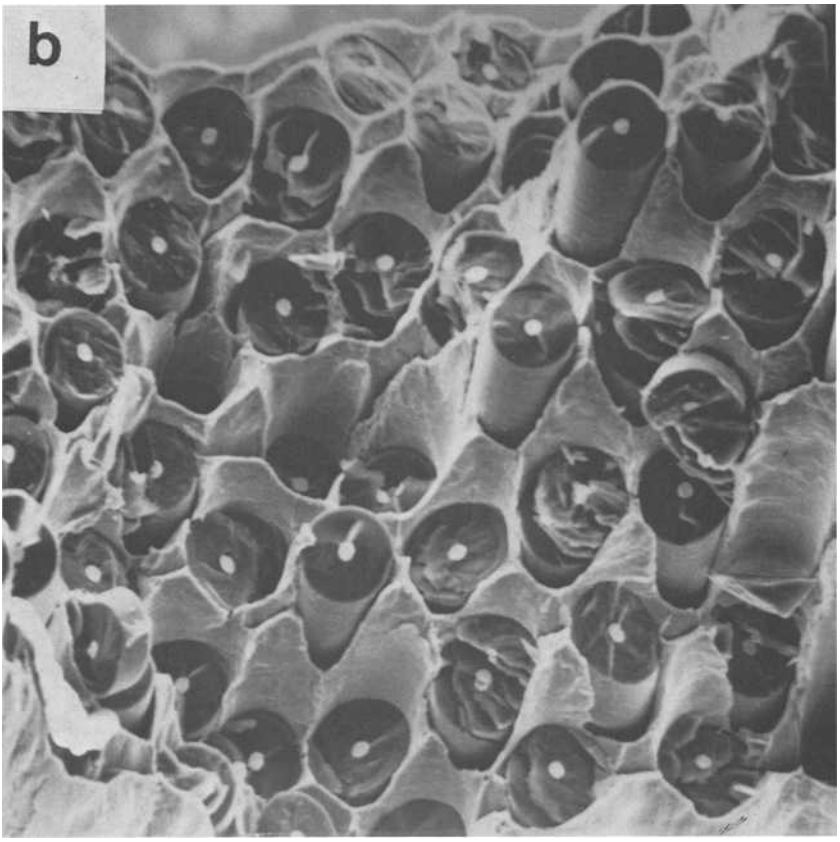

FIG. 4—*Continued.*

up to 8 h. After 24 h exposure, occasional crystals were visible on the surface, and after 72 h the surface was essentially covered with small angular crystals. The strength distribution of the boron fibers is shown in Fig. 8 for $t = 0$ (*a*), 1 (*b*), 8 (*c*), 24 (*d*), and 72 h (*e*). The coefficients of variation in the fiber strength, CV, are close to those of as-received boron fibers used by DiCarlo and Smith [*28*], that is, $CV = 6 \sim 10\%$ except for the value at 1 h exposure.

Work of Fracture, γ_f, by Three-Point Bending Test

The experimentally determined values of γ_F are plotted as open circles in Fig. 9 where (*a*) and (*b*) denote the cases of $V_f = 0.3$ and 0.5, respectively. Figure 9 indicates that the scatter of data is large, particularly at shorter exposure times, and the mean values of γ_F decrease with increasing exposure time, t, except for the data of 1 h exposure. It is noted in Fig. 9 that the volume fraction of fibers, V_f, has some effect on the work of fracture at shorter exposure times, but it diminishes as t increases, which is almost the same trend as for the case of the longitudinal tensile strength of composites (see Fig. 2). Typical fractographs from specimens with $V_f = 0.3$ are shown in Fig. 10 for $t = 1$ h (*a*) and 72 h (*b*). It is seen from Fig. 10 that the fracture surface at $t = 72$ h appears flat indicating a brittle fracture pattern, while in the fracture surface at $t = 1$ h a number of fibers which underwent

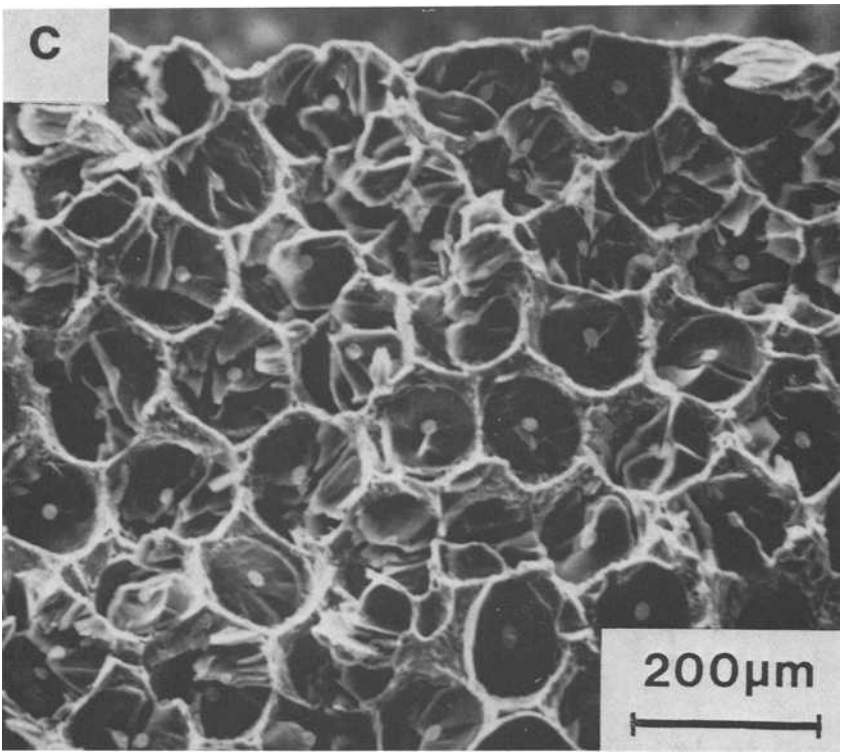

FIG. 4—*Continued.*

extensive pullout are quite visible. These SEM observations are consistent with the values of γ_F measured, that is, the average values of γ_F at $t = 1$ and 72 h are 34.1 and 8.3 kJ/m^2, respectively.

Analytical Models

An attempt is made to construct analytical models to explain the trend of the transverse tensile stress-strain curves and to predict γ_F of B/Al composites.

Model for Transverse Tensile Behavior

The transverse tensile stress-strain curve of B/Al composite indicates two stages, linear and nonlinear stages. In the linear stage the fiber/matrix interface is considered to be perfectly bonded and both matrix and fiber deform elastically under the applied stress, σ_{ij}^0. However, the slopes of the linear stage of B/Al composite with different exposure times do not coincide except for the initial part of the linear stage. Thus, we speculate that in the thermally exposed specimen some of boron fibers were not well bonded to the matrix even in the linear stage of the stress-strain curve. In the nonlinear stage, several possible micromechanical modes of deformation can be considered, for example, plastic deformation in the matrix and the debonding of the fiber/matrix interface.

Based on the previous discussion, we have constructed two models to simulate the behavior

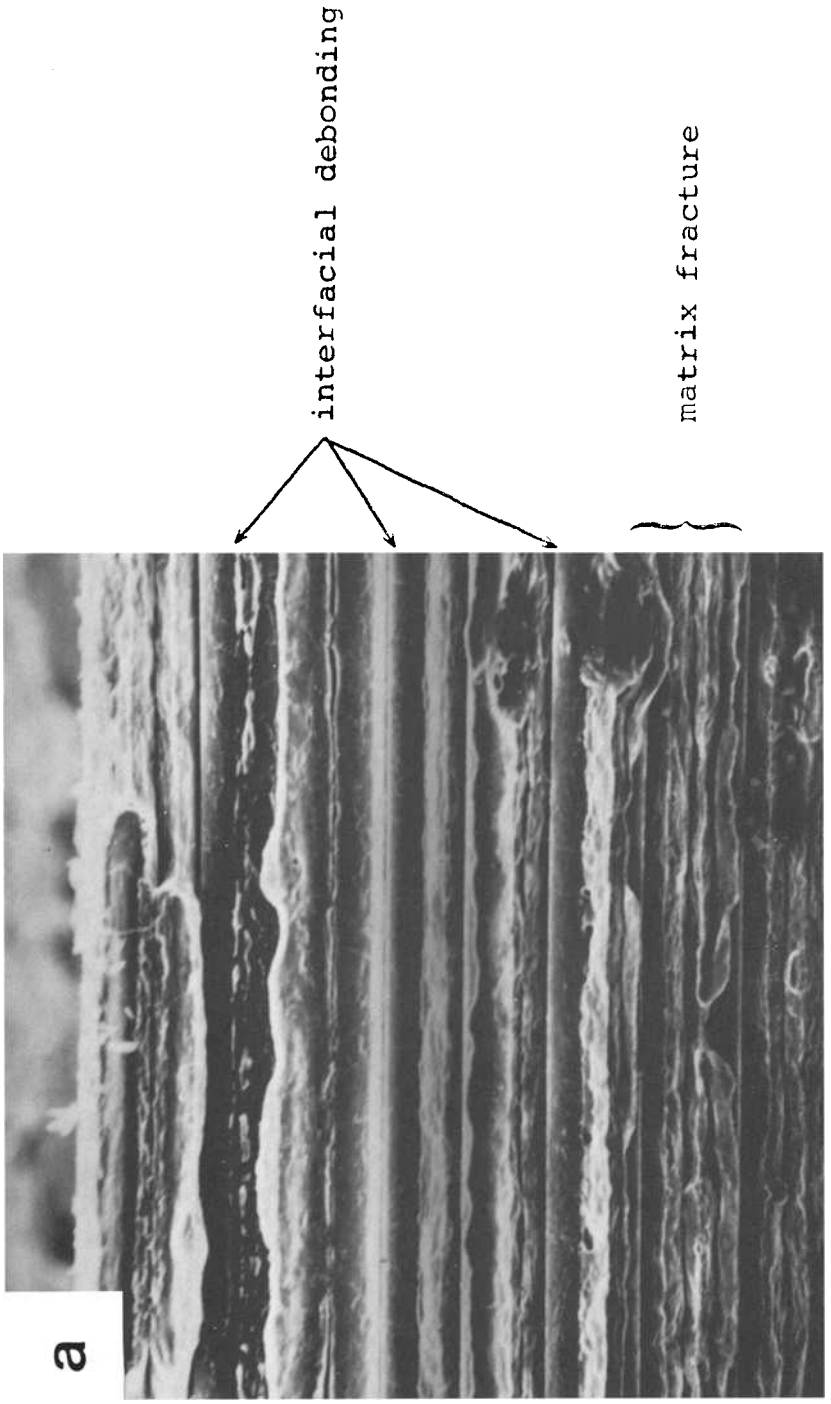

FIG. 5—*SEM photographs of the fracture surface of the transversely tensile tested B/Al* (a) *as-fabricated; exposed at 500°C for* (b) *8 h and* (c) *72 h.*

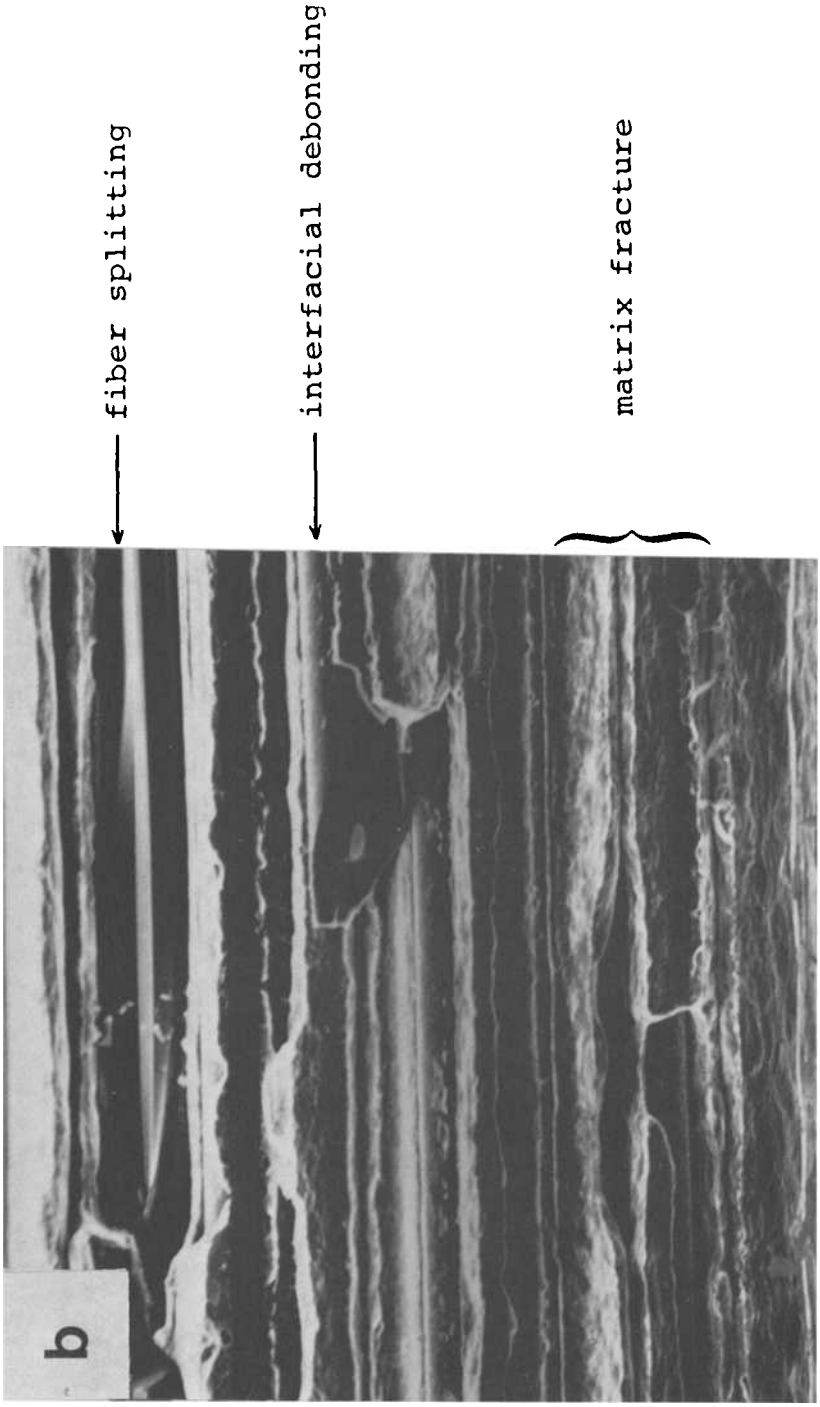

FIG. 5—*Continued.*

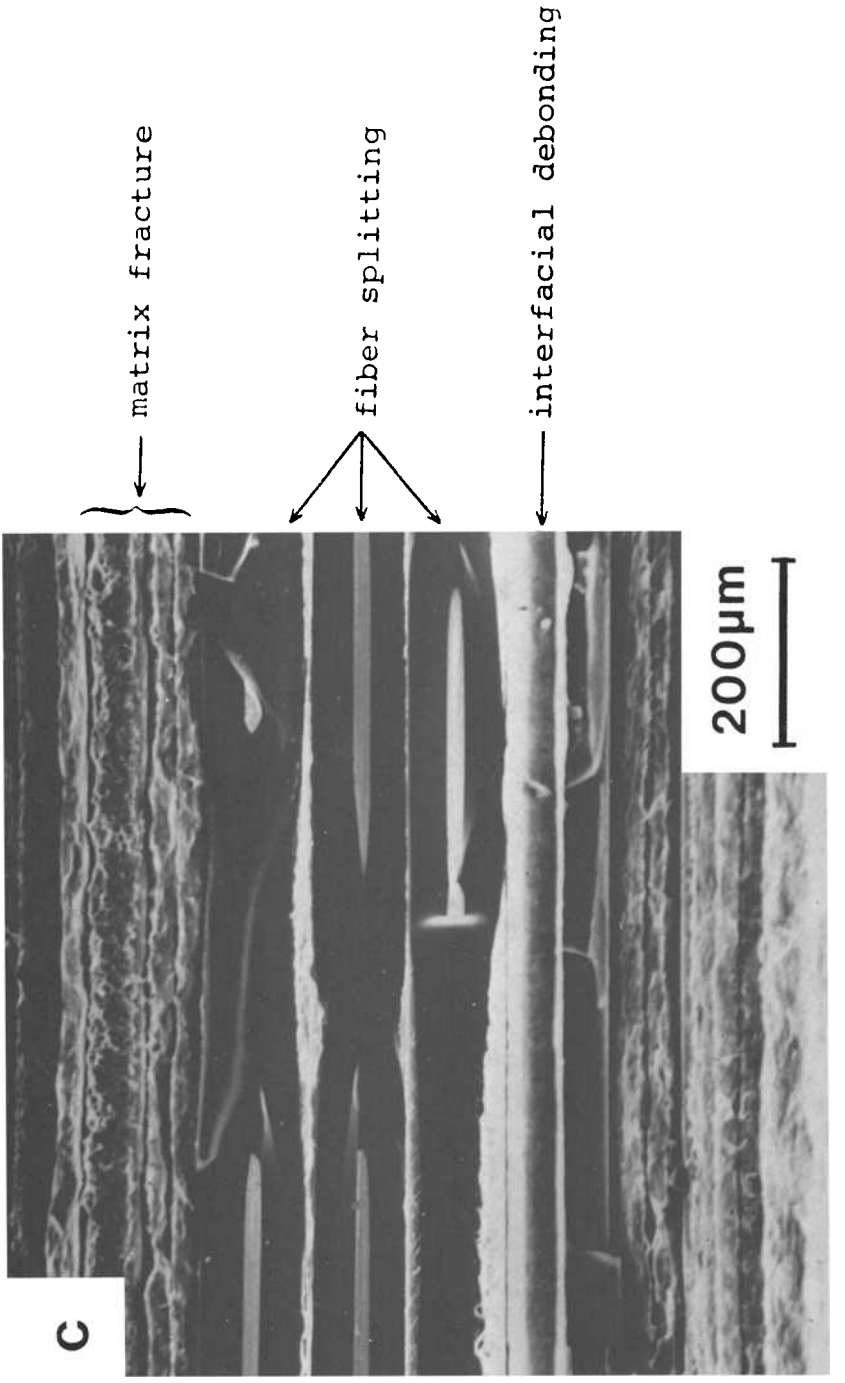

FIG. 5—*Continued.*

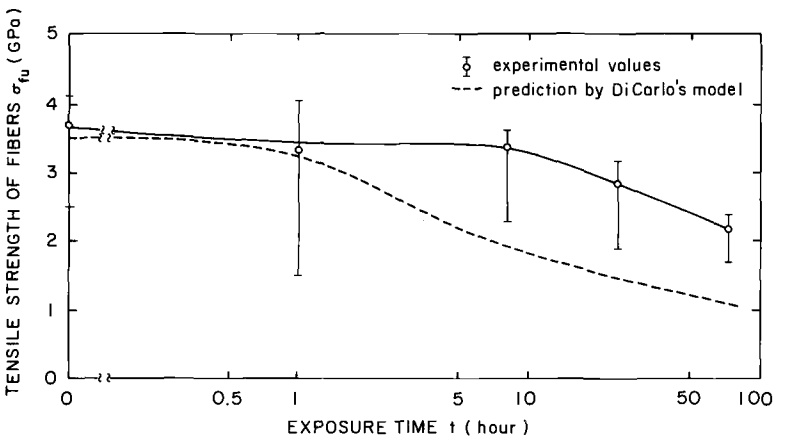

FIG. 6—*Tensile strength, σ_{fu}, of boron fibers extracted from as-fabricated and thermally exposed composite.*

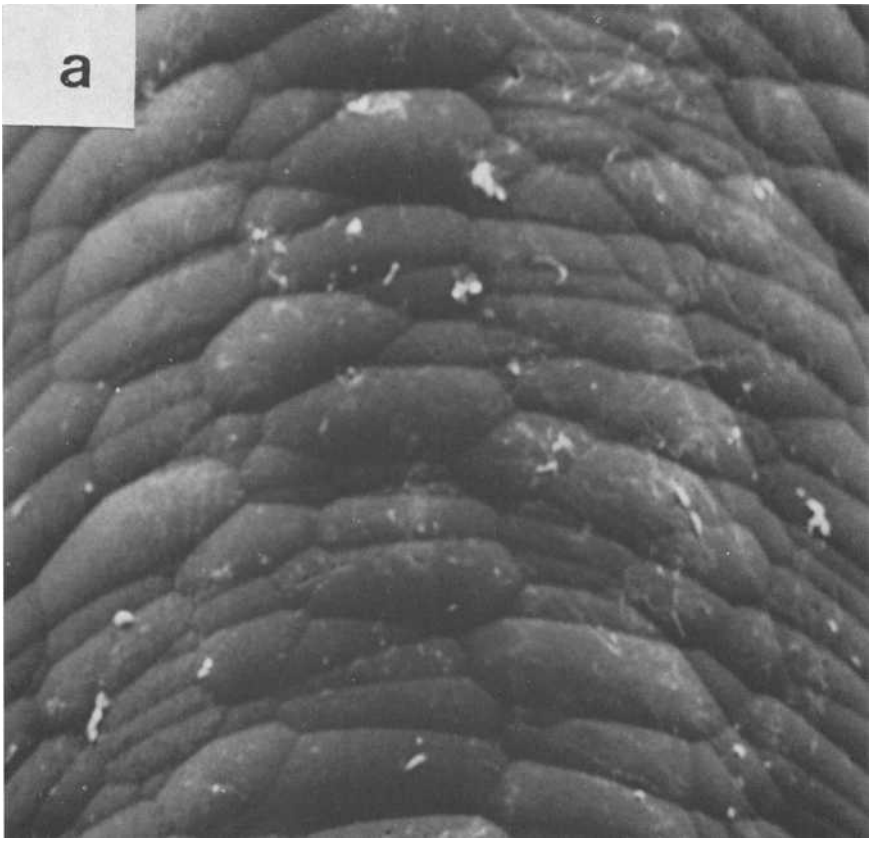

FIG. 7—*SEM photographs of the surfaces of the boron fibers extracted from the composite* (a) *as-fabricated and* (b) *72 h.*

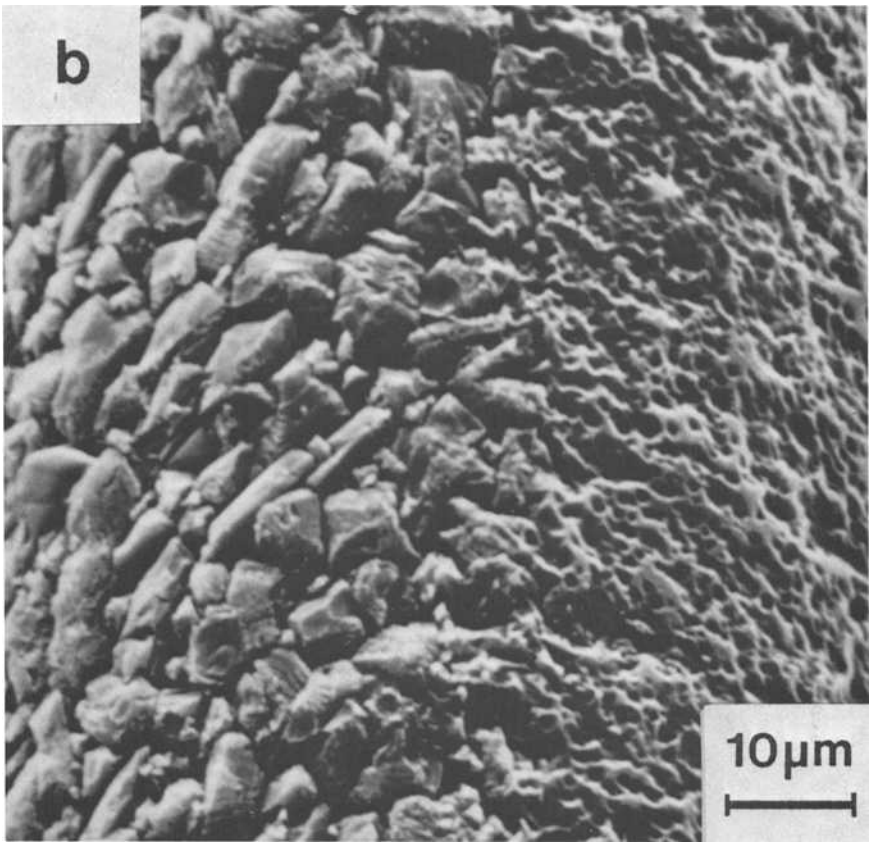

FIG. 7—*Continued.*

of the transverse tensile stress-strain curve. Figures 11 and 12 are the analytical model for the linear stage and nonlinear stage, respectively, where the fiber axes are taken along the X_3-axis. In the linear stage model, both the matrix and fibers (shaded in Fig. 11) are assumed to deform elastically, while it is assumed in the nonlinear stage model (Fig. 12) that the fibers deform elastically but the matrix deforms plastically with uniform plastic strain (ϵ, $-\epsilon/2$, $-\epsilon/2$) [*31,32*]. In both models, Eshelby's equivalent inclusion method will be applied [*33*]. Semi-detailed description of these two models will be given next.

In the linear stage model (Fig. 11) two different types of inhomogeneities are considered to be embedded in an infinite matrix, that is, perfectly bonded fibers, Ω_A, and debonded fibers, Ω_B. Thus, the system of Fig. 11 can be considered as a hybrid composite. A general formulation for hybrid composite has been given by Taya and Chou [*34*] and the method of treating the debonded fiber within the framework of Eshelby's method has been also discussed [*35,36*]. Moreover, the general formulation to compute the effective stiffness of a composite is well documented by Mura [*37*]. Thus, the remaining task in modelling is to assume the volume fraction of the debonded fibers, f_B. f_B is considered to increase with the applied stress σ_{ij}^0. However, the relation between f_B and σ_{ij}^0 is difficult to find.

As to the nonlinear stage model (Fig. 12), most of the formulations used for the linear stage model are also applicable to this model. As far as the computation of the total potential

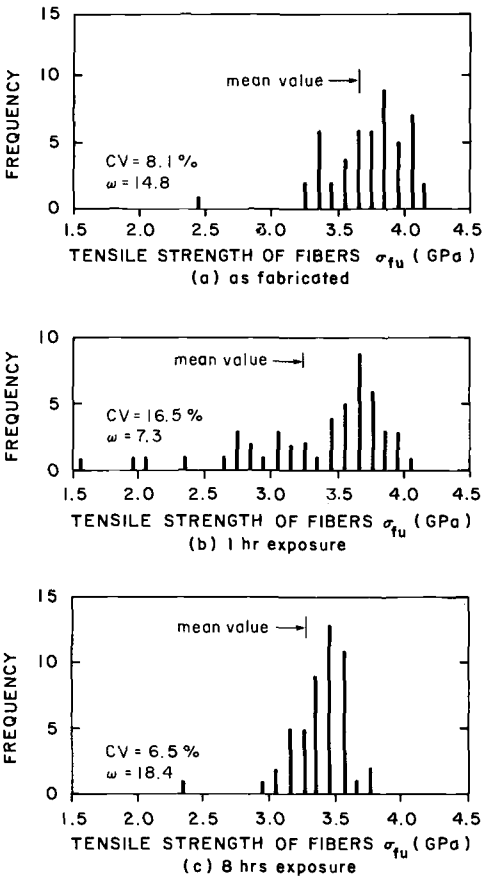

FIG. 8—*Strength distribution of boron fibers extracted from composite* (a) *in as-fabricated condition and exposed to 500°C for,* (b) *1 h,* (c) *8 h,* (d) *24 h, and* (e) *72 h. The total number of fibers tested in each condition is 50. (CV is the coefficient of variation and ω is Weibull modulus).*

energy and the inter stress field in the composite are concerned, the model of Fig. 12 is equivalent to the model in which the plastic strain with opposite sign is prescribed in the fibers and the matrix remains elastic under the applied stress, σ_{ij}^0 [*32*]. In introducing the concept of debonded fibers in a plastically deforming matrix, we encounter the same dilemma as in the linear stage model, that is, the determination of the volume fraction of debonded fibers, f_B. This will be discussed in the next section. We have also attempted to predict the stength of the transversely tested composite, σ_{UT}, by the present model. The key criterion to predict σ_{UT} is to set the average matrix stress along the x_1-axis, (loading direction, see Fig. 12) equal to the breaking stress of the matrix, σ_{mu}.

Comparison Between the Experimental and Analytical Results of the Transverse Stress-strain Curve

The experimental results of the stress-strain curves that were obtained by transverse tension tests conducted on B/Al composites as-fabricated and thermally exposed for several

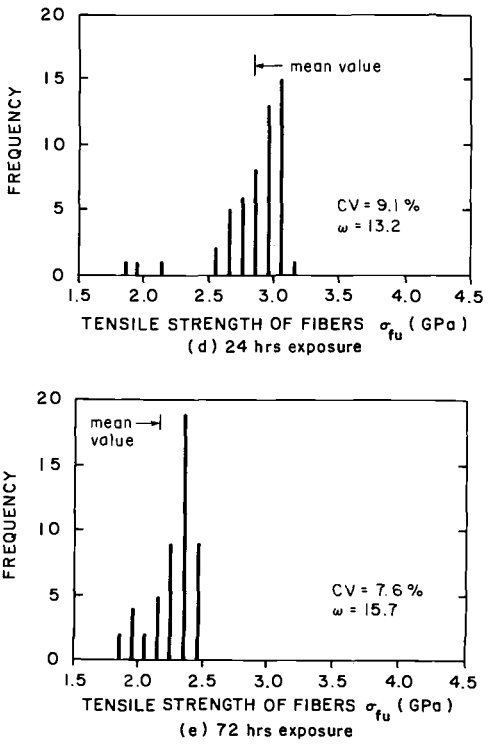

FIG. 8—*Continued.*

time durations, are shown as solid curves with open symbols in Fig. 13, where (*a*) and (*b*) denote the case of $V_f = 0.3$ and 0.5, respectively. In the same figures the analytical results of two cases, the case of perfectly bonded fibers ($f_A = V_f$, $f_B = 0$) and that of completely debonded fibers ($f_A = 0$, $f_B = V_f$) are plotted by thick solid lines. Also the transverse Young's modulus, E_l, of B/Al with perfectly bonded fibers is predicted by the present model, and the results are plotted as dash-dot lines in Fig. 13.

It follows from Fig. 13 that the experimental results are bounded by the analytical ones, and a good agreement between the experimental and analytical E_l is obtained. In order to simulate the nonlinear section of the stress-strain curve, we have attempted to compute the nonlinear stages for a number of f_B, $0 \leqq f_B \leqq 0.3$ in the case of $V_f = 0.3$ by using the stress criterion of the average matrix stress discussed in the preceding section. The results are plotted in Fig. 14 where the matrix breaking stress $\sigma_{mu} = 90$ MPa was used. Due to limited number of different values of f_B taken, the nonlinear stage of the stress-strain curve becomes zigzag path in the figure. In reality, f_B changes continuously from $f_B = 0$ to a certain value which is equal to or less than $f_B = 0.3$ (for example, Fig. 14 shows the case in which the composite fractures at $f_B = 0.24$); thus, the corresponding path should become smooth (shown as a dashed curve in Fig. 14).

In this fracture criterion the matrix breaking stress, σ_{mu}, plays an important role. To be precise, we should consider the dependence of σ_{mu} on the temperature, T, and the exposure time, t, and the effect of fiber splitting. However, we have not used either such a precise value of σ_{mu} or the fiber splitting stress in this model. Another important point to improve the present model is to identify some relationship between the applied stress (or strain) and

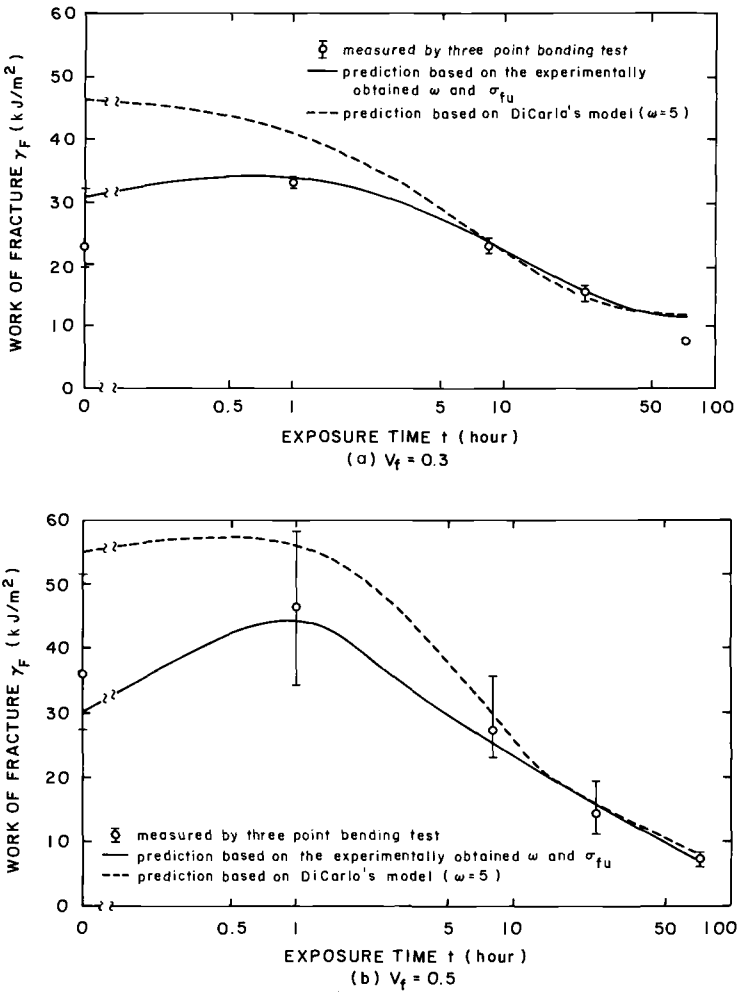

FIG. 9—*Work of fracture,* γ_F, *as a function of exposure time,* t, *for* V_F = *0.3* (a) *and 0.5* (b).

the volume fraction of debonded fibers, f_B. With this relationship, the nonlinear part of the stress-strain curve will become smooth.

Work of Fracture

Analytical Formulation

The analytical model was developed by Taya et al. [*24–28*] for both short and continuous fiber MMCs and modified by Kyono et al. [*27*] to account for the effects of thermal exposure. We will only present a brief summary of the analytical model next.

It was found [*24*] that three mechanisms can contribute to the total fracture energy, W_F, of a three-point bending test specimen with a triangular ligament; namely, elastic strain energy, plastic work along the matrix-fiber interface, and fiber pullout energy. In the for-

mulae describing these three contributions, the fiber ultimate tensile strength, σ_{fu} (hereafter referred to as fiber strength), plays an important role, and σ_{fu} is strongly dependent on the thermal exposure temperature, T, and exposure time, t, which was shown in Eq 1.

The formula to predict γ_F is given by

$$\gamma_F = \frac{1}{2}\left\{\frac{2\pi(1 - \bar{\nu}^2)\bar{\sigma}^2 a_f}{3\bar{E}}(1 + \alpha + \beta) + (1 - \eta)^3 \frac{dV_f\sigma_{fu}^2}{24\tau_y}\right\} \quad (2)$$

where

$$\alpha = \frac{2(1 - \eta)(\sigma_{fu} + \sigma^* - 2\sigma_f)(\sigma_{fu} + \sigma^*)\bar{E}}{\pi\bar{\sigma}^2 E_m}\left\{\frac{4}{5}\left(\frac{\bar{\sigma}}{\sigma_{fu} + \sigma^*}\right)\sqrt{\frac{a_0}{a_f}} - \frac{1}{2\pi}\left(\frac{d}{a_f}\right)\right\} \quad (3)$$

$$\beta = \frac{8\eta(\sigma_{fu} - \sigma_f)\sigma_{fu}\bar{E}}{\pi\bar{\sigma}^2 E_m}\left\{\frac{2}{5}\left(\frac{\bar{\sigma}}{\sigma_{fu}}\right)\sqrt{\frac{a_0}{a_f}} - \frac{1}{2\pi}\left(\frac{d}{a_f}\right)\right\} \quad (4)$$

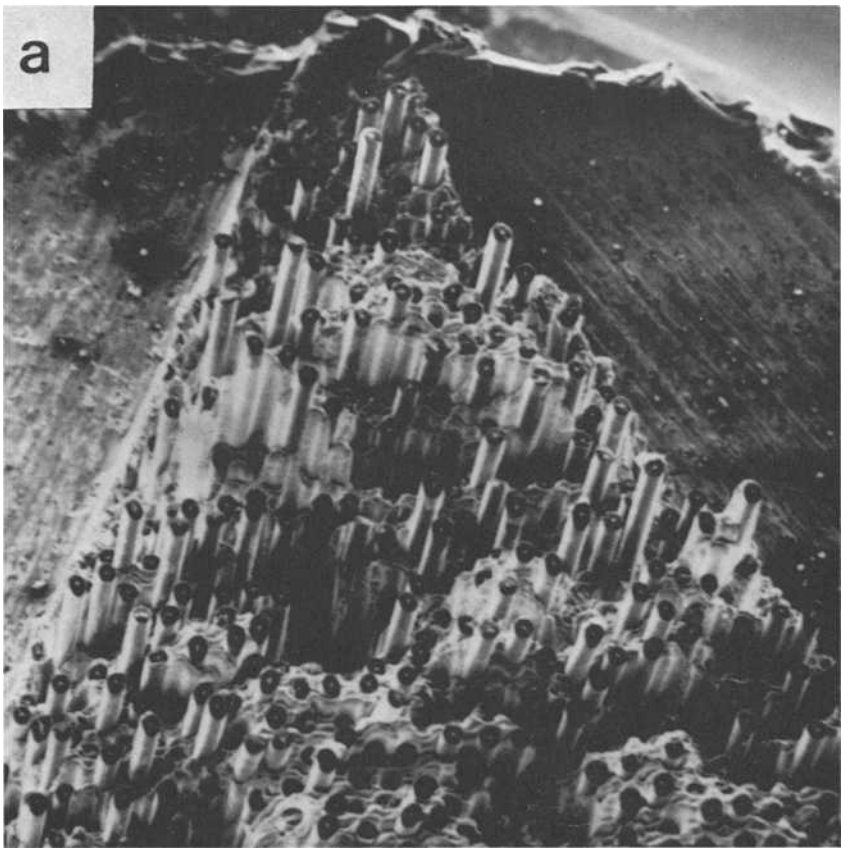

FIG. 10—*SEM photographs of the fracture surfaces by three point bending test of composite exposed at 500°C,* (a) *for 1 h and* (b) *72 h.*

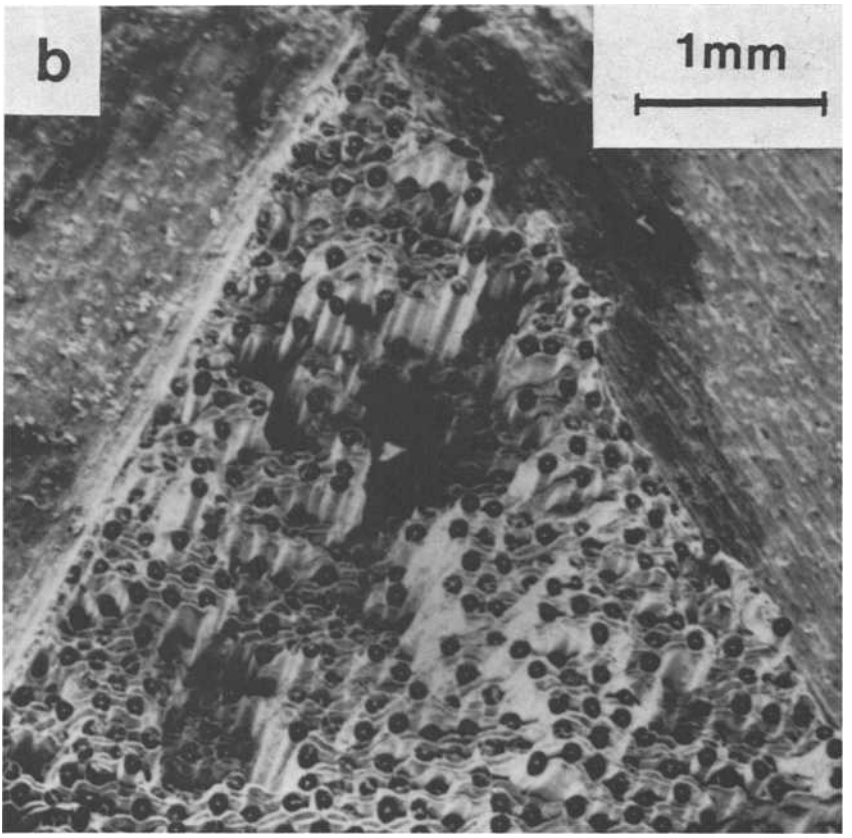

FIG. 10—*Continued.*

In the derivation of Eqs 2, 3, and 4 we have used

$$\overline{E} = V_m E_m + V_f E_f$$

$$\overline{\sigma} = V_m \sigma_m + V_f \sigma_f \tag{5}$$

$$\overline{\nu} = V_m \nu_m + V_f \nu_f$$

where

V_i = volume fraction of the i-phase ($i = m$ and f),
E_i = Young's modulus of the i-phase ($i = m$ and f),
$\overline{\sigma}$ = breaking stress of the composite, and
σ_i = average stress of the i-phase ($i = m$ and f) defined by

$$\sigma_m = \overline{\sigma} \frac{E_m}{\overline{E}} \tag{6}$$

$$\sigma_f = (\overline{\sigma} - V_m \sigma_m)/V_f \tag{7}$$

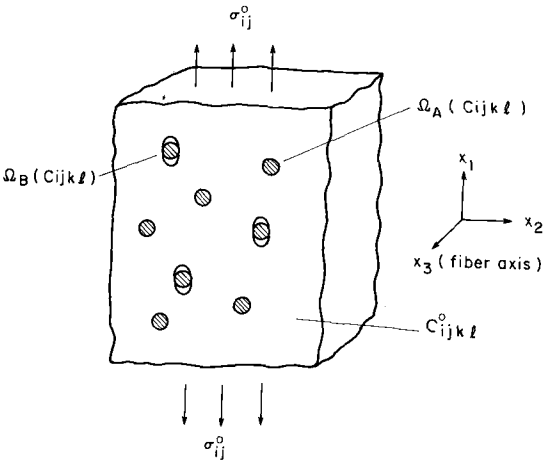

FIG. 11—*Analytical model for the linear stage.*

respectively

ν_i = Poisson's ratio of the i-phase ($i = m$ and f), and
σ^* = the fiber strength at weak points which is set equal to the fiber bundle strength, σ_B, which is related to the Weibull modulus, ω, as [*39*].

$$\sigma_B = \sigma_{fu}\left[\omega^{1/\omega}\exp\left(\frac{1}{\omega}\right)\Gamma\left(1+\frac{1}{\omega}\right)\right]^{-1} \tag{8}$$

where

Γ = Gamma function,
ω = 1.2/CV [*7*],
CV = the coefficient of variation of the distribution of fiber strengths,
η = the ratio of the strength defined by $\eta = \sigma^*/\sigma_{fu}$,
σ_{fu} = fiber ultimate tensile strength obtained by Eq 1 or experimentally, and
a_o = the radius of a penny-shaped crack of initial configuration given by

$$a_o = \frac{1}{2}(b_o - d) \tag{9}$$

where

b_o = average spacing between the centers of fibers for a hexagonal array of fibers
d = fiber diameter, and
a_f = the radius of penny-shaped crack of final configuration given by

$$a_f = \sqrt{\frac{wh}{\theta}} \tag{10}$$

where

w = the width of the specimen, and
h = the thickness of the specimen.

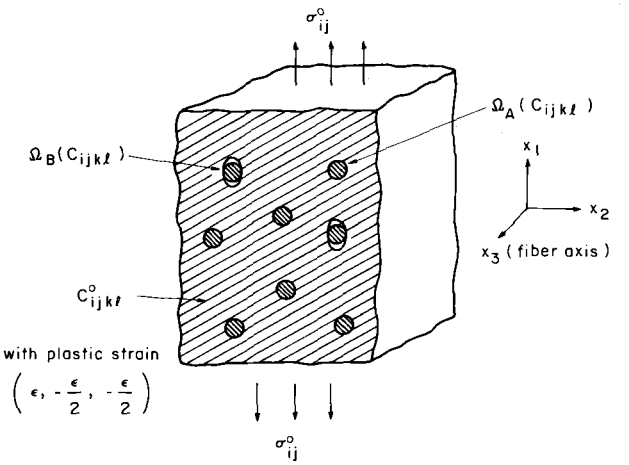

FIG. 12—*Analytical model for the non-linear stage.*

Comparison Between Experimental and Analytical Results of γ_F

An attempt was made to compare the experimental results for γ_F with analytical ones, and this is summarized in Fig. 9.

In evaluation of γ_F given by Eq 2, the fiber breaking stress, σ_{fu}, and fiber bundle strength, σ_B, play important roles. Thus, we have employed two methods to obtain the value of σ_{fu} and σ_B, which is strongly related to Weibull modulus, ω, that is, one by DiCarlo's model [7] (Eq 1) and the other by the present experiment. In DiCarlo's model ω was set equal to 5, while the present experimental results for σ_{fu} yielded a larger value of ω (see Fig. 6). It is clear from Fig. 9 that the analytical results based on DiCarlo's model tend to overestimate

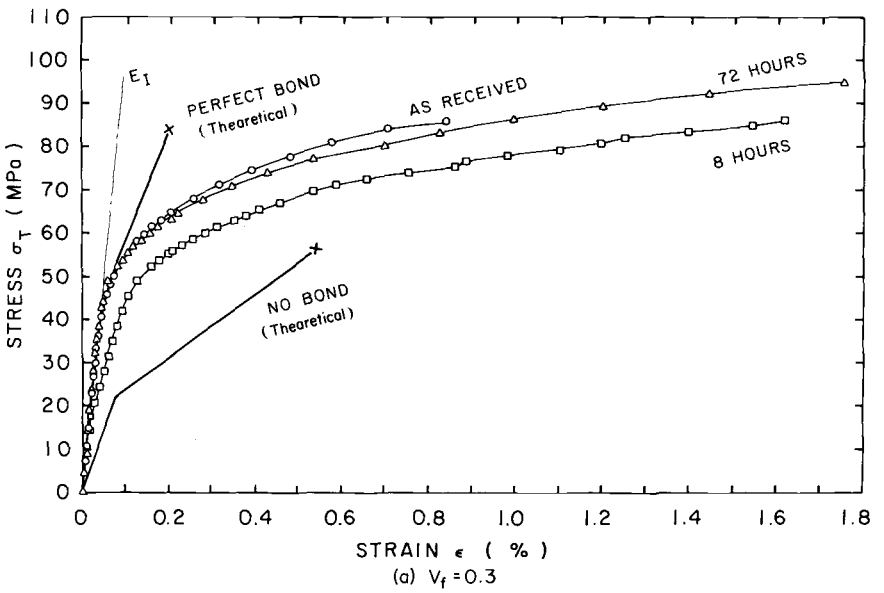

FIG. 13—*Stress-strain curve of transversely tensile tested B/Al.*

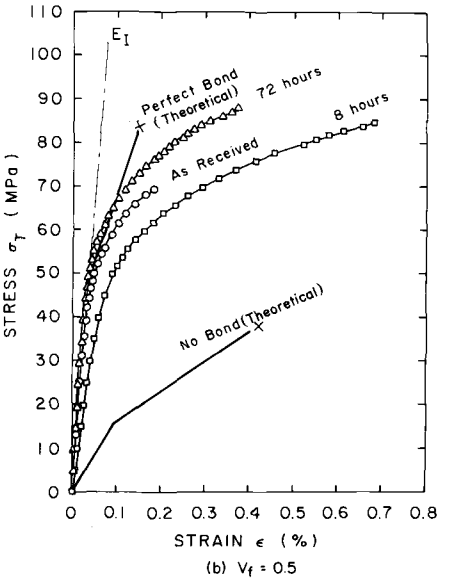

FIG. 13—*Continued.*

γ_F for shorter t but agree well with the experimental ones for larger t, whereas the analytical results based on the experimentally measured σ_{fu} and ω agree well with the experimental ones for the entire range of t. It is noted from the present study that work of fracture is strongly dependent on the distribution of the fiber strength, that is, the mean value of σ_{fu} and Weibull modulus, ω, and also that the fiber pull out tends to increase with V_f.

Conclusion

Three important mechanical properties of continuous fiber MMCs, that is, longitudinal strength, σ_{UL}, transverse strength, σ_{UT}, and work of fracture, γ_F, are studied in this paper.

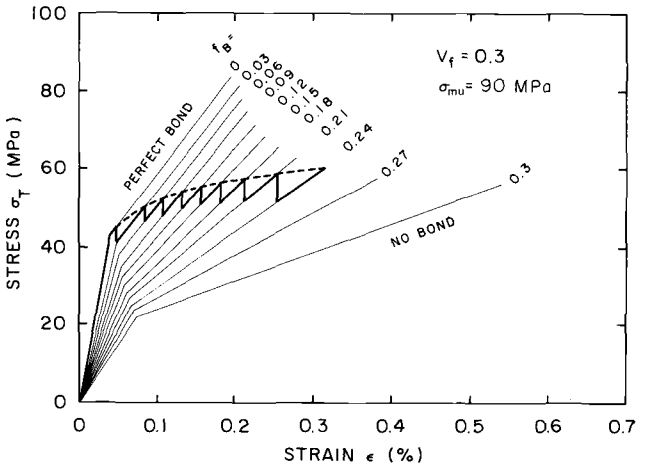

FIG. 14—*Predicted stress-strain curve of B/Al with* $V_t = 0.3$.

Analytical models are also developed to predict σ_{UT} and γ_F. As regards work of fracture, γ_F, a good agreement between the experimental and analytical results was obtained. Though we are successful in explaining the nonlinearity in the transverse tensile stress-strain curve, the model needs to be improved.

Regarding the correlation between three properties, σ_{UL}, σ_{UT}, and γ_F, it can be concluded that as the thermal exposure time at temperature 500°C increases, σ_{UL} and γ_F decreases, but σ_{UT} increases. However, a study on the effect of thermal exposure at lower temperature for example 400°C on the mechanical properties of B/Al composite is recommended for the future.

Acknowledgments

We are grateful to Toray Industries, Inc., Japan for its financial support and to the Center for Composite Materials, University of Delaware, for its partial support; valuable comments from and discussions with Dr. H. Hatta, Mitsubishi Electric Corp., Japan are also appreciated.

References

[1] Metcalfe, A. G. and Klein, M. J., *Interfaces in Metal Matrix Composites, Vol. 1, Composite Materials,* A. G. Metcalfe, Ed., pp. 125–168, Academic Press, New York, 1974.
[2] Klein, M. J. and Metcalfe, A. G., AFML TR-71-189, Air Force Materials Laboratory, 1971.
[3] Klein, M. J. and Metcalfe, A. G., AFML TR-72-226, Air Force Materials Laboratory, 1972.
[4] Wright, M. A. and Intwala, B. D., *Journal of Material Science,* Vol. 8, 1973, pp. 957–963.
[5] Olsen, G. C. and Topkins, S. S., *Failure Modes in Composites IV,* J. A. Cornie and F. W. Crossman, Eds., 1977, pp. 1–21.
[6] Grimes, H. H., Lad, R. A., and Maisel, J. E., *Metallurgical Transactions A.,* Vol. 8A, 1977, pp. 1999–2005.
[7] DiCarlo, J. A., "Mechanical Behavior of Metal-Matrix Composites," J. E. Hack and M. F. Amateau, Eds., The Metallurgical Society of the American Institute of Mining, Metallurgical, and Petroleum Engineers, New York, 1982, pp. 1–14.
[8] Prewo, K. M. and Kreider, K. G., *Metallurgical Transactions,* Vol. 3, 1972, pp. 2201–2211.
[9] Kreider, K. G. and Prewo, K. M., *Composite Materials: Testing and Design (Second Conference) ASTM STP 497,* American Society for Testing and Materials, Philadelphia, 1972, pp. 539–550.
[10] Lin, J. M., Chen, P. E., and DiBenedetto, A. T., *Polymer Engineering Science,* Vol. 11, No. 4, 1971, pp. 344–352.
[11] Adams, D. F. and Doner, D. R., *Journal of Computer Materials,* Vol. 7, 1967, pp. 152–164.
[12] Adams, D. F., *Journal of Composite Materials,* Vol. 4, 1970, pp. 310–328.
[13] Cooper, G. A. and Kelly, A., *Interfaces in Composites, ASTM STP 452,* American Society for Testing and Materials, Philadelphia, 1969, pp. 90–108.
[14] Riggs, D., *New Developments and Applications in Composites,* D. Kuhlman-Wilsdorf and W. C. Harrigan, Eds., TMS-AIME, New York, 1979, pp. 252–260.
[15] Amateau, M. F. and Dull, D. L., *Failure Modes in Composites IV,* J. A. Cornie and F. W. Crossman, Eds., Metallurgical Society of the American Institute of Mining, Metallurgical, and Petroleum Engineers, New York, 1977, pp. 336–358.
[16] Wright, M. A., Welch, D., and Jollay, J., *Journal of Material Science,* Vol. 14, 1979, pp. 1218–1228.
[17] Kanninen, M. F., Rybicki, E. F., and Brinson, H. F., *Composites,* Jan. 1977, pp. 17–22.
[18] Cooper, G. A., *Journal of Material Science,* Vol. 5, 1970, pp. 645–654.
[19] Kelly, A., *Proceedings of the Royal Society,* London, Vol. A319, 1970, pp. 95–116.
[20] Phillips, D. C. and Tetelman, A. S., *Composites,* Sept. 1972, pp. 216–223.
[21] Piggott, M. R., *Journal of Material Science,* Vol. 5, 1970, pp. 669–675.
[22] Wells, J. C. and Beaumont, P. W. R., *Journal of Material Sciences,* Vol. 17, 1982, pp. 397–405.
[23] Wells, J. C. and Beaumont, P. W. R., *Journal of Material Sciences,* Vol. 20, 1985, pp. 1275–1284.
[24] Taya, M. and Daimaru, A., *Journal of Material Science,* Vol. 18, 1983, pp. 3105–3116.
[25] Daimaru, A., *Stiffness, Strength, and Toughness of Metal Matrix Composites: Analytical and Experimental Research,* M.S. thesis, University of Delaware, Newark, June 1984.

[26] Daimaru, A., Hatta, T., and Taya, M., *Recent Advances in Composites in the United States and Japan, ASTM STP 864*, J. R. Vinson and M. Taya, Eds., American Society for Testing and Materials, Philadelphia, 1985, pp. 505–521.
[27] Kyono, T., Hall, I. W., and Taya, M., *Journal of Material Science*, Vol. 21, 1986, pp. 1879–1888.
[28] Mikata, Y. and Taya, M., *Journal of Composite Materials*, Vol. 19, 1985, pp. 489–598.
[29] Kim, W. H., Koczak, M. J., and Lawley, A., *Proceedings of ICCM/2*, B. Norton et al., Eds., Metallurgical Society of the American Institute of Mining, Metallurgical, and Petroleum Engineers, New York, 1978, pp. 487–505.
[30] DiCarlo, J. A. and Smith, R. J., NASA TM-82806, National Aeronautics and Space Administration, Washington, DC, 1982.
[31] Daimaru, A. and Taya, M., *Progress in Science and Engineering of Composites*, T. Hayashi, K. Kawata, and S. Umekawa, Eds., ICCM-IV, Tokyo, 1982, pp. 1099–1106.
[32] Tanaka, K. and Mori, T., *Acta Metallurgica*, Vol. 18, 1970, pp. 931–941.
[33] Eshelby, J. D., *Proceedings of the Royal Society*, London, Vol. A241, 1957, pp. 376–396.
[34] Taya, M. and Chou, T. W., *International Journal of Solids Structures*, Vol. 17, 1981, pp. 553–563.
[35] Taya, M. and Patterson, W. G., *Journal of Material Science*, Vol. 17, 1982, pp. 115–120.
[36] Tanaka, K., Mori, T., and Nakamura, T., *Philadelphia Magazine*, Vol. 21, 1970, pp. 931–941.
[37] Mura, T., *Micromechanics of Defects in Solids*, Martinus Nijhoff Publishers, The Hague, The Netherlands, 1982.

Summary

The first objective of this symposium was to define the testing procedures needed for metal matrix composites. The second objective was to gain an understanding of the physical and theoretical behavior.

The mechanics of how to do tests was addressed by several authors. It is also obvious that the test methods for short fiber reinforced metal matrix composites is quite different from those for long fiber reinforced metal matrix composites. The test specimens made for composites with short fibers (whisker or particulate) and their procedures are based upon test methods derived from isotropic homogenious metals. The best discussion of the methods is the work by co-editor *DiGiovanni et al.* They discuss tensile, flexure, and bearing. Besides ambient temperature tests they did elevated temperature tests. Compression tests are discussed by authors *Awerbuch et al.*, *Chou et al.*, and *Bethoney et al.* The procedures seem to be such that standard test methods could be drafted. The ASTM Committee D-30 on High Modulus Fibers and Their Composites has instituted a task group to draft these standards. Several papers discussed toughness testing, but there does not seem to be a shear test method.

While the methods of evaluating metal matrix composites made with short fibers seem to exist, the methods for evaluating metal matrix composites made with long fibers are not as developed. The most developed test method seems to be the tension test method and, in fact, a standard (D 3552) does exist. The various tension tests are discussed in at least four papers. *Majidi et al.* discussed compression, shear, and toughness tests. *Francini* discussed test methods for tubural configurations. Clearly more effort will be needed in order to define a standard.

One important use of metal matrix composites may well be in thermally stable structures. For this class of applications the important properties are the coefficient of thermal expansion (CTE) and the modulus of elasticity. The CTE measurement methods are discussed very aptly by *Tompkins and Dries*. Several papers discuss the measurement of the modulus by ultrasonic methods rather than by mechanical methods. For these type of applications this appears to be a good technique.

Nondestructive evaluation of materials is important in any application. The work reported here shows that the effort related to metal matrix composites is still in its infancy and more effort is needed.

Beside simply measuring properties, there is a clear need to understand the implication of the findings. The two papers presented by *Chamis and Hopkins* and one by *Adams* clearly helps the investigator to do this.

Finally, if metal matrix composites are to be used, the data must be statistically based. The work by *Wu and Chou* is exemplary in the understanding of scatter in composites. His work shows the effects of the matrix in reducing the scatter. *Harmsworth* discusses the direction that we must proceed in order to obtain true statistically based allowables.

As this summary is being prepared a second conference on testing of metal matrix composites is being planned. The new effort will discuss the efforts in the last two years since this conference was held. The new finds should be also prepared as a special technical publication in the future.

N. R. Adsit
Rohr Industries, Chula Vista, CA 92012;
symposium co-chairman and co-editor.

Author Index

Subject Index

Y

ISBN 0-8031-0967-9